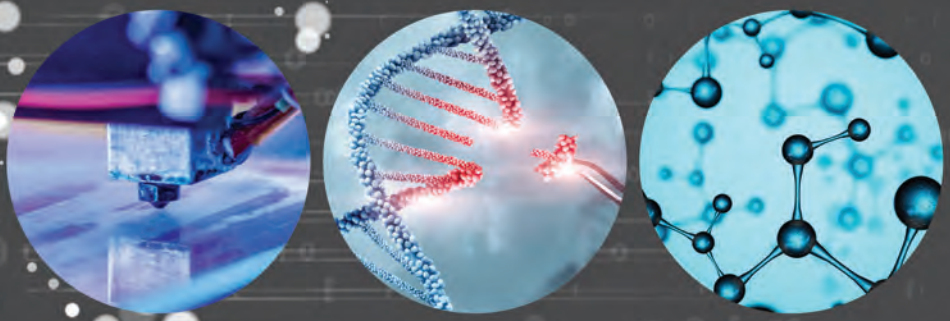

FY21 PROCEEDINGS OF THE U.S. ARMY COMBAT CAPABILITIES DEVELOPMENT COMMAND CHEMICAL BIOLOGICAL CENTER

IN-HOUSE LABORATORY INDEPENDENT RESEARCH AND SURFACE SCIENCE INITIATIVE PROGRAMS

U.S.ARMY

DEVCOM CHEMICAL BIOLOGICAL CENTER

Message from the In-house Laboratory Independent Research Program Manager

I am pleased to present the thirteenth annual edition of the Proceedings of the U.S. Army Combat Capabilities Development Command Chemical Biological Center's (DEVCOM CBC) In-house Laboratory Independent Research (ILIR) and Surface Science Initiative (SSI) Programs. As the Senior Research Scientist (ST) for Chemistry and Director of the ILIR and SSI programs, I am honored to continue the legacy of the Center's Army-funded basic research and innovation programs.

The ILIR and SSI programs represent the core of basic and applied research at DEVCOM CBC. The portfolio not only provides a developmental opportunity for young scientists; it also serves as a science incubator for cutting-edge research and collaborations across academia and the broader Department of Defense (DoD). My goal is to ensure that the scientific endeavors we undertake expand the knowledge base and serve as the foundation for applied programs that transforms how the Army modernizes for the chemical or biological threat.

This annual report includes a detailed description of the ILIR and SSI programs' in-depth project selection and evaluation process. This process, when coupled with our external annual review by experts across the U.S. Government, is critical to ensuring that DEVCOM CBC funds projects with the greatest potential for fulfilling future Army capability needs and receives an honest and unbiased assessment of our research efforts to refine our portfolio each year.

I continue to be impressed with the resiliency of our PIs and their ability to deliver stellar research amid the long-standing challenges presented by COVID-19. In-spite of the limited number of in-person meetings and conferences they have continued to foster new collaborations, along with identifying opportunities to publish and present their work. Adversity has resulted in new methods of communication that has served to broaden the pool of collaborators. It has also led to greater efficiencies in the laboratory and fostered complementary collegial interactions that will benefit the scientific community and research in the future.

Finally, this report concludes with a technical manuscript from each of the ILIR, SSI, and Seedling projects from FY21. In addition, due to scheduling and timing changes, the FY20 Seedling projects were not finalized at the time of publication of the FY20 report and have been included in this report for completeness. Together, these projects covered areas of interest across the chemical, biological, and physical sciences, including: Rational Molecular Synthesis and Novel Materials, Synthetic Biology, Nano Chemical and Biological Sensing, Panomics and Molecular Toxicology, Aerosol Sciences, Algorithm Design and Development, and Surface Science.

If you have questions regarding the ILIR Program or this report, please do not hesitate to contact the DEVCOM CBC Public Affairs Office at usarmy.apg.devcom-cbc.mbx.communications-office@army.mil.

Patricia (Trish) McDaniel, Ph.D.
Senior Research Scientist (ST) for Chemistry

Strategic Mission and Vision

The U.S. Army Combat Capabilities Development Command Chemical Biological Center (DEVCOM CBC) is the Nation's principal research and development resource for non-medical chemical-biological (CB) defense. DEVCOM CBC has the unique ability to advance the mission of the Joint Warfighter and other stakeholders, while leveraging historical expertise, advanced equipment, and state-of-the-art facilities. The Center takes pride in its legacy of solutions born from more than a century of innovation.

Mission

DEVCOM CBC's mission is to provide innovative chemical, biological, radiological, nuclear, and explosive (CBRNE) defense capabilities to enable the Joint Warfighters' dominance on the battlefield and interagency defense of the homeland. This mission recognizes that the Center's range of influence, while rooted in CB warfare defense, can be applied to all types of challenges in chemistry or biology. The Center's emerging capabilities in synthetic biology and materials science are leveraging existing innovations in biotechnology and decontamination sciences to develop next-generation solutions that ensure our warfighters are always prepared to operate on the modern and future battlefield.

Vision

DEVCOM CBC's vision is to be the premier provider of innovative CBRNE solutions for the Army, DoD, the Nation, and our allies. For more than 100 years, the Center has been a distinct asset, providing innovative and economical CB defense technology solutions through scientific and engineering expertise, coupled with our unique facilities and collaboration with partners.

Dr. Marilyn Lee, DEVCOM CBC Chemical Engineer and SSI PI, aims to incorporate cell-free protein synthesis into deployable materials. (Photo credit: DEVCOM CBC)

U.S. Army soldier, assigned to 20th CBRNE Command, analyzes an unknown substance during a training exercise, Aberdeen Proving Ground, MD. (Photo credit: U.S. Army)

DEVCOM CBC sits on the forefront of synthetic biology and has invested in biomanufacturing capabilities at the Center to support these emerging technologies and its mission. (Photo credit: DEVCOM CBC)

DEVCOM CBC Basic Research Portfolio: ILIR, SSI, and Seedling Programs

The purpose of the DEVCOM CBC Basic Research Portfolio is to fund innovative basic research projects that are high-risk but have high potential payoff for fulfilling future Army capability needs. The DoD defines basic research as "systematic study directed toward greater knowledge or understanding of the fundamental aspects of phenomena and of observable facts without specific applications toward processes or products in mind."[1] The In-house Laboratory Independent Research (ILIR) program is funded as part of the Army's Core 6.1 program and adheres to the guidelines outlined in DoD Instruction 3201.04. These requirements dictate that "each DoD component that operates an R&D laboratory or center shall support an ILIR program" and that these laboratories "shall be given wide latitude in the use of ILIR funds…to enable performance of innovative, timely, and promising work without requiring formal and prior approval."[2] The Department of the Army has also established a separate directed basic research effort for studies involving surface science. The SSI program is supported through separate 6.1 funding from the ILIR program.

The ILIR and SSI programs are specifically designed to foster increased innovation within the Center, where they are viewed as a critical part of the Center's efforts to ensure a high level of quality in basic science; to foster innovation in the areas of chemistry and biology; to mentor junior investigators in the art and practice of laboratory science; and to explore new technological innovations and phenomenology at the boundaries of chemistry, biology, mathematics, or physics to expand the state-of-the-possible in support of CBRNE defense missions. These projects are performed over a course of up to three years and are intended to produce peer-reviewed publications, technical reports, patents, and presentations.

While the ILIR and SSI programs are directly funded by the Army 6.1 budget, DEVCOM CBC also uses its Section 2363 authority to fund the Seedling program of smaller, quick-turn, "outside-of-the-box" exploratory research efforts. Under Section 2363, the Director of DEVCOM CBC can "fund innovative basic and applied research that is conducted at the defense laboratory and supports military missions."[3] The Seedling Program is the R&T Directorate's opportunity to invest in the workforce's innovative and promising research ideas to enhance CBC's in-house S&T capabilities.

1 *DoD Financial Management Regulation, DoD 7000.14-R, Vol. 2B, Ch. 5*
2 *In-House Laboratory Independent Research Program, DoDI 3201.04, October 15, 2018*
3 *10 U.S. Code § 2363*

In-house Laboratory Independent Research

Each year, the ILIR program solicits innovative proposals aligned to specific scientific domains. In FY21, the ILIR topics included: Rational Molecular Synthesis and Novel Materials, Synthetic Biology, Nano Chemical and Biological Sensing, Panomics and Molecular Toxicology, Aerosol Sciences, and Algorithm Design and Development. These domains complement DEVCOM CBC's core competencies and possess high potential for technological capability building.

Surface Science Initiative

The SSI is a program of special emphasis and often uses nanoscience-based research to tackle research questions requiring more substantial resource commitments. This research specifically addresses the characterization of chemical and biochemical phenomena occurring at or near solid surfaces and interfaces; the interactions between chemical reactions and transport processes on surfaces; theory and modeling of processes at complex surfaces; and the synthesis and characterization of catalysts that function at the nanoscale.

Seedling Program

Unlike ILIR and SSI projects, Seedling projects are funded for three to six months within a single fiscal year with the intent to explore proof-of-concept ideas or to gather preliminary data on cutting-edge topics in preparation for future proposal calls that further support technical innovations supporting Army and CBRNE defense missions. The Seedling program focuses on funding projects which demonstrate novel solutions to CBRNE defense challenges, have merit for enabling larger proposal efforts to CBC stakeholders, or show clear benefit to the warfighter. Beyond their scientific opportunity, Seedling proposals are also expected to clearly identify potential stakeholders and anticipated return on investment. Seedling projects are intended to fund short-term, "outside of the box" ideas, explore new areas in basic or applied science, and fuel discovery that will lead to more successful submissions for larger funded efforts—both internal and external.

Proposal Review and Selection Process

Each year, submitted ILIR and SSI proposals are reviewed and critiqued by a panel comprised of resident and external senior research scientists from across DoD organizarions and civilian and military faculty members at the United States Military Academy. The review panel evaluates and scores each proposal on its scientific objective, the scientific methods proposed, the qualifications of the investigator, and the budget; with the scientific objective and methods weighted as the most important criteria. The proposals are then ranked according to merit. Only proposals deemed as basic research by the panel are considered for funding. Quality comments from the reviewers are compiled and used, along with the numerical score, as a critical assessment of the proposal. This written feedback is essential for the Center's mentoring of researchers and for justifying the elimination of research programs that are not competitive.

The selected projects are reviewed quarterly; these reviews of project performance provide guidance to the programs' participants, ensuring that projects meet significant milestones, and that substantive new knowledge is being produced and transferred to DEVCOM CBC and the broader scientific community. In FY21, 23 ILIR and SSI proposals were forwarded to the review panel for evaluation; of these, one new ILIR project and one new SSI project were selected for funding. Additionally, four ILIR and six SSI projects funded in FY20 received continued funding in FY21.

Seedling projects also undergo a similar proposal review, selection, and evaluation process as ILIR and SSI projects; however, the Seedling review process is conducted internally at DEVCOM CBC by resident scientists across Divisions of the R&T Directorate. In FY21, a total of 28 proposals were received, and funding was provided to six projects. In addition to end-of-year reporting requirements, Seedling efforts are expected to present at a poster session during the Technical Advisory Board review and/or the Center's internal poster competition, Coffee with Colleagues.

Due to COVID-19 related delays, the FY20 Seedling projects were not completed in time to be included in the FY20 proceedings and are instead published in this report. In FY20, 15 Seedling proposals were submitted, of which 10 projects were funded.

PROPOSAL SCORING CRITERIA

Exceptional 4 Comprehensive and complete in all areas; meets all significant objectives; offers a comprehensive project that exceeds the ILIR vision and is supportable by the proposed approach; has few weaknesses which are easily correctable.

Acceptable 3 Meets most of the significant objectives and is responsive to the ILIR vision; offers a feasible technical solution; weaknesses are readily correctable; proposal is complete to the extent that an award could be made in present terms.

Marginal 2 Minimally meets ILIR vision and objectives (i.e., offers a project vision that is marginally supported by the proposed approach, and/or claims are not documented or substantiated); significant deficiencies exist.

Unacceptable 1 Fails to meet significant characteristics of the ILIR vision and/or objectives stated in the Solicitation; has weaknesses and/or deficiencies that are significant and of such magnitude that they cannot be corrected without extensive discussion/major revision of the proposal.

	REVIEWERS							
	1	2	3	4	5	6	7	AVG
Scientific Objective	4	3	4	3	3	4	3	3.4
Methods and Approach	4	3	3	2	3	2	2	2.7
PI Qualifications	3	3	4	2	3	3	3	3.0
Budget	3	3	3	2	3	3	3	2.9
Overall Evaluation	3.5	3.0	3.5	2.3	3.0	3.0	2.8	**3.0**

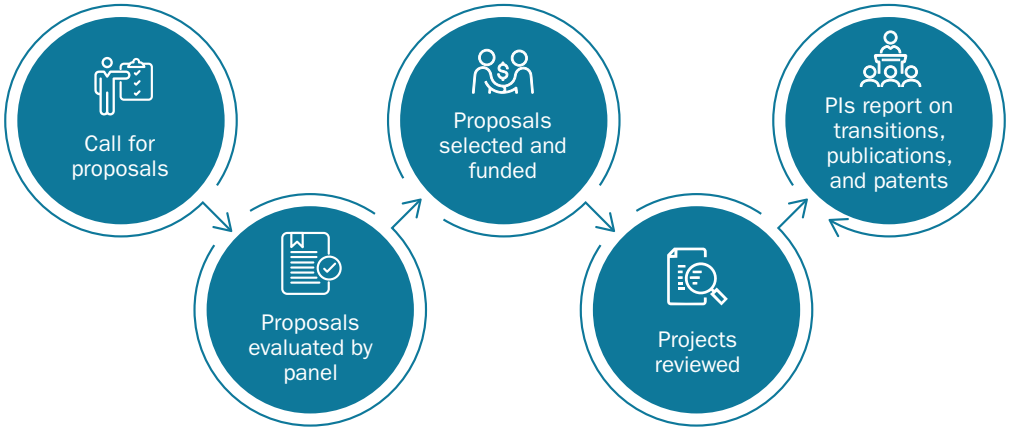

DEVCOM CBC holds an external review in the fourth quarter, known as our Technical Advisory Board (TAB) Review, to assess year-to-date performance of the funded ILIR and SSI projects. Comments and feedback from this review were used to support continued funding, course corrections, or early terminations of each FY21 ILIR/SSI project. These comments and insights are also used to improve the quality and content of the individual research projects, the scientific focus of the ILIR and SSI portfolios, and to guide the overall mission of the programs into the future.

To ensure the safety of all those involved, the FY21 TAB was held virtually. The panel was tasked with producing an unbiased assessment of the content, quality, innovation, accomplishments, and relevance of the R&T basic science programs. In FY21, the panel recommended all projects for continued funding, but provided critical feedback and suggestions to enhance the impact of several projects. Individual scores, portfolio reviews, and the TAB discussion were all used to generate an outbrief to the Director of the ILIR and SSI Programs, the Director of DEVCOM CBC's R&T Directorate, the R&T workforce, and a detailed TAB report.

Overall, the TAB was impressed with the diversity and quality of projects across the board, scoring both programs very well. The panel felt there was excellent productivity throughout the $3.3M portfolio and that the projects spanned a diverse number of topics. The focus of many of the research projects excited the panel with PIs engaged in emerging scientific disciplines, including synthetic biology, metal organic frameworks, and artificial intelligence/machine learning. Further, the basic research portfolio was commended by the TAB panel for the frequent transition of work into new projects—both within the Center's basic research programs and applied programs with support from other government agencies.

FIVE REVIEWERS FROM DIVERSE FEDERAL DEFENSE ORGANIZATIONS SERVED ON THE FY21 TAB PANEL:

- **COL F. John Burpo, Ph.D.**, Department Head and Professor, Department of Chemistry and Life Science, United States Military Academy
- **Dr. Neil Jensen**, Chief, Supervisory Microbiologist, CB Research Center of Excellence, Defense Threat Reduction Agency
- **MAJ Steve DeLeon**, S&T Portfolio Manager, U.S. Army DEVCOM CBC
- **Ms. Wendy Winner**, Programs, Science & Technology Integration, U.S. Army DEVCOM
- **Mr. Christopher O'Malley**, Associate Director for Portfolio Integration, Research & Technology Directorate, DEVCOM CBC

EACH PROJECT WAS EVALUATED BASED ON SEVEN AREAS:

(1) Scientific objectives, opportunity, and significance*

(2) Research methodology*

(3) Connections to the broader community*

(4) Overall capabilities and metrics*

(5) Use of funding

(6) Use of time

(7) Overall presentation

*Criteria 1-4 weighted as most important

The many collaborations between PIs within DEVCOM CBC was also viewed as a positive development from the ILIR and SSI programs.

The TAB panel noted that many of the presenters acknowledged the efforts of PIs collaborating with other DEVCOM CBC PIs on their projects, demonstrating strong collaborations within DEVCOM CBC. The panel stressed PIs should establish collaborations with researchers outside of DEVCOM CBC to avoid scientific isolation and stay current with emerging technologies and techniques. Finally, the panel encouraged DEVCOM CBC administrators to better communicate the organization's short- and long- term goals to the researchers to maximize their impact on the warfighter.

The panel recognized Dr. Nathan McDonald's synthetic designer microbe project and Dr. Casey Bernhards' continued progress identifying off-target effects of CRISPR-Cas technology. In addition to the ILIR projects presented by Drs. McDonald and Bernhards, the TAB also gave top marks to the SSI projects from Drs. Angela Zeigler, Marilyn Lee, and Alex Miklos and remarked that the portfolio contains several strong metal organic framework projects.

Manuscripts from each of the five ILIR projects, seven SSI projects, and six Seedling projects from FY21 are contained within this Proceedings Report. Due to the ongoing SARS-CoV-2 pandemic, FY20 Seedling projects were not completed at the time of publication last year; the ten FY20 Seedling project summaries are also included in this report.

Advancing Young Scientists through the Basic Research Portfolio

A key tenet of the DEVCOM CBC Basic Research Portfolio is to provide opportunities for young researchers to acquire funding and allow them to manage and oversee their own independent research. DEVCOM CBC has continued to engage with the scientific community by training and mentoring the next generation of scientists through a variety of internships, apprenticeships, and fellowships. Many scientists participating in a trainee research program—such as the National Research Council (NRC) and Oak Ridge Institute for Science Education (ORISE) postdoctoral fellowships, or the Summer Undergraduate Research Training (SMART) program and the Minority Undergraduate Student Internship Program (MUSIP)—have served as an integral member of a basic research project team. A point of pride for the Center is the dozens of young scientists from these apprenticeship programs that have joined DEVCOM CBC as civilian staff scientists, with many awarded ILIR, SSI, or Seedling funding to conduct their own research. In FY21, five former NRC and ORISE postdoctoral fellows were PIs of an ILIR or SSI project while two former postdoctoral fellows and two former SMART interns were PIs of an FY20 or FY21 Seedling project.

FY21 Basic Research Program Highlights

FY21 Basic Research Program Productivity

13 Presentations and posters

6 Peer-reviewed publications

1 Patent issued

2 Filed patents

1 Dissertation

Awards and Recognition

Jared DeCoste, Ph.D., CBR Filtration Branch, was the inaugural recipient of the 2021 Joseph D. Wienand National Defense Industrial Association (NDIA) Chemical Biological Radiological Nuclear (CBRN) Division Science Technology Engineering Mathematics (STEM) Excellence Award on 18 August, during the NDIA CBRN Defense Conference. This award recognizes individuals who demonstrate great overall STEM achievement and efforts that significantly impact CBRN defense programs. Dr. DeCoste was recognized for his efforts to design new materials that can decontaminate chemical threats to help protect U.S. and allied warfighters. The award was named in honor of Joseph D. Wienand, who served as director of DEVCOM CBC (then known as the Edgewood Chemical Biological Center) from 2010-2014. Over the years, Wienand championed several STEM programs, and this award acknowledges the lasting impacts he has made and continues to make.

Nathan McDonald, Ph.D., BioTechnology Branch, was awarded an a Federation of European Microbiological Societies (FEMS) Congress Attendance Grant to participate in the World Microbe Symposium in 2021. These grants are used to support European and non-European early career scientists who have received the highest academic degree in their field within the past five years to travel to, attend, and present research at the FEMS Congress of European Microbiologists. Applicants must be an active microbiologist and be the first author of an accepted abstract for the meeting. Dr. McDonald shared his work in a presentation entitled "Engineering the *Escherichia coli* Lipopolysaccharide to mimic *Yersinia pestis*."

In FY21, Air Force Senior Master Sgt. Sarah Katoski was awarded two Department of the Army Achievement Medals for commitment to mission throughout the COVID-19 pandemic as essential personnel response and program support. In addition, SMSgt Katoski was also nominated for the Major General Harold Greene Innovation Award in FY20 for dedication to readiness and unwavering devotion to Soldier performance. This award is named in honor of Major General Harold Greene who was killed in Afghanistan in 2014 while serving as the deputy commanding general of Combined Security Transition Command–Afghanistan. In addition to his role in Afghanistan, Major General Greene also served as the Deputy Commanding General of DEVCOM.

Greg Peterson, of DEVCOM CBC's CBR Filtration Branch, successfully defended his Ph.D. in May 2021 at the University of Delaware. Dr. Peterson conducted his research under the mentorship of Dr. Thomas Epps, III—the Alan & Myra Ferguson Distinguished Professor of Chemical & Biomolecular Engineering of the University of Delaware's Department of Chemical & Biomolecular Engineering. Dr. Peterson's dissertation was titled "Polymer-Metal-Organic Framework Composites for Defense Against Chemical Warfare Agents."

13 Presentations and Posters

- Durke, E.M.; McEntee, M.; He, M.; Dhaniyala, S. Characterization of Particle Charge from Aerosol Generation Process: Investigations of Material Reactivity. *Presented virtually at the American Association for Aerosol Research 38th Annual Conference*, **5–9 October 2020.**

- Lee, M.S. Solvent Tolerance of Freeze-Dried Cell-Free Reactions Enables Materials Applications. *Presented virtually at the American Institute of Chemical Engineers (AICHE) Annual Meeting*, **16–20 November 2020.**

- Lee, M.S. Exploring Cell-Free Functionalized Materials. *Presented virtually at the US-Israel Triservice Biotech Exchange Workshop on Cell-Free Systems*, **14 December 2020.**

- Kulisiewicz, A.; Garibay, S.; Browe, M.; DeCoste, J; Hopgood, B.; Pozza, G.; Kelly, L. Optimization of the metal-organic framework NU-1000 toward photocatalytic oxidation of sulfur mustard stimulants. *Presented virtually at the 261st American Chemical Society National Meeting*, **5–16 April 2021.**

- Decoste, J.B. Tuning the photocatalytic activity of metal-organic frameworks toward the oxidation of sulfur mustard in military relevant conditions. *Presented virtually at the 261st American Chemical Society National Meeting*, **5–16 April 2021.**

- Riley, P.C.; Deshpande, S.V.; Ince, B.S.; Hauck, B.C.; O'Donnell, K.P.; Dereje, R.; Harden, C.S.; McHugh, V.M.; Wade, M.M. Random forest and long short-term memory-based machine learning models for classification of ion mobility spectrometry spectra. *Presented virtually at SPIE Defense + Chemical, Biological, Radiological, Nuclear, and Explosives (CBRNE) Sensing XXII,* **12–16 April 2021.**

- Varady, M.J.; Hulet, M.S.; Savage, A.; Ligda, J.; Sun, R.; Elabd, Y.A. Influence of particle-polymer interface adhesion on chemical transport in polymer composites. *Presented virtually at the Interfaces and Effects in Composite Energetic Materials (IECEM) Symposium*, **13–15 April 2021.**

- Lee, M.S.; Raig, R.; Kuhn, D.; Gupta, M.; Lux, M. Dry Cell-Free Protein Synthesis Formulations are Compatible with Polymer Casting Techniques. *Presented virtually at the Materials Research Society Spring Meeting*, **17–23 April 2021.**

- Zeigler, A.M.; Varady, M.J.; Hulet, Ryu, B.K.; M.S.; Zia, R.N. The Role of Voids and Porosity on the Transport of Macromolecules through 3-D Printed Polymeric Materials. *Presented virtually at the 95th Colloids and Surface Science Symposium (CSSS)*, **14–16 June 2021.**

- Lee, M.S.; Biondo, J.; Raig, R.; Gupta, M.; Lux, M. A New Form of BioActive Materials: Blending Dry Cell-Free Systems and Synthetic Polymers. *Presented virtually at the Synthetic Biology: Engineering, Evolution & Design (SEED) Conference,* **15 June 2021.**

- Lee, M.S.; Biondo, J.; Lux, J.; Gupta, M. Cell-Free Protein Synthesis (CFPS) in Polymer Materials: Biosensing and other applications. *Presented virtually at the 262nd American Chemical Society National Meeting,* **22–26 August 2021.**

- Varady, M.J.; Hinkle, A.R.; Hulet, M.S.; Sweal, M.L.; Savage, A.; Ligda, J.; Strawhecke, K.; Sun, R.; Elabd, Y.A.; Influence of particle-polymer interface adhesion on chemical transport in polymer composites. *Presented virtually at the 262nd American Chemical Society National Meeting*, **22–26 August 2021.**

- Kulisiewicz, A.; Garibay, S.; Browe, M.; DeCoste, J.; Hopgood, B. Optimization of the NU- 1000 metal-organic framework for enhanced quantum efficiency and photocatalytic degradation of a sulfur mustard simulant. *Presented virtually at the 262nd American Chemical Society National Meeting,* **22–26 August 2021.**

6 Peer-reviewed Publications

- McManus, J.B.; Bernhards, C.B.; Sharpes, C.E.; Garcia, D.C.; Cole, S.D.; Murray, R.M.; Emanuel, P.A.; Lux, M.W. Rapid Characterization of Genetic Parts with Cell-free Systems. *J. Visualized Exp.* **2021**, *174 (e62816)*, pp 1–18.
- Peterson, G.W.; Wang, H.; Au, K.; Epps, T.H., III. Metal-organic framework polymer composite enhancement via acyl chloride modification. *Polym. Int.* **2020.** *7 (6)*, pp 783–789.
- Browe, M.A.; Landers, J.; Tovar, T.M.; Mahle, J.J.; Balboa, A.; Gordon, W.O.; Fukuto, M.; Karwacki, C.J. Laponite-Incorporated UiO-66-NH2-Polyethylene Oxide Composite Membranes for Protection against Chemical Warfare Agent Simulants. *ACS Appl. Mater. Interfaces*. **2021**, *13 (8)*, pp 10500–10512.
- Debow, S.; Zhang, T.; Liu, X.; Song, F.; Qian, Y.; Han, J.; Maleski, K.; Zander, Z.B.; Creasy, W.R.; Kuhn, D.L.; Gogotsi, Y.; DeLacy, B.G.; Rao, Y. Charge Dynamics in TiO2/MXene Composites. *J. Phys. Chem. C.* **2021**, *125 (19)*, pp 10473–10482.
- Peterson, G.W.; Lee, D.T.; Barton, H.F.; Epps, T.H., III; Parsons, G.N. Fibre-based composites from the integration of metal-organic frameworks and polymers. *Nat. Rev. Mater.* **2021**, *6 (7)*, pp 605–621.
- Wei, Q.; Kuhn, D.L.; Zander, Z.; DeLacy, B.G.; Dai, H..; Sun, Y. Silica-coating-assisted nitridation of TiO2 nanoparticles and their photothermal property. *Nano. Res.* **2021**, *14 (9)*, pp 3228–3233.

1 Issued Patent

- Peterson, G.W.; Lu, X. Metal organic framework polymer composites. U.S. Patent 11,007,391. **May 18, 2021.**

1 Doctoral Dissertation

- Gregory Peterson, Ph.D. *Polymer-Metal-Organic Framework Composites for Defense Against Chemical Warfare Agents.* Ph.D. Dissertation, University of Delaware, Newark, DE. May 2021.

2 Filed Patents

- Patrick C. Riley, et al. Chemical Detection Training Container and Method for use Thereof. Application number 17/216,295. Filed **03/29/2021**.
- Gregory W. Peterson, et al. Polymer-Based Composite Beads Comprised of Metal-Organic Frameworks and Metal Oxides for Toxic Chemical Removal. Application number 17/476,478. Filed **09/16/2021**.

Meet our FY21 Principal Investigators

In-house Laboratory Independent Research (ILIR) Projects

Casey Bernhards, Ph.D.
Research Biologist, *BioChemistry Branch, BioSciences Division*

Dr. Bernhards earned her Ph.D. in Biological Sciences in 2014 from Virginia Polytechnic Institute and State University. Prior to joining DEVCOM CBC as a Research Biologist in 2021, Dr. Bernhards supported the Center's mission as a National Research Council Postdoctoral Research Fellow while training at the Defense Threat Reduction Agency. Following her postdoctoral training, she continued to support DEVCOM CBC as a Senior Scientist with Excet, Inc. Dr. Bernhards' research primarily focuses on understanding the off-target effects brought about by gene editing using clustered regularly interspaced short palindromic repeats, also known as CRISPR.

Nathan McDonald, Ph.D
Research Biologist, *BioTechnology Branch, BioSciences Division*

Dr. Nathan McDonald earned his Ph.D. in Biological Sciences from the University of Delaware. in 2018, Dr. McDonald continued his training as a National Research Council Postdoctoral Fellow at DEVCOM CBC until 2020 when he transitioned to his current position as a Research Biologist. Dr. McDonald has multiple publications that detail his research on modifying bacterial antigens for use in detection assay development, emerging threat assessment, and enhanced diagnostic and medical countermeasures. In 2021, Dr. McDonald was awarded a Federation of European Microbiological Societies (FEMS) Congress Attendance grant to attend and present at the American Society for Microbiology/FEMS World Microbe Forum.

Sarah Katoski
Biologist, *BioDefense Branch, BioSciences Division*

Ms. Katoski received her master's degree in Biotechnology from the Johns Hopkins University in 2009. She began working at DEVCOM CBC in 2010 as a contractor, later transitioning to civilian service in 2016. Ms. Katoski serves as a molecular biologist and technical specialist providing support to a broad range of major biological defense systems and complex biological detection systems. She was recognized for her expertise by her receipt of the 2019 CBC Excellence in Safety award and a subsequent Director of Army Safety Risk Management Safety Award in FY20 for her part in providing an integrated method for preparing, irradiating, and verifying the inactivation of anthrax spores, enabling their safe use as standard reagents for testing and evaluating detection and diagnostic devices and techniques throughout the DoD.

Patrick Riley
Research Chemist, *Detection Spectrometry Branch, Physical Sciences Division*

Mr. Riley received his bachelor's degree in Chemistry from Salisbury University in 2010. With over 10 years of experience as a Research Chemist at DEVCOM CBC, Mr. Riley's most recent research has focused on utilizing machine learning to develop new alarm algorithms for chemical detection devices to include ion mobility spectrometry-based devices. Mr. Riley's experience in machine learning has extended beyond chemical detection to include participating and leading several efforts to find other applications of machine learning in CBRNE defense. In addition to his own ILIR research, Mr. Riley leads the most recent DEVCOM CBC Grand Challenge–STEWARD, an initiative that focuses on building a foundational understanding of artificial intelligence and machine learning within the Center.

Rabih Jabbour, Ph.D.
Chemist, *Detection Spectrometry Branch, Physical Sciences Division*

Dr. Jabbour earned his Ph.D. in Bioanalytical Chemistry from the University of Arizona in 1999. He has more than 20 years of research experience in academia and industry of chemistry and biology of microorganisms that are of vital interest to the DoD. Dr. Jabbour leads the development of the functional materials and automated biological sample preparation and detection system, and has contributed to various DoD projects such as water monitoring and microbial fate using Raman imaging for Joint Service Agent Water Monitor (JSAWM), microbial mapping by Matrix-Assisted Laser Desorption/Ionization-Mass Spectrometry (MALDI-MS), and biodetection algorithms. Dr. Jabbour has been recognized with several government and industry awards, including the U.S. Army Excellence in Research award, and has published over 43 peer-reviewed articles and proceedings in the fields of chemistry, biochemistry, spectroscopy, molecular biology, bacteriology, and protein chemistry.

Surface Science Initiative (SSI) Projects

Angela Zeigler, Ph.D.
Research Chemist, *Sensors, Signatures, and Aerosol Technologies Branch, Physical Sciences Division*

Dr. Zeigler received her Ph.D. in Chemistry from the Johns Hopkins University in 2014. She began working at DEVCOM CBC as a student intern between 2004–2008, again as a contractor in 2014, and later transitioned to civilian in 2017. Primary duties have included developing concepts for design of CB aerosol spectroscopic equipment—particularly involving UV-visible and infrared wavelength regions for characterization research, and analysis of aerosol simulants and agents in the atmosphere. Additionally, Dr. Zeigler manages related spectroscopic detection programs. She took over as PI of this study following the departure of Dr. Jerry Cabalo from DEVCOM CBC in 2020.

Marilyn Lee, Ph.D.
Chemical Engineer, *BioChemistry Branch, BioSciences Division*

Dr. Lee earned her Ph.D. in Chemical and Biomolecular Engineering from the University of California Berkeley in 2017. Upon graduation, she joined DEVCOM CBC as an Oak Ridge Institute for Science and Education and National Resource Council post-doctoral researcher from 2017 to 2020, before transitioning to a civilian employee as a Chemical Engineer. Her area of research includes improving cell-free biocompatibility with polymers to demonstrate broad implications on the design of sensors and devices harnessing biological activity. In her short time at DEVCOM CBC, Dr. Lee has published multiple articles in top peer reviewed journals.

Alex Miklos, Ph.D.
Research Biologist, *BioChemistry Branch, BioSciences Division*

Dr. Alex Miklos studied Biochemistry at Duke University, ultimately earning his Ph.D. in 2008. Since completing his studies, Dr. Miklos continued his training as a Postdoctoral Fellow at the University of Texas at Austin where he led a project on protein engineering, then switched his focus to early-applied defense research projects that supported DEVCOM CBC as a Senior Scientist at Excet, Inc. In 2012, Dr. Miklos began his career with DEVCOM CBC as a Research Biologist where he has led multiple chemical and biological detection projects, including his current work on biologically engineered metamaterials. Dr. Miklos has contributed to multiple patents and published multiple research papers.

Jared DeCoste, Ph.D.
Research Chemist, *CBR Filtration Branch, CB Protection & Decontamination Division*

Dr. DeCoste earned his Ph.D. in Materials Chemistry in 2009 from Binghamton University. He has been a member of the DEVCOM CBC research team as a government employee, contractor, or National Research Council Post-Doctoral Associate since 2010 studying the fundamental properties of metal-organic frameworks (MOFs). His research interests range from basic research in the fundamentals of porous materials—especially for adsorption and catalysis—to the engineering and scaling of functional nanomaterials. He has led many projects in this area and is regarded as an expert in the field of MOFs for toxic chemical removal in the overarching scientific community. His work at the Center has led to more than 60 publications in top peer-reviewed journals and has been recognized by his peers and superiors through multiple awards—including the Leidos Publication Prize, Coffee with Colleagues Top Poster, DEVCOM CBC Rookie of the Year, and the 2018 Maryland American Chemical Society Chemist of the Year.

Mark Varady, Ph.D.
Research Engineer, *Decontamination Sciences Branch, CB Protection and Decontamination Division*

Dr. Varady received his Ph.D. in mechanical engineering from the Georgia Institute of Technology in 2010. He has been working with DEVCOM CBC since 2012, first as a contractor and then transitioning to a civilian position in 2016. Dr. Varady primarily studies chemical transport mechanisms in polymer-based materials, including multicomponent diffusion, viscoelastic response upon chemical exposure, and details of the polymer-particle interface in composite systems.

Monica McEntee, Ph.D.
Research Chemist, *CBR Filtration Branch, Protection Division*

Dr. McEntee received her bachelor's degree in Chemistry and Mathematics with a minor in Biology in 2010 from Virginia Tech. She received her Ph.D. in Physical Chemistry in 2015 from the University of Virginia. In 2015, she was awarded an ORISE post-doctoral fellowship in the CBR Filtration Branch at DEVCOM CBC studying the fundamental properties of environmental surfaces—sands and soils—as well as their interactions with chemical agent simulant vapors and aerosols and was subsequently hired as a civilian employee in 2017.

Ivan Iordanov, Ph.D.
Physicist, *Decontamination Sciences Branch, CB Protection and Decontamination Division*

Dr. Iordanov earned his Ph.D. in Physics from the Pennsylvania State University in 2012, working on theoretical modeling of the photoelectron spectra of small transition metal clusters using density functional theory and higher-level methods (Coupled-Cluster Singles and Doubles and Symmetry Adapted Cluster-Configuration-Interaction). Afterwards, he joined DEVCOM CBC as a National Resource Council post-doctoral researcher in 2013 and was hired as a civilian employee in 2016. His area of expertise is the use of quantum mechanics-based computational methods to improve understanding of adsorption within porous materials or on surfaces the atomic level.

FY20 and FY21 Seedling Project PIs

Daniel Angelini, Ph.D.
Research Biologist, BioDefense Branch, BioSciences Division
FY21 project keywords: *hydrogel, fentanyl, DNA, trace detection, forensic detection, lateral flow assay, direct analysis in real time-mass spectrometry*

Justin Curtiss
Chemist, Chemical Analysis & Physical Properties Branch, Threat Agent Sciences Division
FY20 project keywords: *hyperspectral, spectroscopy, illumination, Powell lens*

Francis D'Amico
Applied Research Engineer, Sensors, Signatures & Aerosol Technologies Branch, Physical Sciences Division
FY21 project keywords: *biological detection, aerosols, bioaerosols, ultraviolet light induced fluorescence, DNA sequencing, metagenomics*

Shaun Debow
Chemical Engineer, Obscuration & Nonlethal Engineering Branch, Protection Division
FY21 project keywords: *SARS-CoV-2, coronavirus, $Ti_3C_2T_x$ MXene, phi6, bacteriophage, inactivation, inhibition*

Krystina Hess, Ph.D.
Research Bioengineer, BioTechnology Branch, BioSciences Division
FY20 project keywords: *biomanufacturing, synthetic biology, biomaterial, scale-up, downstream processing*

Jennifer Horsmon
Biologist, Molecular Toxicology Branch, Threat Agent Sciences Division
FY20 project keywords: *air-lifted interface, apoptosis, cytokine, cytotoxicity, EpiAirway™,* in vitro*, obscurant, particulates*

Stanley Hulet, Ph.D.
Supervisory Biologist, Operational Toxicology Branch, Threat Agent Sciences Division
FY20 project keywords: *hairless guinea pig, primary cell culture, neurons, cortical neurons, glial cells,* in vitro *cell culture, method development*

Thomas Ingersoll, Ph.D.
Mathematician, Modeling, Simulation & Analysis Branch, Physical Sciences Division
FY21 project keywords: *SARS-CoV-2, Bayesian method, parameter estimation, surveillance, open-population model, underreporting, disease dynamics, Markov chain Monte Carlo*
FY20 project keywords: *SARS-CoV-2, network model, parameter estimation, surveillance, susceptible exposed infectious resistant model, underreporting, disease dynamics, maximum likelihood*

Jana Kesavan, Ph.D.
Research Physicist, Sensors, Signatures, & Aerosol Technologies Branch, Physical Sciences Division
FY20 project keywords: *decontamination, bacteria spores, wiping, vacuuming, blotting, adhesive tape, cold weather*

Ann Kulisiewicz
Research Chemist, CBR Filtration Branch, Protection Division
FY21 project keywords: *metal-organic frameworks, chemical warfare agents, hydrolysis, zirconium*

Eric Languirand, Ph.D
Research Chemist, Chemical Analysis & Physical Properties Branch, Threat Agent Sciences Division
FY20 project keywords: *photothermal, photoacoustic, standoff, acoustic reflection, acoustic waveguide, ultrasound, thermally induced optical reflection of sound*

Nathan McDonald, Ph.D.
Research Biologist, BioTechnology Branch, BioSciences Division
FY20 project keywords: *synthetic biology, temperature, controllers*

James Myslinski, Ph.D.
Research Chemist, Agent Chemistry Branch, Threat Agent Sciences Division
FY20 project keywords: *synthetic biology, temperature, controllers*

Michael Smith
Mechanical Engineer, Smoke & Target Defeat Branch, Protection Division
FY21 project keywords: *countermeasure, carbon fiber, counter unmanned aerial vehicle, unmanned aerial vehicle swarm*

Anne Walker, Ph.D.
Chemical Engineer, Respiratory Protection Branch, Protection Division
FY20 project keywords: *antimicrobial, antiviral, polymer composites, additive manufacturing, coatings, formulation, poly(acylic acid), poly(vinyl alcohol), functional materials*

Table of Contents

In-house Laboratory Independent Research (ILIR) Projects

1 **Elucidating the prevalence of off-target effects of CRISPR-Cas editing in prokaryotes**
Casey B. Bernhards, Alvin T. Liem, Kimberly L. Berk, Pierce A. Roth, Matthew W. Lux*
CRISPR-Cas tools have ushered in a new era of genome editing. However, major knowledge gaps remain including the prevalence of off-target effects—mutations that occur at locations other than the intended locus—from CRISPR-Cas editing in prokaryotes. Understanding these potential unintended signatures of gene-edited prokaryotes may lead to the ability to determine whether an organism has been engineered. Initially, researchers identified appropriate insertion points in *Escherichia coli* and developed a counter selection system for off-target effects. In the second year, efforts focused on engineering this counter selection system to enable quantification of the off-target effects and using *in vitro* sequencing to identify them.

11 **Remodeling the bacterial outer membrane for synthetic designer microbes**
*Erin E. Antoshak, Nathan D. McDonald**
Bacterial outer membranes are associated with survival, pathogenesis, and antimicrobial resistance. Genetic engineering of bacterial surfaces can allow for the characterizations of pathogenicity, detection assay development, and assessment of novel, emerging, and intentionally engineered threats. Researchers aim to engineer a designer microbe with a unique outer membrane lipopolysaccharide by transferring a non-pathogenic lipopolysaccharide biosynthesis system from the pathogenic *Yersinia pestis* host to a receiving non-pathogenic *Escherichia coli* host. In year one, the CRISPR/recombineering system to be used to transfer *Y. pestis* lipopolysaccharide biosynthesis genes to the receiving *E. coli* strain was identified and implemented. Phenotypic and analytical evaluations of the outer membrane were performed to determine if the insertions resulted in the expected result.

19 **Characterization and production of the Coxiella burnetii specific O-antigen carbohydrate virenose in engineered Escherichia coli**
*Nathan D. McDonald, Erin E. Antoshak, Sarah E. Katoski**
Immunity and pathogenicity mechanisms of *Coxiella burnetii*—the causative agent of Q fever—are not fully understood; but lipopolysaccharide in known to play a key role in pathogenesis. As a unique component of *C. burnetii* lipopolysaccharide, L-virenose could serve as a marker for detection and as an antigen for vaccine development. This effort aims to leverage the predicted pathway of L-virenose to express a synthetic construct in an *Escherichia coli* host. Five biosynthetic genes were optimized for expression in *E. coli* to understand how lipopolysaccharide is produced and the biosynthetic pathway of L-virenose. In its second and final year, construction and optimization of the expression vector to enable screening for L-virenose production in *E. coli* was completed, allowing for assessment of the purified enzymes *in vitro* to understand the biology of virenose and *C. burnetii* pathogenesis.

25 **Deep learning for the prediction of experimental spectra**
Patrick C. Riley, Samir V. Deshpande, Brian S. Ince, Ruth Dejere, Kyle P. O'Donnell, Brian C. Hauck*
Alarm algorithms to alert Soldiers of danger grow more complex as new threats emerge—they must be robust enough to prevent false alarms but sensitive enough to detect small doses that prove lethal. Algorithm design for mature systems has left a plethora of data that can be leveraged to train deep learning models to predict experimental spectra of new threats and determine chemical species more precisely. This effort seeks to train a machine learning model to predict chemical spectra for any ion mobility spectrometry (IMS)-based detector. In the first two years of this work, researchers created a theoretical long-short term memory framework that considers instrument parameters and molecular properties to simulate the chemistry of an IMS technology for the prediction of experimental spectra. In its final year, the robustness of model was evaluated against other detector variant.

35 **Effect of quorum sensing molecules on the production of bacterial nanocellulose materials**
Rabih E. Jabbour, Hany F. Sobhi, Hyeonggon Kang*

Bacterial nanocellulose (BNC) is a promising multifunctional material with numerous applications in the areas of medicine, defense, and electronics. However, BNC is difficult to manufacture due to the heterogeneity of bacterial nanocellulose pellicles. This project aimed to determine the impact of quorum sensing molecules—specifically, HSL molecules—on BNC biofilm formation with the aim of utilizing the mechanistic information to bioengineer biofilms with custom-based requirements. In preceding years of this project, the impact of HSLs on the morphological properties of the cellulose films produced by *Gluconacetobacter xylinus* was determined. Quorum sensing pathways were manipulated and the resulting morphological changes in cellulose fiber thickness, structure, and uniformity were evaluated. In its final year, HSL production regulatory circuits were modulated for tailoring BNC for certain applications.

Surface Science Initiative (SSI) Projects

43 **Towards understanding the role of material voids and porosity on transport**
Angela M. Zeigler, Roseanna N. Zia, Brian K. Ryu, Mark J. Varady, Melissa S. Hulet, Bradley R. Ruprecht, Harvey Tsang*

Interest in additive manufacturing for the U.S. Army is gaining traction due to its potential to reduce the burden associated with transporting and maintaining large inventories of custom or complex equipment. The challenge of utilizing 3D printing for CBRN-protective equipment is that there remains inherent porosity and voids (defects) in these materials, meaning it is unclear whether 3D printing equipment can adequately protect the warfighter from chemical toxic agents. This effort sought to determine if breakthrough of harmful chemicals occurs when solvent-borne macromolecules migrate through a porous network, rather than migrating through the dense solid. To study the voids within a 3D print, a mesoscale coarse-grained model was developed. Researchers advanced the computational modeling of transport through material voids via algorithms based on the diffusion of the vapor solvents through the model and the discovered differing breakthrough mechanisms. In the final year, focus was expanded to several interrogating chemical solvents and iterative modifications to the computational model based on the transient breakthrough times—demonstrating the mechanisms determined for the primary breakthrough are in alignment with the initial hypothesis.

53 **Extending bio-functionality in materials via controlled polymer erosion**
Marilyn S. Lee, John R. Biondo, Jeffrey Lux, Casey B. Bernhards, Danielle L. Kuhn, Melissa S. Hulet, Mark J. Varady, Maneesh K. Gupta, Matthew W. Lux*

Cell-free protein synthesis (CFPS) is an emerging platform that offers cell-like functionality independent of cell viability. Up to now, CFPS reactions have been confined to the laboratory, but this project seeks to develop new capabilities to allow CFPS systems to be deployed in the field. Researchers previously demonstrated that lyophilized CFPS lysates tolerated exposure to multiple factors this technology may experience if deployed in the field. During the second year of this project, the CFPS lysates were embedded with polymers that increase the versatility of this technology. These CFPS lysates retained their activity, albeit with some degree of variability, after being processed, demonstrating CFPS polymers could be activated to produce the antimicrobial protein colicin, yielding a potential future application for this technology.

69 **Purification and characterization of a membrane sculpting bacterial BAR domain-containing protein for engineering tunable scaffolds into novel biological metamaterials**
*Daniel A. Phillips, Jennifer A. Lee, Barbara J. Smith, Brian J. Eddie, Duncan R. Sousa, Patricia E. Buckley, Aleksandr E. Miklos**

Optical metamaterials can be used to impart a negative index of refraction to propagate incoming electromagnetic waves parallel to the object as opposed to reflecting directly back to the source, effectively cloaking the object from detection waves. These materials are formed by patterning conductive structures into ordered, three-dimensional arrays on a surface such that the operational electromagnetic wavelength is larger than the spatial interval between the conductive materials, a process by which biology could be manipulated to excel. Proteins containing Bin/Amphiphysin/Rvs (BAR) domains can act as an optical metamaterial by manipulating membrane lipids to affect visible light. This project seeks to understand the structure of one such BAR protein that induces the sculpting of bacterial cell membranes. In year one, the structure and function of the BAR protein were investigated to create tunable biological metamaterial from membrane scaffolds that can perform over a range of electromagnetic wavelengths.

79 **Toward understanding the generation and lifetime of singlet oxygen species in photosensitized rigid crystalline structures**
*Ann M. Kulisiewicz, Sergio J. Garibay, Ivan O. Iordanov, Matthew A. Browe, Gabrielle Pozza, Lisa A. Kelly, Jared B. DeCoste**
Oxygen is considered a non-reactive gas when in its ground triplet state but becomes a mild oxidant when in its singlet state. This project aims to understand the generation and lifetime of singlet oxygen through the controlled irradiation of a photosensitizer. In its second year, several novel metal-organic framework derivatives were synthesized and evaluated based on their photocatalytic activity. Results suggested that the type and position of a functional group can dramatically alter the molecules photocatalytic activity. Further, experiments demonstrated the potential of specific functional groups to self-quench and decrease their reactivity—knowledge invaluable to the design of future MOF-based catalysts intended to mitigate toxic chemicals susceptible to oxidation, including sulfur mustard and hydrogen sulfide.

89 **Cooperative interactions between functionalized particles and binders in polymer composites and their effect on chemical transport**
Mark J. Varady, Melissa S. Hulet, Adam R. Hinkle, Thomas P. Pearl, Melissa L. Sweat, Kenneth E. Strawhecker, Alice M. Savage, Jonathan P. Ligda*
Polymer composite-based coatings consist of solid particles in a polymer matrix which acts like the glue between various particles and additives and plays a key role in chemical resistivity of composite materials. Improved understanding of this structure-property relationship at the interfacial regions will provide strategies to improve composite properties at the macroscale, while maintaining important performance characteristics. This effort initially focused on developing molecular dynamic models of the polymer-particle interface to examine the effect of particle surface modification to alter transport properties. In its third and final year, adhesion force measurements for all silica particle surface modifications were completed and compared with corresponding breakthrough measurements. The results highlight a possible influence of interfacial region for composites with bare silica, while molecular dynamic simulations also revealed an interfacial region with varying transport properties.

101 **Characterization of opioid conformational changes and their effect on binding and reactivity on surfaces**
Monica L. McEntee, Mark D. Winemiller, Andrew J. Walz, Amanda M. Schenning, Michelle L. Sheahy, Ivan O. Iordanov*
An understanding of how opioids interact with surfaces remains incomplete. Different environments alter opioid conformation, but understanding these alterations can help develop future antidotes, establish decontamination protocols, and create sensors to detect these compounds. The goal of this project was to better understand the conformational structure of the fentanyl-class of opioid molecules and what dictates their binding and reactivity on surfaces. Conformational analysis under varying physical and chemical conditions was performed to generate a knowledge base and understand how changes in the chemical environment result in certain opioid confirmations which affect receptor binding. In its final year, this project revealed that uptake of the opioid remifentanil is pH- and solvent-dependent, demonstrating the complexity of its binding capabilities.

113 **A combined density functional theory and grand canonical Monte Carlo approach to modeling multi-component adsorption**
Ivan O. Iordanov, Trent M. Tovar, Lawford Hatcher, Jared B. DeCoste*
Computational modeling is used to improve the understanding of complex phenomena through calculations of variables that are difficult to observe experimentally. This effort sought to contrast and combine first-principles and larger scale atomistic modeling methods to better model gas adsorption in porous media which can help explain the characteristics of novel materials and guide future development. This effort focused on polar gases by using a new forcefield potential database. Improvements were made to the density functional theory comparison by automating the process of binding energy calculations, allowing for meaningful statistical comparisons. The last year of this research focused on using new force field databases for grand canonical Monte Carlo calculations and using density functional theory to improve the model.

FY21 Seedling Projects

123 Biodiversity of the operational aerosol background environment

Francis M. D'Amico, Adina L. Doyle, Mark A. Karavis, Jessica M. Hill, Maria T. Arévalo, Cory R. Bernhards*

Detection and identification systems for biological defense must be able to detect low levels of aerosolized biological agent threats while operating in challenging outdoor environments. Background noise is typically the limiting factor in detector performance but can be overcome by characterizing the aerosol profile and incorporating it into the function of the detector system. This work aimed to develop a data collection and processing method to characterize the operational environment with respect to current and emerging bioaerosol detection technologies. Surveys characterized the biodiversity of the aerosol particles using DNA sequencing and measuring particle size in the respirable range using optical particle monitors and ultraviolet light-induced fluorescence. A pilot data set was created that can be used to support bioaerosol detector technology development and design more operationally relevant test and evaluation protocols.

131 Machine-learning for imperfectly observed networks via Gibbs sampler

Thomas Ingersoll

An important parameter for predictive infectious disease models is R_0, the basic reproductive number. R_0 determines the rate at which new infections occur and responds to intervention strategies such as vaccination, quarantine, social distancing, and is further complicated by shortcomings in surveillance data collection. However, R_0 can be difficult to estimate as its value appears to change in open populations, where subpopulations interact in partial isolation. This effort sought to develop a method for estimating infective disease dynamics parameters when contact rates are heterogeneous, surveillance data are not systematically sampled, and cases are underreported. A hierarchical data-assimilative method was assembled for improving parameter estimates in predictive models when data are imperfectly collected, thereby helping to estimate changes in disease dynamics in a timely manner and inform management decisions and mitigation strategies early in disease outbreaks.

137 MXene inactivation of SARS-CoV-2 proxy φ6

Shaun M. Debow, Steven P. Harvey, Brendan G. DeLacy*

Novel materials that can inhibit transmission and viability of pathogenic viruses—and methods to safely evaluate these novel materials—have gained significant interest due to the SARS-CoV-2 pandemic. To safely evaluate these novel materials, non-pathogenic viral surrogates with lower biosafety requirements can be used instead of novel pathogens. The possibility of using the bacteriophage phi6 to act as a suitable surrogate for SARS-CoV-2 by evaluating phage inhibition after treatment with $Ti_3C_2T_x$ MXene—an emerging class of two-dimensional materials that have recently shown the potential to directly inhibit the SARS-CoV-2 novel coronavirus. Results show no difference in phi6 inhibition after treatment with $Ti_3C_2T_x$ MXene.

145 Novel CWA reactive material by grafting Zr-MOF secondary building units on functionalized supports

Ann M. Kulisiewicz, Sergio J. Garibay, Trenton B. Tovar*

Metal-organic frameworks with Zr-based secondary building units—the primary reactive component for hydrolysis reactions—have shown promise as materials for protection and self-decontamination of chemical warfare agents. However, the variables inherent to metal-organic frameworks structures, including the role of the secondary building units, complicate the understanding of the reactivity of the material. Reactivity of a simplified system consisting of Zr-secondary building unit clusters grafted onto silica supports was explored to develop a novel reactive material and to understand the reactivity of the secondary building units. The modified silica material selectively hydrolyzed the tested substrate, demonstrating the potential use of this silica platform to study and optimize zirconia clusters for decontamination.

153 **Using lung-on-a-chip technology to evaluate the effects of pathogen surrogates**
Daniel J. Angelini, Jennifer R. Horsmon, Tyler D.P. Goralski*

Exposures to the spores of *Bacillus anthracis* can lead to the development of anthrax. Much of the pathology associated with inhalational anthrax is associated with the toxins produced following infection. Previous anthrax research was performed in models that lacked physiological accuracy, were expensive, and raised ethical considerations. To create a cheaper, more physiologically relevant model, this project demonstrated lung-on-a-chip technology could be used to measure the effect *B. anthracis* toxins have on human pneumocytes and lung-specific microvascular tissue. Future studies will be able to incorporate this technology to streamline preliminary studies on a variety of other pathogens and toxins.

159 **UAV swarm defense**
Michael J. Smith, John A. D'Agostino*

Hobby grade, commercially available unmanned aerial vehicles (UAVs) have the potential to carry lethal payloads up to two kilograms and can be used in a combat situation either in single UAV missions or in a swarm of multiple UAVs. Swarms are difficult to counter using conventional kinetic measures, as these technologies are localized and less effective in countering swarms. However, an aerosol cloud containing fibers or spray adhesives could be dispersed in a large area as a countermeasure against UAV swarms. The ability of fibers varying in composition, diameter, and spray adhesives to defeat flying UAVs were examined. The findings show that the fiber length, diameter, and spray adhesive are important variables when it comes to effectiveness of defeat.

FY20 Seedling Projects

165 **Active illumination source for hyperspectral spectrometer in UAV/UGV mounted applications**
Justin M. Curtiss, Eric R. Languirand*

Artificial illumination is required for a line scanning passive hyperspectral spectrometer when operating a system in non-daylight conditions. While more photons will yield a larger reflectance signal return to the sensor, a source that outputs many photons is unlikely to be compatible with a compact hyperspectral spectrometer on a small aircraft or using in a handheld manner. To overcome this issue, a small tungsten halogen source was coupled with off-the-shelf optics to create a source of photons for the spectrometer. Several optical trains were designed to focus the source output to the instruments' field-of-view, and a Powell lens generated a line of light that could be co-aligned to the instrument. The results show that a compact source can allow for a hyperspectral spectrometer to operate with a compact artificial illumination source with minimal decrease in performance.

173 **Antiviral copper-loaded polymer systems**
Anne Y. Walker

Polymers containing copper could allow for rapid production of passive antiviral materials that slow the transmission of microbes, pertinently, SARS-CoV-2. Development of easily deployable copper-loaded systems could allow these materials to be used without having to retrofit equipment with minimal logical burden. To address this shortcoming, a copper-loaded polymer system was developed to serve as passive antiviral composites that could be used as coatings, in textiles, and as 3D printing filaments. This study centered on the formulation of copper-loaded systems made from inexpensive and readily available commodity polymers and copper materials. The initial samples provided a good balance of peel-ability and adhesiveness, while still providing accessibility to copper for the antimicrobial effects. Future efforts will focus on evaluating the antimicrobial effects of these compounds in a series of proof-of-concept experiments.

179 **Cortical neurons for toxicological studies**
*Erin M. Gallagher, Julie A. Renner, Linnzi K. Wright, Theodore S. Moran, Russell M. Dorsey, Stanley W. Hulet**

How threat agents alter the physiology of the human brain is not well understood. This is due to the difficulty of using living brains for *in vivo* studies and a lack of relevant *in vitro* cell lines. Researchers sought to establish an *in vitro* culture model of hairless guinea pig neuronal cells that will complement the Center's current resources and to enable future studies focused on understanding brain functions using assays that characterize toxicity, identifying medical intervention strategies, and the development of a blood brain barrier model. This project resulted in a protocol to harvest guinea pig neurons from fetal tissue and sustain their viability for up to 20 days. Additional studies that can further increase the ability to work with this important cell type were identified.

183 **Determination of the rate of aging inhibited acetylcholinesterase by mass spectroscopy**
*Vanessa Funk, Li Kong, James M. Myslinski**

Organophosphorus nerve agents inhibit the enzyme acetylcholinesterase (AChE) by covalently binding to the catalytically active amino acid Ser203. Nerve agents that possess an alkoxy group—including sarin and VX—become less susceptible to reactivation by antidotes over time through a process called aging. This seedling project was designed to elucidate a method to measure the kinetics of aging various AChE organophosphorus complexes using mass spectroscopy instead of measuring the activity of rescued AChE. The rates of aging AChE inhibited with racemic GB, (R)-VX, and (S)-VX were determined by mass spectroscopy to be similar to the rates obtained from traditional methods and provided insight into the quality of AChE. Furthermore, mass spectroscopy does not suffer the same drawbacks that indirect methods do, making it a viable tool for future nerve agent aging studies.

189 **Development and evaluation of temperature-controlled switches for synthetic biology**
*Julie L. Zacharko, Nathan D. McDonald**

The genomic age has paved the way for developing biological tools and systems for the benefit of society—including the use of genetic switches, controlled by abiotic inputs such as pH or temperature, that can be implemented as controllers of a desired process. The responsiveness and utility of two previously identified temperature responsive elements—Caf1R and TlpA—were investigated in a green fluorescent protein *Escherichia coli* expression system. This study indicated that, unlike a Caf1R-controlled system, a TlpA-controlled system could be manipulated to produce green fluorescent protein expression in a temperature dependent manner, likely suggesting temperature responsive elements can be harnessed as synthetic biology controllers.

193 **Evaluation of cold weather decontamination methods**
Jana Kesavan, Daniel R. McGrady, Aime P. Goad, Amanda M. Schenning, Melissa L. Sweat*

Most chemical or biological decontamination protocols have been driven by the need for fast, efficient, and safe methods that are easy to implement. As such, the focus has primarily been towards "general" environments where water is available and the ambient conditions are amenable to its use. This study focused on identifying common methods for readily available cold weather decontamination methods and evaluation of their respective efficacies—including wiping with both wet and dry wipes, blotting with moistened wipes, vacuuming, and the application and removal of adhesive tape. Results demonstrate that vacuuming and blotting are generally less effective than wiping, and adhesive tape-based measures at removing bacteria from surfaces in cold weather environments. This work provides a baseline against which these methods may be compared efficacies in a controlled laboratory setting.

199 **Inhalation toxicity characterization of obscurants using human tissue**
Jennifer R. Horsmon, Tyler D. Goralski, Danielle L. Kuhn, Daniel J. Angelini*

3D constructs can be utilized to determine the cytotoxicity of human lung tissue when exposed at the air-liquid interface in a more biologically relevant model compared to standard 2D cultures. In this project, EpiAirway™ constructs consisting of human-derived cell cultures of differentiated airway epithelial cells were used to mimic human inhalation exposure to metallic particles and evaluated toxicity. This model offered a higher throughput assessment that was used for screening potential obscurant materials for toxicity. The data suggested that exposure at operationally relevant concentrations to these particles does not cause cytotoxicity in cultured pulmonary cells.

203 **Large scale reflectin production through biomanufacturing**
Krystina L. Hess, Anna M. Crumbley, James M. Myslinski, Robert Levenson, Brandon Malady, Daniel E. Morse*

Biomanufacturing has the potential to replace traditional petrochemical manufacturing of chemicals and materials of interest to the Army. The new DEVCOM CBC biomanufacturing facility can be used to produce materials for defense applications including reflectin—a protein found in the skin cells of squids that can be used in camouflage and photonic applications. A translatable downstream processing method was developed for purifying reflectin from the growth cultures of organisms engineered to produce the protein. The novel method developed can be translated from the lab scale to the pilot scale and was able to provide crucial experience for the biomanufacturing team.

209 **Spatial dynamics of infectious disease**
Thomas E. Ingersoll

R_e, the effective reproductive number, determines the rate at which new infections occur, and responds to intervention strategies such as vaccination, quarantine, and social distancing. However, accurate estimation of R_e is complicated by shortcomings in surveillance data collection, which are difficult to mitigate through changes in sampling methods. This project proposed R_e estimates are not necessary to model changes in disease dynamics; rather, the basic reproductive number R_0 may be used with contact parameters derived from network characteristics within a host population. This project demonstrated a hierarchical data-assimilative method for improving parameter estimates in predictive models when data are imperfectly collected which can then be used to inform management decisions and mitigation strategies.

215 **Standoff photoacoustic spectroscopy by thermally induced optical reflection of sound (THORS)**
Daniel S. Kazal, Brian M. Cullum, Eric R. Languirand, Darren K. Emge*

A recently discovered phenomenon known as thermally induced optical reflection of sound provides a means to optically manipulate sound waves in air without the need for physical acoustic barriers. By photothermally exciting the air with infrared laser light, an abrupt change in compressibility occurs at the edge of the laser beam which results in the reflection of incident acoustic waves on the thermally induced optical reflection of sound barrier. Furthermore, if the excitation source is shaped into an optical tube, an acoustic waveguide forms which can enhance the distance transient acoustic waves can travel due to internal reflection. This project demonstrated the ability to perform standoff photoacoustic measurements of ethanol vapor in ambient air and explored the effect thermally induced optical reflection of sound barriers and channels have on ultrasonic pulses.

ILIR PROJECTS

Elucidating the prevalence of off-target effects of CRISPR-Cas editing in prokaryotes

Casey B. Bernhards[a]*, Alvin T. Liem[b], Kimberly L. Berk[a], Pierce A. Roth[b], Matthew W. Lux[a]*
[a]U.S. Army Combat Capabilities Development Command Chemical Biological Center, Research & Technology Directorate, 8198 Blackhawk Rd, Aberdeen Proving Ground, MD 21010
[b]DCS Corporation, 6909 Metro Park Dr, Suite 500, Alexandria, VA 22310

ABSTRACT

CRISPR-Cas has emerged as a powerful, dual-use gene editing tool that has been used to modify a variety of organisms, from bacteria to humans. Extensive work has gone into understanding off-target effects of CRISPR-Cas systems in higher organisms due to the potential consequences of unintended mutations when used for medical applications, but this area has remained relatively unexplored in prokaryotes. Here, we describe similar work to understand the off-target effects of CRISPR editing in bacteria as a potential method to identify signatures of engineered threats. We describe a two-pronged approach based on a selection system to quantify off-target rates *in vivo*, and a parallel *in vitro* approach that assesses off-target rates using purified molecular components. This report describes work completed in the second year of the project.

Keywords: gene editing, synthetic biology, bioforensics

1. INTRODUCTION

In recent years, the barriers to genetically engineer a wide range of prokaryotic organisms have been dramatically reduced, driven in large part by the application of CRISPR-Cas (Clustered Regularly Interspaced Short Palindromic Repeats and CRISPR-associated) gene editing systems.[1] CRISPR editing has already been demonstrated in at least 36 prokaryotic species,[2] in addition to eukaryotic organisms. Compared to other techniques, CRISPR-Cas gene editing is relatively simple and only a few components are necessary: the Cas enzyme is required to create a double-strand break (DSB) in the DNA, and a small guide RNA (gRNA) and short recognition motif (PAM sequence) are needed for targeting the Cas enzyme to a specific site in the DNA for cleavage.[3] In eukaryotic cells, the natural pathway for repair of CRISPR-induced DSBs is through non-homologous end joining (NHEJ), an error-prone pathway resulting in small insertions or deletions; however, an array of precise edits are possible through homology-directed repair (HDR) by providing a DNA repair template. As most bacteria lack a native NHEJ system, CRISPR editing in prokaryotes relies on the HDR pathway,[4] which crucially leaves no additional markers (antibiotic resistance cassettes, extra bases, or scars) at the site of editing.

The characteristics that have made CRISPR-Cas a powerful genome editing tool, including its ease of use and broad applicability, are the same qualities that have prompted dual-use concerns. There is a need within the Department of Defense to be able to detect genetically engineered threats, particularly those arising from techniques like CRISPR that lack traditional signatures. Despite being touted as a highly-precise gene editing technique, CRISPR off-target effects (unintended modifications elsewhere in the genome) have been reported.[5] Due to the potential ramifications of off-target effects for CRISPR applications like human gene therapy, there has been considerable interest and research in this area for eukaryotic organisms;[6–10] however, there is a significant knowledge gap in our understanding of CRISPR off-target effects in prokaryotes. Importantly, several factors suggest there may be differences observed between off-target effects in eukaryotic and prokaryotic organisms: (1) these groups have different routes of DNA repair (NHEJ versus HDR);[4] (2) due to the lethal nature of unrepaired DSBs in prokaryotic cells, CRISPR-Cas editing may activate the cell's SOS response and increase the cell's mutation rate;[11] and (3) differences in off-target effects have been reported between *in vitro* and *in vivo* experiments in eukaryotic cells,[7,8] suggesting the involvement of other cellular mechanisms. Characterization of off-target effects in prokaryotes may reveal signatures of editing and facilitate detection of CRISPR-modified organisms.

In this work, we aim to genetically modify the model bacterium, *Escherichia coli*, using CRISPR-Cas9 and a combination of counterselection and whole genome sequencing (WGS) to identify off-target effects. The relatively

small size of bacterial genomes and clonal populations that can be isolated following CRISPR-Cas editing make bacteria especially amenable to a WGS-based approach to identify off-target events. In parallel, we aim to apply *in vitro* editing and sequencing techniques specifically designed to identify off-target edits. We hypothesize that CRISPR editing in bacteria creates off-target effects that are detectable through these methods.

2. METHODOLOGIES

2.1 Computational methods

Putative neutral insertion points between convergent genes in bacterial chromosomes were identified using in-house, custom software called targetFinder (https://github.com/ECBCgit/targetFinder). Intergenic gaps identified by targetFinder were further assessed for transcriptomic coverage using RNA-seq datasets obtained from the National Center for Biotechnology Information (NCBI) Sequence Read Archive (SRA). For each organism, 50 RNA-seq datasets were randomly selected and aligned to the organism genome using Bowtie2 software. Samtools software was used to sort the output from Bowtie2 and create a pileup file, and Perl scripts were used to generate gap coverage and coverage statistics files.

2.2 *In vivo* CRISPR edits

A real-time PCR (qPCR)-detectable DNA barcode (Barcode Ec1) was designed using barCoder software[12] for insertion into the *E. coli* MG1655 chromosome. Within each *E. coli* gap identified by targetFinder, a gRNA sequence was designed with GuideFinder software[13] and screened for potential off-target sites using Cas-OFFinder software.[14] Guide RNA sequences were incorporated into plasmid pTargetF (a gift from Sheng Yang, Addgene plasmid #62226)[15] using inverse PCR with primers containing the 20-bp gRNA sequences, followed by isothermal DNA assembly (NEBuilder HiFi DNA Assembly, New England Biolabs). HDR templates containing Barcode Ec1 and ~500 bp of flanking DNA on each side homologous to the chromosomal insertion point were obtained as gBlocks (Integrated DNA Technologies) and cloned into the pTargetF-derivatives containing gRNA sequences using inverse PCR and isothermal DNA assembly. Barcode Ec1 was inserted at sites in the chromosome of *E. coli* MG1655 (BEI Resources, #NR-2653) essentially as previously described[15] using plasmid pCas (a gift from Sheng Yang, Addgene plasmid #62225), which contains the genes for Cas9 and λ-Red recombinase, and pTargetF-derivatives containing both gRNA and HDR template sequences. Successful incorporation of Barcode Ec1 via CRISPR-Cas editing was verified by WGS using a MinION sequencer (Oxford Nanopore Technologies). Barcode Ec1 and gRNA sequences are listed in Table 1.

Table 1. Sequence information.

Construct	Sequence (5′ to 3′)	Description/Use
Barcode Ec1	AAGTTACCGTGGGTTGAGTACGTGTATTA GCTATTCGATTGAGCCTCGGCGATAGCTC TCTGGTCAACCGCTGCACCGTGCAATACT TAGAGCGTACGATAGTGAGCTGAGGATTC TAGAGGTCAAACTGTCGCGGTTACGAG	DNA barcode for insertion into *E. coli* MG1655
Primer Ec1-R	CTCGTAACCGCGACAGTTTG	Part of Barcode Ec1; used as the common reverse primer for qPCR detection of barcoded strains
Probe Ec1	/56-FAM/TCTGGTCAA/ZEN/CCGCTGCACC GTGCAATACTT/3IABkFQ/	Part of Barcode Ec1; used as the common probe for qPCR detection of barcoded strains
Primer Gap2_qPCR-F	GGCGGACGCTCGTTAATATAAG	Specific forward primer for qPCR detection of Barcode Ec1 in Gap 2
Primer Gap3_qPCR-F	TGTTTTGTGCGTGGGAACAG	Specific forward primer for qPCR detection of Barcode Ec1 in Gap 3
Primer Gap4_qPCR-F	ACCATAACGCCTCATTACGC	Specific forward primer for qPCR detection of Barcode Ec1 in Gap 4
Primer Gap5_qPCR-F	CAATCACCTTTCCATCCACCTAAG	Specific forward primer for qPCR detection of Barcode Ec1 in Gap 5
Primer Gap6_qPCR-F	AATACTGACCCACATTCCCGTAAAG	Specific forward primer for qPCR detection of Barcode Ec1 in Gap 6
Primer Gap7_qPCR-F	GAAATTTTTTGATCTCCCCCCAAGT	Specific forward primer for qPCR detection of Barcode Ec1 in Gap 7
Gap 2 gRNA	CGGACGCTCGTTAATATTTA	gRNA sequence for editing Gap 2
Gap 3 gRNA	TGTGCGTGGGAACAGCCTTA	gRNA sequence for editing Gap 3
Gap 4 gRNA	GAAACGCGCTGAGTCAGTCT	gRNA sequence for editing Gap 4
Gap 5 gRNA	CCTCCATGCTTAATATAAGG	gRNA sequence for editing Gap 5
Gap 6 gRNA	CTGACAATTCATACGATTAC	gRNA sequence for editing Gap 6
Gap 7 gRNA	ACTAAGTTTAGATTTCAGGG	gRNA sequence for editing Gap 7

2.3 Phenotypic assays

2.3.1 Growth curves

E. coli strains were grown on Lysogeny Broth (LB) agar plates overnight at 37 °C and isolated colonies were used to inoculate separate tubes of 5 mL LB + 1 % glucose broth. Broth cultures were grown overnight at 37 °C with shaking and then diluted in fresh LB + 1 % glucose broth to reach an optical density at 600 nm (OD_{600}) of approximately 0.05 in a plate reader. Wells of a sterile, clear, flat bottom 96-well plate were loaded with 200 µL of diluted cultures or LB + 1% glucose broth for blank measurements. The plate was covered with an air-permeable seal and incubated in a BioTek Synergy Neo2 plate reader at 37 °C with continuous linear shaking, and OD_{600} measurements were taken every 2 minutes for 24 hours.

2.3.2 Competition experiment

E. coli strains were grown on LB agar plates overnight at 37 °C and isolated colonies were used to inoculate separate tubes of 5 mL LB broth. Pure broth cultures were grown overnight at 37 °C with shaking and then equivalent amounts of each of the 7 strains (wild-type and 6 barcoded strains) were mixed. Mixed cultures were serially passaged twice a day for four days by diluting cultures 1:200 into 5 mL fresh LB and growing at 37 °C with shaking. Samples of the mixed cultures were collected on Day 1 (initial sample) and Day 4 (final sample), and genomic DNA was isolated from the samples with a DNeasy UltraClean Microbial Kit (Qiagen).

DNA copies of each barcoded strain present in samples were quantified with qPCR. Assays were setup as 20 µL reactions in MicroAmp Fast Optical 96-Well Reaction Plates (Applied Biosystems) and consisted of TaqMan Fast Advanced Master Mix (Applied Biosystems), 0.4 µM of the forward primer specific to each barcode, 0.4 µM of the common reverse primer Ec1-R, 0.2 µM of the common probe Ec1, genomic DNA equivalent to 2.8 x 10^4 genomic

copies, and nuclease-free water. Plates were sealed with MicroAmp Optical Adhesive Film (Applied Biosystems) and run on a QuantStudio 6 Flex Real-Time PCR System (Applied Biosystems) using the following protocol: 1 cycle of 50 °C for 2 minutes and 95 °C for 2 minutes, and 40 cycles of 95 °C for 1 second and 58 °C for 10 seconds. Standard curves generated using 10-fold serial dilutions of genomic DNA isolated from pure cultures were used to calculate the number of DNA copies per assay for each barcoded strain. Standard curve properties for each qPCR assay are shown in Table 2. Assays are specific and show no cross-reactivity to other barcoded strains as assessed using genomic DNA equivalent to 4 x 10^3 genomic copies (Figure 1). Sequences for the qPCR primers and probe are provided in Table 1.

Table 2. Standard curve properties of qPCR assays for barcoded *E. coli* strains.

qPCR Assay	Linearity (R^2)	Efficiency (%)
Gap 1	1.000	89.1
Gap 2	1.000	92.0
Gap 3	0.999	90.8
Gap 4	1.000	87.0
Gap 5	0.998	86.2
Gap 6	0.999	78.2

DNA Template Barcode Location

Assay	Gap 1	Gap 2	Gap 3	Gap 4	Gap 5	Gap 6
Gap 1	27.5	ND	ND	ND	ND	ND
Gap 2	ND	27.1	ND	ND	ND	ND
Gap 3	ND	ND	27.8	ND	ND	ND
Gap 4	ND	ND	ND	28.7	ND	ND
Gap 5	ND	ND[a]	ND	ND	27.6	ND
Gap 6	ND	ND	ND	ND	ND	30.0

[a] 1/3 replicates gave a Ct value of 39.3

Figure 1. Cross-reactivity of qPCR assays against barcoded *E. coli* strains. Threshold cycle (Ct) values shown are the mean of three replicates; ND, Not determinable.

2.4 *In vitro* CRISPR experiments

2.4.1 Production of gRNA

For producing *in vitro* transcribed gRNA in-house, gRNA sequences were incorporated into plasmid pCRL1 (a gift from Shengdar Tsai, Addgene plasmid #153997) using inverse PCR with primers containing the 20-bp gRNA sequences, followed by isothermal DNA assembly. A pCRL1 derivative containing the gRNA sequence for *E. coli* Gap 2 (Table 1) was linearized with HindIII-High Fidelity restriction enzyme (New England Biolabs) and purified using a MinElute PCR Purification Kit (Qiagen). The gRNA was transcribed from purified linearized plasmid using a MEGAshortscript T7 Transcription Kit (Invitrogen) for 16 hours at 37 °C. Transcribed gRNA was treated with DNase and purified with a MEGAclear Transcription Clean-Up Kit (Invitrogen). Synthetic gRNA was obtained commercially from Integrated DNA Technologies.

2.4.2 In vitro DNA cleavage

A region of the *E. coli* MG1655 chromosome corresponding to the gRNA sequence/Cas9 cleavage site was PCR amplified. *In vitro* cleavage reactions containing 0.1 µM Cas9 (New England Biolabs), 0.1 µM gRNA (produced in-house or commercially), 125–300 ng PCR product, Buffer 3.1 (New England Biolabs), and nuclease-free water were incubated for 1 hour at 37 °C. Reactions were treated with Proteinase K (New England Biolabs) for 15 minutes at 37 °C and analyzed by agarose gel electrophoresis.

3. RESULTS

3.1 Identification of neutral genomic insertion sites

To identify putative neutral insertion sites for CRISPR-Cas editing in *E. coli,* we previously utilized an algorithm developed in-house, called targetFinder, which locates gaps between convergent genes and performs a series of checks to minimize both the potential of impacting strain function and difficulties with genetic editing.[16] To increase the utility of the targetFinder algorithm to the synthetic biology community, we also applied this tool to an additional nine common synthetic biology chassis organisms (Table 3). The number of gaps identified by targetFinder ranged from six to fourty-four (Table 3) and did not correlate with organism genome size (Figure 2A, R^2=0.1386, *p*-value that slope is non-zero=0.29). The lack of correlation may indicate differences in genome architecture or variable levels of annotations present in reference genome sequences. Most gaps identified were in the 300–500 bp size range (Figure 2B); organisms with significantly larger gaps may indicate the presence of unannotated coding sequences. The gaps for each organism are also well-dispersed across the genome (Figure 2C). Additionally, RNA-seq datasets were analyzed for each organism to assess whether each identified gap had low apparent transcriptional activity relative to the rest of the genome. Transcriptomic coverage analysis was used to downselect three gaps per organism (Table 3), although in most cases, additional gaps are likely suitable. Representative RNA-seq analyses of the gaps identified for *E. coli* are shown in Figure 3A.

Table 3. Putative neutral insertion sites for common synthetic biology chassis organisms.

Organism (Strain)	Chassis Information	NCBI Accession Number(s)	Number of Gaps (300–2,000 bp)	Positions of Suggested Gaps Based on RNA-seq Coverage
Escherichia coli (K-12 MG1655)	Ubiquitous model organism	NC_000913.3	7	1196374–1196866, 3635894–3636207, 4510134–4510689
Bacillus subtilis (168)	Spore former	NC_000964.3	21	1557632–1558033, 2092305–2092898, 2517559–2518022
Vibrio natriegens (ATCC 14048)	Ultra-fast grower	NZ_CP009977.1, NZ_CP009978.1	39	Chr1 1425737–1426304, Chr1 1908244–1908614, Chr2 1626963–1627297
Clostridium acetobutylicum (ATCC 824)	Robust anaerobe	NC_003030.1	19	941388–941786, 2818175–2819125, 3666206–3666506
Marinobacter atlanticus (CP1)	Marine electrogen	NZ_CP011929.1	21	2040995–2041383, 3592251–3592902, 4293010–4293415
Lactobacillus plantarum (WCFS1)	Gut resident	NC_004567.2	44	947235–947886, 1766569–1766899, 2604072–2604453
Bacteroides thetaiotaomicron (VPI-5482)	Gut resident	NC_004663.1	42	663308–664073, 5038842–5039697, 5507675–5508326
Pseudomonas putida (KT2440)	Soil dweller and industrial host	NC_002947.4	23	2168101–2168787, 2171466–2171867, 3414617–3415099
Deinococcus radioduran (R1)	Extremely hardy	NC_001263.1, NC_001264.1	6	Chr1 140911–142587, Chr1 526502–526958, Chr2 262440–262751
Synechocystis sp. (PCC 6803)	Photosynthetic	NC_000911.1	9	2695776–2696124, 2755087–2755430, 3274232–3274545

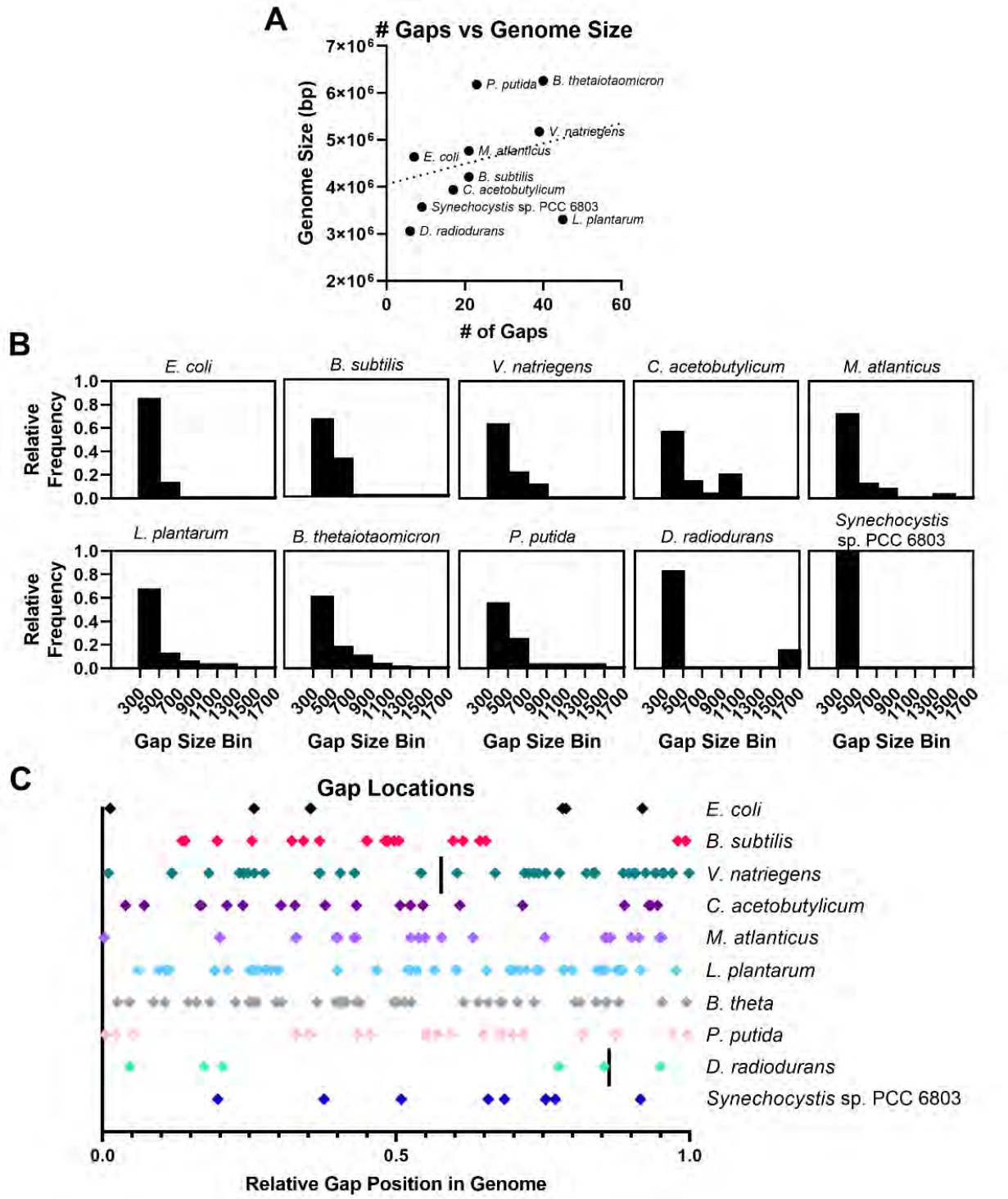

Figure 2. Analysis of gap locations for common synthetic biology chassis organisms. (A) Relationship between the number of gaps identified and the genome size of the organisms. (B) Histograms of gap sizes for each organism. (C) Distribution of gaps across each genome. Diamonds indicate each gap position and vertical lines indicate separation between two chromosomes.

The neutrality of the gaps identified for *E. coli* was further experimentally validated. CRISPR-Cas editing was used to insert a short DNA barcode[12] at each site. One of the seven sites was eliminated at this point due to issues with the commercial synthesis of the HDR template for editing this region. Phenotypic assays of the wild-type and six barcoded

strains were then performed to evaluate the impact of barcode insertion on strain fitness. Growth curves for each strain were highly similar (Figure 3B). Additionally, a competition experiment was performed in which strains were grown together and passaged six times for approximately forty-six doublings. The relative abundance of each barcoded strain, as determined by qPCR, between initial and final samples was consistent (Figure 3C); thus, no apparent fitness defects were observed for the barcoded strains under the conditions tested.

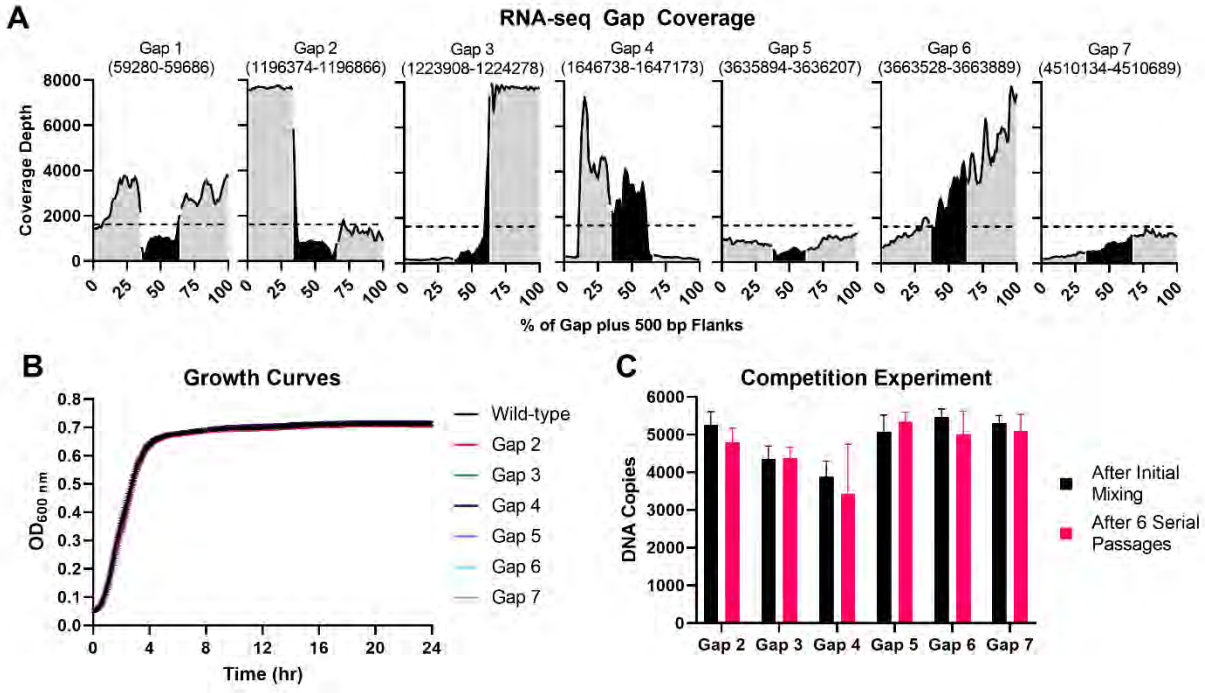

Figure 3. Validation of *E. coli* insertion sites as phenotypically neutral. (A) RNA-seq coverage of each identified *E. coli* gap. Panels display the identified gap (black shading) plus the 500 bp flanking either side (gray shading). Dashed lines indicate the median coverage depth across the genome. (B) Growth curves of wild-type *E. coli* and strains barcoded at each of six putative targets. Error bars represent the standard deviation; *n*=9. (C) Abundance of each strain during repeated passages of competitive growth as assessed by qPCR of the six barcoded strains. Error bars represent the standard deviation; *n*=9.

3.2 Selection strain for off-target effects

Because CRISPR off-target effects are likely to be rare events in bacteria, we devised a counterselection system to isolate instances of off-target DSB formation in bacteria as shown in Figure . *E. coli* strains are under construction in which two of the neutral insertion points identified by targetFinder (Gap 2 and Gap 5) are being used to engineer "on-target" and "off-target" sites. The on-target site consists of a promoterless chloramphenicol resistance gene, and the off-target site contains the *sacB* gene, which makes growth in the presence of sucrose toxic to cells. Both sites contain a gRNA target sequence that can be made less similar through synonymous point mutations in the gRNA region of *sacB*. Successful edits at the on-target site via HDR will result in expression of the chloramphenicol resistance gene (via incorporation of the promoter on the DNA repair template), and cells will be selected by growth on the antibiotic. Cells that survive cleavage at the off-target site through error-prone DNA repair (resulting in a frameshift mutation in *sacB*), will be selected by growth on sucrose. Colony counts from these different scenarios will be used to assess the rates of edits at the engineered sites. WGS will also be performed on resulting colonies to look for additional off-target mutations outside of the engineered site.

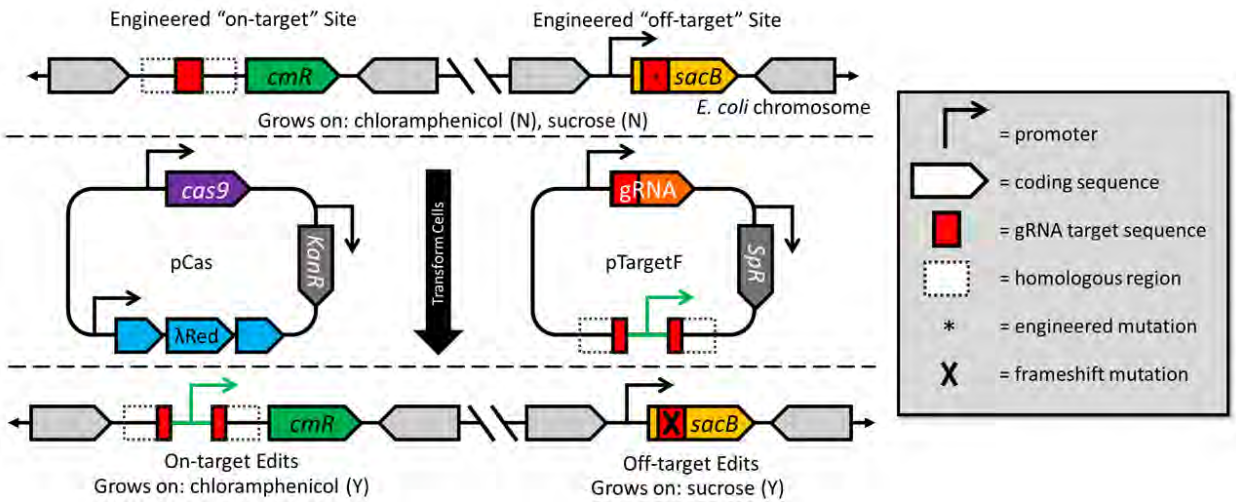

Figure 4. Counterselection strategy to capture potentially rare CRISPR off-target effects. Two engineered sites, an "on-target" and an "off-target" site, are being inserted into neutral sites in the *E. coli* genome. Growth on plates containing chloramphenicol or sucrose will indicate if an edit has occurred at the on-target site, off-target site, or both.

3.3 *In vitro* screening of off-target effects

As a complementary approach to our counterselection and WGS strategies to investigate CRISPR off-target effects, we identified an updated *in vitro* approach, called CHANGE-seq (circularization for high-throughput analysis of nuclease genome-wide effects by sequencing),[17] which has been successfully used for off-target site discovery in eukaryotic organisms. Cleavage sites determined *in vitro* using purified components (i.e., circularized genomic DNA fragments, Cas9, and gRNA) can additionally be utilized for targeted sequencing of *in vivo* CRISPR experiments. As a part of testing the CHANGE-seq methodology, we assessed our ability to generate functional gRNA in-house and cleave DNA *in vitro*. Using a PCR product of the *E. coli* genomic target, purified Cas9, and gRNA produced either commercially through chemical synthesis or in-house via *in vitro* transcription, we were successfully able to achieve CRISPR-mediated cleavage of DNA *in vitro* and show similar performance between gRNA produced commercially or in-house (Figure 5).

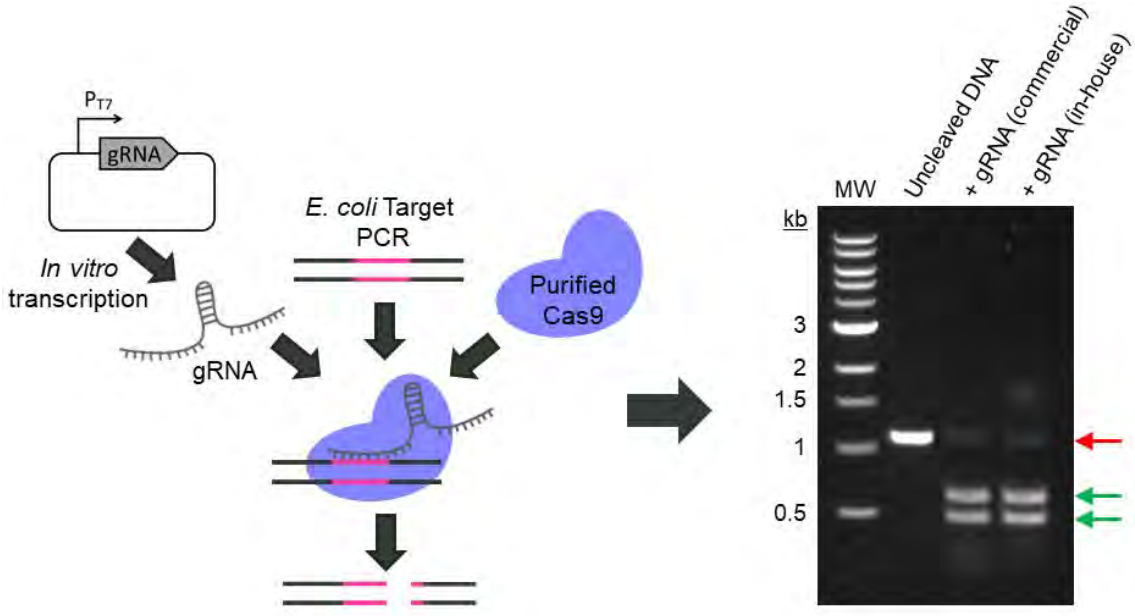

Figure 5. CRISPR cleavage of DNA *in vitro*. Diagram of *in vitro* cleavage experiment (left) and gel electrophoresis of resulting DNA products (right). Red arrow indicates bands corresponding to uncleaved DNA, and green arrows indicate bands corresponding to DNA cleaved by CRISPR components.

4. CONCLUSIONS

This report describes progress toward the goal of quantifying off-target effects of CRISPR editing in prokaryotes. We have identified putative neutral sites for editing in ten common synthetic biology chassis organisms, and experimentally validated the sites identified for *E. coli*. Using these sites, we are in the process of constructing novel *E. coli* selection strains to aid in quantifying potentially rare off-target effects. We have also demonstrated our ability to successfully use CRISPR-Cas gene editing systems, both *in vivo* and *in vitro*, which will enable future work with the intended outcome of the quantification of off-target rates. Knowledge of these rates will inform tools to identify signatures of genetically engineering in emerging threats.

ACKNOWLEDGMENTS

We thank Dr. Henry Gibbons from the U.S. Army Combat Capabilities Development Command Chemical Biological Center (DEVCOM CBC) and Dr. Shengdar Tsai of St. Jude Children's Research Hospital for helpful discussions in support of this work. We also thank Dr. Samir Deshpande and Dr. R. Cory Bernhards (DEVCOM CBC), Dr. Maria Arevalo (Defense Threat Reduction Agency), and Jessica Hill (DCS Corporation) for sequencing and bioinformatics support. Funding was provided by the U.S. Army via the In-house Laboratory Independent Research Program (PE 0601101A Project 91A) at DEVCOM CBC.

REFERENCES

[1] Wang, H.; La Russa, M.; Qi, L.S. CRISPR/Cas9 in Genome Editing and Beyond. *Annu. Rev. Biochem.* **2016,** *85*, pp 227–264.

[2] Vento, J.M.; Crook, N.; Beisel, C.L. Barriers to genome editing with CRISPR in bacteria. *J. Ind. Microbiol. Biotechnol.* **2019,** *46* (9–10), pp 1327–1341.

[3] Jinek, M.; East, A.; Cheng, A.; Lin, S.; Ma, E.; Doudna, J. RNA-programmed genome editing in human cells. *eLife*. **2013**, *2*, e00471.

[4] Cui, L.; Bikard, D. Consequences of Cas9 cleavage in the chromosome of Escherichia coli. *Nucleic Acid Res*. **2016**, *44* (9), pp 4243–4251.

[5] Fu, Y.; Foden, J.A.; Khayter, C.; Maeder, M.L.; Reyon, D.; Joung, J.K.; Sander, J.D. High-frequency off-target mutagenesis induced by CRISPR-Cas nucleases in human cells. *Nat. Biotechnol.* **2013**, *31* (9), pp 822–826.

[6] Hsu, P.D.; Scott, D.A.; Weinstein, J.A.; Ran, F.A.; Konermann, S.; Agarwala, V.; Li, Y.; Fine, E.J.; Wu, X.; Shalem, O.; Cradick, T.J.; Marraffini, L.A.; Bao, G.; Zhang, F. DNA targeting specificity of RNA-guided Cas9 nucleases. *Nat. Biotechnol.* **2013**, *31* (9), pp 827–832.

[7] Cho, S.W.; Kim, S.; Kim, Y.; Kweon, J.; Kim, H.S.; Bae, S.; Kim, J-S. Analysis of off-target effects of CRISPR/Cas-derived RNA-guided endonucleases and nickases. *Genome Res.* **2014**, *24* (1), pp 132–141.

[8] Pattanayak, V.; Lin, S.; Guilinger, J.P.; Ma, E.; Doudna, J.A.; Liu, D.R. High-throughput profiling of off-target DNA cleavage reveals RNA-programmed Cas9 nuclease specificity. *Nat. Biotechnol.* **2013**, *31* (9), pp 839–843.

[9] Kim, D.; Bae, S.; Park, J.; Kim, E.; Kim, S.; Yu, H.R.; Hwang, J.; Kim, J-I.; Kim, J-S. Digenome-seq: genome-wide profiling of CRISPR-Cas9 off-target effects in human cells. *Nat. Methods*. **2015**, *12* (3), pp 237– 243.

[10] Veres, A.; Gosis, B.S.; Ding, Q.; Collins, R.; Ragavendran, A.; Brand, H.; Erdin, S.; Cowan, C.A.; Talkowski, M.E.; Musunuru, K. Low incidence of off-target mutations in individual CRISPR-Cas9 and TALEN targeted human stem cell clones detected by whole-genome sequencing. *Cell Stem Cell*. **2014**, *15* (1), pp 27–30.

[11] Simmons, L.A.; Goranov, A.I.; Kobayashi, H.; Davies, B.W.; Yuan, D.S.; Grossman, A.D.; Walker, G.C. Comparison of responses to double-strand breaks between Escherichia coli and Bacillus subtilis reveals different requirements for SOS induction. *J. Bacteriol.* **2009**, *191* (4), pp 1152–1161.

[12] Bernhards, C.B.; Lux, M.W.; Katoski, S.E.; Goralski, T.D.P.; Liem, A.T.; Gibbons, H.S. barCoder: a tool to generate unique, orthogonal genetic tags for qPCR detection. *BMC Bioinf*. **2021**, *22* (98), pp 1–17.

[13] Spoto, M.; Guan, C.; Fleming, E.; Oh, J. A Universal, Genomewide GuideFinder for CRISPR/Cas9 Targeting in Microbial Genomes. *mSphere*. **2020**, *5* (1), e00086–20.

[14] Bae, S.; Park, J.; Kim, J-S. Cas-OFFinder: a fast and versatile algorithm that searches for potential off-target sites of Cas9 RNA-guided endonucleases. *Bioinformatics*. **2014**, *30* (10), pp 1473–1475.

[15] Jiang, Y.; Chen, B.; Duan, C.; Sun, B.; Yang, J.; Yang, S. Multigene Editing in the Escherichia coli Genome via the CRISPR-Cas9 System. *Appl. Environ. Microbiol*. **2015**, *81* (7), pp 2506–2514.
[16] Bernhards, C.B.; Roth, P.A.; Liem, A.T.; Lux, M.W. Elucidating the prevalence of off-target effects of CRISPR-Cas editing in prokaryotes. *FY20 Proceedings of the Combat Capabilities Development Command Chemical Biological Center In-house Laboratory Independent Research and Surface Science Initiative Programs*; U.S. Army Combat Capabilities Development Command Chemical Biological Center: Edgewood, MD, **2021**, pp 1–8.
[17] Lazzarotto, C.R.; Malinin, N.L.; Li, Y.; Zhang, R.; Yang, Y.; Lee, G.; Cowley, E.; He, Y.; Lan, X.; Jividen, K.; Katta, V.; Kolmakova, N.G.; Petersen, C.T.; Qi, Q.; Strelcov, E.; Maragh, S.; Krenciute, G.; Ma, J.; Cheng, Y.; Tsai, S.Q. CHANGE-seq reveals genetic and epigenetic effects on CRISPR-Cas9 genome-wide activity. *Nat. Biotechnol*. **2020**, *38*, pp 1317–1327.

Remodeling the bacterial outer membrane for synthetic designer microbes

Erin E. Antoshaka,[b], and Nathan D. McDonald[a]*
[a]U.S. Army Combat Capabilities Development Command Chemical Biological Center, Research & Technology Directorate, 8198 Blackhawk Rd, Aberdeen Proving Ground, MD 21010
[b]Excet Inc., 6225 Brandon Ave, Suite 360, Springfield, VA 22150

ABSTRACT

The lipopolysaccharide, also referred to as endotoxin, is a macromolecule component of the outer membrane of Gram- negative bacteria. The lipopolysaccharide defines and characterizes Gram-negative bacteria, facilitating antimicrobial resistance, antigen presentation, virulence, immunomodulation, environmental interactions, and evasion of the host immune response. The lipopolysaccharide can generally be divided into three sections: Lipid A, a core oligosaccharide, and the O-antigen. Further modifications can be caused by phosphates, amino acids and other small molecules increasing the variability of the structure. The lipopolysaccharide macromolecule can be structurally diverse between species and is often the distinguishing factor used for bacterial identification. Advancements in synthetic biology and rapid genome engineering have paved a path towards the creation of safe synthetic microbes with uniquely structured lipopolysaccharides. These engineered organisms can be uniquely leveraged in the development of novel detection assays, improve medical countermeasures, and assess emerging biological threats. Here, we utilize an engineered stain of *Escherichia coli* with key deletions in lipopolysaccharide genes resulting in an endotoxin-free outer membrane. This *E. coli* strain serves as the scaffold in which lipopolysaccharide genes from *Yersinia pestis* will be inserted into the genome, ultimately resulting in an engineered *E. coli* with an outer membrane mimicking that of *Y. pestis*. Building from the inside out, the late acyltransferase genes from *Y. pestis*, lpxM and lpxL, are inserted into the *E. coli* genome at their respective homologous loci via Clustered Regularly Interspaced Short Palindromic Repeats recombineering. The associated temperature dependency observed in *Y. pestis* with these enzymes will be evaluated in the engineered *E. coli.* Having confirmed the functionality of the late acyltransferases, the genes essential to core oligosaccharide synthesis are activated or inserted into the scaffold *E. coli.* The addition and activation of the core oligosaccharide system is expected to result in a fully assembled *Y. pestis* lipooligosaccharide on an *E. coli* backbone. The expression of this lipooligosaccharide will be validated by Matrix-Assisted Laser Desorption/Ionization-Time of Flight, along with biochemical analyses. This work will demonstrate the utility of genome engineering to develop designer microbes displaying specific outer membrane structures.

Keywords: Lipopolysaccharide, *Yersinia pestis*, outer membrane

1. INTRODUCTION

The advances in synthetic biology and genome engineering have allowed researchers to alter organisms, specifically bacteria, in ways never before thought possible. The tools available now have resulted in bacteria which have been engineered for numerous purposes, from drug delivery, biomanufacturing of economically valuable products, probiotics for disease treatment, to biosensors and diagnostics. Research capabilities have matured enough that a novel bacterium, *Mycoplasma laboratorium*, was created from a genome that was 100 % synthetically made. The synthetic biology developments have paved the path for designer medicine, threat detection, and stabilized supply chain among other groundbreaking developments. However, just as easily as these technologies can be used to benefit society, so too can they be used to create dangerous biological threats. The ease of which deadly pathogens can be enhanced, disguised, or even created poses a serious threat to the DoD and the warfighter. Therefore, it is critical to understand the extent to which bacteria can be genetically engineered to grasp where potential threats may exist.

The hallmark feature of Gram-negative bacteria is the outer membrane lipopolysaccharide (LPS). While highly conserved, the LPS macromolecule is structurally diverse across bacteria. Because of this heterogeneity, the LPS has been rigorously characterized in hundreds of bacterial species, resulting in many highly defined structures. For the

bacteria, the LPS is the primary component of the outer leaflet and contributes to the overall stability, permeability, and is essential for survival. Because it is embedded in the outer membrane of the bacteria and extends into the environment, LPS interacts with biotic and abiotic systems through bacterial adhesion, colonization and host immunomodulation, and acts as a virulence factor. Due to the conserved nature of LPS across all Gram-negative bacteria, higher ordered animals have evolved to recognize the structure to elicit an immune response. This robust, host immune response has led to LPS being considered an endotoxin. However, in a constant evolutionary arms race, many bacteria have developed mechanisms to alter various components of the LPS macromolecule to evade recognition and become resistant to antimicrobials.

The LPS molecule can generally be divided into three distinct domains: Lipid A, core oligosaccharide, and O-antigen, each of which possess unique characteristics and properties (Figure 1). While there are exceptions, one Lipid A unit is comprised a of linked D-glucosamine disaccharide backbone, which is phosphorylated at positions 1' and 4' of the carbohydrates.[1] The backbone is acylated with branching fatty acid chains of varying lengths and substitutions depending on the species. This main unit of Lipid A can be further modified by various additions including phosphates, carbohydrates, and other small molecules which can alter the overall charge. Together, it is the Lipid A unit which is responsible for the endotoxic properties of LPS by activation of the innate immune system via recognition by Toll-like receptor TLR4.[1]

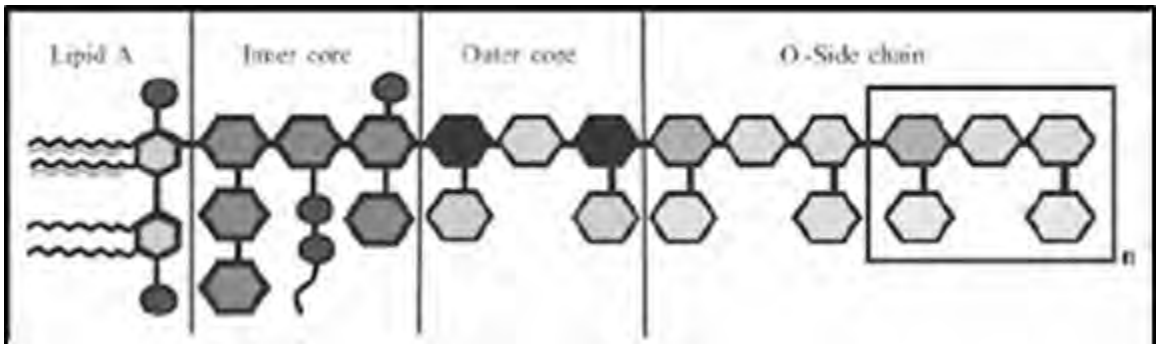

Figure 1. Representative depiction of the lipopolysaccharide structure in Gram-negative bacteria.

Moving outward, linked to the Lipid A is the core oligosaccharide domain of the LPS. The function of the core oligosaccharide is to provide increased rigidity and structure to the outer leaflet of the Gram-negative bacteria through cationic interactions. All bacteria link the core oligosaccharide to the Lipid A via a common carbohydrate, Kdo. The majority of Gram-negative bacteria possess a heptose-heptose-Kdo trisaccharide unit as the core composition, however exceptions to this have been identified.[1] The core oligosaccharide, much like the Lipid A, can also be further modified with substitutions. The most common substitutions to the core oligosaccharide include phosphates, additional carbohydrates and in some cases amino acids. The addition of these small molecules can dictate various interactions between the core oligosaccharide and the environment. Together, the Lipid A and the core oligosaccharide represent the minimal components necessary for bacterial survival. When bacteria only possess the core oligosaccharide and Lipid A, together known as the lipooligosaccharide (LOS), they grow with and are defined by a rough colony morphology.

The final unit of LPS, the O-antigen, is the most genetically and structurally diverse component of the LPS. The O-antigen is comprised of monosaccharides assembled into units, which can be repeated anywhere between one to over one hundred times depending on the bacterium.[1] The structural diversity of O-antigens has allowed for researchers to classify strains within a species by serotyping, which can result in hundreds of variants, as seen with *Escherichia coli* and *Vibrio cholerae*. The structural heterogeneity is a result of dramatic variations within the O-antigen biosynthesis gene clusters of these bacteria. In many cases, the bacteria can regulate the expression of O-antigen genes causing structural changes upon exposure to certain environments, such as during infection of a human host, known as phase variation. Alternatively, prophages can carry biosynthetic pathways and insert them within the genome, rapidly changing display structures.

The overall structure of the LPS in each organism can have profound effects. This macromolecule can itself serve as a virulence factor by a) masking a pathogen to evade the immune response, b) rendering the bacterial cell resistant to antimicrobials both natural and synthetic, c) cause a dramatic immune response which can lead to rapid septic shock, and d) allow for bacteria identification and detection. Because of its role in bacteriology, the structure of LPS has been determined for numerous pathogens, including many select agents associated with biological warfare threats. In

addition, because of the significance of the LPS, the genetics and biogenesis pathways for each of the domains has been defined across hundreds of species. The genomic age has provided researchers with the tools necessary to completely design and build organisms from the ground up. This also means that adversaries and even terrorist groups can create threat agents that have never been seen before. This project proposes to test the following hypothesis: We hypothesize that transferring an LPS biosynthesis system from one organism to another will result in the recipient organism producing the donor organism's LPS. This work seeks to understand how hostile actors could genetically engineer biological agents that threaten human safety outside of typical markers such as toxin expression or antibiotic resistance. This work will also determine the ability of engineered organisms to subvert current detection platforms that rely on surface displayed antigens for increased sensitivity. Finally, this work could potentially be used to generate surrogate bacteria designed to mimic existing threats, without the associated pathogenicity. These surrogates could then be used to further enhance detection, diagnostic, and medical countermeasures without the exposure risks normally associated with biological threat agents.

2. MATERIALS AND METHODS

2.1 Strains, Plasmids, and Constructs

ClearColi® BL21 (DE3) *E. coli* strain was received from Lucigen® and was used for Clustered Regularly Interspaced Short Palindromic Repeats (CRISPR) editing procedures. The CRISPR-Cas two plasmid system utilizes a pCas plasmid (Addgene #62225) for Cas9 expression and a pTargetF plasmid (Addgene #62226) including sgRNA directing it to the target region. The plasmids were obtained from Dr. Casey B. Bernhards from the U.S. Army Combat Capabilities Development Command Chemical Biological Center. The ClearColi® strain was grown in Luria Broth-(LB) Broth (Miller) (Sigma-Aldrich®; St. Louis, MO). The ClearColi® strain containing the temperature-sensitive pCas plasmid was grown at 30 °C, in kanamycin (50 µg/mL) supplemented media. The ClearColi® strain containing the pTargetF plasmid was grown at 37 ºC in media supplemented with spectinomycin (50 µg/mL). The pTargetF plasmid was constructed to incorporate the targeting sgRNA by performing inverse polymerase chain reaction using primers that contain the 20-basepair gRNA target sequence. This is followed by DNA assembly using NEBuilder® HiFi DNA Assembly, New England Biolabs®.

2.2 Donor DNA Amplification

The donor DNA was supplied as gBlocks™ (Integrated DNA Technologies™; Coralville, IA). The gBlock™ was used as a template in a polymerase chain reaction (PCR) amplification reaction. The reaction was performed with the Phusion® High Fidelity DNA Polymerase (New England Biolabs®; Ipswich, MA) following the provided NEB Phusion® protocol and utilizing the primers listed in Table 1. For the thermocycling conditions, the initial denaturation was set at 98 ºC for 30 seconds. Next were 30 cycles of: 98 ºC for 10 seconds, 60 ºC for 30 seconds, and 72 ºC for 15 seconds. The final extension was performed at 72 ºC for 7 minutes. Gel electrophoresis was executed for conformation of the amplified gBlock™ at 120 V for 30 minutes on a 1 % agarose gel with EtBr. The amplified DNA was purified using a DNA Clean & Concentrator-100™ kit (Zymo Research®; Irvine, CA).

2.3 CRISPR-Cas editing

The pCas plasmid was first transformed into the ClearColi® electrocompetent cells using 50 ng of the pCas plasmid extracted using a ZymoPURE midiprep™ kit. These cells were then made electrocompetent by culturing in kanamycin supplemented LB broth grown at 30 ºC with shaking at 225 rpm until the OD_{600} (optical density at 600 nm) reached 0.5–0.7. For induction of the λ-Red genes present in the pCas plasmid, L-arabinose was added to a 10 mM final concentration. There were three washes performed using ice-cold 10 % glycerol. After resuspension, and a final OD600 220–250. the cells were stored at -80 °C. Next, 100 ng of the specific pTargetF plasmid and 400 ng of donor DNA were co-electroporated into the ClearColi®+pCas cells. The electroporation was performed in 1 mm cuvettes at 1.8 kV and the cells recovered at 30 °C for 1 hour at 225 rpm. Next, 150 ul of the cells were spread onto kanamycin-spectinomycin combination plates and were incubated at 30 ºC for 48 hours. A list of primer sequences used in the amplification of the *LpxM* donor DNA, construction of *LpxM* pTargetF, and conformation of the *LpxM* insertion is provided in Table 1.

Table 1. Primers used in this study.

Primer ID	Primer Type	Primer Sequence
5EC*lpxM*ctrl	Forward	ATT AAT TAA CAT CCA TTC GCA GCC G
3EC*lpxM*ctrl	Reverse	CCT ACA GTT CAA TGA TAG TTC AAC AGA TTT CG
pTargetF_F_*LpxM*	Forward	AGT CCT AGG TAT AAT ACT AGT AGC AGC TCC AGC CAA TTG ACG TTT TAG AGC TAG AAA TAG
pTargetF-N20R	Reverse	ACT AGT ATT ATA CCT AGG ACT GAG
Yp_*LpxM*.F	Forward	TCG GTT TCA CCC TCT TTC CG
Yp_*LpxM*.R	Reverse	ATT AGC TGG CAT AGG GCG TC
*LpxM*_Seq_F	Forward	GAA GCG GTT AAT CTG CTG CG
*LpxM*_Seq_R	Reverse	GGA TAA ACC AGC AGG CCG TA
*lpxM*_insert_rev	Reverse	TGG TGT AGC TGC GAC CAT GAA TTC TCT AGA GTC GAC CTG C
*LpxM*_gblock_f	Forward	GTG CAC CGG CGT AAC GCC ACT CAAAAA AAG CAC CGA CTC G
*LpxM*_gblock_rev	Reverse	TCA TGG TCG CAG CTA CAC CA
*lpxM*_gblock_f	Forward	GTG GCG TTA CGC CGG TGC AC

2.4 Growth Curve

Overnight cultures of the following strains were prepared: ClearColi® BL21 (DE3) (*LpxM* edited) in 10 ml of LB broth with 10 mM L-arabinose, and 0.5 mM IPTG at 30° C. ClearColi® BL21 (DE3) were grown in 10 mL LB broth at 37 °C. ClearColi® BL21 (DE3) (containing pCas plasmid) were grown in 10 mL LB broth at 37 °C. Lastly, BL21 *E. coli* was grown in 10mL LB broth at 37 °C. A stock was made for each strain containing 24 ul of culture and 1,176 ul of LB broth (50 mg/ml kanamycin in the edited strain and pCas stocks). In a 96 well plate, three wells in each row were filled with 300 ul of the specific strain stock and the last row was LB broth only. The plate reader was set to read every 5 minutes for 24 hours at 600 nm and 30 °C. The growth curve was repeated a second time.

3. RESULTS

3.1 Identification of key *Yersinia pestis* Lipopolysaccharide biosynthesis genes

To assess the ability to generate a novel outer membrane through synthetic biology and genome engineering, we first needed to create a roadmap of genes and biosynthetic pathways to be targeted. We first selected a reference organism to serve as the "donor" of the outer membrane structure and a second organism to serve as the "recipient", or the strain we would ultimately engineer. *Yersinia pestis* was chosen as the donor organism because *Y. pestis* is an organism of DoD relevance and has a well characterized and annotated genome and LPS structure[2-4]. We chose *E. coli* as the recipient strain to be engineered as this bacterium is well characterized, easy to work with, nonpathogenic, and genetically tractable. To better facilitate the building of an engineered *E. coli* possessing a *Y. pestis* LPS, we specifically chose a strain of *E. coli*, known as ClearColi®, which has been previously genetically modified to not produce endotoxin[5]. The ClearColi® strain is a derivative of the commonly used BL21 lab strain of *E. coli* but with successive gene deletions resulting in the inability of the strain to biosynthesize the outer membrane (Figure 2).

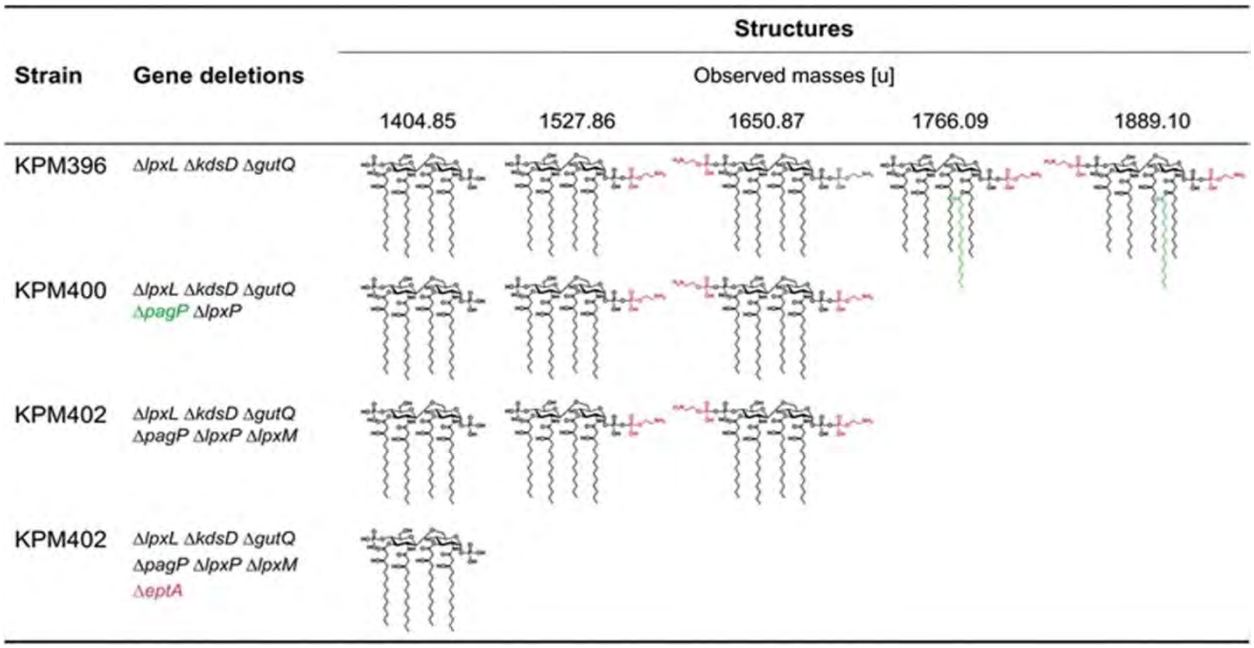

Figure 2. The outermembrane structure of the genetically engineered *E. coli* strain ClearColi®. Successive gene deletions in key LPS biosynthesis genes resulted in an *E. coli* strain with the minimal unit required for an outermembrane. This strain was known as ClearColi® serves as the scaffold strain for engineering.

Using the genetically engineered ClearColi® as a scaffold, we identified the Lipid A and core oligosaccharide genes present in the *Y. pestis* genome, which would need to be transferred to ClearColi®. Utilizing published literature, the National Center for Biotechnology Information, and the Kyoto Encyclopedia of Genes and Genomes databases, the genes and enzymatic pathways required for *Y. pestis* outer membrane biosynthesis were identified (Figure 3).

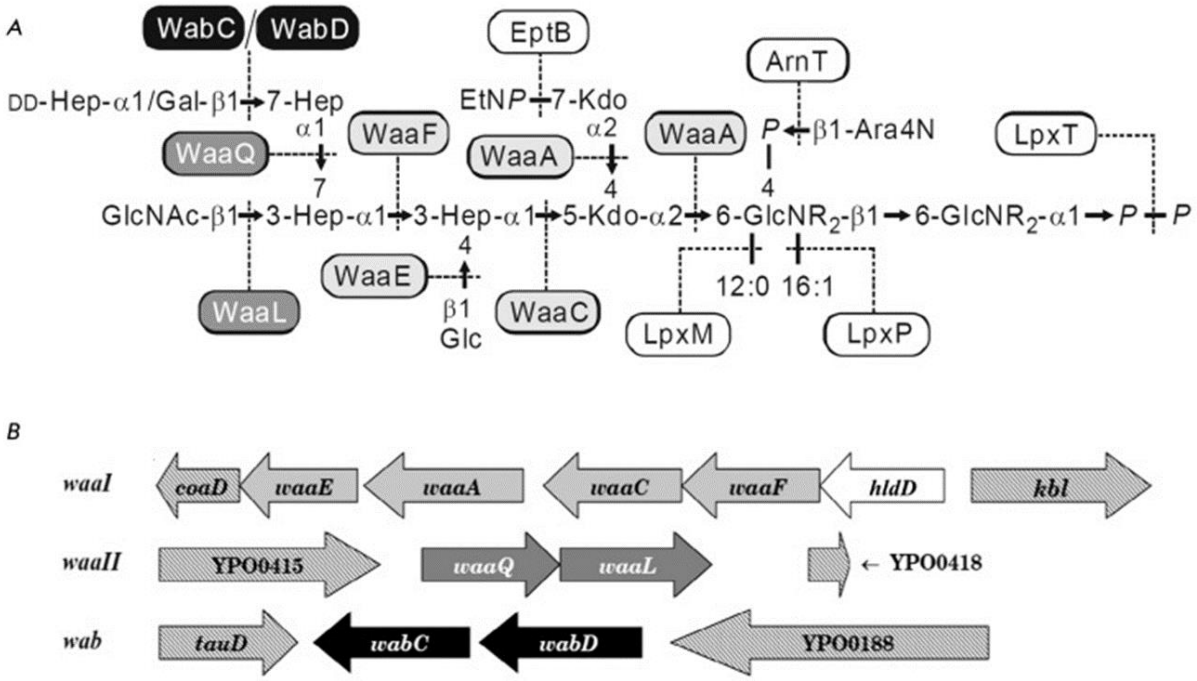

Figure 3. *Yersinia pestis* outer membrane structure and function of associated biosynthesis enzymes. A) Representation of the *Y. pestis* outer membrane including the Lipid A and Core oligosaccharide structures along with the enzymes which catalyze the various reactions. B) The genetic loci associated with core oligosaccharide biosynthesis in *Y. pestis*.

3.2 Engineering the Lipid A of *E. coli* ClearColi®

Having identified the donor organism (*Y. pestis*) and the associated outer membrane biosynthesis genes, along with our recipient ClearColi® strain, we set out to develop a method to conduct the genetic engineering. Traditional methods of gene insertions and recombineering in bacteria, while effective, can be time consuming requiring multiple cloning steps along with several iterations of recombination and plasmid curing. Recently, the implementation of CRISPR-Cas mediated genetic engineering has provided a rapid and effective tool to create site-specific insertions in bacterial chromosomes[6]. We obtained a two-plasmid system consisting of an inducible Cas enzyme and recombination proteins along with a guiding target plasmid. This system is advantageous because the donor insertion DNA can be co-transformed as a linear template, removing the need for additional cloning steps[6, 7].

The initial step in our cloning strategy was to insert the *lpxM* gene from *Y. pestis* into the cognate position of the ClearColi® genome. To ensure that the *lpxM* gene is correctly inserted, we first sequenced the ClearColi® genome to identify the flanking protospacer adjacent motif (PAM) sequences and any scar sequences remaining from the genetic engineering process. For *lpxM*, we verified the scar sequence and identified the PAM needed for the Cas enzyme recognition and the site of cleavage (Figure 4). Having confirmed the sequence on the recipient side, we next set out to design our *Y. pestis lpxM* donor DNA template. For efficient insertion of the *Y. pestis lpxM* gene, ~500 bp of flanking regions were added to either side of the gene homologous to the ClearlColi genome. These flanking regions enable the homologous recombination and insertion of the donor gene. (Figure 4).

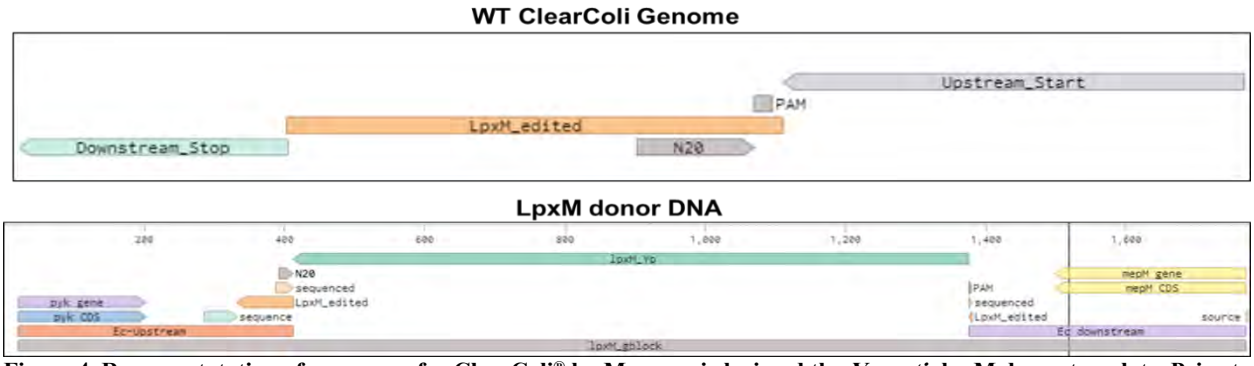

Figure 4. Representatation of sequences for ClearColi® lpxM genomic loci and the *Y. pestis* lpxM donor template. Prior to genome editing, the lpxM genomic loci in ClearColi® was sequenced to identify the scar sequence and PAM site. From this information the template DNA containing the lpxM gene from *Y. pestis* along with flanking regions was obtained.

The donor DNA was designed *in silico* and ordered as synthetic DNA from Integrated DNA Technologies as a gBlock™ which was subsequently amplified by high-fidelity PCR. Together, the donor DNA and the targeting plasmid were co-transformed into the ClearColi® strain containing the pCas recombination vector. The resulting transformants were plated on selective media to identify unique colonies which were able to successfully incorporate the *Y. pestis lpxM* gene. Following selection, only two colonies grew as potential candidates for containing the new *lpxM*. To verify successful insertion of *lpxM*, a colony PCR reaction was run on the two candidates with primers flanking the insertion site. From the colony PCR, a band corresponding to the successful insertion of *lpxM* was present for one of the two colonies screened (Figure 5). Taken together, this data confirmed that we successfully inserted the *Y. pestis lpxM* gene into the cognate genomic loci in our ClearColi® strain, resulting in the strain ClearColi:*lpxM*.

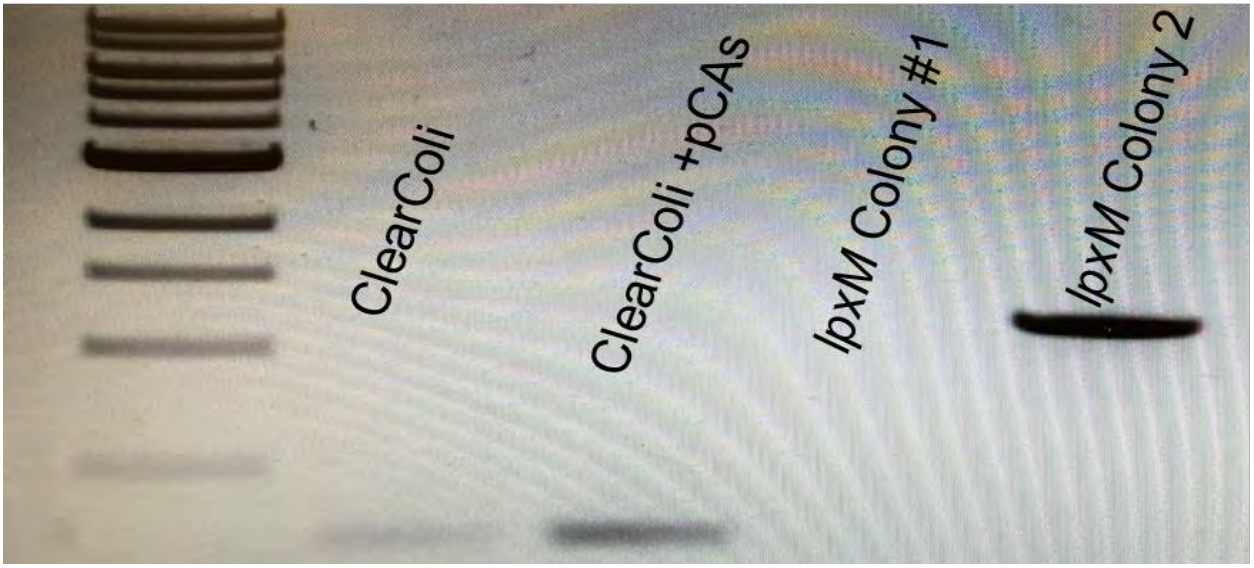

Figure 5. Colony PCR verification of *lpxM* insertion to ClearColi®. A colony PCR was conducted on the two transformants resulting from the engineering transformation with colonies flanking the insertion site.

Having verified the successful construction of ClearColi:*lpxM*, we set out to assess whether this insertion had any effects on the overall growth of the engineered strain compared to other strains of *E. coli*. A growth assay was conducted with several strains of *E. coli* in the optimal media, Luria-bertani broth, overnight to examine if there were any detrimental or beneficial effects of *lpxM* insertion. After 24 hours of growth, we found that the ClearColi:*lpxM* did not have any significant growth defects or advantages compared to the other ClearColi® strains, all of which however were defective compared to the *E. coli* BL21 parent strain (Figure 6).

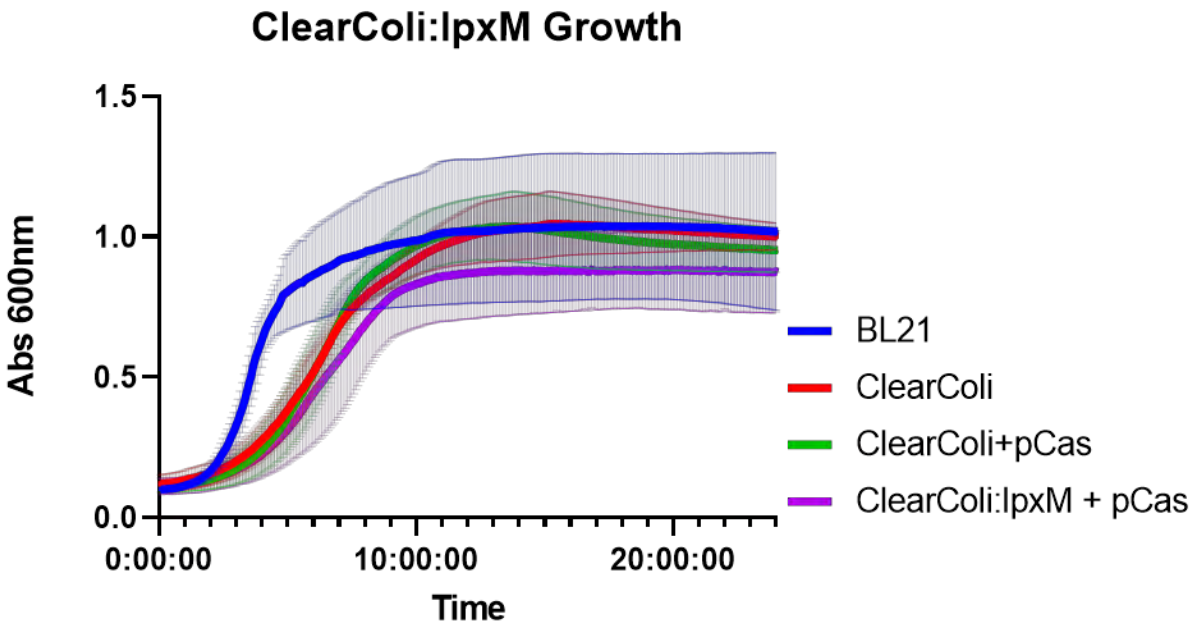

Figure 6. Growth analysis of *E. coli* strains in LB media. A growth curve was conducted in triplicate with two biological replicates. Solid lines represent mean and error bars are standard deviation.

4. CONCLUSION

Here, we describe our efforts to redesign a bacterial outer membrane through synthetic biology and rapid genome engineering. We first identified the biosynthetic pathways for LPS biosynthesis in our donor organism *Y. pestis*. These are the pathways which must be transferred and functional in our engineered strain in order to obtain the novel outer membrane. In addition, we identified and obtained our scaffold strain, which lacks an outer membrane, on which we would build out the pieces of LPS from *Y. pestis*. Finally, we demonstrated that we could successfully transfer a *Y. pestis* LPS biosynthesis gene, *lpxM*, into our donor organism, *E. coli*. Continuing work on this effort will add the biosynthesis genes in a processive manner. Along the engineering process, the outer membrane will be evaluated through biochemical and analytical methods verifying the functionality. Ultimately, this work informs the threats and benefits associated with the ability to modify and redesign bacterial membranes.

ACKNOWLEDGMENTS

Funding was provided by the U.S. Army via the In-house Laboratory Independent Research Program (PE 0601101A Project 91A) at the Combat Capabilities Development Command Chemical Biological Center.

REFERENCES

[1] Knirel, Y. A.; Valvano, M. A. *Bacterial Lipopolysaccharides: Structure, Chemical Synthesis, Biogenesis and Interaction with Host Cells*. Springer, Vienna: 2011.
Knirel, Y. A.; Anisimov, A. P. Lipopolysaccharide of Yersinia pestis, the Cause of Plague: Structure, Genetics, Biological Properties. *Acta Naturae*. **2012**, *4* (3), pp 46–58.

[2] Chandler, C. E.; Harberts, E. M.; Pelletier, M. R.; Thaipisuttikul, I.; Jones, J. W.; Hajjar, A. M.; Sahl, J. W.; Goodlett, D. R.; Pride, A. C.; Rasko, D. A.; Trent, M.S.; Bishop, R.E.; Ernst, R.K. Early evolutionary loss of the lipid A modifying enzyme PagP resulting in innate immune evasion in *Yersinia pestis. Proc. Natl. Acad. Sci. U.S.A*. **2020**, *117* (37), pp 22984–22991.

[3] Prior, J. L.; Hitchen, P. G.; Williamson, D. E.; Reason, A. J.; Morris, H. R.; Dell, A.; Wren, B. W.; Titball, R. W. Characterization of the lipopolysaccharide of Yersinia pestis. *Microb. Pathog*. **2001**, *30* (2), pp 49–57.

[4] Mamat, U.; Wilke, K.; Bramhill, D.; Schromm, A. B.; Lindner, B.; Kohl, T. A.; Corchero, J. L.; Villaverde, A.; Schaffer, L.; Head, S. R.; Souvignier, C.; Meredith, T. C.; Woodard, R. W. Detoxifying *Escherichia coli* for endotoxin-free production of recombinant proteins. *Microb. Cell Fact*. **2015**, *14* (57), pp 1–15.

[5] Jiang, Y.; Chen, B.; Duan, C.; Sun, B.; Yang, J.; Yang, S. Multigene editing in the *Escherichia coli* genome via the CRISPR-Cas9 system. *Appl. Environ. Microbiol*. **2015**, *81* (7), pp 2506–2514.

[6] Li, Q.; Sun, B.; Chen, J.; Zhang, Y.; Jiang, Y.; Yang, S. A modified pCas/pTargetF system for CRISPR-Cas9-assisted genome editing in Escherichia coli. *Acta Biochim. Biophys. Sin*. **2021**, *53* (5), pp 620– 627.

Characterization and production of the *Coxiella burnetii* specific O-antigen carbohydrate virenose in engineered *Escherichia coli*

Nathan D. McDonald[a], Erin E. Antoshak[a,b], Sarah E. Katoski[a]*
[a]U.S. Army Combat Capabilities Development Command Chemical Biological Center, Research & Technology Directorate, 5183 Blackhawk Rd, Aberdeen Proving Ground, MD 21010
[b]Excet Inc., 6225 Brandon Ave, Suite 360, Springfield, VA 22150

ABSTRACT

Coxiella burnetii, a Gram-negative bacterium and the causative agent of Q fever, is regarded as a potential biological warfare agent. Only the phase I strains of *C. burnetii* are considered pathogenic and these strains bear a unique O-antigen in the lipopolysaccharide. This O-antigen contains the carbohydrate virenose which is only found in phase I *C. burnetii* strains, making it a unique biomarker for Q fever. Despite this, the O-antigen carbohydrate virenose remains poorly understood. Virenose serves as a valuable target for detection assays as well as a potential antigen in *C. burnetii* vaccine development. While comparative proteomics analysis studies for the biosynthesis of D- or L-enantiomers of virenose *in silico* have identified a putative biosynthetic route, the complete biosynthetic pathway of virenose has yet to be experimentally determined. We hypothesize that L-virenose biosynthesis can be validated utilizing a non-native host through synthetic engineering of the predicted L-virenose pathway. Here we leverage synthetic biology to recreate the Virenose biosynthesis pathway in *Escherichia coli* and assess the ability of this engineered strain to produce the carbohydrate.

Keywords: Lipopolysaccharide, virenose, *Coxiella burnetii*

1. INTRODUCTION

The unique mechanisms of immunity and pathogenicity of *Coxiella burnetii*, the causative agent of Q fever, are not fully understood, hindering advances in early diagnosis, treatments, and the prevention of infection. Lipopolysaccharides (LPS) are a component of the outer membrane of Gram-negative bacteria and play a key role in pathogenesis. *C. burnetii's* LPS has the ability to undergo irreversible antigenic (or phase) variations defined as Phase I and Phase II strains.[1, 2] These phase variations present a unique antigen/immunogen shift that are particularly valuable for differentiating between the chronic, less infectious Phase II strain and the more acute infectious Phase I strain.[1, 2]

The outer carbohydrates of the LPS, known as O-antigens, represent the more variable section of the LPS and are implicated in *C. burnetii's* antigenic specificity.[1] The rare O-antigen carbohydrates virenose and dihydrohydroxystreptose are major virulence determinants unique to *C. burnetii.* Virenose, an O-antigen carbohydrate found only in the virulent Phase I strain of *C. burnetii*,[3] is a methylated-6-deoxyhexose and serves as a unique biomarker for the disease. Only the virulent Phase I isolates of *C. burnetii* bear this O-antigen; however, despite its uniqueness, the complete biosynthetic pathway of virenose has yet to be experimentally determined (Figure 1).

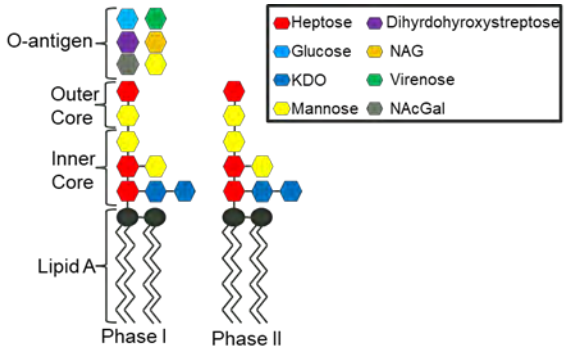

Figure 1. LPS structure of Phase I and Phase II *C. burnetii.*

Chromosomal deletion studies looking at key biosynthesis genes of Phase II isolates of *C. burnetii,* have identified nine genes predicted to be involved in the biosynthesis of virenose and dihydrohydroxystreptose.[3-5] Additionally, a study using comparative proteomics *in silico* analysis showed the biosynthesis of D- or L- enantiomers of virenose is likely comprised of five enzymatic steps and, based on the genes associated with the chromosomal changes in Phase II strains of *C. burnetii*, the pathway elucidated was most likely that of L-virenose (Figure 2).[5] We hypothesize that the putative *C. burnetii* L-virenose pathway can be synthetically engineered into *Escherichia. coli* to validate the biosynthetic pathway and provide a source of recombinant virenose.

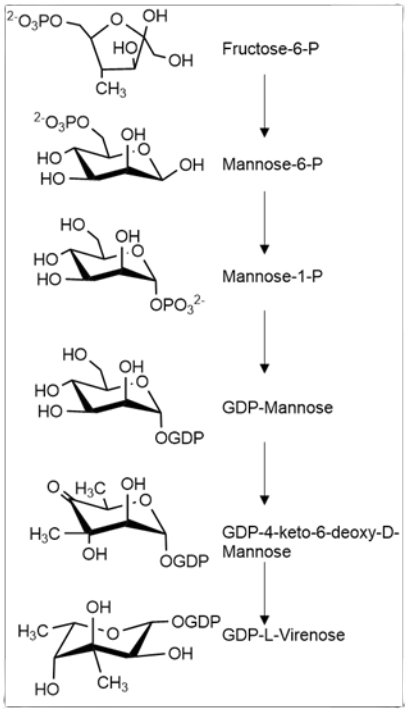

Figure 2. Predicted biosynthetic pathway of GDP-L-virenose.

The field of synthetic biology and genome engineering has facilitated the identification and characterization of biosynthetic pathways of countless molecules of interest. The ability to produce non-native products in engineering conducive organisms such as *Escherichia coli* or *Saccharomyces cerevisiae* has been described in many cases.[6, 7] Utilizing engineered biosynthesis pathways can be cost effective and are often more efficient than complex multi-step organic synthetic routes. Furthermore, many microbial species are being engineered as biofactories for the production and characterization of rare carbohydrates which can have significant applications across many fields.[7-9] Here, we leverage synthetic biology to study the biosynthesis and recombinant production of virenose. expression, optimization, purification, and validation of recombinant L-virenose will be accomplished in the host organism *E. coli*. Additionally, the putative virenose biosynthesis enzymes will be purified and independently verified for specific catalytic activity and involvement in virenose production.

2. MATERIALS AND METHODS

2.1 Obtaining and amplifying virenose biosynthesis genes

The sequence information for each of the five genes predicted to be involved in the biosynthesis of L-virenose were obtained from the National Center for Biotechnology Information database using the locus tags provided in Table 1. The sequences were codon optimized for expression in *E. coli* using the Codon Optimization tool available from Integrated DNA Technologies™ (Coralville, IA). The codon-optimized sequences were purchased as gBlocks™ from Integrated DNA Technologies™ and were routinely used as templates in polymerase chain reaction (PCR) amplification assays. The PCR assays were conducted utilizing Phusion® High Fidelity DNA Polymerase (New England Biolabs®, Ipswich. MA) per manufacturer's instructions. The thermocycling conditions for the PCR reactions were as follows: 98 °C 30 seconds, 30 cycles of 98 °C for 10 seconds, 60 °C for 30 seconds, 72 °C for 90 seconds,

and a final extension was held at 72 °C for 10 minutes. The amplified DNA was separated via gel electrophoresis run at 100 V on a 1 % agarose gel. DNA was visualized with Ethidium Bromide and UV light. The amplified PCR products were purified using a QIAquick® Gel extraction kit (QIAGEN; Germantown, MD) following the manufacturer's recommended protocol. The purified gene PCR products were used for downstream cloning procedures.

2.2 Cloning the virenose biosynthesis genes

Purified PCR gene products were used to clone into either the protein purification vector pET21-B+ or the gene expression plasmid pMGX-HK. Both the PCR products and the plasmids were digested utilizing either XhoI/NdeI for pET-21b+ or NdeI/BamHI for pMGX-HK. The restriction digest was carried out at 37 °C for 2 hours. The digested DNA products were purified following the QIAGEN QIAquick® Gel extraction kit manufacturer's protocol. The digested and purified DNA products were used for ligation reactions with T4 DNA ligase (New England Biolabs®;Ipswich, MA). The ligation reactions were carried out following the manufacturer's suggested protocol and incubated at 16 °C overnight. Following the ligation, the reactions were used to transform either *E. coli* DH5α or BL21. The transformants were validated by either restriction digest or sequencing.

2.3 Expression test for protein purification

To determine the expression levels of the virenose biosynthetic enzymes for purification, an expression test was conducted. *E. coli* transformants harboring the protein expression plasmids were grown in Overnight Express™ Instant TB Medium (Sigma-Aldrich®; St. Louis, MO) at 37 °C. Following incubation, the bacterial cultures were pelleted by centrifugation at 13,000 x g for 5 minutes. Bacterial pellets were resuspended in an equal volume of Laemmli buffer and boiled at 98 °C for 5 minutes. The samples were separated on a polyacrylamide gel and proteins were stained using the SimplyBlue™ safe stain following the manufacturer's (Invitrogen™; Carlsbad, CA) recommended protocol.

2.4 Mass spectroscopy analysis of recombinant virenose.

The E. coli strain, Bl21+pMGX_0691_0688 was grown overnight in M9 minimal media™ (Thermo Fisher Scientific®; Waltham, MA). The expression of the genes was induced via addition of isopropyl b-D-1-thiogalactopyranoside at 0.1mM. After growth, the cells were harvested and lysed via successive freeze-thaw cycles. The lysed cells were clarified via centrifugation and the clarified lysate, predicted to contain the virenose, was collected for HPLC-MS analysis. purified on the Waters preparative HPLC/MS with the method as follows: flow rate 20 mL/minute, 0.1 % formic acid in Millipure H2O as eluent A and 0.1 % formic acid in HPLC grade acetonitrile as eluent B. Inlet file (A/B): 0 minute 95/5, 4 minutes 5/95, 4.5 minutes 5/95 and 4.8–5 minutes 95/5. The product was collected based on [M-H]- ESI neg.

3. RESULTS

To test our hypothesis and attempt to fully characterize the biosynthesis pathway of virenose from *C. burnetii*, we first needed to optimize and obtain the genes encoding the predicted enzymes of the pathway. A previous study utilized a bioinformatics investigation of the *C. burnetii* genome to predict the enzymes involved in the biosynthesis of virenose.[5] This study identified several potential routes for virenose biosynthesis in *C. burnetii* with one route expected to be the most likely. This pathway is predicted to involve six enzymatic steps catalyzed by five unique enzymes (Table 1).

Table 1. Genes predicted to biosynthesize virenose.

Gene	Predicted function	Locus tag	Size (bp)
rfbA	Mannose-1-P-guanylytransferase/mannose-6-P isomerase	Cbu_0671	1433
N/A	Phosphomanomutase	Cbu_0294	1415
gmd	GDP-mannose 4,6 dehydrataase	Cbu_0689	1046
N/A	Methyltransferase	Cbu_0691	1238
wcaG	GDP-L-Fucose synthase	Cbu_0688	998

In our attempt to recapitulate virenose biosynthesis in a non-native host, we chose to test the function of these five enzymes. Previously we obtained the DNA sequence for five genes from the National Center for Biotechnology Information database and chose standard lab *E. coli* as the non-native host to evaluate virenose biosynthesis. After successfully obtaining the optimized genes from *C. burnetii*, we utilized two approaches to characterize their potential role in virenose biosynthesis. Our first approach is to assemble each of the genes into a polycistronic operon under the control of a single inducible promoter that functions in *E. coli* (Figure. 3). 9

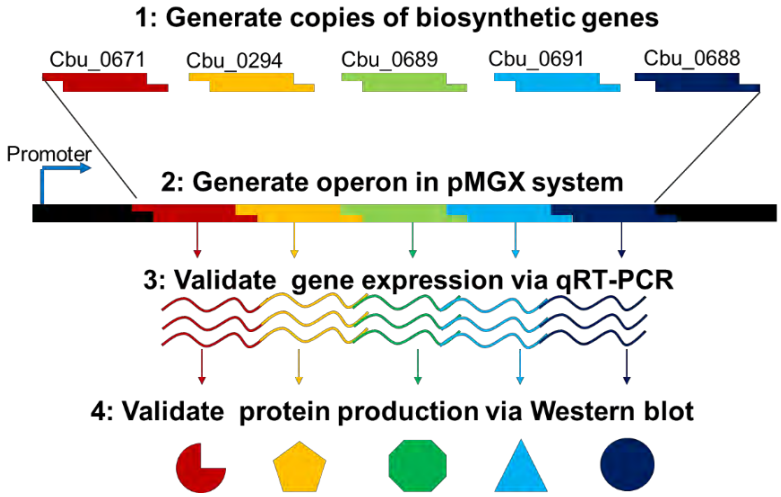

Figure 3. Generating virenose biosynthetic pathway operon workflow.

We utilized a previously described plasmid system which has been used to characterize biosynthetic pathways.[9] The five genes were cloned individually into the pMGX-HK vector with the goal of systemically cloning the individual genes into a single operon. PCR analysis confirmed that we successfully ligated the Methyltransferase (CBU_0691) and GDP-L-Fucose synthase (CBU_0688) genes into our plasmid; however, we failed to validate the construct via protein expression of an intermediate product (Figure 4).

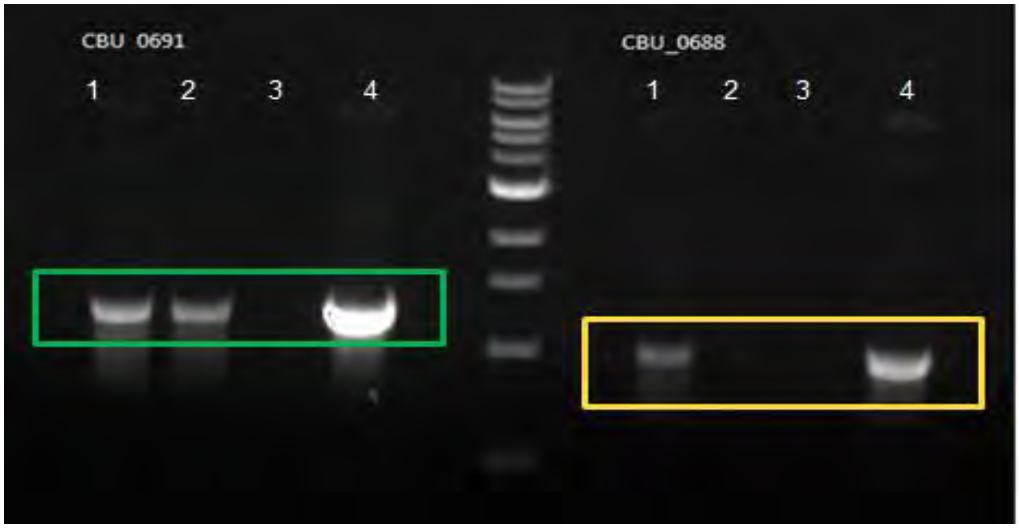

Figure 4. Confirmation of individual genes by PCR and gel analysis.

Having successfully generated the inducible construct containing the genes CBU_0691/CBU_0688 we could next screen our *E. coli* strain for virenose biosynthesis. While our construct only contains two of the five genes predicted in the virenose biosynthesis pathway, these two genes are expected to be specifically required for the biosynthesis. Because of this, we predicted that expression of these two genes could hijack the common intermediates of hexose biosynthesis in *E. coli*, specifically GDP-4-keto-6-deoxy-mannose. The engineered *E. coli* strain was grown in minimal media to remove background interference from the culture conditions and the cells were lysed, releasing any recombinantly produced virenose prior to HPLC/MS analysis. Evaluation with mass spectrometry further confirmed that our engineered strain was not expressing masses that correspond to virenose GDP or virenose.

The extracted ion chromatographs (Figure 5) illustrate our intermediate construct has the identical mass spectrometry pattern of that to our negative control sample.

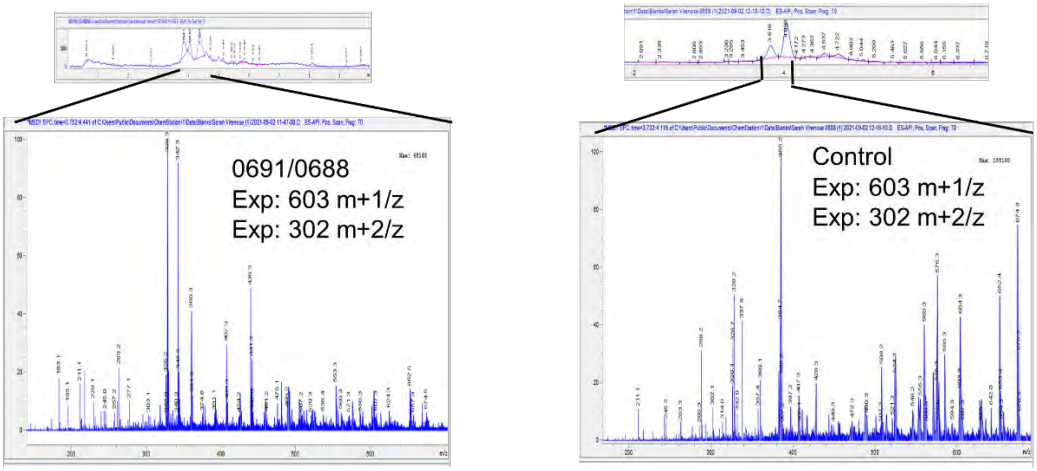

Figure 5. Ion chromatographs of the intermediate and control.

Our second approach to determine if the *C. burnetii* enzymes can catalyze virenose biosynthesis was to evaluate the function of each enzyme *in vitro*. Purifying each of these enzymes and assessing the functions *in vitro* allows us to determine the role in virenose biosynthesis outside of the context of the non-native host background. The five genes were individually cloned into the protein expression vector pET-21b+ which also includes a 6x-histidine tag on the proteins necessary for affinity chromatography. After generating the constructs, we tested the expression of the proteins prior to the purification (Figure 6).

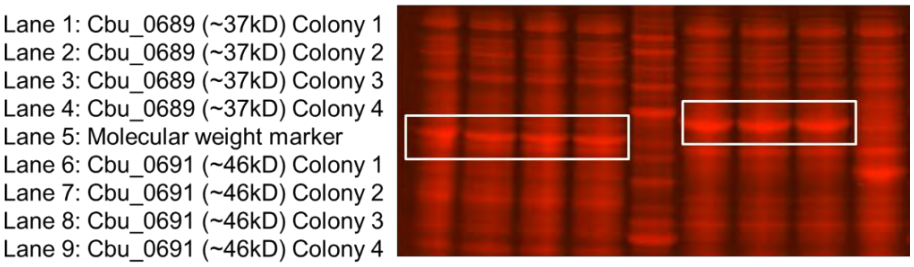

Figure 6. Representative expression test of Cbu_0689 and Cbu_0691.

Initially, the proteins expressed well; however, when the cultures were scaled up for IMAC protein purification and enzyme characterization, the product yields and concentration were insufficient to evaluate activity. Future work will be focused on implementing alternative purification tags and purification conditions to increase the solubility and decrease the non-specific binding of off-target proteins.

4. CONCLUSION

C. burnetii poses a threat to our nation and warfighters abroad. It is important to combat *C. burnetii* on two fronts—detection and prevention. Because the LPS is such a critical aspect of *C. burnetii* pathogenesis, it is important to gain a better understanding of the biology of the LPS biosynthesis. As a unique and key component of the phase I *C. burnetii* LPS, virenose has the potential to serve a marker for detection and as an antigen for vaccine development. Here, we set out to recreate the biosynthesis pathway of virenose in *E. coli* to understand how this key carbohydrate is produced. We successfully obtained codon optimized genes for encoding the enzymes predicted to be required for virenose production in *C. burnetii*. These genes were transferred to a specialized expression vector designed for generating biosynthesis operons for characterization. Future work will focus on assembling each of the genes into a single expression vector to screen for virenose production in *E. coli*. In addition, we demonstrated that we could express the virenose biosynthesis enzymes to fully characterize the mechanism of the pathway. The ability to assess the purified enzymes *in vitro* is an essential component of understanding the biology of virenose and *C. burnetii* pathogenesis. The future of this work will include enzymatic assays to assign function to the enzymes of interest.

The use of bacterial carbohydrates and antigens for vaccines has been successfully implemented for a number of dangerous pathogens, demonstrating the utility of this approach.[10] Recent work has focused on developing carbohydrate-based vaccines for antibiotic resistant bacteria, in particular, because of the increased challenges of treating infections.[10] This is pertinent to *C. burnetii* as Q fever can be difficult to treat by traditional antibiotics. Further demonstrating the need for *C. burnetii* vaccine development is the negative side effects associated with current products available.[11] Currently, the Q fever vaccine Q-VAX® (Seqirus™; Maidenhead, UK) is approved for use in Australia for workers at particularly high risk of *C. burnetii* exposure. Unfortunately, this vaccine comes with severe systemic side effects when vaccinated individuals had previously been exposed to *C. burnetii* and developed immunity. The vaccine-associated side effects require patients to be prescreened for immunity prior to vaccination, which is costly, time consuming, and not feasible on a large scale. A carbohydrate-based vaccine for *C. burnetii* may eliminate these off-target effects resulting in an immunization which can be made widely available. An additional benefit of characterizing virenose biosynthesis is the utilization of the carbohydrate for developing handheld detection assays for the warfighter. The current detection strategies are based on phase II *C. burnetii* strains which lack the outer O-antigen and are non-pathogenic.[12] Having an antigen-based detection platform against virenose will provide a specific and sensitive readout allowing for rapid responses from warfighters and enhanced decision making abilities.

ACKNOWLEDGMENTS

Funding was provided by the U.S. Army via the In-house Laboratory Independent Research Program (PE 0601101A Project 91A) at the Combat Capabilities Development Command Chemical Biological Center.

REFERENCES

[1] Abnave, P.; Muracciole, X.; Ghigo, E. Coxiella burnetii Lipopolysaccharide: What Do We Know? *Int.l J. Mol. Sci.* **2017**, *18* (12), pp 2509.
[2] Hackstadt, T. Antigenic variation in the phase I lipopolysaccharide of Coxiella burnetii isolates. *Infect. Immun.* **1986**, *52* (1), pp 337–340.
[3] Beare, P. A.; Jeffrey, B. M.; Long, C. M.; Martens, C. M.; Heinzen, R. A. Genetic mechanisms of Coxiella burnetii lipopolysaccharide phase variation. *PLoS Pathog.* **2018**, *14* (3), e1006922.
[4] Toman, R.; Škultéty, L. T.; Ftáček, P.; Hricovíni, M. NMR study of virenose and dihydrohydroxystreptose isolated from Coxiella burnetii phase I lipopolysaccharide. *Carbohydr. Res.* **1998**, *306* (1–2), pp 291–296.
[5] Flores-Ramirez, G.; Janecek, S.; Miernyk, J. A.; Skultety, L. *In silico* biosynthesis of virenose, a methylated deoxy-sugar unique to Coxiella burnetii lipopolysaccharide. *Proteome Sci.* **2012**, *10* (67).
[6] Keasling, J. D. Synthetic biology and the development of tools for metabolic engineering. *Metab. Eng.* **2012**, *14* (3), pp 189–195.
[7] Li, Z.; Gao, Y.; Nakanishi, H.; Gao, X.; Cai, L. Biosynthesis of rare hexoses using microorganisms and related enzymes. *Beilstein J. Org. Chem.* **2013**, *9* (1), pp 2434–2445.
[8] Granström, T. B.; Takata, G.; Tokuda, M.; Izumori, K. Izumoring: A novel and complete strategy for bioproduction of rare sugars. *J. Biosci. Bioeng.* **2004**, *97* (2), pp 89–94.
[9] Hassan, M. I.; Lundgren, B. R.; Chaumun, M.; Whitfield, D. M.; Clark, B.; Schoenhofen, I. C.; Boddy, C. N. Total Biosynthesis of Legionaminic Acid, a Bacterial Sialic Acid Analogue. *Angew. Chem.* **2016**, *55* (39), pp 12018–12021.
[10] Astronomo, R. D.; Burton, D. R. Carbohydrate vaccines: developing sweet solutions to sticky situations? *Nat. Rev. Drug Discovery.* **2010**, *9* (4), pp 308–324.
[11] Zhang, G.; Samuel, J. E. Vaccines against Coxiella infection. *Expert Rev. Vaccines.* **2004**, *3* (5), pp 577–584.
[12] Wegdam-Blans, M.C.A.; Wielders, C.C.H.; Meekelenkamp, J.; Korbeeck, J.M.; Herremans, T.; Tjhie, H.T.; Bijlmer, H.A.; Koopmans, M.P.; Schneeberger, P.M. Evaluation of commonly used serological tests for detection of Coxiella burnetii antibodies in well-defined acute and follow-up sera. *Clin. Vaccine Immunol.* **2012**, *19* (7), pp 1110–1115.

Deep learning for the prediction of experimental spectra

Patrick C. Riley[a]*, Samir V. Deshpande[a], Brian S. Ince[a], Ruth Dejere[b], Kyle P. O'Donnell[b], Brian C. Hauck[a]
[a]U.S. Army Combat Capabilities Development Command Chemical Biological Center, Research & Technology Directorate, 8198 Blackhawk Rd, Aberdeen Proving Ground, MD 21010
[b]Science & Technology Corporation, 21 Enterprise Pkwy, Suite 150, Hampton, VA 23666

ABSTRACT

A supervised deep neural network model's training data set directly impacts its generalization to other similar devices. Often, a large sum of data must be collected at great expense and time to achieve a deep neural network to classify or approximate a given training data set. A mature chemical detection technology— such as the ion-mobility spectrometry-based Joint Chemical Agent Detector—has an existing large data set from the development of alarm algorithms intended to alert soldiers of the presence of hazardous chemicals. Alarm algorithms require that instruments and environmental impacts to peak behavior are captured such that the detectors alert as intended when used in complex operating environments. Here, the design of a theoretical long short-term memory framework is presented that considers both instrument parameters and molecular properties to simulate the chemistry of an ion mobility spectrometry technology for which it was trained and to predict experimental spectra. This network, by accounting for these sources of variance traditionally measured in laboratories, can simulate additional data, reducing the cost and time needed to developed alarm algorithms for ion-mobility spectrometry-based detectors or provide a method for reducing cost in the development of future chemical detection technologies.

Keywords: deep neural network, machine learning, ion-mobility spectrometry, false alarm reduction

1. INTRODUCTION

Ion-mobility spectrometry (IMS)-based chemical detectors are frequently used for the detection of explosives, toxic industrial compounds, and chemical warfare agents (CWAs).[1] These detectors rely on a library of statistically determined peak positions for the identification of potentially hazardous chemicals. Fielded IMS technology is not the only analytical instrumentation that relies on library searches for the presumptive identification of spectral data. In all cases, the development of these spectral libraries can take years of data collection across several instruments and various environmental conditions. Machine learning (ML) has been shown to be useful in the development of algorithms for identification, by designing classification models from preexisting data libraries.[2,3,4]

However, several challenges exist concerning the quantity and quality of data in preexisting libraries that were developed without ML in mind. To address limitations in the quantity of data, models can be developed that utilize synthetically generated data. In IMS, work has been done to synthetically generate the collision cross section (CCS) value of an ion to reduce false positives in metabolite identification.[5,6] The CCS value is a physiochemical property of an ion and is the basis for the separation of ions in IMS, as larger molecules have an increased chance of collision with the drift gas. CCS is defined in equation 1, where e is the elementary charge, N is the drift gas number density, μ is the reduced mass of the ion-neutral pair, k is Boltzmann's constant, T is the neutral drift gas temperature, and K is the mobility of the ion (not normalized against standard pressure and temperature),

$$\Omega = \frac{3e}{16N}\left(\frac{2\pi}{\mu kT}\right)^{1/2}\left(\frac{1}{K}\right). \quad (1)$$

While CCS is a powerful predictor of ion separation, the reduced mobility value (K_0) is used to describe the behavior of an ion within an IMS detector. K_0 is calculated by measuring the time it takes ions to travel a discreet path within an electric field and a carrier gas. This discreet path in the instrument is referred to as the drift region and the time it takes for ions to travel in the drift region is referred to as the drift time (t_d). The K_0 value of the ions is calculated from

the t_d of the ion, the path length of the drift region (L), the applied voltage (V), temperature (T), and pressure (P) of the drift gas, as shown in,

$$K_0 = \frac{L^2}{Vt_d}\left(\frac{273.15}{T}\right)\left(\frac{P}{760}\right). \quad (2)$$

Equation 2 and previous work has demonstrated that the K_0 of a specific chemical in a given IMS instrument is dependent upon temperature, pressure, water content, and manufacturing variance. This variance in K_0 or peak position in IMS instrumentation will subsequently increase the size of an alarm region for a specific chemical, as shown in Figure 1.[7,8] Work has been done to decrease the size of this region by using highly accurate K_0 values to calibrate IMS instrumentation, reducing variance in measured peak position. These K_0 values were acquired using the accurate ion mobility instrument (AIMI) which is a one-of-a-kind world instrument designed with the explicit purpose of obtaining the most accurate K_0 values with an error of 0.001.[9]

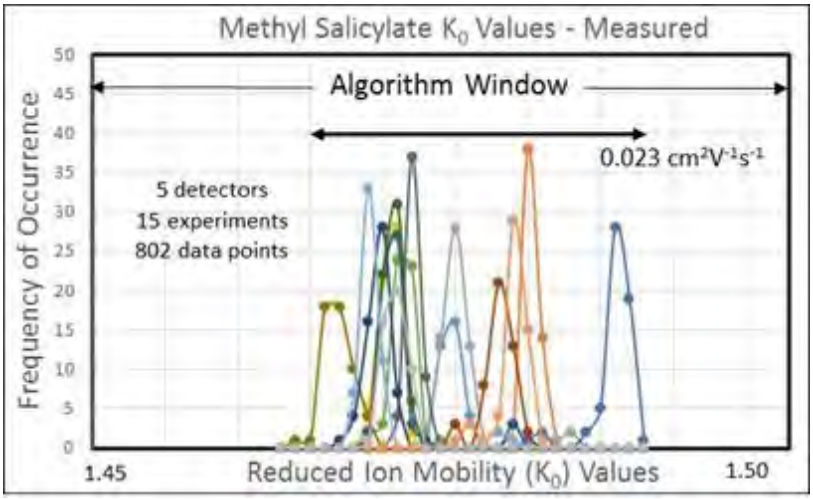

Figure 1. Variance in peak position of methyl salicylate across multiple detectors and conditions.

To acquire highly accurate K_0 values on AIMI, a large number of man hours is required to obtain values of potential calibrants at numerous conditions for each compound. This challenge of collecting data for research and development purposes is not limited to the AIMI data set. Often, other low throughput analytical techniques have limited data, or experimental data is limited given the nature of specific compounds. For instance, the size of data sets pertaining to CWA's or other toxic chemical research is often limited given the number of laboratories and researchers capable of performing the dangerous work. The relationship between AIMI and improving IMS alarm algorithms is connected to improving false alarm rates for CWAs in fielded IMS systems. This relationship further exacerbates the potential expense and time in collecting accurate IMS data.

2. METHODS

2.1 Data set

Two training data sets were acquired and curated for two IMS instruments: AIMI and a Joint Chemical Agent Detector (JCAD). AIMI uses a drift cell with the stacked-ring design capable of measuring the variables affecting K_0 values to ± 0.1 % accuracy. The JCAD is an ambient air drift tube IMS intended to be used in the presumptive identification of CWA and TIC vapors in non-laboratory conditions. All chemicals used for the two training data sets were obtained from Sigma-Aldrich® (St. Louis, MO). Dimethyl methylphosphonate (DMMP), di-*tert*-butylpyridine (D*t*BP), and triethyl phosphate (TEPO) were obtained as 97 %, 97 %, and 99.8 % pure standard, respectively. Di(propylene glycol) monomethyl ether (DPM), was obtained as a 99% pure standard consisting of a mixture of isomers.

All AIMI training data was collected in the positive ion detection mode and a time-of-flight mass spectrometer (Ionwerks™, Inc.; Houston, TX) was used to mass identify all mobility peaks. Two different ionization sources were used for data collection—a ^{63}Ni ionization source for DMMP and a corona ionization source for all other chemicals. The training data for the JCAD was collected for both the positive ion and negative ion detection mode simultaneously.

Unlike AIMI, the JCAD is equipped with two drift cells that operate in tandem allowing for the dual collection. However, the JCAD is not equipped with a mass spectrometer and is incapable of mass identification of mobility peaks.

Table 1 provides the total spectra counts for both AIMI and the JCAD across the four chemicals and none. Data are labeled none when there is only reactant ion peak (RIP) and no other relevant peaks. From AIMI, a total of 111, 87, 83, 89, and 0 data points were collected for DMMP, DtBP, TEPO, DPM, and none respectively. The total data collected for the JCAD was 103,177, 54,568, 216,885, 26,199, and 230,258 for DMMP, DtBP, TEPO, DPM and none, respectively. The low throughput of AIMI meant calibrant spectra were prioritized over collection of clean background data. Thus, while background spectra were collected for AIMI, they are traditionally not collected in quantities useable for ML-related modeling.

Table 1. Total spectra count for both AIMI and the JCAD across the four chemicals and none.

Chemical	Spectra Counts per IMS	
	AIMI	JCAD
DMMP	117	103177
DtBP	83	54568
TEPO	89	216885
DPM	87	26199
None	N/A	230258

2.2 Feature selection

The two training data sets were separated into two spectra categories, instrument parameters and molecular properties (IP/MP). A total of 32 features considered IP/MP were initially selected for each chemical compound from the AIMI data set. The 32 features were down selected to 14 to prevent overfitting of the data and decrease model run time. Several highly correlated features were determined to be sources of bias due to their discreet nature. For example, pressure P (torr) was considered an instrument parameter; but, as a feature, had two discreet values across the four chemicals collected. This occurred during data collection when DMMP was collected at high altitude and the other three compounds at sea level. The final correlation matrix of the selected features is shown in Figure 2, where features ending in _1, _2, or _3 represent a feature specific to the reactant ion peak, monomer peak, or dimer peak, respectively.

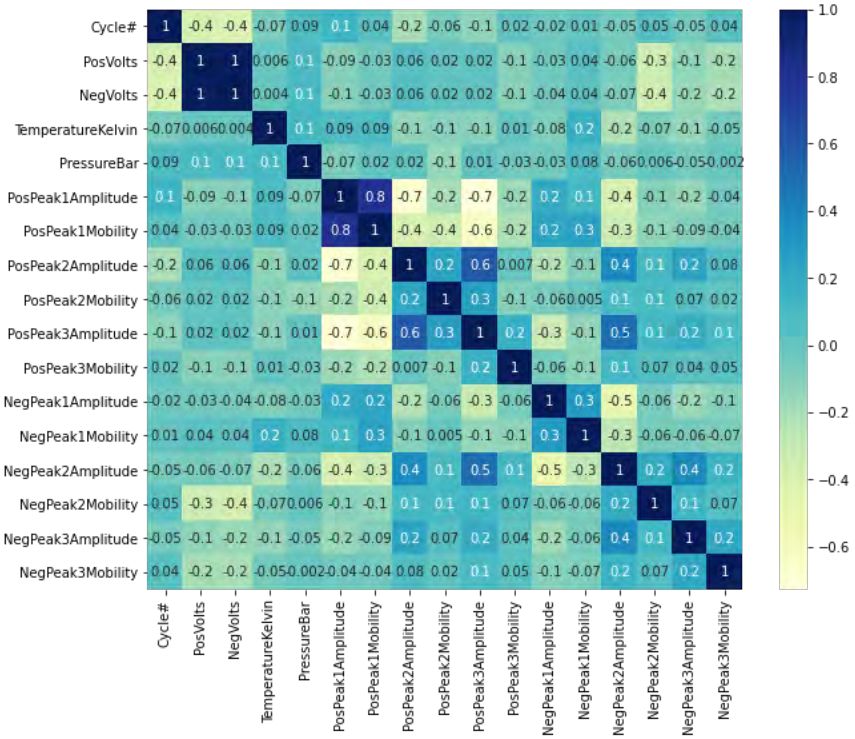

Figure 2. Final correlation matrix of the selected features.

The second set of training data sets were composed of spectral bins, where each spectral bin represents the total signal measured at a single drift time or K_0 value if corrected. Thus, spectral bins are represented as a K_0 (x coordinate) and the amplitude (y coordinate). Figure 3 provides a typical IMS spectrum showing the Gaussian shape of three typical IMS peaks, the reactant ion peak (RIP) the monomer peak, and the dimer peak, shown as peak 1, 2, and 3, respectively.

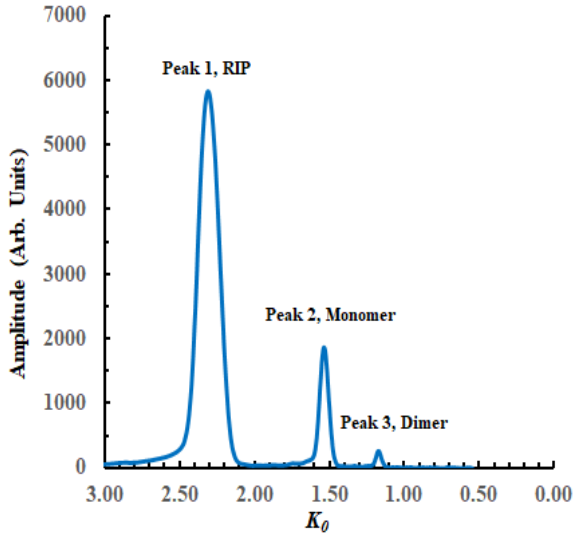

Figure 3. Example IMS spectrum depicting RIP, monomer, and dimer, as Peak 1, Peak 2, and Peak 3, respectively.

Each IMS detector can report a different number of spectral bins, where the AIMI spectra contain a total of 1,500 features, representing spectral bins composed of a measured signal amplitude. The JCAD spectra contains 1,021 features, representing signal amplitude. JCAD spectra were trimmed to 839 features to remove noise that appears at the start of each spectrum, corresponding to a K_0 range of 3.0 to 0.5.

2.3 Models

Three different ML algorithms were used to train classification models and evaluate the predictive power of the training data sets; Random Forest (RF), a deep feedforward network or multi-layered perceptron (MLP), and a type of recurrent neural network (RNN), long short-term memory (LSTM). When used in classification, RF is an ensemble technique that uses multiple decision trees to provide the mode of the labels. Figure 4 shows an example of a RF where a class is selected based on the output of a number of decision trees, where Class B would be the final selected label.

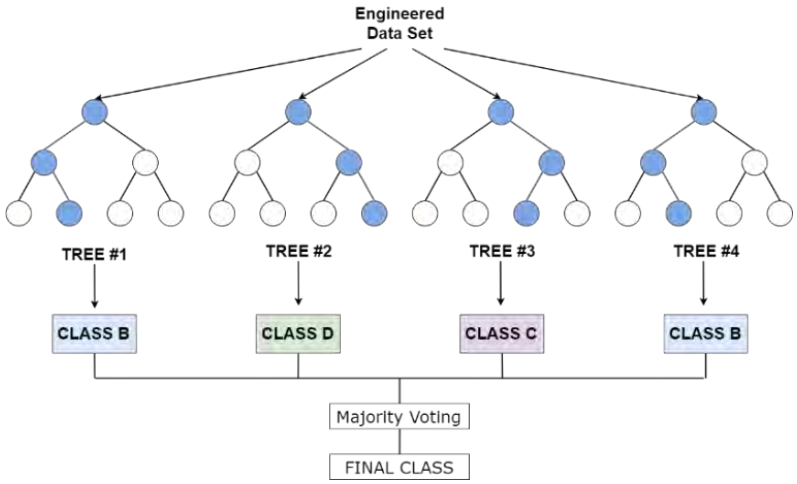

Figure 4. Random Forest Classification example diagram depicting 4 trees with 3 different class labels predicted.

RF has been shown to provide high accuracy for data set sizes similar to the AIMI training set and provides interpretability through feature importance.[10,11] Feature importance is a measurement of how powerful a specific

feature was in predicting the target label. When assessing the feature importance of a classification model, the default method utilizes Gini importance or mean decrease in impurity.[12,13]

When used for classification, MLP's are a type of artificial neural network that uses the function $y = f^*(x)$ to map some number of inputs x to y. Figure 5 shows densely connected MLP's composed of an input layer, at least two hidden layers, and an output layer. [14,15]

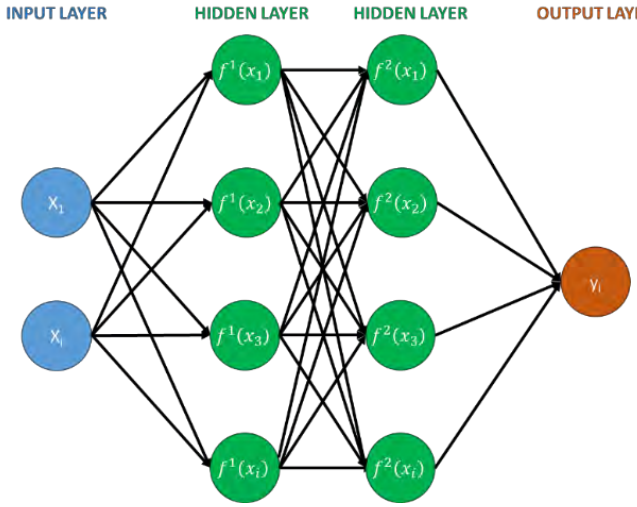

Figure 5. Diagram of simple 4 layer neural network containing 2 hidden layers, an input layer, and an output layer.

This MLP is considered densely connected since all inputs map to each node, forming a chain of functions. The MLP, being one of the simplest neural networks, provides a baseline performance on the predictive power of the features selected in the training data set.

The final model used to evaluate the predictive power of the features is LSTM. LSTM is a type of RNN. RNN's, as opposed to the MLP discussed above, have feedback connections that allow for an internal state memory which is excellent in predicting temporal behavior.[16,17] LSTM is used as opposed to RNN's because of a vanishing gradient problem. Where the gradient, or the change of the output with respect to the inputs, is extremely small causing weights at various nodes to not update. When the weights of the nodes stop updating, the model's error or loss cannot decrease stopping the learning process. LSTM solves the vanishing gradient by using a series of gates as shown in Figure 6 to update the internal state memory, decoupling it from the hidden layers making the cell's internal memory more stable.

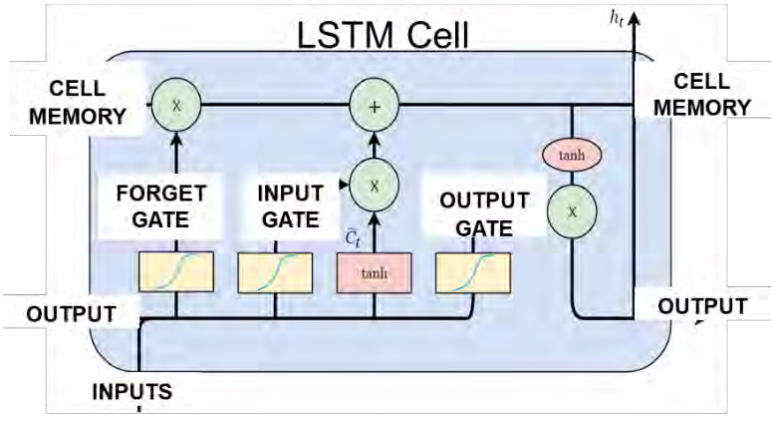

Figure 6. LSTM memory cell diagram showing flow of operations.

Ion behavior of an individual spectrum is inherently temporal, and spectra are often collected continuously, which makes LSTM well suited for predicting the behavior of an IMS system. However, spectra are not necessarily collected continuously and may be collected in a non-continuous manner. Utilizing both, MLP and LSTM, to investigate the feature's predictive power helps assess the impact of this temporal and non-continuous behavior of the data on prediction.

2.4 System specifications

All modelling and data processing was performed on a Lambda Labs Quad desktop equipped with Ubuntu 18.04 LTS operating system, Intel®Core™ i-9-9820X CPU, and 2 NVIDIA® GeForce® RTX 2080 Ti GPUs. The code was written in Python version 3.6, running in Jupyter Notebook 6.1.0. Key data processing software used was NumPy 1.18.1 and pandas 1.0.5. Data modeling was performed using scikit-learn 0.23.1, TensorFlow 2.3.0, and Keras 2.4.3. Lastly, figure generation performed in the above software packages was done with Matplotlib 3.2.2 and seaborn 0.10.1.

2.5 RF feature selection

All modelling and data processing was performed on a Lambda Labs Quad desktop equipped with Ubuntu 18.04 LTS operating system, Intel®Core™ i-9-9820X CPU, and 2 NVIDIA GeForce RTX 2080 Ti GPUs. The code was written in Python version 3.6, running in Jupyter Notebook 6.1.0. Key data processing software used was numpy 1.18.1 and pandas 1.0.5. Data modeling was performed using scikit-learn 0.23.1, tensorflow 2.4.1, and Keras 2.4.3. Lastly figure generation performed in the above software packages was done with matplotlib 3.2.2 and seaborn 0.10.1.

3. RESULTS

3.1 Impact of data set size on accuracy

RF, MLP, and LSTM classification algorithms were trained using the IP/MP feature set and spectral bin feature set to predict the class label. Table 5 shows a selection of hyper-parameters used for each model and the corresponding accuracy of each.

Table 2. Classification accuracy of RF, MLP, and LSTM for each detector across two feature sets.

Classification Accuracy for DPM, DMMP, TEPO, DtBP, and None					
Data Type	**Instrument**	**Number of Data points (total, train/test)**	**RF (score)**	**MLP (train/val/test accuracy)**	**LSTM (loss,acc)**
Ins/Mol	AIMI	(370, 296/74)	1.0000	(0.3136, 0.2500, 0.3378)	(1.3321, 0.4223)
Spectra	AIMI	(370, 296/74)	0.99331	(1.0000, 1.0000, 1.0000)	(0.0128, 0.9967)
Ins/Mol	JCAD	(631087, 503903/127184)	0.94352	(0.6844, 0.6824, 0.6844)	(0.8160, 0.6762)
Spectra	JCAD	(631087, 315543/315544)	0.91054	(0.8672, 0.8561, 0.8580)	(0.1589, 0.9427)

The resulting classification models used here test data set size versus total features on model accuracy. Regardless of the size of the data set, accuracy was improved with LSTM by changing the feature space to raw spectral bins. Due to the variance in

3.2 RF model feature importance calculation

The results of the classification models indicated that training a model on instrument parameters and molecular properties is challenging in the absence of any spectral features. To select the smallest number of features, a random forest classifier was trained, and feature importance was used down select the fewest features. The calculation of feature importance can be used to rank a particular feature when the model makes a classification providing interpretability of the model. The default measurement of feature importance in RF classification is mean decrease impurity or Gini importance. Gini importance is calculated by the frequency (f_i) of a label (i) at a node, given a number of unique labels (C), as shown in

$$\sum_{i=1}^{C} f_i(1 - f_i). \tag{3}$$

However, when features of high cardinality are used in training a RF classifier, Gini importance has been shown to often incorrectly assign importance to features based on domain knowledge.[18,19] When dealing with features of high cardinality for a time-series data set, permutation feature importance should be used to obtain a more accurate representation of true feature importance. Permutation feature importance in scikit-learn is defined as the relationship between the decrease in a model's score and the shuffling of a random feature value. This computation can be performed agnostic of the model and was permutated 10 times per feature. Figure 7a shows the top 25 features as determined by Gini importance, and Figure 7b shows the top 25 features as determined by permutation importance. The results demonstrate that Gini importance selected for features in a simple descending order, while permutation importance selected a wide variety of features.

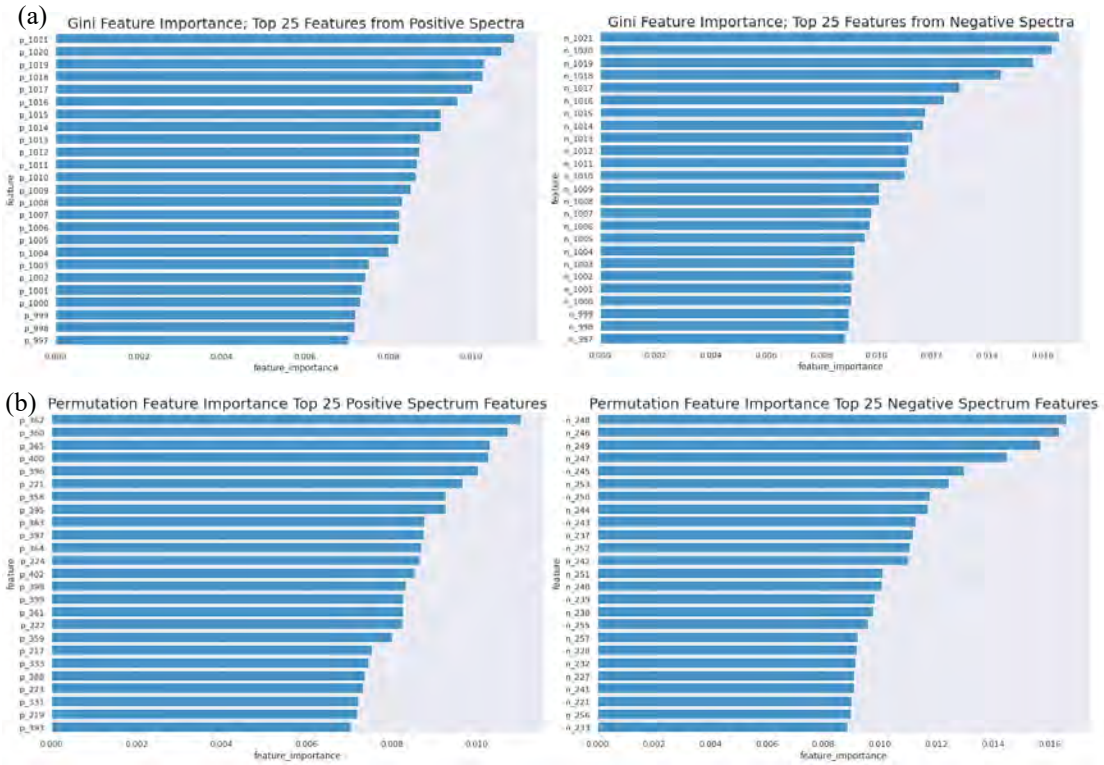

Figure 7. Gini (a) and Permutation (b) feature importance for the top 25 features from the positive and negative detection modes.

Further examination of the permutation importance on a spectrum of DPM demonstrates that permutation selected features match subject matter knowledge by selecting for the RIP and monomer regions before the dimer and trimer regions, as shown in Figure 8.

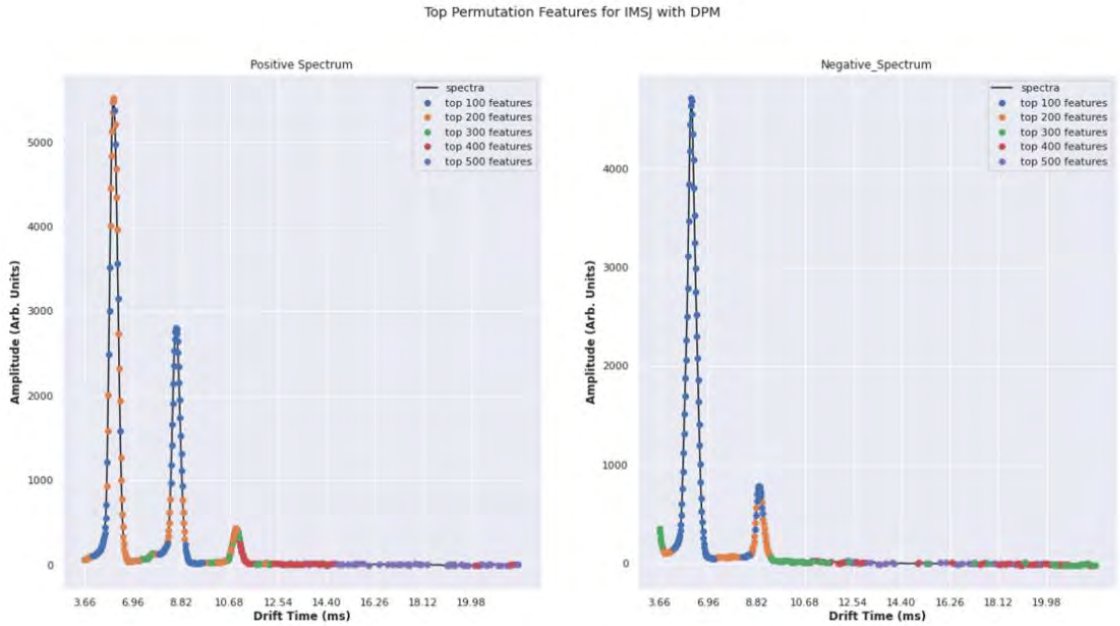

Figure 8. DPM positive and negative mode spectra displaying the RF permutation-based drift time bin selection for the first 100, 200, 300, 400, and 500 features in blue, orange, green, red, and purple, respectively.

3.3 Spectral prediction

A combination of features for temperature, pressure, calculated K_0 values for the three largest peaks, and spectral features were used to train an LSTM model to predict spectrum amplitude at a given drift time per chemical. Where peak 1, peak 2, and peak 3 correspond to the K_0 value for the RIP, monomer, and dimer, respectively. The resulting loss, accuracy, and F1 score calculated from the test data set for the various trained models is shown in Table 3. Here, accuracy is misleading, as amplitude can vary greatly, meaning when compared to the true positive of a given spectrum the amplitude will often be wrong. Since the number of potential predicted values is high and there is a balance between wanting a false positive and false negative prediction, F1 provides a more intuitive measure of how well

Table 3. List of Loss, Accuracy, and F1 scores for various models trained using a combination of IMS parameters and Spectral Features.

IMS Parameters	Spectral Features	Loss	Accuracy	F1
All	50	30026.2051	0.3584	0.9218
No Temp	50	39187.3516	0.3128	0.9460
No Pressure	50	39085.7030	0.3292	0.9565
No Temp/Pressure	50	46471.0938	0.3109	0.9487
No Peak 3	50	31119.5742	0.3441	0.9993
No Peak 2	50	41437.5820	0.3113	1.0261
No Peak 1	50	31209.5918	0.3589	0.9679
No Peak 1,2,3	50	34835.0000	0.3290	1.0152
None	50	53048.0000	0.2563	1.0052
All	40	30243.5273	0.3597	0.9513
All	30	36629.6992	0.3141	0.8149
All	20	37684.0547	0.2940	0.9818
All	10	55883.2109	0.2065	1.0405

ACKNOWLEDGMENTS

We would like to thank the U.S. Army Combat Capabilities Development Command Chemical Biological Center In-house Laboratory Independent Research Program (PE 0601101A Project 91A) and Defense Threat Reduction Agency, Research and Development Directorate, Chemical and Biological Technologies Department (CB10874) for funding this work. In addition, we wish to thank Charles 'Steve' Harden, Ph.D., (STC) for his subject matter expertise in IMS, Mr. Vince M. McHugh (retired DEVCOM CBC) and Chia-Wei Tsai, Ph.D. (DTRA RD-CBI) for their technical guidance, and Trish P. McDaniel, Ph.D. (DEVCOM CBC) for her program and technical support of this project.

REFERENCES

Examples:

[1] Eiceman, G.A.; Stone, J.A. Peer Reviewed: Ion Mobility Spectrometers in National Defense. *Anal. Chem.* **2004**, *76* (21), pp 390A–397A.

[2] Bell, S.; Nazarov, E.; Wang, Y.F.; Eiceman, G.A. Classification of ion mobility spectra by functional groups using neural networks. *Anal. Chim. Acta.* **1999**, *394* (2-3), pp 121–133.

[3] Riley, P.C.; Deshpande, S.V. *Machine learning based spectral interpretation in chemical detection*; Artificial Intelligence and Machine Learning for Multi-Domain Operations Applications, International Society for Optics and Photonic, **2019**; p 110061X.
[4] Torres-Tello, J.; Guaman, A.V.; Ko, S-B. Improving the Detection of Explosives in a MOX Chemical Sensors Array with LSTM Networks. *IEEE Sens. J.* **2020,** *20* (23), pp 14302–14309.
[5] Zhou, Z.; Shen, X.; Tu, J.; Zhu, Z.J. Large-Scale Prediction of Collision Cross-Section Values for Metabolites in Ion Mobility-Mass Spectrometry. *Anal. Chem.* **2016**, *88* (22), pp 11084–11091.
[6] Meier, F.; Köehler, N.D.; Brunner, A.D.; Wanka, J.M.H.; Voytik, E.; Strauss, M.T.; Theis, F.J.; Mann, M. Deep learning the collisional cross sections of the peptide universe from a million experimental values. *Nat. Commun.* **2021**, *12* (1), p 1185.
[7] Eiceman, G.A.; Karpas, Z. Hill, H.H. *Ion mobility spectrometry*. CRC press: 2005.
[8] Hauck, B.C.; Davis, E.J.; Clark, A.E.; Siems, W.F.; Harden, C.S.; McHugh, V.M.; Hill Jr., H.H. Determining the water content of a drift gas using reduced ion mobility measurements. *Int. J. Mass Spectrom.* **2014**, *368*, pp 37–44.
[9] Hauck, B.C.; Harden, C.S.; McHugh, V.M., Current status and need for standards in ion mobility spectrometry. *Int. J. Ion Mobility Spectrom.* **2018,** *21* (4), pp 105–123.
[10] Ho, T.K. *Random decision forests*, Proceedings of 3rd International Conference on Document Analysis and Recognition, IEEE: **1995**; pp 278–282.
[11] Breiman, L. Random Forests. *Machine Learning.* **2001,** *45* (1), pp 5–32.
[12] McKinney, W. *Data Structures for Statistical Computing in Python*, Proceedings of the 9th Python in Science Conference, Austin, TX: **2010**; pp 51–56.
[13] Pedregosa, F.; Varoquaux, G.; Gramfort, A.; Michel, V.; Thirion, B.; Grisel, O.; Blondel, M.; Prettenhofer, P.; Weiss, R.; Dubourg, V.; Vanderplas, J.; Passos, A.; Cournapeau, D.; Brucher, M.; Perrot, M.; Duchesnay, É. Scikit-learn: Machine Learning in Python. *J. Mach. Learn. Res.* **2011**, *12* (85), pp 2825–2830.
[14] Abadi, M.; Agarwal, A.; Barham, P.; Brevdo, E.; Chen, Z.; Citro, C.; Corrado, G.S.; Davis, A.; Dean, J.; Devin, M.; Ghemawat, S.; Goodfellow, I.; Harp, A.; Irving, G.; Isard, M.; Jia, Y.; Jozefowicz, R.; Kaiser, L.; Kudlur, M.; Levenberg, J.; Mane, D.; Monga, R.; Moore, S.; Murray, D.; Olah, C.; Schuster, M.; Shlens, J.; Steiner,B.; Sutskever, I.; Talwar, K.; Tucker, P.; Vanhoucke, V.; Vasudevan, V.; Viegas, F.; Vinyals, O.; Warden, P.; Wattenberg,M.; Wicke, M.; Yu, Y.; Zheng, X. TensorFlow: Large-Scale Machine Learning on Heterogeneous Distributed Systems. *arXiv preprint arXiv:1603.04467* **2016**.
[15] Abadi, M.; Barham, P.; Chen, J.; Chen, Z.; Davis, A.; Dean, J.; Devin, M.; Ghemawat, S.; Irving, G.; Isard, M.; Kudlur, M.; Levenberg, J.; Monga, R.; Moore, S.; Murray, D.G.; Steiner, B.; Tucker, P.; Vasudevan, V.; Warden, P.; Wicke, M.; Yu, Y.; Zheng, X. *TensorFlow: A System for Large-Scale Machine Learning*, 12th {USENIX} symposium on operating systems design and implementation ({OSDI} 16), **2016**; pp 265–283.
[16] Hochreiter, S.; Schmidhuber, J. Long Short-Term Memory. *Neural Comput.* **1997**, *9* (8), pp 1735–1780.
[17] Liu, J.; Zhang, J.; Luo, Y.; Yang, S.; Wang, J.; Fu, Q. Mass Spectral Substance Detections Using Long Short-Term Memory Networks. *IEEE Access.* **2019**, *7*, pp 10734–10744.
[18] Menze, B.H.; Kelm, B.M.; Masuch, R.; Himmelreich, U.; Bachert, P.; Petrich, W.; Hamprecht, F.A. A comparison of random forest and its Gini importance with standard chemometric methods for the feature selection and classification of spectral data. *BMC Bioinf.* **2009**, *10* (1), pp 1–16.
[19] Louppe, G.;Wehenkel, L.;Sutera, A.;Geurts, P. Understanding variable importances in forests of randomized trees. *Advances in neural information processing systems 26.* **2013**.

This page intentionally left blank

Effect of quorum sensing molecules on the morphology of bacterial nanocellulose biofilms

Rabih E. Jabbour[a*], Hany F. Sobhi[b] Hyeonggon Kang[b]

[a]U.S. Army Edgewood Chemical Biological Center, Research & Technology Directorate, 5183 Blackhawk Rd, Aberdeen Proving Ground, MD 21010

[b]Coppin State University, Center for Organic Synthesis, Department of Natutral Sciences, Baltimore, MD, 21216

ABSTRACT

Bacterial nanocellulose produced by several bacterial species, including *Gluconacetobacter xylinus*, is a promising versatile material with unique physiochemical properties with potential applications in medicine, defense, electronics, optics, and food. Bacterial nanocellulose has several advantages over plant cellulose, including high purity and crystallinity, large surface area, durability, and biocompatibility. While advantageous in many ways, bacterial nanocellulose materials can be difficult to manufacture and process into useable forms. In many instances, bacterial nanocellulose pellicles are not uniform in their composition which is often due to the heterogeneity of cell density that leads to large clusters of dense cellular growth. The aim of this research proposal is to study the mechanism of quorum sensing (QS) molecules, specifically homoserine lactones, and their effect on the production of bacterial nanocellulose utilizing a synthetic biology approach. We hypothesize that the bacterial nanocellulose morphology can be controlled through manipulation of the QS pathways of the bacterium. In the third and final year of this effort, we investigated the effect of different concentrations of signaling molecules on the morphological parameters of the bacterial cellulose biofilm. The resulted data showed that there is a direct correlation between the concentration of the QS molecules introduced during growth phase and the morphological properties of the bacterial nanocellulose films produced. The morphological studies were performed with scanning electron microscope and atomic force microscopy. These experimental data provided a direct testing of the hypothesis that signal molecules directly contribute to the formation and to the morphological properties of the bacterial cellulose biofilm.

Keywords: Bacterial nanocellulose, quorum sensing, homoserine lactones, scanning electron microscopy, atomic force microscopy, morphology

1. INTRODUCTION

Bacterial nanocellulose (BNC) is a unique biofilm with promising multifunctional properties in various applications including tissue engineering, medicine, defense, food, fabrics, and electronics. Nanocellulose can be obtained from two main sources: plants and bacteria (mainly from the *Gluconacetobacter* bacterial genus). However, the plant-based nanocellulose material is energetically costly and laborious to manufacture. Additionally, while the small rod-like structures can be used in the production of thin films and other materials, the physical properties of the materials are often reduced compared to that of the bacterial-based ones that has superior chemo-physical properties over the plant nanocellulose.

BNC is formed at the air media interface of active *Gluconacetobacter xylinus* cultures. BNC nanofibers are synthesized from glucose units by *Acetobacter* cellulose synthase operon proteins and secreted by forming an interconnected cellulose "pellicle" around cells.[1-3] BNC pellicles are comprised of long cellulose fibrils that intertwine with another and are highly free from other chemical compounds, i.e., lignin and pectin. Because of their physical properties, BNC films often demonstrate a higher strength and flexibility than plant-based films.[4] BNC can also be easily modified and functionalized through genetic engineering and/or

synthetic biology approaches.[5-11] However, BNC materials can be difficult to manufacture and process into useable forms due to bacteria growth conditions and changes in bacterial behavior during production stage of the biofilm which can result in non-uniform pellicles. This is often due to heterogeneity of cell density which often leads to large clusters of dense cellular growth. While methods have been developed to circumvent some of these BNC production issues, pellicle abnormalities and irregularities are still encountered and a streamlined protocol that controls the fibril density, mechanical properties of the film, or rate of production has not been developed to date.

Homoserine lactones (HSLs) are QS molecules that enable bacterial cells to communicate with one another and regulate replication, growth, and behavior of their community. HSLs consist of various acyl side chain of 4-14 carbon atoms and may also contain double bonds. The carbon chain of homoserine lactones can be hydroxylated or oxidized to a carbonyl-carbon; resulting in different physicochemical properties. Homoserine lactones are the most common QS signals in Gram-negative bacteria and coordinate important temporal events more specifically the formation of biofilms in nature and in human[12-13]. There is little regarding the correlation between the bacterial cellulose production, fibril density, pellicle thickness, in response to different HSL QS molecules. As such we will address vital questions related to the impact of the QS signals of the HSL on the morphological properties of the bacterial cellulose. Understanding the effect HSL as a signaling molecule has on the production of BNC is vital to producing desired biofilms that can be utilized in various applications. To understand the effect signaling molecules have on the production of the BNC, we need to determine the surface characterization of the BNC produced after altering the type and concentration of the homoserine lactone molecules present. The surface characterization will provide relevant information to develop customized methods to produce specific BNC with specific morphological properties.[18-20] The final year of this study will investiage the effect of adding different HSL signaling molecules at different concentrations to the bacterial growth media. Various concentrations of the HSL molecules were utilized, and samples were collected from each experimental condition. Subsequent morphological analyses showed that different signaling molecules affected the structural uniformity of the BNC film. The cellulose fibrils thickness, structure, and distribution were also correlated to the type and concentration of the signaling molecules used during the growth phase. The results showed that there is a direct correlation between the utilized HSL acting as QS, molecules and the morphological properties of the produced BNC biofilms.

2. MATERIALS AND METHODS

2.1 Bacterial strains

The ATCC 10245 *Gluconacetobacter xylinus* strain (Manassas, VA) was used to produce BNC. The *G. xylinus* strain was cultured in Hestrin and Schramm medium (HS medium) with 2 % glucose (wt/vol). The stock bacterial culture was added to the 10 mL of HS media in 50-mL conical tubes and was grown at 27 ºC for 3-7 days depending on the amount of biofilm formation. The growth was done under static culture in which no agitation of the culture broth was performed. Once the bacterial cellulose biofilm is formed it was removed for further processing and characterization.

2.2 Cellulose production and purification

The bacterial cellulose was formed after approximately 72 hours of bacterial growth. The formation of bacterial cellulose occurred in static culture after cells were grown in 50 mL conical tube containing 10 mL of HS medium at 27°C for 3-7 days. The cellulose pellicles were then isolated and purified by treating them with 0.5% NaOH at 100 ºC for 1 hour, followed by extensive washing with milliQ-H_2O to remove the excess NaOH solution and reduce the pH to between 4–5. Following the water wash, the pellicles were dried out at 30 ºC for 24 hours and then weighed on an analytical balance. The mass obtained was normalized to include the culture volume used during the growth stage to compare the different yields of

the pellicles based on the different homoserine lactones studied. Pellicles who are cleaned but not processed were kept in 0.1M sodium azide solution.

2.3 Analysis of surface morphology of BNC biofilm by SEM and AFM

Scanning electron microcopy (JSM 7100F, Jeol USA, Inc) and Atomic Force Microscopy (NT-MDT) were both utilized for the surface morphology analysis of the various cellulose samples. Cellulose samples were coated with ~ 2 nm of gold using a sputtering method to reduce charging and beam damage effects from the electron beam of the SEM instrument. The SEM beam energy was set to 5 kV to obtain the images. Energy Dispersive Spectroscopy (EDS, JED-2300) was used to determine the elemental content of the analyzed materials.

AFM images were obtained by securing each on an AFM holder using a carbon tape and was taken in semi-contact mode using a silicon cantilever and visualized using Topography and Mag modes. The Mag image is the amplitude of oscillation of the cantilever. The two images clearly show the structures of the cellulose samples. The images were obtained in various scan regions.

3. RESULTS AND DISCUSSIONS

3.1 Effect of homoserine lactones (HSLs) on the morphology of BNC biofilms

Three different HSL molecules were added to different batches of growth media inoculated with *G. xylinus.* BNC biofilms were subsequently produced in each growth condition, collected, and processed for morphological analysis using SEM. SEM provides useful morphological information about the potential 2D-spatial variation due to the presence of different HSLs and was used to determine any changes in the BNC fiber diameter and distribution. Four different pellicle samples were analyzed, three of which were produced in the presence of HSL signaling molecules with one produced in the absence of any HSL molecule as a control. Figure 1 shows a comparison between the control-BNC, N-Decanoyl-DL-homoserine lactone (DHL)-BNC fibers, N-Dodecanoyl-L-homoserine lactone (DDHL)-BNC, and N-(3-Oxododecanoyl)-L-homoserine lactone (ODDHL)-BNC fibers through different magnifications. There is variability in the structure and diameter size for the pellicles when comparing the control to the HSLs modified fibers. The control cellulose is more uniformly distributed throughout the sample relative to DDHL-BNC fibers (Figures 1A-C, 1G-I). The DDHL-BNC fibrils are are structurally deformed relative to the control. This deformity could be the result of the DDHL molecules disrupting the formation mechanism of the cellulose fibrils. The DDHL-BNC fibrils are high non-uniformity cellulose fibers and have high porosity compared to the control-BNC samples. Investigating the in-depth projections of these BNC fibrils showed that the DDHL-BNC fibrils had more layers than that of the control-BNC samples and within the same layer the width of the fiber diameter has more variation in the DDHL-BNC sample. The SEM data are important for utilizing BNC fibrils in applications that require high porosity including filtration and sample extractions. It is noteworthy that the DDHL-fibrils have less water capacity than the control-BNC ones and this observation was noticed during the sample processing in which the sample was weighed wet and dry to determine their respective water holding capacity.

There is variability in the structure, diameter, and distribution of the pellicles when comparing the control and ODDHL-BNC fibers. The cellulose in the control sample was less uniformly distributed compared to the ODDHL-BNC fibers. The ODDHL-BNC fibrils are well formed and tightly packed with high density of BNC fibers in the field of view relative to the control-BNC images. The ODDHL-BNC fibers were better-formed, less structurally deformed compared to the DDHL-BNC fibers. The ODDHL-BNC fibrils showed less porosity and higher fiber density as compared to that of the control-BNC or the DDHL samples. Investigating the in-depth projections of these BNC fibrils layers showed that the ODDHL-BNC fibrils are distributed in more closely packed layers compared to the control-BNC fibrils with more spatial separation on the Z-axis projection and with significant difference in density of fibrils. The SEM data are

important in terms of utilizing such ODDHL-BNC fibrils in applications that require high fibril density, more uniformity and less porosity such as electronic display circuitry and sensing applications.

Figures 1a-c and 1d-f show a comparison between the control-BNC and the N-Decanoyl-DL-homoserine lactone (DHL)-BNC fibers. There is variability in the structure and diameter of the pellicles when comparing the control to the DHL-BNC fibers. In Figure 1a, the untreated cellulose was less uniformly distributed compared to the DHL-treated BNC fibers (Figure 1d). The DHL-BNC SEM image showed well formed, tightly packed fibrils compared to the control-BNC SEM images. The DHL-BNC fibrils have similar morphology compared to ODDHL-BNC fibers, with the former having more uniformity and less variability in the fiber morphology when considering fiber width, thickness, and distribution. The DHL-BNC were observed to be well-formed and more structural uniform as observed with the ODDHL-BNC. The DHL-BNC fibrils showed uniform porosity and higher fiber density as compared to that of the control-BNC samples. Investigating the in-depth projections of these BNC fibrils showed that the DHL-BNC fibrils are distributed in closed packed layers as compared to the control-BNC fibrils that have more spatial separation on the Z-axis projection and with significant difference in the density of fibrils in various layers. The SEM data are important in terms of utilizing such DHL-BNC fibrils in applications that require high fibril density, more uniformity and less porosity such as electronic display circuitry, wearable sensor and detection technologies. Finally, the average diameter of the control and DDHL-BNC fibers was calculated using the SEM analysis software. These measurements showed that the average diameter of the ODDHL-BNC (42.2 nm) sample was slightly larger than the control-BNC (34.1 nm) sample (Figure 2). It should be noted that the DHL-BNC fibrils were the most uniform in terms of fiber diameter and, unlike the other HSL molecules, the DHL-BNC showed better fiber integrity and formation.

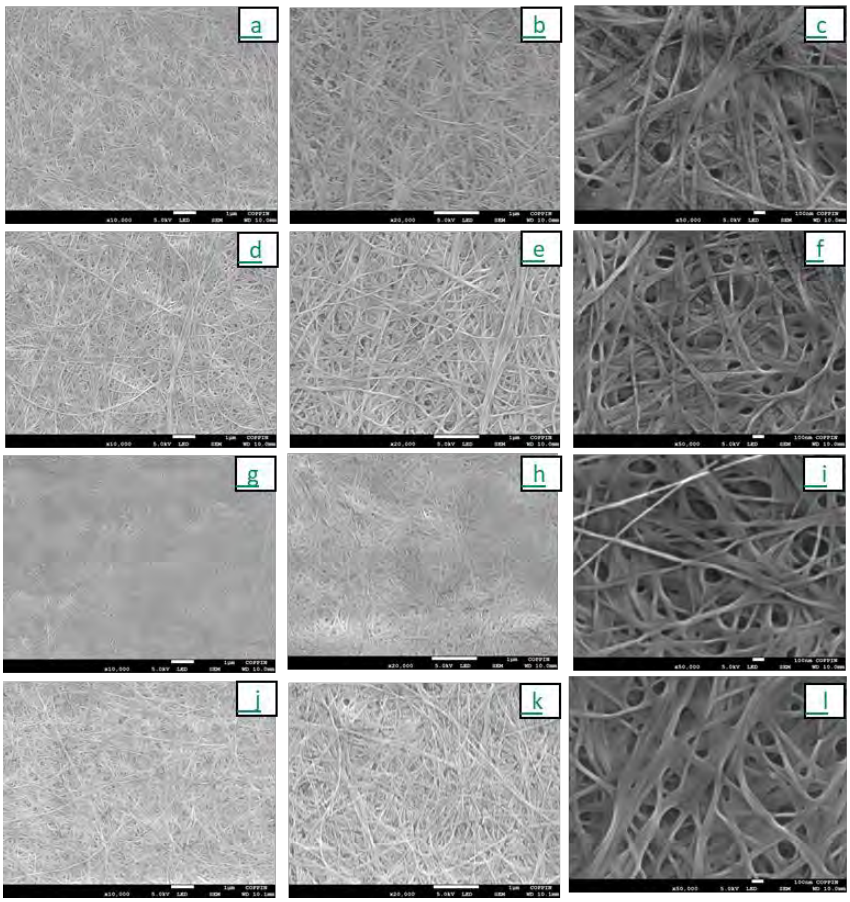

Figure 1. Morphological images of cellulose produced in the presence of various homoserine lactones. Harvested BNC fibers were visualized using SEM at three different magnifications (10,000 x, 20,000 x, and 50,000 x): Untreated, control cellulose fibrils (a-c), DHL-treated cellulose fibrils (d-f), DDHL-treated BNC fibrils (g-i), and ODDHL (j-l).

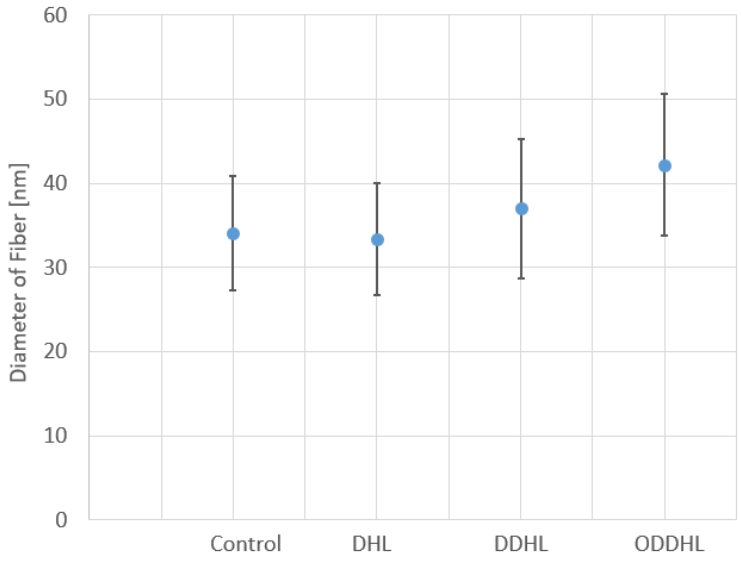

Figure 2. Average diameter of untreated BNC fibers compared to BNC fibers treated with DHL, DDHL, and ODDHL

Comparing SEM data for all HSLs used in the production of the BNC fibrils in these experiments showed that HSLs affect the formation and the morphological properties of the BNC pellicles. The HSLs' effect on the morphological properties of the BNC pellicles varied based on the molecule used, the DHL-BNC fibrils had the best morphological properties compared to other HSLs, namely the ODDHL- and DDHL-BNC fibrils. One common effect among the three HSLs used was the enlargement of the fiber average diameter as compared to that of the control-BNC samples (Figure 2). The average diameter of the ODDHL-BNC (42 nm) sample was higher than that of the control-BNC (34 nm). While this explanation is based on experimental morphological data, further genomic and mechanistic investigations of the factors affecting the enlargement of the pellicle in the presence of HSLs are needed. Future experiments will address the impact of genetic materials responsible for the secretion of HSLs and how such factors can impact the formation of BNC pellicles on molecular level. Overall, the SEM data showed that the presence and type of HSLs present during the bacterial growth phase play a role in the morphology and mechanism of formation of BNC pellicles that can go on to be utilized for various applications. Comprehensive surface characterization of BNC pellicles isolated from different HSLs growth conditions are vital steps to produce tailored biofilms that can have multifunctional properties. For example, DHL-BNC fibrils showed a well uniform layers of BNC fibers with the most uniform distribution in diameter sizes compared to other HSLs. Hence DHL-BNC fibril can be utilized with application that requires uniformity and ruggedness of the biofilm, such as electronic, food, drug delivery and sensing technologies. While other HSLs produced BNC fibrils with different morphology with properties that can be utilized for applications other than the mentioned one in the DHL-BNC example.

Atomic Force Microscopy (AFM) experiments have been initiated to understand the 3D-spatial variation of the pellicle morphology. These experiments will provide 3D images of the morphological changes and help to determine if these changes are a direct result of the presence of HSLs in the growth media of *G. xylinus*. Figure 3 shows a Mag mode image and the topography of each cellulose sample obtained by AFM. The Mag image is the amplitude of oscillation of the cantilever. The two images show the structure of the cellulose sample and allow us to measure the width of the cellulose fibers. The images were obtained in various scan regions. The images shown in Figure 3 are obtained in 5 μm × 5 μm areas from the 256 × 256 scan points. Details of the surface structure of nanocellulose fibers at the nanometer scale were observed in the topology and Mag mode images. Based on the AFM topography images, the roughness was calculated. In the roughness measurement, the DHL-BNC fibrils showed a little high roughness value compare to the control and the DDHL BNCs, but the values are in the range of the error bar and the less formed fibril structure may affect the low roughness value.

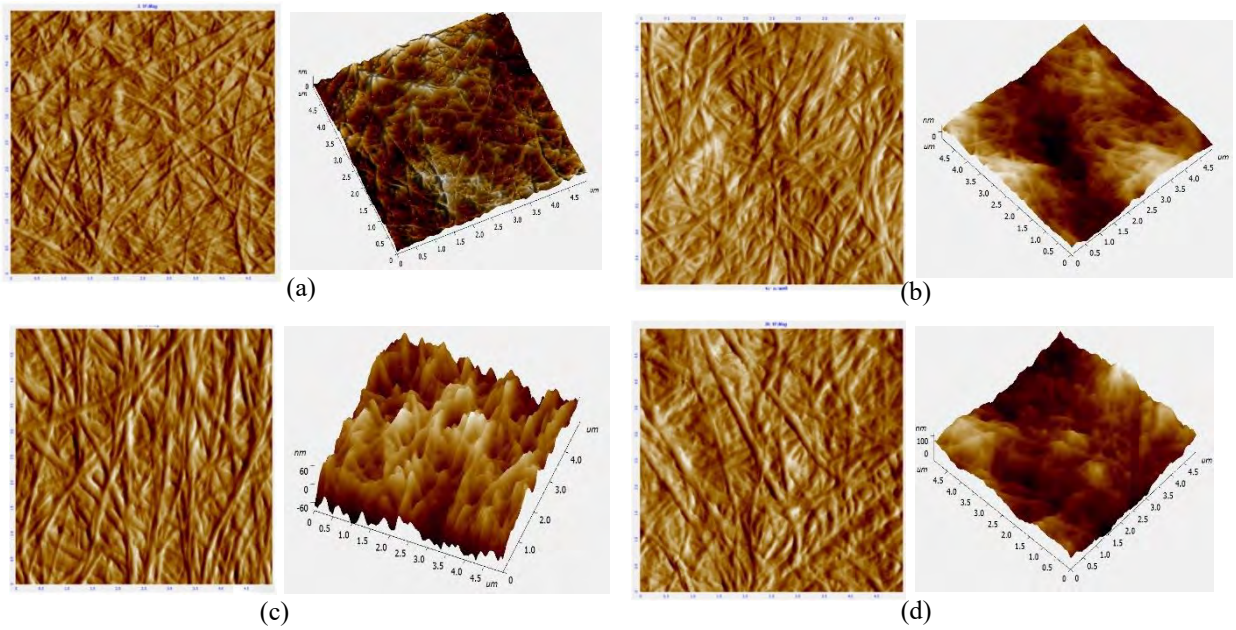

Figure 3. AFM images for the BNC samples (a)AFM image in Mag mode and 3D topography for Control. (b) AFM image in Mag mode and topography for DHL(c) AFM image in Mag mode and 3 D topography for DDHL. (d) AFM image in Mag mode and 3 D topography for ODDHL.

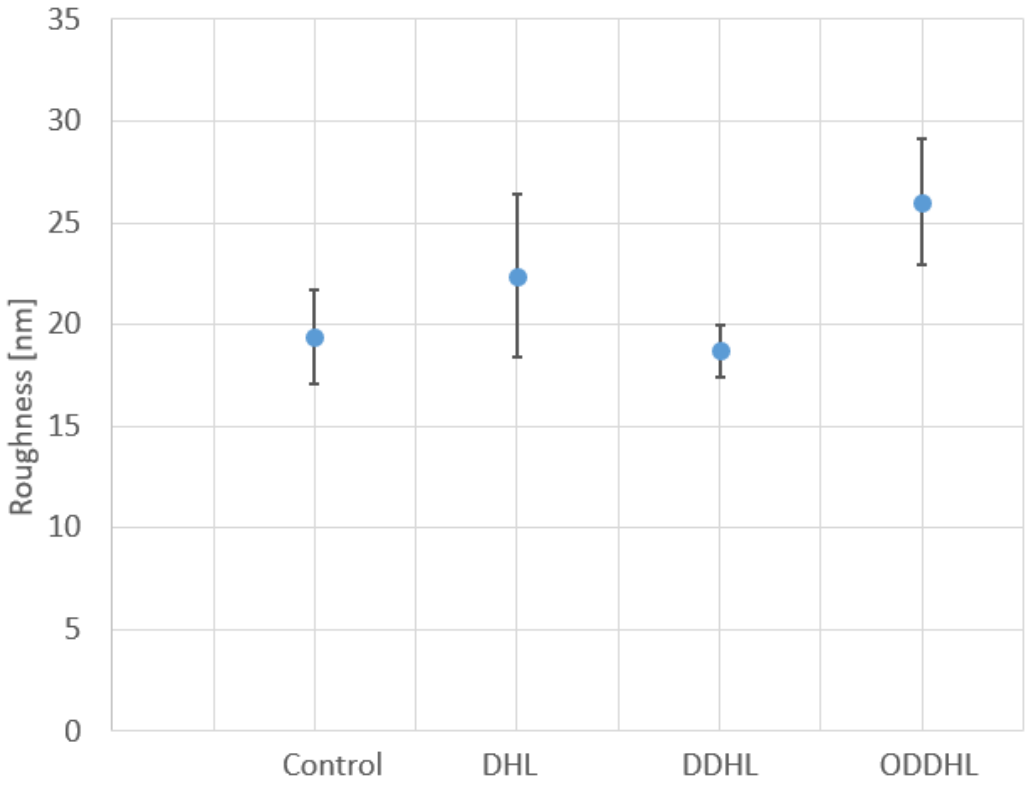

Figure 4. Roughness of the BNC samples.

The four cellulose samples were analyzed by EDS to measure the four cellulose samples (Figure 6). Carbon and Oxygen were detected in all cellulose samples in common as the major elements in addition to Sodium. A very small amount of Silicon, and Phosphorus, which were generated in the process of the sample fabrication for DHL.

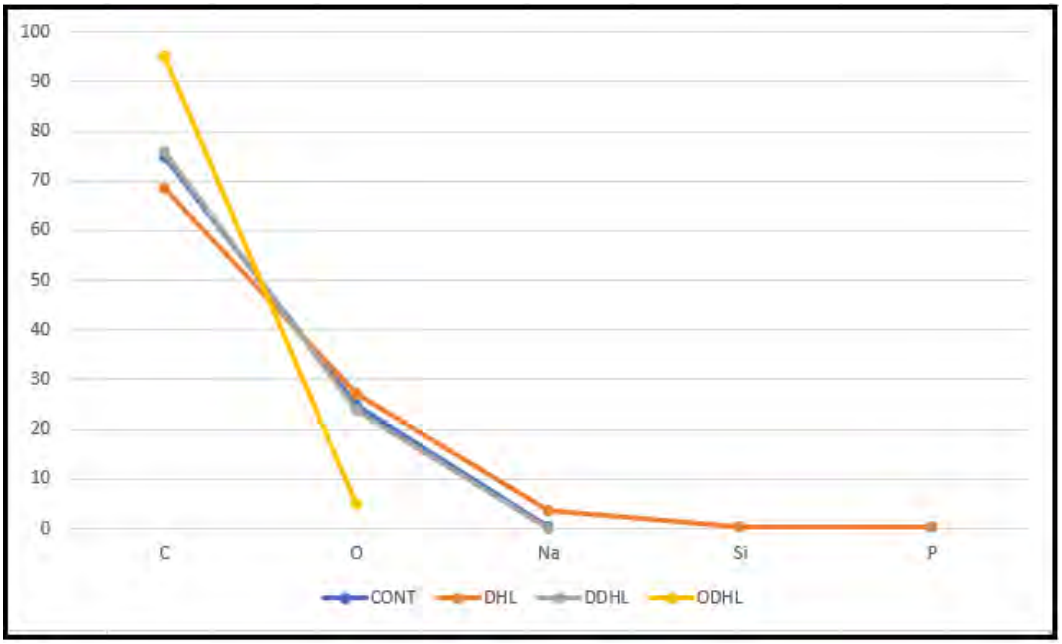

Figure 5. EDS element analysis of Control, DHL, DDHL, and ODDHL treated BNC.

4. CONCLUSIONS

The result of the final year of research funded by ILIR revealed the morphological changes that occur in the presence or absence of specific quorum sensing molecules, in this case homoserine lactones, during bacterial growth phase. The presence of various HSL molecules affects the signaling circuitry that is responsible for the formation of the bacterial cellulose fibrils. How HSL molecules manipulate signaling cascades and gene expression is yet to be worked out, previously published literature has eluded to HSLs impacting these cell processes. Modifications of HSLs were observed to affect the width of the BNC, in particular with ODDHL leading to the formation of the widest bacterial fibrils compared to the control sample. Atomic force microscopy provided a closer look at the 3D projection of the bacterial pellicles to identify the roughness and smoothness of the surface of the bacterial pellicles. The HSL showed variable effects on the surface properties of the bacterial fibrils, specifically with the presence of ODDHL leading to the roughest surface among all the tested HSL molecules.

This work will transition its focus into production of custom-made bacterial cellulose for specific applications. Understanding the effect HSL molecules have on the morphology of bacterial cellulose biofilm will be documented and applied in producing on-demand bacterial cellulose. The superior physicochemical properties of the bacterial cellulose over plant ones will lead to more DoD applications especially in the wearable sensing technologies for chemical and biological threats.

ACKNOWLEDGMENTS

Funding was provided by the U.S. Army via the In-house Laboratory Independent Research Program (PE 0601101A Project 91A) at the Combat Capabilities Development Command Chemical Biological Center.

REFERENCES

[1] Lee K-Y; Buldum G.; Mantalaris, A.; Bismarck, A. More than meets the eye in bacterial cellulose: biosynthesis, bioprocessing, and applications in advanced fiber composites. *Macromol Biosci*. **2014**. *14* (1), pp 10–32.
[2] Rognoli, V.; Bianchini, M.; Maffei, S.; Karana, E. DIY materials. *Mater Des*. **2015**, *86* (5), pp 692–702.

[3] Wong, H.C.; Fear, A.L.; Calhoon, R.D.; Eichinger, G.H.; Mayer, R.; Amikam, D.; Benziman, M.; Gelfand, D.H.; Meade, J.H.; Emerick, A.W. Genetic organization of the cellulose synthase operon in *Acetobacter xylinum*. *Proc. Natl. Acad. Sci. U.S.A.* **1990**, *87* (20), pp 8130–8134.
[4] Williams, W.S.; Cannon, R.E. Alternative Environmental Roles for Cellulose Produced by *Acetobacter xylinum*. *Appl. Environ. Microbiol.* **1989**, *55* (10), pp 2448–2452.
[5] Zhong, C.; Gurry, T.; Cheng, A.A.; Downe, J.; Deng, Z.; Stultz, C.M.; Lu, T.K. Strong underwater adhesives made by self-assembling multiprotein nanofibres. *Nat Nanotechnol.* **2014**, *9* (10), pp 858–866.
[6] Chen, A.Y. Deng, Z.; Billings, A.N.; Seker, U.O.S.; Lu, M.Y.; Citorik, R.J.; Zakeri, B.; Lu, T.K. Synthesis and patterning of tunable multiscale materials with engineered cells. *Nat Mater.* **2014***, 13* (5), pp 515–523.
[7] Yadav, V.; Paniliatis, B.J.; Shi, H.; Lee, K.; Cebe, P.; Kaplan, D.L. Novel In Vivo-Degradable Cellulose-Chitin Copolymer from Metabolically Engineered *Gluconacetobacter xylinus*. *Appl. Environ. Microbiol.* **2014**, *76* (18), pp 6257–6265.
[8] Mohite, B.V.; Patil, S.V. Physical, structural, mechanical and thermal characterization of bacterial cellulose by *G. hansenii* NCIM 2529. *Carbohydr. Polym.* **2014**, *106*, pp 132–141.
[9] Hsieh, Y.C.; Yano, H.; Nogi, M.; Eichhorn, S.J. An estimation of the Young's modulus of bacterial cellulose filaments. *Cellulose*. **2008**, *15* (4), pp 507–513.
[10] Rusli, R.; Eichhorn, S.J. Determination of the stiffness of cellulose nanowhiskers and the fiber-matrix interface in a nanocomposite using Raman spectroscopy. *Appl. Phys. Lett.* **2008**, *93* (3), pp 033111.
[11] Gelin, K.; Bodin, A.; Gatenholm, P.; Mihranyan, A.; Edwards, K.; Stromme, M. Characterization of water in bacterial cellulose using dielectric spectroscopy and electron microscopy. *Polymer*. **2007**, *48* (26), pp 7623–7631.
[12] Yuen, J.D.; Walper, S.A.; Melde, B.J.; Daniele, M.A.; Stenger, D.A.; Electrolyte-Sensing Transistor Decals Enabled by Ultrathin Microbial Nanocellulose. *Sci. Rep.* **2017**, *7*, pp 40867.
[13] Rudrappa, T.; Biedrzycki, M.L.; Bais, H.P. Causes and consequences of plant-associated biofilms. FEMS *Microbiol. Ecol.* **2008**, *64* (2), pp 153-166.
[14] Silverstein, R. M.; Bassler, G. C.; Morrill, T. C. Spectrometric Identification of Organic Compounds, 4th ed.; Wiley: New York, **1981**.
[15] Soares, S.; Camino, G.; Levchik, S. Comparative study of the thermal decomposition of pure cellulose and pulp paper. *Polym. Degrad. Stab*. **1995**, *49* (2), pp 275–283.
[16] Pastorova, I.; Botto, R. E.; Arisz, P. W.; Boon, J. J. Cellulose char structure: a combined analytical Py-GC-MS, FTIR, and NMR study. *Carbohydr. Res.* **1994**, *262* (1), pp 27–47.
[17] Hardy, B. J.; Sarko, A. Molecular dynamics simulations and diffraction-based analysis of the native cellulose fibre: structural modelling of the I-α and I-β phases and their interconversion. *Polymer*. **1996**, *37* (10), pp 1833-1839.
[18] Bodin, A.; Bäckdahl, H.; Fink, H.; Gustafsson, L.; Risberg, B.; Gatenholm, P. Influence of cultivation conditions on mechanical and morphological properties of bacterial cellulose tubes. *Biotechnol. Bioeng*. **2007**, *97* (2), pp 425-434.
[19] Gea, S.; Reynolds, C. T.; Roohpour, N.; Wirjosentono, B.; Soykeabkaew, N.; Bilotti, E.; Peijs, T. Investigation into the structural, morphological, mechanical and thermal behaviour of bacterial cellulose after a two-step purification process. *Bioresour. Technol*. **2011**, *102* (19), pp 9105-9110.
Grande, C. J.; Torres, F. G.; Gomez, C. M.; Troncoso, O. P.; Canet-Ferrer, J.; Martinez-Pastor, J. Morphological Characterisation of Bacterial Cellulose-Starch Nanocomposites. *Polym. Polym. Compos.* **2008**, *16* (3), pp 181-185.

SSI PROJECTS

Towards understanding the role of material voids and porosity on transport

Angela M. Zeigler[a]*, Roseanna N. Zia[b], Brian K. Ryu[b], Mark J. Varady[a], Melissa S. Hulet[c], Bradley R. Ruprecht[d], Harvey Tsang[e]
[a]U.S. Army Combat Capabilities Development Command Chemical Biological Center, Research & Technology Directorate, 8198 Blackhawk Rd, Aberdeen Proving Ground, MD 21010
[b]Department of Chemical Engineering, Stanford University, 443 Via Ortega, Stanford, CA 94305
[c]Leidos, 1750 Presidents St, Reston, VA 20190
[d]U.S. Army Combat Capabilities Development Command Chemical Biological Center, Engineering Directorate, 8198 Blackhawk Rd, Aberdeen Proving Ground, MD 21010
[e]U.S. Army Combat Capabilities Development Command Army Research Laboratory, 2800 Powder Mill Road, Adelphi, MD, 20783

ABSTRACT

Additive manufactured materials are limited in field use as a result of inherent porosity and voids. A fundamental understanding of how the mesoscale structure affects the chemical transport diffusion through three dimensional printed polymeric materials allows for full exploitation of the technology. Understanding of the efficacy of such materials includes detailed understanding of the migration rates through the material of solvent-suspended particles of various sizes and how the rate varies with the tortuosity of the void network. Studies of flow through porous media are well-established in the literature, but the geometry and connectivity of pore structures that arise from different additive manufacturing techniques have not been well studied, preventing the development of predictive models for mass transport. Using a combination of experiments and computational studies, we constructed a framework for our methods in the first year of the project. In our second year, we further developed algorithms for characterizing the tortuosity of additively printed material and how changes in this tortuosity affect the migration rate of solvent-suspended macromolecules. Changes in morphology emerging from fused deposition modeling, selective laser sintering, and stereolithography are modeled computationally and studied experimentally. In our third year, we expanded both computational and experimental methods for a higher-level qualitative agreement.

Keywords: additive manufacturing, 3D printing, transport, voids, porosity, diffusion, mesoscale, Micro-CT

1. INTRODUCTION

Three-dimensional (3D) printing, a phenomenon closely related to additive manufacturing, has emerged as a technology of interest to the Army due to its potential in easing logistics burdens and building Army readiness as related to the 2018 Army Strategy.[1] Applications for 3D-printed materials may include body armor, weapon components, or even personal protective equipment (PPE). Also, in light of the COVID-19 pandemic, there has been an exponential increase in printing PPE and medical supplies as a last resort to aid in the sudden supply shortage.[2] However, there is a significant knowledge barrier to implement 3D printing as a long-term solution, as the effects of porosity and defects on permeability of polymeric materials are not well known.[3,4] Therefore, a fundamental understanding of the effect of transport across voids and the porous network would allow for full exploitation of the technology.

Depending on the additive manufacturing method utilized, there may be an inherent presence of voids or other subsurface defects.[5,6] Fused deposition modeling (FDM) is a method that requires heating of the polymeric material as it is extruded through a small nozzle. For the desired product, the nozzle is programmed to build the piece layer-by-layer, from bottom to top, and the melted polymer fuses to the previous layer as it is deposited. This method potentially allows for voids or defects to form between the fused layers. Other printing parameters, such as the printing head temperature, mechanical layering speed, etc., may also create subsurface voids. Selective laser sintering (SLS)

is a powder bed-based method where a CO_2 laser is programmed to form the shape of the desired product by melting and fusing the powder together layer-by-layer as powder is continuously added. The potential of unfused granules from the feedstock could allow for potential voids or defects in the substructure.[7] Stereolithography (SLA) uses a photochemical process to optically cure a product pulled from a liquid vat of the polymeric material. The material is cured typically by a UV lamp layer-by-layer starting from the top to bottom. Again, there is a potential for voids or defects to form between the cured layers. In each case, only specific polymeric materials may be utilized depending on the method; therefore, the impact of understanding the mechanisms of transport through these polymeric materials may affect the degree to which they can serve as protective material.

Our first year, or FY19, proceedings report focused on establishing the necessary experimental and modeling infrastructure for the research. This infrastructure was the foundation for the investigation of the influence of voids and porosity on transport of a chemical of interest through a bulk polymer. We limited this study to a reasonable scope, utilizing the following: (1) the FDM method of a black polycarbonate acrylonitrile butadiene styrene (PC-ABS) thermoplastic, (2) the SLS method with glass filled nylon (PA-GF), and (3) the SLA method using an elastomeric polyurethane (EPU40).

Three microscopy methods were performed to capture the dimensions of pores and voids in the 3D printed material. Confocal optical microscopy in visible wavelengths and scanning electron microscopy (SEM) were performed. However, it was difficult to extract quantifiable data and porosity was not visible on the surfaces imaged. Therefore, measurements of the substructure of the 3D-printed polymeric materials proceeded with the method of X-ray microtomography (micro-CT). Lastly, an experimental design was constructed for measuring the transient breakthrough times of the solvents and preliminary tests were performed.

Our second year, or FY 20, proceedings report focused on further developing the computational model to predict the 'tortuosity', meaning pore interconnectedness which cannot be quantified from visual data. To our knowledge, no established technique exists yet in laboratory samples, computational models, or theory that unambiguously *measures* both feature-size distribution and connectivity.[8,9] Due to the effects of COVID-19, progress focused primarily on the advancements of the computational modelling efforts, followed comparison to limited experimental breakthrough laboratory efforts permitted to take place.

For our third and final year, or FY21, we further evaluated the chemical permeation of the three 3D-printed material types with a range of chemical vapors that included alcohols and chemical simulants, and then calculating the diffusion coefficients from the measured data. We further developed the computational modelling by incorporating the additional experimental breakthrough and micro-CT data to obtain a higher level of quantitative agreement.

2. EXPERIMENTAL APPROACH

2.1 Microscopy methods

Micro-CT is a non-invasive microscopy method that utilizes X-rays to record images of an object that is rotated around an axis; this technology is analogous to medical facility computerized axial tomography X-ray imaging, or CAT scans. A 3D image is constructed from the data using image reconstruction software or computerized algorithms. The advantage of this technology is that a spatial resolution of ~100 nm is possible. The 3D-printed parts of our study were characterized using micro-CT instrumentation at the Combat Capabilities Development Command (DEVCOM) Army Research Laboratory (ARL) in Adelphi, MD. The data received was encoded as an MPEG movie file, where each pixel in an image represents a voxel that is a volume element in the data. A length scale was present in the data that permitted the determination of the length of each voxel. The micro-CT data contain raw voxel intensities, which require further post-processing to obtain meaningful information of voids.

2.2 Computational modeling

The large-scale atom/molecule massively parallel simulator is a computational platform developed to successfully model physical dynamics of very large-scale systems of interacting molecules, with a more recent version used to represent Newtonian liquids.[10] Large-scale atom/molecule massively parallel simulator is optimized for parallel processing, capable of distributing the dynamics of millions of macromolecules across thousands of processors.

For development of the model, the first key physical feature of the pore microstructure in 3D-printed solids was utilized, namely, an amorphous distribution of interconnected pores. The base of the initial model was developed by

constructing a porous solid via self-assembly of colloids – microscopically small particles dispersed in a solvent that exert attractive forces on one another, leading to self-assembly into an amorphous network of thick strands interpenetrated by a network of interconnected, solvent-filled pores.

To approach the next challenge of 'tortuosity', we developed methods for implementing skeletonization[11] techniques to extract condensed features of the void structure to analyze the 3D micro-CT data. This step enables efficient analysis of experimentally obtained large micro-CT scan data. This was performed by establishing implementation for 3D skeletonization methods to examine the void structure and implementation. Skeletonization methods (formally, medial axis transformations) are commonly used in computational image analysis of 2D or 3D images. These transformations compress the images while preserving the most important structural features present in images, such as approximate size, shape, and connectivity.[12,13]

2.3 Laboratory breakthrough measurements

The final design for our real-time monitoring of chemical breakthrough measurements is shown in Figure 1. An in-house assembled source was coupled to an MKS atmospheric mass spectrometer for detecting chemical permeation in real-time. The source includes a computer aided design stainless steel sandwich source with recessed channels for O-rings to hold the sample in place as well as isolate the top and bottom of a sample from each other. A saturator cell held in a temperature and relative humidity-controlled system, provided a saturated chemical vapor stream for each chemical of interest, exposing just the top side of the sample to the chemical. A dry nitrogen sweep flow is introduced to the bottom side of the sample where the inlet of a mass spectrometer detects very low levels of vapor as it permeates the sample. Flows on both sides of the sample are adjusted to minimize the pressure differential across the sample. A LabVIEW program from National Instruments™ was set up to make the turning on and off of the saturated vapor more precise and repeatable. The solvent vapor diffusivity was computed through the solid sample using steady state concentrations of solvent in the saturated vapor and nitrogen gas. The sample was then monitored over a period of days to detect breakthrough. If breakthrough occurred or was stopped by the operator following a pre-determined number of days, the next sample was tested.

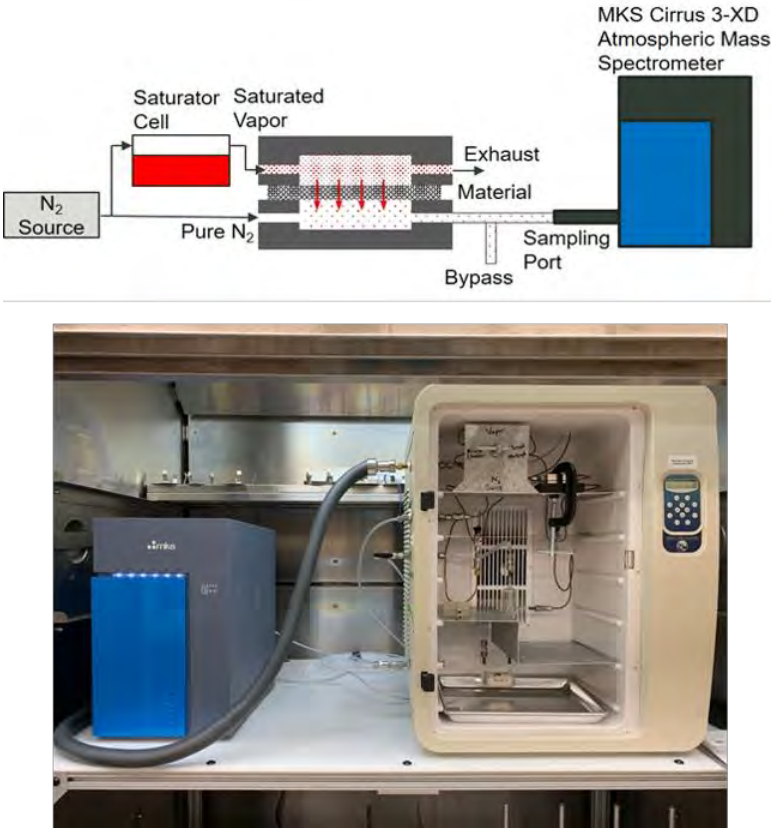

Figure 1. (top) Design for breakthrough measurements. Schematic of the finalized design structure. (bottom) Photograph of the lab set-up within engineering controls.

Data that has been collected and analyzed on several chemicals, including ethanol, isopropyl alcohol, 2-chloroethyl ethyl sulfide (2-CEES), and dimethyl methylphosphonate (DMMP). We also looked at 3 varying thickness measurements of samples; approximately 1 inch x 1 inch x varying thickness (0.02 inch (~0.5 mm), 0.05 inch (~1.2mm), and 0.1 inch (~2.5mm)). These thickness measurements were chosen as the approximate thickness needed for a first single complete layer of a 3D print. The measurements were doubled, and then doubled again for mapping of porosity and permeation based on increasing the layer thickness. The measurements obtained from experiments were then utilized to calculate the permeation diffusion coefficients and to estimate the ratio of porosity and tortuosity, if applicable.

3. RESULTS AND DISCUSSION

3.1 PC-ABS/FDM method

For the chemical breakthrough times of the polycarbonate acrylonitrile butadiene styrene (PC-ABS) 3D-printed samples, via the FDM method, breakthrough measurements were performed for each sample. The breakthrough profile obtained was an accumulation of sample exposure over days and the breakthrough magnitude, or molar flux, of the solvent was monitored. Overall, we observed similarities in profile and breakthrough times with MeOH, EtOH and IPA, with a primary breakthrough occurring almost immediately, followed by a second breakthrough observed several hours later, which was then followed by a steady state, meaning no further breakthrough activity was observed. Chemical simulants 2-CEES and DMMP both showed a sharp intensity profile indicating a primary breakthrough, followed by a steep decline and then a steady state of no further activity. The effective diffusion rate coefficients and ratio of porosity and tortuosity, if applicable, were then calculated using the steady state method.[14]

The output reading in real-time is a computed partial pressure, $\boldsymbol{p_i}$, of vapor that can then be converted to concentration given the appropriate calibration curve for the given chemical. The molar flux, n_i'', of permeating chemical can then be calculated using Equation 1:

$$n_i'' = \mathrm{Q}\frac{p_i}{RT}. \quad (1)$$

Where Q is the volumetric flow rate of the N2 sweep flow on the bottom of the sample. If the chemical permeation rate reaches a steady-state, an effective diffusion coefficient of the chemical through the material (thickness = L), $D_{i,eff}$, can be computed using Fick's first law assuming the diffusivity is constant throughout the material, Equation 2:

$$n_{i,eq}'' = \frac{D_{i,eff}}{L}\frac{p_{i,vap}-p_i}{RT}. \quad (2)$$

If the diffusion is through an open pore network, the diffusivity of the chemical in N_2, $D_{i,N2}$ can be used to estimate the ratio of porosity and tortuosity, ε/τ using Equation 3:

$$D_{i,eff} = \frac{\varepsilon}{\tau}D_{i,N2}. \quad (3)$$

From these calculations, the resulting effective diffusion coefficients for PC-ABS are presented in Table 1. The thickest samples, ~2.4 mm, are not represented in the below table due to failure of permeation after several days of exposure, resulting in being manually stopped by the operator.

Table 1. The values of the effective diffusion coefficient, $D_{i,eff}$, and ratio of porosity and tortuosity (ε/τ) for the PC-ABS material exposed to each chemical calculated based on sample thickness (L) and molar flux ($n''_{i,eq}$).

Chemical	L (mm)	$n''_{i,eq}$ (mol/m^2/s)	$D_{i,eff}$ (m^2/s)	ε/τ
MeOH[15]	0.57	5.67×10^{-3}	6.85×10^{-7}	0.045
	1.48	3.14×10^{-3}	9.36×10^{-7}	0.052
EtOH[16]	0.597	1.38×10^{-2}	7.5×10^{-6}	0.68
	1.48	1.38×10^{-2}	1.81×10^{-5}	1.64
IPA[17]	0.6	7.2×10^{-3}	3.90×10^{-6}	0.406
	1.48	4.7×10^{-3}	5.23×10^{-6}	0.54
2-CEES	0.58	~0	~0	N/A
DMMP	0.58	~0	~0	N/A

For the PC-ABS material, we hypothesize that the primary breakthrough mechanism is diffusion, via an open-cell void network, meaning that the voids within this material are mostly all interconnected or open. This leads to quick breakthrough and was also found in the analysis of the micro-CT. There is also a secondary mechanism of a chemical interaction taking place between the simulants CEES and DMMP and the PC-ABS filaments altering void morphology, swelling the material and reducing the void size.

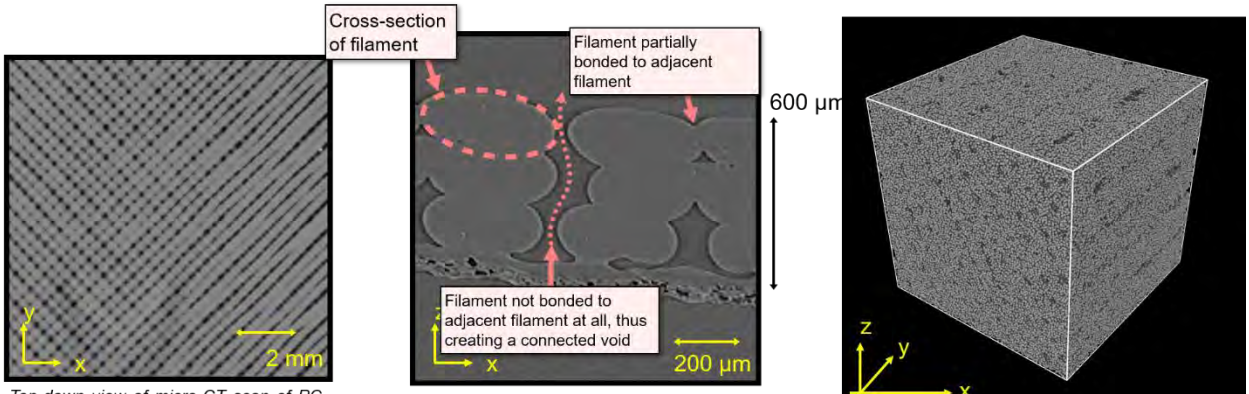

Top-down view of micro-CT scan of PC-ABS sample. Pores (black) occur periodically between layers of PC-ABS filament (gray)

Magnified side view of micro-CT scan of PC-ABS sample.

Figure 2. (left) Top-down view of micro-CT processed data of PC-ABS sample structure. (center) Side view of micro-CT processed data of PC-ABS sample structure revealing extent and inconsistencies of filament bonding (right) 3D computational model representation of PC-ABS samples.

For the PC-ABS samples, incorporating both the calculated diffusion coefficients, and analysis of the micro-CT data into the computation model yields quantitative agreement. Figure 2 shows an example of the processed micro-CT data and model. The left and center schematics of Figure 2 are of the micro-CT analysis showing where the periodic voids are visible; and we clearly see sections where filaments are not fused tightly, leaving large voids in between, leading to interconnected void pathways. The right schematic of Figure 2 is the resulting 3D computational model representation after experimental data has been incorporated.

3.2 PA-GF/SLS Method

For the chemical breakthrough times of the PA-GF 3D-printed samples via the SLS method, breakthrough measurements were performed for each sample. The breakthrough profile obtained was an accumulation of sample

exposure over days and the breakthrough magnitude or, molar flux, of the solvent was monitored. Overall, we observed similarities in profile and breakthrough times with MeOH and IPA, with a primary breakthrough occurring immediately, but not as immediately compared to the PC-ABS material, and then followed by a second breakthrough observed several hours later, followed by a steady state, meaning the breakthrough flux is constant after this time. The profile of 2-CEES was observed to have similar characteristics compared to the alcohols. EtOH was not completed for GF-PA. For DMMP, it showed a sharp intensity profile indicating a primary breakthrough, followed by a steep decline to zero flux. From the steady state method[14] calculations, the resulting effective diffusion coefficients for PA-GF are presented in Table 2. As with the previous PC-ABS, some of the thicker samples of ~1.2 mm and ~2.5 mm are not represented in the below table due to failure of permeation after several days of exposure. This may indicate a change in morphology from thermal effect, where doubling the thickness of the sample may have an impact on the printing process. However, these observations would need further study. Also, EtOH was not tested with the PA-GF samples.

Chemical	L (mm)	$n''_{i,eq}$ (mol/m^2/s)	$D_{i,eff}$ (m^2/s)	ε/τ
MeOH[15]	0.53	1.26x10^{-3}	1.30x10^{-7}	0.0087
	1.2	3.08x10^{-7}	7.04x10^{-10}	N/A
	2.4	~0	N/A	N/A
IPA[17]	0.5	5.2x10^{-4}	1.52x10^{-7}	0.0158
	1.2	~0	N/A	N/A
	2.45	~0	N/A	N/A
2-CEES	0.52	4.72x10^{-6}	1.43x10^{-8}	N/A
DMMP	0.58	~0	~0	N/A

Table 2. The values of the effective diffusion coefficient, $D_{i,eff}$, and ratio of porosity and tortuosity (ε/τ) for the PA-GF material exposed to each chemical calculated based on sample thickness (L) and molar flux ($n''_{i,eq}$).

We summarize here that the primary breakthrough mechanism happening with the PA-GF is via a closed-cell void network, meaning that diffusion is happening through the pores, but that the voids are not as interconnected, like the open-cell. As the sample increases in thickness, the voids become more spaced out and therefore it is difficult to obtain a breakthrough time, even after letting these experimental runs after days for the thicker samples. For DMMP, there is a secondary chemical interaction mechanism again, we extrapolate may be related to DMMP absorption and degradation due to the presence of the glass fused components, that result in sealing off of the pore network.[18]

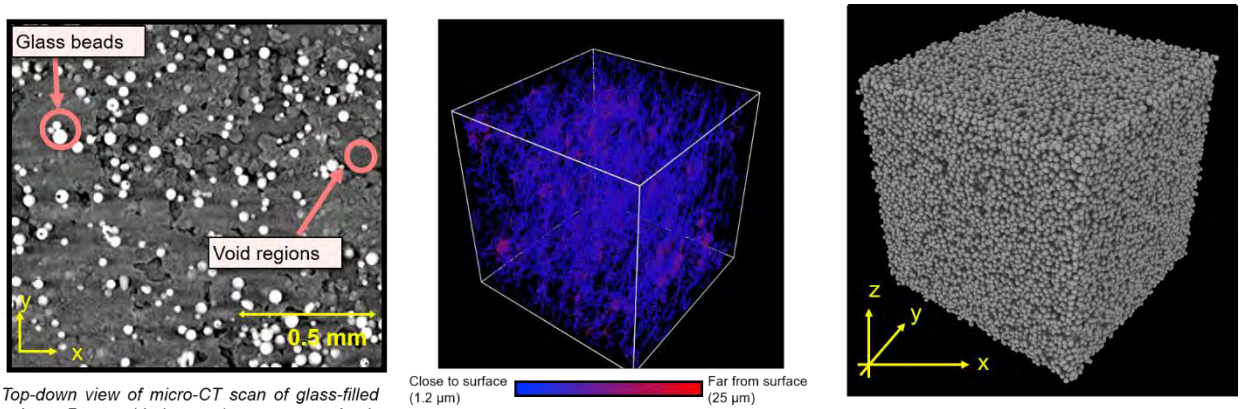

Top-down view of micro-CT scan of glass-filled nylon. Pores (dark gray) are randomly distributed.

Video of 3D skeleton void structure inside glass-filled nylon sample. Colors represent thickness of voids. Length of one side of the cube is 400µm.

Figure 3. (left) Top down view of micro-CT processed data of PA-GF sample structure revealing glass beads and void regions. (center) 3D skeleton void structure of the computational model highlighting how close and far from surface the disconnected voids are located (right) 3D computational model representation of PA-GF samples.

For the glass filled nylon samples, we again incorporated the micro-CT data and experimental diffusion coefficients. Figure 3, shows an example of the processed micro-CT data and model. The micro-CT scan in left schematic of Figure 3 clearly reveals the glass bead components and void regions as highlighted. The void regions are seemingly randomly distributed and disconnected, confirming our mechanism conclusion from experimental measurements. In stitching the scans together in the computational in the center view, we can observe the interspersing of void structures and thickness and how far or close to the surface they are utilizing a thermal imaging type legend shown in the center schematic of Figure 3. The right schematic in Figure 3 is the resulting 3D computational model representation after experimental data has been incorporated.

3.3 EPU40/SLA Method

For the chemical breakthrough times of the elastomeric polyurethane (EPU40) 3D-printed samples via the SLA method, breakthrough measurements were performed for each sample. The breakthrough profile obtained was an accumulation of sample exposure over days and the breakthrough magnitude or molar flux of the solvent was monitored. Overall, we observed similarities in profile and breakthrough times with MeOH, EtOH, IPA and 2-CEES with a primary breakthrough occurring gradually overtime, ultimately reaching a steady state, meaning the flux is constant after this time. For DMMP we failed to obtain a breakthrough even at the thinnest sample so far over a period of days.

However, calculating the effective diffusion coefficients by applying the steady state method[14] is not valid in this case as partitioning into the polymer requires knowledge of the solubility of each chemical in the polymer. Instead, the time lag method[20] is a viable alternative that produces reasonable values, typically observed based on Fick's laws.[19] From the time lag method[20] calculations, the resulting diffusion coefficients for EPU40 are presented in Table 3. As with the previous 3D-printed material, some of the thicker samples of ~1.2 mm and ~2.5mm are not represented in the below table due to failure of permeation after several days of exposure. The thinnest ~0.5mm samples were not tested with all chemical vapors.

Table 3. The values of the time lag diffusion coefficient, D_{lag}, for the EPU40 material exposed to each chemical calculated based on sample thickness (L) and time lag (t_{lag}).

Chemical	Material/ Method	L (mm)	t_{lag} (s)	D_{lag} (m²/s)
MeOH	EPU40/SLA	1.8	29043	1.86×10^{-11}
EtOH	EPU40/SLA	1.24	14579.5	1.75×10^{-11}
		1.94	54440.2	1.15×10^{-11}
IPA	EPU40/SLA	2.0	67325	9.90×10^{-12}
2-CEES	EPU40/SLA	2.0	64701	1.03×10^{-11}
	GF-Nylon/SLS	0.53	28646	1.63×10^{-12}

We deduce that this EPU40 material has one primary mechanism as solution diffusion through the polymer, not making use of voids or a void network, and therefore extended time elapses before chemical breakthrough is observed. No other secondary mechanisms were observed.

For the EPU40 samples, we again incorporated the micro-CT data and experimental diffusion coefficients. Figure 4 shows an example of the processed micro-CT data and model. The left and center schematics in Figure 4 show that although the outer surface may appear rigid or bumpy, there is clearly a lack of voids within the mesoscopic structure. The right schematic in Figure 4 is the resulting 3D computational model representation after experimental data has been incorporated. The lack of voids validates the solution diffusion through the solid polymer mechanism.

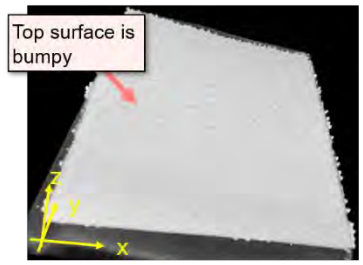

3D view of EPU40 elastomer sample constructed from micro-CT scan. Top surface shows circular bumps .

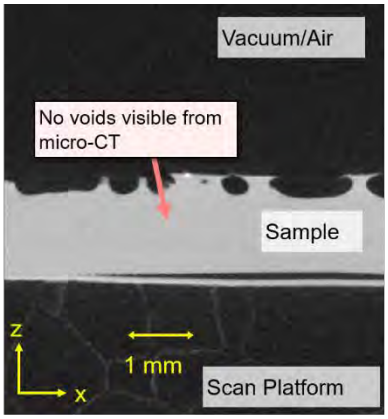

Side view image of EPU40 elastomer sample. No voids are visible within the sample itself.

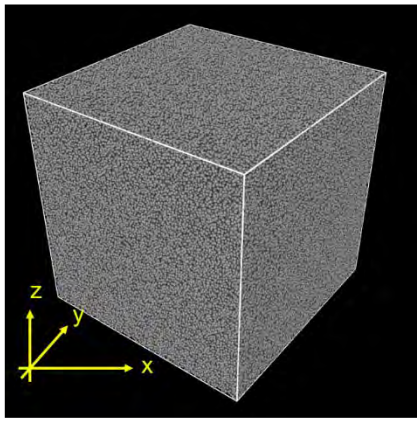

Figure 4. (left) Top-down view of micro-CT processed data of EPU40 sample structure showing inconsistencies at the top surface. (center) Side view of micro-CT processed data revealing no void structure observed (right) 3D computational model representation of EPU40 samples.

4. CONCLUSIONS

Two significant advances were made in the progress in our third year. First, we attained representation of each primary mechanism breakthrough, in which the quantity of voids present was observed to be dependent on the type of material being studied. These mechanisms have been characterized as (1) diffusion via an open cell network for the PC-ABS material, (2) diffusion via a closed-cell void network for the GF-PA material, and (3) diffusion through the solid polymer for the EPU40 material. Secondary mechanisms of chemical reactivity with the material was also accounted for to an extent based on chemical affinity of each material.

The second significant advancement we attained was the mapping of the specific void network of each 3D print material (assumption at near full density fill parameters). Our computational modeling provided high qualitative accuracy with our developed skeletonization algorithms in describing the tortuosity. To our knowledge, this is the first time quantification of "tortuosity" has been accomplished to describe both pathways and interconnectedness within any computational model.

We continue to leverage this data in obtaining future funding for void mapping and transport properties based on manipulation of parameters during the 3D printing process. We could then continue modification based on the newest experimental results revealing secondary migration mechanisms and leverage this data to tune fabrication parameters for optimal material performance based on the application required. Detailed characterization of solvent transport provides an understanding of the mechanism of how the structure of voids and connectivity affect the solvent flow traversing the network.

ACKNOWLEDGMENTS

The authors thank the U.S. Army DEVCOM Chemical Biological Center for funding this work via the Surface Science Initiative Program (PE 0601102A Project VR9). The authors also thank the original principal investigator Dr. Jerry Cabalo, now at the Chemical Security Analysis Center at the Department of Homeland Security.

REFERENCES

[1] Milley, M.; Esper, M. *The Army Strategy*; The U.S. Army: Washington D.C., 2018; pp 1–11.
[2] *3D Printing in FDA's Rapid Response to COVID-19. 2020*; U.S. Food & Drug Administration: U.S. Government Printing Office: Washington, DC, 2020.
[3] Mizokami, K. The U.S. Army Is Working on 3D Printed Body Armor. https://www.popularmechanics.com/military/research/a28425864/us-army-28425863d-printing-body-armor/ (accessed July 27, 2019), *Popular Mechanics*, July 18, 2019.
[4] Robson, S. Yokota airmen improve gas mask with 3D printer, potentially saving Air Force $8 million or more. https://www.stripes.com/news/yokota-airmen-improve-gas-mask-with-3d-printer-potentially-saving-air-force-8-million-or-more-1.531504 (accessed July 27, 2019), *Stars and Stripes,* June 7, 2018.
[5] Cerniglia, D.; Scafidi, M.; Pantano, A.; Rudlin, J. Inspection of additive-manufactured layered components. *Ultrasonics.* **2015**, *62*, pp 292–298.
[6] Lewis, G.K.; Schlienger, E. Practical considerations and capabilities for laser assisted direct metal deposition. *Mater. Des.* **2000**, *21* (4), pp 417–423.
[7] Zhang, D.; Niu, W.; Cao, X.; Liu, Z. Effect of standard heat treatment on the microstructure and mechanical properties of selective laser melting manufactured Inconel 718 superalloy. *Mater. Sci. Eng., A.* **2015**, *644*, pp 32–40.
[8] Berg, S.; Rücker, M.; Ott, H.; Georgiadis, A.; van der Linde, H.; Enzmann, F.; Kersten, M.; Armstrong, R.T.; de With, S.; Becker, J.; Wiegmann, A. Connected pathway relative permeability from pore-scale imaging of imbibition. *Adv. Water Resour.* **2016**, *90*, pp 24–35.
[9] Ahrenholz, B.; Niessner, J.; Helmig, R.; Krafczyk, M. Pore-scale determination of parameters for macroscale modeling of evaporation processes in porous media. *Water Resour. Res*. **2011**, *47* (7), W07543.
[10] Plimpton, S. Fast Parallel Algorithms for Short-Range Molecular Dynamics. *J. Comput. Phys.* **1995**, *117* (1), pp 1–19.

[11] Cao, J.; Tagliasacchi, A.; Olson, M.; Zhang, H.; Su, Z. Point Cloud Skeletons via Laplacian Based Contraction. In *Proceedings of the SMI 2010 Shape Modeling International Conference,* Aix-en-Provence, France, 21–23 June 2010; IEEE Computer Society, 2010; Vol 1, pp 187–197.
[12] Lee, T.C.; Kashyap, R.L.; Chu, C.N. Building Skeleton Models via 3-D Medial Surface Axis Thinning Algorithms. *CVGIP Graph. Model. Image Process.* **1994**, *56* (6), pp 462–478.
[13] Arcelli, C.; Sanniti di Baja, G.; Serino, L. Distance-Driven Skeletonization in Voxel Images. *IEEE Transactions on Pattern Analysis and Machine Intelligence.* **2011**, *33* (4), pp 709–720.
[14] Crank, J. "The Mathematics of Diffusion", Oxford Univ. Press, London, **1975**, p 44.
[15] GSI Chemical Database. https://www.gsi-net.com/en/publications/gsi-chemical-database/single/343-methanol.html (accessed 18 February 2021).
[16] Lugg, G. A. Diffusion coefficients of some organic and other vapors in air. *Anal. Chem.* **1968**, *40* (7), pp 1072–1077.
[17] GSI Chemical Database. https://www.gsi-net.com/en/publications/gsi-chemical-database/single/324.html (accessed 18 February 2021).
[18] Wilmsmeyer, A.R.; Gordon, W.O.; Davis, E.D.; Troya, D.; Mantooth, B.A.; Lalain, T.A.; Morris, J.R. Infrared Spectra and Binding Energies of Chemical Warfare Nerve Agent Simulants on the Surface of Amorphous Silica. *J. Phys. Chem. C.* **2013**, *117* (30), pp 15685−15697.
[19] Tosun, İ. *Modelling in Transport Phenomena: A Conceptual Approach*; Elsevier: Oxford, UK, **2002**.
[20] Crank, J. "The Mathematics of Diffusion", Oxford Univ. Press, London, **1975**, pp 51–52.

Extending bio-functionality in materials via controlled polymer erosion

Marilyn S. Lee[a], John R. Biondo[b], Jeffrey Lux[c,d], Casey B. Bernhards[a], Danielle L. Kuhn[a], Melissa Hulet[a], Mark Varady[a], Maneesh K. Gupta[c], Matthew W. Lux[a]*
[a]U.S. Army Combat Capabilities Development Command Chemical Biological Center, Research & Technology Directorate, 5183 Blackhawk Rd, Aberdeen Proving Ground, MD 21010
[b]Excet Inc; 5183 Blackhawk Rd, Aberdeen Proving Ground, MD 21010
[c]US Air Force Research Laboratory, 2179 12th St., B652/R122 Wright-Patterson Air Force Base, OH 45433 USA
[d]UES Inc., 4401 Dayton-Xenia Rd., Dayton, OH 45432 USA

ABSTRACT

Advances in synthetic biology have granted the ability to dictate a variety of functions through genetic and protein design. These functions include sensing, catalyzing chemical reactions, and producing desired molecules and materials. While these capabilities have been extensively developed in whole cell cultures, or *in vitro* in solution, important applications may also be pursued for biological systems in solid materials. Challenges obstructing this concept include difficulties in maintaining cell viability or protein activity, both during the harsh processing steps involved in producing many synthetic materials, and with long-term use of the material. One technology that shows promise in circumventing these issues is cell-free (CF) systems. CF reactions can be dried and stored for months to a year and are able to maintain activity upon rehydration. Further, dried CF reactions have shown remarkable stability to both heat and organic solvents, lending them to applications in synthetic materials that would be impossible using whole living cells. These characteristics have inspired us to reconfigure the reaction environment and embed CF systems in polymer matrices towards enabling new form factors and controlling water-induced activation.

Keywords: Cell-free protein synthesis, polymers, synthetic biology, protein stability, sensing, biosynthesis

1. INTRODUCTION

Many new innovations in dynamic materials stem from biological inspiration because living organisms are continually reshaping the materials within themselves and their environment. Some examples of interesting functions driven by bioactivity include sensing, catalytic enzyme activity, and biosynthesis. It is recognized that embedding synthetic materials with these functions could unlock many applications, such as protective masks that sense threats and alert the user to exposure, self-decontaminating coatings, or objects that change shape, color, or mechanical property in response to stimuli.

An ongoing challenge preventing these applications is maintaining the stability of the bio-system during material processing and overuse of the material. It is difficult to maintain cell viability and prevent protein denaturation in variable field conditions and harsh fabrication steps. One technology that shows promise in circumventing these issues is cell-free (CF) systems. CF systems are comprised of cell lysates, or broken cells, that contain all the enzymes, cofactors, DNA, and active components of a cell. These components can be reactivated and supplied with resources to carry out sensing or catalysis without the burden of maintaining cellular survival and replication (Figure 1A).[1-5] CF reactions are advantageous among biochemical formulations because of their stability through the lyophilization process while maintaining transcription, translation, and metabolic processes that enable life-like complexity and dynamics. CF reactions can be dried and stored up to a year at room temperature, and retain activity upon rehydration.[6,7] Results from the first year of this SSI project demonstrated that dry CF powder derived from *Escherichia coli* is also stable through treatment with several types of organic solvents and temperatures up to 90 °C for up to 30 minutes. It was observed that both the type of solvent and the CF recipe used affect the viability of the CF system following solvent processing. These results allowed CF components to be solvent cast and heat cast into

synthetic polymers Poly(lactic-co-glycolic acid) (PLGA) and polycaprolactone (PCL), respectively, with recoverable activity (Figure 1C).[8,9]

One can compare these findings to studies of lyophilized purified proteins. A variety of individual enzymes and proteins have enhanced stability to organic solvents and high temperatures, some of which have even been cast into polymers.[10-13] However, this has not been the case for all proteins. Moreover, buffer conditions often need to be arduously optimized on a protein-specific basis to maximize activity recovery following hydration. The advantage of CF systems is the ability to stabilize and reactivate transcription and translation and large portions of metabolic activity for generalizable functions. Attaining the ability to preserve CF systems during polymer casting and subsequent use could enable broader flexibility with less optimization effort because we can program an array of functions by simply adding DNA that contains the directions for producing a protein of interest.

Looking ahead, the use of polymers in combination with CF reactions has implications for improving the utility of CF systems. There is great potential to leverage materials to modulate hydration, and therefore activation of lyophilized reactions (Figure 1C). Polymers have been widely used to control the timing of cargo release in products that include anything from pharmaceuticals to fertilizers.[14,15] The same principles may be used to extend the lifetime of activity of a detection device. For instance, continual activation of fresh bio-active cargo, such as enzymes, embedded in a material may be achieved by polymer erosion.[16,17] Polymer-CF composites are also a way to introduce localization and specify diffusion barriers *in vitro*, which can lead to enhanced performance in multistep reactions, more complex cooperative functions, and signaling across distances.[18-20]

Here, we describe further advances made in the exploration of polymer-casting CF systems. 3D printing was explored in two ways. Heat tolerance of CF powder was put to the test in heat extrusion 3D printing. UV-curable resins used in stereolithography (SLA) 3D printing were screened to reveal that CF protein synthesis can be reactivated in some cases. Additionally, CF powder was 3D printed in an SLA printer and the printed object successfully produced green fluorescent protein via CF activity after a water wash.

We also sought to improve the dispersion and uniformity of CF powder in polymer formulations and develop new methods to measure CF-polymer composite properties and activity. Finally, two more advanced CF functions were tested after lyophilization: organic solvent exposure and polymer casting. The first function was a heavy metal transcription factor sensor to detect arsenic as a water contaminant and produce green fluorescent protein (GFP) as an output. The second function was production of the antimicrobial protein, colicin, which is assessed via *E. coli* growth inhibition assay. When combined with polymer materials, we envision these functions could be applied in water filters and anti-microbial coatings.

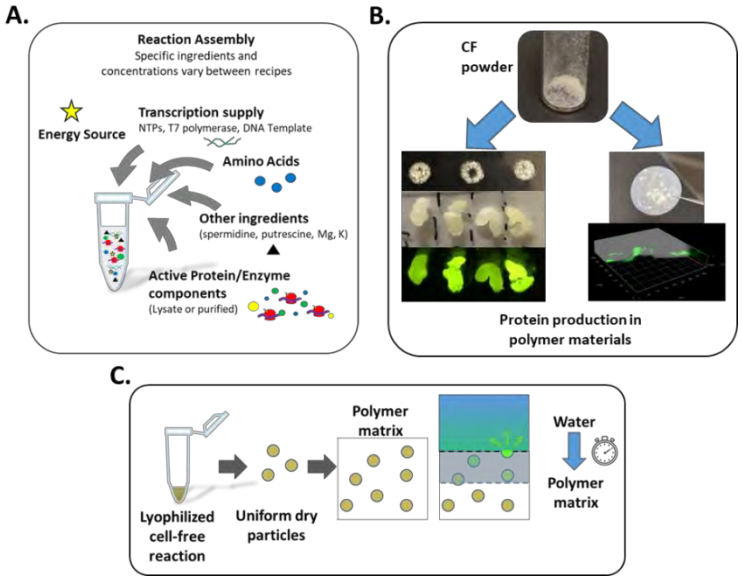

Figure 1. (A) Illustration of the composition of a CFPS reaction. (B) Dried CF powder pictured alone and after inclusion in polymer composites using acetone to solvent cast PLGA (left) and using thermal compression to cast PCL (right). Protein synthesis activity is detected in polymer composites via the production of GFP as imaged by photography with blue light (left) and confocal microscopy (right). (C) Illustrated example of a delayed activation concept design where lyophilized CFPS reaction material is embedded with a polymer matrix that delays rehydration.

2. RESULTS AND DISCUSSION

2.1 Lyophilized CF powder composites with various UV-cured resins

CF reactions made with *E. coli* lysate were mixed based on the PANOx-SP recipe (Kwon et al.).[21] These were challenged with exposure to six different commercially available photo-curable resins (Table 1). All but resin 2 are designed for SLA 3D printing. Resin 2 is a PolyJet photopolymer, used for a different type of 3D printing process where print heads deposit resin droplets that are then UV-cured. 15 uL reactions were distributed in the wells of a microplate, then treated with resin and UV light as described in Figure 2A. The CF transcription and translation activity were measured by production of green fluorescent protein as a result of adding of plasmid DNA encoding GFP under the control of a strong and constitutive T7 promoter (Figure 2B, C).

Table 1. UV-curable resins.

Resin #	Name, Description	Supplier, catalog number
1	3D Rapid Model Resin, Clear	Monocure 3D, NSW, Australia, M/3DR3582C
2	VeroClear	Stratasys, Los Angeles, CA, USA, RGD810
3	Simple, Clear	SIRAYA Tech, USA
4	Tenacious, Clear and Flexible	SIRAYA Tech, USA
5	Build, Smoky Black	SIRAYA Tech, USA
6	Blu	SIRAYA Tech, USA

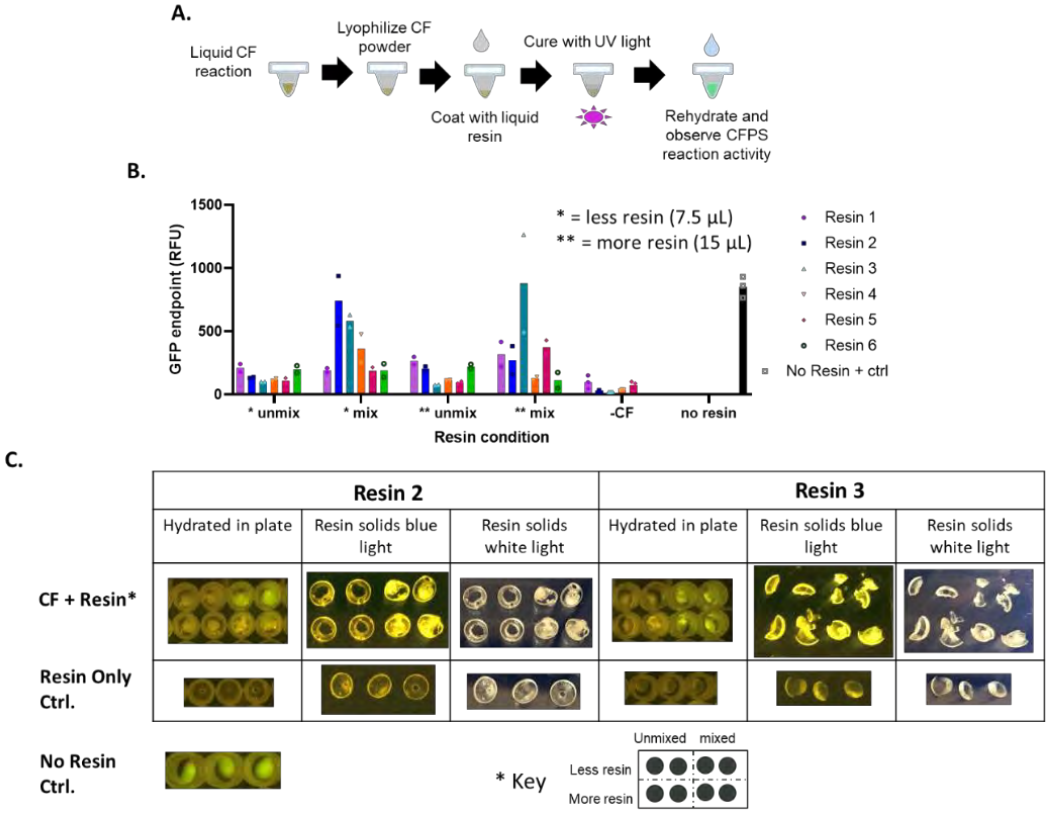

Figure 2. (A) Treatment sequence for CF reactions includes lyophilization, suspension in a liquid resin, curing to solidify resin with UV light, and assessment of CF activity via monitoring the appearance of GFP after rehydration. (B) Microplate reader measurements of endpoint concentration of GFP in reaction mixtures after treatments with either 7.5 or 15 µL of 6 different resins, with or without mixing. In the "no resin" control, no resin was added but the well was exposed to UV light. In the "-CF" control, fluorescence readings were measured for cured resins that were not mixed with CF powder. (C) Images taken for best performing resins 1 and 2. *Resin level and mixing condition described by sample position as illustrated in key.

For each resin tested, high and low amounts of resin were compared, and mixing prior to UV cure was varied to determine if the activity was sensitive to casting variables. Some resins are intrinsically fluorescent, so the "-CF" control was used to get a background reading for each resin. All resins showed CF activity higher than the background reading in at least one composite formulation, but most resin composites exhibited reduced activity of less than 50% than that of the no resin control. The best performing samples were resins 2 and 3, which resulted in CF activity comparable to the no resin control in some formulations. CF activity in resin 2 appeared to be more sensitive to the amount of resin. Both resin 2 and 3 composites performed best with mixing. Images of the resin solids and solution phase fluorescence readings indicate that the majority of GFP signal is localized to the solution. Taken together, these trends in mixing and the release of GFP into solution could indicate that activity is dependent on the amount of surface exposed CF powder. This is expected for resins that repel or exclude water. Custom resins or improved knowledge of resin formulations are required to fully explore underlying factors that remain opaque with proprietary printing resins. Yet, we can conclude that it is possible with selection of the correct formulation to recover CF bioactivity after resin exposure and UV-curing. Further exploration of water infiltration and reaction localization will define characteristics important for application of these materials.

2.2 3D Printing CF-polymer composites

Since lyophilized CF powder has demonstrated tolerance to both melt processed and UV cured polymers, we next sought to assess the feasibility of 3D printing bio-active CF composites. Heat extrusion printing was the first method tested, taking advantage of heat tolerance explored in FY20. To approach extrusion printing, CF powder must first be mixed with melted polymer to form pellets or nurdles which may then be formed into a filament. Most 3D printers utilizing heat are fed by filament, but there are some that can use nurdles directly, such as the Allevi bioprinter used here. Filament production requires relatively large quantities of polymer composite sample (10 –100 g) and was not approachable with our current production scale (~0.1g) for CF powder. PCL was used in FY20 to heat press films and was used again as a matrix for 3D printing because of its relatively low melting temperature of 60 °C. Lyophilized CF powder was folded into PCL melted at 80 °C, then the PCL was flattened and cut into small pellets (Figure 3A). The overall mass loading ratio of CF powder to PCL was 0.05.

Next, print settings on the Allevi bioprinter were assessed for printing PCL. This printer uses a mobile heated syringe print head, which is pneumatically controlled to dispense a PCL melt. The best PCL print accuracy was attained with syringe temperature of 90 °C, 40 psi pneumatic pressure, and 1 mm/s print head. It was possible to print with lower temperature, higher pressure, and/or faster print speed, however the prints tended to have more flaws. One drawback of using a heated syringe to melt nurdles directly instead of using a filament printer is that all starting material is exposed to elevated temperatures for the entirety of the print time. For this reason, printed CF-PCL objects would have to be limited in size to prevent CF powder heat inactivation. It was found in FY20 that CF powder can only withstand temperatures at 80 °C for 30 minutes or less.

Due to limitations in the available quantities of CF-PCL composite nurdles and the restrictions imposed by print size and speed, the heat extrusion process was approximated by using a metal syringe heated to 90 °C to extrude CF-PCL by hand instead of using the printer (Figure 3B). Crude shapes were formed as shown in Figure 3A. Finally, these shapes were sliced into small PCL pieces to be rehydrated in a sealed 24-well microplate for 2 hours, followed by imaging under blue light and orange filter to capture GFP fluorescence. GFP fluorescence was observed indicating the CF bioactivity can withstand the second heat treatment and applied shear force in the syringe. Thus, it is conditionally feasible to 3D print a bioactive PCL material using heat extrusion. To approach this as a useful application, it is likely that filament would need to be formed, which would add yet another intermediate heat step. Optimization of each of these steps to minimize material residence time at high heat is an important prerequisite that requires larger scales of CF powder for testing.

The second 3D printing method tested is SLA printing, which uses UV light projected in a pattern to cure resin in 2D layers attached to a vertically rising platform (Figure 3D). Resin 3, SIRAYA Tech "Simple" in clear, was selected from the screen of resins described in section 2.1. Prior to lyophilization, 1.7 mL of aqueous CF reaction was mixed with 66.7 mg of microcrystalline cellulose added as a bulking agent. After lyophilization, this resulted in 197 mg of CF-cellulose powder. This powder was mixed with 112 g or 100 mL Resin 3 (approximately 0.0017 weight ratio CF-cellulose powder). This mixture was loaded into the SLA printer reservoir and was used to print a lattice cube with support structures to attach it to the printer platform. Two more cube shapes were printed with the remainder of the resin. However, because of settling of the CF-cellulose powder in the reservoir overtime, very little CF solids seemed to be embedded in the later prints. All SLA cube prints were rehydrated by placing the entire cube into the well of a

24-well plate and washing with 250 µL water. This is not enough water to submerge the entire cube, but the high surface-area lattice structure does hold onto water via surface tension and maintains a high level of water contact. The wells were sealed with a plate sealer and incubated at 37 °C overnight. The following day, the wells were photographed under blue light with an orange lens filter to capture GFP fluorescence (Figure 3C). Water extracted from the wells was also imaged. The first cube printed produced visible GFP, while later prints from the same batch of resin did not. Overall, this experiment indicates it is possible to use CF powder in SLA 3D-printing to achieve a bio-active polymer object, though there are hurdles to making the process more robust. Improved mixing, improved powder dispersion, and/or increased CF powder quantities in the resin reservoir are all likely to improve the distribution of active CF activity within SLA-printed objects. An interesting difference between PCL and SLA resin materials was noted. GFP fluorescence localized to the PCL solids in the heat extruded sample, but fluorescence signal was primarily observed in the wash water for the SLA printed resin sample. These observations hint at differences in material behaviors, like water and solute transport that could play an important role in device function. Further investigations are necessary to understand these effects and achieve predictable activity in CF-functionalized materials.

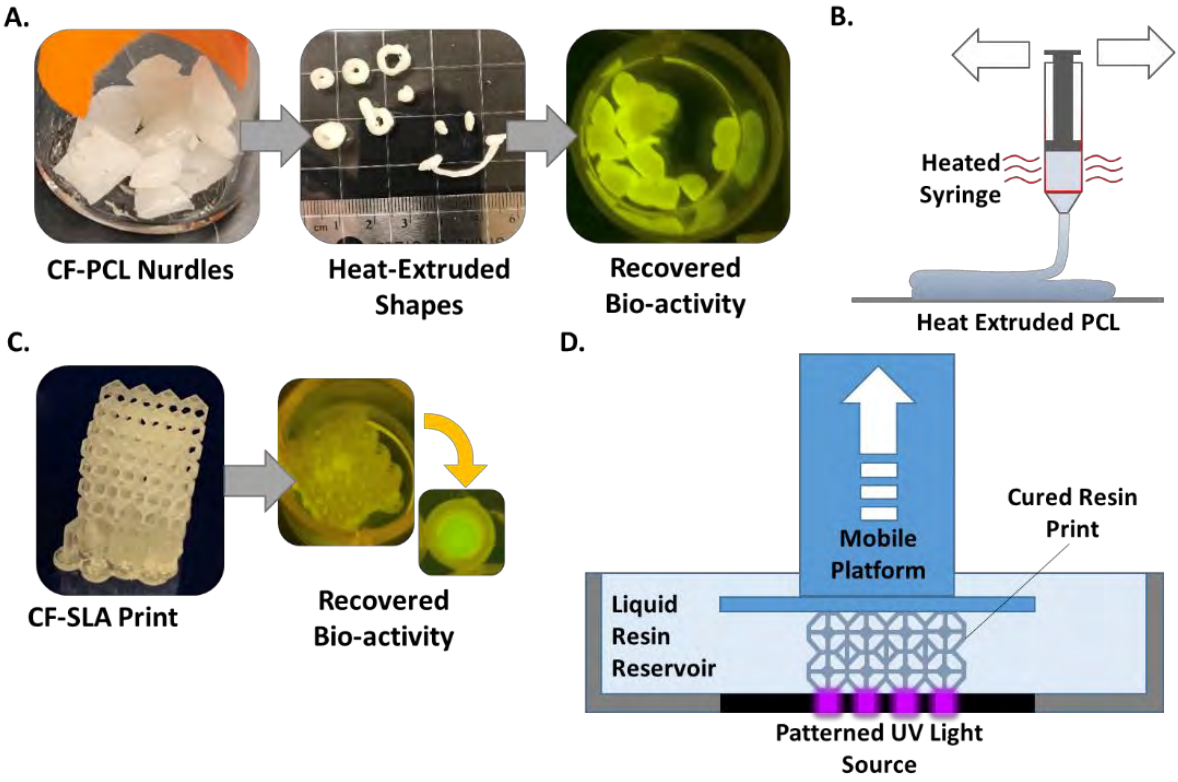

Figure 3. (A) Photographed stages in heat-extrusion printing of CF-PCL composite. Lyophilized CF powder is embedded in PCL nurdles after a preliminary melt step (left). Nurdles are placed in a metal syringe and heated to 90 °C and extruded by hand into coarse shapes (middle). Extruded CF-PCL is cut into small pieces and incubated in water at 37 °C for 2 hours to assess GFP production via CF activity (right). (B) Illustration of heat extrusion of CF-PCL. (C) Lyophilized CF powder embedded in a polymer lattice cube object via SLA 3D-printing. Incubating the lattice in a water wash at 37 °C overnight yielded GFP produced by CF bioactivity. (D) Illustration of SLA 3D-printer.

2.3 Efforts to improve dispersion and reduce clumping in CF-polymer composites

CF powder is largely insoluble in organic solvents and liquid polymer resins or melts. A problem observed in multiple casting methods is a tendency for the CF powder to clump and aggregate, both during dry handling and when mixed into a suspension with the liquid polymer or organic solvent solution. This leads to non-uniformity observed in the morphology of the material as well as variability in the levels of recovered activity. Several factors were identified as potentially influencing aggregation: ambient humidity during powder handling and the hygroscopic nature of CF components, powder particle size, and non-favorable interactions with polymer and/or solvent in solution. Additives to improve powder handling, or protein-solvent interactions, were tested as countermeasures. Using sieves to control particle size of the dried powder was also examined as a potential solution.

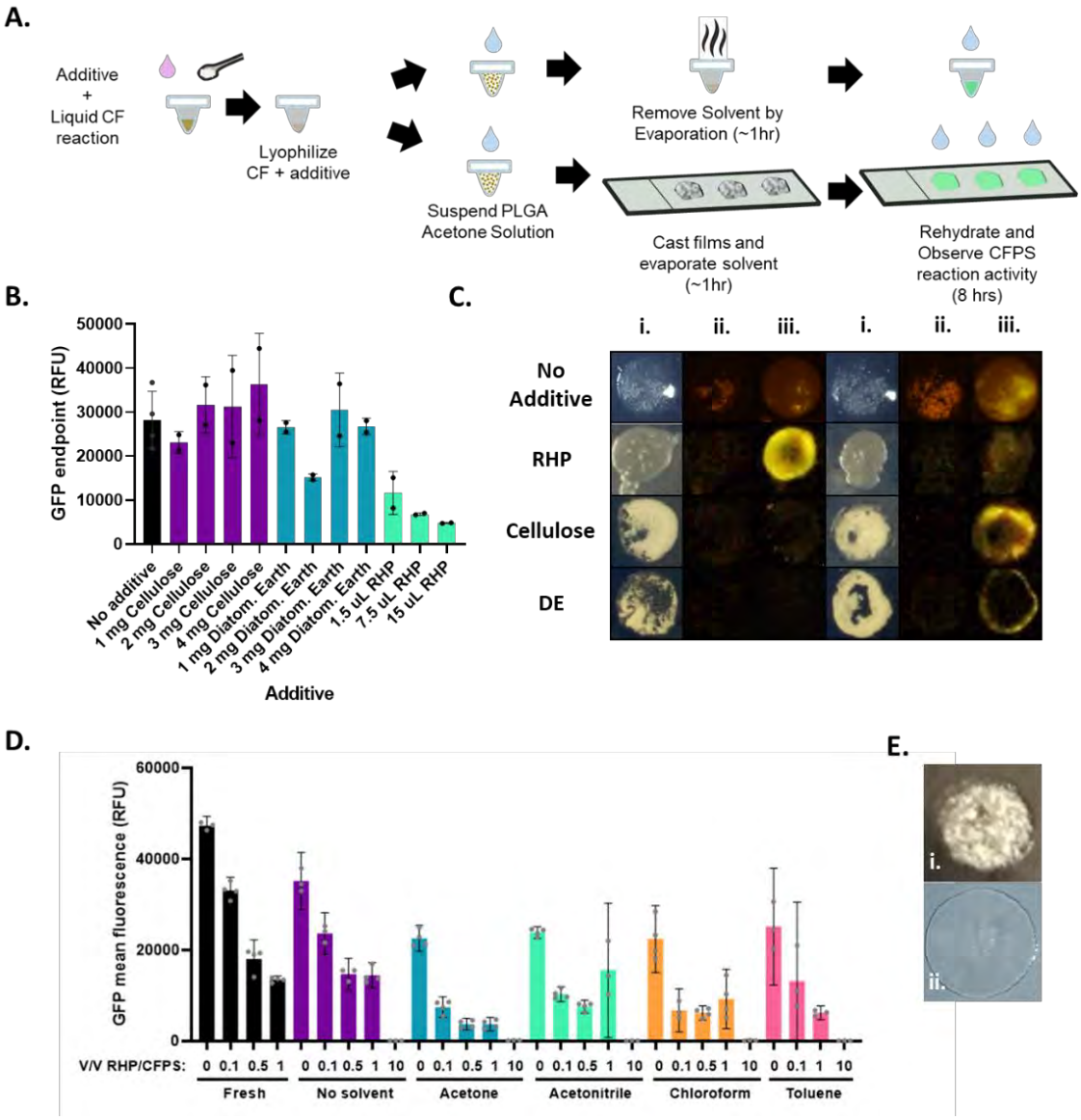

Figure 4. Exploring the effects of additives on CF activity and CF-polymer film morphology. (A) Diagram showing the treatment sequence to test additives in CF-polymer composites. (B) CF-polymer protein synthesis productivity in microplate at an 8 hour endpoint, in the presence of various amounts of additives. (C) CF-polymer protein synthesis productivity in films at an 8-hour endpoint, in the presence or absence of additives. (D) 8 hour endpoint GFP productivity in CF protein synthesis reactions mixed with RHP additive and exposed to various organic solvents. (E) Photographs of acetone-cast PLGA films containing cellulose powder untreated (i) or passed through a 230 mesh sieve (ii).

Three additives tested include microcrystalline cellulose and Diatomaceous Earth (DE) as bulking agents to improve powder handling, and Random Hetero Polymer (RHP) developed to improve the tolerance of lyophilized proteins to organic solvents.[13] As a first test, these additives were screened at various ratios for their effect on protein synthesis activity and morphology in CF-polymer films. Cellulose powder, DE powder, or RHP stock solution were mixed with the aqueous CF solution prior to lyophilization in the wells of a microplate (Figure 4A). Then, PLGA dissolved in acetone was added to each well, the acetone was either allowed to evaporate from the well, or the suspension was cast as a film on glass. The CF-polymer composites were then hydrated either in wells, or on slides. The appearance of GFP fluorescence was measured by a microplate reader for the samples in wells (Figure 4B) or by photography under blue light and with an orange lens filter for the film samples (Figure 4C). The quantified fluorescence in wells shows that RHP addition reduces GFP productivity relative to the control without any additive. Additions of cellulose and DE did not show a clear decrease in activity at most concentrations, though the 2 mg DE samples had somewhat reduced productivity.

The film samples exhibited much more variable fluorescence production. For each additive condition, only 1 in 2 samples showed significant visible fluorescence. This variability can be due to several factors, including the loss of suspended CF components during pipet casting, or inconsistent water exposure across the surface of the films, in addition to the previously observed variable dispersion during casting. Nevertheless, the morphology of cast films can be compared between different additives. Though RHP reduced activity in the microplate samples, it significantly improved the dispersion and uniformity in the PLGA film. While in other films, the fluorescence production is localized to portions of the film, the RHP film had more uniformly distributed fluorescence. However, there was still variability in overall activity since only 1 in 2 films had significant fluorescence. Notably, the lyophilized RHP and CF mixture could not be ground into a powder, but rather formed a viscid solid that could dissolve in acetone. The bulking agent additives, Cellulose and DE, both functioned to improve powder handing and reduced clumping, but they increased the net amount of insoluble solids in the CF-polymer composite, which affect polymer properties. Further, there was an increased tendency for the powder to form a ring around the edge of the film. The film samples containing DE had less fluorescence overall and all fluorescence was confined to the outer edge.

RHP was examined further in a solvent screen, to determine if RHP's effects on activity were dependent on the type of solvent used. RHP stock solution was mixed with CF reactions prior to lyophilization in the wells of a microplate. Then organic solvents acetone, acetonitrile, chloroform, or toluene were added to the lyophilized solids. The solvents were removed by pipet, with residual solvent allowed to evaporate before the CF powder was rehydrated and GFP production was quantified (Figure 4D). The trends were similar for every solvent tested: increasing RHP concentration tends to reduce GFP productivity.

Next, the use of sieves was explored to control particle size of the CF powder, and observe how this affected acetone-cast CF-polymers. The use of sieves with CF powder can be difficult due to excessive clumping. CF ingredients are quite hygroscopic, so increased exposure to ambient air results in increased cohesion. To get reliable particle size results, cellulose was used as a bulking agent to improve flowability. Still, passing CF-cellulose powder through a sieve resulted in losing most of the materials at the milligram scale. Thus, it was determined that sieves could only be thoroughly tested at a larger scale of material. In the absence of that capability in FY21, cellulose alone was used as a stand-in for CF powder to understand the effects of particle size on dispersion in solvent cast films. Figure 4E illustrates the difference in morphology in acetone-cast PLGA with un-treated cellulose (i) versus cellulose passed through a 230 mesh (63 µm particle size) sieve. There is clearly improved dispersion at smaller particle sizes, indicating this is a worthwhile future approach. The use of a sieve is not the only method by which particles could be formed using CF components. Coated particles may be formed by spray drying or by using emulsion or microfluidic methods to form defined particles prior to drying. Spray drying using a custom small-scale setup will be attempted in year 3 (Figure 5).

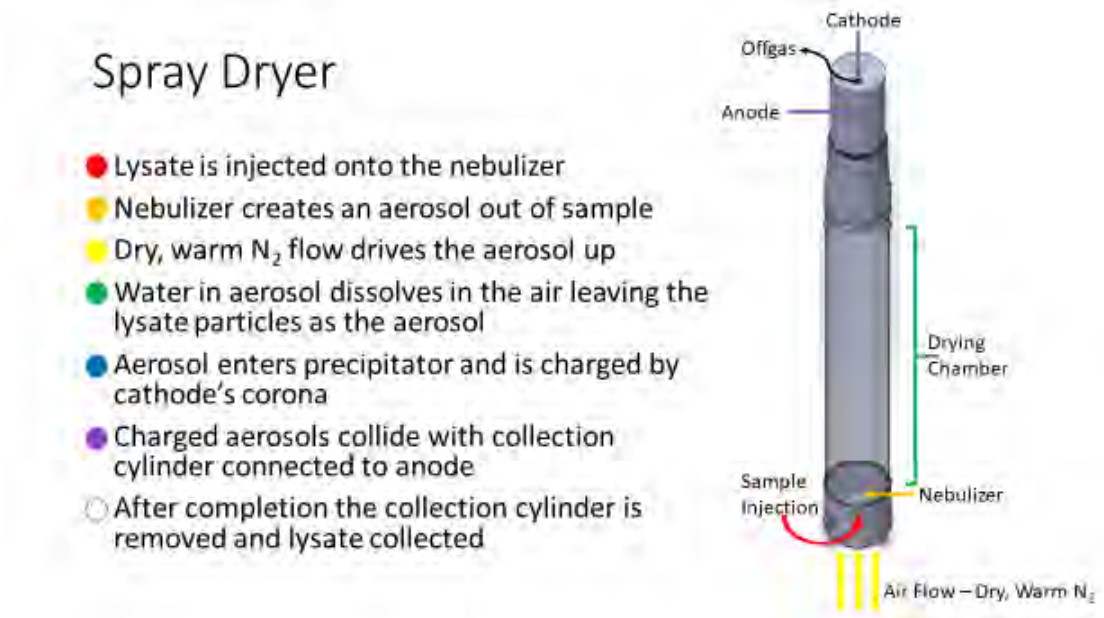

Figure 5. Illustration of proposed small-scale spray drying apparatus.

2.4 Time-lapse CF-polymer film microscopy

Implementing CF bio-reactions within solid materials introduces new challenges for measuring activity and underlying phenomena such as mass transport. It is critical to understand how these factors relate to composite formulation and casting methods because of their large impacts on bio-functionality. Microscopy time-lapse imaging with image stitching was used to observe morphology of eight whole CF-polymer films during the rehydration and GFP production process. Three representative films out of eight are shown in Figure 6. These images show the dynamics of water infiltration and GFP production and demonstrate localized activation of protein synthesis activity within films. The PLGA polymer matrix is initially transparent, with CF particle inclusions visible. The dried CF material appeared to contain both crystalline and amorphous phases with variable particle sizes of 10-100 µm (much larger than the size of an *E. coli* cell (~1 µm)). As water infiltrated the material, the PLGA became cloudy and hydrolysis of the polymer started to occur. Water infiltration occurs within the first 30 minutes of water exposure, and GFP production was detected between 20 minutes and 1 hour after addition of water. Particles of dried CF material were co-localized with the emerging GFP fluorescence, though not all particle inclusions reactivate to produce fluorescence which could be caused by non-uniform distribution of CF components. Over the incubation time, the sharp edges of crystalline, lyophilized components became blurred and water expanded pockets within the PLGA. In contrast to CF-PLGA films imaged via photography, all eight films imaged produced some degree of the GFP fluorescence. The microscopy method provides increased sensitivity and filling slide wells with water allows full submersion of the films. This method will provide detailed data with enough throughput to have replicates and side-by-side comparisons as additives, polymers, and casting method are modified in composite preparations.

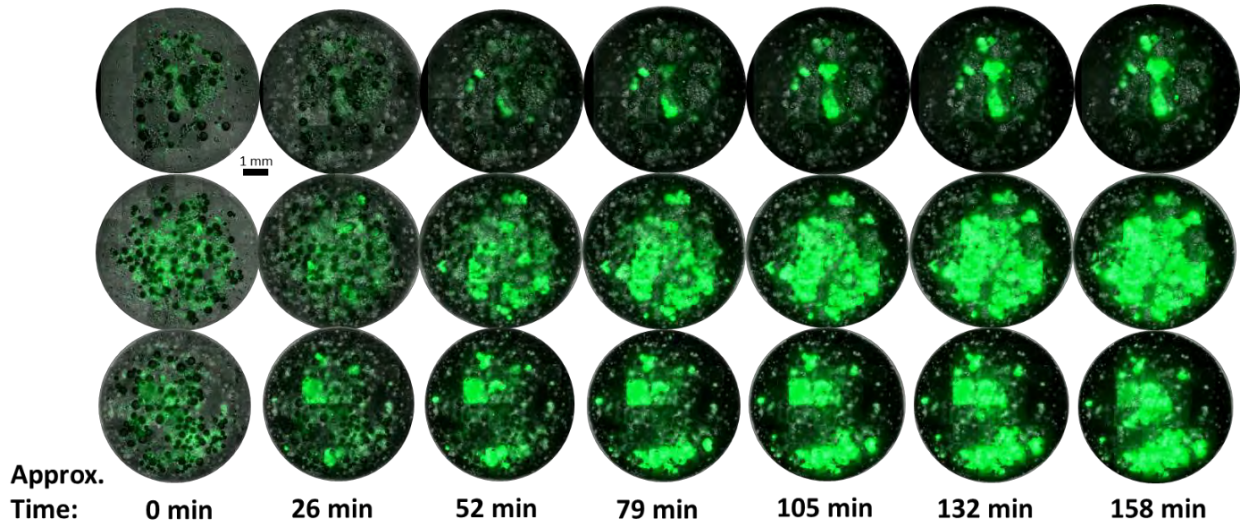

Figure 6. CF-PLGA films were solvent cast using acetone into 8-well microscope slides followed by rehydration and real-time imaging via widefield microscopy with incubation at 37 °C.

2.5 Measuring water infiltration in CF-polymer composite films

Quantifying the diffusivity of water and other solutes in polymer films may be done using breakthrough Fourier transform infrared (FTIR) spectroscopy. An illustration of the breakthrough apparatus and data collected for PCL samples are shown in Figure 7. The film sample is placed between a pressurized water reservoir and an Attenuated Total Reflectance (ATR) crystal element used to collect an infrared spectrum at points over time. The peaks of these spectra can be assessed for the changes to the polymer, appearance or breakthrough of the water solvent or dissolved solutes, or changes to composite cargoes. Here, the peak for water was integrated for each time point to create a breakthrough curve that is fit to Fick's law to find diffusivity. Thus far, diffusivity values are similar between pure PCL and PCL composite samples, though the cellulose additive does slow water diffusion somewhat, and diffusivity is quite variable in the CF-PCL composite. This technique will be used to analyze water diffusivity in more PCL replicate samples as well as PLGA samples in future work.

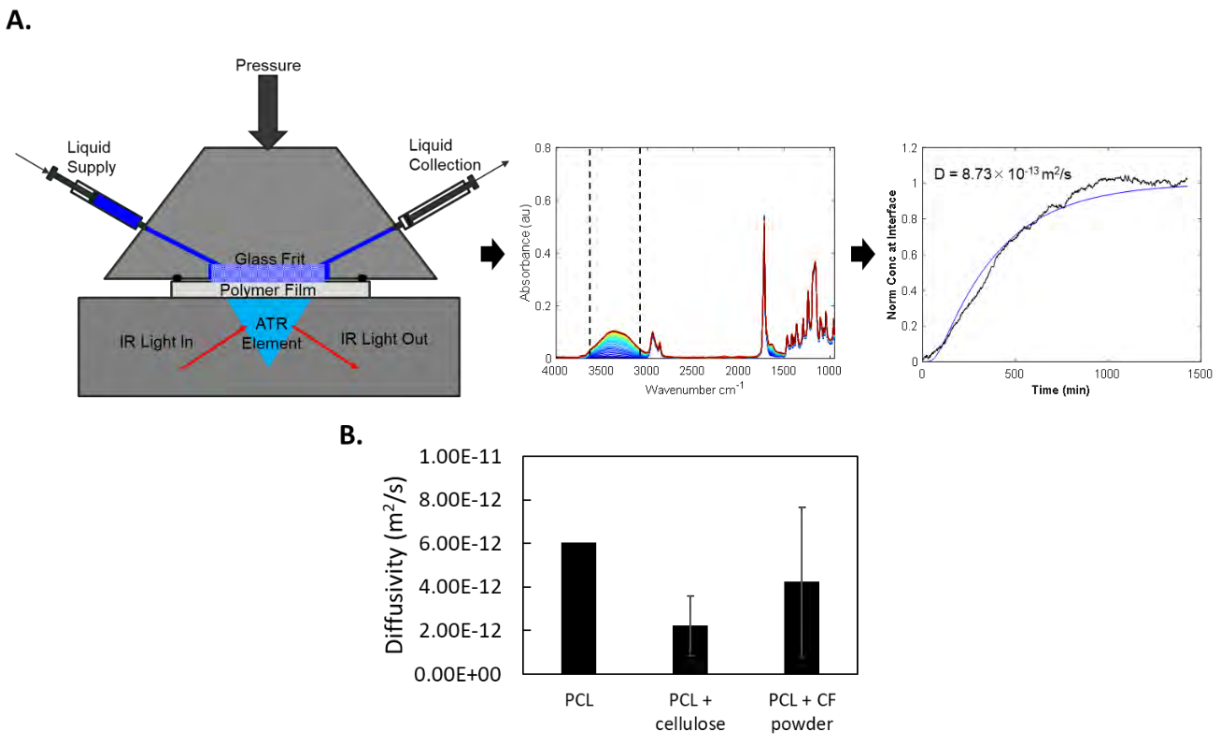

Figure 7. (A) A flow chart showing data collection for water diffusivity in films. Breakthrough FTIR spectroscopy apparatus diagram (left). Example output spectra with color coding blue to red indicating early to late times (middle). Peak between dotted lines at 3100-3600 cm^{-1} is integrated to produce the water breakthrough curve (right). The water breakthrough data is fitted to Fick's second law to estimate diffusivity. (B) Diffusivity values estimated for heat pressed PCL and PCL-composites.

2.6 Sensing arsenic with solvent cast CF-polymers

There are many functions possible using CF systems beyond simply producing GFP. We sought to demonstrate that these more complex functions are also robust for exposure to organic solvent and polymer solutions. The first such application is an arsenic sensor designed for water quality testing in a CF platform. An arsenic sensing polymer material could be used in a filter or bottle to alert the user to drinking water contaminants. The sensor used here has been designed for liquid lysate-based myTXTL CF reactions, but was untested for lyophilizated or solvent-processed treatments. The sensor is encoded in two linear DNA fragments amplified by polymerase chain reaction (PCR) (Figure 8A). The first segment is referred to as "repressor DNA" and codes for the constitutive P_{70a} promoter-activated production of the ArsR repressor protein. In the second DNA segment, called the "reporter DNA", a P_{ars} promoter controls production of GFP reporter. The repressor DNA is pre-incubated in CF reactions such that the repressor protein is present initially. Then, reporter DNA is added on ice prior to lyophilization, polymer processing, or CF reaction incubation. Arsenic is introduced at 0, 10, or 50 µM during the rehydration step and GFP is detected with incubation at 30 °C. Endpoint GFP levels are plotted for several different CF reaction processing treatments in Figure 8. Increased GFP signal was detected in the presence of arsenic for both fresh and lyophilized samples (Figure 8B, C). Further treatments with organic solvents decreased the GFP signal in the presence of arsenic. Chloroform and ethyl acetate treatments prevented discrimination between samples with/without arsenic, while acetone treatment maintained a lower positive signal with arsenic present. When the lyophilized CF reactions were exposed to PLGA dissolved in acetone, the activity in the presence of arsenic was improved and comparable to the untreated control on average, but variability was very high. From this data we can conclude the transcription factor-based sensing mechanism for arsenic can maintain functionality after lyophilization, and solvent casting processes, but optimization to improve robustness and sensitivity is needed.

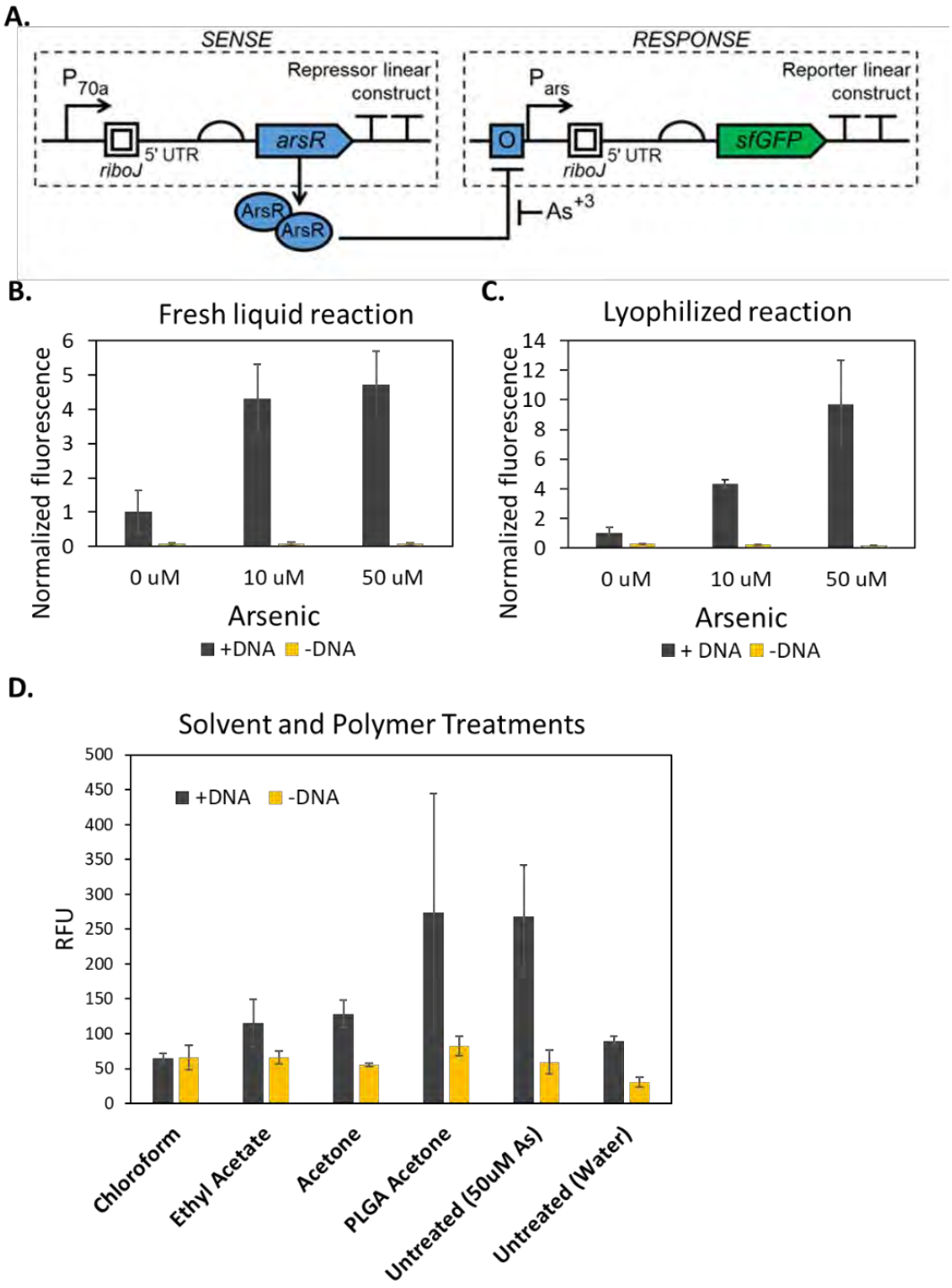

Figure 8. (A) Diagram of genetic construct for Arsenic sensor controlled by the P_{ars} promoter and ArsR transcription factor repressor. ArsR is constitutively produced under the P70a promoter. In the presence of arsenic, ArsR de-represses P_{ars} transcription to allow production of GFP reporter. (B) Endpoint GFP signal for CF reactions containing arsenic sensor DNA in fresh and untreated aqueous reactions. (C) Endpoint GFP signal for CF reactions containing arsenic sensor DNA in lyophilized and rehydrated reactions. (D) Endpoint GFP signal for CF reactions containing arsenic sensor DNA in lyophilized reactions treated with various solvents or PLGA dissolved in acetone, before solvent evaporation and reaction rehydration. All reactions except for the "Untreated (water)" reactions contained 50 µM arsenic. Error bars represent standard deviation of at least three replicates.

2.7 Producing antimicrobial colicin with solvent cast CF-polymers

A second application of CF-polymers is the production of useful molecules to add function to a material. One example is the production of an antimicrobial protein to counteract harmful contamination in a coating or device. Here we test whether colicin can be produced after exposure to the solvent-casting process. Colicin is a protein capable of inhibiting *E. coli* growth and is of interest to combat infections. Colicin-functionalized materials could be used in medical equipment and implants like ventilators or catheters to prevent device-associated infections. Colicin was expressed from a linear DNA fragment with a constitutive T7 promoter. The colicin DNA was added to CF reactions prior to lyophilization. Then, dried reactions with and without DNA were exposed to acetone, a solution of PLGA in acetone, or left untreated. After solvent evaporation, reactions were rehydrated and incubated for two hours at 37 °C to stimulate production of colicin. Aliquots of CF reactions were added to a subculture of *E. coli* bacteria and cell density was recorded over time (Figure 9). CF reactions containing colicin DNA efficiently inhibited the growth of *E. coli* in all cases. Untreated and PLGA-treated samples showed complete inhibition, while acetone-treated samples had a small amount of growth. This result mirrors the arsenic sensor results in that the addition of polymer improves activity relative to the solvent-only treatment. CF-polymers are a promising new material platform that can deliver multiple functions for different applications.

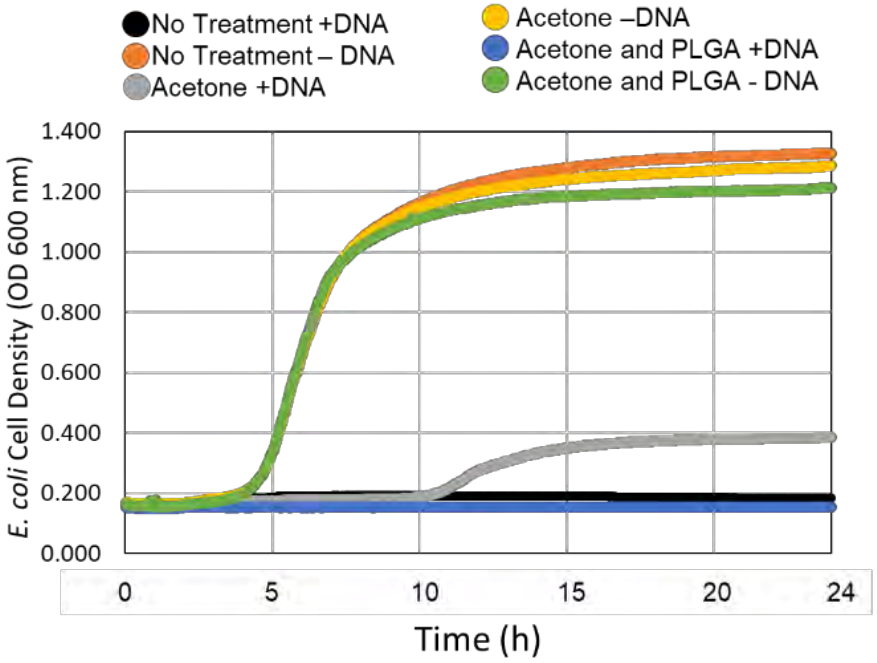

Figure 9. Cell density growth curve for *E. coli* after addition of CF reactions. CF reactions were mixed +/- colicin DNA, lyophilized, and subjected to one of three conditions prior to rehydration and incubation: no treatment, exposure to acetone, or addition of acetone-cast PLGA.

3. METHODOLOGY

3.1 Reagents and DNA

Unless otherwise noted, all reagents were purchased from MilliporeSigma® (St. Louis, MO). The default plasmid template for constitutive expression of GFP via CF was pY71sfGFP with Genbank accession number MT346027. Plasmid DNA was purified from transformed *E. coli* using a PureYield™ plasmid miniprep kit (Promega Corporation; Madison, WI), followed by ethanol precipitation to further concentrate and purify the DNA. The sequence of linear DNA for colicin E1 with a 6x-Histidine tag was published by Ouyang et al.[22] Linear fragments for colicin and arsenic sensor were ordered as gblocks™ (Integrated DNA Technologies; Newark, NJ). The gblocks were amplified by PCR using Q5 PCR™ master mix (New England Biolabs), to obtain increased quantities. DNA was stored in RNase and DNase-free water at -20 °C until reaction assembly. The RHP additive was provided by Professor Saadyah Averick, Allegheny Health Network Research Institute.

3.2 CF reaction preparation

PANOx-SP cell extract is prepared from shake flask cultures of *E. coli* BL21 Star (DE3) according to the growth and sonication protocol detailed previously by Kwon and Jewett.[21]

Lysates were aliquoted, flash frozen in liquid nitrogen, and stored at -80 °C until use in CFPS reaction assembly. To assemble reactions, CFPS components were thawed on ice, then combined with DNAse free water to reach the final concentrations listed in the FY20 report for PANOx-SP.[9] If expressing GFP from the PY71 sfGFP plasmid, the final DNA concentration was 6.5 nM. See descriptions on DNA below for the arsenic sensor and colicin production experiments. A DNA stabilizer, GamS (NEB), was added at 30 µg/mL to arsenic sensor and colicin CF reactions containing linear DNA, but not added to GFP reactions containing plasmid DNA. Reaction mixtures were well mixed and distributed 15 µL per well into 96 well, v-bottom, polypropylene plates (Costar 3357), or distributed at 0.1-1mL in glass lyophilization vials for larger scale CF powder preparations.

For additive experiments, RHP, cellulose, and DE were added to CF reactions at the concentrations noted in the text and well mixed prior to lyophilization.

3.3 Lyophilization of CFPS reactions

To lyophilize CFPS reactions in a microplate, the 96 well plate is dipped in liquid nitrogen and transferred to a shelf-type lyophilizer (SP Scientific, VirTis Wizard 2.0) with initial temperature set to -40 °C. When the lyophilizer chamber is sealed, the vacuum is initiated to reach approximately 200–300 mTorr. Then, primary drying is initiated with a shelf temperature of -20 °C and maintained for four hours. The secondary drying step changes the shelf temperature to 15 °C and is maintained overnight or approximately 17 hours. Microplate samples removed from the lyophilizer were immediately treated with solvent, or solvent and polymer, as indicated and rehydrated to monitor protein synthesis activity. Larger volumes of CFPS reaction may be lyophilized in vials. A longer secondary drying step of at least 48 hours is necessary to achieve good powder formation. Lyophilized CF powders can be stored in a desiccator for at least two months. When powder that has been stored is used to make and test CF-polymer materials, untreated powder is rehydrated as a control to measure activity after storage in comparison polymer-cast samples.

3.4 Testing CF powder composites with various UV-cured resins

15 µL CF reactions were lyophilized in a microplate, then 6 types of resin (Table 1) were added to wells at either 7.5 or 15 µL. For each resin type and resin amount, half of the wells were mixed to evenly distribute CF powder and others were not mixed. Resins were solidified by exposing the entire plate to a UV trans illuminator at 360 nm for 10 minutes. 15 µL of water was added to each well to rehydrate CF powder and the plate was sealed and placed in a 37 °C incubator overnight. The next day, an endpoint GFP fluorescence measurement was recorded with a Biotek Synergy H1 plate reader, excitation/emission (ex/em): 485/528 nm, with gain of 100. Images of the plate and the extracted resin solids were also captured using photography under white light and under blue light with an orange tinted lens filter. After the solids were removed from the plate, a second fluorescence reading was measured for the solution phase. Control wells without any resin added or without any CF powder added were also processed with UV light, hydrated, and measured for fluorescence.

3.5 PCL Heat extrusion

CF-PCL nurdles were made from CF powder lyophilized at the 1 mL scale in glass lyophilization vials. Lyophilized CF powder was folded into PCL melted at 80 °C, then the PCL was flattened and cut into small pellets. The overall mass ratio of CF powder to PCL was 0.05. CF-PCL nurdles were loaded into the metal syringe of the Allevi 1 bioprinter (Allevi; Philadelphia, PA). CF-PCL was melted by heating the syringe on the printer set to 90 °C. When the syringe reached the set temperature after several minutes, it was removed from the printer and a syringe plunger was used by hand to extrude PCL shapes. The shapes were cooled, then chopped into ~3 mm pieces and placed into the wells of a 24-well microplate. PCL pieces were washed with excess 250 µL of water and incubated for 2 hours at 37 °C to reactivate CF protein synthesis activity. Endpoint GFP readings were measured in the plate with a microplate reader, ex/em: 485/528 nm, with extended gain. (Biotek Synergy Neo2). Photographs were also taken under blue light with an orange tinted lens filter.

3.6 SLA 3D printing

The SLA 3D printer used was Phrozen Sonic Mini (Phrozen Technology; Hsinchu City, Taiwan). The resin selected for use was SIRAYA Tech Simple model resin. The STL file for the printed object was the ProFab Lattice Cube by

ProFab3D published on Thingiverse (thingiverse.com/thing:2522147). The slicing software used was Chitubox. The cubic print was sized at 1 cm^3. Prior to lyophilization, 1.7 mL of aqueous CF reaction was mixed with 66.7 mg of microcrystalline cellulose added as a bulking agent. After lyophilization, this resulted in 197 mg of CF-cellulose powder. This powder was mixed with 112 g or 100 mL Resin 3 (approximately 0.0017 weight ratio CF-cellulose powder). This mixture was loaded into the SLA printer reservoir and was used to print a lattice cube with support structures to attach it to the printer platform.

3.7 Solvent treatments and solvent polymer casting

All solvent treatments are performed in a chemical fume hood. For exposure to organic solvent without polymer, 100 µL of each solvent was added to the lyophilized CFPS reaction mixture in designated wells of a polypropylene microplate (Costar 3357). No solvent was added to lyophilized control reactions. Wells were sealed with a flexible polypropylene storage mat (Costar 3080) to prevent evaporation. Reactions were incubated with solvent for one hour at room temperature. Following solvent incubation, plates were briefly spun at low speed in a centrifuge to settle the insoluble CFPS reaction components, then solvents were removed by aspiration with a pipette without disturbing the pellet. The residual solvent was removed by evaporation. After solvent removal, all reactions were rehydrated with 15 µL of DNase free water to return CFPS reaction components to their original aqueous concentration.

For acetone-cast PLGA treatments, 0.35 g PLGA 50:50 L:G was dissolved in 1 mL acetone. 15 µL of the PLGA acetone solution was added to each well and mixed with the CF or CF-additive powder. For film experiments, the mixture of PLGA, acetone, and CF powder was drop cast using a pipet with a wide bore tip onto a glass substrate. The acetone was allowed to evaporate to form a CF-PLGA film. For plate experiments the acetone was simply allowed to evaporate from the plate without drop-casting, leaving CF-PLGA at the bottom of the well.

Films were rehydrated on simple glass slides by added a 30 uL droplet of water, films rehydrated in 8-well slides for microscopy were rehydrated with 200 µL water. GFP formation and film morphology after rehydration were tracked over 8 hours either through automated photography with blue light and orange lens filter in at 37 °C incubator, or by microscopy as described below.

For plate experiments, immediately after rehydration, plates were sealed with a polypropylene mat, transferred to a BioTek Synergy H1 microplate reader, and incubated at 30 °C for 8 hours. Formation of GFP fluorescence was monitored by plate reader with excitation/emission: 485/528 nm with a gain of 100.

3.8 Microscopy

Microscopy images were captured of CF-PLGA films in 8-well microscope slides (Ibidi, 80826). The microscope used was a Zeiss LSM 800 Axio Observer inverted microscope (Carl Zeiss, LLC, Thornwood, NY, USA) in wide field mode with a Colibri 7 LED light source. The objective was an EC Plan-Neofluar 10x/0.30 Ph1 WD = 5.2 M27. Images were collected in two channels that are shown overlaid. The GFP fluorescence channel uses the 475 nm LED at 10 % intensity, 150 ms exposure time with filter set 90 HE LED. The DIC channel shows film morphology with auto exposure. Images are captured with an Axiocam 506 camera. Image stitching and time lapse captured whole films in 8 wells approximately every 26 minutes for 8 hours using automated stage, automated focus, and incubation enclosure set to 37 °C.

3.9 FTIR procedure

Time-resolved FTIR spectra (60 scans, 4 cm-1 resolution) were obtained on a FTIR (Thermo Scientific Nicolet iS50R) coupled with a single reflection diamond ATR accessory (golden gate, Spec AC) using the pressure-contact method developed by Santos and Elabd.[23] In this setup a free polymer film was placed in contact with the ATR element, a glass frit (Chemglass, borosilicate fritted disc, 10 mm) was placed on top of the film and pressure was applied by a liquid exposure cell while sealing around the perimeter of the film with an o-ring as shown in Figure 7A. FTIR spectra collection was started at a rate of 1 min-1 for 10 minutes before introducing water to capture the baseline spectrum of the pure polymer. The water was pushed into the exposure cell via syringe, saturating the glass frit, and the excess was collected by a second syringe. This ensured that the surface of the polymer film was exposed to a constant amount of water throughout the experiment. Collection of the FTIR spectra continued for 2880 min (2 days) to monitor the water absorption by the polymer over time.

Difference spectra were computed by subtracting the reference pure polymer spectrum from all the spectra collected throughout the experiment. The concentration of water in the polymer film at the interface with the ATR element was quantified by integrating the difference spectra over the wavenumber range 3,100–3,600 cm-1 yielding a breakthrough

curve for water. The breakthrough curve was normalized using the integrated area (3,100–3,600 cm-1) after equilibrium has been reached. The diffusion process was modeled using Fick's second law assuming a constant diffusivity of the water in the polymer film. The constant diffusivity of the water was adjusted to minimize the error between the model-predicted normalized concentration at the backside of the polymer film and the experimentally observed normalized breakthrough curve using the MATLAB nonlinear least squares optimization function (nlinfit, MATLAB 2019b).

3.10 Arsenic sensor

The arsenic sensor was implemented in CF reactions with or without solvent and PGLA treatments as described above, with small modifications to the method. First, the CF reactions were mixed on ice with all components except the DNA. Then, linear repressor DNA was added at a concentration of 2 nM and the reaction was incubated at 30 °C for 1 hour to pre-express ArsR repressor protein. After 1 hour, the reactions were returned to ice while reporter DNA was added to a concentration of 40 nM. For fresh prepared reactions without any treatment, concentrated arsenic solution was added to achieve 0, 10 or 50 µM concentration. For untreated lyophilized reactions or lyophilized reactions treated with solvent and/or PLGA, the reactions were flash frozen in liquid nitrogen directly after addition of reporter DNA and placed at -80 °C until lyophilizaton. Drying, solvent, and polymer treatments were carried out as described above. Arsenic solutions were added at rehydration to achieve the designated concentration. Arsenic sensor reactions were incubated in a Biotek Synergy H1 microplate reader at 30 °C for 8 hours. Fluorescence was measured at ex/em: 485/528 nm, with gain of 100.

3.11 Colicin assay

E. coli MG1655 cultures were prepared to assay colicin antimicrobial activity. On day 1 of the experiment, the strain was streaked from freezer stock onto LB agar. Then on day 2, colonies were used to inoculate 3 biological replicates in 5 mL LB media with 1 % glucose in 50 mL conical tubes. These starter cultures were grown overnight at 37 °C, and 250 rpm orbital shaking. On day 3, *E. coli* starter cultures were diluted 1:100 in LB + 1 % glucose and grown until an OD_{600} of 0.05 or $4x10^8$ cells/mL. Then the *E. coli* subcultures are diluted to ~10^4 cells/mL and are distributed at 200µL per well in a sterile Costar 96-well flat bottom plate (#3370). All unused wells are filled with 200 µL blank media.

On day 2 of the experiment, linear colicin DNA was added at 40 nM final concentration to 15 µL CF reactions in a 96-well microplate prior to lyophilization. When lyophilization was complete on day 3, dried reactions with and without DNA were exposed to acetone, a solution of PLGA in acetone, or left untreated. After solvent evaporation, reactions were rehydrated with 15 µL of water and incubated for two hours at 37 °C to stimulate production of colicin. 10µL aliquots of CF reactions were added to each well of the prepared microplate of diluted *E. coli* cultures.

The *E. coli* culture plate was sealed with a Breathe-Easy® oxygen permeable plate sealer (Sigma Z380059). The plate was incubated at 30 °C in a Biotek Synergy Neo2 microplate reader for 24 hours with linear shaking at 567 cpm, a 1 °C temperature gradient to prevent condensation and evaporation and reading optical density every 2 minutes.

4. CONCLUSIONS

We have demonstrated that lyophilized CF reactions tolerate several polymer casting processes, including solvent casting, melt casting, and UV resin curing, and maintain high levels of transcription and translation activity. PLGA, PCL, and SLA resin polymers have all shown compatibility. Further, heat extrusion and SLA 3D printing processes were used to make CF-functionalized bio-active objects as proof of concept. Additional studies are needed to better define the factors at play in composite casting uniformity and the interaction between polymer, CF powder, and water as bioactivity is reactivated. Bulking agents and RHP additives were tested and achieved some benefits in powder handling and solvent-casting uniformity, respectively. However, variability in GFP productivity was still an issue. We noted that controlling particle size via sieve was not possible with low CF reagent quantities, though there are other approaches like microfluidics or emulsion encapsulation that could enable particle size control. Improving dispersion and polymer cast uniformity will be enabled by increased scale of CF reagent preparation, study of spray drying and particle size control, and expanded screens of additives and other casting variables like loading and polymer concentrations.

Applying microscopy and breakthrough FTIR spectroscopy to measure water infiltration and GFP production rates are important developments to capture detailed information and gain insights on the effects of polymer encapsulation under varying formulation conditions. Results from these techniques will support model building so that more complex form factors and functions can be constructed with predictable results in the future. Initial measurements of activity in polymer formats confirm our hypothesis that the properties of the polymer greatly impact the hydration rate, and therefore activation of the CF reaction. We predict that detailed understanding of water intrusion into the composite material and its effect on CFPS activation will fuel the design of coatings and fibers that continuously release CFPS components for an extended activity lifetime. This understanding will include optimization of parameters such as polymer and CFPS formulation and improved casting methodology. Other potential benefits include exploiting new device form factors and controlling localization in CF reactions to improve function.

Finally, towards application of CF-polymers, we demonstrated the function of an arsenic sensor and production of physiologically relevant levels of colicin antimicrobial protein in CF reactions exposed to solvent-cast PLGA polymer. These preliminary results unlock promising future applications to make materials capable of sensing and self-decontamination. Indeed, combining myriad variations in polymer chemistries and casting methods with the vast array of DNA-encoded biological functions has virtually boundless potential for new and dynamic material performance.

ACKNOWLEDGMENTS

Funding was provided by the U.S. Army via the Surface Science Initiative Program (PE 0601102A Project VR9) at the Combat Capabilities Development Command Chemical Biological Center.

REFERENCES

[1] Silverman, A.D.; Karim, A.S.; Jewett, M.C. Cell-free gene expression: an expanded repertoire of applications. *Nat. Rev. Genet.* **2020**, *21* (3), pp 151–170.

[2] Pardee, K.; Green, A.A.; Ferrante, T.; Cameron, D.E.; DaleyKeyser, A.; Yin, P.; Collins, J.J. Paper-Based Synthetic Gene Networks. *Cell.* **2014**, *159* (4), pp 940–954.

[3] Pardee, K.; Green, A.A.; Takahashi, M.K.; Braff, D.; Lambert, G.; Lee, J.W.; Ferrante, T.; Ma, D.; Donghia, N.; Fan, M.; Daringer, N.M.; Bosch, I.; Dudley, D.M.; O'Connor, D.H.; Gehrke, L.; Collins, J.J. Rapid, Low-Cost Detection of Zika Virus Using Programmable Biomolecular Components. *Cell* **2016**, *165* (5), pp 1255–1266.

[4] Pardee, K.; Slomovic, S.; Nguyen, P.Q.; Lee, J.W.; Donghia, N.; Burrill, D.; Ferrante, T.; McSorley, F.R.; Furuta, Y.; Vernet, A.; Lewandowski, M.; Boddy, C.N.; Joshi, N.S.; Collins, J.J. Portable, On-Demand Biomolecular Manufacturing. *Cell* **2016**, *167* (1), pp 248–259.

[5] Noireaux, V.; Liu, A.P. The New Age of Cell-Free Biology. *Annu. Rev. Biomed. Eng.* **2020**, *22* (1), pp 51–77.

[6] Smith, M.T.; Berkheimer, S.D.; Werner, C.J.; Bundy, B.C. Lyophilized Escherichia coli-based cell-free systems for robust, high-density, long-term storage. *BioTechniques* **2014**, *56* (4) pp 186–193.

[7] Pardee, K. Perspective: Solidifying the impact of cell-free synthetic biology through lyophilization. *Biochem. Eng. J.* **2018**, *138*, pp 91–97.

[8] Lee, M.S.; Raig, R.M.; Gupta, M.K.; Lux, M.W. Lyophilized Cell-Free Systems Display Tolerance to Organic Solvent Exposure. *ACS Synth. Biol.* **2020,** *9* (8), pp 1951–1957.

[9] Lee, M.S.; Raig, R.M.; Kuhn, D.; Blum, S.; Gupta, M.K.; Lux, M.W. Extending Bio-Functionality in Materials via Controlled Polymer Erosion. FY20 Proceedings of the US Army Combat Capabilities Development Command Chemical Biological Center In-house Laboratory Independent Research and Surface Science Initiative Programs, 2020; pp 57–70.

[10] Klibanov, A.M. Improving enzymes by using them in organic solvents. *Nature.* **2001,** *409*, pp 241–246.

[11] Schmitke, J.L.; Stern, L.J.; Klibanov, A.M. Comparison of x-ray crystal structures of an acyl-enzyme intermediate of subtilisin Carlsberg formed in anhydrous acetonitrile and in water. *Proc. Natl. Acad. Sci. U.S.A.* **1998**, *95* (22), pp 12918–12923.

[12] DelRe, C.; Jiang, Y.; Kang, P.; Kwon, J.; Hall, A.; Jayapurna, I.; Ruan, Z.; Ma, L.; Zolkin, K.; Li, T.; Scown, C.D.; Ritchie, R.O.; Russell, T.P.; Xu, T. Near-complete depolymerization of polyesters with nano-dispersed enzymes. *Nature.* **2021,** *592* (7855), pp 558–563.

[13] Panganiban, B.; Qiao, B.; Jiang, T.; DelRe, C.; Obadia, M.M.; Nguyen, T.D.; Smith, A.A.A.; Hall, A.; Sit, I.; Crosby, M.G.; Dennis, P.B.; Drockenmuller, E.; Olvera de la Cruz, M.; Xu, T. Random heteropolymers preserve protein function in foreign environments. *Science.* **2018**, *359* (6381), pp 1239–1243.
[14] Tibbitt, M.W.; Dahlman, J.E.; Langer, R. Emerging Frontiers in Drug Delivery. *J. Am. Chem. Soc.* **2016**, *138* (3), pp 704–717.
[15] Tian, H.; Liu, Z.; Zhang, M.; Guo, Y.; Zheng, L.; Li, Y.C. Biobased Polyurethane, Epoxy Resin, and Polyolefin Wax Composite Coating for Controlled-Release Fertilizer. *ACS Appl. Mater. Interfaces.* **2019**, *11* (5), pp 5380–5392.
[16] Ding, D.; Zhu, Q. Recent advances of PLGA micro/nanoparticles for the delivery of biomacromolecular therapeutics. *Mater. Sci. Eng., C.* **2018**, *92*, pp 1041–1060.
[17] Kamaly, N.; Yameen, B.; Wu, J.; Farokhzad, O.C. Degradable Controlled-Release Polymers and Polymeric Nanoparticles: Mechanisms of Controlling Drug Release. *Chem. Rev.* **2016**, *116* (4), pp 2602–2663.
[18] Yocum, H.C.; Pham, A.; Da Silva, N.A. Successful Enzyme Colocalization Strategies in Yeast for Increased Synthesis of Non-native Products. *Front. Bioeng. Biotechnol.* **2021**, *9*.
[19] Niederholtmeyer, H.; Chaggan, C.; Devaraj, N.K. Communication and quorum sensing in non-living mimics of eukaryotic cells. *Nat. Commun.* **2018**, *9* (1).
[20] Efrat, Y.; Tayar, A.M.; Daube, S.S.; Levy, M.; Bar-Ziv, R.H. Electric-Field Manipulation of a Compartmentalized Cell-Free Gene Expression Reaction. *ACS Synth. Biol.* **2018**, *7* (8), pp 1829–1833.
[21] Kwon, Y.-C.; Jewett, M.C. High-throughput preparation methods of crude extract for robust cell-free protein synthesis. *Sci. Rep.* **2015**, *5* (1).
[22] Ouyang, X.; Zhou, X.; Lai, S.N.; Liu, Q.; Zheng, B. Immobilization of Proteins of Cell Extract to Hydrogel Networks Enhances the Longevity of Cell-Free Protein Synthesis and Supports Gene Networks. *ACS Synth. Biol.* **2021**, *10* (4), pp 749–755.
[23] Santos, M.C.; Bendiksen, B.; Elabd, Y.A. Diffusion of Liquid Water in Free-Standing Polymer Films Using Pressure-Contact Time-Resolved Fourier Transform Infrared Attenuated Total Reflectance Spectroscopy. *Ind. Eng. Chem. Res.* **2017**, *56* (12) pp 3464–3476.

Purification and characterization of a membrane sculpting bacterial BAR domain-containing protein for engineering tunable scaffolds into novel biological metamaterials

Daniel A. Phillips[a,b], Jennifer A. Lee[a,c], Barbara Smith[d], Brian J. Eddie[e], Duncan Sousa[d], Patricia E. Buckley[a], Aleksandr E. Miklos[a]*

[a]U.S. Army Combat Capabilities Development Command Chemical Biological Center, Research & Technology Directorate, 8198 Blackhawk Rd, Aberdeen Proving Ground, MD 21010

[b]Oak Ridge Institute for Science and Education, 1299 Bethel Valley Rd, Oak Ridge, TN 37830

[c]Defense Threat Reduction Agency, 8725 John J Kingman Rd #6201, Fort Belvoir, VA 22060

[d]Johns Hopkins University School of Medicine, 855 N Wolfe St, Baltimore, MD 21205

[e] U.S. Naval Research Laboratory, Center for Bio/Molecular Science and Engineering, 4555 Overlook Ave SW, Washington, DC 20375

ABSTRACT

Metamaterial construction relies upon the ability to introduce precise features in surfaces at size scales proportional to the wavelength of the radiation being manipulated. Biology excels at forming precise structures on the nanometer to micrometer scale, but a fundamental understanding of the processes involved in their formation is essential to harnessing the ability to engineer these structures in a controlled manner. The ordered tubules formed through the interaction between Bin/Amphiphysin/Rvs domain-containing proteins and lipids fall within the diameter and length range required to affect visible light. A novel bacterial Bin/Amphiphysin/Rvs domain-containing protein was investigated for its membrane sculpting capabilities both within the context of *in vitro* interaction between purified protein and liposomes, and *in vivo* through protein expression and membrane extension formation. Predicted structures generated of Bin/Amphiphysin/Rvs domain-containing protein show a characteristic Bin/Amphiphysin/Rvs domain-like appearance and provide potential targets for engineering through targeted mutagenesis. Negative stain transmission electron microscopy experiments show that purified Bin/Amphiphysin/Rvs domain-containing protein resembles previously characterized Bin/Amphiphysin/Rvs domain proteins with intrinsic curvature and the predicted structure model. These initial experiments will serve to baseline future iterations of engineered membrane sculpting proteins towards the goal of using Bin/Amphiphysin/Rvs domain protein-mediated tubule formation to generate tunable scaffolds for templating conductive structures, paving the way for biologically engineered metamaterials.

Keywords: Metamaterials, synthetic biology, membrane sculpting, BAR domain, cell-free, tunable, obscurants

1. INTRODUCTION

Optical metamaterials (OMMs) impart a negative index of refraction, allowing electromagnetic fields to bend in unconventional directions.[1,2] OMMs are formed by patterning conductive structures into ordered, three-dimensional arrays on a surface such that the operational electromagnetic wavelength is larger than the spatial interval between the conductive materials.[3] The array of conductive materials creates surface plasmons, causing the incident electromagnetic waves to propagate parallel to the surface, rather than reflected back. This detail is very important for the long-term goal of optical cloaking technology and bending light around an object. For such materials to alter the way light reflects off a surface, a 3D structure must be within 10 to 100 nm in diameter,[3] making synthesis of OMMs that are functional within this range costly and difficult. Similarly, manufactured OMMs are bulky, cumbersome, and are seldom adaptable or responsive. In the context of developing a surface coating for the Warfighter at larger scales, these design constraints pose a significant challenge.

By contrast, biology excels at producing micro- and nanoscale ordered structures. Structural color occurs when non-pigmented but conductive biopolymers are ordered in the same 3D manner as man-made metamaterials. Visible light encounters the surface, but the precise ordering of the proteins creates a plasmonic effect, selectively reflecting a specific wavelength of light and producing color.[4,5] Examples of biological structures resulting in metamaterial-like

properties (iridescence) can be found in bacterial colonies.[6] Bacterial cells can naturally form a complex, protective structure containing bacteria and a secreted extracellular matrix, referred to as a biofilm. With the right components, bacterial synthesis offers a cost-effective and scalable method to produce optical metamaterials.

Microscale lipid membrane features can also impart structural coloration on the macroscale, as evidenced by the brilliant blue color observed in the marble berry.[7,8] Forming lipids into precise structures requires the assistance of scaffolding or membrane sculpting proteins. In eukaryotic cells, membrane sculpting mechanisms are ubiquitous due to the necessity of membrane trafficking, organelle biogenesis, vesicle transport, and protein-lipid scaffolding.[9,10,11] The Bin/Amphiphysin/Rvs (BAR) domain family achieves membrane sculpting activity through electrostatic interactions between positively charged residues on the protein and negatively charged lipids. The intrinsic curvature of certain members of the BAR domain family promotes tubule formation through this protein-lipid association.[11] Recently, researchers coupled membrane sculpting BAR domain protein activity to light-actuated activity, resulting in controlled membrane deformation capabilities.[12] A bacterial membrane shaping BAR domain-like protein (BdpA) was identified in the conductive outer membrane extensions and vesicles produced naturally by *Shewanella oneidensis*. When expression of this protein is induced in cells, long-distance (>10 μm) outer membrane structures with a diameter less than 100 nm can be generated, posing a promising target for further characterization of biophysical activity and utilization through synthetic biology.

Here, we aim to solve the structure of BdpA and further characterize its membrane sculpting capabilities. This characterization will allow targeted mutagenesis of the protein towards the goal of altering the physical parameters of the resultant membrane tubules generated through protein-lipid interaction. The ability to alter dimensions and aspect ratios of membrane structures is an essential first step into producing tunable biological metamaterials from membrane scaffolds capable of performing over a range of electromagnetic wavelengths.

2. RESULTS

2.1 Expression and purification of BdpA

2.1.1 Expression tests in Eschericia coli

Heterologous expression of BdpA was tested in *Eschericia coli* cells across a range of temperatures, inducer concentrations, and proprietary media optimized for protein expression. Isopropyl β-d-1-thiogalactopyranoside (IPTG) inducer concentration did not meaningfully affect soluble protein yield but inducing cells overnight at 16 °C resulted in improved solubility (Figure 1a). The Western blot of the expression tests show no significant difference between inducer concentrations; therefore, the lowest inducer concentration of 50 μM IPTG was chosen moving forward. Out of each growth medium tested using the 16 °C overnight induction, Hyper broth yielded the highest concentration of soluble protein at the correct molecular weight of 56 kDa after immobilized metal ion chromatography (IMAC) purification (Figure 1c). Several other media formulations yielded similar (or higher) total protein yield after IMAC purification, but the elutions screened had fewer contaminating bands from the samples grown and induced in Hyper broth.

2.1.2 IMAC purification and size exclusion chromatography of codon-optimized BdpA

Following expression condition and construct codon optimization, BdpA was tested with an array of buffer additives to improve purification, protein stability, and monodispersity in solution (not shown). Here, size exclusion chromatography (SEC) highlights the results of this optimization, showing pure BdpA eluting from the SEC column. BdpA eluted in the first three peaks, suggesting that BdpA forms multimers in a similar manner to classic BAR domain-containing proteins.[13] The larger peak following the first three BdpA peaks was suspected to be Triton X-100 micelles, since a one percent solution of the detergent was used for purification, and Triton X-100 exhibits a strong absorbance at 280 nm.

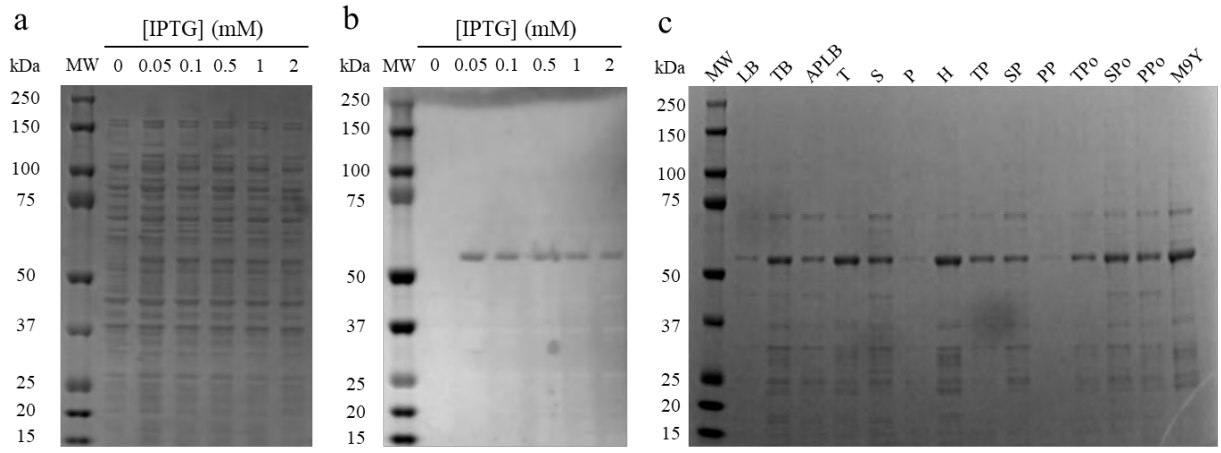

Figure 1. Expression tests of BdpA in *E. coli* cells. a) SDS-PAGE of His-tagged BdpA expression (56 kDa) at indicated concentrations of IPTG. b) Western blot of the expression tests against the 6x-His tag. c) Expression and IMAC purification of His-tagged BdpA from cultures grown in different media. Luria-Bertani (LB), Terrific Broth (TB), Animal Product-free LB (APLB), Turbo (T), Superior (S), Power (P), Hyper (H), Turbo Prime (TP), Superior Prime (SP), Power Prime (PP), Turbo Primeolate (TPo), Superior Primeolate (SPo), Power Primeolate (PPo), Glucose M9Y (M9Y).

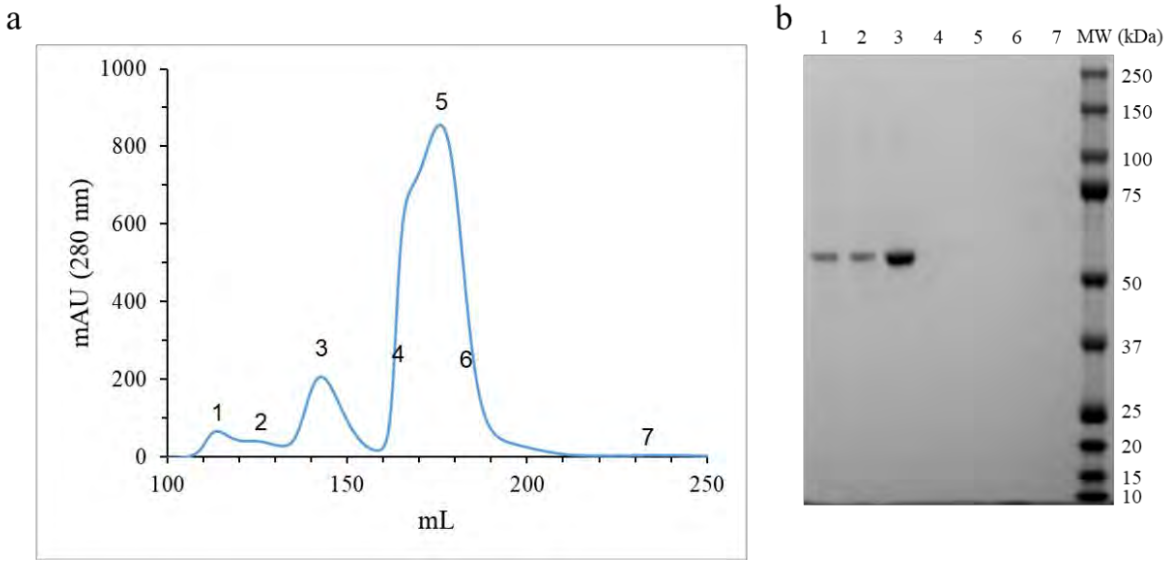

Figure 2. Size exclusion chromatography of BdpA. a) Chromatogram of absorbance at 280 nm. b) SDS-PAGE of a fraction from the indicated peak numbers from the chromatogram. Peaks four, five, and six are Triton X-100.

2.2 Predicted structure of BdpA

In silico methods were employed to generate an *ab initio* predicted structure of BdpA in the absence of homology models. The predicted structure appeared as a jellyroll-like fold corresponding to the galactose-binding domain-like (GBD) region at the N-terminus of the protein, followed by a coiled coil in the predicted BAR domain section (Figure 3a). Homooligomerization models generated through trRosetta reveal a dimer with intrinsic "banana-shaped" curvature (Figure 3b), consistent with many other BAR domain-containing proteins.[13] The multisequence alignment of BdpA homologs in other bacteria suggest variability and flexibility near the GBD, as well as within the dimerization interface of the coiled coils. We suspect that mutagenesis of the residues within these variability regions are promising targets for affecting membrane tubule diameter. Likewise, deletion of the specific protein domains could affect membrane sculpting functionality.

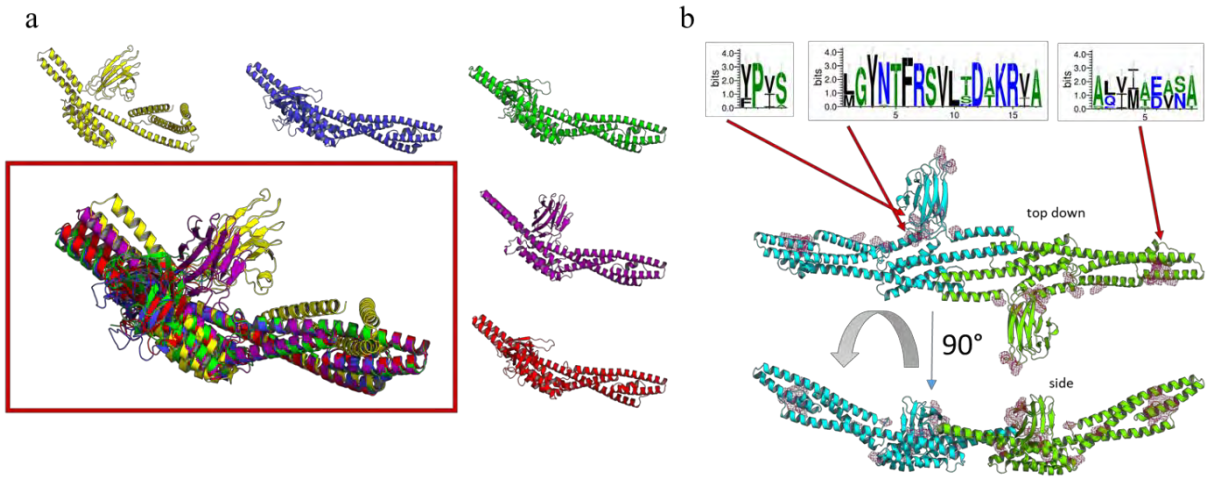

Figure 3. Predicted structure of BdpA. a) Structure variability of the top 5 predicted models generated using trRosetta show flexibility in the GBD region. b) Predicted dimer from docking2 with sequence cartoons show the most frequent amino acid residues at each site highlighted in red on the dimer model.

2.3 Transmission electron microscopy of BdpA

2.3.1 Negative stain TEM of purified BdpA

A solved structure of BdpA will provide valuable insight into how to engineer the protein through targeted mutagenesis. For structural analysis, the purified protein must be monodispersed on a grid such that individual particles can be analyzed. A dilution series of BdpA was prepared from a starting concentration of one mg/mL. A 1:100 dilution of the protein (10 µg/mL) provided the best particle dispersal on the grids and allowed the first glimpse at the protein structure. Here, "banana-like" dimers can be seen by transmission electron microscopy (TEM) after negative staining (Figure 4).

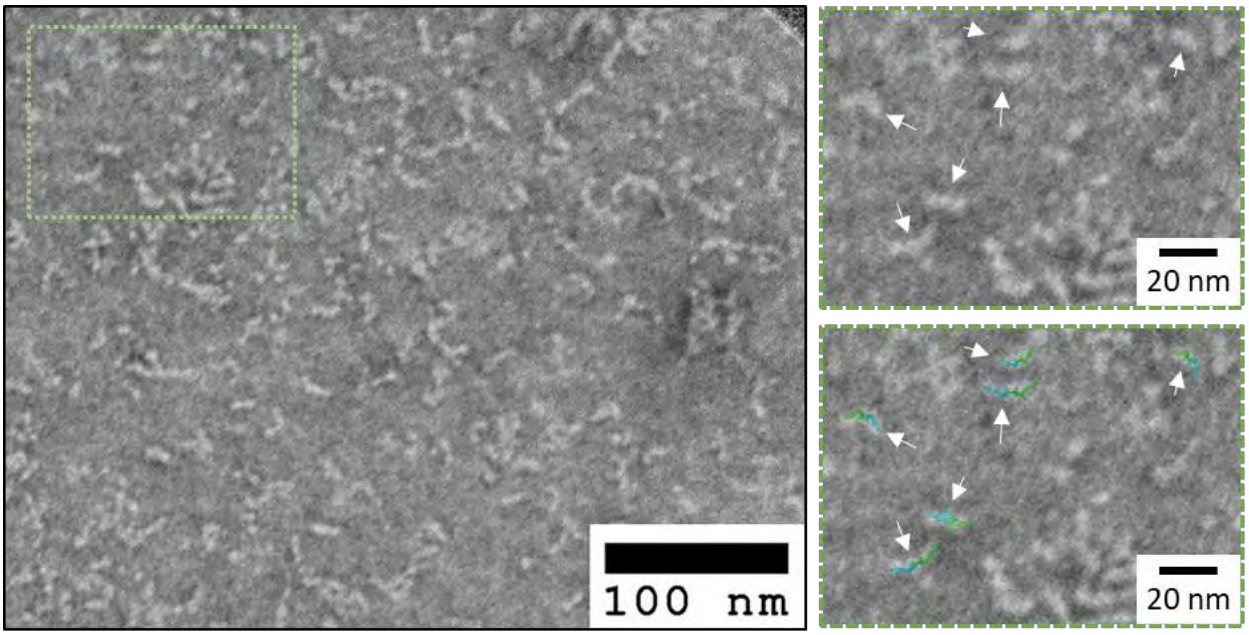

Figure 4. Negative stain TEM of BdpA. Structures appear as coiled coils with BAR domain-like curvature showing similarity to the predicted structure from Figure 3. Enlarged inset image of the green box (top right) has white arrows pointing to BAR domain protein-like shapes, and bottom right inset shows these structures overlaid with the predicted dimer structure.

2.3.2 In vitro tubule formation

Lipid binding and curvature alteration are hallmarks of BAR domain protein activity. Through electrostatic interaction, purified BAR domain-containing proteins co-incubated with liposomes can form tubules.[9,10,11,13] Cell-free protein synthesis (CFPS) reactions offer a way to rapidly test protein expression and interaction in the absence of cells. To test *in vitro* tubule formation activity of BdpA, we engineered expression constructs comprised of the BAR domain-containing region alone (BdpA BAR only), BdpA without the cleavable signal peptide (BdpA no SP), and BdpA without the BAR domain region (BdpA GBD-like domain only). These constructs were expressed in CFPS reactions using a PURExpress® *In Vitro* Protein Synthesis Kit supplemented with liposomes prepared from the lipopolysaccharide (LPS) of *S. oneidensis* and labeled with the fluorescent, lipophilic dye FM 4-64 to visualize membrane structures. A network of tubule-like structures can be observed when the expression construct contained the BAR domain, but not in the GBD-only expression reaction nor the plasmid-free negative control (Figure 5a). This test demonstrated membrane curvature activity of the BAR domain region of BdpA, but higher resolution imaging is required to observe and measure the dimensions of the resultant tubule-like structures.

In vitro tubule formation assays of BAR domain proteins are typically performed by incubating purified protein with liposomes followed by imaging the reactions on grids using negative stain TEM. The presence of BdpA in the reactions resulted in tubules with a diameter less than 100 nm (Figure 5b). When the same samples were imaged by cryo-TEM, tubules were observed with BAR domain protein-like striations (Figure 5c).

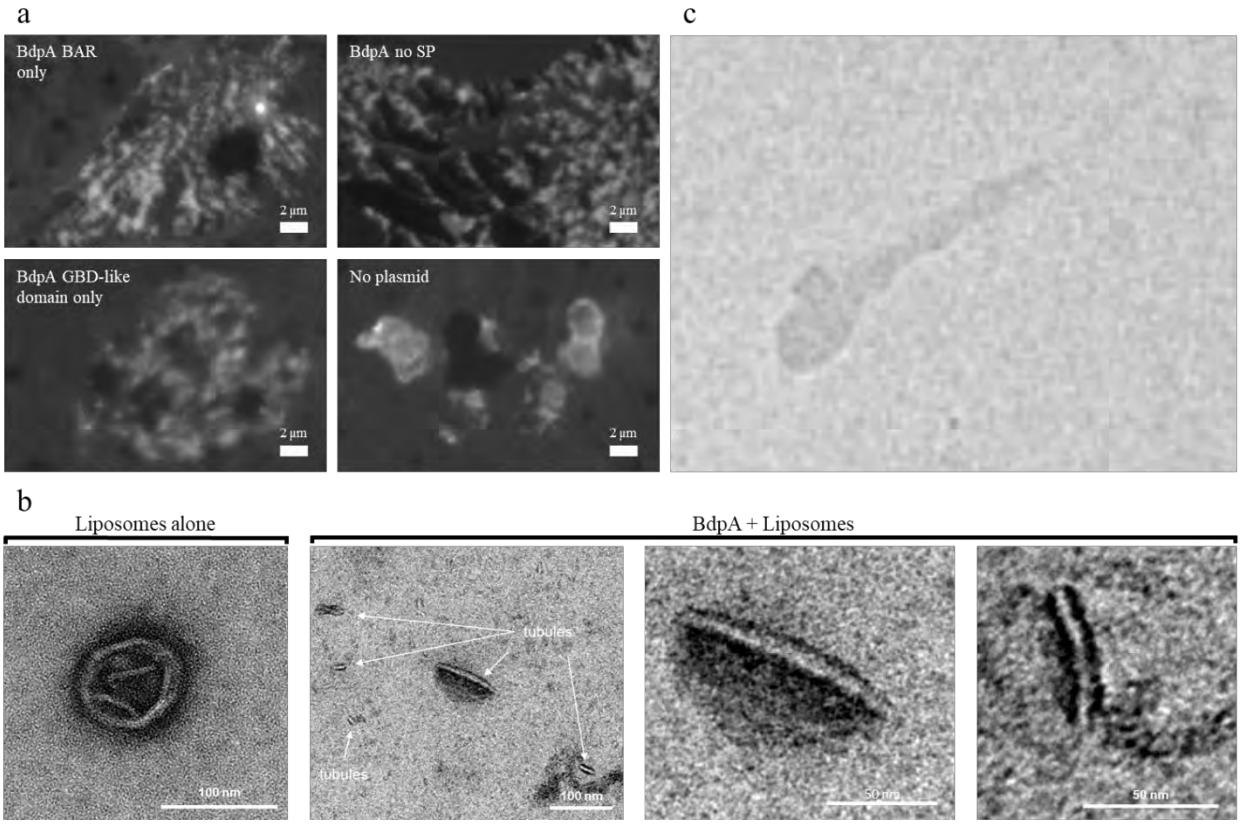

Figure 5. Demonstration of *in vitro* membrane sculpting activity of BdpA. a) Fluorescence microscopy images of CFPS reactions using PURExpress with BdpA expression constructs and LPS-derived liposomes labeled with FM 4-64 lipophilic dye. b) Negative stain TEM images of *in vitro* tubule formation assays using either liposomes alone (left) or liposomes with purified BdpA (right). c) Cryo-TEM of *in vitro* tubule formation using BdpA and liposomes.

2.4 Variation of *in vivo* BdpA membrane extension phenotypes

When BdpA expression is induced in cells, membrane extensions are produced and can be visualized by fluorescence microscopy after addition of FM 4-64. We tested BdpA expression across a range of inducer concentrations and within different cell types to see if extension phenotypes would be affected. During induction in *E. coli* cells, phenotypes varied between outer membrane vesicles (OMVs), web-like outer membrane extensions (OMEs), or tubule-like OMEs

(Figure 6). Inducer concentrations did not significantly alter the distribution of OME phenotypes (Figure 6b). However, expression of BdpA in different species revealed significant variation in the OME phenotypes between strains. *S. oneidensis* and *Marinobacter atlanticus, b*oth exhibited more tubules, while *E. coli* produced predominately web-like OMEs (Figure 6c-e). We suspect the variation between strains is either due to the lipid composition of the LPS in the outer membrane, or a consequence of a cell line engineered for heterologous overexpression of proteins.

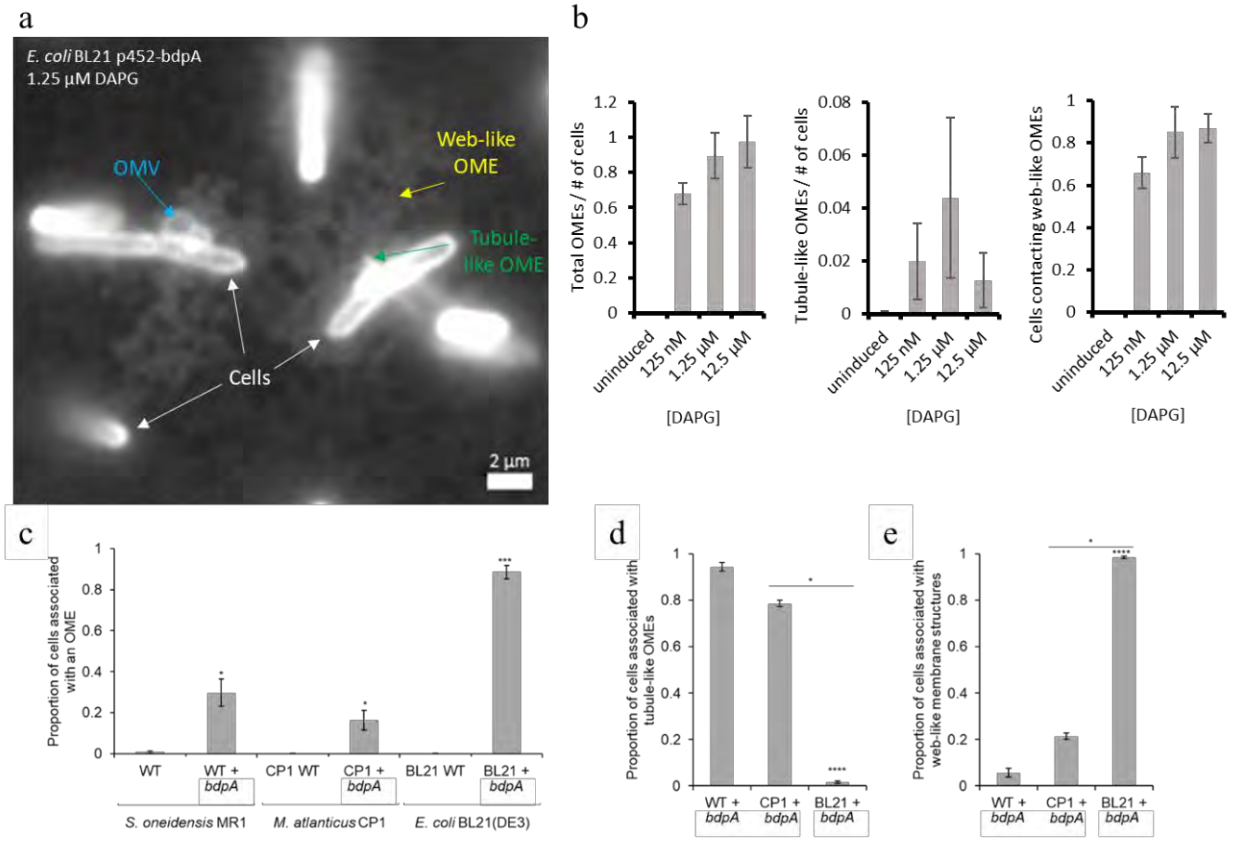

Figure 6. Membrane extension phenotypes *in vivo*. a) Representative image of OME phenotypes produced upon induction of BdpA expression in cells labeled with FM 4-64. Scale = 2 µm. b) OME phenotypes observed from BdpA induction at varied concentrations of 2,4-diacetylphloroglucinol (DAPG) inducer in *E. coli* cells. c) Proportions of cells associated with an OME after induction of BdpA expression in *S. oneidensis* (WT), *M. atlanticus* (CP1), and *E. coli* (BL21). d) Proportion of cells associated with tubule-like OMEs, and e) associated with web-like OMEs between species following BdpA induction. Asterisks indicate statistical significance ($p < 0.05$, Welch's *t*-test).

3. DISCUSSION

Considerable evidence is mounting that BdpA is a functional, bacterial BAR domain protein. Protein purification and size exclusion chromatography revealed that BdpA is capable of forming oligomers with itself, and homodimerization is critical to eukaryotic BAR domain protein biophysical activity. Through preliminary TEM experiments, the purified protein was observed having a characteristic "banana-like" shape that was anticipated through *ab initio* structure prediction methods. Finally, the protein was capable of sculpting liposomes into tubules *in vitro* in a manner similar to other BAR domain-containing proteins. Future experiments will optimize the *in vitro* tubule formation conditions to improve tubule frequency and stability, and later iterations will include mutagenesis to alter the phenotype of the resultant membrane tubules.

Within the greater context of using these biological structures to template materials, we have provided a baseline for future protein engineering tests. Currently, the diameter of tubules produced *in vitro* is sufficient for a scaffold structure for templating conductive materials into metamaterials, but the length of the tubules is insufficient to provide the requisite aspect ratio. Optimizing handling conditions to minimize shear forces could improve tubule length;

similarly, an engineered BdpA protein that forms tighter, more stable oligomers could increase stability and tubule scaffold rigidity. Conversely, tubules resulting from BdpA expression in cells fit the length and diameter requirements, and biopolymer templating of extensions could be achieved through co-expression under the right conditions.

4. METHODS

4.1 Protein purification

BdpA constructs were ordered and cloned into the pET-28a expression vector with an N-terminal 6x-His tag, GSSGSS linker, and a thrombin cleavage site by Twist Bioscience. Plasmid constructs were transformed into chemically competent *E. coli* BL21(DE3) pLysS cells for protein expression. For protein expression, transformed cells were grown as overnight cultures in 30 mL Hyper broth (Athena ES) supplemented with 50 µM kanamycin and 25 µM chloramphenicol at 30 °C with 250 rpm shaking. Three cultures of 1 L Hyper broth with 50 µM kanamycin and 25 µM chloramphenicol were inoculated with 10 mL of the overnight culture and incubated at 37 °C with 250 rpm shaking until the OD_{600} of one culture was reached. Cultures were then cooled for 15 minutes in an ice bath, induced with 50 µM IPTG, and incubated overnight at 16 °C for 16 hours. Cultures were centrifuged, and the cell pellet was resuspended in 300 mL of lysis buffer (50 mM Tris, 500 mM NaCl, 40 mM imidazole, 1% Triton X-100, 1 mM DTT, 6 tablets of EDTA-free cOmplete protease inhibitor (Millipore Sigma), pH 8.0). Resuspended cells were lysed by microfluidization, centrifuged, and the clarified lysate was filtered through 0.45 µm filters before loading onto a 5 mL HisTrap Ni-NTA resin column on an AKTAxpress (Cytiva) FPLC machine. After loading, the column was washed with Buffer A (50 mM Tris, 500 mM NaCl, 40mM imidazole, 1% Triton X-100, 1 mM DTT, pH 8.0) until the A280 signal stabilized back to baseline. The imidazole gradient was increased to 80 mM until the A280 signal returned to baseline again. Finally, the imidazole concentration was ramped up to 500 mM, and fractions were collected of the purified protein. Fractions containing purified protein were dialyzed overnight into 4 L of 50 mM Tris, 500 mM NaCl, 0.1 % Triton X-100, 1 mM DTT, pH8.0. Secondary purification size exclusion chromatography was performed by injecting 6 mL of the dialyzed elution onto a HiLoad Superdex S200 26/60 gel filtration column and collecting fractions. Fractions containing BdpA were determined by SDS-PAGE. These fractions were pooled, concentrated using a 30 k MWCO spin concentrator, and the remaining Triton X-100 was desalted out using a HiTrap 5 mL Desalting column. Protein was diluted into 1 mg/mL aliquots and either used immediately or stored at 4 °C.

4.2 *Ab initio* structure prediction

A total of 278 BdpA homologs were identified across a range of bacterial species by BLAST. These homologs were used to build a multiple sequence alignment for ab initio structure prediction by trRosetta (Yang et al., 2020). Structures were visualized in the PyMOL Molecular Graphics System, Version 2.0 (Schrödinger, LLC). The BdpA dimer structure model was predicted using the RosettaDock and docking2 software on ROSIE (Lyskov and Gray, 2008; Chaudhury et al., 2011; Lyskov et al., 2013).

4.3 Liposome preparation

For CFPS membrane sculpting assays, LPS liposomes were made by rehydrating 0.5 mg of purified *S. oneidensis* LPS with 500 µL PURExpress *In Vitro* Protein Synthesis Kit (New England BioLabs) reaction mix, sonicating the lipid suspension at 30 °C for 10 minutes, then passing the sonicated mixture through 0.2 µm filters within a syringe liposome extruder 6 times (Avanti Polar Lipids). Liposome suspensions were prepared immediately prior to use, then labeled with FM 4-64 (ThermoFisher).

For negative stain TEM, LPS liposomes were prepared by rehydrating 1 mg of purified *S. oneidensis* LPS with 50 mM Tris, 250 mM NaCl, pH 8.0 buffer. Lipid suspensions were sonicated at 30 °C for 10 minutes, then passed through a series of sequentially smaller pored filters (1.0, 0.8, 0.4, and 0.2 µm) within a syringe liposome extruder 6 times per filter while incubating the extruder block at 30 °C.

4.4 CFPS membrane sculpting assay

Plasmids of protein constructs in the pET-28(a) vector were purified from glycerol stocks purchased from Twist Bioscience. All CFPS reactions were performed using the PURExpress reaction mix according to the manufacturer's specifications. Plasmids were diluted to 10 ng/µL, then 2 µL of each plasmid (or ddH_2O for plasmid-free control) were added to a separate 3 µL aliquot of the PURExpress reaction mixture. The plasmid reaction mix and the liposome reaction mix were combined in a 1:1 ratio in a total of 10 µL. Reactions were immediately transferred to a chambered

cover glass slide and images were collected on a Zeiss LSM 800 confocal microscope with a Plan-Apochromat 63x/1.4 numerical aperture oil immersion M27 objective. Widefield fluorescence images were taken using a LED-Module 511 nm light source with 583–600 nm filters and a 91 He CFP/YFP/mCherry reflector. Excitation and emission spectra were 506 nm and 751 nm, respectively. Images were recorded using the Zeiss Zen software (Carl Zeiss Microscopy, LLC).

4.5 Negative stain TEM and *in vitro* tubule formation

Dilutions of 1 mg/mL purified BdpA were briefly incubated on copper grids. Samples (8 µL) were adsorbed to glow discharged (EMS GloQube) ultra-thin (UL) carbon coated 400 mesh copper grids (EMS CF400-Cu-UL), by floatation for 2 minutes. Grids were rinsed in three drops (one minute each) of buffer (50 mM Tris, 250 mM NaCl, pH 8.0) and negatively stained in two consecutive drops of 1 % uranyl acetate (UA, aq.), and quickly aspirated. Grids were imaged on a Hitachi 7600 TEM operating at 80 kV with an AMT XR80 CCD (8 megapixel).

In vitro tubule formation assays were similarly performed as above with the following modifications. Purified BdpA was incubated with LPS liposomes at a 1:1 ratio of 0.1 mg/mL each. Samples were negatively stained in two consecutive drops of 0.75 % uranyl formate (UF, aq.) and quickly aspirated. Grids were imaged on a Hitachi 7600 TEM operating at 80 kV with an AMT XR80 CCD (8 megapixel) or a Talos L120C with a Thermo-Fisher Ceta (cooled 16 Mpixel CMOS, 16-bit 1–25 fps).

For cryo-TEM of the *in vitro* tubule formation assays, samples were prepared as before, but were plunge frozen on grids into liquid ethane using a Vitrobot Mark IV System (Thermo Scientific). Images were taken using a Thermo Scientific™ Titan Krios cryo-TEM.

4.6 *In vivo* BdpA expression and OME formation

To test for OME phenotypes resulting from BdpA induction in WT *S. oneidensis* (WT + *bdpA*), *M. atlanticus* (CP1 + *bdpA*), and *E. coli* (BL21 + *bdpA*), overnight cultures for each strain were diluted in LB for *S. oneidensis*, BB for *M. atlanticus*[14], or LB for *E. coli* to an OD_{600} of 0.05 and induced with the indicated concentration of DAPG for 1 hour at 30 ˚C (or 37 ˚C for *E. coli*) with 200 RPM shaking agitation. Prior to pipetting, ~1cm of the p200 pipette tip was trimmed to minimize shear forces during transfer. A 100 µL aliquot of each culture was labeled with 1 µL 1M FM 4-64, and 10 µl deposited onto chambered cover glass. Each sample was imaged immediately after deposition onto the glass slides.

Imaging experiments were performed on at least 3 individual biological replicate experiments per strain and are representative images from 5-10 fields of view per replicate from 700 cells for *S. oneidensis* WT, 472 cells for *S. oneidensis* WT + *bdpA*, 4041 cells for *M. atlanticus* CP1 WT, 150 cells for *M. atlanticus* CP1 + *bdpA*, 2190 cells for *E. coli* BL21 WT, and 2623 cells for *E. coli* BL21 + *bdpA*. The proportion of cells producing either type of membrane feature was calculated by dividing the number of cells for which a membrane feature was observed by the number of total cells for each strain; the proportions from each independent experiment were averaged for each strain to obtain the mean proportions for each strain that were plotted in bar graphs. The proportion of cells associating with OMEs observed from each biological replicate culture was recorded, as well as if the associated OME resembled either a tubule-like or web-like structure. Tubule-like OMEs were defined as narrow, unbranching membrane extensions. Cells that were associated with a branching, reticular membrane were counted as producing a web-like OME. Statistical significance of the proportions of cells associated to each of the OME phenotypes between strains was determined by Welch's *t*-test.

ACKNOWLEDGMENTS

We would like to thank Robert Ernst at the University of Maryland, Baltimore for preparing the purified LPS used in this study, and Brian Eddie for his technical help counting membrane extensions. We especially thank Katherine Rhea for the intellectual conversations about troubleshooting and training on specific equipment. Daniel Phillips and Aleksandr Miklos wrote the proposal, acquired funding, planned and supervised research, generated predicted structure models, and wrote the report. Daniel Phillips and Jennifer Lee purified proteins. Jennifer Lee performed expression and buffer additive testing, as well as intellectual discussions. Barbara Smith and Duncan Sousa performed TEM experiments. Daniel Phillips, Jennifer Lee, and Aleksandr Miklos interpreted data. Funding was provided by the U.S. Army via the Surface Science Initiative Program (PE 0601102A Project VR9) at the Combat Capabilities Development Command Chemical Biological Center.

REFERENCES

[1] Pendry, J.B.; Smith, D.R. Reversing Light With Negative Refraction. *Phys. Today*, **2004**, *57* (6), pp 37–43.

[2] Pendry, J.B.; Schurig, D.; Smith, D.R. Controlling Electromagnetic Fields. *Science*. **2006**, *312* (5781), pp 1780–1782.

[3] DuFort, C.C.; Dragnea, B. Bio-enabled synthesis of metamaterials. *Annu. Rev. Phys. Chem.* **2010**, *61*, pp 323–344.

[4] Ruiz-Clavijo, A.; Tsurimaki, Y.; Caballero-Calero, O.; Ni, G.; Chen, G.; Boriskina, S.V.; Martín-González, M. Engineering a Full Gamut of Structural Colors in All-Dielectric Mesoporous Network Metamaterials. *ACS Photonics*. **2018**, *5* (6), pp 2120–2128.

[5] Yang, W.; Xiao, S.; Song, Q.; Liu, Y.; Wu, Y.; Wang, S.; Yu, J.; Han, J.; Tsai, D-P. All-dielectric metasurface for high performance structural color. *Nat. Commun.* **2020**, 11, p 1864.

[6] Johansen, V.E.; Catón, L.; Hamidjaja, R.; Oosterink, E.; Wilts, B.D.; Rasmussen, T.S.; Sherlock, M.M.; Ingham, C.J.; Vignolini, S. Genetic manipulation of structural color in bacterial colonies. *Proc. Natl. Acad. Sci.* **2018**, *115* (11), pp 2652–2657.

[7] Vignolini, S.; Rudall, P.J.; Rowland, A.V.; Reed, A.; Moyroud, E.; Faden, R.B.; Baumberg, J.J.; Glover, B.J.; Steiner, U. Pointillist structural color in Pollia fruit. *Proc. Natl. Acad. Sci.* **2012**, *109* (39), pp 15712–15715.

[8] Middleton, R.; Sinnott-Armstrong, M.; Ogawa, Y.; Jacucci, G.; Moyroud, E.; Rudall, P.J.; Prychid, C.; Conejero, M.; Glover, B.J.; Donoghue, M.J.; Vignolini, S. Viburnum tinus Fruits Use Lipids to Produce Metallic Blue Structural Color. *Curr. Biol.* **2020**, *30* (19), pp 3804–3810.

[9] Daum, B.; Auerswald, A.; Gruber, T.; Hause, G.; Balbach, J.; Kühlbrandt, W.; Meister, A. Supramolecular organization of the human N-BAR domain in shaping the sarcolemma membrane. *J. Struc. Bio.* **2016**, *194* (3), pp 375–382.

[10] Daumke, O.; Roux, A.; Haucke, V. BAR domain scaffolds in dynamin-mediated membrane fission. *Cell*. **2014**, *156* (5), pp 882–892.

[11] Frost, A.; Perera, R.; Roux, A.; Spasov, K.; Destaing, O.; Egelman, E.H.; De Camilli, P.; Unger, V.M. Structural basis of membrane invagination by F-BAR domains. *Cell*. **2008**, *132* (5), pp 807–817.

[12] Jones IV, T.; Liu, A.; Cui, B. Light-Inducible Generation of Membrane Curvature in Live Cells with Engineered BAR Domain Proteins. *ACS Synth. Biol.* **2020**, *9* (4), pp 893–901.

[13] Simunovic, M.; Evergren, E.; Callan-Jones, A.; Bassereau, P. Curving Cells Inside and Out: Roles of BAR Domain Proteins in Membrane Shaping and Its Cellular Implications. *Annu. Rev. Cell Dev. Biol.* **2019**, *35* (1), pp 111–129.

[14] Bird, L.J.; Wang, Z.; Malanoski, A.P.; Onderko, E.L.; Johnson, B.J.; Moore, M.H.; Phillips, D.A.; Chu, B.J.; Doyle, J.F.; Eddie, B.J.; Glaven, S.M. Development of a Genetic System for Marinobacter atlanticus CP1 (sp. nov.), a Wax Ester Producing Strain Isolated From an Autotrophic Biocathode. *Front. Microbiol.* **2018**, *9*, p 3176.

This page intentionally left blank

Toward understanding the generation and lifetime of singlet oxygen species in photosensitized rigid crystalline structures

Ann M. Kulisiewicz,[a] Sergio J. Garibay,[b] Ivan Iordanov,[a] Matthew Browe,[a] Gabrielle Pozza,[c] Lisa A. Kelly,[c] Jared B. DeCoste[a]

[a]U.S. Army Combat Capabilities Development Command Chemical Biological Center, Research & Technology Directorate, 5183 Blackhawk Rd, Aberdeen Proving Ground, MD 21010

[b]Leidos, Inc., P.O. Box 68, Edgewood Chemical Biological Center, Aberdeen Proving Ground, Maryland 21010, United States

[c]Department of Chemistry and Biochemistry, University of Maryland Baltimore County, Baltimore, Maryland 21250, United States

ABSTRACT

Oxygen is generally considered a non-reactive gas in its ground triplet state; however, upon excitation to its singlet state it becomes a mild oxidant that can be utilized in fine chemical synthesis, waste water treatment, cancer therapy, as insecticides or herbicides, and in the destruction of toxic chemicals, including sulfur mustard. The generation of singlet oxygen and its subsequent lifetime is of utmost importance to these applications. One way to generate singlet oxygen is through the irradiation of a photosensitizer with the appropriate wavelength of light. Various photosensitizers have been incorporated into porous metal-organic frameworks to date, but fundamental studies on photosensitizer proximity, charge transfer, and photosensitizer composition have been largely unexplored. We hypothesize that the quantum yield of metal-organic framework photosensitizers toward singlet oxygen generation and subsequent lifetime of these species in metal-organic frameworks is maximized by the high density of the photosensitizer in positions that discourage quenching. This can be controlled by the topology of the metal-organic frameworks and the nature of the photoactive species. Several NU-1000 derivatives—NU-1000, NU-1000-*o*-Cl_4, NU-1000-*m*-Cl_4, NU-1000-*m*-$(NO_2)_4$, NU-1000-*o*-$(NO_2)_4$, NU-1000-*o*-$(NH_2)_4$, NU-1000-*o*-$(CH_3)_4$—have been synthesized and analyzed for their reactivity with 2-chloroethyl ethyl sulfide (2-CEES). In addition, several of the metal-organic frameworks linkers were analyzed for singlet oxygen generation through transient absorption spectroscopy and computational modeling was utilized to predict the band gap of the linkers to guide experimental design as well as corroborate experimental data.

Keywords: metal-organic framework, photocatalysis, singlet oxygen, sulfur mustard, 2-chloroethyl ethyl sulfide

1. INTRODUCTION

In recent years many groups have been examining ways to incorporate photosensitizers in systematic ways into porous structures such as metal-organic frameworks (MOFs).[1-4] These photosensitizers have included organic linkers based on pyrene or porphyrins, metal complexes including $Ru(bpy)_3$, and metals (including lanthanides) within the framework. While all these approaches have been successful in generating singlet oxygen, fundamental studies in how different metals and organic linkers interact with one another based on their proximity are lacking. Singlet oxygen generation is of particular interest as it can be of great use in fine chemical synthesis, waste water treatment, cancer therapy, as insecticides or herbicides, and in the destruction of sulfur mustard.[5] The mild nature of singlet oxygen makes it ideal as it is non-hazardous and prevents the over oxidation to less desired products as in the case of sulfur mustard to the sulfone, which is a vesicant.

MOFs are interesting materials for studying these fundamental interactions. They consist of metal/metal oxide secondary building units (SBUs) linked together in a regular pattern by organic linkers, forming crystalline structures. Most of these structures are very porous in nature and have large internal surface areas.[6] The porous nature and ability to understand the location of each functional moiety within its structure make MOFs ideal for fundamentally studying the effect photosensitizer proximity, charge transfer, and photosensitizer composition have on the quantum efficiency and lifetime of singlet oxygen.

The generation of singlet oxygen by a photosensitizer requires a process where an electron is excited, typically by UV or visible light, followed by an intersystem crossing to a MOF triplet state, which transfers the energy to create the excited singlet oxygen species (Figure 1). While the inherent activity MOFs have toward species such as the mustard simulant 2-chloroethyl ethyl sulfide (2-CEES) have been examined, understanding the fundamental underpinnings of the photophysics and how that can affect the production of singlet oxygen has been relatively unexplored in the literature.[2-4]

Pyrene (NU-1000),[2, 3] porphyrins (PCN-222),[4] and Ru complexes(UiO-67-Ru(bpy)$_3$[1] have been examined in MOF organic linkers as species that can produce singlet oxygen. However, there has been very limited work done with respect to synthesis of pyrene linker derivatives of NU-1000 and there have been no systematic studies detailing its effects on photocatalysis and singlet oxygen generation. To date the only reported functionalization of H_4TBAPy within a MOF was in the form of an amine functionalization on the benzoic acid portion of the linker.[7] Derivatives of the H_4TBAPy linker can be readily synthesized via the conventional palladium cross-coupling reaction between 1,3,6,8-tetrabromopyrene and functionalized 4-methylcarbonylphenylboronic acid derivatives, followed by deprotection of the ester (Figure 2). By modifying the C and D positions on the H_4TBAPy linker, we can determine the effect of substituents that vary in electronegativity on the lifetime of the excited triplet state of the MOF and subsequent generation of singlet oxygen. These effects were determined directly by transient absorption spectroscopy (TAS) and confirmed by computational measurements of band gap energies and the rate of photocatalytic oxidation of 2-CEES (Figure 3). We show here that the carboxylic acid form of the linker has an enhanced triplet state lifetime relative to the ester precursor indicating that the linker bound within the MOF structure should have inherent enhanced photocatalytic activity. We also show that heavy halogen groups incorporated onto the *meta* and *ortho* positions of benzene ring in the linker will extend the lifetime of the triplet state of the MOF and that heavy halogen groups *ortho* to the pyrene will have the largest enhancement on the reactivity as previously observed with tetraphenylporphyrins.[8] However, it is also indicated from our results that the topology of the MOF plays a large role in the activity and could cause potential self-quenching effects.

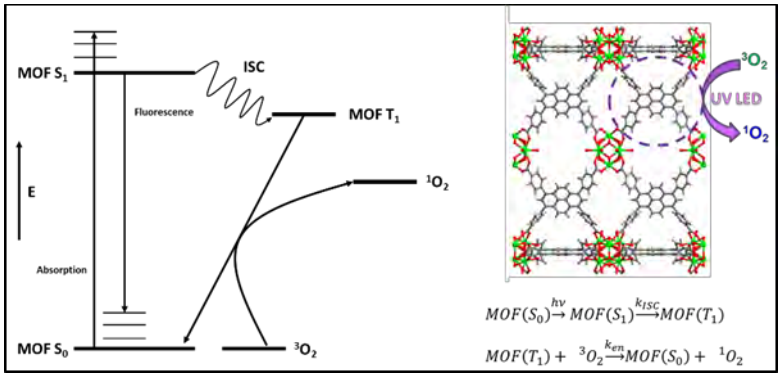

Figure 1. The photosensitized production of singlet oxygen by a MOF linker occurs via irradiation of light to excite an electron into an excited state for the MOF linker. This is followed by an intersystem crossing to the MOF linker triplet state. Returning of the electron to the ground state releases a photon of appropriate energy to excite the oxygen from its triplet state to singlet state.

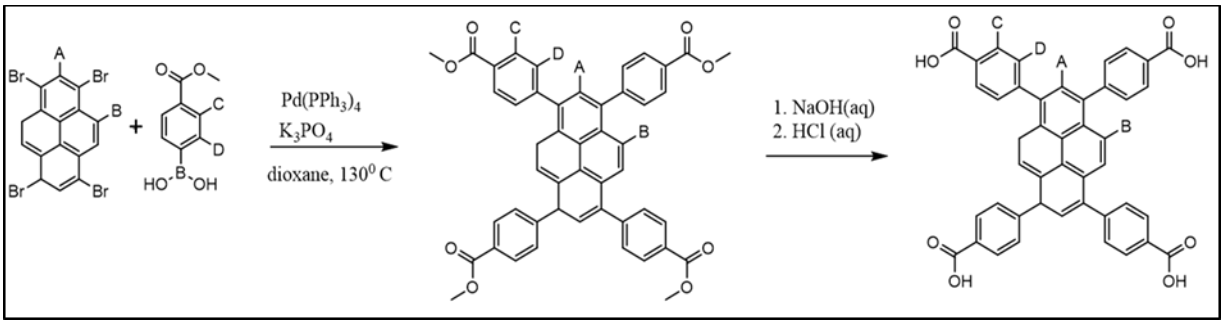

Figure 2. Synthesis of the tetratopic H4TBAPy linker found in NU-1000 and NU-901 occurs through a palladium cross-coupling reaction followed by a deprotection workup. Positions A and B on the pyrene ring and C and D on the benzoic acid ring are hydrogen atoms in H4TBAPy; however, these locations can be functionalized prior to the cross-coupling reaction leading to a variety of functionality that may alter the photophysics of the pyrene system.

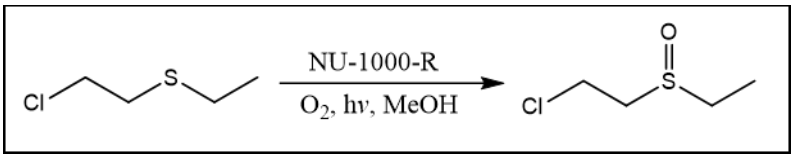

Figure 3. Reaction scheme of 2-CEES with a functionalized NU-1000 photosensitizer to form its sulfoxide oxidation product.

2. EXPERIMENTAL METHODS

2.1 Synthesis

2.1.1 Linker synthesis

All reagents were purchased from commercial sources and used without further purification. H_4TBAPy and functionalized derivatives were synthesized following published procedures.[7]

2.1.2 Synthesis of NU-1000

$ZrOCl_2{\cdot}8H_2O$ (98 mg, 0.3 mmol) and benzoic acid (2 g, 16.4 mmol) were mixed in 8 mL of dimethylformamide (DMF) in an 8-dram vial and ultrasonically dissolved. The clear solution was incubated in an oven at 100 ºC for 1 hour. After cooling down to room temperature, H_4-TBAPy (40 mg, 0.06 mmol) and trifluoro acetic acid (50 uL, 0.65 mmol) were added and ultrasonically mixed. The yellow solution was incubated in an oven at 100 ºC for 18 hours. The yellow material was isolated by centrifuge (5 minutes, 7,500 rpm) and solvent exchanged with fresh DMF three times (10 mL each) followed by acetone three times (10 mL each). The material was dried in a vacuum oven at 80 ºC for 1 hour, and then activated at 120 ºC for 18 hours.

2.1.3 Synthesis of NU-1000-o-Cl_4

$ZrOCl_2{\cdot}8H_2O$ (65 mg, 0.2 mmol) and benzoic acid (2.68 g, 22 mmol) were mixed in 8 mL of DMF in an 8-dram vial and ultrasonically dissolved. The clear solution was incubated in an oven at 80 ºC for 1 hour. After cooling down to room temperature, H_4-TBAPy-*o*-$(Cl)_4$ (49 mg, 0.06 mmol) and trifluoro acetic acid (50 uL, 0.65 mmol) were added and ultrasonically mixed. The yellow solution was incubated in an oven at 100 ºC for 18 hours. The yellow material was isolated by centrifuge (5 minutes, 7,500 rpm) and solvent exchanged with fresh DMF three times (10 mL each) followed by methanol three times (10 mL). The material was dried in a vacuum oven at 80 ºC for 1 hour, and then activated at 120 ºC for 18 hours.

2.1.4 Synthesis of NU-1000-m-Cl_4

$ZrOCl_2{\cdot}8H_2O$ and benzoic acid (2.68 g, 22 mmol) were mixed in 8 mL of DMF in an 8-dram vial and ultrasonically dissolved. The clear solution was incubated in an oven at 80 ºC for 1 hour. After cooling down to room temperature, H_4-TBAPy-*m*-$(Cl)_4$ (49 mg, 0.06 mmol) and trifluoro acetic acid (50 uL, 0.65 mmol) were added and ultrasonically mixed. The yellow solution was incubated in an oven at 100 ºC for 18 hours. The yellow material was isolated by centrifuge (5 minutes, 7,500 rpm) and solvent exchanged with fresh DMF three times (10 mL each) followed by methanol three times (10 mL). The material was dried in a vacuum oven at 80 ºC for 1 hour, and then activated at 120 ºC for 18 hours.

2.1.5 Attempted Synthesis of NU-1000-o-$(NO_2)_4$ (PCN-224-o-$(NO_2)_4$)

$ZrOCl_2{\cdot}8H_2O$ (48 mg, 0.15 mmol) and benzoic acid (1 g, 8.2 mmol) were mixed in 4 mL of DMF in an 8-dram vial and ultrasonically dissolved. The clear solution was incubated in an oven at 80 ºC for 1 hour. After cooling down to room temperature, H_4-TBAPy-*o*-$(NO_2)_4$ (26 mg, 0.03 mmol) and trifluoro acetic acid (25 uL, 0.33 mmol) were added and ultrasonically mixed. The solution was incubated in an oven at 100 ºC for 18 hours. The yellow material was isolated by centrifuge (5 minutes, 7,500 rpm) and solvent exchanged with fresh DMF three times (10 mL each) followed by methanol three times (10 mL). The material was dried in a vacuum oven at 80 ºC for 1 hour, and then activated at 120 ºC for 18 hours.

2.1.6 Attempted Synthesis of NU-1000-m-$(NO_2)_4$ (NU-901-m-$(NO_2)_4$)

$ZrOCl_2 \cdot 8H_2O$ (48 mg, 0.15 mmol) and benzoic acid (1 g, 8.2 mmol) were mixed in 4 mL of DMF in an 8-dram vial and ultrasonically dissolved. The clear solution was incubated in an oven at 80 ºC for 1 hour. After cooling down to room temperature, H_4-TBAPy-*m*-$(NO_2)_4$ (26 mg, 0.03 mmol) and trifluoro acetic acid (25 uL, 0.33 mmol) were added and ultrasonically mixed. The solution was incubated in an oven at 100 ºC for 18 hours. The yellow material was isolated by centrifuge (5 minutes, 7,500 rpm) and solvent exchanged with fresh DMF three times (10 mL each) followed by methanol three times (10 mL). The material was dried in a vacuum oven at 80 ºC for 1 hour, and then activated at 120 ºC for 18 hours.

2.1.7 Synthesis of NU-1000-o-$(NH_2)_4$

$ZrOCl_2 \cdot 8H_2O$ (48 mg, 0.15 mmol) and benzoic acid (1g, 8.2 mmol) were mixed in 4 mL of DMF in an 8-dram vial and ultrasonically dissolved. The clear solution was incubated in an oven at 80 ºC for 1 hour. After cooling down to room temperature, H_4-TBAPy-*o*-$(NH_2)_4$ (22 mg, 0.03 mmol) and trifluoro acetic acid (25 uL, 0.33 mmol) were added and ultrasonically mixed. The yellow solution was incubated in an oven at 100 ºC for 18 hours. The material was isolated by centrifuge (5 minutes, 7,500 rpm) and solvent exchanged with fresh DMF three times (10 mL each) followed by methanol three times (10 mL). The material was dried in a vacuum oven at 80 ºC for 1 hour, and then activated at 120 ºC for 18 hours.

2.1.8 Synthesis of NU-1000-o-$(CH_3)_4$

$ZrOCl_2 \cdot 8H_2O$ (98 mg, 0.3 mmol) and benzoic acid (2 g, 16.4 mmol) were mixed in 8 mL of DMF in an 8-dram vial and ultrasonically dissolved. The clear solution was incubated in an oven at 80 ºC for 1 hour. After cooling down to room temperature, H_4-TBAPy-*o*-$(CH_3)_4$ (44 mg, 0.06 mmol) and trifluoro acetic acid (50 uL, 0.65 mmol) were added and ultrasonically mixed. The yellow solution was incubated in an oven at 100 ºC for 18 hours. The material was isolated by centrifuge (5 min, 7500 rpm) and solvent exchanged with fresh DMF three times (10 mL each) followed by methanol three times (10 mL). The material was dried in a vacuum oven at 80 ºC for 1 hour, and then activated at 120 ºC for 18 hours.

2.2 Characterization

2.2.1 Powder X-ray diffraction

Powder x-ray diffraction (PXRD) patterns were measured on a Rigaku® MiniFlex 600 diffractometer equipped with a D/teX Ultra detector with Cu-Kα radiation (λ = 1.5418 Å) over a range of 2θ = 3–50 ° at a scan rate of 5 ° min^{-1}.

2.2.2 Attenuated total reflectance-Fourier transform infrared

Attenuated total reflectance-Fourier transform infrared (ATR-FTIR) spectra were measured on a Bruker Tensor 27 spectrometer from 4000–400 cm^{-1} at a resolution of 2 cm^{-1}.

2.2.3 N_2 physisorption

N_2 isotherms were measured using a Micromeritics® ASAP® 2420 analyzer at 77 K. Samples were off-gassed at 120 °C under vacuum for ~16 hours. The Brunauer-Emmett-Teller (BET) method was used to calculate specific surface area in m^2/g.

2.2.4 UV-vis spectroscopy

Solid state UV-vis measurements of MOF samples from 200–800 nm were collected on a JASCO® V-650 UV-vis spectrophotometer equipped with a 150 mm integrating sphere.

2.3 Photocatalysis Experiments

For 2-CEES oxidation experiments, 2.2 mg of the MOF was dispersed in 1 mL anhydrous methanol and sealed in a 17 mm x 83 mm glass microwave vial. After purging with O_2 for 20 minutes, 23 µL (0.2 mmol) 2-CEES and 5 µL (0.04 mmol) internal standard (1-bromo-3,5-difluorobenzene) were added to the microwave vial with a 25 µL glass syringe. The vial was then exposed to either UV (396 nm) or blue (465 nm) LED irradiation using an LED setup constructed from solderless LEDs purchased from RapidLED that were then mounted onto a U-shaped aluminum sheet (Figure 4). Aliquots of 25 µL from the reaction vial were withdrawn using a syringe at 5 minute intervals,

filtered, and diluted with 1 mL of methanol into a gas chromatography vial. The samples were then subjected to a gas chromatography with flame ionization detector to monitor the reaction progress.

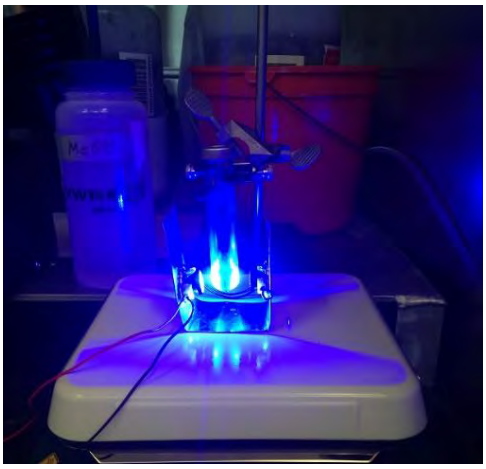

Figure 4. Homemade LED setup for photocatalysis experiments.

2.4 Transient absorption spectroscopy via nanosecond laser flash photolysis

Production, decay, and oxygen-reactivity of the triplet excited states (T_1) of the TBAPy compounds (-H_4, -OEt-, *o*-Me, and *m*-NO_2) were studied using laser flash photolysis (LFP). The third harmonic (355 nm) of a Q-switched Nd:YAG laser (Continuum® Surelite™ II, pulse width ca. 8 ns) was used for laser flash excitation. Pulse energies of up to 50 mJ cm^{-2} $pulse^{-1}$ were typically employed. The sample was excited through a 1 cm x 2 mm aperture. Laser-induced transmittance changes were monitored using white light from a 75 W Xenon source (Oriel® Instruments) focused through the sample, then re-imaged on the entrance slit of a Teledyne Princeton Instruments SP-2150 monochromator equipped with a 500 nm blazed grating. The monochromated light was detected with a Hamanatsu R-928 PMT, and the current was routed through a back-off circuit which stored and compensated for Io. The real-time current was recorded across 50 Ω on a Teledyne T3DSO2304 digital oscilloscope. The timing pulses to trigger the laser flashlamps, Q-switch, Uniblitz® (Vincent Associates) probe shutter, back-off circuit and oscilloscope were generated using a National Instruments PCIe Counter/Timer card. Data collection and analyses were controlled and performed using LabView 18 for Windows 10.

Powdered TBAPy samples were obtained from DEVCOM CBC and dissolved in spectroscopy grade DMF to achieve an absorbance of ca. 0.20 at the 355-nm excitation wavelength. Samples were deoxygenated or fully oxygenated by bubbling (for ca. 20 minutes) with either argon or oxygen, respectively. The T_1-T_n absorption of the TBAPy samples was monitored at the maximum of their absorption spectrum (between 500 and 550 nm, depending on the sample). Concomitant recovery of the ground-state bleach was also monitored at 380 nm.

2. 5 Computational Band Gap Measurements

The Highest Occupied Molecular Orbital (HOMO)- Lowest unoccupied molecular orbital (LUMO) gap calculations for H4TBAPy and TCPP derivatives were performed using the Gaussian 16 electronic structure package.[9] Calculations were performed at the B3LYP/3-21G level of theory using default optimization criteria. Initial molecular specifications were constructed by building the molecules in the Avogadro molecular editor and performing a preliminary single-point energy minimization procedure using the Universal force field and steepest descent algorithm. The value for the HOMO-LUMO gap was calculated by simply subtracting the reported HOMO and LUMO energies.

3. RESULTS

Under similar reaction conditions the majority of functionalized H_4TBAPy linkers generated MOFs with **csq** topology that were analogous to NU-1000. However, both *meta* and *ortho* nitro functionalized H_4TBAPy linkers generated MOFs with **scu** and **she** topologies characteristically similar to NU-901 and PCN-224 respectively. While powder X-ray diffraction (PXRD) can clearly distinguish the **she** MOF from **csq/scu** topologies (Figure 5), the **scu** topology was

confirmed through nitrogen adsorption experiments (Figures 6 and 7).[8, 10] The solid-state UV-vis spectra was collected for each functionalized MOF derivative that was synthesized (Figure 8). The addition of chlorine groups onto the linker appears to narrow the absorption spectra of the material while the addition of the nitro, amino, and methyl groups appear to broaden the absorption spectra of the material. In particular, NU-901-*m*-$(NO_2)_4$ shows a particularly broad absorption profile as compared to the other synthesized NU-1000 derivatives. This material also appears much darker in color than the other synthesized materials—a dark brown powder as compared to powders that vary from light tan-yellow (PCN-224-*o*-$(NO_2)_4$ and NU-1000-*o*-$(NH_2)_4$) to bright yellow (NU-1000, NU-1000-*o*-Cl_4, NU-1000-*m*-Cl_4, NU-1000-*o*-$(CH_3)_4$) in color. While the NU-1000-*o*-$(NH_2)_4$ and PCN-224-*o*-$(NO_2)_4$ derivatives also broaden the absorption spectrum, they do not broaden the absorption spectrum as much as the NU-901-*m*-$(NO_2)_4$ derivative, likely leading to the lighter color of those powders as compared to NU-1000-*m*-$(NO_2)_4$.

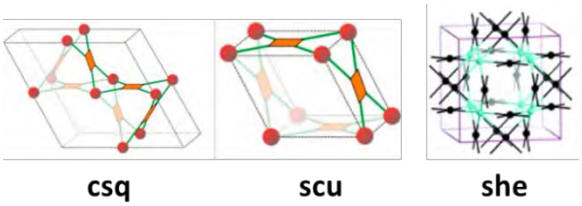

Figure 5. MOF topologies for NU-1000, NU-1000-*o*-Cl_4, NU-1000-*m*-Cl_4, NU-1000-*o*-$(CH_3)_4$, NU-1000-*o*-$(NH_2)_4$ (csq), NU-901-*m*-$(NO_2)_4$ (scu), and PCN-224-*o*-$(NO_2)_4$ (she). The csq and scu topologies have similar PXRD patterns but can be distinguished through nitrogen adsorption experiments.

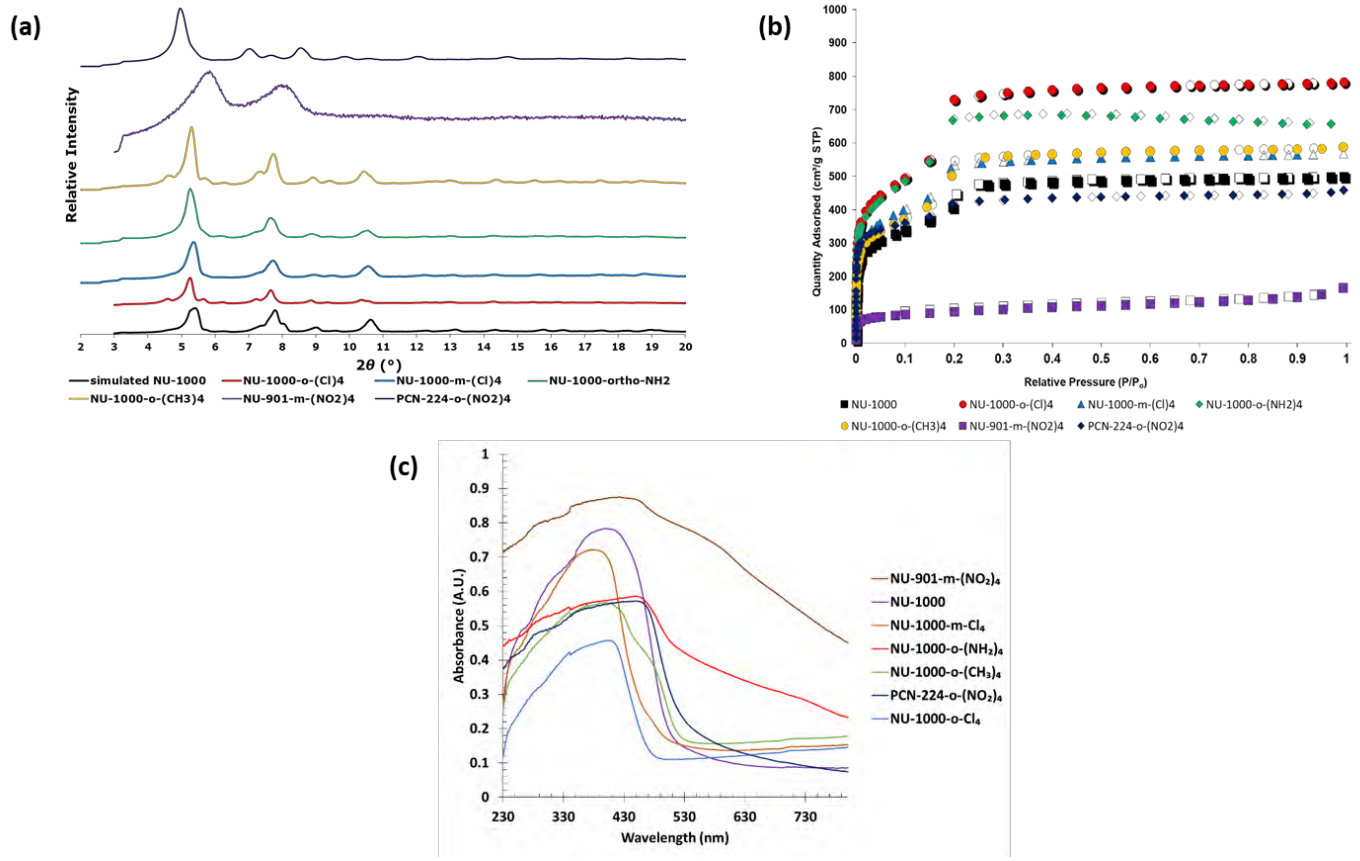

Figure 6. (a) PXRD pattern for the synthesized MOF derivatives (b) Nitrogen adsorption isotherms of the synthesized MOF derivatives. (c) Solid-state UV-vis spectra for the synthesized MOF derivatives.

Each functionalized MOF was reacted with 2-CEES in the presence of UV (395 nm) and blue (465 nm) LED light. The reactions were conducted so that there was a catalytic amount of MOF present relative to the amount of 2-CEES present in the reaction solution (approximately 100:1, 2-CEES:H_4TBAPy). PCN-224-*o*-$(NO_2)_4$, NU-901-*m*-$(NO_2)_4$, and NU-1000-*o*-$(NH_2)_4$ showed very little to no reactivity compared to the baseline material and NU-1000-*o*-$(CH_3)_4$

showed reactivity similar to that of the baseline material. However, NU-1000-*o*-Cl_4 and NU-1000-*m*-Cl_4 showed marked enhancement in reactivity (Table 1). Interestingly, these materials showed a narrower absorption spectrum as compared to the less reactive derivatives. However, previously reported computational data suggests that functionalization of the benzene ring with these moieties does not significantly affect the band gap.

Table 1. Calculated half-lives for the oxidation of 2-CEES by the synthesized NU-1000 derivatives.

MOF	UV LED ($t_{1/2}$, min)	Blue LED ($t_{1/2}$, min)
NU-1000	3	40
NU-1000-*o*-Cl_4	5.5	7.5
NU-1000-*m*-Cl_4	1	25
NU-901-*m*-$(NO_2)_4$	N.R.	N.R.
PCN-224-*o*-$(NO_2)_4$	N.R.	N.R.
NU-1000-*o*-$(NO_2)_4$	1	-
NU-1000-*o*-$(NH_2)_4$	45	N.R.
NU-1000-*o*-$(CH_3)_4$	11	40
NU-1000-*m*-I_4	22	45

Therefore, the enhancement in reactivity is hypothesized to be a result of the heavy chlorine atoms facilitating the intersystem crossing that leads to the reactive triplet state of the MOF as previously observed in TCPP linkers.[11] In addition, the enhanced reactivity of NU-1000-*o*-Cl_4 relative to NU-1000-*m*-Cl_4 under blue LED conditions can be attributed to the red-shift of the *ortho*-substituted derivative relative to that of the *meta*-substituted derivative, leading to enhanced absorption and therefore faster reactivity (Figure 7).

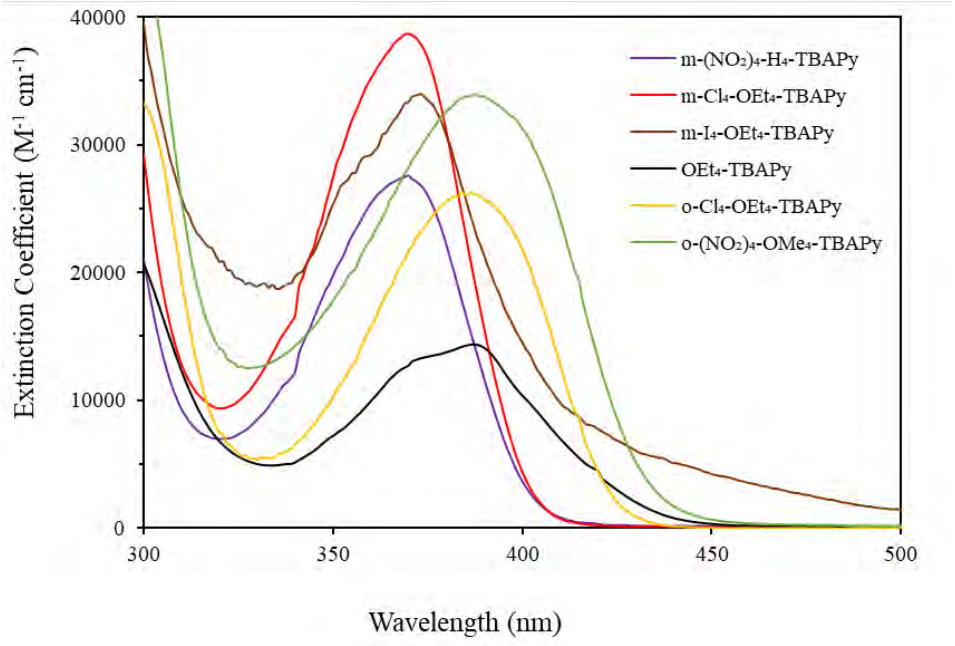

Figure 7. Absorbance profiles of functionalized H_4TBAPy derivatives.

The ability to reach the triplet state of the MOF is one of the primary factors to produce singlet oxygen and enhancement of photocatalytic reactivity (Figure 1). While the more darkly colored materials (NU-901-*m*-$(NO_2)_4$, PCN-224-*o*-$(NO_2)_4$, and NU-1000-*o*-$(NH_2)_4$) have overall wider absorption spectra, this spectral enhancement doesn't appear to translate into an enhancement of the excitement of the material to the triplet state as evident by the lack of

reactivity of these materials with 2-CEES. Rather, it is hypothesized that these materials absorb a great deal more light over a wider range of wavelengths but proceed to undergo a self-quenching mechanism as adjacent functionalized linkers can then absorb any transferred energy rather than using it to promote the MOF to the excited triplet state, particularly in the case of NU-901-*m*-$(NO_2)_4$ and PCN-224-*o*-$(NO_2)_4$ as their topology causes the linkers to be in closer proximity to each other than the **csq** topology of NU-1000.

This proposed self-quenching pathway was further confirmed by TAS measurements. The lifetime of the triplet excited state for several of the H_4TBAPy linkers was determined in DMF (Table 2). The ester derivative of the linker showed a shorter triplet state lifetime as compared to the carboxylic acid derivative indicating that the acid form of the linker contained within the MOF should have enhanced reactivity overall and that the MOF structure should contribute to an enhanced triplet state lifetime and subsequent reactivity with 2-CEES. While each of the linkers tested showed fairly long triplet state lifetimes, H_4TBAPy-*m*-$(NO_2)_4$ exhibited the longest triplet state lifetime. This is consistent with the UV-vis data which showed a higher absorptivity of NU-1000-*m*-$(NO_2)_4$ in the visible region as compared to the other NU-1000 derivatives. However, the diminished reactivity of the linker when contained within the MOF framework indicates that the MOF topology is contributing to a self-quenching mechanism that is diminishing the overall reactivity of the MOF.

The diminished reactivity of NU-1000-*o*-I_4 and NU-1000-*m*-I_4 relative to the chloride derivatives can also be attributed to a non-radiative self-quenching mechanism. TAS measurements on the linker derivatives determined that the quantum yield measurement, molar extinction coefficient, and wavelength of absorbance are all sufficient for reactivity. However, the reactivity profile is much slower for the iodide derivatives compared to their chloride counterparts indicating that there is a competing non-radiative process that is quenching the triplet state prior to the formation of singlet oxygen (Table 3). While these results are indicative a self-quenching mechanism, direct confirmation can be achieved through TAS measurements on the MOF derivatives themselves. However, TAS measurements are traditionally limited to materials that are soluble which is not the case for the MOF materials. Therefore, we have prepared the MOFs in PDMS, an optically transparent polymer, cast directly into polystyrene cuvettes for collecting spectral measurements.

Table 2. Summary of T1 lifetimes of various NU-1000 linker derivatives collected in DMF.

NU-1000 Linker	τ_{T1} (µS)
H_4TBAPy	50.0
H_4TBAPy-OEt	34.7
H_4TBAPy-*o*-$(CH_3)_4$	49.0
H_4TBAPy-*m*-$(NO_2)_4$	59.7

Table 3. Summary of singlet oxygen quantum yield measurements for NU-1000 linker derivatives.

NU-1000 Linker	Molar Extinction Coefficient ($M^{-1}cm^{-1}$)	Wavelength (nm)	Φ_Δ ACN
TBAPy-OEt_4	(1.430±0.006) x10^4	386	0.73±0.04
o-Cl-TBAPy-OEt_4	(2.62±0.04) x10^4	386	0.34±0.04
m-Cl-TBAPy-OEt_4	(3.87±0.03) x10^4	370	0.68±0.05
m-NO_2-TBAPy-OEt_4	(2.76±0.04) x10^4	370	--
o-NO_2-TBAPy-OMe_4	(3.39±0.08) x10^4	388	0.054±0.002
m-I-TBAPy-OEt_4	(3.38±0.06) x10^4	374	0.50±0.03

These novel NU-1000 derivatives also offer the opportunity to perform optimized solid-state dynamic photocatalytic experiments for flow-through degradation of CWAs. A micro breakthrough system was developed and used to determine the ability of NU-1000 to degrade 2-CEES in a flow-through system. When 2-CEES flowed through a packed bed of NU-1000 under UV light conditions, 2-CEES removal was estimated to be >70 mol/g (approximately 100 turnovers of 2-CEES/pyrene) relative to 12.4 mol/g when 2-CEES was exposed to the packed catalyst bed in the dark (Figure 8). In addition, the catalytic ability of the material did not diminish over time and in fact led to condensation of product on the surface of the bed rather than 2-CEES breaking through the catalyst bed (Figure 8). While this system will need to be further studied and optimized, these initial results show promise for a novel photodynamic system for the degradation of chemical warfare agents that will produce less waste and has the advantage of being able to be regenerated and reused several times over.

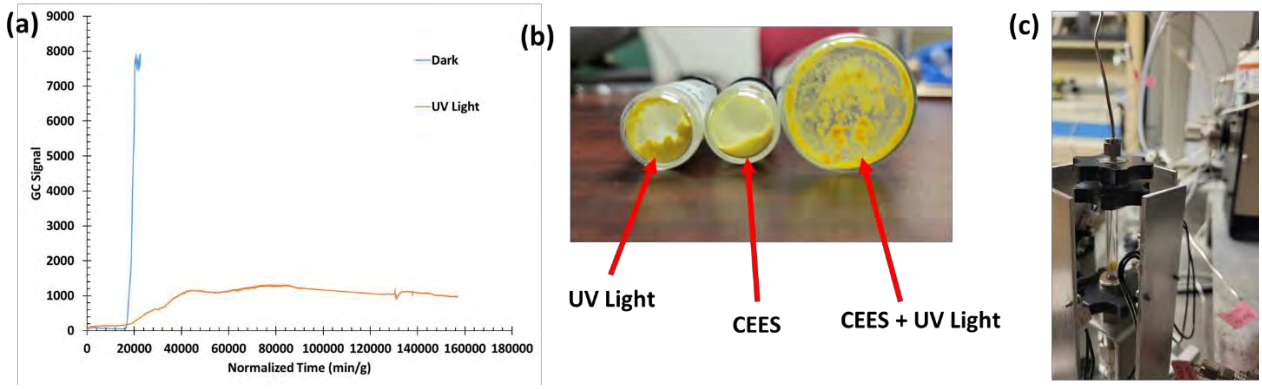

Figure 8. (a) Micro breakthrough results for NU-1000 exposed to 2-CEES under dark and UV light conditions (b) Photos of the NU-1000 powder before and after exposure to 2-CEES (c) Photo of micro breakthrough system

4. CONCLUSIONS/FUTURE WORK

Several novel MOF variants were successfully synthesized with functional groups (–Cl, –I, $–NO_2$, $–NH_2$, $–CH_3$) positioned either *ortho*- or *meta*- to the carboxylic acid on the linker. Photocatalytic experiments showed that chlorine atoms significantly improve the photocatalytic reactivity of the material consistent with our hypothesis that heavy halogen groups would enhance the triplet state of the MOF, thereby enhancing photocatalytic reactivity. However, a non-radiative self-quenching process was found to diminish reactivity of the iodide derivative, despite expectations that the heavier iodide atom would enhance reactivity. In addition, the *ortho*-substituted derivatives showed a red-shift in absorbance relative to the *meta*-substituted derivatives providing an explanation for the enhanced reactivity of NU-1000-*o*-Cl_4 relative to NU-1000-*m*-Cl_4 under blue light conditions. Previously reported computational data suggests that these moieties do not significantly affect the band gap of the material confirming that the lifetime of the triplet state of the MOF is the primary factor affecting the generation of singlet oxygen and reactivity of the photocatalyst with 2-CEES and should be the factor most considered when designing a MOF photocatalyst for the generation of singlet oxygen.

In addition, it was determined that possible self-quenching mechanisms should be carefully considered in the design of MOF photocatalysts. This was evidenced by the fact that PCN-224-*o*-$(NO_2)_4$, NU-901-*m*-$(NO_2)_4$, and NU-1000-*o*-$(NH_2)_4$ absorb more light than the more reactive chlorine derivatives but do not exhibit enhanced photocatalytic reactivity. TAS experiments of the various functionalized linkers in solution further confirmed this theory as H_4TBAPy-*m*-$(NO_2)_4$ showed the longest triplet state lifetime indicating that the linker is an appropriate photosensitizer and should enhance reactivity but does not in the crystalline structure indicating that the proximity of linkers within the structure could be causing a self-quenching pathway diminishing the triplet state lifetime. Solid state TAS experiments of the NU-1000 derivatives printed into optically transparent cuvettes will be used to confirm this mechanism. These results not only enhance the general knowledge of these materials but also contribute toward design principles for future MOF-based photocatalysts for the mitigation of toxic chemicals susceptible to oxidation including sulfur mustard, hydrogen sulfide, and other organic pollutants, particularly for a dynamic flow-through system which has already shown promise in this work.

ACKNOWLEDGMENTS

Funding was provided by the U.S. Army via the Surface Science Initiative Program (PE 0601102A Project VR9) at the U.S. Army Combat Capabilities Development Command (DEVCOM) Chemical Biological Center (CBC). This research was performed while Sergio J. Garibay held a National Research Council post-doctoral research associateship award at DEVCOM CBC.

REFERENCES

[1] Maza, W.A.; Morris, A.J. Photophysical Characterization of a Ruthenium(II) Tris(2,2′-bipyridine)-Doped Zirconium UiO-67 Metal–Organic Framework. *J. Phys. Chem. C.* **2014**, *118* (17), pp 8803–8817.

[2] Howarth, A.J.; Buru, C.T.; Liu, Y.; Ploskonka, A.M.; Hartlieb, K.J.; McEntee, M.; Mahle, J.J.; Buchanan, J.H.; Durke, E.M.; Al-Juaid, S.S.; Stoddart, J.F.; DeCoste, J.B.; Hupp, J.T.; Farha, O.K. Postsynthetic Incorporation of a Singlet Oxygen Photosensitizer in a Metal–Organic Framework for Fast and Selective Oxidative Detoxification of Sulfur Mustard. *Chem. Eur. J.* **2017**, *23* (1), pp 214–218.

[3] Liu, Y.; Buru, C.T.; Howarth, A.J.; Mahle, J.J.; Buchanan, J.H.; DeCoste, J.B.; Hupp, J.T.; Farha, O.K. Efficient and selective oxidation of sulfur mustard using singlet oxygen generated by a pyrene-based metal–organic framework. *J. Mater. Chem. A.* **2016**, *4* (36), pp 13809–13813.

[4] Liu, Y.; Howarth, A.J.; Hupp, J.T.; Farha, O.K., Selective Photooxidation of a Mustard-Gas Simulant Catalyzed by a Porphyrinic Metal–Organic Framework. *Agnew. Chem., Int. Ed.* **2015**, *54* (31), pp 9001–9005.

[5] DeRosa, M.C.; Crutchley, R.J. Photosensitized singlet oxygen and its applications. *Coord. Chem. Rev.* **2002**, *233–234*, pp 351–371.

[6] Tranchemontagne, D.J.; Mendoza-Cortes, J.L.; O'Keeffe, M.; Yaghi, O.M. Secondary building units, nets and bonding in the chemistry of metal-organic frameworks. *Chem. Soc. Rev.* **2009**, *38* (5), pp 1257–1283.

[7] Islamoglu, T.; Ortuño, M.A.; Proussaloglou, E.; Howarth, A.J.; Vermeulen, N.A.; Atilgan, A.; Asiri, A.M.; Cramer, C.J.; Farha, O.K. Presence versus Proximity: The Role of Pendant Amines in the Catalytic Hydrolysis of a Nerve Agent Simulant. *Agnew. Chem., Int. Ed.* **2018**, *57* (7), pp 1949–1953.

[8] Kirchon, A.; Feng, L.; Drake, H.F.; Joseph, E.A.; Zhou, H.-C. From fundamentals to applications: a toolbox for robust and multifunctional MOF materials. *Chem. Soc. Rev.* **2018**, *47* (23), pp 8611–8638.

[9] Frisch, M.J.; Trucks, G.W.; Schlegel, H.B.; Scuseria, G.E.; Robb, M.A.; Cheeseman, J.R.; Scalmani, G.; Barone, V.; Petersson, G.A.; Nakatsuji, H.; Li, X.; Caricato, M.; Marenich, A.V.; Bloino, J.; Janesko, B.G.; Gomperts, R.; Mennucci, B.; Hratchian, H.P.; Ortiz, J.V.; Izmaylov, A.F.; Sonnenberg, J.L.; Williams-Young, D.; Ding, F.; Lipparini, F.; Egidi, F.; Goings, J.; Peng, B.; Petrone, A.; Henderson, T.; Ranasinghe, D.; Zakrzewski, V.G.; Gao, J.; Rega, N.; Zheng, G.; Liang, W.; Hada, M.; Ehara, M.; Toyota, K.; Fukuda, R.; Hasegawa, J.; Ishida, M.; Nakajima, T.; Honda, Y.; Kitao, O.; Nakai, H.; Vreven, T.; Throssell, K.; Montgomery, J.A., Jr.; Peralta, J.E.; Ogliaro, F.; Bearpark, M.J.; Heyd, J.J.; Brothers, E.N.; Kudin, K.N.; Staroverov, V.N.; Keith, T.A.; Kobayashi, R.; Normand, J.; Raghavachari, K.; Rendell, A.P.; Burant, J.C.; Iyengar, S.S.; Tomasi, J.; Cossi, M.; Millam, J.M.; Klene, M.; Adamo, C.; Cammi, R.; Ochterski, J.W.; Martin, R.L.; Morokuma, K.; Farkas, O.; Foresman, J.B.; Fox, D.J. *Gaussian 16*, Revision C.01, Gaussian, Inc.: Wallingford, CT, 2016.

[10] Gomez-Gualdron, D.A.; Gutov, O.V.; Krungleviciute, V.; Borah, B.; Mondloch, J.E.; Hupp, J.T.; Yildirim, T.; Farha, O.K.; Snurr, R.Q. Computational Design of Metal-Organic Frameworks Based on Stable Zirconium Building Units for Storage and Delivery of Methane. *Chem. Mater.* **2014**, *26* (19), pp 5632-5639.

[11] Nifiatis, F.; Athas, J.C.; Gunaratne, D.D.; Gurung, Y.; Monette, K.M.; Shivokevich, P.J. Substituent Effects of Porphyrin on Singlet Oxygen Generation Quantum Yields. *Open Spectrosc. J.* **2011**, *5*, pp 1–12.

Cooperative interactions between functionalized particles and binders in polymer composites and their effect on chemical transport

Mark J. Varady[a]*, Melissa S. Hulet[b], Adam R.Hinkle[c], Thomas P. Pearl[c], Melissa L. Sweat[a], Kenneth E. Strawhecker[d], Alice M. Savage[d], Jonathan P. Ligda[d], Yossef A. Elabd[e]
[a]U.S. Army Combat Capabilities Development Command Chemical Biological Center, Research & Technology Directorate, 8198 Blackhawk Rd, Aberdeen Proving Ground, MD 21010
[b]Leidos, 1750 Presidents St, Reston, VA 20190
[c]DCS Corporation, 6909 Metro Park Dr, Suite 500, Alexandria, VA 22310
[d]U.S. Army Research Laboratory, 2800 Powder Mill Rd, Adelphi, MD 20783
[e]Department of Chemical Engineering, Texas A&M University, 3122 TAMU Room 200, College Station, TX 77843

ABSTRACT

Protective coatings on military assets are complex polymer composites consisting of a high loading of several different particle types to achieve the desired coating functionality. The transport properties at the particle-polymer interface can differ significantly from those in the polymer bulk, and when the interfacial regions overlap at sufficiently high loading, undesirable fast chemical transport pathways can open. Improving the chemical resistance of protective coatings while maintaining the desired properties requires a detailed understanding of how the interface can be tuned to improve the interfacial transport properties. Because paint coatings consist of so many different components, such basic studies are difficult to perform and deconvolve all the factors contributing to performance. In this work, polyurethane-silica composites are used as model systems to capture the essential elements of the problem while enabling a clearer picture of how system modifications influence performance. Specifically, the surface chemistry of the silica particles is modified by silanization and polymer grafting to alter the interaction with the polymer matrix. The effect of these changes on the particle-polymer interface are assessed experimentally using atomic force microscopy-based colloidal force spectroscopy on single particles and imaging cross-sectioned composites. In parallel, molecular dynamics simulations of the interface elucidate structural changes in the polymer and corresponding diffusivity changes of different penetrant chemicals. Comparing how specific modifications to the particle surface influence the nature of the interface versus how they influence chemical transport is an important step in developing structure-property relationships for chemical transport in polymer composites and developing more rational approaches to controlling transport properties.

Keywords: Transport phenomena, diffusion, polymer composites, atomic force microscopy, colloidal force spectroscopy, interface adhesion, chemical resistance, molecular dynamics

1. INTRODUCTION

Protective coatings on military assets are complex polymer composites consisting of different solid particle types and sizes bound together by a polymer binder matrix. The particles provide rheology modification for processing and application, required optical and signature management properties of the coating, and camouflage. To achieve all these functions, the particle (or solids) loading in the polymer binder must be relatively high, up to 60 wt%. In these high-loading composite coatings, it has been observed that the breakthrough of a chemical is significantly faster than for the corresponding pure polymer. Since the particles used in these systems are impermeable, this suggests that the transport properties of the polymer are modified by the presence of the particles. At the polymer-particle interface, the arrangement of polymer chains can be different than in the bulk, and the nature of the interface is mediated by interactions between the polymer and particle. Thus, to understand and control chemical transport in polymer composites, it is necessary to determine how changes in the polymer-particle interface manifest as changes in the

overall transport properties of the system to identify effective strategies for modifying the particle surface to improve chemical resistance.

It has been demonstrated that polymer structure and properties near a solid interface depend on the polymer-solid interaction strength and can differ significantly from the bulk polymer. Typical bulk polymer characterization methods such as differential scanning calorimetry or broadband dielectric relaxation spectroscopy can be used to infer the influence of an interfacial region by varying the particle loading in the composite and/or the chemical nature of the particle surface. For example, Bansal et al.[1] used differential scanning calorimetry to show that increasing the loading of silica in polystyrene (PS) lowered the glass transition temperature (T_g) of the composite due to unfavorable interactions between the matrix and solid resulting in higher PS chain mobility. The authors found that grafting PS chains onto the surface of the silica particle negated the decrease in T_g. Similarly, Mapesa et al.[2] used broadband dielectric relaxation spectroscopy to infer that chain dynamics of polymethylmethacrylate (PMMA) are significantly slower at the interface with silica particles due to strong hydrogen bonding interactions. Many studies have related stronger particle-polymer interaction and increased T_g with corresponding increases in composite modulus.[3-5] Similar correlations have been drawn between chemical diffusion in polymer composites including PEG-silica composites[6] and mixed matrix membranes.[7-9]

Directly measuring polymer structure and properties near solid interfaces is more difficult and typically has been performed with more specialized equipment. For example, neutron reflectometry can provide detailed information on polymer structure near solid interfaces and has been used to show decreased PMMA chain mobility close to an interface (~10 nm)[10] and surface-induced structuring of ion transport channels in Nafion.[11] Positron annihilation lifetime spectroscopy is another specialized technique that is used to determine the free volume in a polymer, which is a primary factor in the diffusivity of small penetrant molecules. Sharma et al[12] used positron annihilation lifetime spectroscopy to show that the strong interaction between PMMA and alumina results in a denser region with smaller free volume holes at the interface. Atomic force microscopy (AFM) is a lower cost, more accessible tool that has also been used to directly interrogate polymer-solid interfaces. Examples of this include using AFM-based nanoindentation on model 2D composites to show stiffening of PS near a glass interface.[13] Phase contrast and torsional harmonic AFM imaging of cross-sectioned nitrile butadiene rubber-carbon black composites that reveal an interfacial region with increased modulus,[14] and contact resonance AFM of polyvinylacetate-silica composite cross-sections showing higher polymer stiffness near the interface have also been observed.[15]

Given that much of the work around polymer composites has strongly suggested particle-polymer interaction strength as the predominant factor influencing the nature of the interfacial region, having a quantitative measure of this interaction strength is useful. The AFM-based colloidal probe technique is one mature experimental method for quantifying adhesion between a single small particle (1–50 μm diameter) attached to the end of an AFM cantilever and a polymer surface.[16-18] For example, Pham et al.[19] studied the adhesion between silica particles and polydimethylsiloxane and showed that accounting of capillary forces is required to accurately predict the adhesion force. Colloidal probe AFM has also been used to study the influence of adhesion in metal-polymer composites by using polyamide and polyethylene colloidal probes to measure the adhesion with aluminum and steel planar surfaces.[20]

Molecular dynamics (MD) models of the particle-polymer interface provide a complementary computational technique for probing details of the polymer structure as well as penetrant diffusion dynamics. Dutta and Bhatia[21] used MD to construct a model of a polyimide-zeolite interface and showed that the interfacial region is denser and improves CO_2/CH_4 selectivity. Cheng et al.[22] utilized a similar MD simulation to assess variations in relaxation dynamics of glycerol near a silica surface as a function of temperature.[22]

This work leverages techniques similar to the AFM-based imaging, colloidal probe, and MD described above to elucidate the nature of the interfacial region in polyurethane (PU)-silica composites and how it changes with chemical modification of the silica surface. Specifically, the surface is modified with (a) different silane chemistries to vary the degree of hydrogen bonding with the PU matrix and (b) polymer grafting to entangle with the PU matrix. Both AFM imaging and MD simulations provide information on the interfacial region thickness and properties while AFM colloidal probe measurements provide a measure of adhesion between the silica and PU. These are correlated with observed diffusion dynamics of the probe molecule methanol in the PU-silcia composites as a function of loading as measured by attenuated total reflectance-Fourier transform infrared (ATR-FTIR) spectroscopy. Particular focus is on advancements made in FY21: AFM imaging of cross-sectioned composites and image analysis to obtain semi-quantitative information on the interfacial regions and MD simulations for different silica surface chemistries and varying penetrant size and polarity.

2. MATERIALS AND METHODS

2.1 Materials

PU was synthesized by the U.S. Army Combat Capabilities Development Command Army Research Laboratory, and described in a previous publication.[23]

Silica and functionalized silica particles were obtained from Polysciences, Inc.® (0.5 and 5 µm silica, carboxyl functionalized silica, and amine functionalized silica).

Silica particles were functionalized with decyltrimethoxysilane and dodecyltrimethoxysilane (Gelest). The silica particles were washed by dispersing ~0.1 g in 1.5 mL ethanol (EtOH), mixing at a speed of 18,000 rpm (Scilogex D160) for 5 minutes, sonicating for 15 minutes, centrifuging for 20 minutes at 4000 rpm and pulling off the supernatant EtOH. The washing procedure was repeated 3 times prior to silanization to remove any impurities from the particle surface. Following the procedure recommended by Gelest, 200 mL of the silane was added dropwise with mixing into 5 mL of 95 % EtOH/H2O solution adjusted to pH ~5 by addition of acetic acid. After mixing for 5 minutes, 1.5 mL of the solution was added to the washed silica particles, mixed for 5 minutes at 18,000 rom, sonicated for 15 minutes, and centrifuged for 20 minutes at 4,000 rpm. The washing procedure described above was then repeated 3 times to remove excess silane not bound to the silica surface. The silanized silica particles were then placed in a vacuum oven at 70 ºC for at least 24 hours to dry.

Silica particles used for creating in-house colloidal probes were dispersed on a 1 in. glass slide. The glass slide was sonicated in a methanol (MeOH) bath for 15 minutes followed by drying in a dry N2 stream and placing in a UV/ozone cleaner for 20 minutes. A 35 µL droplet of ~0.01 mg/mL silica particles in MeOH was deposited on the clean glass slide and dried in a 70 ºC oven for at least 1 hour.

Solutions of 100 mg/mL PU in cyclopentanone (Sigma-Aldrich®, > 99 % purity) were prepared and spin cast onto attenuated total reflectance (ATR) crystals (Pike Technologies, Germanium 45 deg, 80 mm x 10 mm x 4 mm) or glass slides (Fisher Scientific™, 1 inch diameter). For the ATR crystals, 200 µL of solution was spread onto the ATR crystal and rotated at 300 rpm for 5 minutes in a spin coater (WS-650 Series Spin Processer, Laurell Technologies®). For the glass slides, 200 µL of solution was spread onto the glass slide and rotated at 1,500 rpm for 5 minutes in a spin coater.

Silica-polymer composites were created by dispersing varying masses of 0.5 µm particles in 1 mL of cyclopentanone using a homogenizer (Scilogex D160) operating at ~18,000 rpm for 5 minutes before mixing with the 100 mg/mL polymer solutions for 15 minutes at 18,000 rpm, followed by sonication for 15 minutes.

2.2 Methods

Composites were cross-sectioned using either a Leica EM UC7 ultramicrotome or a Leica EM TIC020 triple beam ion miller. For both techniques, a ~500 µm thick PU-silica composite was rough-cut to expose the cross-section. The samples were cooled to -80 °C and cut in 500 nm slices with a glass knife before performing a finishing cut using 150 nm slices with a diamond knife (45 deg, Diatome). Cross-sectioned samples were annealed above the Tg of PU at 80 °C for at least 24 hours prior to AFM imaging to relieve any stress induced by the cutting process.

Colloidal force spectroscopy was performed with a Nanosurf™ Flex Axiom AFM. Each colloidal AFM probe was calibrated prior to use by using the thermal tuning capability of the instrument to obtain the resonant frequency and spring constant of the cantilever. Additionally, the deflection sensitivity (relating photodetector voltage to cantilever deflection) of each colloidal probe was obtained by measuring the photodetector voltage as a function of *z*-position as the colloidal probe is pressed into a rigid silicon wafer. Both the cantilever spring constant and deflection sensitivity are required for obtaining quantitatively accurate measurements of the particle-polymer interaction force. Standard force spectroscopy was performed by approaching the colloidal probe to the polymer surface using default settings, performing a 2 µm indentation over 2 seconds followed by a pull-off over 2 seconds. Modifications to the standard force spectroscopy procedure were also investigated and are described in the Results and Analysis section.

Imaging of composite cross sections was performed with both amplitude modulation (AM) – frequency modulation (FM)[24,25] and loss tangent AFM[26,27] (Molecular Force Probe (MFP)-3D, Asylum Research). In each case, the cross-sectioned composite sample was placed on a temperature control stage and allowed to equilibrate. After thermal equilibration of the sample, the AFM tip was brought into contact with the sample then retracted slightly before tuning the operating frequency to ensure that the cantilever was driven at resonance during the imaging scans. Analysis of all images was performed in MATLAB (R2019b).

Details of the chemical breakthrough experiments have been described in previous publications.[23] Briefly, a controlled vapor concentration was created by flowing dry N_2 gas through a custom blown, glass saturator cell (Glassblowers, Inc.) that was saturated with the desired liquid chemical. The vapor concentration delivered (i.e., effective partial pressure or activity) was modulated by combining the saturated vapor flow with dry N_2 and setting the corresponding mass flow controllers in the desired ratio with a total flow rate of 50 SCCM in all cases. This flow was passed over the top of the polymer-coated ATR crystal and infrared light was shone through the backside of the crystal, creating an evanescent wave at the polymer-crystal interface. Monitoring the intensity of the reflected infrared light as a function of wavelength allows the presence of species with corresponding absorption bands to be detected. Because the evanescent wave penetrates less than 600 nm into the polymer, this measurement only detects species near the polymer-crystal interface. Integration over the absorption band(s) corresponding to a particular species of interest allows quantification of the amount of species absorbed as a function of time.

The MD systems have been prepared with 28 PU chains of 20 monomer units and 80 penetrant molecules randomly packed into a simulation cell that is initially compressed to a density of approximately 1.5 g/cm3. In cases where the surface chemistry has been modified, functional groups of carboxyl (-COOH) or amine (-NH2), approximately 40 groups in number, were attached to each side of the silica as shown in Figure 1 (right). The silica slab itself was held as a fixed, rigid structure which reflects the impermeable nature of the large (micron-size) silica particles in the actual coating. The functional groups were studied both as rigid and as flexible structures to understand how to best model their presence and effect on penetrant diffusion.

The systems were first equilibrated under NVT conditions at 300 K for 20 ns using the LAMMPS MD software and the polymer consistent force field provided by the commercially available software BIOVA Materials Studio. The systems were then relaxed using NPT integration and thermostating while raising the temperature to 300 K, 400 K, and 500 K at 1 atm for another 20 ns. The compressed systems had the approximate dimensions 6 x 6 x 12 nm^3. The pressure relaxation was allowed only in the extended (12 nm) dimension, i.e., in the direction perpendicular to the plane of the silica slab, and the in-plane box dimensions were held fixed. This constraint was imposed to preserve the interface between the polymer and the silica as well as a fixed cross-sectional area of 30.25 nm^2. The constraint also permitted periodic boundaries in all directions.

3. RESULTS AND ANALYSIS

3.1 AM-FM AFM imaging

Overview images were obtained over a ~20 µm square area to identify particles that had been cleanly cross-sectioned, then images were acquired over ~5 µm and ~1.5 µm areas of interest to better spatially resolve the interfacial regions around the sectioned particles. Topography (Z) and phase (ϕ_1) are the standard outputs from AM-AFM, commonly known as tapping mode, in which the tip-sample distance is adjusted to maintain a constant cantilever oscillation amplitude. Variation in $\phi_1$over the sample is indicative of material property variations, although this information is also convolved with tip-sample interaction, which can be influenced by things like adhesion and capillary forces. AM-FM AFM additionally excites a higher frequency resonance (typically the first harmonic) at a much lower oscillation amplitude and maintains this at resonance (90 degree phase) by adjusting the drive frequency while also maintaining the oscillation amplitude by adjusting the drive voltage. The difference between the free resonance and modulated frequency (Δf_2) provides information on the sample stiffness (stiffer samples cause higher frequency shift) while the variation in drive voltage (dissipation, A_2) provides information on vibrational energy loss in the sample (higher dissipation means greater loss). Figure 6 shows a closely spaced pair of particles in a cross-sectioned PU-unfunctionalized silica composite over a 1.4 µm window using the topography, phase, frequency, and dissipation channels. Similar images were obtained in several different locations and for composites made with NH_2, COOH and DDTMS functionalized silica particles. The topography map shows that the particles are only ~10 nm higher than the surrounding polymer matrix, indicating successful sectioning. The phase map offers the clearest delineation of the particle from the surrounding polymer matrix, while both Δf_2 and A_2 clearly reveal an interfacial region surrounding the particle.

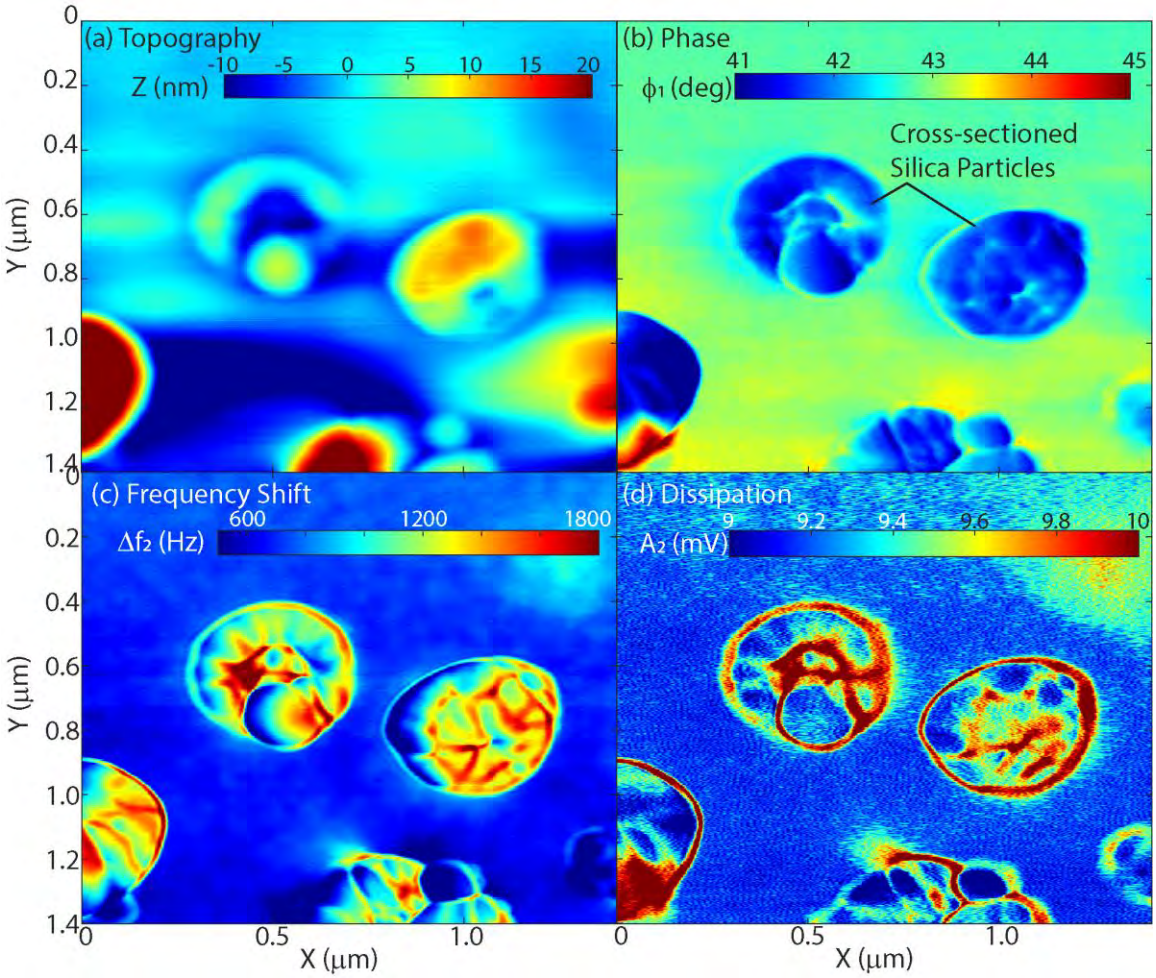

Figure 1. AM-FM images of cross-sectioned PU-silica (bare) composite over 1.4 µm square area: (a) topography, (b) phase, (c) second mode frequency shift, and (d) dissipation.

To reliably compare similar images across composites with different silica surface chemistry, it is necessary to quantify relevant properties in both the interfacial and bulk polymer region using a consistent methodology across all images. A piecewise linear closed curve was individually drawn around each particle to define regions of interest (ROIs) and a phase threshold was specified to define the boundaries of each particle. A second bounding curve was drawn enclosing all particles and the bulk polymer. Subtracting the particle ROIs from this larger ROI defined the bulk polymer ROI. The interfacial regions were defined by incrementally expanding normal to the particle boundaries and checking whether the values of Δf_2 and A_2 differed significantly between the bulk polymer and added interface increment. Specifically, the increment is added to the interface if the mean values within the interface region fall outside of the standard deviation of the bulk polymer region. Figure 2 shows an example of the definition of the interface boundary for the same composite shown in Figure 6, revealing an average interface thickness of 55 nm.

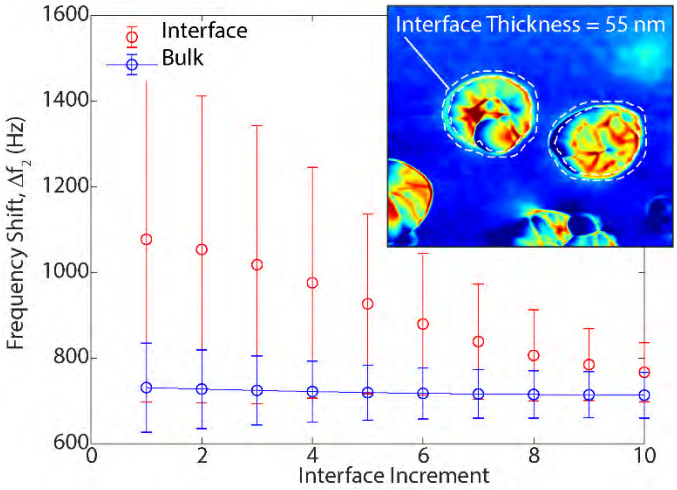

Figure 2. Definition of interface region using AM-FM image of PU-silica(bare) composite showing the values of Δf_2 for each added interface increment (red) and bulk polymer (blue). The inset shows the interfacial region (dashed white lines) overlaid on the image of Δf_2.

With the interfacial and bulk polymer regions defined, it is possible to compare the values of the AFM outputs between the regions. Figure 3 shows a comparison of distributions of Δf_2 and A_2 for all pixels in each region of the PU-silica composite. The mean values Δf_2 and A_2 are higher in the interfacial region indicating that the polymer is both stiffer and lossier adjacent to the silica surface. This is indicative of the polymer being denser in the interfacial region, which aligns with previous studies of strong particle-polymer interaction. The distributions are also broader in the interfacial region, which could reflect the gradual variation in polymer properties from the particle surface to the bulk.

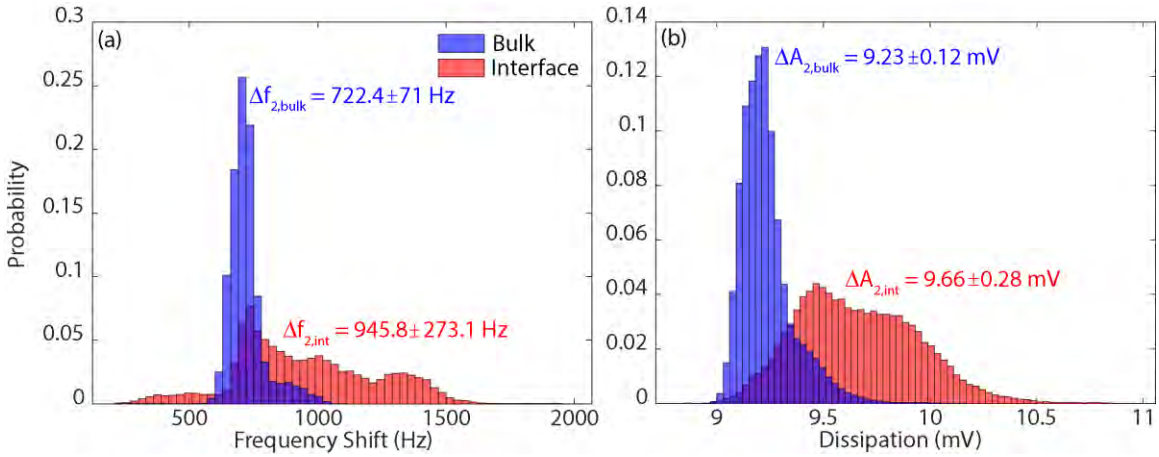

Figure 3. Histograms of (a) frequency shift, Δf_2, and (b) dissipation, A_2, in bulk (blue) and interfacial (red) regions of cross-sectioned PU-silica composite along with means and standard deviations.

Direct comparison of the above results across different composite samples is difficult because the stiffness and dissipation not only depend on the material properties, but are convolved with the cantilever properties tip shape, and operating parameters, which can vary significantly from experiment to experiment. However, comparison between the interfacial and bulk regions within a given sample is possible, and it is the relative difference between interfacial and bulk regions and how this changes with particle surface chemistry that is the primary interest of this work. To facilitate comparison across samples, the ratio of mean interface and bulk values is used in Figure 5. It is clear that the interfacial region in the composite with bare (unfunctionalized) silica particles departs from the bulk more than for the functionalized particles. The surface of bare silica particles is expected to be populated with hydroxyl (Si-OH) groups that will more strongly hydrogen bond with the PU matrix than the functionalized particles, which explains the trend in interface properties shown in Figure 4. Previously reported breakthrough dynamics in PU-silica composites showed a sharper slowdown in MeOH diffusion with increasing loading of bare silica particles compared to carboxyl or amine functionalized silica particles, aligning with the findings here.[28]

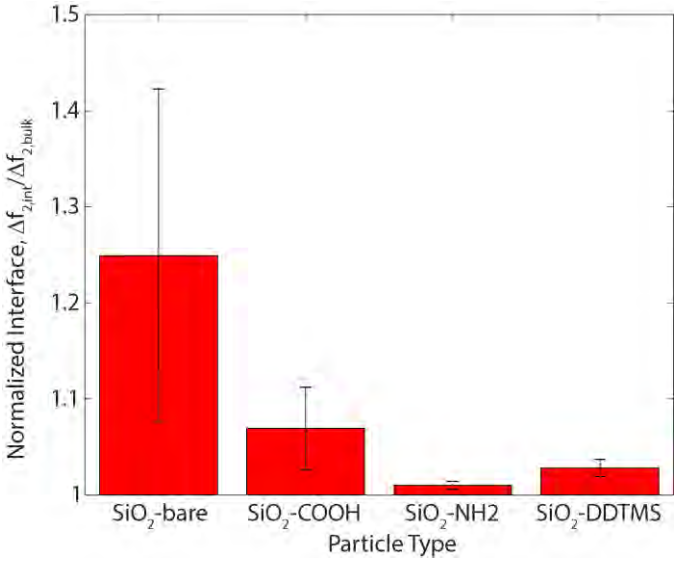

Figure 4. Ratio of interface and bulk frequency shift for different silica surface chemistries.

3.2 Molecular dynamics studies

Computational investigations have been leveraged to provide molecular-scale insight into the fundamental chemistry undergirding polymer-penetrant interactions and the effect of particle-surface modification via the addition of specific functional groups. The modeling seeks to complement concurrent transport experiments and to help provide a more revealing description of the underlying physics at molecular scales. An important component of this computational work has been to understand how to effectively model (represent) the interfacial region of the polymer-particle composite to reveal molecular level phenomena, including property changes induced by surface modification, that affect the diffusive transport of penetrant molecules.

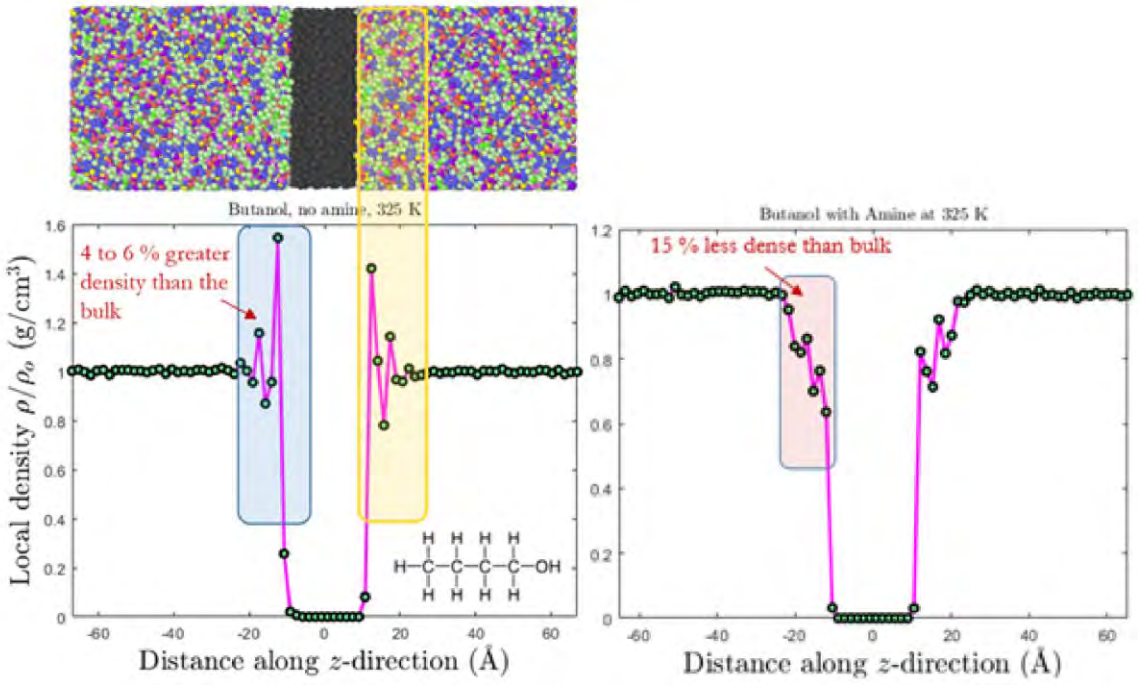

Figure 5. The molecular dynamics system with polymer and butanol on both sides of amorphous silica slab (top). The plots show the average local density of the PU along the horizontal direction using bins of approximately 0.1 nm wide with no silica functionalization (left) and with amine functionalized silica (right).

MD calculations have been performed to characterize the interfacial region between a silica particle and the surrounding PU which is believed to experience local transport properties that differ in a significant way from the bulk (non-interfacial) PU. The presence of a functional group on the silica surface affects the local density of the polymer near the interface as shown in Figure 5. When the silica is unfunctionalized, the interfacial PU density is found to be elevated relative to the bulk. This result is consistent with results found in other polymer composite systems where the formation of densified polymer layers is seen at the surface.[21] This is likely to impact penetrant transport by increasing the resistance (enhanced selectivity) the diffusing penetrant experiences near the silica surface. Densified interfacial regions are observed in the presence of both butanol and butane and across a temperature range of 300 K to 500 K in the simulations. This trend contrasts the density profiles of the amine-functionalized systems, where the polyurethane density is considerably lower, in some cases more than 20 % lower than the bulk as shown in Figure 5.

During the NPT production leg of the simulations, mean-square displacements (MSD) of the penetrant molecules were computed, and provide a direct, quantitative measure of the diffusion dynamics, including the ability to assess the effect of the added functional groups modifying the silica. Figure 6 shows diffusion coefficients for systems with penetrants butanol, butane, and dimethylsilanediol (DMSD) in the presence of bare silica and silica functionalized with carboxyl and amine groups.

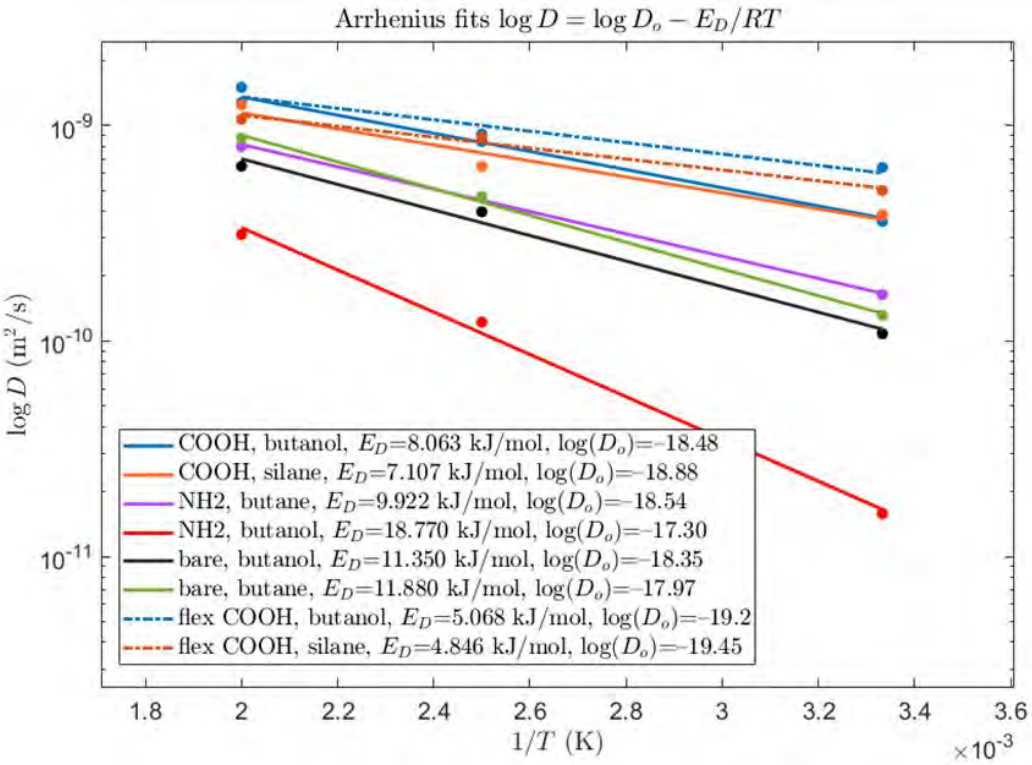

Figure 6. The diffusion coefficients computed from the MSD data for each MD system, and the temperature-dependent Arrhenius behavior.

The simulations thus far suggest that the transport behavior as quantified by diffusion coefficient is dependent upon multiple properties of the system, most importantly the PU density and specific surface modifications of the silica. The density, in particular, is quite difficult to control and to equilibrate given the nature of the constraints imposed on such small, yet intricate systems. Nonetheless, the results thus far have helped to identify the dominant physics and what remaining analyses are necessary to draw further conclusions. The data presented in Figure 6 correspond to a range of average system densities of 1.37 g/cm^3 to 1.49 g/cm^3, which may likely have a significant effect on the overall MSD and hence the diffusion coefficient. The systems functionalized with COOH have an average density of approximately 1.37 g/cm^3 while those with NH_2 and bare silica are denser at 1.49 g/cm^3. So, while it appears upon comparing the NH_2 and bare silica surfaces that the NH_2 has a clear effect on the transport in the system with butanol, it's not certain whether a less dense system would behave the same. The carboxyl group seems to increase the transport relative to the bare systems but, again, the densities differ, obfuscating a definitive conclusion.

Simulations are currently nearing completion that aim to untangle the interplay between the role of the functional groups and the system density. It has already been determined, e.g., that the density of the COOH-systems cannot be increased beyond 1.37 g/cm^3, and it equilibrates to this value even when initially compressed to a greater density. The remaining simulations will present diffusion data for NH_2 and bare silica at a lower density of 1.37 g/cm^3 which will enable final comparisons across systems without the hindrance of density differences. A set of simulations of bulk polymer-penetrant (not composite or interface) are also in the process of completing and can be compared directly with the composite systems. This should provide a clearer understanding of how to interpret the properties of the composite setup and its relationship to the bulk.

While these results show that density differences even ~ 0.1 g/cm^3 can have a first-order effect on the diffusion coefficients of penetrants in the polymer, the ability of surface modification of the silica to have a similar, strong effect depends on several factors. The most important of these is the potential for strong hydrogen bonding between the penetrant and the functional group. Inter-species pair correlations describe the probability of finding elemental constituents within molecules of one species in a certain proximity of the constituents of another species, e.g., the probability of finding an O atom of the penetrant within the H-bond distance of an N-atom in the polymer. A partial radial distribution function (RDF) can be used to provide such a quantitative metric for how, e.g., the penetrant and functional groups interact, and is distinguished from the complete RDF which would also include the intra-species constituent correlations. It was seen that polar molecules like butanol and DMSD readily form hydrogen bonds with the COOH and NH_2 functional groups on the silica. Figure 7 shows the partial RDFs for several of the MD systems. The top left plot shows that there is little interaction between any penetrant and PU chains, while there is a small peak in the RDF for butanol – butanol interactions, indicating a degree of hydrogen bonding among the butanol molecules themselves.

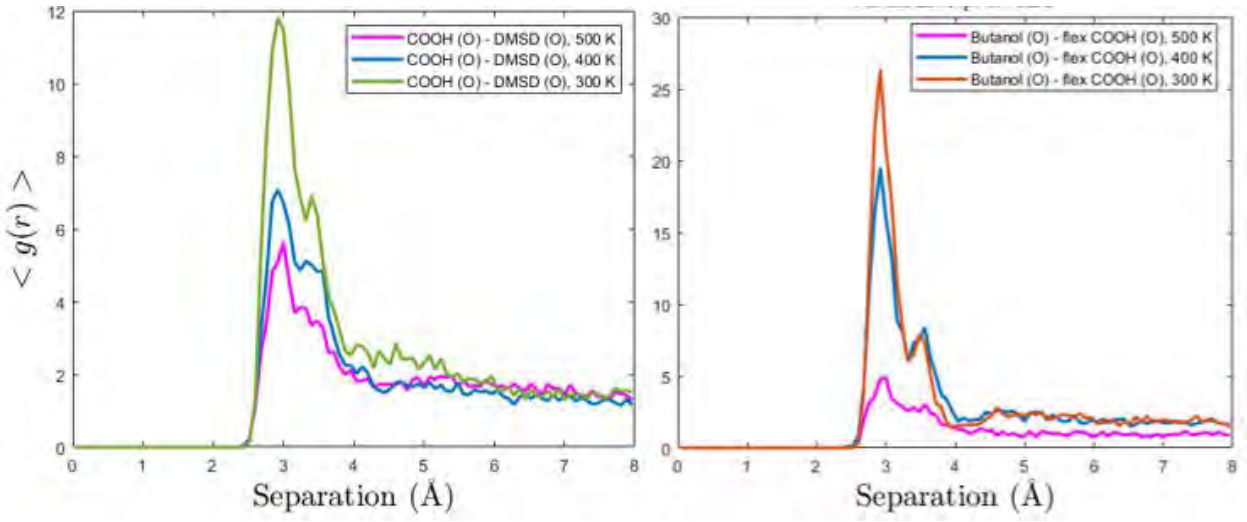

Figure 7. The inter-species, partial radial distribution functions. Little interaction is seen between the polymer and the penetrants, while strong hydrogen bonding occurs between the polar penetrants (butanol and DMSD) and the functional groups COOH and NH2.

The most striking result of the pair-correlation data is the interaction between penetrants butanol and DMSD, both polar molecules, and the N and O atoms in the functional groups. This bonding is strongest at 300 K and attenuates with increasing temperature (Figure 7). The strongest signal of this type of interaction occurs between butanol and amine groups which are not rigidly attached to the silica slab or in one case where some of the groups have unattached themselves from the silica but remain near the interface. The result of this is a very strong degree of hydrogen bonding between the amine groups and the polar penetrant as shown in Figure 7 in the RDF peak at the H-bond distance of approximately 2.8 Å. This leads to accumulated butanol at the amine-rich interface, and drop in the diffusion coefficient by nearly an order of magnitude at room temperature. This phenomenon, that is most pronounced when a fraction of the functional groups is detached from the silica, suggests that additives with similar chemistry may reduce agent transport in composites, and that molecular simulation might be able to reveal the fundamental chemistry underlying this effect.

4. CONCLUSIONS AND NEXT STEPS

Methods for directly imaging cross-sectioned composites using AM-FM AFM and characterizing differences in the polymer properties in the interfacial region compared to the bulk were developed. These techniques showed that PU composites with unfunctionalized silica particles have a stiffer and denser interfacial region compared with those made with functionalized particles, aligning with previously reported chemical breakthrough dynamics in the same composite materials, demonstrating how changing the silica surface chemistry can influence overall chemical transport dynamics. Molecular dynamics simulations modeling the interfacial region of PU-silica composites revealed similar qualitative variations in PU density near the interface compared to the bulk. The MD simulations also enabled the calculation of diffusion coefficients of polar and non-polar penetrant molecules and found that strong hydrogen bonding interactions with the silica surface slowed the diffusion rate significantly.

The experimental and computational tools developed in this work enable the effect of specific changes in particle surface chemistry to be determined and could play a role in the development of future polymer-based protective coatings. It is important to highlight that protective coatings are multifunctional materials that must satisfy many, often competing objectives. Thus, a true coatings development program must holistically examine how changes in formulation influence *all* of the performance characteristics. This program focused solely on the chemical transport dynamics in a model composite system. Future work should not only consider other important performance aspects of model composites (e.g., modulus, strain at failure), but also of real coatings. The tools developed in this work provide a first step in tuning the surface chemistry of solid additives for improving coatings performance with an emphasis on chemical resistance.

ACKNOWLEDGMENTS

The authors would like to thank Dr. Brent Mantooth for his insights on transport in polymer composites. Funding was provided by the U.S. Army via the Surface Science Initiative Program (PE 0601102A Project VR9) at the Combat Capabilities Development Command Chemical Biological Center.

REFERENCES

[1] Bansal, A.; Yang, H.C.; Li, C.Z.; Cho, K.W.; Benicewicz, B.C.; Kumar, S.K.; Schadler, L.S. Quantitative equivalence between polymer nanocomposites and thin polymer films. *Nat. Mater.* **2005**, *4* (9), pp 693–698.

[2] Mapesa, E.U.; Street, D.P.; Heres, M.F.; Kilbey II, S.M.; Sangoro, J. Wetting and Chain Packing across Interfacial Zones Affect Distribution of Relaxations in Polymer and Polymer-Grafted Nanocomposites. *Macromolecules.* **2020**, *53* (13), pp 5315–5325.

[3] Aoyama, S.; Park, Y.T.; Macosko, C.W.; Ougizawa, T.; Haugstad, G. AFM Probing of Polymer/Nanofiller Interfacial Adhesion and Its Correlation with Bulk Mechanical Properties in a Poly(ethylene terephthalate) Nanocomposite. *Langmuir.* **2014,** *30* (43), pp 12950–12959.

[4] Maillard, D.; Kumar, S.K.; Fragneaud, B.; Kysar, J.W.; Rungta, A.; Benicewicz, B.C.; Deng, H.; Brinson, L.C.; Douglas, J.F. Mechanical Properties of Thin Glassy Polymer Films Filled with Spherical Polymer-Grafted Nanoparticles. *Nano Lett.* **2012**, *12* (8), pp 3909–3914.

[5] Senses, E.; Akcora, P. An Interface-Driven Stiffening Mechanism in Polymer Nanocomposites. *Macromolecules.* **2013**, *46* (5), pp 1868–1874.
Su, N.C.; Smith, Z.P.; Freeman, B.D.; Urban, J.J. Size-Dependent Permeability Deviations from Maxwell's Model in Hybrid Cross-Linked Poly(ethylene glycol)/Silica Nanoparticle Membranes. *Chem. Mater.* **2015**, *27* (7), pp 2421–2429.

[6] Bachman, J.E.; Smith, Z.P.; Li, T.; Xu, T.; Long, J.R. Enhanced ethylene separation and plasticization resistance in polymer membranes incorporating metal-organic framework nanocrystals. *Nat. Mater.* **2016**, *15* (8), pp 845–849.

[7] Galizia, M.; Chi, W.S.; Smith, Z.P.; Merkel, T.C.; Baker, R.W.; Freeman, B.D. *50th Anniversary Perspective*: Polymers and Mixed Matrix Membranes for Gas and Vapor Separation: A Review and Prospective Opportunities. *Macromolecules,* **2017**, *50* (20), pp 7809–7843.

[8] Lin, R.J.; Hernandez, B.V.; Ge, L.; Zhu, Z.H. Metal organic framework based mixed matrix membranes: an overview on filler/polymer interfaces. *J. Mater. Chem. A.* **2018**, *6* (2), pp 293–312.

[9] Lin, E.K.; Kolb, R.; Satija, S.K.; Wu, W.-L. Reduced polymer mobility near the polymer solid interface as measured by neutron reflectivity. *Macromolecules.* **1999**, *32* (11), pp 3753–3757.
[10] Kim, S.; Dura, J.A.; Page, K.A.; Rowe, B.W.; Yager, K.G.; Lee, H.-J.; Soles, C.L. Surface-Induced Nanostructure and Water Transport of Thin Proton-Conducting Polymer Films. *Macromolecules.* **2013**, *46* (14), pp 5630–5637.
[11] Sharma, S.K.; Sudarshan, K.; Sahu, M.; Pujari, P.K. Investigation of free volume characteristics of the interfacial layer in poly(methyl methacrylate)-alumina nanocomposite and its role in thermal behaviour. *RSC Adv.* **2016**, *6* (72), pp 67997–68004.
[12] Zhang, M.; Askar, S.; Torkelson, J.M.; Brinson, L.C. Stiffness Gradients in Glassy Polymer Model Nanocomposites: Comparisons of Quantitative Characterization by Fluorescence Spectroscopy and Atomic Force Microscopy. *Macromolecules.* **2017**, *50* (14), pp 5447–5458.
[13] Qu, M.; Deng, F.; Kalkhoran, S.M.; Gouldstone, A.; Robisson, A.; Van Vliet, K.J. Nanoscale visualization and multiscale mechanical implications of bound rubber interphases in rubber-carbon black nanocomposites. *Soft Matter.* **2011**, *7* (3), pp 1066–1077.
[14] Cheng, S.W.; Bocharova, V.; Belianinov, A.; Xiong, S.M.; Kisliuk, A.; Somnath, S.; Holt, A.P.; Ovchinnikova, O.S.; Jesse, S.; Martin, H.; Etampawala, T.; Dadmun, M.; Sokolov, A.P. Unraveling the Mechanism of Nanoscale Mechanical Reinforcement in Glassy Polymer Nanocomposites. *Nano Lett.* **2016**, *16* (6), pp 3630–3637.
[15] Kappl, M.; Butt, H.-J. The Colloidal Probe Technique and its Application to Adhesion Force Measurements. *Part. Part. Syst. Charact.* **2002**, *19* (3), pp 129–143.
[16] Leite, F.L.; Bueno, C.C.; Da Roz, A.L.; Ziemath, E.C.; Oliveira, O.N. Theoretical Models for Surface Forces and Adhesion and Their Measurement Using Atomic Force Microscopy. *Int. J. Mol. Sci.* **2012,** *13* (10), pp 12773-12856.
[17] Leite, F.L.; Herrmann, P.S.P. Application of atomic force spectroscopy (AFS) to studies of adhesion phenomena: a review. *J. Adhes. Sci. Technol.* **2005**, *19* (3-5), pp 365–405.
[18] Pham, J.T.; Schellenberger, F.; Kappl, M.; Butt, H.-J. From elasticity to capillarity in soft materials indentation. *Phys. Rev. Mater.* **2017**, *1* (1), p 8.
[19] Fuellbrandt, M.; Kesal, D.; von Klitzing, R. Multiscaling Approach for Non-Destructive Adhesion Studies of Metal/Polymer Composites. *ACS Appl. Mater. Interfaces.* **2015**, *7* (30), pp 16247–16256.
[20] Dutta, R.C.; Bhatia, S.K. Structure and Gas Transport at the Polymer-Zeolite Interface: Insights from Molecular Dynamics Simulations. *ACS Appl. Mater. Interfaces.* **2018**, *10* (6), pp 5992–6005.
[21] Cheng, S.W.; Mirigian, S.; Carrillo, J.-M.Y.; Bocharova, V.; Sumpter, B.G.; Schweizer, K.S.; Sokolov, A.P. Revealing spatially heterogeneous relaxation in a model nanocomposite. *J. Chem. Phys.* **2015**, *143* (19), p 16.
[22] Boyne, D.A.; Varady, M.J.; Lambeth, R.H.; Eikenberg, J.H.; Bringuier, S.A.; Pearl, T.P.; Mantooth, B.A. Solvent-Assisted Desorption of 2,5-Lutidine from Polyurethane Films. *J. Phys. Chem. B.* **2018**, *122* (7), pp 2155–2164.
[23] Kocun, M.; Labuda, A.; Meinhold, W.; Revenko, I.; Proksch, R. Fast, High Resolution, and Wide Modulus Range Nanomechanical Mapping with Bimodal Tapping Mode. *ACS Nano.* **2017**, *11* (10), pp 10097–10105.
[24] Labuda, A.; Kocun, M.; Meinhold, W.; Walters, D.; Proksch, R. Generalized Hertz model for bimodal nanomechanical mapping. *Beilstein J. Nanotechnol.* **2016**, *7*, pp 970–982.
[25] Proksch, R.; Kocun, M.; Hurley, D.; Viani, M.; Labuda, A.; Meinhold, W.; Bemis, J. Practical loss tangent imaging with amplitude-modulated atomic force microscopy. *J. Appl. Phys.* **2016**, *119* (13), p 11.
[26] Proksch, R.; Yablon, D.G. Loss tangent imaging: Theory and simulations of repulsive-mode tapping atomic force microscopy. *Appl. Phys. Lett.* **2012**, *100* (7), p 3.
[27] Varady, M.J.; Hulet, M.S.; Hinkle, A.R.; Pearl, T.P.; Sweat, M.L.; Strawhecker, K.E.; Savage, A.S.; Ligda, J.P.; Elabd, Y.A. *Cooperative interactions between functionalized particles and binders in polymer composites and their effect on chemical transport*; DEVCOM Chemical Biological Center: Aberdeen Proving Ground, MD, **2020**; pp 71–80.

This page intentionally left blank

Characterization of opioid conformational changes and their effect on binding and reactivity on surfaces

Monica L. McEntee*, Mark D. Winemiller, Andrew J. Walz,
Amanda M. Schenning, Michelle L. Sheahy, Ivan O. Iordanov
U.S. Army Combat Capabilities Development Chemical Biological Center, Research & Technology Directorate, 8198 Blackhawk Rd,
Aberdeen Proving Ground, MD 21010

ABSTRACT

Opioids contain multiple groups, including aliphatic chains, ketone groups, and cyclic rings, that can influence how the molecules bind to and react with surfaces through hydrogen bonding or hydrolysis, all of which is partially dependent on the solvent present. This report, however, focuses on the conformational structure of the opioid molecule. To determine the effects a solvent has on an opioid's conformation, we performed density functional theory calculations of carfentanil on silica, in either methanol or water, with different combinations of solvents and surfaces and performed opioid uptake studies in various solutions. Hydrolysis studies of remifentanil and its derivatives were performed and monitored by nuclear magnetic resonance spectroscopy to relate opioid hydrolysis rates to conformer structure. A comparison of density functional theory binding energies revealed that carfentanil-solvent and carfentanil-silica interactions could not fully explain experimental results, rather lowering of the solvent self-interaction energy of water during solvation drives the binding of carfentanil to the silica surface. Remifentanil uptake studies on silica in pure solvent showed that increasing solvent polarity decreases uptake of remifentanil by the silica surface. In buffered aqueous solutions, as pH is increased, remifentanil is hydrolyzed to its corresponding salt; however, at pH 7, the salt is not detected in solution and is presumably taken up by the silica surface. In buffered/non-buffered deionized water/solvent mixtures, there is a convolution of solvent and pH effects. Lastly, nuclear magnetic resonance spectroscopy hydrolysis experiments of remifentanil derivatives revealed that molecular conformation greatly affects the hydrolysis rate of the terminal methyl ester and that removal of the ring nitrogen prevents hydrolysis while removal of groups at position four of the ring greatly increases the hydrolysis of remifentanil derivatives.

Keywords: remifentanil, carfentanil, conformational changes, surface binding, opioid, nuclear magnetic resonance, liquid chromatography-mass spectrometry

1. INTRODUCTION

The synthetic opioid fentanyl and its derivatives were originally developed for their potential benefit to act as quick-acting painkillers. For example, the opioids fentanyl and carfentanil are orders of magnitude more potent than morphine, and remifentanil and sufentanil have short onset times and high lipid solubility, factors that increase their potency. Fentanyl and its derivative compounds have contributed substantially to drug overdoses, and the potential for dermal absorption can pose a significant risk to first responders and military personnel. This study focuses on carfentanil and remifentanil and is a continuation of the carfentanil research documented in an earlier technical report[1]. Remifentanil is a very potent opioid that is soluble in both water and methanol but hydrolyzes quickly in water compared to other opioids such as carfentanil. The goal of this work is to determine what affects the opioid conformational structure and the carrier solvents have on properties such as hydrolysis rate and surface binding of these opioids.

2. METHODS AND PROCEDURES

2.1 Synthesis and characterization of remifentanil and derivatives

The synthesis procedures for remifentanil, carfentanil salt, and carfentanil freebase were performed from a derivation from the literature and are described in more detail elsewhere. Conformational changes in different solvents and pH

ranges were measured using nuclear magnetic resonance spectroscopy (NMR). All ^{1}H NMR spectra were recorded on a Bruker Advance III HD 500 MHz instrument and referenced to the residual solvent peaks. A macro was used so that gradient shimming would be performed before the collection of each ^{1}H spectrum after a specified time interval. At the conclusion of a run, another macro was used to process and integrate all the ^{1}H NMR spectra against the internal standard allowing for a greater number of points to be collected and eliminating bias during analysis. The following pH solutions were used: a pH 2 solution of HCl was prepared using an Accumet Research AR25 Dual Channel pH/Ion Meter that had been calibrated with Thermo standard solutions at a pH 4, 7, and 10; all other buffers were prepared to 0.3 M and measured with the pH meter— a pH 4 was prepared using acetic acid/sodium acetate, a pH 6 was prepared using acetic acid/ammonium acetate, and a pH 7.5 was prepared using sodium dihydrogen phosphate/disodium hydrogen phosphate.

2.2 Uptake studies of remifentanil on mesoporous silica

Single point equilibrium sorption experiments were constructed to evaluate sorption of remifentanil on the porous SiO_2 substrate, mesoporous silica (MCM-41). MCM-41 was suspended in various solutions containing dissolved remifentanil oxalate, at a targeted initial concentration of 2 µg/mL remifentanil (excluding oxalate salt). The suspensions were allowed to equilibrate with stirring overnight (18 to 24 hours) at ambient temperature. Control samples with no solid substrate were also carried through the equilibration conditions to account for any opioid sorption to the glass vial or degradation through hydrolysis during the study. Following the equilibration period, the solutions were analyzed by liquid chromatography-mass spectrometry (LC-MS) for both remifentanil and the hydrolysis product, remifentanil acid (CAS No. 132875-68-4), illustrated in Figure 1.

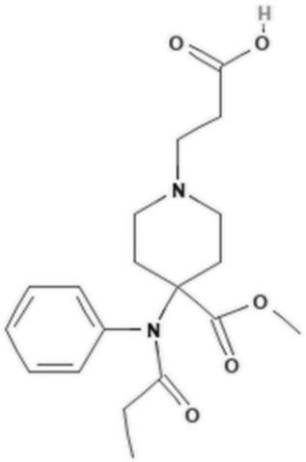

Figure 1. Remifentanil acid, CAS No. 132875-68-4.

MCM-41 was obtained through Sigma-Aldrich® (St. Louis, MO) and the remifentanil oxalate salt was synthesized in house by the Agent Chemistry Branch using the synthesis procedure developed by Waals et al. The remifentanil acid reference standard used during the sample analysis was obtained through Cerilliant, Inc. (Round Rock, Texas).

Remifentanil oxalate solutions were prepared in five organic solvents (methanol, ethanol, isopropanol, chloroform, and hexane), in aqueous solutions buffered at four pH conditions (1.68, 4, 7, and 10) and in several 50/50 mixed aqueous-methanol solutions. A deionized water (DIW) control condition was carried through the experiment as well. Sorption equilibration samples were prepared by adding 10 ± 0.5 mg of MCM-41 to a one mL aliquot of each remifentanil solution and stirred at ambient temperature for 18–24 hours. The control samples were carried through the entire experiment except for the addition of the solid substrate. All samples were centrifuged to separate the MCM-41 substrate from the supernatant. The supernatant was sampled, diluted in methanol to a concentration within the LC-MS analytical calibration range and analyzed.

Remifentanil was quantified using an Applied Biosystems API5500 QTrap Triple-Quadrupole MS, equipped with the TurboV Ion Source. Sample introduction and chromatography were performed with an Agilent 1290 Infinity series UHPLC, which included the Agilent Infinity Binary Pump, Degasser, Thermal Column Compartment, High Performance Automatic Liquid Sampler, and the Automatic Liquid Sampler Thermostat. Sample effluent was directed from the UHPLC directly to the TurboV ion source of the API5500MS. The instrument operation and data analysis were performed with the Applied Biosystems Analyst software package (v. 1.5.1.) [Carlsbad, CA]. Detailed analytical instrument parameters are listed in Table 1.

Table 1. Analytical Instrument Parameters

UHPLC Parameters			
Mobile Phase A: 0.1 % Formic Acid in Deionized Water			
Mobile Phase B: 0.1 % Formic Acid in Acetonitrile			
Gradient			
Time (minutes):	A %		B %
0	70		30
0.5	70		30
1.25	20		80
1.5	20		80
1.6	70		30
2.25	70		30
Flow Rate: 0.5 mL/min			
Analytical Column: Waters Acquity HSS T3, 1.8 µm, 2.1 x 50 mm			
Typical Column Pressure: 330 bar			
Analytical Column Temperature: 40 ºC			
Injection Volume: 1 µL			
Auto-sampler Temperature: 5 ºC			
Post-injection Needle Wash: 10 seconds of Mobile Phase B			
Mass Spectrometer (MS) Parameters			
Scan Type: Multiple Reaction Monitoring (MRM)			
Polarity: Positive Mode			
Curtain Gas: 30			
CAD Gas: Medium			
Source Temperature: 500 °C			
GS1: 45			
GS2: 55			
Declustering Potential: 100			
Exit Potential: 10			
Collision Energy: 25 (for all analytes)			
MRM for Carfentanil:	395.2	>	335.2
MRM for Remifentanil:	377.2	>	228.1
MRM for Remifentanil Acid:	363	>	259

2.3 Density Functional Theory calculations

All plane wave Density Functional Theory (DFT) calculations were performed using the Quantum opEn-Soure Package for Research in Electronic Structure, Simulation, and Optimization (Espresso) software package. Core electrons were approximated using SSSP pseudopotentials and the exchange correlation was approximated using the Perdew–Burke-Ernzerhof functional. Van der Waals interactions were included through Grimme's D2 approximation. All presented structures were geometrically optimized with convergence thresholds of $10^{-5}/10^{-4}$ Ry for the energies/forces. For initial calculations involving "solvent-free" binding, a vacuum-slab model of a hydrogenated silica surface was established within a 19.65 x 19.65 x 40.29Å cell, corresponding to a double layer of silica with a 30Å vacuum region. Further calculations involving solvation were conducted using in-house code that implements the Monte-Carlo process to insert solvent molecules to create randomized solvation structures and to create the initial state for the ab initio calculation.

3. RESULTS AND DISCUSSION

3.1 Hydrolysis of remifentanil and its derivatives

The hydrolysis of the terminal methyl ester in remifentanil and several of its derivatives was investigated to ascertain, to what extent, the role solution phase conformation plays in the hydrolysis of remifentanil. Figure 2 shows the structure of the three remifentanil derivatives (molecules 1–3) and remifentanil (molecule 4). All hydrolysis reactions were conducted in 0.3 M buffered aqueous solutions that were held at a pH 10. Figure 3 shows the hydrolysis of 0.015 M remifentanil in a pH 10 solution. The half-life of this reaction was determined to be 3.2 hours.

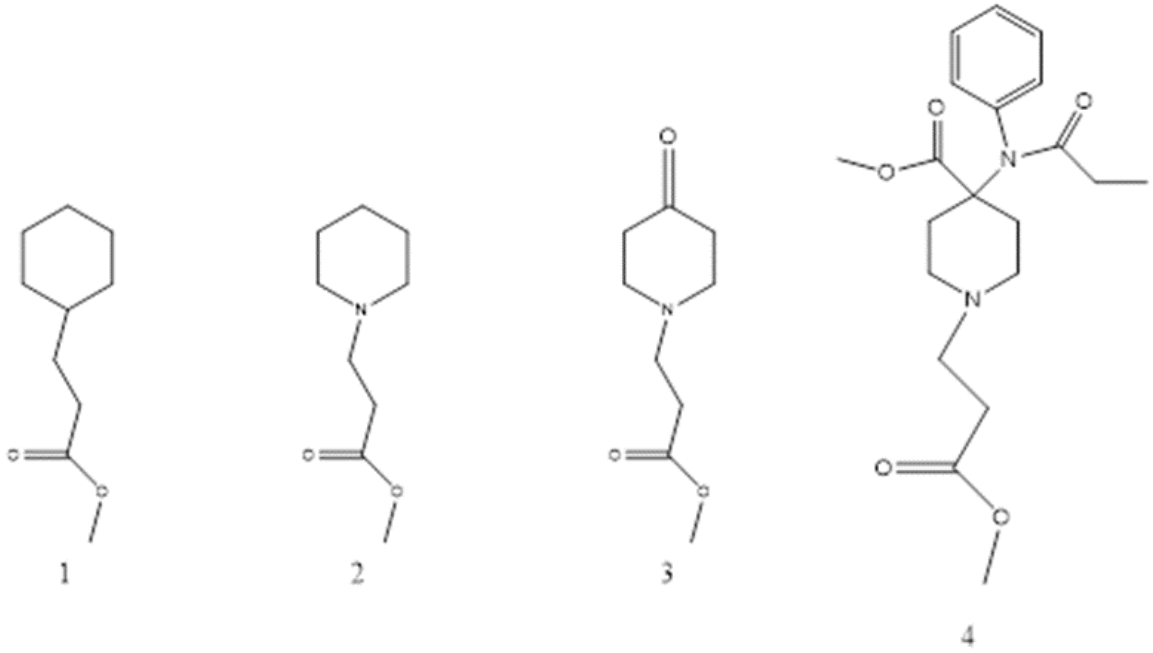

Figure 2. (1) Compounds methyl 3-cyclohexylpropanoate, (2) methyl 3-(piperidin-1-yl)propanoate, (3) methyl 3- (4-oxopiperidin-1-yl)propanoate, (4) and remifentanil.

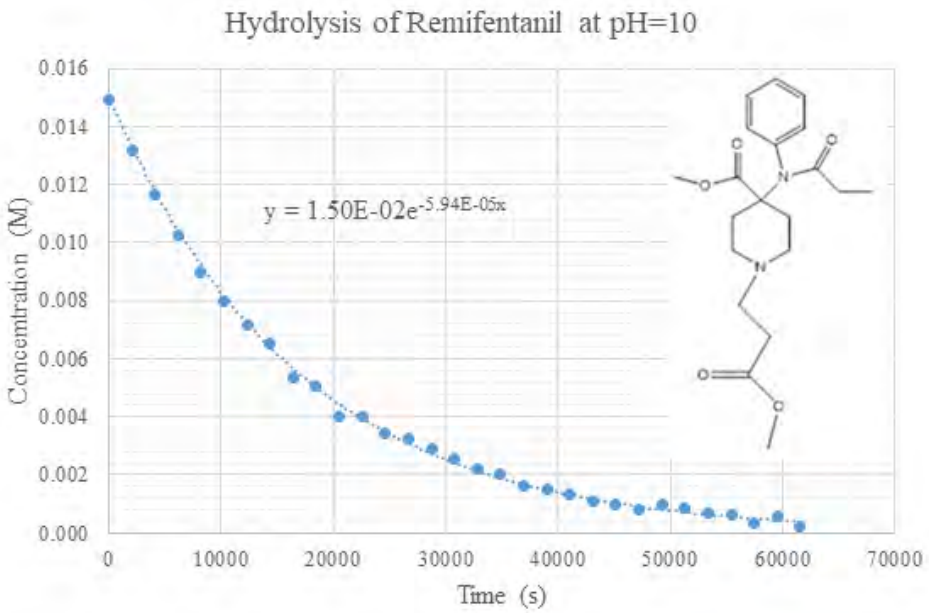

Figure 3. Hydrolysis of 0.015 M remifentanil at pH 10. The half-life was determined to be 3.2 hours.

The hydrolysis of methyl 3-(4-oxopiperidin-1-yl)propanoate (molecule 3, Figure 2) was chosen as the starting point of this study as it is the product from the first step of the synthetic sequence used to synthesize remifentanil. The hydrolysis of molecule 3 in solution at pH 10 is shown in Figure 4, and the half-life of this reaction was determined to be 2.8 hours.

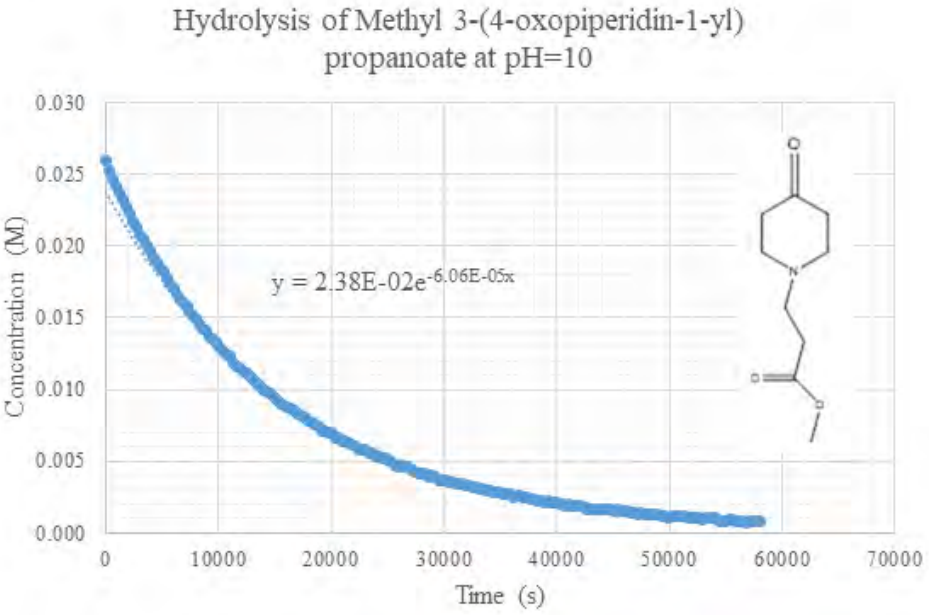

Figure 4. Hydrolysis of 0.026 M methyl 3-(4-oxopiperidin-1-yl) propanoate (molecule 3) at pH 10. The half-life was determined to be 2.8 hours.

The ketone group of molecule 3 is long established in the six-member ring conformational analysis as highly influential and so, was removed to form methyl 3-(piperidin-1-yl) propanoate (molecule 2, Figure 2). The hydrolysis of molecule 2 at pH 10 is shown in Figure 5, and its half-life was determined to be 11.7 minutes. The removal of the ketone from molecule 3 led to a roughly order of magnitude increase in the rate of hydrolysis of the methyl ester from a half-life of 168 minutes to 11.7 minutes. As a control, methyl 3-cyclohexylpropanoate (molecule 1, Figure 2), was observed at a pH 10 and no hydrolysis of the methyl ester was detected, which confirmed the importance of the ring

nitrogen, and hence the role of conformation in these molecules. Because no conjugation to the methyl ester exists in any of molecules 1–4, the rate at which neighboring group participation can occur will be the rate of hydrolysis observed by the methyl ester and is therefore, a direct result of the conformation of the molecule.

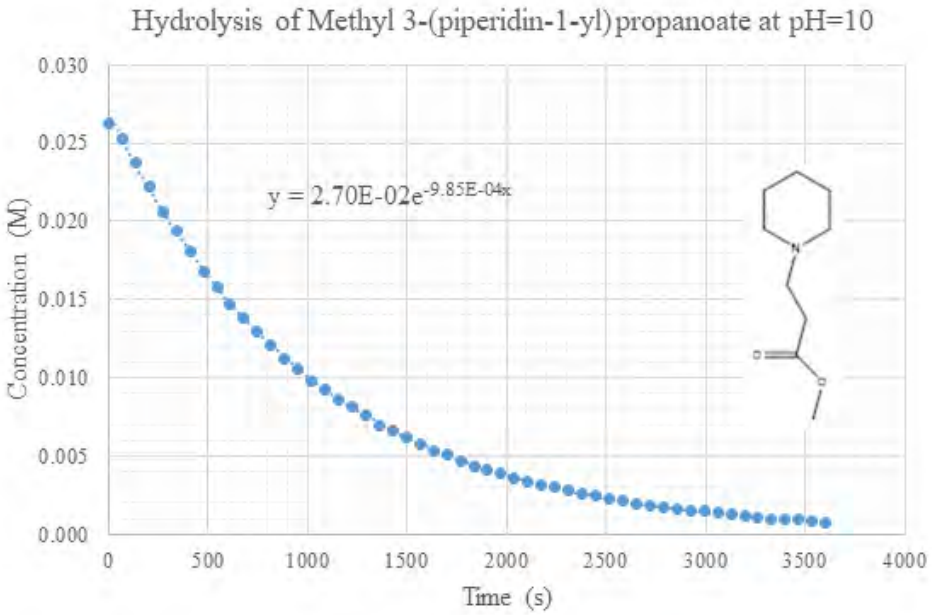

Figure 5. Hydrolysis of 0.026 M methyl 3-(piperidin-1-yl)propanoate (molecule 2) at pH 10. The half-life was determined to be 11.7 minutes.

After varying the reactive groups on remifentanil, a second series of molecules was synthesized, based on molecule 2, in which the chain length to the methyl ester was lengthened. The assumption was that the rate of hydrolysis of these molecules would decrease as the degrees of freedom increased. It was observed that as the chain length increased, the rate of hydrolysis did in fact decrease. Figure 6 shows the hydrolysis of methyl 5-(piperidin-1-yl) pentanoate. The data shown in Figure 6 reveals that when the chain length was increased by two carbons, with respect to molecules 1–4, the half-life increased from 12 minutes to almost 5.5 hours compared to molecule 2.

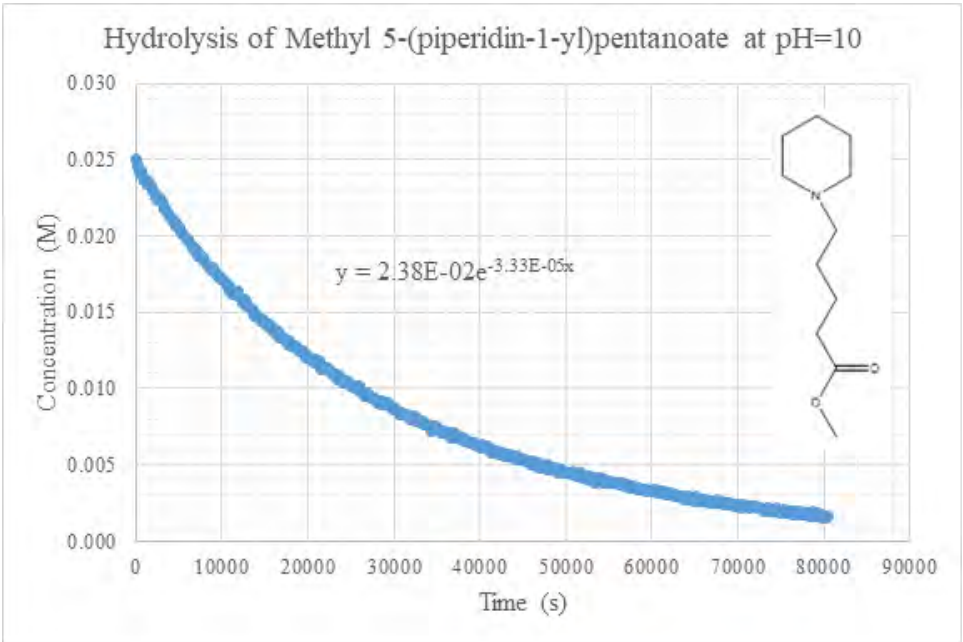

Figure 6. Hydrolysis of 0.025M methyl 5-(piperidin-1-yl)pentanoate at pH 10. The half-life of this reactions was determined to be 5.4 hours.

Lastly, a series of derivatives were synthesized, in which the alkyl groups were added to the alkyl ring with the goal of trying to observe if adding the groups could induce enough of a conformational change to see as large of a change in the hydrolysis rate as the four position ketone located on molecule 3 was able to induce. The structures of these derivatives are shown below in Figure 7. However, although these derivatives were synthesized, the hydrolysis of the derivatives has not been examined, except for molecule 9. The results for the hydrolysis of molecule 9 are shown in Figure 8.

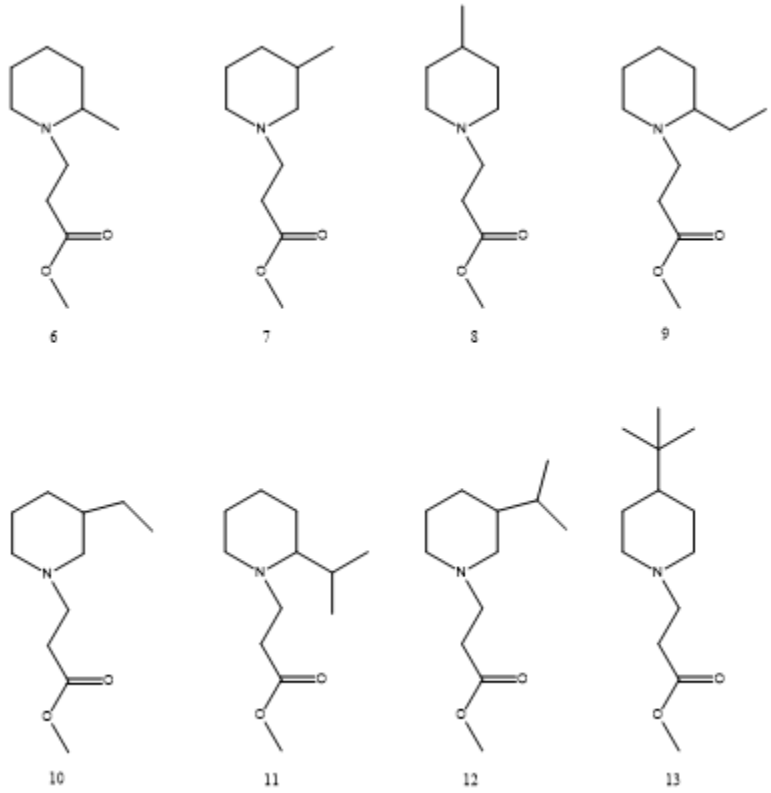

Figure 7. Alkyl substituted remifentanil derivatives synthesized to study the effects of alkyl substituents and ring position on the hydrolysis of the methyl ester in molecule 2.

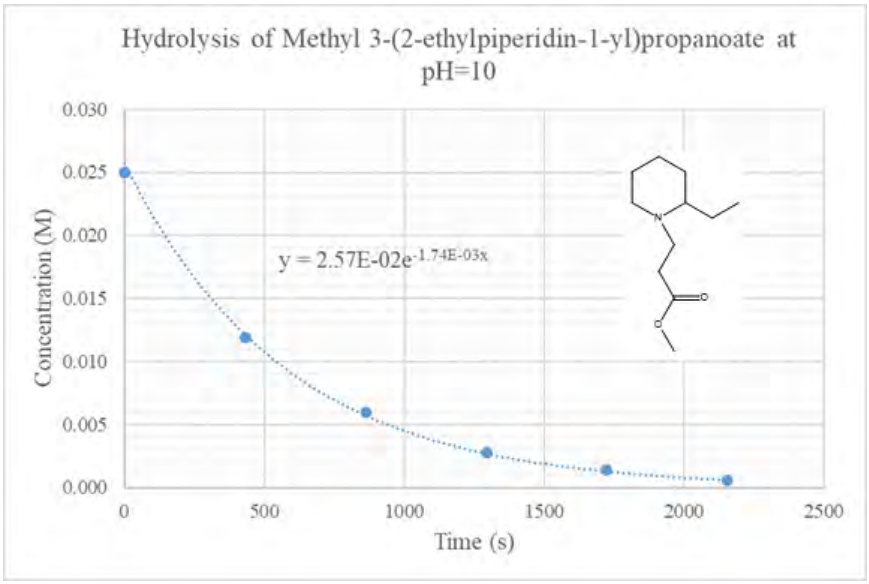

Figure 8. Hydrolysis of 0.025 M methyl 3-(2-ethylpiperidin-1-yl)propanoate (molecule 9) at pH 10. Half-life of 6.9 minutes.

The results shown in Figure 8 were for only one experiment; however, if these results are validated, the hydrolysis rate would be doubled simply by adding an ethyl group at the 2-position of the alkyl ring and would justify synthesizing molecules with a ketone in the two and three positions of the alkyl ring. Table 2 summarizes the results of the hydrolysis experiments for molecules 1–4 as well as methyl 3-(2-ethylpiperidin-1-yl)propanoate (molecule 9). The results of the hydrolysis study provided excellent results that serve as the basis for future experiments. An in-depth conformational analysis that utilizes both NMR and infrared techniques could help elucidate the mechanisms that cause such large differences in hydrolysis rates.

Table 2. Summary of remifentanil derivative hydrolysis reaction half-lives.

Derivative	Structure	Hydrolysis Half-life
Remifentanil	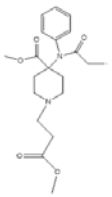	3.2 Hours
Methyl 3-(4-oxopiperidin-1-yl)propanoate	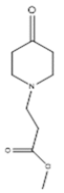	2.8 Hours
Methyl 3-(piperidin-1-yl)propanoate		11.7 Minutes
Methyl 3-cyclohexylpropanoate		N/A
Methyl 5-(piperidin-1-yl)pentanoate		5.4 Hours
Methyl 3-(2-ethylpiperidin-1-yl)propanoate	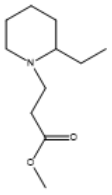	6.9 Minutes

3.2 Remifentanil uptake on MCM-41 mesoporous silica

Equilibrium sorption studies were conducted to evaluate the potential for uptake of remifentanil from various solutions onto MCM-41. The data collected from the sorption experiments was compared to results from control conditions in which there was no silica present in the solution. The difference in remifentanil concentration between the control sample and the corresponding sorption sample was used to evaluate remifentanil uptake. Both remifentanil and the hydrolysis product were measured for each experiment to distinguish between the loss of remifentanil through uptake on the silica, and the loss due to hydrolysis in the solution. If remifentanil were chemically stable in all the solvents used, a simple measurement of the difference between initial and final concentration in the supernatant would provide a basis for uptake measurement. However, since hydrolysis is known to occur in aqueous solvents, the difference in final concentrations of remifentanil in each sample, with respect to its associated control, was used to evaluate uptake.

Initially, uptake experiments on silica (MCM-41) were conducted in non-aqueous solvents to exclude effects from water. Figure 9 shows the remifentanil and hydrolysis product equilibrium concentrations in the sorption and control samples that were dissolved in pure organic solvents. From the control experiments, remifentanil is soluble in all of the solvents, except hexane, and that hydrolysis did not occur in any of these solvents during the equilibration period used. The remifentanil concentration in the supernatant from the MCM-41 samples, when compared to the corresponding control samples, demonstrates that remifentanil uptake on MCM-41 decreases with increasing solvent polarity (chloroform >> isopropyl alcohol > ethanol > methanol). The loss of remifentanil in the MCM-41 samples is attributed to uptake since as expected, the remifentanil hydrolysis product was not detected in any of these samples.

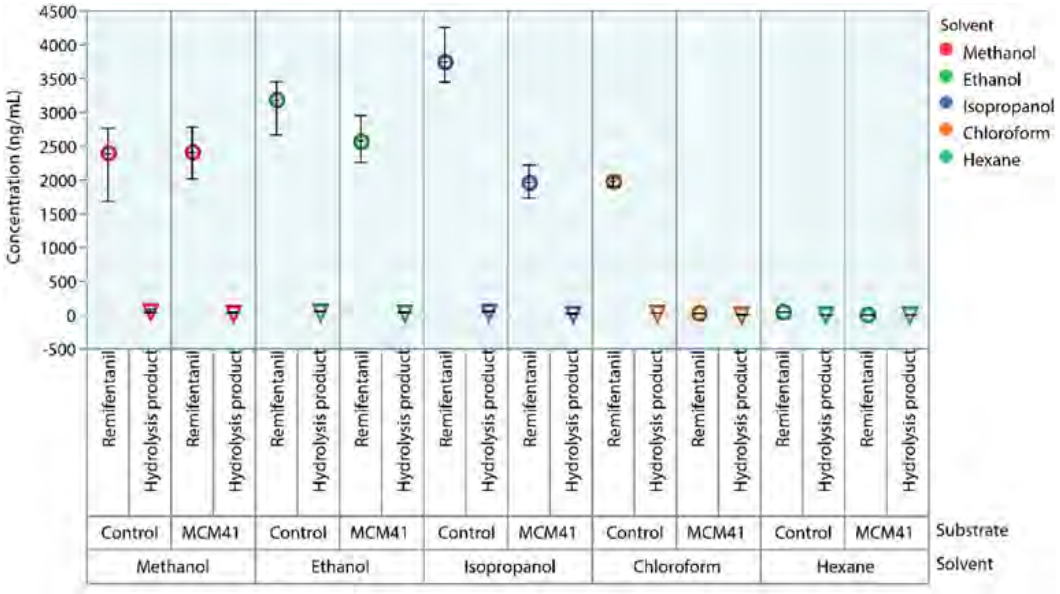

Figure 9. Concentration of remifentanil and the associated hydrolysis product in pure solvents post-uptake experiment. Open circles correspond to remifentanil and open triangles correspond to the hydrolysis product.

Uptake experiments were then conducted in both buffered and non-buffered DIW solutions to investigate the effect of pH on remifentanil uptake on the silica surface. Figure 10 shows the remifentanil and hydrolysis product concentrations for buffered and non-buffered DIW solutions post uptake. From the control experiments, as the pH increases, the remifentanil concentration decreases and the corresponding hydrolysis product increases; this is a direct result of hydrolysis at higher pH values. The uptakes for remifentanil at pH 7, pH 10, and in non-buffered DIW are irrelevant since there is a near complete conversion of remifentanil to the hydrolysis product in both the samples and controls. At pH 1.68 and pH 4, the marked difference in remifentanil concentration between the control and uptake samples as well as the absence of the hydrolysis product suggests uptake of remifentanil by MCM-41.

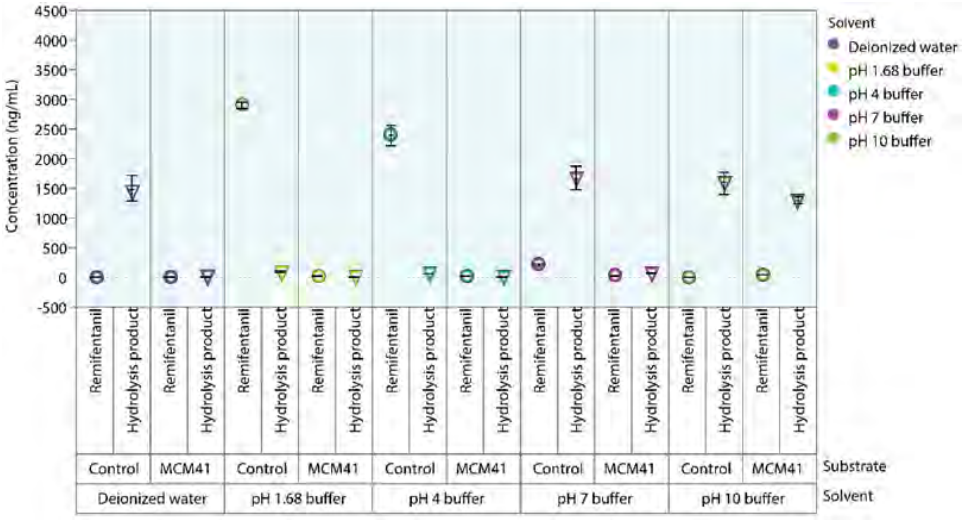

Figure 10. Concentration of remifentanil and the corresponding hydrolysis product in buffered and non-buffered DIW solutions, post-uptake experiment. Open circles correspond to remifentanil and open triangles correspond to the hydrolysis product.

Lastly, uptake experiments were conducted in both buffered and non-buffered mixed DIW/solvent solutions to investigate the effects of a co-solvent on the hydrolysis and/or uptake of remifentanil on the silica surface. Figure 11 shows the remifentanil and hydrolysis product concentrations for DIW/solvent mixtures post-uptake experiments.

There is much information that can be gleaned from this data. In the buffered methanol solvents, there is a slight difference in concentration between the silica and control samples, indicating there may be a small amount of remifentanil uptake by the silica. However, as the solvent pH increases, the concentration of remifentanil in both the controls and the samples decreases. This decrease is accompanied by formation of the hydrolysis product, particularly at or above the solution pH of 7. In the buffered methanol solutions, remifentanil uptake (as measured by comparison to the remifentanil concentration in the control) is consistent across the pH range, except for pH 10 where it appears that silica may be slightly inhibiting hydrolysis. Salt uptake is essentially the same when hydrolysis occurs above pH 4.

In the non-buffered DIW/solvent solutions, significant remifentanil uptake is only observed in the mixed solution of DIW and methanol, with only minor uptake observed in the water-ethanol and water-isopropanol mixtures. The concentration of the hydrolysis product generated is similar across the three solvent mixtures. Lastly, the uptakes in the DIW/methanol mixture would be expected to be similar to the uptake in the pH 7 buffered/methanol solution however, there is a marked difference between the uptakes in each solution. This phenomenon suggests that the buffer cannot be assumed to be a spectator in these experiments. Additional replicates of these conditions would be suggested to further decipher the trends in these data points.

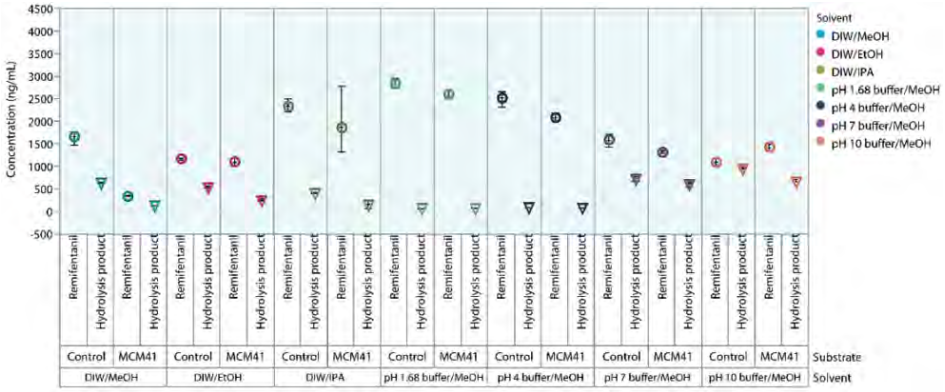

Figure 11. Concentration of remifentanil and the corresponding hydrolysis product in buffered and non-buffered DIW/solvent mixtures post-uptake experiment. Open circles correspond to remifentanil and triangles correspond to the hydrolysis product. Note that in the graph, methanol, ethanol and isopropanol were abbreviated to MeOH, EtOH, and IPA, respectively.

3.3 DFT calculations of carfentanil on silica and in solution

Given the relatively large molecular size of fentanyl compounds, their surface interactions can be significantly shifted due to solvation effects. Additionally, the overall weak interactions of fentanyl compounds implies that a decrease in the self-interaction energy of a solvent may not be negligible when calculating the degree of surface binding versus solvation of fentanyl compounds in the presence of both surface and solvent. The main goal of the simulations was to explain the apparently better solvation of carfentanil in methanol compared to water in the presence of porous silica. The initial simulations were focused on the interaction between the silica surface and carfentanil in the absence of any solvent. A vacuum-slab model of a hydrogenated silica surface was developed that occupied a 19.65 Å x 19.65 Å x 40.29 Å cell; this cell corresponds to a double layer of silica with a 30 Å vacuum region. Calculations of the binding of carfentanil to the silica surface showed a low binding energy in the range of ~1.2–1.3 eV, depending on the orientation of the carfentanil molecule. The relative insensitivity of the binding energy to the binding orientation and low total energy suggests that binding occurs primarily through physisorption due to weak Van der Waals interactions. Additionally, there is limited to no-existent dipole-dipole interactions, despite the presence of some polar groups on both carfentanil and the hydrogenated silica surface. Similar surface binding calculations were also performed for remifentanil, which also showed a low binding energy ~1.0–1.1eV, consistent with physisorption. To study the effect of the solvent, solvation was calculated explicitly by implementing a custom, in-house code that populates the empty regions within the simulation cell with solvent molecules in a randomized manner**,** which in turn, creates the initial state for the ab-initio calculation. Previous experimental work suggested that carfentanil binds preferentially to the silica surface in aqueous solution but remains solvated when in methanol. And so, the purpose of these DFT calculations is to attempt to determine the cause and rationalize this solvation behavior. Binding energies of carfentanil to the surface and to solvent were initially calculated separately to determine which interaction is stronger and whether these values can explain what is seen experimentally. Table 3 shows the values obtained from the DFT calculations. The data indicates that the water-carfentanil binding is a significantly stronger interaction than methanol-carfentanil binding; this is the reverse of what is seen experimentally. Therefore, there must be another effect that was not accounted for.

Table 3. Calculated DFT binding energies for carfentanil with either a solvent or the silica surface as well as for a solvent-surface system.

Solvent	Solvent Binding (eV)	Surface Binding (eV)	Co-Binding (eV)
Water	-2.28	-1.15	-3.19
Methanol	-1.73	-1.70	-3.46

In the calculation described above, the self-interaction energy of the solvents was not considered. However, it appears that this energy cannot be neglected to correctly account for the energetic effects of solvation versus surface binding. Given the extensive hydrogen bonding of water and the proportionally large size of carfentanil, solvation of carfentanil may significantly disturb the hydrogen bond networks within a water cluster and the lost self-interaction energy of the solvent most likely will not be offset by the weak carfentanil-water interactions. However, modeling this effect with DFT would prove rather difficult since it would require a significant number of iterations to obtain proper statistics. However, it is possible to approximate this effect by calculating the energy loss of removing a sphere of radius approximately equal to that of carfentanil using the known self-energy densities of methanol and water. Carfentanil has a diameter on the order of ~9–11Å, depending on its arrangement. The minimum size of 9Å was used to calculate the water displacement effect, since this would provide a minimum for the energy. Even with the smallest approximate radius, the self-interaction energy of the water sphere was calculated to be 6.12 eV versus only 2.20 eV for methanol. This water self-interaction energy is significantly larger than that of the water-carfentanil binding and may explain why carfentanil preferentially binds to the silica when dissolved in water. In the case of methanol, the self-interaction energy is approximately the same order of magnitude as the methanol-carfentanil binding energy. This suggests that the solvation of carfentanil in methanol is much more favored than its adsorption to silica. It should be noted however, that this type of energetic analysis is only approximate, and that classical MD simulations could be used to include entropic effects, providing a more complete analysis of fentanyl solvation. However, such calculations would require significant efforts to create new model potentials for fentanyl compounds as well as their interactions with solvents and surfaces of interests.

4. CONCLUSIONS

The hydrolysis of the methyl ester of remifentanil and its derivatives revealed the importance of conformers in remifentanil reactivity. Specifically, it was found that substituents located at the four position of the nitrogen ring hinder hydrolysis and that the removal of these groups resulted in an order of magnitude increase in hydrolysis rate. Removal of the ring nitrogen or lengthening of the alkyl chain respectively prevents hydrolysis or halves the hydrolysis rate, with respect to remifentanil.

Uptake studies of remifentanil on silica revealed many trends. In non-aqueous solvents, remifentanil uptake decreases with increasing solvent polarity in the order, chloroform >> isopropanol > ethanol > methanol. For buffered aqueous solutions, remifentanil is hydrolyzed to the corresponding salt as pH is increased. There is significant uptake for both remifentanil and its hydrolysis product except in the case of pH 10. However, at low pH values (1.68 and 4) little hydrolysis occurs and remifentanil is completely hydrolyzed at pH 7 and pH 10. Therefore, uptake measurements are essentially irrelevant for remifentanil at pH 7 and pH 10 and for the hydrolysis product at pH 1.68 and pH 4. Interestingly enough, uptake of the hydrolysis product is suppressed at pH 10 and the buffer is shown to not be a bystander since remifentanil is fully hydrolyzed in DIW but not in pH 7 buffered solution. For mixed aqueous/organic solvents, remifentanil is again hydrolyzed as the pH is increased. However, organic solvents seem to limit the rate of hydrolysis substantially and silica appears to inhibit hydrolysis at pH 10. In buffered, DIW/organic solvent solutions, the percent uptake for remifentanil is basically constant in all cases excluding pH 10 and there is little uptake of the hydrolysis product when hydrolysis does occur (pH > 4). In non-buffered mixed aqueous/solvent solutions, remifentanil uptake appears to be very solvent dependent and increases with the trend, methanol > isopropanol > ethanol. The hydrolysis product uptake follows the same trend, but the variation is not as great. As with the aqueous only solutions, the remifentanil and hydrolysis product uptakes for the non-buffered and buffered DIW/methanol solutions should be equivalent; however, the buffer is found to inhibit both uptake and hydrolysis of remifentanil as well as the uptake of the hydrolysis product.

Previous experiments showed that the carfentanil uptake on silica is much higher in aqueous solutions than in methanol. Calculated DFT binding energies of carfentanil-solvent and carfentanil-silica systems appear to support the reverse, showing that solvation is energetically more favorable in aqueous solutions than in methanol. However, further DFT calculations of self-interaction energies reveal that these energies significantly outweigh carfentanil-solvent and carfentanil-silica interaction energies and show that solvation of carfentanil in water is much less favored than in methanol.

ACKNOWLEDGMENTS

Funding was provided by the U.S. Army via the Surface Science Initiative Program (PE 0601102A Project VR9) at the Combat Capabilities Development Command Chemical Biological Center.

REFERENCES

[1] McEntee, M.; Schenning, A.; Iordanov, I.; Peterson, G.; Sheahy, M. Sorption of Carfentanil and Remifentanil Salts on Porous Materials; CCDC CBC-TR-1651; U.S. Army Combat Capabilities Development Command Chemical Biological Center: Aberdeen Proving Ground, MD, 2021; UNCLASSIFIED Report

A combined density functional theory and grand canonical Monte Carlo approach to modeling multi-component adsorption

Ivan O. Iordanov[a]*, Trenton M. Tovar[b], Lawford Hatcher[c], Jared B. DeCoste[a]
[a]U.S. Army Combat Capabilities Development Command Chemical Biological Center, Research & Technology Directorate, 8198 Blackhawk Rd, Aberdeen Proving Ground, MD 21010
[b]Leidos, 1750 President St, Reston, VA 20190
[c]Minority Undergraduate Student Internship Program, 8198 Blackhawk Rd, Aberdeen Proving Ground, MD 21010

ABSTRACT

Novel nano-scale materials often require computational support to provide a mechanistic understanding of their unusual properties. Probing adsorption of gases in nanoporous materials typically requires calculating both thermodynamic properties through classical methods and local binding energies calculated with quantum methods. In this work, we use grand canonical Monte Carlo and density functional theory methods to examine the binding of small polar and non-polar gases on Zeolitic imidazolate framework-8 and the binding of carfentanil in a wide variety of metal-organic frameworks. We find that the polarity of the gas does not have a significant effect on the adsorption loading in Zeolitic imidazolate framework-8. We also find experimentally that there is an atypical time-gated chemisorption reaction for NO adsorbed on UiO-66-NH_2. Finally, we look at the relationship between the binding energy of the opiate carfentanil, and the size of the pores of metal-organic frameworks. The result is a volcano plot—showing the optimal pore size for binding of carfentanil to be commensurate with its size, ~4.5 Å.

Keywords: density functional theory, computational chemistry, adsorption, molecular-organic frameworks, grand canonical Monte Carlo, porous materials

1. INTRODUCTION

Adsorption in porous materials has numerous diverse applications ranging from filtration of toxic chemicals, to gas separation and CO_2 sequestration. Given the importance of porous materials, there has been significant interest in improving porous materials—such as amorphous carbons or zeolites—as well as inventing new classes of porous materials. Metal-organic frameworks (MOFs) are a relatively new class of porous materials invented by the Omar Yaghi group.[1] MOFs are a modular material consisting of inorganic metallic centers called secondary building units (SBU) connected by organic linkers. By changing out the linkers or SBUs, nearly infinite combinations of MOFs can be created, allowing for nearly endless variation in the properties of the material. The combination of the number of possible MOF structures, their crystallinity, as well as the intrinsic dependence of their properties on their atomistic structure make MOFs an excellent class of materials for investigation and optimization though computational means.

Extensive high-throughput computational studies have been done, searching for a MOF optimal for a particular application (e.g., CO_2 sequestration)[2,3] or property (e.g., high surface area).[4] These studies enable relatively fast screening of thousands of MOFs, which would be prohibitively difficult to do solely experimentally. It is also common practice to include hypothetical MOFs,[5] or functionalized MOFs that have not been currently synthesized, allowing computational studies to guide future synthesis when optimizing for a particular purpose. Furthermore, due to the complex geometry and chemistry of these structures, computational studies are often done in conjunction with experimental work to jointly provide mechanistic understanding. Classical forcefield methods, such as the grand canonical Monte Carlo (GCMC) method, are typically used when modeling thermodynamics-related properties of MOFs, such as adsorption and diffusion, as well as structural motifs like defects that can have patterns on a multiple-unit cell-length scale. On the other hand, chemical reactions and detailed structural analysis of individual unit cells are typically done using density functional theory (DFT) due to its high accuracy and ability to handle chemical reactions. In this work, we use both methods to study adsorption within MOFs, with the goal of improving the adsorption of weakly interacting species within MOFs.

2. METHODS

2.1 Density functional theory

DFT is an *ab initio* quantum chemical method used to calculate atomic properties with high accuracy. Unlike previous quantum mechanics-based methods—such as configuration interaction—in DFT, the total energy is a functional of the total electron density instead of the multi-electron wavefunction.[6] This simplification makes much larger simulations feasible, while typically maintaining a similar level of precision as other quantum mechanics-based methods. The primary approximation in DFT is in the treatment of the exchange and correlation interactions between electrons, which is approximated through different exchange and correlation functionals. Multiple functionals have been developed over the years[7] to improve the accuracy of DFT for different classes of problems. Due to the large size and crystalline nature of MOFs and most other porous materials, crystalline MOF calculations are usually performed using the Perdew-Burke-Ernzerhof (PBE) functional.[8] PBE is one of the oldest, fastest, and most widely implemented generalized gradient approximation functionals, with a generally comparable accuracy to other generalized gradient approximation functionals, and we have used it in all the calculations in this work.

Due to the crystallinity of MOFs, we have elected to use plane-wave basis sets within periodic boundary conditions to model the full unit cell of the MOF structure. The calculations were done using the open-source Quantum Espresso code, which implements plane-wave DFT and many related properties calculations. The lattice vectors are taken from experimental X-ray diffraction measurements and used as-is; although, we have checked the lattice parameters by running cell relaxation calculations to confirm that there are no significant distortions. Electron orbitals are described using mixed pseudopotentials from the standard solid-state pseudopotentials efficiency database,[9] with 50/400 Ry cutoffs for the wavefunctions/electron density. Initially, calculations were also performed using the projector augmented wave pseudopotentials included with Quantum Espresso. The difference in binding energies for adsorbates depending on the pseudopotential used were less than 0.01 eV. All calculations included a semi-empirical van der Waals correction due to Grimme et al.[10] because of the importance of van der Waals interactions for physisorption. Due to the size of the cells, all calculations only included the Γ k-point.

2.2 Grand canonical Monte Carlo

While DFT has many advantages in atomistic simulations, it is difficult to run DFT simulations on time scales long enough to provide meaningful statistical ensemble averages for thermodynamic properties, like temperature or pressure of gases. To run long/large enough simulations, the quantum interactions between electrons must be approximated using classical forcefield potentials. GCMC simulations are the primary framework for full-scale simulations of adsorption. Using classical forcefields, simulations can be run for any temperature/pressure combination, allowing for full isotherms to be simulated through a series of calculations. GCMC calculations were done using the RASPA software package,[11] using a combination of built-in and TraPPE potentials[12] for the adsorbates. The framework is kept fixed, thus not needing a forcefield parametrization, and the built-in RASPA generic MOF values are used for the Lennard-Jones parametrization.

2.3 Isotherms and synthesis

Zeolitic imidazolate framework-8 (ZIF-8) was synthesized as described by Pan et al.[13] Separate aqueous solutions of $Zn(NO_3)_2{\cdot}6H_2O$ and 2-methylimidazole were mixed by stirring at room temperature for 1 hour. The product was collected by centrifuging and was washed three times with deionized water before methanol exchange. Isotherms for CO and NO were measured on a Micromeritics® 3Flex 3500 instrument. Before measurements, all samples were degassed under vacuum at 120 °C to remove water and record an accurate weight.

3. RESULTS

3.1 Adsorption in ZIF-8

Initial work focused on adsorption of small polar and non-polar gases in ZIF-8. ZIF-8 consists of small (~10 Å-diameter) pores containing zinc metal centers that are connected with imidazole linkers.[14] ZIFs can be considered a subset of MOFs with more restrictive SBU/linker combinations; they have been investigated intensely due to their topological similarity to zeolites. Our initial hypothesis was that there will be stronger binding between the polar gases and the framework compared to the non-polar ones.

DFT calculations (Figure 1) show that there is no correlation between polarity of the gas and its binding energy. The most likely reason is that the van der Waals interactions dominate the overall binding, due to relatively small or inaccessible framework dipole moments. Examining the binding orientations and locations of the adsorbates (Figure 2) confirms that the optimal binding is near the linkers, optimizing the van der Waals interactions through close proximity with multiple parts of the framework. The binding geometry suggests that the binding energy could be increased by creating pores or other geometric motifs with sizes commensurate with the adsorbate size, which we will consider in Section 3.3. Adsorption isotherm experiments broadly confirmed the computational results, showing that there is no increase in adsorption loading with polarity.

	CH_4	CO_2	CO	NO	N_2	O_2
DFT BE (eV)	0.196	0.227	0.191	0.185	0.172	0.267
Loading 0.01 bar	0.004	0.009	0.001			
Loading 0.1 bar	0.330	0.617	0.017			

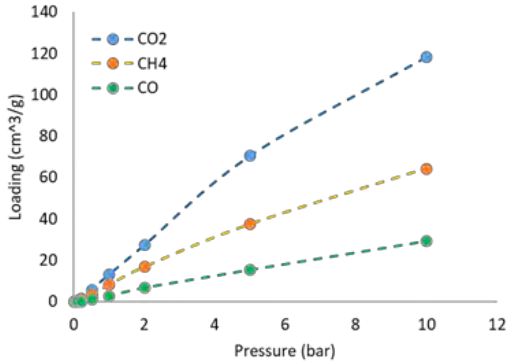

Figure 1. (left) DFT binding energies and low pressure GCMC adsorption loadings for polar and non-polar gases. GCMC adsorption values follow same ordering as DFT binding energies. (right) Full GCMC isotherms showing adsorption at higher pressures.

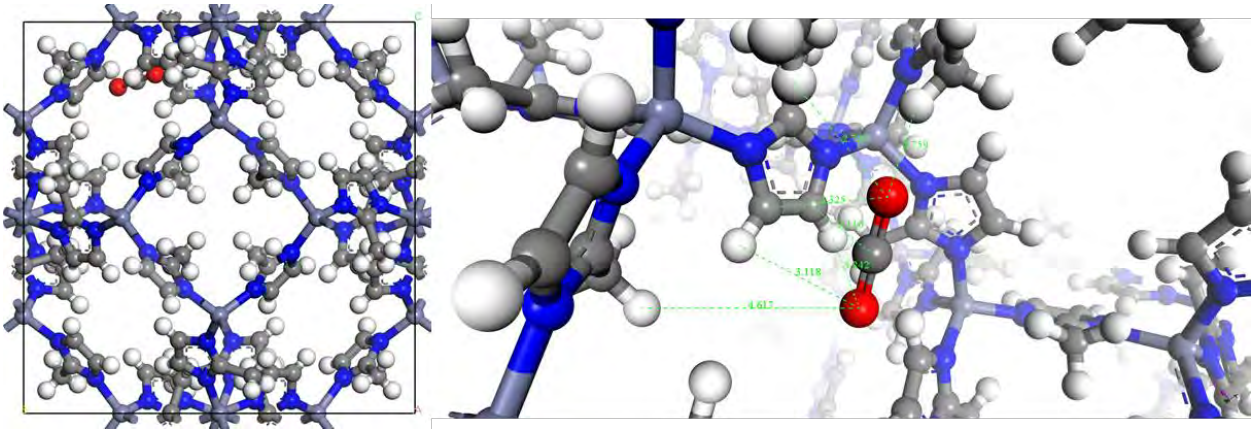

Figure 2. CO2 adsorption in ZIF-8. Full unit cell on the left, zoom in on binding site on right. Note the close proximity of multiple linkers to the adsorbate at the binding site, showing how "enveloping" sites can improve van der Waals binding energy.

3.2 NO adsorption and reaction in UiO-66-NH_2

Subsequent to our work on adsorption of polar and non-polar gases in ZIF-8, we ran an adsorption isotherm for NO within UiO-66-NH_2, a very well-studied MOF with potential filtration applications. NO was found to have a rather peculiar isotherm (Figure 3), with very low uptake at low pressures, followed by an irreversible step uptake at higher pressures. This dynamic is in contrast to the NO isotherms on ZIF-8 and UiO-66, both of which showed reversible weak physisorption. The initial low uptake of the NO isotherm on UiO-66-NH_2 indicates an initiation period before chemisorption can occur. This is very different than previously reported isotherms of NO on MOFs. Typically, MOFs with coordinatively unsaturated metal sites show a step isotherm; however, the step occurs immediately at the lowest measured pressure point.[15] When the sample is re-evacuated, a second isotherm shows only reversible physisorption. Interestingly, the physisorptive uptake is higher than the initial uptake on a fresh UiO-66-NH_2 sample; meaning, the treated sample has a stronger interaction with NO.

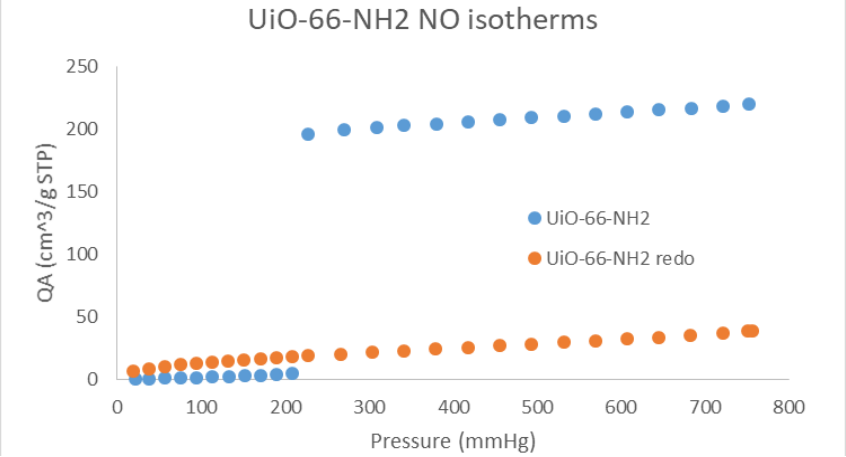

Figure 3. NO isotherms on fresh UiO-66-NH2 (blue) and UiO-66-NH2 already treated with NO (orange).

Reaction of NO with pendant amines has been shown for IRMOF-3 and UMCM-1-NH_2.[16] However, the reaction takes place at high NO pressures, and an isotherm was never measured. To explore the pressure effect, UiO-66-NH_2 was exposed to NO at pressures of 189 mmHg (below the step) and 760 mmHg (above the step). The two samples were digested with nitric acid and the solution was measured by nuclear magnetic resonance (NMR), shown in Figure 4. For both samples, NMR spectroscopy shows the doublet peaks of the bdc-NH_2 linker shift from an untreated sample. However, the shift is different for each treatment pressure meaning that different species formed at each pressure. This indicates that the initiation phase forms a stable complex before reaction to the final product. N_2 isotherms after the reactions show only ~25 % lower surface areas, suggesting UiO-66-NH_2 maintains most of its structure after the reaction. *In situ* diffuse reflectance infrared Fourier transform spectroscopy experiments and further DFT/GCMC calculations are planned to further explore the reaction.

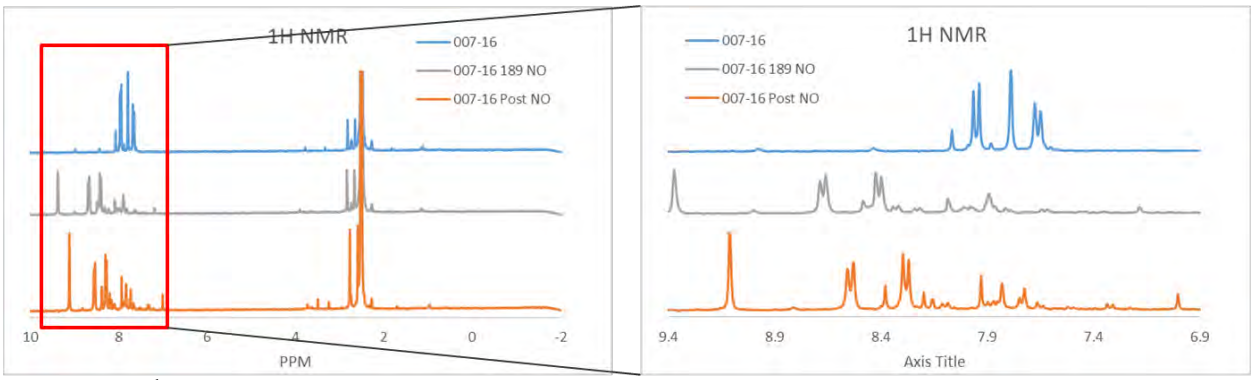

Figure 4. ^{1}H NMR of UiO-66-NH_2 (blue), UiO-66-NH_2 treated at 189 mmHg NO (gray), and UiO-66-NH_2 treated at 760 mmHg (orange).

3.3 Pore size effect for adsorption

Pore size effects are known to have important effects in gas adsorption and separations applications, for example, in adsorption in the hierarchical pores of amorphous carbon and in the cracking of hydrocarbons using zeolites in the petrochemical industry. However, there has been comparatively little research in tailoring nano-scale pores in MOFs to increase physisorption adsorption at low pressures. Most research has focused on larger pores for increased adsorption at high pressure or chemical modifications for improved binding. In this section, we describe our initial work in investigating this approach to improve adsorption.

3.3.1 Pore size effect for carfentanil

Carfentanil is a dangerous opiate—approximately 10,000 times more potent than morphine.[17] Understanding how it interacts with surfaces and how to protect personnel or neutralize it is of general interest to the Army. Aside from its practical importance, it is also a useful test molecule for improving adsorption through pore size modulation due to its large size and generally unreactive nature. Therefore, we have done DFT binding energy calculations for carfentanil in a variety of MOFs, looking to establish a pore size verses binding energy relationship.

The results can be seen in Figure 5, which shows a typical volcano plot relationship between pore size and binding energy, centered around the approximate radius of carfentanil, ~4.5 Å. The pore sizes shown were measured as the radii of spheres contained within the pores and not allowed to overlap the van der Waals radii of the surrounding atoms. Such a measurement can cause some discrepancy as the real pore geometry deviates from the spherical shape, but it approximates most of the cage-like pores of MOFs and provides a consistent basis for comparison. Given that the adsorbate itself does not have a perfectly spherical shape and is able to bend to accommodate geometrical features, it is not expected for there to be perfect correlation between pore size and adsorbate size, but the results are quite consistent with a pore size/adsorbate size binding improvement effect. Note that some MOFs have multiple pores with different sizes and are listed at different locations depending on each pore size.

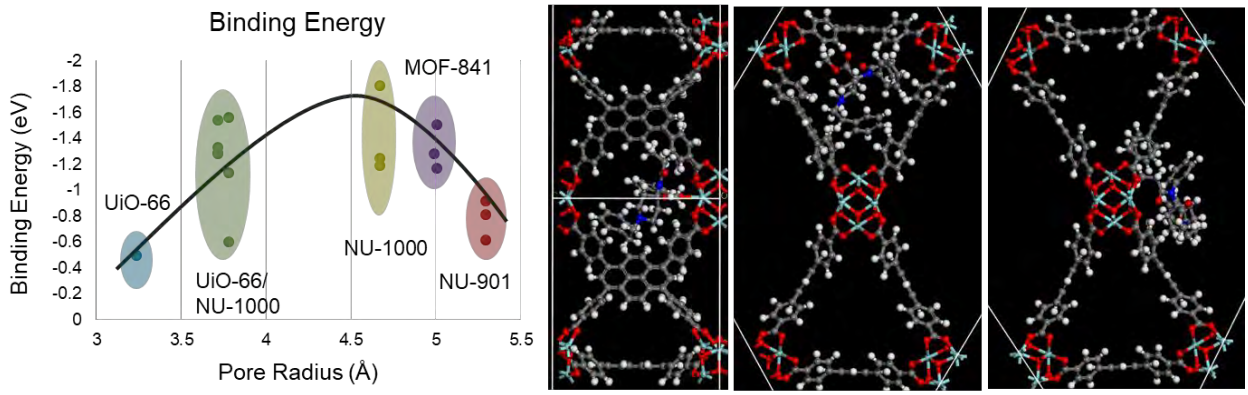

Figure 5. Binding energy of carfentanil versus MOF pore size. Volcano plot curve shows maximum near carfentanil radius (4.5 Å). (left) Largest pore of NU-1000 is not shown, although it is consistent with the trend, with a binding energy of 0.7 eV and a 14.4 Å pore radius. (right) Carfentanil within the three pores of NU-1000; smallest, medium, and largest from left to right.

The adsorption of carfentanil is primarily due to van der Waals interactions; however, we also find that carfentanil can create a hydrogen bond between the oxygen in the ester group and undercoordinated metal sites on Zr_6O_8 SBUs, if the geometry allows it. By twisting the carfentanil structure to allow/deny hydrogen bond formation, its contribution to the total binding can be approximated as ~0.5 eV—significant but still lower than the overall van der Waals binding. Multiple binding energies are shown in Figure 5 for most pores since multiple binding orientation converged, showing the spread in binding energy due purely to binding orientation as opposed to pore size. The inclusion of hydrogen bonding (or lack thereof) is the reason for the larger spread in binding energies shown for NU-1000 and UiO-66.

Overall, these results show a promising pathway to improving physisorption of analytes in MOFs in a way that will be size-selective as opposed to reliant on chemical reactivity. This approach could improve adsorption of chemical warfare agents in protective equipment, since chemical warfare agents have larger sizes than most ambient chemicals, and pore sizes could be tuned to improve their adsorption while allowing smaller molecules through. Future work will further investigate this possibility and use this as a basis for future projects.

3.3.2 Modifying pore size through modulators

In the previous section, we described the process of changing out different MOFs in order to optimize the pore size to bind a particular analyte with a similar size. However, instead of changing the MOF itself, there are two other options that allow for finer control of pore sizes without changing the underlying MOF structure and its topology. The first is to attach functional groups to the MOF linkers. Functional groups are typically attached to the benzene rings of the linkers to change the chemical reactivity of the MOF; however, attaching bulky hydrocarbons should allow for changes in pore sizes without changing the chemical properties of the material. The second option is to attach so-called "modulators" to the undercoordinated sites that are part of the normal topology of some MOFs—such as NU-901 and NU-1000. Both MOFs have four unoccupied sites, each of which allows for the attachment of a linker through two carboxylate acids. If a modulator with just one carboxylic acid is attached, we can decrease the size of the pores or change their shape without changing the connectivity of the pore network. We have already done DFT calculations on the binding energies of the modulators to the SBU of previously synthesized NU-901 analogs (Figure 6) and are looking into using these optimized structures for binding energy calculations of hydrocarbons. The combination of functionalizing linkers and attaching modulators should allow for fine modulation of pore sizes and improved optimization of the binding of different analytes.

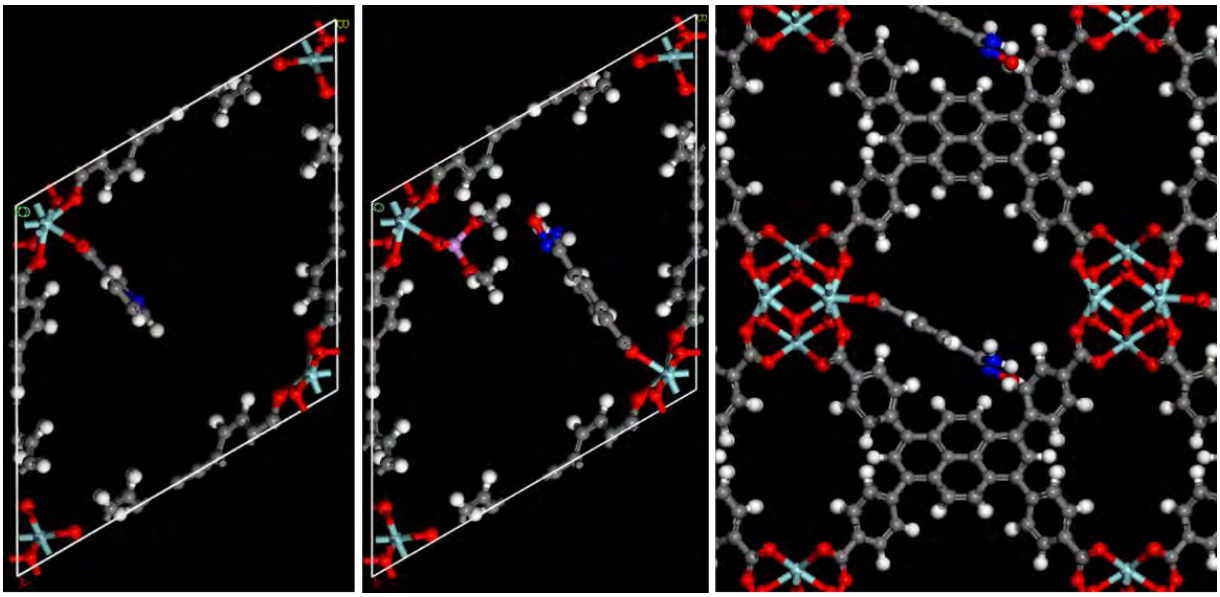

Figure 6. (left) Modulators attached to NU-901: pyridine, (middle) DMP and oxime, and (right) oxime. Note that NU-901 has two pores and, depending on which of the four sites on the SBU the modulator is attached to, it can extend in either pore. The two figures on the left show modulators in the large pore, whereas the last rotates the view through 90 degrees to show the small pore with a modulator nearly spanning the length of the pore. Addition of modulators that are approximately as large as the pore can effectively split the pore and effectively increase the surface area of the MOF.

3.4 Large-scale DFT adsorption calculations

Typically, adsorption calculations using ab-initio methods like DFT in the literature are done with hand-crafted input files, where the user tries out a couple of plausible adsorption sites and reports the results. Due to the significant computational cost of ab-initio methods, this limited process was considered an acceptable trade-off, sometimes complimented by cheaper Monte-Carlo force-field calculations in order to determine initial positions. The availability of ever more computational power and the recent push towards automated and statistically validated approaches, often used as inputs to machine learning codes, led us to consider developing an approach where adsorption calculations in MOFs can be done in a mostly automated way. We think this approach will be particularly useful with new MOFs, where the adsorption sites are less well known.

3.4.1 Initial large-scale simulations – UiO-66

An automated script was used to prepare multiple DFT input files with different adsorption locations and run them in parallel. The adsorption locations were randomized for position and orientation, within a constraint of being further then ~1.5Å away from the MOF framework atoms. Afterwards, a full DFT geometry optimization is performed based on the randomized initial geometry of the analyte. Using this setup, we could run 10s to 100s of parallel calculations for each analyte with minimal human input. The results of initial calculations on polar and non-polar gases using this process are shown in Figure 7. The maximum binding energies suggest that the dipole moment by itself is not the most important variable in determining adsorption energies. Instead, it appears that the ability to create hydrogen bonds for ammonia/methanol creates much stronger binding then that of SO_2/CH_3Cl, despite similar polarity. In fact, the binding energies of the non-hydrogen bonding species are very similar, and appear to be primarily influenced by the size of the species, and not the polarity. This appears to contradict the GCMC results, which show a clear difference between polar and non-polar species. Part of the reason may be due to adsorbent-adsorbent interactions, which are not considered in the DFT calculations, and can be expected to be stronger between polar species.

Since we are considering a distribution of binding energies over many sites and orientations, there are several interesting physical insights to be gleaned from the results. First, as one could expect, the hydrogen-bonding species methanol/ammonia show a much greater site/orientation dependence then the other species, despite the local geometry optimization that is part of each calculation. However, there is an unexpected difference between them, with ammonia showing very weak binding outside of its optimal configuration, while methanol displays a much wider spread of binding energies, with many more viable configurations. This implies that methanol is less site-dependent then ammonia, and could be expected to adsorb more easily, even if the optimal binding sites are blocked or already full.

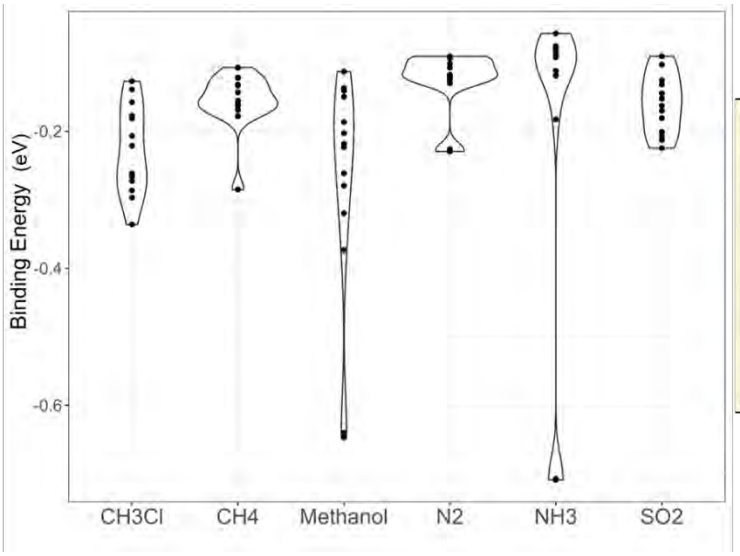

	Max	Aver	STDEV	Dip
Methanol	-0.65	-0.28	0.17	1.7
CH_4	-0.28	-0.16	0.04	0
N_2	-0.23	-0.13	0.04	0
CH_3Cl	-0.34	-0.23	0.06	1.87
SO_2	-0.22	-0.16	0.04	1.63
NH_3	-0.71	-0.23	0.25	1.47

Figure 7. (left) Violin plot of DFT binding energy distributions for adsorbate polar and non-polar gases. (right) Corresponding maximum, average and standard deviation of binding energies in eV, along with dipole moment in debye. Dipole moment is not strongly correlated with binding energies.

In order to test the robustness of these calculations, a much larger set of calculations was performed just for the case of ammonia adsorption on UiO-66. In this case, a 100 and 1,000 repeat set of calculations was done (Figure 8). Notably, the results are quite similar between both calculations, as well as the previous NH_3/UiO-66 run shown in Figure 7. These results suggest that the smaller calculation runs in the ~50 repeat range can be sufficient, although it is always possible to increase the run number to improve accuracy. It is notable in both Figures 7 & 8 that most randomly assigned locations/orientations result in very minimal binding energies. This is because most of the empty space in the MOF is far away from the surface, which prevents any significant adsorption interactions. Consequently, the code was optimized by rejecting random locations that were too far from any surface atom, which eliminates many unnecessary calculations that will result in near zero binding energies.

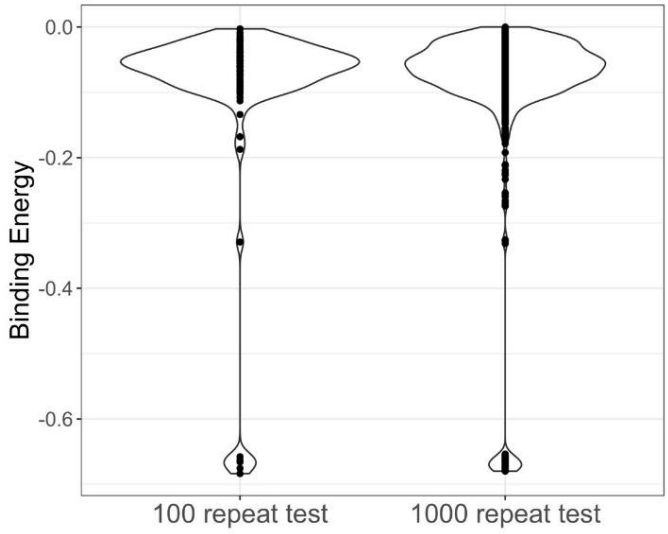

Figure 8. Larger scale repeat test for adsorption of ammonia on UiO-66. Overall, the energy distribution is quite similar between the 100 and 1000 repeat test, suggesting that 100-repeat calculations have a good chance of finding all important binding sites, when adsorbing small molecules in MOFs.

3.4.2 MOF-808 calculations

Further calculations were done for the adsorption of small gases in MOF-808. MOF-808 is interesting primarily because it has six open sites for every SBU, in contrast to UiO-66, which is fully coordinated (unless there are defects).

These open sites can be terminated in different ways. Usually MOF-808 is formate, terminated after synthesis, but it can be activated to remove the formate, replacing each formate with a hydroxyl. Large-scale simulations showed that both terminations seem to show similar binding energy distributions, so we focused on the formate structure in this work. The most interesting result of these calculations is that there are two primary binding sites on the Zr6 MOF SBU that is commonly used for CWA removal across a variety of MOFs (including UiO-66, MOF-808 and NU-1000). The first is the "enveloped" site, where a small gas molecule can simultaneously interact with several linkers and the SBU through weak Van der Waals forces, adding up to a significant total binding energy despite the weakness of the interactions. The second binding site is at the μ_3-OH of the SBU, which allows for hydrogen-bond like polar/polar interactions with polar adsorbates, that are significantly stronger than the enveloped site binding energies (Figure 9). Polar adsorbates prefer the μ_3-OH site, and have overall stronger binding to MOF-808, and other MOFs with the Zr6 SBU like UiO-66. However, the "enveloped" site is comparable (~2–3x smaller), and it is likely that for larger CWA molecules both the polar and non-polar interactions are important when binding to the MOF.

Due to the random sampling used in this project to determine adsorption sites, we can also see that there's a significant difference in the amount of strong adsorption sites that different molecules find on the MOF. Notably, water and CH_3Cl appear to bind most easily to MOF-808, with water having a very broad, nearly even distribution of binding energies from 0.0–0.5eV, with much less of the typical clustering near zero that most other adsorbates have. Presumably, this is because water is less sensitive to the binding location or orientation than other adsorbates and can more easily re-arrange into a strong local minimum of the binding. Ultimately, this type of analysis is only suggestive, and it would take larger simulations with multiple adsorbates to determine the true distribution of sites and energies. Nonetheless, this type of work can provide better information about the adsorption sites on a MOF than typical singular calculations where the sites are chosen by hand.

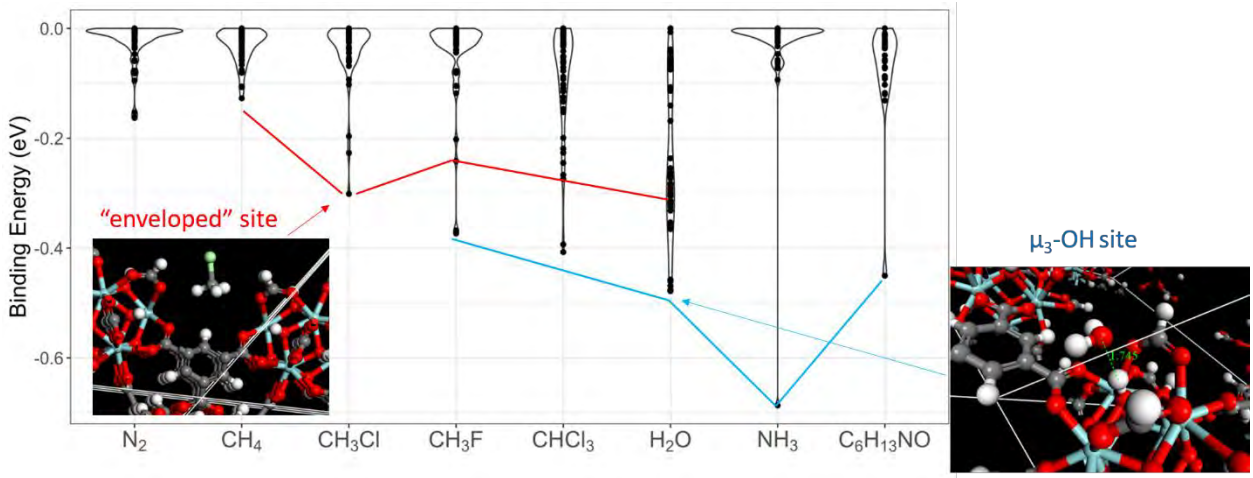

Figure 9. Binding energy distributions for several adsorbates on MOF-808. The red line follows the binding energies associated with the "enveloped" site, which is due to weak physisorption, whereas the blue line follows the binding energies of the hydrogen-bond like polar interactions at the μ3-OH site. Insets show corresponding minimal binding orientations for CH3Cl and H2O, that are representative of the enveloped and μ3-OH sites.

4. CONCLUSION

Computational and experimental methods were used to investigate and improve adsorption in MOFs. Initial work focused on small polar/non-polar gases in ZIF-8, showing that van der Waals interactions dominate adsorption even for polar gases, and that the preferred binding orientation allows for interactions with multiple linkers to improve the binding. Experimental isotherms confirmed that polarity does not have a large effect in this case, but we also found an atypical chemisorption/reaction of NO on UiO-66-NH_2. In this case, there is a delay between dosing and reaction, as well as possible pressure dependence of the products. Later work was focused on large-scale DFT simulations, to provide a general framework for calculations of adsorption in MOFs and other novel porous materials. These types of calculations both provide better reliability and confidence in the resulting binding energies, as well as a potentially useful distribution of possible binding energies in the structure.

ACKNOWLEDGMENTS

Funding was provided by the U.S. Army via the Surface Science Initiative Program (PE 0601102A Project VR9) at the U.S. Army Combat Capabilities Development Command Chemical Biological Center. This research was performed while Lawford Hatcher was a Minority Undergraduate Student Internship Program student at U.S. Army Combat Capabilities Development Command Chemical Biological Center.

REFERENCES

[1] Zhou, H.-C.; Long, J.R.; Yaghi, O.M. Introduction to Metal–Organic Frameworks. *Chem. Rev.* **2012**, *112* (2), pp 673–674.
[2] Jasuja, H.; Zang, J.; Sholl, D.S.; Walton, K.S. Rational Tuning of Water Vapor and CO_2 Adsorption in Highly Stable Zr-Based MOFs. *J. Phys. Chem. C.* **2012**, *116* (44), pp 23526–23532.
[3] Han, S.; Huang, Y.; Watanabe, T.; Dai, Y.; Walton, K.S.; Nair, S.; Sholl, D.S.; Meredith, J.C. High-Throughput Screening of Metal–Organic Frameworks for CO_2 Separation. *ACS Comb. Sci.* **2012**, *14* (4), pp 263–267.
[4] Colón, Y.J.; Snurr, R.Q. High-throughput computational screening of metal–organic frameworks. *Chem. Soc. Rev.* **2014**, *43* (16), pp 5735–5749.
[5] Wilmer, C.E.; Leaf, M.; Lee, C.Y.; Farha, O.K.; Hauser, B.G.; Hupp, J.T.; Snurr, R.Q. Large-scale screening of hypothetical metal–organic frameworks. *Nat. Chem.* **2012**, *4*, pp 83–89.
[6] Kohn, W.; Sham, L.J. Self-Consistent Equations Including Exchange and Correlation Effects. *Phys. Rev.* **1965**, *140* (4A) pp A1133–A1138.
[7] Yu, H.S.; He, X.; Li, S.L; Truhlar, D.G. MN15: A Kohn–Sham global-hybrid exchange–correlation density functional with broad accuracy for multi-reference and single-reference systems and noncovalent interactions. *Chem. Sci.* **2016**, *7* (8), pp 5032–5051.
[8] Perdew, J.P.; Burke, K.; Ernzerhof, M. Generalized Gradient Approximation Made Simple. *Phys. Rev. Lett.* **1996**, *77* (18), pp 3865–3868.
[9] Lejaeghere, K.; Bihlmayer, G.; Björkman, T.; Blaha, P.; Blügel, S.; Blum, V.; Caliste, D.; Castelli, I.E.; Clark, S.J.; Dal Corso, A.; de Gironcoli, S.; Deutsch, T.; Dewhurst, J.K.; Di Marco, I.; Draxl, C.; Dułak, M.; Eriksson, O.; Flores-Livas, J.A.; Garrity, K.F.; Genovese, L.; Giannozzi, P.; Giantomassi, M.; Goedecker, S.; Gonze, X.; Grånäs, O.; Gross, E.K.U.; Gulans, A.; Gygi, F.; Hamann, D.R.; Hasnip, P.J.; Holzwarth, N.A.W.; Iuşan, D.; Jochym, D.M.; Jollet, F.; Jones, D.; Kresse, G.; Koepernik, K.; Küçükbenli, E.; Kvashnin, Y.O.; Locht, I.L.M.; Lubeck, S.; Marsman, M.; Marzari, N.; Nitzsche, U.; Nordström, L.; Ozaki, T.; Paulatto, L.; Pickard, C.J.; Poelmans, W.; Probert, M.I.J.; Refson, K.; Richter, M.; Rignanese, G.-M.; Saha, S.; Scheffler, M.; Schlipf, M.; Schwarz, K.; Sharma, S.; Tavazza, F.; Thunström, P.; Tkatchenko, A.; Torrent, M.; Vanderbilt, D.; van Setten M.J.; Van Speybroeck, V.; Wills, J.M.; Yates, J.R.; Zhang, G.-X.; Cottenier, S. Reproducibility in density functional theory calculations of solids. *Science.* **2016**, *351* (6280), pp aad3000-1–aad3000-7.
[10] Grimme, S.; Ehrlich, S.; Goerigk, L. Effect of the damping function in dispersion corrected density functional theory. *J. Comput. Chem.* **2011**, *32* (7), pp 1456–1465.
[11] Dubbeldam, D.; Calero, S.; Ellis, D.E.; Snurr, R.Q. RASPA: molecular simulation software for adsorption and diffusion in flexible nanoporous materials. *Mol. Simul.* **2015**, *42* (2), pp 81–101.
[12] Eggimann, B.L.; Sunnarborg, A.J.; Stern, H.D.; Bliss, A.P.; Siepmann, J.I. An online parameter and property database for the TraPPE force field. *Mol. Simul.* **2013**, *40* (1–3), pp 101–105.
[13] Pan, Y.; Liu, Y.; Zeng, G.; Zhao, L.; Lai, Z. Rapid synthesis of zeolitic imidazolate framework-8 (ZIF-8) nanocrystals in an aqueous system. *Chem. Comm.* **2011**, *47* (7), pp 2071–2073.
[14] Fairen-Jimenez, D.; Galvelis, R.; Torrisi, A.; Gellan, A.D.; Wharmby, M.T.; Wright, P.A.; Mellot-Draznieks, C.; Düren, T. Flexibility and swing effect on the adsorption of energy-related gases on ZIF-8: Combined experimental and simulation study. *Dalton Trans.* **2012**, *41* (35), pp 10752–10762.
[15] Xiao, B.; Wheatley, P.S.; Zhao, X.; Fletcher, A.J.; Fox, S.; Rossi, A.G.; Megson, I.L.; Bordiga, S.; Regli, L.; Thomas, K.M.; Morris, R.E. High-Capacity Hydrogen and Nitric Oxide Adsorption and Storage in a Metal-Organic Framework. *J. Am. Chem. Soc.* **2007**, *129* (5), pp 1203–1209.
[16] Nguyen, J.G.; Tanabe, K.K.; Cohen, S.M. Postsynthetic diazeniumdiolate formation and NO release from MOFs. *CrystEngComm.* **2010**, *12* (8), pp 2335–2338.
[17] George, A.G.; Lu, J.J.; Pisano, M.V.; Metz, J.; Erickson, T.B. Carfentanil–an ultra potent opioid. A*m. J. Emerg. Med*. **2010**, *28* (4), pp 530–532.

This page intentionally left blank

FY21
SEEDLING PROJECTS

Biodiversity of the operational aerosol background environment

Francis M. D'Amico*, Adina L. Doyle, Mark A. Karavis, Jessica M. Hill, Maria T. Arévalo, R. Cory Bernhards
U.S. Army Combat Capabilities Development Command Chemical Biological Center, Research & Technology Directorate, 8198 Blackhawk Rd, Aberdeen Proving Ground, MD 21010

ABSTRACT

Detection and identification systems for biological defense must operate in challenging outdoor environments and be capable of detecting very low levels of aerosolized biological agent threats. Natural background is typically the limiting factor for detector performance in the field in terms of sensitivity and false alarm rate. Therefore, it is important to characterize the aerosol profile in the operational environment to understand how it impacts performance of detection systems. Such knowledge can lead to enhanced detection algorithms and improved test and evaluation methods. The objective of this work was to develop a data collection and processing method to characterize the operational environment with respect to current and emerging bioaerosol detection technologies. The method aims to quantify the biological aerosol particle load versus particle size in the respirable range (0.5–10 μm) using modern optical particle monitors and ultraviolet light induced fluorescence. The method also characterizes the biodiversity of the aerosol particles using DNA sequencing applied to physical aerosol samples collected onto dry filters. Sequencing results provide a taxonomical breakdown of the biological aerosol constituents to identify bacteria, fungi, and virus components. To demonstrate the aerosol background differences versus geographical locations, data was collected in a mid-Atlantic location, as well as a desert location. The product of this effort is a pilot data set that can be used by technology developers to support bioaerosol detector technology development and design more operationally relevant test and evaluation protocols. Extended background collection campaigns are very expensive in terms of resources and manpower but the methodology workflow refined in this work will enable researchers to develop more effective cost estimates and streamlined protocols for future collection efforts.

Keywords: biological detection, biological identification, aerosols, bioaerosols, ultraviolet light induced fluorescence, DNA sequencing, metagenomics

1. INTRODUCTION

1.1 Motivation

Modern biological aerosol (bioaerosol) detection and identification systems used to defend against aerosolized biological agent threats are built on underlying technologies including ultraviolet laser induced fluorescence (UV-LIF), polymerase chain reaction (PCR), and DNA sequencing. Operating such systems in field environments is challenging as they must be designed to detect and identify a sparse bioaerosol threat that may be interspersed among man-made and naturally occurring aerosols. This so-called "operational background" is complex and formed by aerosol particles of sizes ranging from 0.1–30 μm, which is the operational range of many commercial detection systems and off-the-shelf particle monitoring devices. The composition of the operational background is a function of geographical location, season, and time of day among many other factors. Therefore, product developers want to know the nature of the background environment in different operational locations and times, so they can develop effective detection algorithms to achieve low false alarm rates and high sensitivity to the low-level threats. Knowledge of the constituent makeup of different operational environments also allows developers to design more effective test methods to evaluate detector performance. Long-term background sampling campaigns across multiple locations to characterize each environment is expensive and time consuming. However, development of a standardized and streamlined collection and processing protocol could help product developers more efficiently determine and mitigate background noise otherwise present during field deployment.

1.2 Scope

The effort described here uses commercial particle monitoring and sampling equipment to collect background aerosol data, which are then processed to characterize the outdoor environment in two geographical locations. The first

location represents a mid-Atlantic environment (Aberdeen Proving Ground (APG) in Edgewood, MD) and the second location is a desert environment (Dugway Proving Ground (DPG) in Dugway, UT). Data elements were obtained from three primary sources: 1) real-time aerosol particle monitors that measure single particles and record both their size and fluorescence intensity using ultraviolet light induced fluorescence (UV-LIF), 2) high volume air samplers that collect ambient aerosols onto different filter types, which are processed in the laboratory with DNA sequencing methods to determine the biological constituents, and 3) meteorological instrumentation that characterizes the ambient environment. Together, these products form a high-dimension data set that describes the background aerosol environment in parameters critical to evaluation of the dominant technologies used in modern biological detection and identification systems.

2. METHODOLOGY

2.1 Aerosol particle monitoring

Real-time monitoring of background aerosol particles is performed using an environment monitoring platform that was developed for unattended outdoor aerosol sampling called the Environment Background Aerosol Collection System. [1] The Environment Background Aerosol Collection System supports multiple aerosol monitoring devices on an isokinetic sampling manifold that collects air through a standard EPA PM-10 inlet at a sample flow rate of 16.7 liters per minute. The platform also hosts a meteorological station: Vaisala model WXT530 (Vaisala Inc., Louisville, CO).

The primary aerosol monitor used in this work was the Wideband Integrated Bioaerosol Sensor (WIBS), model WIBS-5/NEO (Droplet Measurement Technologies, Longmont, CO). The WIBS is used to count particles, determine their size, and measure their fluorescence intensity. It is a single-particle instrument, meaning it detects every particle that flows into the device. Particles are measured using optical scattering with a continuous-wave diode laser operating at 660 nm. The WIBS is a multi-channel UV-LIF system that uses excitation wavelengths of 280 nm and 370 nm to excite the aerosol particles using Xenon flash lamps. [2] It measures fluorescence emission in both the ultraviolet (UV, 300–400 nm) and visible (VIS, 420–650 nm) bands. The 280 nm excitation wavelength is matched to the absorption peak of tryptophan, an amino acid present in organisms such as bacteria, and 370 nm targets nicotinamide adenine dinucleotide and flavins which are found in all living cells. [2,3]

WIBS produces three important data products: total aerosol particle concentration, particle size, and particle fluorescence intensity in three optical channels. Particle concentration is a measure of the total aerosol load in the environment and is a function of particle size. Fluorescent biological aerosols are typically in the size range of 1.0 µm and greater, and fluorescent particles below 1.0 µm are generally considered to be of man-made origin.[4] The number of fluorescent particles is a fraction of the total particle concentration, and the magnitude of this fraction is proportional to the bioaerosol particle concentration in the environment.

2.2 Aerosol physical sampling

The goal of physical sampling is to acquire a sample of ambient particles sufficient for laboratory analysis using analytical methods, specifically qPCR and DNA sequencing, to determine and quantify the biological constituents present in the environment. The general method is to use a high-volume air sampler to capture aerosol particles onto a dry filter. Two high volume samplers were used in this study: the SASS 3100 (Research International, Inc.; Monroe, WA), and the Dry Filter Unit (DFU) (Northrop Grumman Corporation®).

The SASS 3100 operates at an air flow rate of 50–300 liters of air per minute, which is used to pull aerosols onto a dry electret filter mounted onto a faceplate on the instrument. Electret filters are a special type of dry filter made of electrically charged polymer fibers, which enhance collection efficiency for particle sizes of interest. The SASS 3100 has been used in similar investigations in aerosol microbiome research.[5]

The DFU is a materiel item developed by the US Navy and used to collect airborne particles from ambient air to enable identification and subsequent notification of a biological attack. It operates at a sample flow rate of 1,000 liters of air per minute and collects samples onto a polyester felt filter. It has seen recent use in background aerosol monitoring.

The SASS 3100 and DFU were both deployed side-by-side and operated continuously for periods of 8–24 hours. Filters were mounted according to manufacturer specifications. The DFU samples from a vertical tube and has a screen

cover at the inlet to prevent large particles and insects from entering the sampling manifold. The SASS 3100 does not have a protective screen, so it is oriented in a downward position at approximately 45° to avoid deposits of large particles onto the filter surface. After the sampling period, the filters were collected with sterile forceps and placed into 50 ml conical tubes for storage at 4 °C.

2.3 Laboratory DNA sequencing method

The samples from both the DFU and SASS air filters were eluted with PBS + 0.01 % Triton via vortexing for 5 minutes in a 50 mL conical tube. The samples were lysed using a OmniLyse device for 2 minutes (Claremont BioSolutions). Next, the DNA was purified using a DNeasy® PowerSoil® Pro Kit (QIAGEN, Hilden, Germany) quantified using Qubit analysis. Library preparation was performed using the Rapid PCR Barcoding Kit (Oxford Nanopore Technologies™, Oxford, UK). Following PCR amplification, the samples were purified using an AMPure bead protocol and Qubit analysis was performed to measure the DNA concentration. The samples were loaded onto a GridION sequencing instrument (Oxford Nanopore Technologies™) and sequenced for 12–24 hours.

3. DATA

3.1 Real-time aerosol particle data

Aerosol particle monitoring data is shown in Figure 1 for a one-week period from 7/25–8/1/2021 at the mid-Atlantic location. Figure 2 shows the same data elements for a one-week period from 9/5–9/12/2021 at the location. There is generally a much higher average background concentration for the mid-Atlantic versus the desert. However, the average background fluorescent particle fraction for particles greater than 1.0 µm, which is a proportional measure of biological aerosol particles, was generally higher in the mid-Atlantic. This is likely because the desert is a slightly cleaner environment. These plots illustrate the background aerosol profile is highly dynamic, both in terms of overall particle concentration and fluorescence. A more in-depth analysis of particle size distribution and meteorological data is needed to explain the nature of the temporal trends.

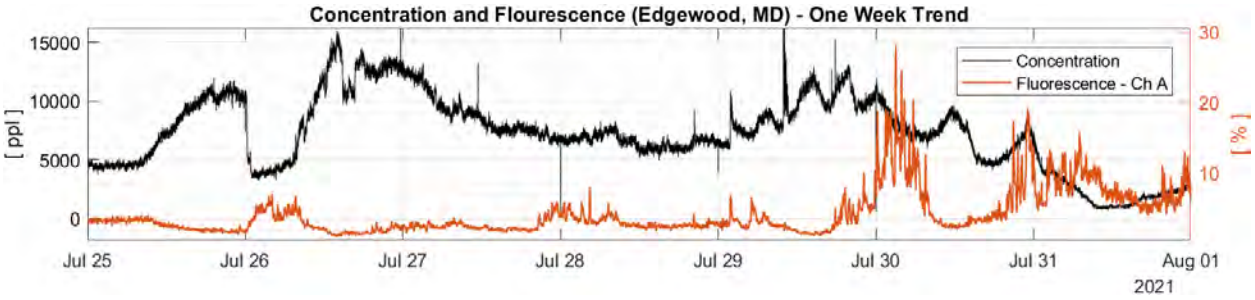

Figure 1. Temporal plot of ambient aerosol concentration and fluorescence for a seven-day period at APG.

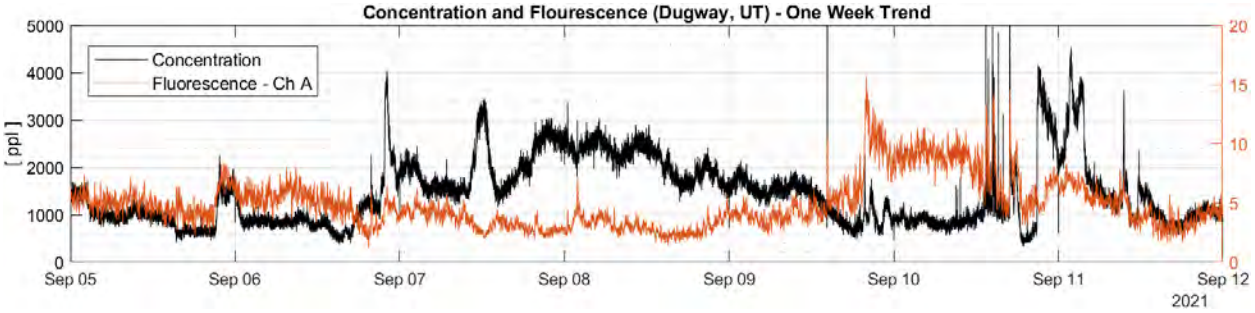

Figure 2. Temporal plot of ambient aerosol concentration and fluorescence for a seven-day period at DPG.

Particle size distributions help assess the impact of particle sizes on overall aerosol concentration and fluorescence. The background is largely dominated by particles below 1.0 µm, which may be fluorescent, but not typically biological

aerosols. The total particle size distribution (TPSD) looks at the contribution of all particles, and the fluorescent particle size distribution (FPSD) looks at only the contribution of fluorescent particles.

The data collected in the mid-Atlantic APG site is shown in Figure 3, which plots the total particle size distribution (TPSD) as a gray bar plot and fluorescent particle size distribution (FPSD) as line plots with color markers for two of the WIBS UV-LIF channels, A and C. The left plot shows the TPSD and FPSD for the time period 00:00–04:00 on 7/27/2021, and the right plot shows the distributions for the same time period on 7/30/2021. The key observation with this data is the size distributions are dynamic and have different features that depend on the presence of smaller or larger particles. The feature at 3.0 µm on 7/30 is typical of a high fluorescence environment (Figure 3b).

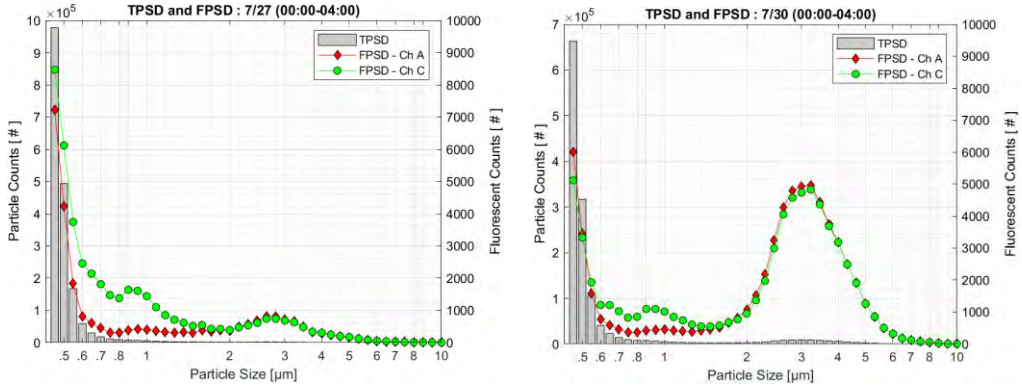

Figure 3. Example particle size distribution plots for mid-Atlantic region.

The example shown in Figure 4 shows size distributions from the desert environment at DPG. This background environment is characterized by a wider TPSD below 1.0 µm during low fluorescence periods (left plot) and a very broad TPSD and FPSD during high fluorescence periods (right plot). The broad feature we see in the mid-Atlantic aerosol background is not as prominent in the desert environment. These differences impact the response of UV-LIF bioaerosol trigger technologies in different ways.

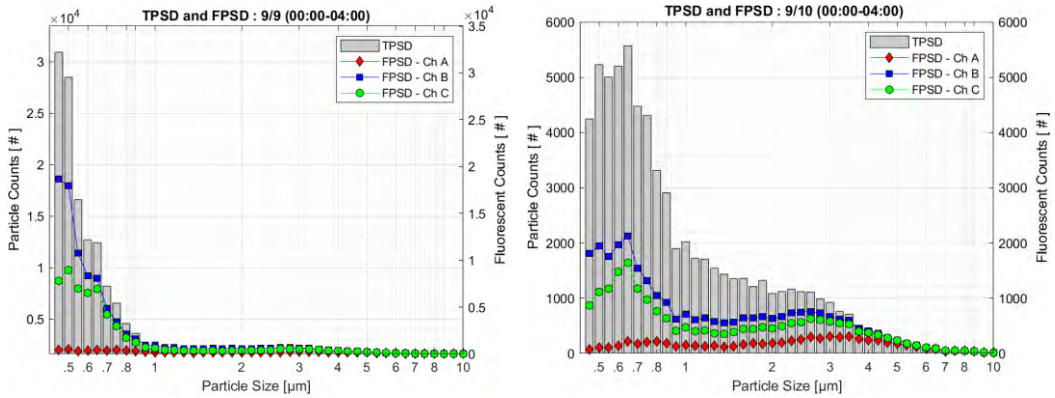

Figure 4. Example particle size distribution plots for desert region.

3.2 DNA sequencing data

The DNA sequencing data was analyzed using the minimap2 aligner against the RefSeq database from NCBI to identify what organisms were present in the samples. Tables 1–4 show examples of results from both DFU and SASS air filters from APG and DPG. The top nine organisms based on number of reads mapped are listed for each sample (Table 1).

Tables 1 and 2 show results from a 24-hour sample collected on 14–15 Sept 2021 at DPG in the desert environment. Results for SASS versus DFU sequencing show a comparable taxonomy. Two of the top organisms (*Rubrobacter* and *Geodermatophilus obscurus*) are natural aerobic Gram-positive bacteria, which have been found in, or known to survive in desert soil and rock surfaces. Another Gram-positive bacterium was also found among the top hits (*Blastococcus saxobsidens*), as well as a common plant fungus (*Botrytis cinerea*). Some of these organisms are bacterial spores that are resistant to prolonged UV exposure, which makes them well suited for a desert climate.

Table 1. Top nine organisms identified by nanopore sequencing for a DFU air filter collection at DPG.

Organism	Genome Size	Reads Mapped	Unique Reads	% Unique Reads
Rubrobacter sp. SCSIO 52909 chromosome complete genome	4,378,772	9,723	6,037	62.1
Geodermatophilus obscurus DSM 43160 complete sequence	5,322,497	8,540	5,462	64.0
Botrytis cinerea B05.10 chromosome 4 complete sequence	2,468,882	5,375	4,011	74.6
Skermanella sp. W17 chromosome complete genome	5,869,433	4,986	3,066	61.5
Rubrobacter xylanophilus DSM 9941 complete genome	3,225,748	4,601	845	18.4
Nocardioides sp. JS614 complete sequence	4,985,871	3,169	504	15.9
Blastococcus saxobsidens DD2 complete genome	4,875,340	2,511	671	26.7
Microvirga ossetica strain V5/3m chromosome complete genome	5,843,140	2,458	1,136	46.2
Rubrobacter sp. SCSIO 52915 chromosome complete genome	4,156,492	2,277	1,148	50.4

Table 2. Top nine organisms identified by nanopore sequencing for a SASS air filter collection at DPG.

Organism	Genome Size	Reads Mapped	Unique Reads	% Unique Reads
Geodermatophilus obscurus DSM 43160 complete sequence	5,322,497	6,272	4,345	69.3
Rubrobacter sp. SCSIO 52909 chromosome complete genome	4,378,772	4,129	2,628	63.6
Botrytis cinerea B05.10 chromosome 4 complete sequence	2,468,882	2,733	1,866	68.3
Massilia sp. WG5 chromosome complete genome	6,013,801	1,915	427	22.3
Rubrobacter xylanophilus DSM 9941 complete genome	3,225,748	1,805	346	19.2
Blastococcus saxobsidens DD2 complete genome	4,875,340	1,626	493	30.3
Nocardioides sp. JS614 complete sequence	4,985,871	1,389	208	15.0
Malassezia restricta chromosome IV complete sequence	846,651	1,316	3	0.2
Microvirga ossetica strain V5/3m chromosome complete genome	5,843,140	1,308	531	40.6

Tables 3 and 4 show results from an overnight 24-hour sample collected on 30–31 July 2021 at APG. All the organisms identified are commonly found in nature, and often found aerosolized. Many of these organisms are found on plants which are abundant in the mid-Atlantic environment. For example, *Pseudomonas syringae* found on the SASS filter is a ubiquitous plant pathogen. Interestingly, the SASS and DFU show very different organism taxonomy. The field filter samples had visible residue, mostly what appeared to be dust from large particles, and the SASS filter had an insect on the surface, which was removed before storage. The DFU has a screen on the inlet to prevent large particles from getting on the filter. The SASS does was oriented at a 45-degree angle downward to avoid buildup of large particles that might fall onto the filter surface. Analysis is ongoing and other samples are being collected and processed at the time of this report.

Table 3. Top nine organisms identified by nanopore sequencing for a DFU air filter collection at APG.

Organism	Genome Size	Reads Mapped	Unique Reads	% Unique Reads
Burkholderia sp. PAMC 26561 chromosome 1 complete sequence	3,397,021	123,876	33,257	26.8
Burkholderia sp. PAMC 28687 strain PAMC28687 chromosome 1 complete sequence	3,260,450	119,186	50,508	42.4
Burkholderia insecticola chromosome 1 complete sequence	3,013,410	58,658	142	0.2
Burkholderia sp. PAMC 26561 chromosome 2 complete sequence	1,611,937	48,230	21,154	43.9
Burkholderia sp. PAMC 26561 chromosome 3 complete sequence	1,623,425	42,005	19,541	46.5
Burkholderia sp. PAMC 28687 strain PAMC28687 chromosome 3 complete sequence	1,495,500	41,332	16,704	40.4
Burkholderia sp. PAMC 28687 strain PAMC28687 chromosome 2 complete sequence	1,696,029	38,305	16,820	43.9
Paraburkholderia phytofirmans PsJN chromosome 1 complete sequence	4,467,537	31,486	50	0.2
Paraburkholderia xenovorans LB400 chromosome 1 complete sequence	4,895,836	31,011	124	0.4

Table 4. Top nine organisms identified by nanopore sequencing for a SASS air filter collection at APG.

Organism	Genome Size	Reads Mapped	Unique Reads	% Unique Reads
Sphingomonas sp. PAMC26645 chromosome complete genome	4,283,956	535,432	239,367	44.7
Sphingomonas taxi strain ATCC 55669 complete genome	3,859,099	218,015	10,500	4.8
Pseudomonas fluorescens Pf0-1 complete genome	6,438,405	159,170	5,696	3.6
Pseudomonas syringae pv. syringae B728a complete sequence	6,093,698	119,502	4,706	3.9
Pseudomonas protegens Pf-5 complete sequence	7,074,893	103,690	234	0.2
Pseudomonas syringae pv. tomato str. DC3000 complete sequence	6,397,126	102,990	1,425	1.4
Sphingomonas wittichii RW1 complete sequence	5,382,261	85,636	836	1.0
Pantoea agglomerans strain C410P1 chromosome complete genome	4,182,028	82,323	535	0.6
Pantoea vagans C9-1 complete sequence	4,024,986	80,095	70	0.1

4. RESULTS

The particle monitoring data show concentration and fluorescence trends at high temporal resolution over periods of weeks. The two one-week examples from each of the two environments indicates the background fluorescence fraction for bioaerosol particles can range from 5–25 % of the total particle load. Both particle concentration and fluorescence are dynamic metrics that can change in timeframes on the order of 5 minutes. Particle size distributions also vary with time. All these parameters impact the performance of modern UV-LIF bioaerosol detector technology.

The sequencing data show stark differences in the microbial background of the two different environments (mid-Atlantic and desert). There are also significant differences between the sequencing results of the two dry filter types in the mid-Atlantic data. Follow-on collections and analysis will be performed to assess the source of this discrepancy. A screen attachment is being fabricated for the SASS 3100 to prevent large particles and insects from binding to the filter surface. Additional collections are scheduled for December 2021.

A key finding is the impact of aerosol particles that contain humic substances from soil. Humic acid is a well-known PCR inhibitor.[6] At the beginning of this study, DNA/RNA purification was done using the MasterPure™ Complete DNA and RNA Purification Kit. However, low DNA concentrations were observed, even after PCR amplification. The sample period was changed from 8 hours to 24 hours but DNA concentrations were still low. Later, a different DNA/RNA purification kit was used, QIAGEN DNeasy® PowerSoil® Pro Kit (Hilden, Germany), which neutralizes humic acid. The DNA yield and sequencing results improved significantly using this kit suggesting the humic acid may have been affecting PCR detection.

5. CONCLUSIONS

In this study, a method to collect and process natural aerosol background data for the purpose of characterizing the operational environment for bioaerosol detection systems was developed. The pilot data sets produced in this effort include real-time particle data that describe the dynamic nature of the aerosol background and DNA sequencing results that describe the biodiversity and relative abundance of biological organisms. The resulting data products can be used to improve detection algorithms, test methodologies, and assess performance in the field to ensure our detection technology minimizes adverse events such as as false alarms. For example, the non-biothreat *Burkholderia* species that were found in the mid-Atlantic environment could potentially cause false alarms with existing PCR-based biological identification technologies since two *Burkholderia* species of interest (*Burkholderia mallei* and *Burkholderia pseudomallei*) are commonly targeted on biothreat panels.

A critical finding of this study is the impact of soil/dust particles that inhibit the sample preparation process for DNA sequencing. Switching to the PowerSoil Kit overcame this inhibition so any future studies should use the PowerSoil Kit, which is consistent with methods used in related research on the aerosol microbiome.[7] The highest known risk entering this effort was the dry filter sampling and processing for DNA sequencing, which was expected to be an iterative process. The methods were subsequently improved and are now suitable for more extended field sampling

campaigns. These campaigns will provide critical information that will help reduce false alarms for currently fielded biological detection and identification technologies and enable confident decision making for our warfighters.

ACKNOWLEDGMENTS

Funding was provided by the Director, Combat Capabilities Development Command Chemical Biological Center under the authorities and provisions of Section 2363 of the FY 2018 NDAA to develop new technologies, engineer innovations, and introduce game-changing capabilities. Supplemental funding was provided by Joint Program Executive Office for Chemical, Biological, Radiological and Nuclear Defense (JPEO-CBRND).

REFERENCES

[1] D'Amico, F.M.; Dybwad, M.; Skogan, G.; Bøifot, K.O.; Hurley, J.M.; Bennett, B. Integrated multi-purpose bioaerosol testbed for characterization of UV-LIF-based particle counting and sizing instruments and environmental background monitoring, *Proceedings SPIE 11416, Chemical, Biological, Radiological, Nuclear, and Explosives (CBRNE) Sensing XXI*, 114160F, **May 2020**.

[2] Kaye P.H.; Stanley, W.R.; Hirst, E.; Foot, E.V.; Baxter, K.L.; Barrington, S.J. Single particle multichannel bio-aerosol fluorescence sensor. *Opt. Express.* **2005***, 13* (10), pp 3583–3593.

[3] Hairston, P.P; Ho, J.; Quant, F.R. Design of an instrument for real-time detection of bioaerosols using simultaneous measurement of particle aerodynamic size and intrinsic fluorescence. *J. Aerosol Sci.* **1997**, *28* (3), pp 471–482.

[4] Huffman, J.A.; Treutlein, B.; Pöschl, U. Fluorescent biological aerosol particle concentrations and size distributions measured with an Ultraviolet Aerodynamic Particle Sizer (UV-APS) in Central Europe. *Atmos. Chem.Phys.* **2010**, *10* (7), pp 3215–3233.

[5] Bøifot, K.O.; Gohli, J.; Skogan, G.; Dybwad, M. Performance evaluation of high-volume electret filter air samplers in aerosol microbiome research. *Environ. Microbiome. 15* (14), pp 2–16.

[6] Sidstedt, M.; Jansson, L.; Nilsson, E.; Noppa, L.; Forsman, M.; Rådström, P.; Hedman, J. Humic substances cause fluorescence inhibition in real-time polymerase chain reaction. *Anal. Biochem.* **2015**, *487,* pp 30–37.

[7] Bøifot, K.O.; Gohli, J.; Moen, L.V. Dybwad, M. Performance evaluation of a new custom, multi-component DNA isolation method optimized for use in shotgun metagenomic sequencing-based aerosol microbiome research. *Environ. Microbiome*. **2020**, *15* (1), pp 1–23.

This page intentionally left blank

Machine-learning for imperfectly observed networks via Gibbs sampler

Thomas E. Ingersoll
U.S. Army Combat Capabilities Development Command Chemical Biological Center, Research & Technology Directorate, 8198 Blackhawk Rd, Aberdeen Proving Ground, MD 21010

ABSTRACT

A method for estimating infective disease dynamics parameters when contact rates are heterogeneous, surveillance data are not systematically sampled, and cases are underreported is presented in this report. An important parameter for predictive infectious disease models is R_0, the basic reproductive number. R_0 determines the rate at which new infections occur, and responds to intervention strategies such as vaccination, quarantine, and social distancing. However, R_0 can be difficult to estimate as its value appears to change in open populations, where subpopulations interact in partial isolation. These changes in value result in changes in disease dynamics as reflected in rates of spread. Accurate estimation of R_0 is further complicated by shortcomings in surveillance data collection, shortcomings that are difficult to mitigate through changes in sampling methods. Estimation of R_0 may be achieved through application of a hierarchical model which considers detection probabilities and affected population size. These characteristics may be inferred from imperfect surveillance data using Bayesian methods, which can be highly automated. A hierarchical data-assimilative method for improving parameter estimates in predictive models when data are imperfectly collected is demonstrated below. Timely estimates of changes in disease dynamics can inform management decisions and mitigation strategies early in disease outbreaks when such decisions are most likely to be effective.

Keywords: CoViD-19, Bayesian method, Parameter estimation, Surveillance, Open-population model, Underreporting, Disease dynamics, Markov Chain Monte Carlo.

1. INTRODUCTION

1.1 Purpose

This report details a Bayesian-likelihood method for estimating infective disease dynamics parameters in metapopulations, where open subpopulations exist in partial spatial isolation from a larger population, surveillance data are not systematically sampled, and cases are underreported. We hypothesize the basic reproductive number for an infectious disease, R_0, may be estimated along with size of the affected subpopulation (K), using only surveillance data, that is, without a-priori knowledge of population structure (Figure 1).

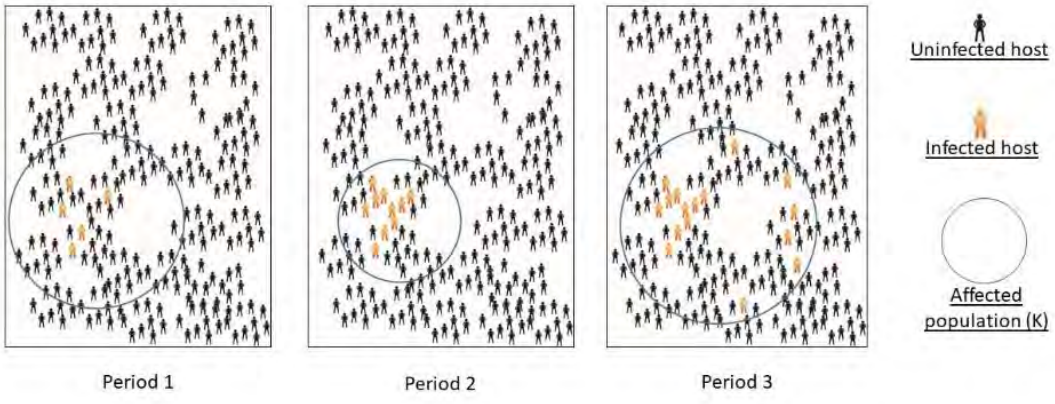

Figure 1. Spatial distribution of a hypothetical disease outbreak showing the size of affected subpopulations (circles). Infected cases are in orange, while susceptible individuals are in black.

Further, such estimates of K can then be used to inform mitigation strategies such as quarantine and ring vaccination, while estimates of R_0 can be used to populate predictive models. A method for automating these parameter estimates using Gibbs samplers is detailed in this report.

1.2 Background

Parameter estimates for predictive disease models typically rely on unsystematically sampled data. Sampling is limited to case reports of patients already known to be ill, which results in underreporting. Because only suspected cases are included in sampling, asymptomatic cases are overlooked, leading to an underestimation of the number of infected hosts. Furthermore, host populations do not exhibit homogeneous contact rates. That is, portions of the population exist in partial isolation from others, resulting in populations that are not well-mixed.[1] Underreporting, and incomplete mixing complicate our ability to estimate growth parameters for the spread of infectious disease, parameters such as R_0, the basic reproductive number. Rate parameters may appear to change erratically as the disease passes through different portions of the affected population, as additional surveillance resources are brought to bear, or as mitigation measures are attempted.

Methods using hierarchical models are well-established for correcting underreporting.[2] A method for estimating detection probability using count data from surveillance is found using Isaac Newton's Binomial Theorem[3]

$$P = \binom{n}{d} (p)^d (1-p)^{n-d} \,. \tag{1}$$

For our purposes, n is the true count of infected hosts which cannot be directly observed. The data, d, is the day's count from the surveillance, p is the detection probability, and P is the probability of the parameters n and p, given the datum d. Given that, in the absence of false-positives, n must be greater than or equal to d, d is a floor value for the true count. The maximum-likelihood estimates of n and p are those which produce the highest value of P, which is achieved though iteration. The result is a method for estimating the detection probability and true count. Newton's Theorem can thus be used to adjust observed imperfect counts to estimates of the true number of cases in the population.

A model that describes population growth in resource limited environments is given by the logistic equation,

$$\frac{dN}{dt} = e^{\alpha\left(1-\frac{N}{K}\right)} \,. \tag{2}$$

For our purposes, N is the number of infected hosts, α is the growth coefficient, and K is the affected population size, that population which is well-mixed with the infected hosts.

The growth coefficient is related to R_0 according to

$$\alpha = 1 + \frac{R_0 - 1}{D}, \tag{3}$$

where D is the incubation time, in days[5]. Since R_0, and thus α, are assumed to be fixed characteristics of the pathogen[6] they are unchanging unless a new pathogenic strain arises through mutations.

Hierarchical models that correct for unsystematic sampling have been used to overcome problems with data collection, and accurately estimate disease dynamics parameters.[1] That is, these estimates are free of over and underestimates. However, these models use machine-learning techniques that require close supervision, including hand calculated estimates of boundary and starting values. This results in a labor and time-consuming analysis. The best chances of managing a disease outbreak occur in its earliest stages, before the disease becomes established in a larger population.[5] Therefore, the utility of models to inform decision-making would be improved though methods that automate and speed their calculation, allowing predictions and assessments to proceed in a timely fashion.

A method for automating parameter estimation can be found using Markov Chain Monte Carlo (MCMC) methods and Gibbs samplers. MCMC methods use large numbers of iterative simulations to estimate the value of complex integrals,[7] such as those for likelihood values of hierarchical models. Because these methods are Bayesian, they may be more suitable for predicting individual observations than maximum-likelihood methods[8] such as those used by Ingersoll.[1] Individual Bayesian estimates for daily changes in the affected population size (K) are detailed in this report.

1.3 Data sources

Open-source data for the CoViD-19 pandemic are available for the Diamond Princess Cruise Ship.[9] Diamond Princess began the sampling period with a population of 2,670 passengers and 1,100 staff. By the end of the sampling period, all those infected had been removed shoreward into quarantine.[10] Additionally, by the end of the sampling period complete surveillance had been attained, so that all passengers had been repeatedly tested for SARS-CoV-2 using polymerase chain-reaction methods. Because testing frequency increased, and all passengers were tested repeatedly by the end of the sampling period, a valid model with underreporting should converge on testing results towards the end of the period, and estimated rates of detection should increase across the period towards $p = 1$.

2. METHODS

2.1 The detection model

A maximum-likelihood estimate of daily detection probability was produced using Newton's Theorem (Figure 2, open dots). These values were then used to create a logistic model for detection probabilities across the entire data series (Figure 2, red trace).

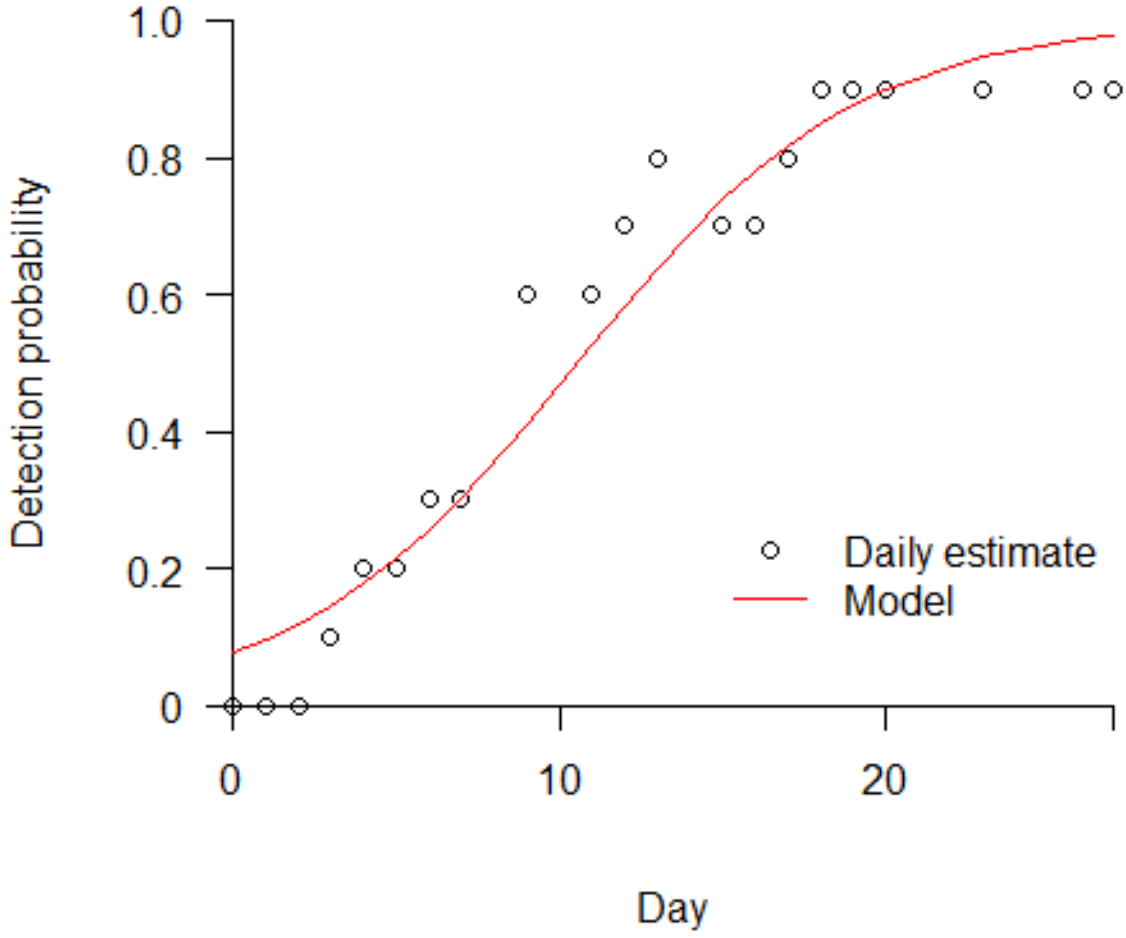

Figure 2. Logistic model for detection probability.

2.2 The logistic growth model

The observed counts of infective cases (Figure 3, black dots) were multiplied by the inverse of the detection probability to produce a daily estimate of the true count of infective hosts (Figure 3, red dots). An MCMC model was then implemented in the software OpenBUGS[11] producing daily estimates of the affected population size and its confidence interval (Figure 3, blue traces), along with an estimate of the growth coefficient. A run of 10,000 iterations was used, discarding the first 2,000 as burn-in.

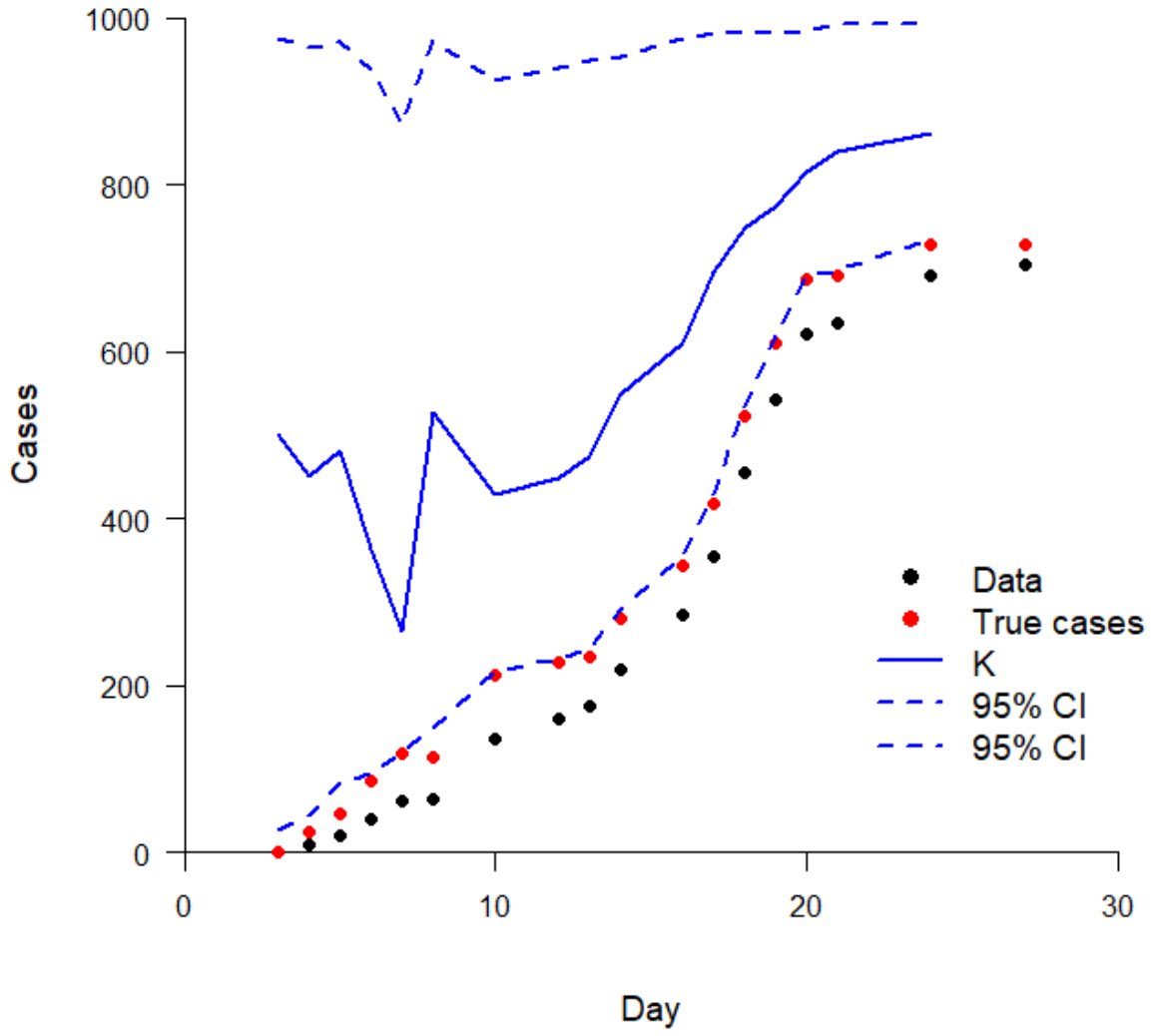

Figure 3. Estimating daily changes in the size of the affected population (K).

Note that the expected value for the affected population size (solid blue trace) tended to decrease until Day 7, due to quarantine efforts. However, the outbreak managed to escape quarantine and the affected population tended to grow between Day 10 and the end of the study period. Because estimation relied on data from subsequent time periods, no estimate was available for the final day (Day 27).

The estimated basic reproductive number is given in Table 1.

Table 1. Estimated R_0.

R_0	Upper 95 % C.I.	Lower 95 % C.I.
1.54	3.04	1.01

3. DISCUSSION

3.1 The Diamond Princess outbreak

According to the model (Figure 3, solid blue trace), SARS-CoV-2 initially spread aboard the Diamond Princess in a population of about 500 individuals. This was later reduced by Day 7 to about 265 individuals, which can be attributed to isolation of infective cases following declaration of a shipboard quarantine on Day 6.[10] The quarantine was, however, not fully effective as epidemic growth resumed following Day 7. Detection probability (Figure 2, red trace) was low at first, and approached $p = 1$ towards the end of sampling period as passengers were subject to repeated testing. Because of its moderate infectivity (Table 1, R_0 of 1.54), partial isolation from the rest those onboard, and low initial levels of detection, the disease was able to persist onboard undetected for an unknown number of days and spread throughout the primary affected population until links with a larger population on Days 7 and 11 triggered a steep period of spread. The pattern of spread seen early in the outbreak, with low-level persistence followed by eruption into exponential growth, cannot be explained by well-mixed, closed population models.[1] Exponential growth never reached its maximum, because the effects of emigration began to take over on Day 19, as passengers disembarked into stricter levels of quarantine.[10] It's possible that movement associated with disembarkation triggered the links on Days 9 and 11, as isolation was interrupted when passengers were repatriated via group air travel.[10] According to the data, no new cases occurred after Day 27.

3.2 The value of modeling K

The affected population size for a particular daily interval (K, Figure 3, solid blue trace) was the size of that population in which spread behaved as if well-mixed. Outside this population, the disease was not spreading at the time. K and its upper confidence boundary (Figure 3, upper dashed blue trace) could be used as a guideline for the size of population that should be under quarantine, to suppress an outbreak with a calculable probability of success. For example, the upper 95 % boundary on Day 7 suggests that at least 871.7 individuals would have to be in quarantine for a 97.5 % chance of containing the outbreak. The public health response[10] suggests that this level of quarantine was not attained by Day 7, which explains the growth in the outbreak that followed.

3.3 Model shortcomings

A highly detailed Susceptible, Exposed, Infected, Recovered (SEIR) model for a networked population was previously employed.[1] The model for the current study was a far simpler logistic model for open-populations due to budget constraints and fails to capture epidemic behavior as completely as the SEIR model. In particular, the SEIR model does a better job of accounting for time lags between the exposed and infective state[1] but requires extensive user input in the maximum-likelihood environment. The author recommends a networked SEIR model be programmed for the MCMC environment, should resources become available so parameter estimates are increasingly automated.

3.4 Success of the demonstration

It was successfully demonstrated that MCMC via Gibbs sampler increased automation for disease dynamics models, by reducing the need for hand-calculated boundary and starting values. While MCMC is more computationally complex than maximum-likelihood methods, it requires less user supervision once programmed, thus can be performed in a shorter time with less expert labor investment. MCMC methods could be generalized to work for a variety of new and emerging diseases, producing useful results to aid decision making early within disease outbreaks, before expert analysts are available for deployment.

ACKNOWLEDGMENTS

Funding was provided by the Director, Combat Capabilities Development Command Chemical Biological Center under the authorities and provisions of Section 2363 of the FY 2018 NDAA to develop new technologies, engineer innovations, and introduce game-changing capabilities.

REFERENCES

[1] Ingersoll, T.E. Spatial dynamics of infectious disease. Proceedings of the Edgewood Chemical Biological Center. **2021**.
[2] Royle, J. A., and R. M. Dorazio. Hierarchical Modeling and Inference in Ecology. Elsevier, London. **2008**.
[3] Kline, M. *History of mathematical thought*. Oxford University Press. **1972**.
[4] Verhulst, P.F. Notice sur la loi que la population poursuit dans son accroissement. Correspondance Mathématique et Physique. 10: 113–121. **1838**.
[5] Anderson, R. and R. May, Infectious Diseases of Humans, Dynamics and Control, Oxford University Press, New York, **1991**.
[6] Kermack, W.O., and McKendrick, A.G., A contribution to the mathematical theory of Epidemics, Proceedings of the Royal Society, A115, 700–721. **1927**.
[7] Robert, C. and G. Casella. Monte Carlo Statistical Methods. Springer-Verlag, New York. **2004**.
[8] McCarthy, M. A., Bayesian Methods for Ecology. Cambridge University Press, Cambridge. **2007**.
[9] Center for Systems Science and Engineering (CSSE). *COVID-19 Dashboard*. Johns Hopkins University (JHU). **2021**.
[10] CDC. Public Health Responses to COVID-19 Outbreaks on Cruise Ships — Worldwide, February–March 2020, *CDC Weekly*. **2020**, *69*(12), pp347–352.
[11] Spiegelhalter DJ, A. Thomas, N.G. Best, and D. Lunn. WinBUGS Version 2.0 Users Manual. MRC Biostatistics Unit, Cambridge. URL http://mathstat.helsinki.fi/openbugs/. **2004**.

MXene Inactivation of SARS-CoV-2 Proxy φ6

Shaun Debow[a]*, Steven Harvey[a]*, Brendan DeLacy[b]
[a]U.S. Army Combat Capabilities Development Command Chemical Biological Center, Research & Technology Directorate, 8198 Blackhawk Rd, Aberdeen Proving Ground, MD 21010
[b]Ballydel Technologies, Inc. 200 Powder Mill Road, Wilmington, DE 19803

ABSTRACT

Novel materials to inhibit transmission and viability of highly pathogenic viruses, and methods to safely evaluate these novel materials, have gained significant interest within the scientific community since the beginning of the SARS-CoV-2 pandemic. One approach to safely evaluate novel materials is to identify suitable, non-pathogenic viral surrogates having lower biosafety requirements. Surrogates can reduce safety risks to personnel by simplifying handling procedures, lower experimental costs and resources required for Biosafety Level 3 containment and increase the number of laboratories participating in complementary research, thus resulting in faster screening of novel materials capable of inactivating or inhibiting a target virus. Herein, we have investigated the phi6 bacteriophage, an enveloped ribonucleic acid virus, to act as a suitable surrogate for the enveloped ribonucleic acid SARS-CoV-2 coronavirus. To better understand the potential for the phi6 bacteriophage to perform as a surrogate, we evaluated inhibition of the phage after treatment with $Ti_3C_2T_x$ MXene, an emerging class of two-dimensional materials that have recently shown the potential to directly inhibit the SARS-CoV-2 novel coronavirus. Our results show no difference in phi6 inhibition after treatment with $Ti_3C_2T_x$ MXene.

Keywords: SARS-CoV2, coronavirus, $Ti_3C_2T_x$ MXene, phi6, bacteriophage, inactivation, inhibition.

1. INTRODUCTION

1.1 Background

Disinfection and inactivation of the ribonucleic acid (RNA) SARS-CoV-2 virus on surfaces has typically required hazardous chemicals,[1] harmful radiation (UV_{254}),[2] concentrated ozone[3] or high temperatures.[4,5] These chemicals and conditions can pose a significant hazard to operators treating surfaces, other nearby collateral, or temperature sensitive materials. Identifying novel, non-hazardous materials and safe methods to evaluate efficacy is important to reduce adverse outcomes posed by hazardous materials or conditions. Recently published research from Turkey suggests that the 2D material $Ti_3C_2T_x$ MXene may effectively inactivate and decontaminate SARS-CoV-2 on surfaces under ambient conditions.[6] Elucidating viral inactivation and surface effects on MXene could enable self-decontaminating personal protective equipment or of high-touch surfaces.[3,7,8] Evaluating SARS-CoV-2 inactivation is expensive due to the high cost of both Biosafety Level 3 facilities and qualified personnel capable of handling SARS-CoV-2, a Centers for Disease Control and Prevention select agent. Alternatively, the enveloped RNA bacteriophage phi6 has been used as a surrogate for several enveloped human respiratory viruses (e.g. Ebola[9], influenza (H5N1)[9], and common-cold coronaviruses[2]), with a recent study suggesting that phi6 may be a good surrogate for SARS-CoV-2.[2] We have evaluated the potential for phi6 to act as a suitable surrogate by studying viral inhibition by novel $Ti_3C_2T_x$ MXene substrates.

1.2 SARS-CoV-2

The SARS-CoV-2 coronavirus is the causative agent for the Coronavirus Disease 2019. It is a single-stranded RNA phospholipid-bilayer-enveloped virus of the coronaviridae family, with a diameter of approximately 90 nm.[10] The structure as illustrated in Figure 1 (left), shows the coronavirus having a spherical geometry with spike proteins protruding from its phospholipid envelope.[2] In simple terms, these spike proteins enable the coronavirus to attach to a human angiotensin-converting enzyme 2,[11] undergo receptor-mediated endocytosis, and release its nucleocapsid containing the single-stranded RNA payload into the host cell cytoplasm, infecting the host.

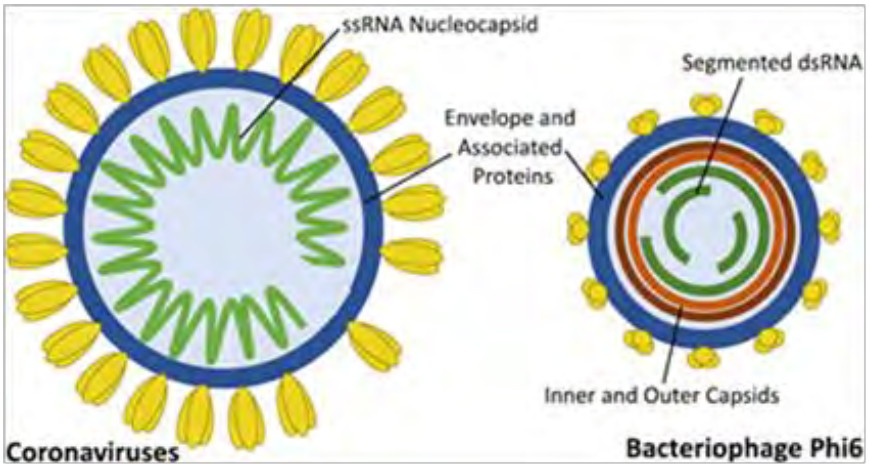

Figure 1. Graphical representation of Coronaviruses (left) and the Bacteriophage Phi 6 (right); figure from Silverman.[2]

1.3 Phi6 bacteriophage

The pseudomonas phage phi6 is a double-stranded RNA phospholipid-bilayer-enveloped virus of the cystoviridae family.[12] As illustrated in Figure 1 (right), the phi6 bacteriophage is very similar to a coronavirus, it has a spherical geometry and a diameter of approximately 85 nm, and its outer surface is decorated with protruding attachment spikes.[2,12] We must note that the phi6 bacteriophage attachment spikes differ from the attachment spikes on the coronavirus. They enable infection of *Pseudomonas syringae* bacteria through recognition of the pilin receptor and adsorption to the host pili, not human cells.[12,13]

1.4 Phi6 as a proxy for SARS-COV-2

Multiple studies have demonstrated that phi6 is a good surrogate for lipid-enveloped viruses, including coronaviruses causing the common cold, SARS-1, and Middle Eastern Respiratory Syndrome.[2,3,7,9,14,15] We have shown that there are many structural and chemical similarities between the phi6 bacteriophage (cystoviridae family) and the coronavirus (coronaviridae family). A study by Silverman and coworkers has presented a systematic review of and meta-analysis of available data to support evaluating phi6 as a surrogate for human coronaviruses in wastewater.[2] We will leverage this existing knowledge to evaluate phi 6 as a potential surrogate, specifically for the novel SARS-CoV-2 virus belonging to the genus betacoronavirus.[2]

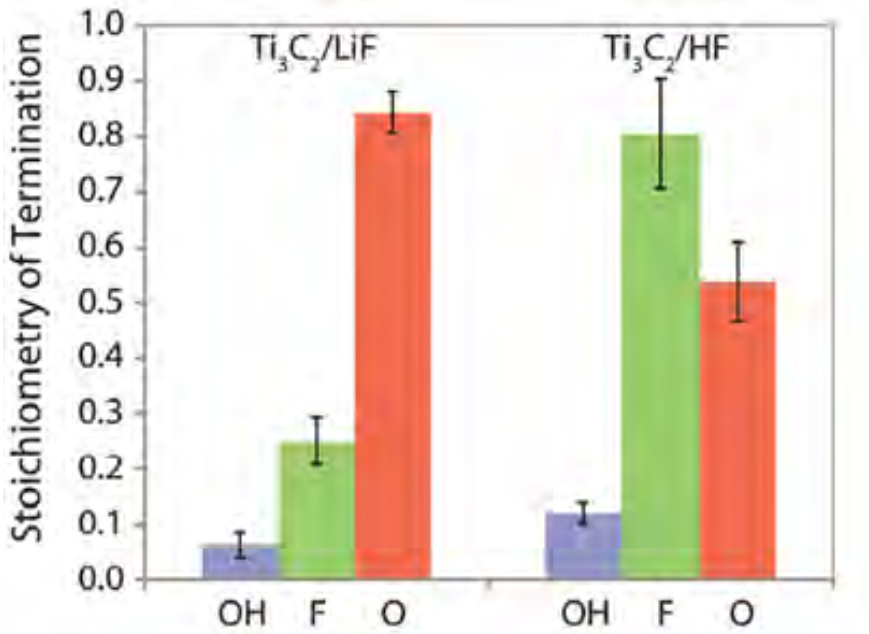

Figure 2. Stoichiometry of MILD and HF etched $Ti_3C_2T_x$ MXene; figure from Hope.[17]

1.5 MXenes and antimicrobial activity

At the nanoscale, MXenes are layered two-dimensional materials having a composition of $M_{n+1}X_nT_x$, where M represents an early transition metal, X being nitrogen or carbon, T representing a variable surface termination (such as F, Cl, O, OH) and where n = 1, 2, or 3.[18] Rich surface terminations result in a hydrophilic character that enables good dispersion in aqueous suspension, provide an electronegative surface and reactive sites, while metallic and carbon layers promote electron conduction. Surface terminations will vary based upon the method to prepare MXene. Two common methods are direct etching with concentrated hydrofluoric acid (HF) and a milder method (MILD) using lithium fluoride and hydrochloric acid (HCl) to produce HF in-situ. The stoichiometry of these terminations is shown in Figure 2 for each etching method. The unique characteristics have enabled MXenes to find applications in water purification and desalination,[19] super capacitors,[20-24] photocatalysts,[25] microwave absorption and shielding,[26,27] and as antimicrobial fibers.[28] Recently, MXenes have been reported to inhibit or inactivate bacteria, viruses, and fungi.[28-35] In some cases, MXene has been shown to maintain antibacterial activity after incorporation into electrospun nanofibers, extending the number of potential applications.[28] In this study, we evaluated inactivation of phi6 by $Ti_3C_2T_x$ MXene.

2. METHODOLOGY

2.1 Microbe growth and assay

2.1.1 Microbes and preparation

The cystoviridae phi6 *Pseudomonas* phage and *Pseudomonas syringae* were used in this study. Luria Broth (LB) from acumedia® (New Brunswick, NJ) was prepared at a concentration of 20 g/L and sterilized at 121 °C for 20 minutes in an autoclave. *P. Syringae* was grown overnight in LB broth at 28 °C with shaking.

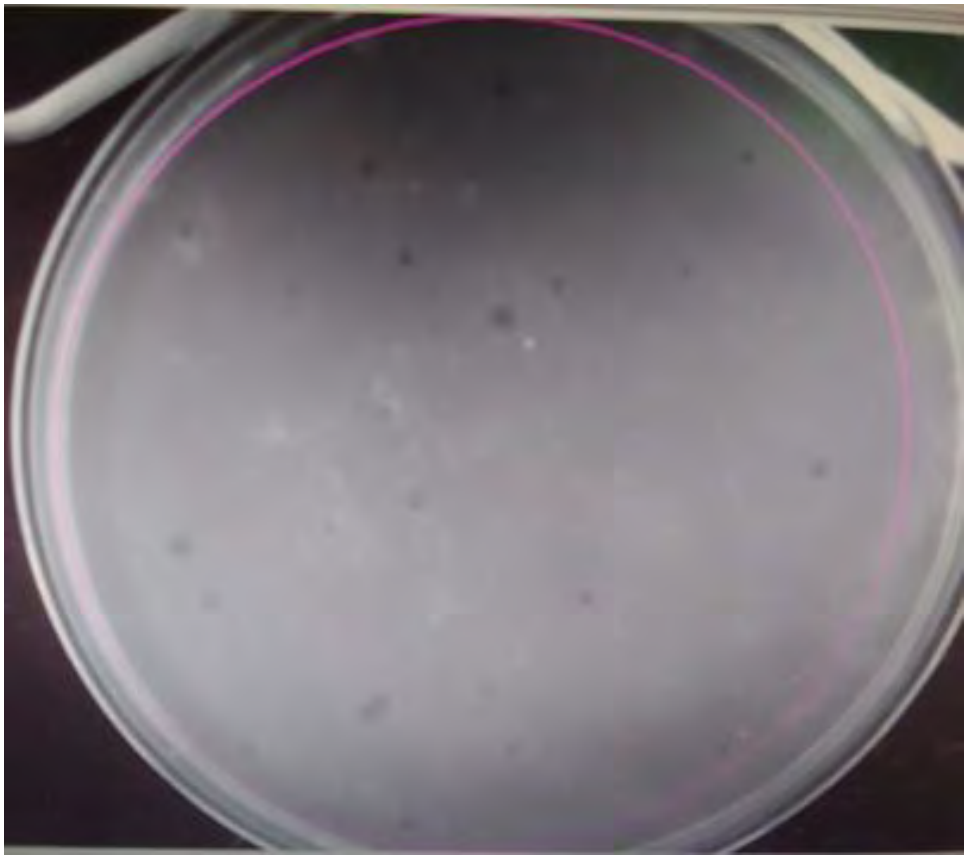

Figure 3. A typical growth plate showing phi6 plaques in a lawn of *P. syringae* following overnight incubation.

2.1.2 Phi6 assay

Phi6 were prepared from purified plaques and stored at -70 °C. For use, defrosted phage were diluted in sterile LB and 100 µL of phage was mixed with 100 µL of *P. syringae* for 10 minutes to which 4 mL of soft LB agar (7.5 g/L agar) was added at 55 °C and plated on LB plates immediately, followed by growth overnight at 28 °C. Plates with approximately 10–100 plaques (typically 10^{-6} dilutions of phi6) were manually counted. To determine effects of MXene on the phage, 100 µL of appropriately diluted MXene was incubated with phi6 prior to addition of bacteria and processed as above. Initial tests determined variability of plaque counts to be less than five-fold. A typical plate is shown in Figure 3.

2.2 Preparation of $Ti_3C_3T_x$ MXene, MILD method

$Ti_3C_2T_x$ was prepared using previously reported methods to selectively etch Al layers from a layered Ti_3AlC_2 MAX phase precursor using a modified mild etching procedure.[36] Briefly, 1.6 g of lithium fluoride was dissolved in 20 mL of 6 M aqueous HCl, and 2 g of Ti_3AlC_2 MAX powder was added to this solution. The reaction was carried out at 40 °C for 40 hours under stirring. The resulting suspension was washed with deionized water several times until the pH of the supernatant was near 6. The precipitate was collected and reacted with dimethylsulfoxide at room temperature for 20 hours under stirring. The resulting suspension was washed with deionized water 3 times using centrifugation (supernatant was discarded and new deionized water was added for each washing) and bath sonication for 1 hour. The exfoliated nanosheets were obtained by centrifuging the suspension at 3,500 rpm and the supernatant was collected. This produced a MXene suspension having a concentration of 5.45 mg/mL, which was used in each series of the phi6 assay.

2.3 Preparation of $Ti_3C_3T_x$ MXene, HF method

$Ti_3C_2T_x$ was prepared using previously reported methods to selectively etch Al layers from a layered Ti_3AlC_2 MAX phase precursor using a modified hydrofluoric acid and hydrochloric acid procedure.[37] Briefly, 6 g of Ti_3AlC_2 MAX phase, 72 mL HCl, 36 mL deionized (DI) water and 12 mL HF were mixed for etching. A 12:6:2 ratio (HCl:H2O:HF) per 1 g of MXene was used. The solution was etched for 24 hours at 35 °C, washed with DI water by sequential centrifugation until a neutral pH was reached. After washing, 6 g of LiCl in 60 mL of DI water was used to aid delamination and stirred for 16 hours at 35 °C. The washing process was repeated until a neutral pH was reached. MXene sediment was removed by collecting the supernatant after centrifugation at 3,500 RPM for 30 minutes, the remaining sediment was discarded. The resulting MXene was diluted with DI water to form a suspension with a concentration of 10.9 mg/mL; this was used in each series of the phi6 assay.

2.4 Surface alkalized $Ti_3C_3T_x$ MXene

$Ti_3C_2T_x$ MXene was surface alkalized by treatment with potassium hydroxide following a previously reported method.[38] Briefly, 50 mg of $Ti_3C_2T_x$ MXene HF was mixed with 10 mL of 2M potassium hydroxide and stirred for 4 hours at 35 °C, to substitute F surface terminations with OH. The suspension was then washed twice with DI water and filtered using a MilliporeSigma® (St. Louis, MO) vacuum-assisted filter funnel with a 100 nm pore-size hydrophilic filter Celgard membrane. The treated MXene was then collected and washed two more times using DI water with centrifugation for 15 minutes at 8,000 RPM. This surface modified MXene was used in each series of the phi6 assay.

3. RESULTS AND DISCUSSION

3.1 Results of phi6 – *P. Syringae* assays

Assays were prepared as described in section 2.1.2 for $Ti_3C_2T_x$ MXene, prepared using both the MILD and HF etching methods; $Ti_3C_2T_x$ MXene with surface alkalization; and, both precursor Ti_3AlC_2 MAX phases used in the MILD and HF etching methods.

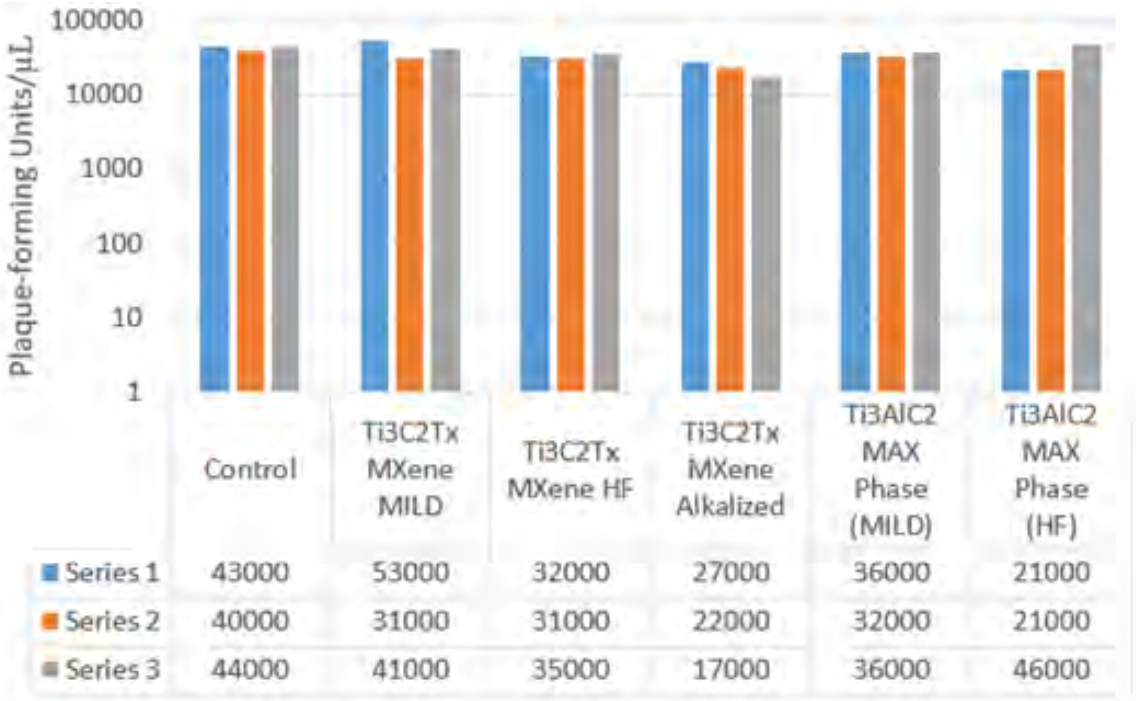

Figure 4. Experimental series results.

Three experimental series were conducted for each assay utilizing MXene or MAX phase and for the control. Results from the control assays demonstrated a high reproducibility as shown in Figure 4, having an average of 42,333 PFU/µL (± 2,082). The control assays utilized methods previously described but without addition of any MXene or MAX phase.

Three experimental series also were prepared for each MXene. The results shown in Figure 4 indicate none of the assays prepared after MXene treatment demonstrated any significant phi6 inactivation. The averages and deviation for each MXene series were: $Ti_3C_2T_x$ MXene (MILD) 41,667 PFU/µL (± 11,015); $Ti_3C_2T_x$ MXene (HF) 32,667 PFU/µL (± 2,082); and $Ti_3C_2T_x$ MXene Alkalized 22,000 PFU/µL (± 5,000).

Additional assays were prepared to evaluate any effect of each precursor MAX phase on phi6 inactivation. The MAX phase lacks the same surface terminations and stoichiometry found on etched MXene, such as F, OH, O. The averages and deviations for each MAX phase were found to be $Ti_3C_2T_x$ MAX Phase (MILD) 34,667 PFU/µL (± 2,309); and $Ti_3C_2T_x$ MAX Phase (HF) 29,333 PFU/µL (± 14,433). Testing the MAX phase would determine if surface area and surface terminations affected inactivation. No significant inactivation was observed for either MAX phase variant.

3.2 Discussion

Previously reported results demonstrated that MXene can provide SARS-CoV-2 inactivation up to 99 %.[6] We sought to identify a suitable surrogate using the phi6 bacteriophage to reduce the hazards, costs, and time to perform inactivation studies for MXene. Results have shown that phi6 bacteriophage is not significantly inhibited by MXene and doesn't perform as a viable surrogate to approximate previously reported SARS-CoV-2 inactivation. We hypothesize this variation is associated with differences between the phi6 and SARS-CoV-2 spike attachment proteins. These proteins may affect virus-substrate interactions and thus inactivation. Future research for substrate-induced inactivation should focus on proxies more closely related to the SARS-CoV-2 coronavirus, such as the bovine coronavirus (BCoV) strain Mebus, which has been suggested as a potential candidate for SARS-CoV-2.[39] Any use of a closely related virus would require a strict safety assessment due to the potential for human infection and illness.

4. CONCLUSION

Phi6 bacteriophage was investigated as a surrogate for the SARS-CoV-2 coronavirus when introduced to a MXene substrate, a material previously reported to inhibit SARS-CoV-2.[6] To evaluate suitability as a surrogate, *P. syringae* – phi6 assays were developed and used to measure phi6 inhibition after phi6 was exposed to $Ti_3C_2T_x$ MXene substrates. Results show that phi6 is not inhibited by MXene and doesn't perform as a viable surrogate to approximate previously reported SARS-CoV-2 inactivation. This variation is potentially associated with differences in spike attachment proteins between the phi6 bacteriophage and coronaviruses. Future research should focus on similarity of the spike attachment of the surrogate and SARS-CoV-2 coronavirus. A recently released pre-print suggests the BCoV strain Mebus as a potential candidate for human coronaviruses.[39] A strict safety assessment would be necessary to determine potential hazards associated with BCoV testing due to its potential to cause mild illness in humans. Safely evaluating novel materials by utilizing suitable viral surrogates remains a challenge and an area of opportunity for future research.

ACKNOWLEDGMENTS

Funding was provided by the Director, Combat Capabilities Development Command Chemical Biological Center under the authorities and provisions of Section 2363 of the FY 2018 NDAA to develop new technologies, engineer innovations, and introduce game-changing capabilities. The authors extend their sincere gratitude to the Senior Research Scientists, internal and external senior scientists, and professionals who invested their time to evaluate the initial proposal. The authors would like to further thank Drexel University and Texas A&M University for their support of this project.

REFERENCES

[1] Kwok, C.S; Dashti, M.; Tafuro, J.; Nasiri, M.; Muntean, E-A.; Wong, N.; Kemp, T.; Hills, G.; Mallen, C.D. Methods to disinfect and decontaminate SARS-CoV-2: a systematic review of in vitro studies. *Ther. Adv. Infect. Dis*. **2021**, *8*, pp 1–12.

[2] Silverman, A.I.; Boehm, A.B. Systematic Review and Meta-Analysis of the Persistence and Disinfection of Human Coronaviruses and Their Viral Surrogates in Water and Wastewater. *Environ. Sci. Technol. Lett.* **2020**, *7* (8), pp 544–553.

[3] Franke, G.; Knobling, B.; Brill, F.H.; Becker, B.; Klupp, E.M.; Campos, C.B.; Pfefferle, S.; Lütgehetmann, M.; Knobloch, J.K. An automated room disinfection system using ozone is highly active against surrogates for SARS-CoV-2. *J. Hosp. Infect*. **2021**, *112*, pp 108–113.

[4] Kim, Y-I.; Casel, M.A.B.; Kim, S-M.; Kim, S-G.; Park, S-J.; Kim, E-H.; Jeong, H.W.; Poo, H.W.; Choi, Y.K. Development of severe acute respiratory syndrome coronavirus 2 (SARS-CoV-2) thermal inactivation method with preservation of diagnostic sensitivity. *J. Microbiol.* **2020**, *58* (10), pp 886–891.

[5] Campos, R.K.; Jin, J.; Rafel, G.H.; Zhao, M.; Liao, L.; Simmons, G.; Chu, S.; Weaver, S.C.; Chiu, W.; Cui, Y. Decontamination of SARS-CoV-2 and Other RNA Viruses from N95 Level Meltblown Polypropylene Fabric Using Heat under Different Humidities. *ACS Nano*. **2020**, *14* (10), pp 14017–14025.

[6] Unal, M.A.; Bayrakdar, F.; Fusco, L.; Besbinar, O.; Shuck, C.E.; Yalcin, S.; Erken, M. T.; Ozkul, A.; Gurcan, C.; Panatli, O.; Summak, G. Y.; Gokce, C.; Orecchioni, M.; Gazzi, A.; Vitale, F.; Somers, J.; Demir, E.; Yildiz, S.S.; Nazir, H.; Grivel, J.-C.; Bedognetti, D.; Crisanti, A.; Akcali, K.C.; Gogotsi, Y.; Delogu, L.G.; Yilmazer, A. 2D MXenes with antiviral and immunomodulatory properties: A pilot study against SARS-CoV-2. *Nano Today.* **2021**, *38*, p 101136.

[7] Brown, T.W.; Chen, W.; Casanova, L.M. Survival and disinfection of an enveloped surrogate virus on Tyvek suits used for health care personal protective equipment. *Am. J. Infect. Control.* **2016**, *44* (12), pp 1734–1735.

[8] Liu, Q.; Brookbank, L.; Ho, A.; Coffey, J.; Brennan, A.B.; Jones, C.J. Surface texture limits transfer of S. aureus, T4 bacteriophage, influenza B virus and human coronavirus. *PLoS One.* **2020**, *15* (12), p e0244518.

[9] Whitworth, C.; Mu, Y.; Houston, H.; Martinez-Smith, M; Noble-Wang, J.; Coulliette-Salmond, A.; Rose, L. Persistence of Bacteriophage Phi 6 on Porous and Nonporous Surfaces and the Potential for Its Use as an Ebola Virus or Coronavirus Surrogate. *Appl. Environ. Microbiol.* **2020**, *86* (17*)*, pp e01482-20.

[10] Klein, S.; Cortese, M.; Winter, S.L.; Wachsmuth-Melm, M.; Neufeldt, C.J.; Cerikan, B.; Stanifer, M.L.; Boulant, S.; Bartenschlager, R.; Chlanda, P. SARS-CoV-2 structure and replication characterized by in situ cryo-electron tomography. *Nat. Commun.* **2020**, *11*, p 5885.
[11] Hoffmann, M.; Kleine-Weber, H.; Schroeder, S.; Krüger, N.; Herrier, T.; Erichsen, S.; Schiergens, T.S.; Herrier, G.; Wu, N-H.; Nitsche, A.; Müller, M.A.; Drosten, C.; Pöhlmann, S. SARS-CoV-2 Cell Entry Depends on ACE2 and TMPRSS2 and Is Blocked by a Clinically Proven Protease Inhibitor. *Cell*. **2020**, *181* (2), pp 271–280.e8.
[12] Poranen, M.M.; Mäntynen, S. ICTV Virus Taxonomy Profile: Cystoviridae. *J. Gen. Virol.* **2017**, *98* (10), pp 2423–2424.
[13] Callanan, J.; Stockdale, S.R.; Shkoporov, A.; Draper, L.A.; Ross, R.P.; Hill, C. RNA Phage Biology in a Metagenomic Era. *Viruses*. **2018**, *10* (7), p 386.
[14] Aquino de Carvalho, N.; Stachler, E.N.; Cimabue, N.; Bibby, K. Evaluation of Phi6 Persistence and Suitability as an Enveloped Virus Surrogate. *Environ. Sci. Technol.* **2017**, *51* (15), pp 8692–8700.
[15] Ye, Y.; Chang, P.H.; Hartert, J.; Wigginton, K.R. Reactivity of Enveloped Virus Genome, Proteins, and Lipids with Free Chlorine and UV_{254}. *Environ. Sci. Technol.* **2018**, *52* (14), pp 7698–7708.
[16] Pal, M.; Berhanu, G.; Desalegn, C.; Venkataramana, K. Severe Acute Respiratory Syndrome Coronavirus-2 (SARS-CoV-2): An Update. *Cereus*. **2020**, *12* (3), p e7423.
[17] Hope, M.A.; Forse, A.C.; Griffith, K.J.; Laukatskaya, M.R.; Ghidu, M.; Gogotsi, Y.; Grey, C.P. NMR reveals the surface functionalisation of Ti_3C_2 MXene. *Phys. Chem. Chem. Phys.* **2016**, *18* (7), pp 5099–5102.
[18] Alhabeb, M.; Maleski, K.; Anasori, B.; Lelyukh, P.; Clark, L.; Sin, S.; Gogotsi, Y. Guidelines for Synthesis and Processing of Two-Dimensional Titanium Carbide ($Ti_3C_2T_x$ MXene). *Chem. Mater*. **2017**, *29* (18), pp 7633–7644.
[19] Li, R.; Zhang, L.; Shi, L.; Wang, P. MXene Ti_3C_2: An Effective 2D Light-to-Heat Conversion Material. *ACS Nano*. **2017**, *11* (4), pp 3752–3759.
[20] Ling, Z.; Ren, C.E.; Zhao, M.-Q.; Yang, J. Gimmarco, J.M.; Qiu, J.; Barsoum, M.W.; Gogotsi, Y. Flexible and conductive MXene films and nanocomposites with high capacitance. *Proc. Natl. Acad. Sci. U.S.A.* **2014**, *111* (47), pp 16676–16681.
[21] Tian, Y.; Yang, C.; Que, W.; Liu, X.; Yin, X.; Kong, L.-B. Flexible and free-standing 2D titanium carbide film decorated with manganese oxide nanoparticles as a high volumetric capacity electrode for supercapacitor. *J. Power Sources.* **2017**, *359*, pp 332–339.
[22] Wen, Y.; Rufford, T.E.; Chen, X.; Li, N.; Lyu, M.; Dai, L.; Wang, L. Nitrogen-doped $Ti_3C_2T_x$ MXene electrodes for high-performance supercapacitors. *Nano Energy*. **2017**, *38*, pp 368–376.
[23] Xin, Y.; Yu, Y.-X. Possibility of bare and functionalized niobium carbide MXenes for electrode materials of supercapacitors and field emitters. *Mater. Des.* **2017**, *130*, pp 512–520.
[24] Xu, S.; Wei, G.; Li, J.; Ji, Y.; Klyui, N.; Izotov, V.; Han, W. Binder-free $Ti_3C_2T_x$ MXene electrode film for supercapacitor produced by electrophoretic deposition method. *Chem. Eng. J.* **2017**, *317*, pp 1026–1036.
[25] Peng, C.; Yang, X.; Li, Y.; Yu, H.; Wang, H.; Peng, F. Hybrids of Two-Dimensional Ti_3C_2 and TiO_2 Exposing {001} Facets toward Enhanced Photocatalytic Activity. *ACS Appl. Mater. Interfaces.* **2016**, *8* (9), pp 6051–6060.
[26] Han, M.; Yin, X.; Li, X.; Anasori, B.; Zhang, L.; Cheng, L.; Gogotsi, Y. Laminated and Two-Dimensional Carbon-Supported Microwave Absorbers Dervied from MXenes. *ACS Appl. Mater. Interfaces.* **2017**, *9* (23), pp 20038–20045.
[27] Li, X.; Yin, X.; Han, M.; Song, C.; Xu, H.; Hou, Z.; Zhang, L.; Cheng, L. Ti_3C_2 MXenes modified with in situ grown carbon nanotubes for enhanced electromagnetic wave absorption properties. *J. Mater. Chem. C.* **2017**, *5* (16), pp 4068–4074.
[28] Mayerberger, E.A.; Street, R.M.; McDaniel, R.M.; Barsoum, M.W.; Schauer, C.L. Antibacterial properties of electrospun $Ti_3C_2T_z$ (MXene)/chitosan nanofibers. *RSC Adv.* **2018**, *8* (62), pp 35386–35394.
[29] Rasool, K.; Helal, M.; Ali, A.; Ren, C.E.; Gogotsi, Y.; Mahmoud, K.A. Antibacterial Activity of $Ti_3C_2T_x$ MXene. *ACS Nano.* **2016**, *10* (3), pp 3674–3684.
[30] Shamsabadi, A.A.; Gh, M.S.; Anasori, B.; Soroush, M. Antimicrobial Mode-of-Action of Colloidal $Ti_3C_2T_x$ MXene Nanosheets. *ACS Sustainable Chem. Eng.* **2018**, *6* (12), pp 16586–16596.
[31] Sun, W.; Wu, F.-G. Two-Dimensional Materials for Antimicrobial Applications: Graphene Materials and Beyond. *Chem.- Asian J.* **2018**, *13* (22), pp 3378–3410.
[32] Miao, H.; Teng, Z.; Wang, C.; Chong, H.; Wang, G. Recent Progress in Two-Dimensional Antimicrobial Nanomaterials. *Chemistry*. **2019**, *25* (4), pp 929–944.
[33] Huang, K.; Li, Z.; Lin, J.; Han, G.; Huang, P. Two-dimensional transition metal carbides and nitrides (MXenes) for biomedical applications. *Chem. Soc. Rev.* **2018**, *47* (14), pp 5109–5124.

[34] Zheng, J.; Li, J.; Zhang, L.; Chen, X.; Yu, Y.; Huang, H. Post-graphene 2D materials-based antimicrobial agents: focus on fabrication strategies and biosafety assessments. *J. Mater. Sci.* **2020**, *55* (17), pp 7226–7246.
[35] Wang, W.; Feng, H.; Liu, J.; Zhang, M.; Liu, S.; Feng, C.; Chen, S. A photo catalyst of cuprous oxide anchored MXene nanosheet for dramatic enhancement of synergistic antibacterial ability. *Chem. Eng. J.* **2020**, *386*, p 124116.
[36] Sarang, K.T.; Zhao, X.; Holta, D.; Radovic, M.; Green, M.J.; Oh, E.-S.; Lutkenhaus, J.L. Minimizing two-dimensional $Ti_3C_2T_x$ MXene nanosheet loading in carbon-free silicone anodes. *Nanoscale*. **2020**, *12* (40), pp 20699–20709.
[37] Wang, X.; Mathis, T.S.; Sun, Y.; Tsai, W,-Y.; Shpigel, N.; Shao, H.; Zhang, D.; Hantanasirisakul, K.; Malchik, F.; Balke, N.; Jiang, D.-E.; Simon, P.; Gogotsi, Y. Titanium Carbide MXene Shows an Electrochemical Anomaly in Water-in-Salt Electrolysis. *ACS Nano*. **2021**, *15* (9), pp 15274–15284.
[38] Ye, M.; Wang, X.; Liu, E.; Ye, J.; Wang, D. Boosting the Photocatalytic Activity of P25 for Carbon Dioxide Reduction by using a Surface-Alkalinized Titanium Carbide MXene as Cocatalyst. *ChemSusChem*. **2018**, *11* (10), pp 1606–1611.
[39] Karthigeyan, K.P.; Flanigan, C.; Machado, D.J.; Kiziltas, A.A.; Janies, D.A.; Chen, J.; Cooke, D.; Lee, M.V.; Saif, L.J.; Henegar, S.; Jahnes, J.; Mielewski, D.F.; Kwiek, J.J. Heat efficiently inactivates coronavirus inside vehicles. bioRxiv preprint: DOI: 10.1101/1021.09.08.459486

Novel CWA reactive material by grafting Zr-MOF secondary building units on functionalized supports

Ann M. Kulisiewicz[a], Sergio J. Garibay[a,b], Trenton B. Tovar[a]
[a]U.S. Army Combat Capabilities Development Command Chemical Biological Center, Research & Technology Directorate, 5183 Blackhawk Rd, Aberdeen Proving Ground, MD 21010
[b]Leidos, Inc., 3465 Box Hill Corporate Center Dr., Abingdon, MD 21009

ABSTRACT

Metal-organic frameworks with Zr-based secondary building units have shown promise as materials for protection and self-decontamination of chemical warfare agents. In particular, Zr-based secondary building units have been previously determined to be the primary reactive component in these materials for hydrolysis reactions. However, the multitude of variables inherent to metal-organic frameworks structures (e.g. pore size, pore structure, connectivity, crystal size, functional groups, and monocarboxylic acid modulators used in synthesis) complicate the understanding of the reactivity of the material, especially the role of the secondary building units. In this work, we have explored the reactivity of a simplified system consisting of Zr- secondary building unit clusters grafted onto silica supports to both develop a novel reactive material and to better understand the reactivity of the secondary building units component of the metal-organic frameworks independent of the other variables inherent to metal-organic frameworks structures. Silica supports functionalized with sulfuric acid or phosphoric acid groups were used to tether individual Zr- secondary building units clusters to the surface. The tethered Zr- secondary building units cluster were then activated to remove some of the monocarboxylic acid modulators and generate unsaturated reactive sites. The final products were characterized by powder x-ray diffraction and N_2 isotherm to confirm porosity of the material and retained crystallinity of the secondary building units cluster post-attachment. Hydrolysis reactivity of these materials was assessed through Nuclear Magnetic Resonance experiments under buffered conditions in the presence of dimethyl 4-notrophenyl phosphate, a nerve agent simulant.

Keywords: metal-organic framework, catalysis, acid-modified silica

1. INTRODUCTION

Developing protective equipment for chemical warfare agents (CWAs) and other toxic compounds is a key goal of the military. Current protective equipment traps CWAs by physical adsorption, so desorption becomes a possible cross-contamination hazard during disposal. As such, significant effort has been put into developing materials that can both adsorb and subsequently react with CWAs to self-detoxify. One promising set of materials for this application is metal-organic frameworks (MOFs).

MOFs are materials consisting of metal nodes, referred to as secondary building units (SBUs), bridged in a crystalline arrangement by organic linkers to create a porous framework. By varying the SBU and linker, a wide array of MOFs can be synthesized with different structural or chemical properties tailored to a specific application. MOFs containing $Zr_6O_4(OH)_4^{12+}$ SBUs have recently shown promise as catalytically active materials for nerve agent hydrolysis. This includes UiO-66, UiO-67, NU-1000, NU-901, MOF-808, and many variants of these structural topologies with functionalized linkers. For each of these MOFs, the hydrolysis reaction mechanism of VX and GB depends only on the SBU and not the linker.[1] Despite having the same reaction site and mechanism, the reaction rate varies greatly based on both the MOF and the agent. Currently, the reason why some Zr-MOFs perform better for agent hydrolysis is not understood.

One of the key limitations for why reactivity is poorly understood is the inability to quantify the number of active sites within a MOF. Different Zr-MOFs can have connectivity of six, eight, or twelve linkers per SBU, potentially revealing more active Zr sites. Due to pore size, it has been hypothesized that some agents cannot access the interior of some MOFs based on steric constraints, thus reactivity is limited only to sites on the surface causing crystal size to become the main determinant for reactivity. However, crystal sizes are determined by synthesis conditions and can vary

greatly. In some MOFs, the presence of defect sites, which cannot be accurately quantified, and which also depend on synthesis conditions, have been shown to greatly impact reactivity.

MOF linkers can further complicate the understanding of reactivity profiles. While linkers do not participate in the hydrolysis reaction, linker topology can create steric effects at the SBU which can affect the adsorption and subsequent reactivity of the MOF with CWAs. In addition, functionalized linkers could induce electronic effects on the SBU thereby affecting reactivity. Current efforts are attempting to develop MOF design rules based on correlations of these many variables with respect to reactivity to predict the ideal MOF for CWA protection. However, these studies do not seek to understand the basic interactions of the agent with the SBU that drives hydrolysis reactivity. Therefore, we proposed to study hydrolysis reactions on Zr-MOF SBU clusters independent of the MOF structure in an effort to better understand the reactivity of the Zr-SBU cluster and to develop a novel reactive material. The reactive material consists of an inert, mesoporous silica support functionalized with different acid groups to tether a quantifiable number of Zr-SBU clusters to the surface. This material was then assessed for hydrolysis activity when reacted with dimethyl 4-notrophenyl phosphate (DMNP), a nerve agent simulant, under buffered aqueous conditions.

2. EXPERIMENTAL METHODS

2.1 Synthesis

2.1.1 SBU cluster synthesis

All reagents were purchased from commercial sources and used without further purification. Zr_6-, and Zr_{12}-SBUs was synthesized according to modified literature procedures from Pappas et al.[2] and Bezrukov et al.[3] respectively.

$[Zr_6(O)_4(OH)_4(H_2O)_8(Gly)_8]$ 12Cl $8H_2O$ cluster synthesis: In an 8-dram vial, 0.403 g of $ZrOCl_2$ $8H_2O$ (1.25 mmol) was dissolved in 12 ml H_2O. Glycine was added to this vial (0.375 g, 5 mmol), followed by 0.1 mL 8 mM HCl (aq) solution. After briefly stirring the solution (5 min) the vial was heated to 98 °C for 4 days which slowly evaporated off the water. The gel was recrystallized with 4-6 mL of hot DI water at 100 °C on a hot plate. Upon heating at 100 °C and evaporation ~ 3 mL of water remained. The vial was removed from the hot plate and allowed to cool for two hours, resulting in a white solid. The cluster was solvent exchanged three times with 3 ml $CHCl_3$.

$Zr_{12}O_8(OH)_8(AA)_{24}$ cluster synthesis: $ZrOCl_2$ $8H_2O$ (1.16 g, 3.6 mmol) was dissolved with dimethylformamide (DMF) (1.8 mL) in an 8-dram vial with magnetic stir bar. Acetic acid (7.95 mL, 139 mmol) was added to the vial and the solution was stirred for 5 minutes until solution became clear. The vial was capped and placed in a pre-heated oven at 110 °C for 24 hours. The white crystalline solid was filtered and washed with 50 mL of a 1:1 DMF:Acetic acid solution. The solid was transferred to an 8-dram vial and solvent exchanged with 3 ml $CHCl_3$ three times. Residual chloroform was evaporated with N_2 (g) at room temperature.

2.1.2 Synthesis of sulfuric acid treated SBA-15

Sulfuric acid treated silica particles (SBA-15) were synthesized according to literature procedures from Crisci et al.[4] 0.67 g Pluronic 123 was dissolved in 23 mL 1.6 M HCl at 35 °C. The resulting solution was combined with 1.4 mL of TEOS and 140 mg NaCl and stirred for 1 hour. The solution was then equally divided into 3 vials, with 12 µL of 3-mercapto-trimethoxysilane (MPTMS) added to vial 1 and 48 µL of MPTMS added to vial 2 in 12 µL increments every 15 minutes. 1.4 mmol H_2O_2 was added to all 3 vials, followed by 24 hours of stirring. The three samples were put in Parr bombs and heated to 100 °C for 24 hours. The samples were filtered and washed with water. From each sample, the Pluronic surfactant was extracted with ethanol under reflux. The samples were washed with ethanol and the extraction was repeated. The 2 samples with MPTMS were washed with water and suspended in HCl for 3 hours. The HCl treated samples were filtered and washed with water, dried in air at 60 °C overnight, and then dried under vacuum at 150 °C.

2.1.3 Synthesis of phosphoric acid treated SBA-15

From 2.1.2, the sample that did not contain MPTMS was suspended in a H_3PO_4/acetone solution. The sample was stirred at 60 °C until the acetone evaporated. The sample was dried in air at 60 °C overnight and then dried under vacuum at 150 °C.

2.1.4 Synthesis of SBU cluster treated acid functionalized SBA-15

70 mg of phosphoric or sulfuric acid functionalized SBA-15 was added to an 8-dram vial. A solution of Zr-SBU cluster (70 mg) in 12 mL of DMF was added to the vial and capped. The vial sulfuric acid functionalized SBA-15 was placed in a 55 °C oven while the phosphoric acid functionalized SBA-15 was placed in a 100 °C pre-heated oven for 18 hours. The vials were solvent exchanged with fresh 12 mls of DMF and acetone three times.

2.2 Characterization

2.2.1 Powder X-ray diffraction

Powder x-ray diffraction (PXRD) patterns were measured on a Rigaku® MiniFlex™ 600 diffractometer equipped with a D/teX Ultra detector with Cu-Kα radiation (λ = 1.5418 Å) over a range of 2θ = 3–50 °C at a scan rate of 5 degrees minute^{-1}.

2.2.2 Attenuated total reflectance-Fourier transform infrared

Attenuated total reflectance-Fourier transform infrared spectra were measured on a Bruker® Tensor™ 27 spectrometer from 4000–400 cm^{-1} at a resolution of 2 cm^{-1}.

2.2.3 N_2 physisorption

N2 isotherms were measured using a Micromeritics® ASAP™ 2420 analyzer at 77 K. Samples were off-gassed at 120 °C under vacuum for ~16 hours. The Brunauer-Emmett-Teller method was used to calculate specific surface area in m2/g.

2.3 Catalysis experiments

Cluster modified SBA-15 (12 mol% ~8.6 to 8.7 mg) were added to a vial. A mixture (9:1) of H_2O:D_2O (0.9/0.1 mL) was added to the vial and capped. The vial was briefly (1 minute) sonicated then transferred to a Nuclear Magnetic Resonance (NMR) tube. N-ethylmorpholine (50 µL) was added to the solution within the NMR tube. DMNP (4 µL, 25 µmol) was added to the top sidewalls of the NMR tube. The tube was capped and carefully inverted thrice to mix the components. The tube was inserted into the NMR instrument and conversion was monitored by ^{31}P NMR.

3. RESULTS

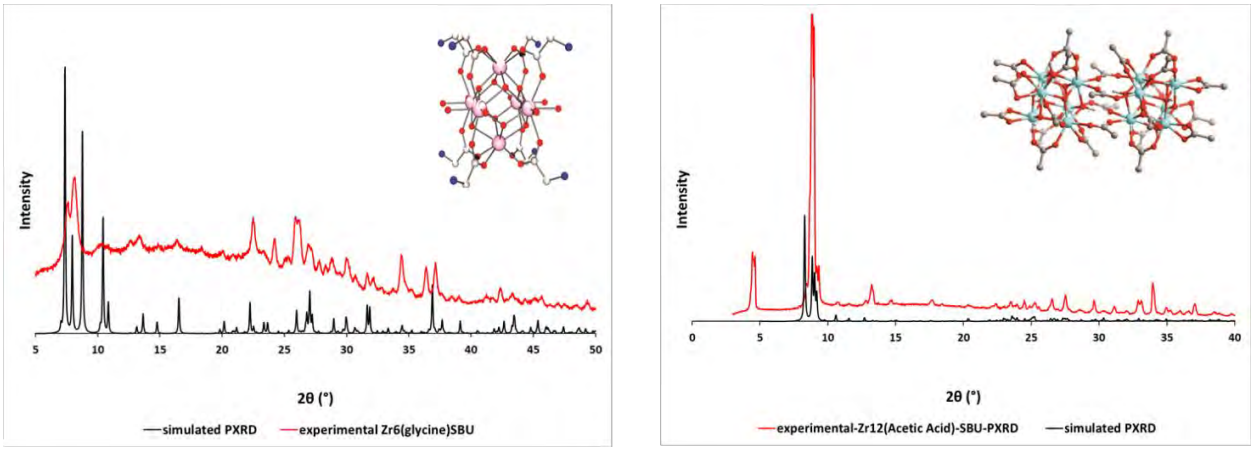

Figure 1. (Left) Simulated PXRD pattern of Zr_6(glycine)-SBU cluster (bottom, black) and experimental PXRD pattern of Zr_6(glycine) SBU (top, red) with the representation of the Zr_6-SBU cluster derived from single X-ray diffraction data. (Right) Simulated PXRD pattern of Zr_{12}(acetic acid) SBU (bottom, black) and experimental PXRD pattern of Zr_{12}(acetic acid) (top, red). Note that simulated spectra begin at 5 ° with the representation of the Z_{12}-SBU cluster derived from single X-ray diffraction data.

The zirconium clusters were synthesized through modified literature procedures using excess mono-carboxylic acids under heating. As observed in Figure 1, the PXRD patterns of the synthesized clusters closely resembled that of their simulated patterns derived from their single crystal X-ray diffraction structures. With both Zr_6- and Zr_{12}- type SBU

clusters in hand, we explored their catalytic properties in the hydrolysis of DMNP under aqueous conditions through ^{31}P NMR spectroscopy. Like many Zr-MOFs, hydrolysis of DMNP with the Zr-SBU clusters requires basic conditions or amine co-catalyst for effective reactivity. As expected, the Zr-SBU clusters which have mono-carboxylic acids bound to zirconium sites do not facilitate DMNP hydrolysis under strictly aqueous (pH = 7) conditions (Table 1). However, the use of N-ethylmorpholine (NEM) engenders the Zr-SBUs to facilitate DMNP hydrolysis (Table 1). Presumably, the NEM facilitates the dissociation of mono-carboxylic acids which induces DMNP access to the resulting Zr-OH, -H_2O catalytic sites for hydrolysis. The Zr_6-SBU fully facilitates the hydrolysis of DMNP after 18 hours with a half-life ($t_{1/2}$) of 69 minutes. Interestingly, the Zr_{12}-SBU performs relatively faster with a DMNP half-life of 12 minutes. This may be attributable to the relatively larger number of available Zr-OH, -H_2O catalytic sites of the Zr_{12}-SBU than the Zr_6-SBU cluster (2:1, respectively). To better facilitate DMNP hydrolysis with the SBU cluster, HCl-activation was performed to displace the mono-carboxylic acids from the SBU.

Table 1. DMNP hydrolysis in 0.45 M N-ethyl morpholine buffer.

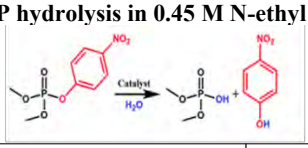

Material	Half-life (min.), DMNP, water	Half-life (min.), DMNP, 0.45 M NEM buffer
Zr_{12}-SBU	N.R.	12
Zr_6-SBU-glycine	N.R.	69
HCl activated Zr_{12}-SBU	--	7
P-SBA-15	--	>220
H-SO_3H-SBA-15	--	1080
Zr_{12}-SBU-P-SBA-15	--	69
Zr_{12}-SBU-H-SO_3H-SBA-15	--	15
Zr_{12}-SBU-L-SO_3H-SBA-15	--	8

As seen in Figure 2, both SBUs retain their crystallinity after HCl-activation. As expected, the HCl-activated Z_{12}-SBU cluster facilitated faster DMNP hydrolysis than the as synthesized Zr_{12}-SBU cluster under 0.45 M NEM aqueous conditions $t_{½}$ = 7 minutes versus 12 minutes, respectively (Table 1).

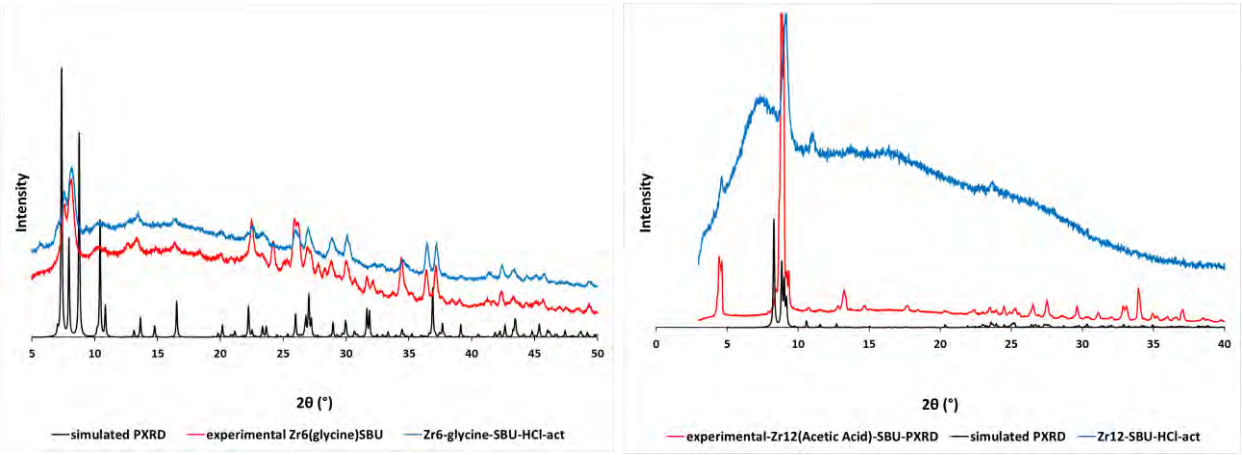

Figure 2. (Left) Simulated PXRD pattern of Zr_6-SBU (bottom, black), experimental PXRD pattern of Zr_6-SBU (middle, red) and after HCl-activation (blue, top). (Right) Simulated PXRD pattern of Zr_{12}-SBU (bottom, black), experimental PXRD pattern of Zr_{12}-SBU (middle, red) and after HCl-activation (blue, top).

Silica particles (SBA-15) were modified with sulfuric acid and phosphoric acid. The synthesized particles were characterized by ATR-IR and N_2 isotherms to determine crystallinity and porosity. As seen in Figure 3, the IR spectrum of phosphoric acid functionalized SBA-15 (P-SBA-15) contain peaks around 1323 cm^{-1} and 626 cm^{-1} corresponding to the P=O and P-OH stretches respectively. After phosphoric acid functionalization the N_2 adsorption significantly decreases (Figure 3). The observed decrease in porosity might be due to the high degree of residual H_3PO_4 within the pores of P-SBA-15 or a high level of functionalization. Indeed, when P-SBA-15 was utilized for DMNP hydrolysis under 0.45 M NEM aqueous conditions, residual H_2PO_4 is observed in the ^{31}P NMR spectrum at

2.5 ppm. Interestingly, P-SBA-15 is not selective towards DMP, instead it primarily and slowly ($t_{½}$ = >220 minutes) generates the undesired P-O-Me cleavage product methyl 4-nitrophenyl phosphate (M4NP). Due to the enhanced performance of the Zr_{12}-SBU as compared to the Zr_6-SBU, the modified SBA-15 materials were reacted with Zr_{12} clusters to generate Zr_{12}-modified SBA-15. Dissolved Zr_{12}-SBU cluster was introduced to P-SBA-15 through heating overnight. Residual clusters were removed through successive solvent exchange.

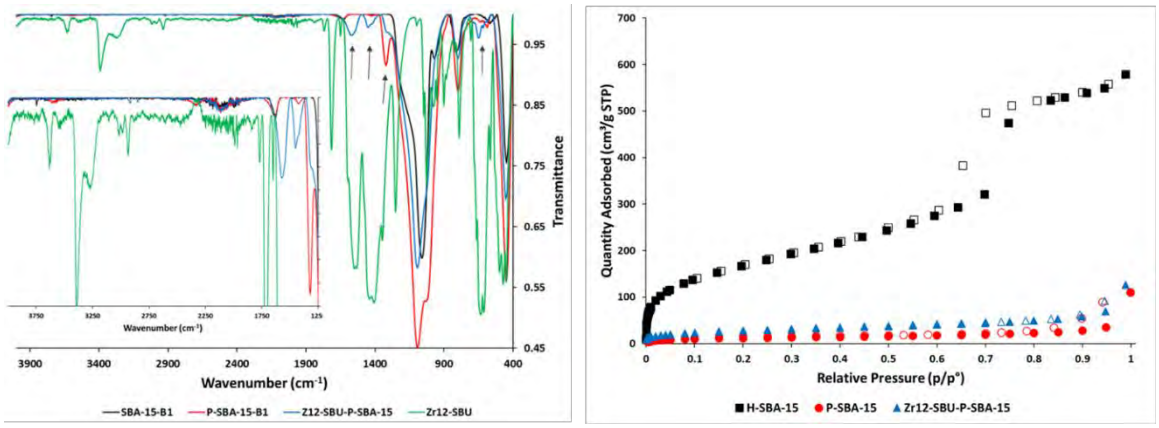

Figure 3. (Left) IR spectra of SBA-15 (black), P-SBA-15 (red), Zr_{12}-SBU-P-SBA-15 (blue), and Zr_{12}(acetic acid) SBU (green). Inset zoom of spectra from 3,900 to 1,200 cm^{-1}. (Right) N_2 adsorption isotherms of SBA-15 (black squares), P-SBA-15 (red circles), and Zr12-SBU-P-SBA-15 (blue triangles). Solid symbols represent adsorption, empty symbols represent desorption.

As seen in Figure 3, the stretches associated with P=O and P-OH in P-SBA-15 shift or decrease after introduction of the Zr_{12}-SBU. More importantly, new C=O stretches corresponding to the acetic acid within the Zr_{12}-SBU appear. However, the stretches associated with the Zr-O-H stretches of the cluster at 3390 cm^{-1} completely disappear after introduction into P-SBA-15 presumably through the binding of Zr to the Si centers or phosphoric acid within P-SBA-15. However, the PXRD of Zr_{12}-SBU-P-SBA-15 does not display crystallinity (Figure 4). The lack of crystallinity could be due relatively low amount of Zr retained in the SBA-15 the EDX-SEM indicates the Si:P:Zr ratio is 1: 0.5: 0.09 respectively. Remarkably, Zr_{12}-SBU-P-SBA-15 facilitates the fast (t ½ = 69 minutes) and selective hydrolysis of DMNP to DMP under 0.45 M NEM aqueous conditions. The stark contrast in DMNP hydrolysis reactivity and selectivity is clearly attributable to the introduction of the Zr_{12}-SBU clusters into SBA-15.

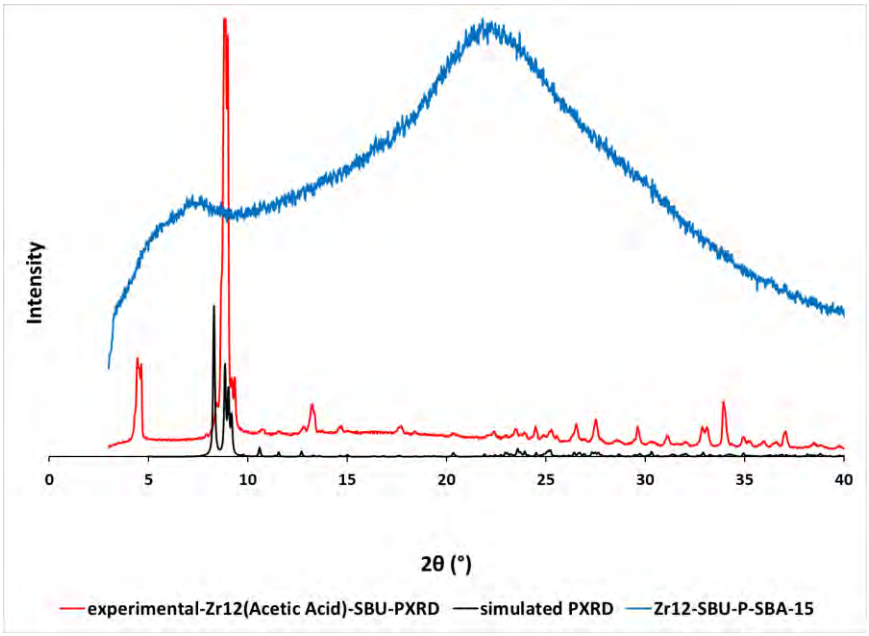

Figure 4. Simulated PXRD pattern of Zr_{12}(acetic acid) SBU (bottom, black) and experimental PXRD pattern of Zr_{12}(acetic acid) (middle, red) note that simulated spectra begins at 5 °, and experimental PXRD pattern of Zr_{12}-SBU-P-SBA-15 (top, blue).

SBA-15 was modified different amounts of SO_3H to generate H-SO_3H-SBA-15 and L-SO_3H-SBA-15 (H = high, L = low). EDX-SEM analysis indicates that H-SO_3H-SBA-15 has a 3.9-fold greater sulfide content than L-SO_3H-SBA-15. The IR spectrum of H-SO_3H-SBA-15 contains a peak at 688 cm^{-1} corresponding to the S-OH stretch (Figure 5).

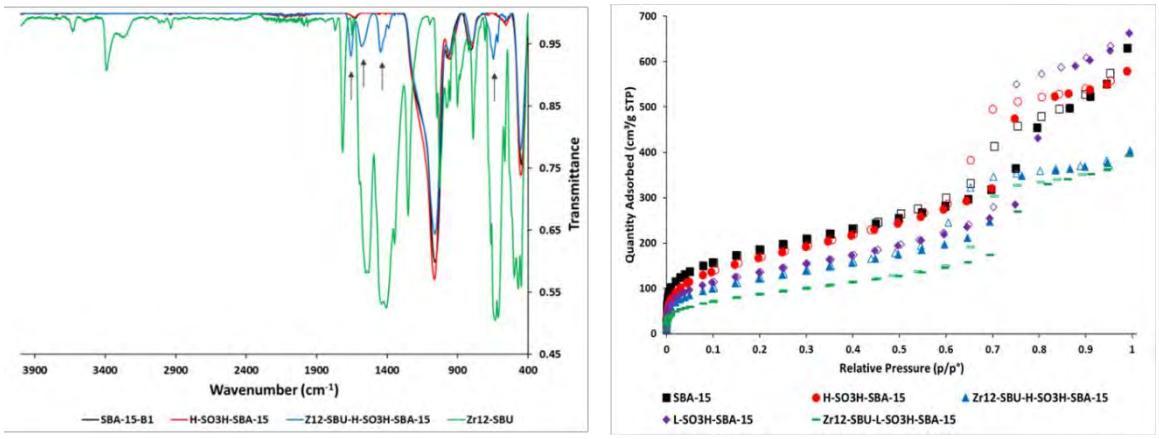

Figure 5. (Left) IR spectra of SBA-15 (black), H-SO_3H-SBA-15 (red), Zr_{12}-SBU- H-SO_3H-SBA-15 (blue), and Zr_{12}(acetic acid) SBU (green). (Right) N_2 adsorption isotherms of SBA-15 (black squares), H-SO_3H-SBA-15 (red circles), Zr_{12}-SBU-H-SO_3H-SBA-15 (blue triangles), L-SO_3H-SBA-15 (purple diamonds), and Zr_{12}-SBU-L-SO_3H-SBA-15 (green line). Solid symbols represent adsorption, empty symbols represent desorption.

Upon introduction of the Zr_{12}-SBU the S-OH stretch disappears and new stretches at 1586 cm^{-1} and 1480 cm^{-1} corresponding to the acetic acid within the Zr_{12}-SBU. Like P-SBA-15, H-SO_3H-SBA-15 slowly and primarily generates M4NP when it was utilized in the hydrolysis of DMNP in 0.45 M NEM aqueous conditions. Modification of SBA-15 with SO_3H reduces the porosity. Similar to Z_{12}-SBU-P-SBA-15, Zr_{12}-SBU-H-SO_3H-SBA-15 does not have crystallinity (Figure 6). The introduction of the Zr_{12}-SBU into H-SO_3H-SBA-15 changes the catalytic properties in the hydrolysis of DMNP. Zr_{12}-SBU-H-SO_3H-SBA-15 facilitates the fast (t ½ = 15 minutes) and selective hydrolysis of DMNP to DMP under 0.45 M NEM aqueous conditions. Interestingly, there is a stark 3-fold greater Zr content within Zr_{12}-SBU-L-SO_3H-SBA-15 than its analog Zr_{12}-SBU-H-SO_3H-SBA-15 (Si:Zr ratios 1:0.24 and 1:0.083, respectively). Based on the elemental analysis of their precursors (3.9:1 H- versus L-respectively), it was expected that H-SO_3H-SBA-15 would have bound relatively more Zr_{12}-SBU- within the pores of SBA-15. This dramatic increase in the zirconium content appears to significantly affect hydrolysis as Zr_{12}-SBU-L-SO_3H-SBA-15 quickly and selectively converts DMNP into DMP (t ½ = 8 minutes).

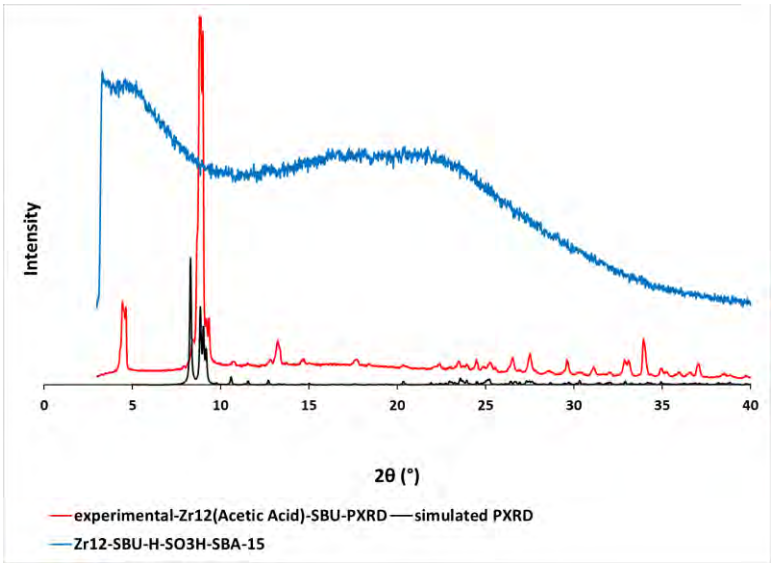

Figure 6. Simulated PXRD pattern of Zr_{12}(acetic acid) SBU (bottom, black) and experimental PXRD pattern of Zr_{12}(acetic acid) (middle, red) and experimental PXRD pattern of Zr12-SBU-H-SO_3H-SBA-15 (top, blue).

4. CONCLUSION/FUTURE WORK

A novel modified silica material decorated with zirconia clusters was developed in this work and has been shown to selectively hydrolyze DMNP to the desired DMP product in less than 10 minutes under buffered conditions. The modified silica without the bound zirconia clusters, however, shows slow hydrolysis to the less desired product, M4NP. In addition, the bound zirconia clusters analogous reactivity as compared to the unbound zirconia clusters indicating that the silica support does not hinder reactivity. These initial experiments demonstrate the potential use of this silica platform to study and optimize zirconia clusters for CWA decontamination. In addition, these novel materials are scalable and can be readily transitioned into relevant form factors such as fibers and polymer coatings. Future work with these materials will include the addition of functionalities to enhance reactivity under neutral aqueous conditions, variations in the amount of zirconia clusters on the particles to determine optimal reactivity, incorporation of this porous materials into fibers and coatings, and studies to determine reactivity of these materials with agents.

ACKNOWLEDGMENTS

Funding was provided by the Director, Combat Capabilities Development Command Chemical Biological Center under the authorities and provisions of Section 2363 of the FY 2018 NDAA to develop new technologies, engineer innovations, and introduce game-changing capabilities.

REFERENCES

[1] Troya, D. Reaction Mechanism of Nerve-Agent Decomposition with Zr-Based Metal Organic Frameworks. *J. Phys. Chem. C.* **2016**, *120* (51), pp 29312–29323.

[2] Pappas, I.; Fitzgerald, M.; Huang, X.-Y., Li, J.; Pan, L. Thermally Resolved in Situ Dynamic Light Scattering Studies of Zirconium(IV) Complex Formation. *Cryst. Growth Des.* **2009**, *9* (12), pp 5213–5219.

[3] Bezrukov, A.A.; Törnroos, K.W.; Le Roux, E.; Dietzel, P.D.C. Incorporation of an intact dimeric Zr_{12} oxo cluster from a molecular precursor in a new zirconium metal-organic framework. *Chem. Commun*. **2018**, *54* (22), pp 2735–2738.

[4] Crisci, A.J.; Tucker, M.H.; Lee, M.-Y.; Jang, S.G. Dumesic, J.A.; Scott, S.L. Acid-Functionalized SBA-15-Type Silica Catalysts for Carbohydrate Dehydration. *ACS Catal.* **2011**, *1* (7), pp 719–728.

This page intentionally left blank

Using lung-on-a-chip technology to evaluate the effects of pathogen surrogates

Daniel J. Angelini*, Jennifer R. Horsmon, Tyler D.P. Goralski
U.S. Army Combat Capabilities Development Command Chemical Biological Center, Research & Technology Directorate, 8198 Blackhawk Rd, Aberdeen Proving Ground, MD 21010

ABSTRACT

Exposures to the spores of *Bacillus anthracis* can lead to the development of the disease known as anthrax. While the spores can infect the host through multiple routes, inhalation results in the most severe form of disease if left untreated. Much of the pathology associated with inhalational anthrax is associated with toxins produced once the infection is established in the host organism. Anthrax research has been typically performed using whole animal infections or two-dimensional cell culture exposed to the anthrax toxins; however, two-dimensional cell culture can lack physiological accuracy, and animal studies are costly, can have ethical considerations, and often require large amounts of agent to perform exposures. Recently, advances in cell culture technology have led to the development of *in vitro* organs-on-a-chip that recreate *in vivo* organ microenvironments. Emulate has recently developed chips that are comprised of a top and bottom channel separated by a porous membrane, which house different cell types and microvasculature associated with the various organs. This system also provides constant media flow to the tissues, as well as mechanical stretch and the ability to place the cells under air-liquid interface. In this study, we use alveolus lung chips manufactured by Emulate to examine the pathophysiological effects of anthrax toxin on human pneumocytes and lung specific microvascular tissue.

Keywords: anthrax, inflammation, organ-on-a-chip, toxin

1. INTRODUCTION

1.1 Anthrax

The Gram-positive bacterium *Bacillus anthracis* is the causative agent of the disease anthrax.[1] The bacterium occurs naturally in the environment in its vegetative state, or as a spore when essential environmental and nutritional needs are depleted. The spore form of the bacteria is classified as a tier 1 select agent due to the severe pathology associated with the disease, and ease with which spores have been propagated and disseminated for biological warfare in the past.[1] Traditionally, human anthrax occurs through cutaneous, inhalational, or intestinal exposures to *B. anthracis* spores[1], however injection has also been demonstrated as a potential route of exposure.[2,3] Of the described types of anthrax exposures, inhalational and intestinal are considered the most difficult to diagnose and treat, leading to poor clinical outcomes.[3] Once the spores have entered a host organism, the spores are phagocytosed by macrophages and germinate into vegetative cells. The resultant vegetative cells produce toxins that cause pathological effects including cellular death and edema.[1,3]

1.2 Anthrax toxins

B. anthracis bacterium contain two plasmids known as pXO1 and pXO2 that play an essential role in the production of the three factors responsible for the formation of anthrax toxin and therefore the pathogenesis of the disease.[3,4] These three factors are known as protective antigen (PA), edema factor (EF), and lethal factor (LF). Once produced, PA will combine with either EF to form edema toxin (ET) or LF to form lethal toxin (LT).[4] After the formation of ET and LT, these toxins are capable of entering cells through anthrax-specific cell surface receptors, followed by a disruption of intracellular signaling.[4] Exposure to these toxins either *in vivo* or *in vitro* have been shown to alter cellular morphology and induce apoptosis in both pulmonary epithelial and endothelial cells.[5–7] Alterations to these cells is a key aspect of anthrax disease pathology.

1.3 Organ-on-a-chip technology

Traditionally, researchers have relied on whole animal, *ex vivo* organ culture, or two-dimensional tissue culture to examine the pathophysiological effects of chemical or biological agents. Recent advances in both cell culture techniques and microfluidics have allowed for the development of organ-on-a-chip technologies, known as microphysiological systems, that can mimic the physiology of various *in vivo* organs, such as lung, liver, and intestines.[8–13] The cells used in microphysiological systems contain multiple cell types and are grown with three-dimensional architecture.[8-13] In addition, these systems include fluid flow and other processes specific to certain organs, such as the stretch and Air-Liquid Interface (ALI) that would be associated with breathing in the lung.[9,10,12,13] In this study, we examined some of the pathophysiological effects of the anthrax toxins associated with *B. anthracis* infection on an alveolus organ-on-a-chip system.

2. METHODOLOGY

2.1 Cell culture

Human primary alveolar epithelial cells (HPAEC) and human lung microvascular endothelial cells (HMVEC-L) were purchased from Lonza (Walkersville, MD). These cells were thawed and expanded in tissue culture flasks in either SABM™ Basal media supplemented with bovine pituitary extract, hydrocortisone, human epidermal growth factor (hEGF), epinephrine, transferrin, insulin, retinoic acid, triiodothyronine, 1 % penicillin/streptomycin, and 5 % fetal bovine serum (FBS) (HPAEC) or EGM™-MV medium supplemented with hEGF, human vascular endothelial growth factor (hVEGF), R3-insulin-like growth factor-1 (R3-IGF-1), ascorbic acid, hydrocortisone, human fibroblast growth factor-β, gentamycin/amphotericin-B, and 5 % FBS (HMVEC-L). All media and supplements were purchased from Lonza.

2.2 Organ-chip preparation

The Chip-S1™ (Emulate, Inc.; Boston, MA) is a microfluidic device composed of a stretchable material that contains both a top and bottom channel separated by a porous membrane (7 µm-pore size) allowing for cell-cell interactions.[12,13] To prepare for the addition of cells, both the top and bottom channels of the chips were washed and activated according to the manufacturer's recommended protocol (Emulate, Inc.). Briefly, ER-1 solution in ER-2 buffer was added to each channel and then exposed to ultraviolet light to activate the surface. Following chip activation, both the top and bottom channels of the chips were coated with an extracellular matrix (ECM) specific to the cell type to be seeded. The top channel, or epithelial side, was coated with a mixture of collagen IV, fibronectin, and laminin. The bottom channel, or endothelial side, was coated with a mixture of collagen IV and fibronectin. All ECM proteins were obtained from Sigma-Aldrich® (St. Louis, MO).

2.3 Organ-chip cell seeding

Once the channels had been coated with the appropriate ECM, HPAECs were seeded on the top channel at a density of 1 x 10^6 cells/mL. The cells were then allowed to attach for at least 4 hours and then washed and refed with epithelial media, described above, supplemented with dexamethasone, keratinocyte growth factor, 8-br-cAMP, isobutyl methylxanthine, and 2 % FBS [Sigma-Aldrich® or Thermo Fisher Scientific, Inc. (Waltham, MA)]. The cells were then placed back at 37 °C with 5 % CO_2 for two days with daily media changes. The HMVEC-Ls were seeded to the bottom channel at a density of 5 x 10^6 cells/mL. The chips were inverted to allow for endothelial cell attachment for 4 hours. Once the cells attached, the chips were flipped, the media was changed in each channel, and the chips were placed back at 37 °C with 5 % CO_2 overnight.

2.4 Development of alveolus-on-a-chip

The seeded chips were then attached to the Pods (Emulate, Inc.) which contain individual inlet and outlet media reservoirs for both the top and bottom channels. Once the chips had been attached to the Pods, the inlet reservoirs were filled with the respective media and the Pods were inserted into the Zoë (microfluidic regulator) which is in the cell culture incubator (37 °C with 5 % CO_2). The Zoë is set to a flow rate of 30 µL/hour for both the top and bottom channels. The next day, the media was removed from the top channel and replaced with air to create the ALI. The bottom channel media was replaced with Complete ALI medium, consisting of Medium 199 supplemented with hEGF, human basic FGF, hVEGF, hydrocortisone, heparin, di-butyl cAMP, L-glutamax, dexamethasone, 1 %

penicillin/streptomycin, and 2 % FBS. All media supplements were purchased from Thermo Fisher Scientific, Inc. or Sigma-Aldrich®. Two days after the initiation of the ALI, a 5 % mechanical stretch at a frequency of 0.2 Hz was started to replicate a breathing motion. The media was changed every other day until exposures.

2.5 Anthrax toxins

In this study, we examined three individual anthrax factors: PA, EF, and LF. All factors were obtained from List Biological Laboratories (Campbell, CA). PA and EF were provided lyophilized in buffer and reconstituted with cell-culture grade water to a concentration of 1 mg/mL prior to use. LF was provided as a frozen liquid with a concentration of 1 mg/mL. All toxins were studied at an exposure concentration of 2 µg/mL.

2.6 Toxin exposure procedure

The following conditions were prepared in Complete ALI medium: media alone, PA, EF, LF, PA + EF, PA + LF, or PA + EF + LF. Each of the media conditions were added to the bottom channel inlet reservoir and the Zoë set to a flow rate of 600 µL/hour for 5 minutes. The Zoë was then set back to a flow rate of 30 µL/mL for the remainder of the 24-hour exposure. At the end of the incubation, the chips were visualized using a Keyence BZ-X Fluorescence Microscope on the brightfield phase contrast setting.

2.7 Cytokine array

Outflow media from each experimental condition was collected at the conclusion of the experiment. The collected outflow was examined for the presence of cytokines using the Human Multiplex Cytokine ELISA (Creative Diagnostics; Shirley, NY). The ELISA had the capability of detecting eight different inflammatory cytokines: interluekin-1α (IL-1α), IL-1β, IL-6, IL-8, granulocyte-macrophage colony-stimulating factor (GM-CSF), Interferon-γ (IFNγ), monocyte chemotactic and activating factor (MCAF), and tumor necrosis factor-α (TNFα). The ELISA protocol was performed according to the manufacturer's recommended protocol and the results were displayed as upregulated or downregulated compared to media control.

2.8 Immunofluorescence microscopy

The top and bottom channels of the chips were fixed with 4 % paraformaldehyde in phosphate-buffered saline (PBS) for 15 minutes at room temperature followed by three washes with PBS and then stored at 4 °C. The chips were permeabilized/blocked with a solution of 1 % saponin, 1 % BSA, and 10 % normal goat serum in PBS for 1 hour. The chips were then washed with PBS and treated with either mouse anti-PECAM-1 (bottom channel; Abcam; Cambridge, MA) or rabbit anti-podoplanin (top channel; Abcam) antibodies in 1 % BSA and 10 % normal goat serum in PBS for 1 hour. The chips were washed and then exposed to either goat anti-mouse IgG conjugated to Alexa Flour 488 (bottom channel; Abcam) or goat anti-rabbit conjugated to Texas red (top channel; Abcam) antibodies in 1 % BSA, 10 % normal goat serum, and 0.01 % Hoescht 33342 (Thermo Fisher Scientific, Inc.) in PBS for 1 hour. Finally, the chips were washed with PBS and visualized using a Keyence BZ-X Fluorescence Microscope.

3. RESULTS

3.1 Development of alveolus-on-a-chip

To confirm the development of a functional epithelial monolayer, the top channel was stained with the mucin-type glycoprotein podoplanin (Figure 1). This protein is a used as a marker for the development of Type I pneumocytes. There was significant staining for podoplanin in these epithelial cells indicating proper differentiation. In addition, we examined the endothelial channel for the presence of the endothelial cell marker PECAM-1 (Figure 2). These cells also formed a monolayer structure with significant staining on the cellular boundaries. The presence of these cells in both the epithelial and endothelial channels of the organ chips indicates that an alveolus-like structure has formed.

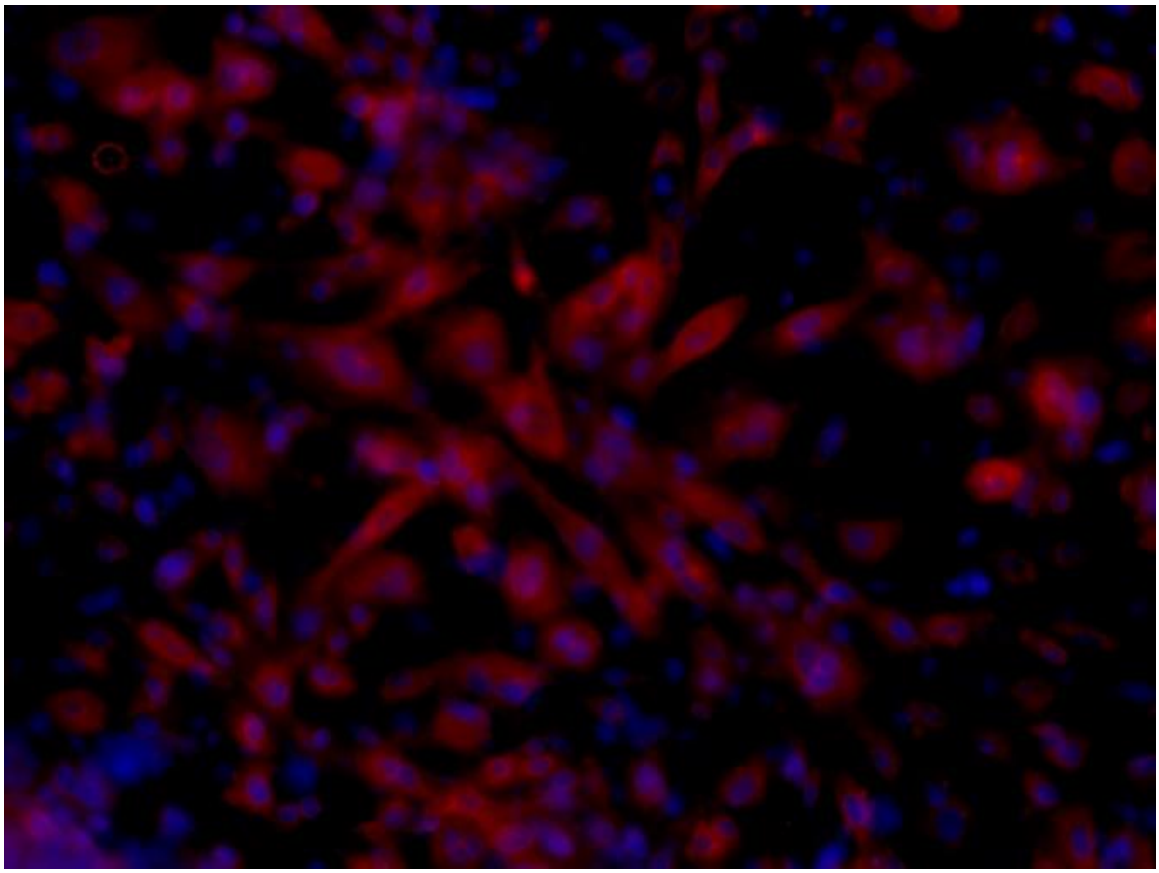

Figure 1. Expression of Podoplanin on the Alveolus-on-a-Chip. Podoplanin was stained on the epithelial channel of the alveolus-on-a-chip using rabbit anti-podoplanin IgG followed by visualization by a Texas red–conjugated goat anti-rabbit IgG antibody (green) Nuclei were counterstained Hoechst 33342 (blue).

3.2 Expression of inflammatory cytokines

A multiplex ELISA cytokine array containing IL-1α, IL-1β, IL-6, IL-8, GM-CSF, IFNγ, MCAF, and TNFα was used to determine the effect of anthrax toxins on the expression levels of inflammatory cytokines in the cell culture media. Following a 24-hour treatment with media alone, PA, EF, LF, PA + EF, PA + LF, or PA + EF + LF, a reduction in cytokines was observed (Table 1). Particularly, reductions in IL-1α and IL-1β levels were seen following any of the treatments performed. Moreover, reductions in expression of IL-6, IL-8, and MCAF were also seen following treatment with PA + LF and PA + EF + LF. Recent findings suggest that anthrax toxins reduce the expression of IL-1α and IL-1β *in vivo* in order to evade the immune response during the initial *B. anthracis* infection[4].

Table 1. Expression of Inflammatory Cytokines in Cell Culture Media in Treated versus Untreated Controls. Key: ↑ upregulated versus untreated control; ↓ downregulated versus untreated control; − unchanged versus untreated control

	IL-1α	IL-1β	IL-6	IL-8	GM-CSF	IFNγ	MCAF	TNFα
PA	↓	↓	−	−	−	−	−	−
EF	↓	↓	−	−	−	−	−	−
LF	↓	↓	−	−	−	−	−	−
PA + EF	↓	↓	−	−	−	−	−	−
PA + LF	↓	↓	↓	−	↓	−	↓	−
PA + EF + LF	↓	↓	↓	−	↓	−	↓	−

3.3 Effect of anthrax toxins on alveolus-on-a-chip

Fully developed alveoli were exposed to anthrax toxins through the endothelial channel for 24 hours. The endothelial channel was chosen as the exposure route because of the similarity of exposure in a human clinical setting.[1] Following exposure to anthrax toxin or media alone, the cells in the chips were fixed, permeabilized, and probed with anti-PECAM-1 antibodies on the endothelial channel. The media control endothelium appeared as a monolayer with consistent localization of PECAM-1 at the intercellular boundaries (Figure 2). Treatment with PA + EF + LF, which would allow for the formation of both anthrax toxins, induced loss of endothelial cells from the basal membrane. This loss is consistent with the induction of apoptotic or necrotic cellular death. This observed loss of cells is consistent with other *in vitro* and *in vivo* exposures to anthrax toxins.[4,5,7]

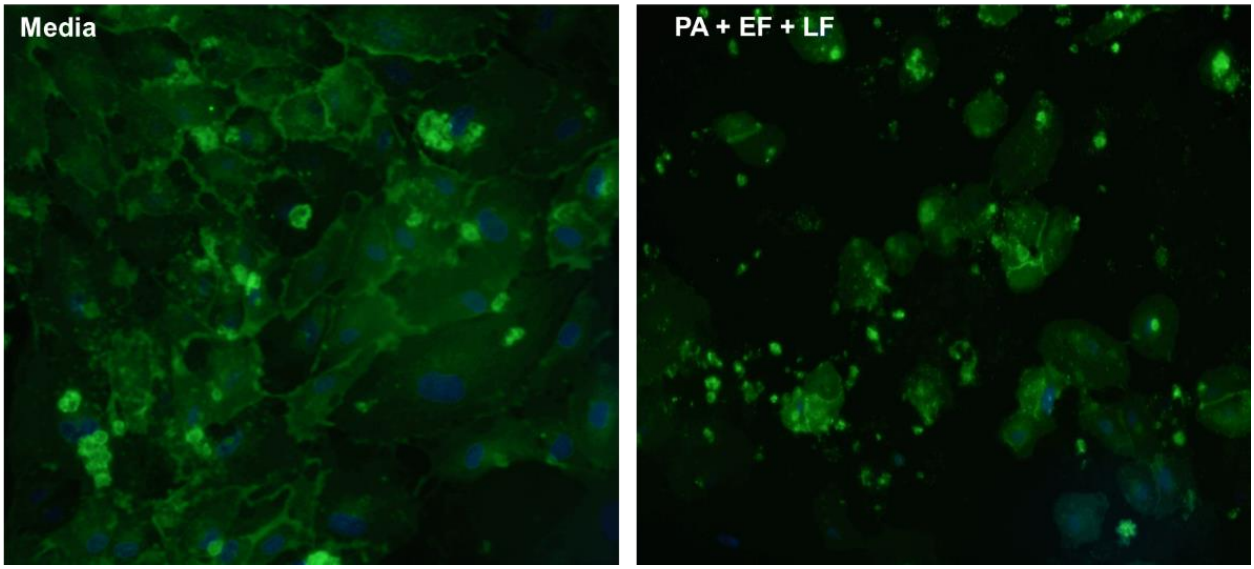

Figure 2. Expression of PECAM-1 Following Anthrax Toxin Treatment. PECAM-1 was stained on the endothelial channel of the alveolus-on-a-chip using mouse anti-PECAM-1 IgG followed by visualization by an Alexa Fluor 488–conjugated goat anti-mouse IgG antibody (green) Nuclei were counterstained Hoechst 33342 (blue).

4. CONCLUSION

In the current study, we successfully implemented a functional human alveolus-on-a-chip in our laboratory. These chips were cultured under ALI, with the appropriate flow and stretch associated with a fully intact alveolus, and the differentiated chips displayed appropriate epithelial (podoplanin; Type I pnuemocytes) and endothelial cell markers (PECAM-1). Human alveolus chips were exposed to anthrax toxins on the endothelial channel for 24 hours. Following exposure to these toxins, we observed reductions in basal levels of inflammatory cytokines (e.g., IL-1α, IL-1β). Finally, we observed a consistent loss of endothelial cells on chips that were exposed to both anthrax toxins (e.g., ET, LF). The observations that were made from the alveolus-on-a-chip in this study were consistent with other results seen in both in vitro and in vivo models examining anthrax toxin. Further studies will be required to perform a complete interrogation of the effects of anthrax toxins using alveolus-on-a-chip technology.

ACKNOWLEDGMENTS

Funding was provided by the Director, Combat Capabilities Development Command Chemical Biological Center under the authorities and provisions of Section 2363 of the FY 2018 NDAA to develop new technologies, engineer innovations, and introduce game-changing capabilities. The authors would also like to thank Dr. Nicole Rosenzweig, Ms. Stacey Broomall, and Ms. Shakena Norton for continued scientific and administrative support.

REFERENCES

[1] Chambers, J.; Yarrarapu, S.N.S.; Mathai, J.K. Anthrax Infection. In *StatPearls*, Treasure Island (FL), **2021**,

[2] Ringertz, S.H.; Høiby, E.A.; Jensenius, M.; Maehlen, J.; Caugant, D.A.; Myklebust, A.; Fossum, K. Injectional anthrax in a heroin skin-popper. *Lancet.* **2000,** *356* (9241), pp 1574–1575.

[3] Savransky, V.; Ionin, B.; Reece, J. Current Status and Trends in Prophylaxis and Management of Anthrax Disease. *Pathogens.* **2020**, *9* (5) p 370.

[4] Friebe, S.; van der Goot, F.G.; Bürgi, J. The Ins and Outs of Anthrax Toxin. *Toxins.* **2016,** *8* (3). pp 1–15

[5] Langer, M.; Duggan, E.S.; Booth, J.L.; Patel, V.I.; Zander, R.A.; Silasi-Mansat, R.; Ramani, V.; Veres, T.Z.; Prenzler, F.; Sewald, K.; Williams, D.M.; Coggeshall, K.M.; Awasthi, S.; Lupu, F.; Burian, D.; Ballard, J.D.; Braun, A.; Metcalf, J.P. *Bacillus anthracis* Lethal Toxin Reduces Human Alveolar Epithelial Barrier Function. *Infect. Immun.* **2012**, *80* (12), pp 4374–4387.

[6] Lucas, R.; Hadizamani, Y.; Gonzales, J.; Gorshkov, B.; Bodmer, T.; Berthiaume, Y.; Moehrlen, U.; Lode, H.; Huwer, H.; Hudel, M.; Mraheil, M.A.; Toque, H.A.F.; Chakraborty, T.; Hamacher, J. Impact of Bacterial Toxins in the Lungs. *Toxins.* **2020**, *12* (4), pp 1–34.

[7] Warfel, J.M.; Steele, A.D.; D'Agnillo, F. Anthrax Lethal Toxin Induces Endothelial Barrier Dysfunction. *Am. J. Pathol.* **2005,** *166* (6), pp 1871–1881.

[8] Apostolou, A.; Panchakshari, R.A.; Banerjee, A.; Manatakis, D.V.; Paraskevopoulou, M.D.; Luc, R.; Abu-Ali, G.; Dimitriou, A.; Lucchesi, C.; Kulkarni, G.; Maulana, T.I.; Kasendra, M.; Kerns, J.S.; Bleck, B.; Ewart, L.; Manolakos, E.S.; Hamilton, G.A.; Giallourakis, C.; Karalis, K. A Novel Microphysiological Colon Platform to Decipher Mechanisms Driving Human Intestinal Permeability. *Cell. Mol. Gastroenterol. Hepatol.* **2021**, *12* (5), pp 1719–1741.

[9] Huh, D.; Leslie, D.C.; Matthews, B.D.; Fraser, J.P.; Jurek, S.; Hamilton, G.A.; Thorneloe, K.S.; McAlexander, M.A.; Ingber, D.E. A human disease model of drug toxicity-induced pulmonary edema in a lung-on-a-chip microdevice. *Sci. Transl. Med.* **2012**, *4* (159), p 159ra147.

[10] Huh, D.; Matthews, B.D.; Mammoto, A.; Montoya-Zavala, M.; Hsin, H.Y.; Ingber, D.E. Reconstituting organ-level lung functions on a chip. *Science.* **2010**, *328* (5986), pp 1662–1668.

[11] Kim, H.J.; Huh, D.; Hamilton, G.; Ingber, D.E. Human gut-on-a-chip inhabited by microbial flora that experiences intestinal peristalsis-like motions and flow. *Lab Chip.* **2012**, *12* (12), pp 2165–2174.

[12] Nawroth, J.C.; Lucchesi, C.; Cheng, D.; Shukla, A.; Ngyuen, J.; Shroff, T.; Varone, A.; Karalis, K.; Lee, H.-H.; Alves, S.; Hamilton, G.A.; Salmon, M.; Villenave, R. A Microengineered Airway Lung Chip Models Key Features of Viral-induced Exacerbation of Asthma. *Am. J. Respir. Cell Mol. Biol.* **2020**, *63* (5), pp 591–600.

[13] Si, L.; Bai, H.; Rodas, M.; Cao, W.; Oh, C.Y.; Jiang, A.; Moller, R.; Hoagland, D.; Oishi, K.; Horiuchi, S.; Uhl, S.; Blanco-Melo, D.; Albrecht, R.A.; Liu, W.-C.; Jordan, T.; Nilsson-Payant, B.E.; Golynker, I.; Frere, J.; Logue, J.; Haupt, R.; McGrath, M.; Weston, S.; Zhang, T.; Plebani, R.; Soong, M.; Nurani, A.; Kim, S.M.; Zhu, D.Y.; Benam, K.H.; Goyal, G.; Gilpin, S.E.; Prantil-Baun, R.; Gygi, S.P.; Powers, R.K.; Carlson, K.E.; Frieman, M.; tenOever, B.R.; Ingber, D.E. A human-airway-on-a-chip for the rapid identification of candidate antiviral therapeutics and prophylactics. *Nat. Biomed. Eng.* **2021**, *5* (8), pp 815–829.

UAV Swarm Defense

Michael J. Smith[a], John A. D'Agostino[a],
[a]U.S. Army Combat Capabilities Development Command Chemical Biological Center, Research & Technology Directorate, 8198 Blackhawk Rd, Aberdeen Proving Ground, MD 21010

ABSTRACT

This program successfully demonstrated defeat of two models of Unmanned Aerial Vehicles quad copters. A total of 52 trials were conducted, 40 of which were successful in defeating the Unmanned Aerial Vehicles. Fiber length, diameter, and spray adhesive appear to be the major variables in determining the effectiveness of defeat.

Keywords: Countermeasure, Carbon Fiber, Counter Unmanned Aerial Vehicle, Unmanned Aerial Vehicle Swarm

1. INTRODUCTION

Smaller, hobby grade, commercially available Unmanned Aerial Vehicles (UAV) have the potential to carry lethal payloads up to two kilograms. These UAVs can be used in a combat situation either in single UAV missions or in a swarm of multiple UAVs. Swarms are difficult to counter using conventional kinetic measures such as anti-aircraft fire, nets, or jammers. These technologies are localized and thus are less effective in countering UAV swarms. Leveraging Chemical Biological Center's aerosol science expertise, the Smoke and Target Defeat Branch explored the interaction of aerosol clouds in defeating UAVs via propeller entanglement. An aerosol cloud defeat mechanism has the advantage of being able to cover a larger area, making this countermeasure more effective against UAV swarms.

2. BACKGROUND AND OBJECTIVES

2.1 Background

Quadcopter type UAVs were selected for this effort as they are commercially available and widely used. After consulting with UAV suppliers, the DJI Phantom 4 was identified as a popular platform in which the design was more resistant to countermeasures than other models. In addition, a DJI Phantom 3 was tested for comparison.

To most efficiently entangle the UAV propellers, a high aspect ratio material is desired that contains a high length to diameter ratio. The length allows for the fibers to efficiently wrap into the propeller, and the small diameter allows for the material to be ingested inside the motor enclosure for more effective disruption. The goal is to create enough friction between the propeller and the UAV body to slow the propeller from spinning.

Fiber materials allow for both a small diameter and a high aspect ratio. Fibers are typically sold on tows which contain thousands of individual fiber filaments on a roll. These tows are traditionally used to produce fabrics and are also chopped to produce reinforced fiber panels.

There are many different types of fiber materials available commercially. During this effort, HexTow IM2A carbon fiber, HexTow AS4 carbon fiber, AS4W carbon fiber, polypropylene, and acrylic fibers were chosen based on availability and desired material parameters.

2.2 Objective

The objective of this project is to quantify the effectiveness of a various aerosol cloud's ability to defeat UAVs. Key variables examined during the effort include material type, fiber length, UAV model, or the addition of an adhesive.

3. EXPERIMENTAL SETUP

3.1 UAVs

The Phantom 3 and Phantom 4 UAVs were tested in this event. The platform specifications are similar with the primary difference being the geometry of the motor and motor arm as shown in the Figure 1 below.

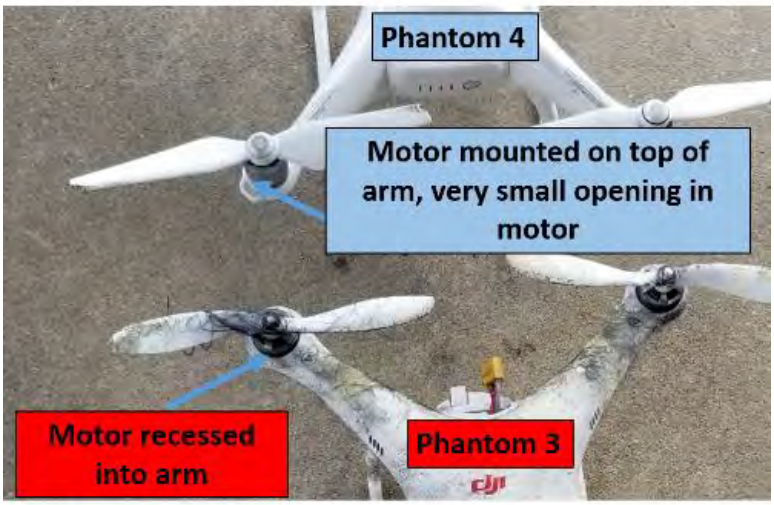

Figure 1. Phantom 3 versus Phantom 4 motor arm mount differences.

3.2 Belt chopper

A belt chopper made by Engineering Technologies, Inc. was used to cut the fiber tows to various lengths. A fiber tow is fed through a pipe and into the cutter head. The cutter head is a wheel containing removable blades spaced at even increments around the circumference. The cutter head spins at a fixed rpm and makes a cut each time the blade meets the fiber at the cutting surface. Once the fiber is cut, an air amplifier fed by an industrial air compressor entrains the fibers and feeds them out from the cutter head and into the air. By adding or removing cutter head blades, the cut length of the fiber can be varied.

Figure 2. Belt chopper set up outside of the test enclosure, polypropylene being loaded into cutter head

3.3 Test enclosure

A test enclosure (Figure 2) was constructed to allow for controlled dissemination of aerosol clouds. The test enclosure is 12 ft deep by 7 ft wide by 7ft high. An opening on the end allowed for fibers to be disseminated into the enclosure. Mesh windows were used on the far end as well as the sides to allow for air to pass through, preventing the enclosure from building up air pressure. A plywood floor was constructed to make cleaning of the test enclosure possible as seen above.

3.4 Procedure

At the start of the trial the UAV and the fiber roll were weighed. The UAV was then set to hover inside the test enclosure. At the start of the trial the belt cutter was turned on which began to disseminate fibers inside the test enclosure. When the UAV lost control and hit the floor, the belt cutter was turned off and the trial was considered a successful defeat. The fiber roll and UAV were then reweighed to measure the weight of fiber disseminated.

In preparation for the next trial, the UAV motors would be removed and cleaned out. Then the test enclosure would be swept, and the fibers inside would be disposed of to ensure no contamination of the next trial.

Four separate tests were run in the manner described above, along with the addition of spraying 3M™ Super 77™ spray adhesive right as the fibers exited the cutter head.

4. RESULTS

4.1 Overview

The general phenomena observed during experimentation is shown below in Figure 3. The UAV is flying normally in the center of the test enclosure. Upon exposure to fibers the propellers begin to wrap with the fibers. This causes some loss of control, but the platform continues to operate requiring more throttle to remain airborne. Typically, a few seconds later, complete loss of control is observed and the UAV crashes to the ground.

Figure 3. Progression of fiber collection on the UAV propellers from left to right.

Experiments demonstrated that fibers were readily and quickly ingested into the propeller and motors of the UAV which caused a loss of power and control, thus defeating the UAV. Photos of this are shown below in Figure 4.

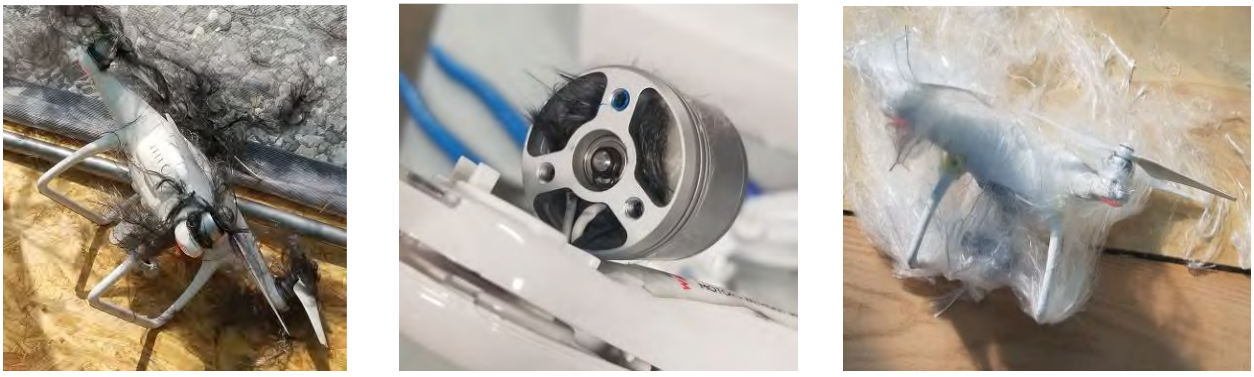

Figure 4. IM2A UAV defeat (left), IM2A Ingested in Motor (center), Polypropylene UAV defeat (right).

4.2 Material type

The material type influences the diameter, density, and tensile strength used in defeating the UAVs. The below table shows the material type and percentage of successful defeat experienced during testing across all trials. As can be seen from the table, almost all materials used had some success in defeating the UAVs.

Table 1. Material type defeat probability.

Material	Diameter (microns)	Density (g/cm^3)	Filament Count	Tensile Strength (MPa)	# of Trials Conducted	# of Defeats	Successful Defeat (%)	Average Fiber Weight to Defeat (g)
HexTow IM2A Carbon Fiber	5.2	1.78	12,000	5,343	20	17	**85**	**11**
HexTow AS4 Carbon Fiber	7.1	1.79	12,000	4,447	13	5	**38**	**-**
AS4W Carbon Fiber	7.5	1.79	6,000	4,100	2	0	**0**	**20.1**
Acrylic	-	-	-	-	10	8	**80**	**40.5**
Polypropylene	-	-	-	-	6	6	**100**	**356**

"-" indicates currently no data is available

AS4W carbon fiber performed the worst out of all materials tested. This carbon fiber is a legacy experimental tow and did not disseminate effectively when fed through the belt cutter. Most of the cut fiber settled quickly to the test enclosure floor.

Post-test observations show the smaller diameter fibers are more readily ingested inside the motor causing a defeat. This was apparent in IM2A (5.2 µm diameter) carbon fiber compared to the AS4 carbon fiber (7.1 µm diameter). Both fibers have similar properties, but the IM2A was much more effective in entangling the propellers and motors due to the smaller diameter. Photos of the fiber inside the motor are shown above in Figure 4.

4.3 Fiber length

The length of the fibers influences how the propellers of the UAV become entangled as well as how long the fibers can remain airborne in a cloud form. The IM2A fiber was down selected to explore the length variable since it had successful defeats and had the lowest average fiber weight to defeat. Fiber lengths ranged from 5.6–44.9 cm and the results are shown in Figure 3.

Average time to kill was measured by starting a stopwatch when the first fiber contacted the UAV and stopped when the UAV crashed. Average fiber weight to defeat was measured by weighing the fiber roll before and after the trial. The performance factor metric was created to display the effectiveness indicated by the average time to kill and the average fiber weight to defeat. This was calculated by multiplying the average time to kill by the average fiber weight to defeat and taking the inverse. The result was then multiplied by 100 for ease of display.

Length (cm)	Average Time to Kill (s)	Average Fiber Weight to Defeat (g)	Performance Factor
5.6	-	-	-
7.5	4.0	21.7	1.15
11.2	2.0	9.4	5.32
22.5	4.00	8.16	3.06
44.9	10.33	12.8	0.76

(- denotes did not defeat)

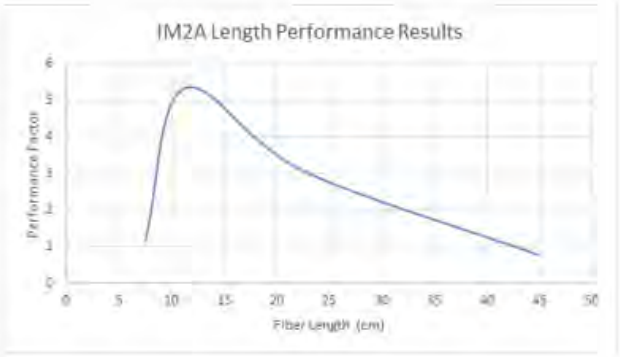

Figure 5. IM2A performance factor versus length.

As shown in Figure 5, the performance of the IM2A fiber is optimized at lengths ranging from 10 to 15 cm. As fiber length is decreased below 10 cm there is a fall in performance due to the length of time required for defeat. For lengths above 15 cm the performance reduction is less severe and is caused by the time to kill and weight to defeat both increasing as length increases.

4.4 Adhesive

3M™ Super 77™ Spray Adhesive was applied to the fibers and results were compared to dry fibers of equal specifications. When adhesive was applied, this effectively made the fiber length longer. At a cut length of 5.6 cm using IM2A fiber two trials showed no defeat of the UAV. When these two trials were repeated with spray adhesive used the UAV was defeated in 1 second. This demonstrates that the spray adhesive improved the chances of defeat. A performance factor of 8.2 was calculated using the method above including the weight of adhesive used.

4.5 UAV model

The model of UAV used influenced difficulty of defeat. The Phantom 3 was easier to defeat than the Phantom 4. Using AS4 fiber cut to 7.5 centimeters a Phantom 3 was 50% likely to be defeated while the Phantom 4 was 0% likely. It is hypothesized that the motor mount geometry greatly influences how much effect an entangled fiber has on the flight characteristics as seen in Figure 1.

4.6 Overall conclusions

This program successfully demonstrated defeat of two models of UAV quad copters. 52 total trials were conducted. Of these 52 trials 40 were successful in defeating the UAV. Fiber length, diameter, and spray adhesive appear to be the major variables in determining the effectiveness of defeat.

Changing these parameters not only changed whether a defeat occurred, but also changed the time it took for the defeat to occur, and the weight of material required for defeat. Operationally the quicker the defeat the better, as this allows for less standoff distance and less material required results in a lower logistical burden.

4.7 Recommendations for future experimentation

This effort was fundamental in understanding the key variables of this defeat mechanism, but due to funding and time constraints more experiments are recommended. More experimental trials are needed to better define key defeat parameters and to better understand how these variables effect the probability and time to defeat.

In addition, research into separation of fibers from the cutter head is desired as the cloud generated was often not homogeneous. To counter a swarm, a large homogeneous cloud is desired. Possible approaches include using precut fibers, as well as higher shear air nozzles.

Discussions with experts at Georgia Tech Research Institute indicated that hexacopter and octacopters will likely be even tougher to defeat since they are able to fly with one or multiple propellers defeated. Future iterations of these experiments should include testing these types of UAVs.

All UAVs were operated with no additional weight outside of the standard camera and gimbal payloads. This is representative of a scouting mission loadout. In the case of a UAV carrying a lethal payload such as an improvised explosive device, it is likely that the UAV would be flying with more weight. Although not tested, it is expected that defeat would be easier for a UAV carrying more weight since lower power loss would be required for defeat. This theory should be tested in the experimental set up to confirm this hypothesis.

ACKNOWLEDGMENTS

The authors would like to acknowledge Frank Mackowiak, and Jerry Eyet of Excet Inc. for their assistance with the experimentation phase of the effort and Dr. Ken Collins of the Smoke and Target Defeat Branch, for his expertise in countermeasure technologies. In addition, background knowledge and lessons learned were supplied by John Stewart and Pat Bartlett of Georgia Tech Research Institute and Bryce Cline of Flymotion. Dennis Metz of Sci Tech Inc. supported this project by ordering supplies for his support. Funding of this project was provided by the Director, Combat Capabilities Development Command Chemical Biological Center under the authorities and provisions of Section 2363 of the FY 2018 NDAA to develop new technologies, engineer innovations, and introduce game-changing capabilities via the Seedling and IDEAS programs.

FY20
SEEDLING PROJECTS

Active illumination source for hyperspectral spectrometer in UAV/UGV mounted applications

Justin M. Curtiss*, Eric R. Languirand
U.S. Army Combat Capabilities Development Command Chemical Biological Center, Research & Technology Directorate, 8198 Blackhawk Rd, Aberdeen Proving Ground, MD 21010

ABSTRACT

Artificial illumination is required for a line scanning passive hyperspectral spectrometer when operating a system of this type in non-daylight conditions. While in general, more photons will yield a larger reflectance signal return to the sensor, a source that outputs a large number of photons is unlikely to be compatible with a compact hyperspectral spectrometer on a small aircraft or using in a handheld manner. Therefore, in this paper, we investigate a small tungsten halogen source coupled with off-the-shelf optics to create a compact artificial illumination source to provide photons for the spectrometer. After characterizing the compact halogen source and comparing its output characteristics to larger sources currently in use, several optical trains were designed to focus the sources output to the instruments' field-of-view. To further increase the photon density on the surface, proof-of-concept experiments were performed with a commercially available Powell lens to generate a line of light that could be co-aligned to the instrument. The results detailed herein show that a compact source can allow for a hyperspectral spectrometer to operate with a compact artificial illumination source with a minimal decrease in performance.

Keywords: hyperspectral, spectroscopy, illumination, Powell lens

1. INTRODUCTION

Rapid interrogation of a surface for chemical threats is paramount to maintaining soldier lethality through protection. A hyperspectral spectrometer can scan a large area for anomalies and potential contamination but require a photon source to obtain a signal.[1] Alternative illumination sources to solar irradiance were researched and coupled to the spectrometer to provide compact, artificial photon source allowing for night and indoor operation, which is normally restricted to daylight hours. A commercially available tungsten halogen bulb produces similar wavelengths and intensity to solar irradiance and due to its size, can be engineered into a compact package for unmanned aerial vehicles (UAV) or handheld sensor applications. In this paper, multiple optical designs were used to focus the halogen sources output to maximize reflectance in the spectrometer and a Powell lens (Thorlabs, Inc.; Newton, NJ) was used in proof-of-concept experiments to co-align a source to the spectrometers field-of-view (FOV). An anomaly detection algorithm was applied to the resultant data to determine improvements in performance with the artificial sources when compared to solar irradiance.[2,3]

2. BACKGROUND

A passive hyperspectral spectrometer requires an external illumination source to collect a reflectance spectrum from a surface. In general, solar irradiance provides the required photons; however, this is not possible at night, under cloud cover, or indoors limiting the systems utility. External illumination sources that output the required photons for the spectrometer to operate efficiently are large and have power requirements that are not compatible with a UAV or unmanned ground vehicles (UGV) mounted or handheld application. Active sources such as quantum cascade, interband cascade, or diode lasers can fit within a UAV platform size/power requirements and have similar or greater photon output when compared to solar irradiance, but do not provide continuous coverage across the spectral range of interest, which can lead to data gaps.[4–6] A tungsten halogen source provides broadband illumination across the ultraviolet, visible, and infrared spectral range similar to solar irradiance, and when co-aligned with the spectrometers FOV, could provide the necessary photons for the spectrometer at any time of day.[7] A Powell lens can be used to focus the photons from the tungsten source to a line that is complimentary to the spectrometers FOV.[8] This arrangement

would allow a compact tungsten source to be utilized as a photon emitter that is also compatible with a UAV or handheld application.

3. EQUIPMENT

A Headwall Photonics Microhyperspec® spectrometer was used in this research, affixed with a variable focal length lens (StingRay Optic; Keene, NH) set to 1 meter, with a 320 x 256-pixel array and 0.4–1.7 µm range. The spectrometer scanned an area on the ground approximately 4 mm x 600 mm and was translated over the surface using a linear stage. Data collected by the linear array was reconstructed into a three-dimensional hyperspectral image for analysis.

Three illumination sources were used in this research: 1000-watt tungsten bulb (Osram; Munich, Germany) in a PAR64 housing, 80-watt infrared radiation halogen flood lamp (Philips; Amsterdam, Netherlands) mounted in an aluminum reflective housing, and 300-watt halogen reflector bulb (Impact ELH; New York, NY) . The 1000-watt bulb was chosen as it is a high intensity source with similar spectral output to solar irradiance and has been used in operations at security check points, making potential integration of the spectrometer less intrusive. An infrared radiation halogen flood lamp was chosen as a low-cost solution for indoor testing illumination as it is widely available at most hardware stores and has a similar solar spectrum to the sun. The halogen reflector bulb is a compact source, 2-inch diameter and less than 1 lb., with high photon output similar to solar irradiance that could be integrated easily with the Microhyperspec® spectrometer. For comparison, the 1000-watt tungsten bulb and housing weighs approximately 15 lbs with a diameter of 10-inches and the halogen bulb with housing weighs approximately 5 lbs with an 8-inch diameter. A wattage output of 300 was chosen as a middle ground between the flood and stage light, though multiple other wattages are available ranging from 50 to 500 watts.

Commercially available optical lenses and components were used to focus light from the compact halogen source to co-align its output to the spectrometers FOV. Two-inch diameter, 60 mm focal length, plano-convex lenses, and a 40 mm focal condenser lens were mounted and adjusted to partially collimate the light from the compact halogen source to increase the photon flux at the spectrometer FOV. An acrylic Fresnel lens (Thorlabs, Inc.; Newton, NJ) was also used as a method to collimate the light from the halogen source. A 9 mm diameter, commercially available Powell lens was used generate a line of focused light from a source, to better match the spectrometer FOV. In addition, a 532 nm laser (JUNO Compact Series; Kanagawa, Japan) was used for proof-of-concept experiments to understand the Powell lens operation and how the change in input diameter affects the output properties. These optical components, coupled with the compact halogen source, were used to increase the photon flux at the spectrometers FOV.

4. EXPERIMENTAL

To establish a baseline for comparison, initial photon flux output profiles and surface measurements were collected with both the stage and flood light sources. Each source was placed 1 meter from the surface in front of a 24-inch wide scale, with the brightest area of the source centered at 12-inches. An LT300 light meter (Extech™; Boston, MA) was used to measure the photon flux, the number of photons per second per unit area, across the 24-inch scale in two-inch increments, creating photon output profile of each source. Both sources were then positioned to illuminate a 24-inch square gravel and dirt surface with Teflon™ samples, as depicted in Figure 1, over which the spectrometer traveled, collecting a hyperspectral data cube of the sample. Due to the weight of the stage light, it remained stationary; however, data was collected with the flood lamp in a stationary position and moved by a linear stage at a speed of 50 mm/s along with the spectrometer. Data collected from these experiments were then processed through an anomaly detection algorithm as a baseline for comparison to determine if improvements are made by the compact halogen source. The anomaly algorithm treated each surface, dirt and gravel, as different backgrounds, with the Teflon™ representing a chemical contamination; when processing a sample area of dirt, the two Teflon™ strips and small patch of gravel should appear as an anomaly. These experiments were then repeated with the compact halogen source.

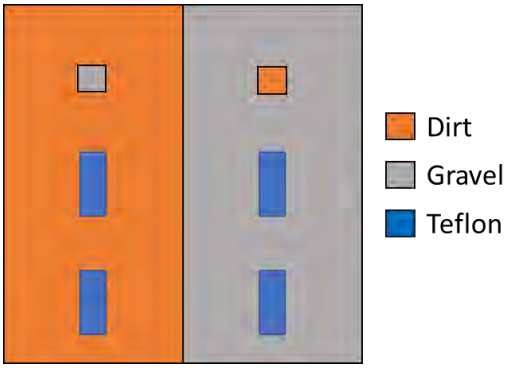

Figure 1. Depiction of sample set-up.

For the compact halogen source, the two-inch optical lenses were used in multiple combinations to gather and focus the light to increase the photon flux within the center potion of the scale. Two arrangements of optical lenses were chosen, one used a pair of 40 mm focal length convex lenses, while the other used a 40 mm focal length convex lens and a 50 mm focal length condensing lens. The photon flux measurements were then repeated with each lens combination as well as with the unfocused source, with an output diameter of 16- and 24-inches on the surface chosen to illuminate the instrument FOV. As above with the flood lamp experiments, the compact source was used to illuminate the dirt and gravel surface in both a stationary position as well as tracking with the spectrometer. The experiments were then repeated with focusing lenses used to increase the photon flux at the spectrometer FOV and all the resultant data was processed using the same anomaly algorithm.

To understand the principles of the Powell lens, a 532 nm laser (JUNO Compact Series; Kanagawa, Japan) was used as a collimated, single wavelength source. The laser output was directed through a 400 µm diameter diffusor and the scattered light was collimated with a 25 mm diameter, 50 mm focal length optical lens. The expanded, collimated light was then passed through a variable diameter aperture and then through the Powell lens, who's output was imaged with a camera. Output of the Powell lens was imaged with different diameter input beams and the intensity and profile characteristics were analyzed to observe how the input beam affected the output. These experiments were then repeated with a low intensity light emitting diode source as a proof-of-concept that the Powell lens can be used to focus a broadband source into a line that could be co-aligned to the hyperspectral spectrometer.

5. RESULTS AND DISCUSSION

To compare the output profile of each source and have a basis of comparison to quantify improvements made by the focusing optics for the compact halogen source, the three light sources were projected onto a ruled 24-inch wide scale, the same width as the spectrometer FOV. The light intensity was measured at two inch increments across the scale for each source. Compared first were the stage, flood, and non-focused compact halogen sources with the intensity profiles shown in Figure 2.

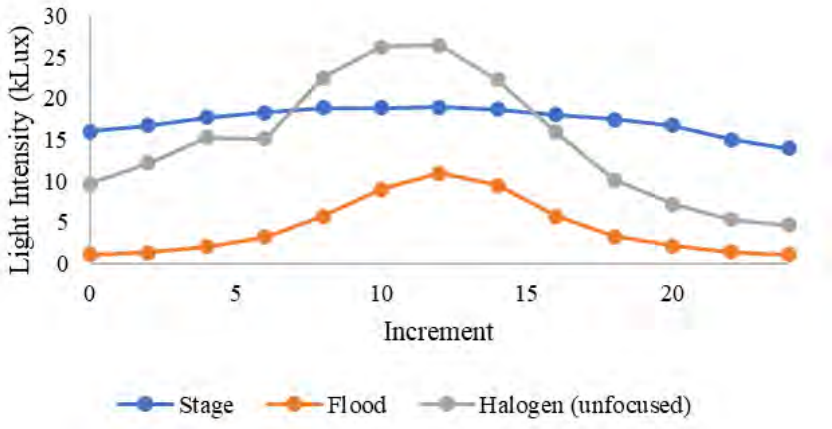

Figure 2. Intensity profile of non-focused sources.

The stage light provides the most even illumination across the scale with a change of 4.92 kLux and higher average output of 17.35 kLux when compared to the flood and halogen source at 4.36 and 14.85 kLux average, respectively; solar photon flux collected was 95 kLux for comparison. The compact halogen source had the highest peak output at the center of the scale, but a greater delta of 21.80 kLux. From this data, the compact halogen source demonstrated that it may be a viable illumination source but will provide uneven photon density within the instrument FOV. This will cause a hot spot in the middle of the FOV with a weaker signal towards the edges.

Multiple methods to gather, focus, collimate, and co-align the compact halogen source to the spectrometer were investigated during this research, to include a Fresnel lens (Thorlabs, Inc.; Newton, NJ), paired convex lenses, and a condenser lens. A baseline of illumination profile was established with the unfocused source, with a maximum output of 26.5 kLux at one meter, as shown in Figure 2. Initial results with the Fresnel lens appeared to be promising, with a photon flux measurement of 38.5 kLux at the center of the beam that was fairly collimated, increasing the maximum photon density and decreasing the divergence of the source. However, after a few minutes, the heat from the halogen source began to delaminate and melt the Fresnel lens, as it was made from acrylic. A commercially available or custom-made glass replacement lens could not be sourced as modern Fresnel lenses are plastic and pressed in dies rather than traditional Fresnel lenses which are cut from solid glass. Because the Fresnel lens did collimate the light, it may have been an option to couple with the Powell lens, which requires a collimated source.

The pair of plano-convex 60 mm focal length lenses and the combination of a condenser and plano-convex lens worked well to gather and focus the light from the source and were made of glass, thus more resilient against heat. Adjusting the distance of the lenses from the source and each other altered the output diameter of the source at one meter with 24 inches being achieved, matching the instrument FOV, and 16-inch diameter maximizing the photon output density.

Two optical assemblies were constructed to focus and collimate the output from the compact halogen source, creating a focused area of 16-inch and 24-inch. The combination of the condenser lens and convex lens produced a greater peak intensity than the paired convex lenses, as shown in Figure 3.

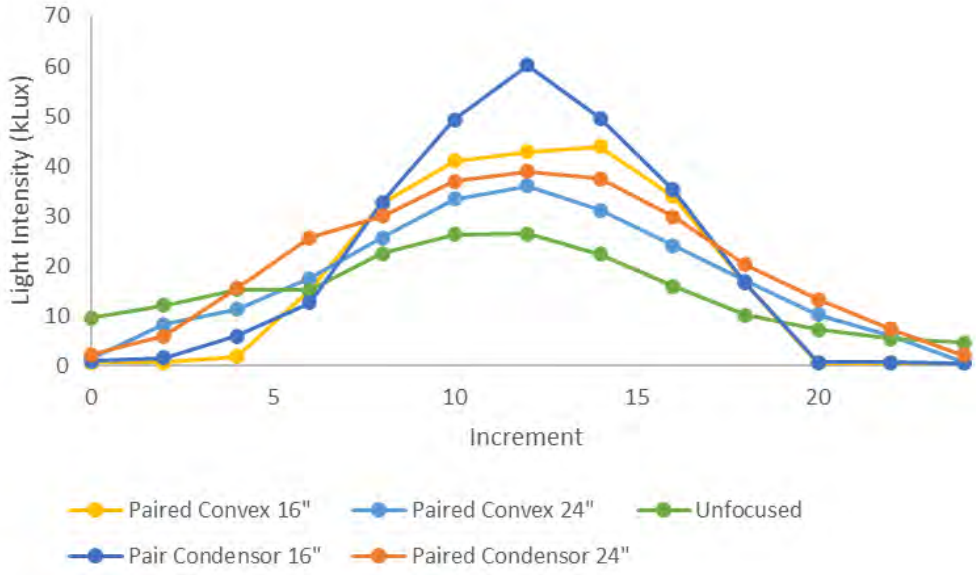

Figure 3. Intensity profile of compact halogen source with focusing lenses.

Comparing the 16- to 24-inch diameter areas, the 16-inch peak intensity was higher as the photons are more focused than with the 24-inch diameter area, resulting in a higher photon density. However, as previously observed when comparing the non-focused sources, there is a greater photon density in the center and with lower intensity at the edges, resulting in a hot spot. With the 16-inch diameter area, the outer 6 inches on each end of the scale have a photon output reading of less than 1 kLux, meaning there would be little signal to the instrument at the outer regions of its FOV. To compensate for this, the focusing lens of the instrument could be adjusted to view a narrower width on the ground or multiple compact sources could be used to fully illuminate the area. Flat field correction of the collected data could also be used to correct for the uneven illumination. Overall, the condenser/convex lens combination created the greatest photon flux on the surface at 1 meter when compared to the other sources evaluated and produced a photon flux 72 % that of solar irradiation.

While the combination of lenses increased the photon density of the compact source within the FOV of the instrument, a collimated beam was not able to be achieved limiting the use of the Powell lens in this application. Therefore, proof-of-concept experiments were conducted with a commercially available Powell lens using a 532 nm laser and broadband light source, acting as stand-ins for the compact halogen source. A Powell lens requires that the input beam is well collimated, and therefore the compact halogen source could not be used as collimation was not achieved with the methods used. Collimation of the halogen source used may not be possible as it is not a point source, but rather an extended source or a source that has many focal lengths from a given point. Because the bulb is a filament housed in a faceted parabolic reflector, each reflective surface acts as a mirror and thus its own extended source with its own focal length.[9] To collimate an extended source violates the second law of thermodynamics as the entropy of the system cannot be reduced, i.e., cannot create more order, collimated, light from a non-ordered, extended, source. For the proof-of-concept experiments, a laser was used which is collimated, and the broadband source utilized a pinhole to create a point source, which can therefore be collimated and not violate the second law of thermodynamics.

With each of these collimated sources, a line of light was generated with the Powell lens onto a surface, similar to the FOV of the spectrometer. A pixel-distance calibrated digital image of each line was captured and six segments of the generated line were analyzed using Otsu's method for thresholding where the data was binarized as either background or data. The value of the data point for the cross section was then plotted for each pixel across the width of the array, as shown in Figure 4 and Figure 5, for the laser and broadband sources, respectively.

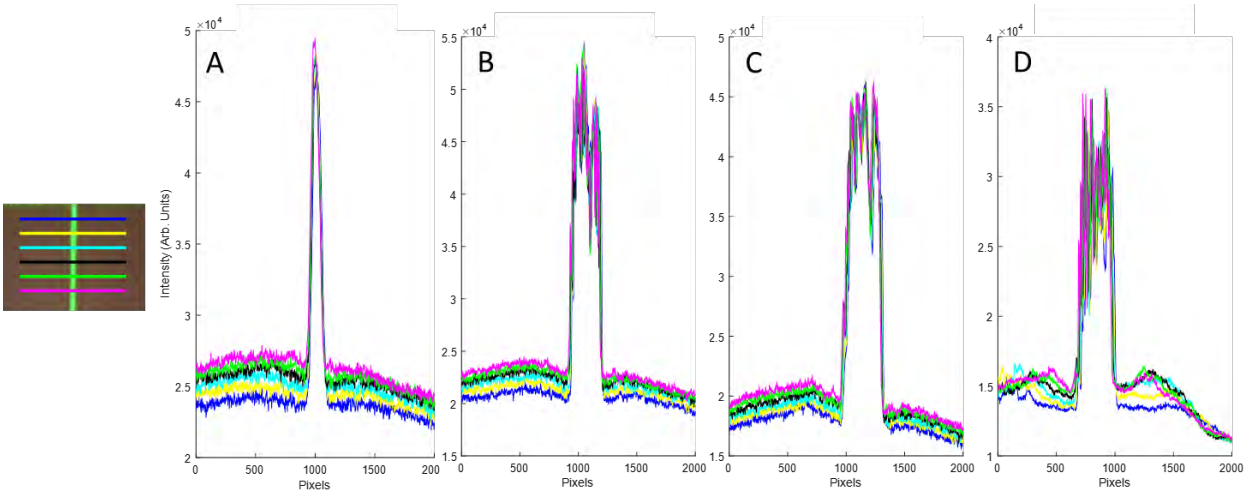

Figure 4. Image analysis results of 532 nm laser through Powell lens at diameters of 2–25 mm; A: 2 mm, B: 5 mm, C: 10 mm, D: 25 mm.

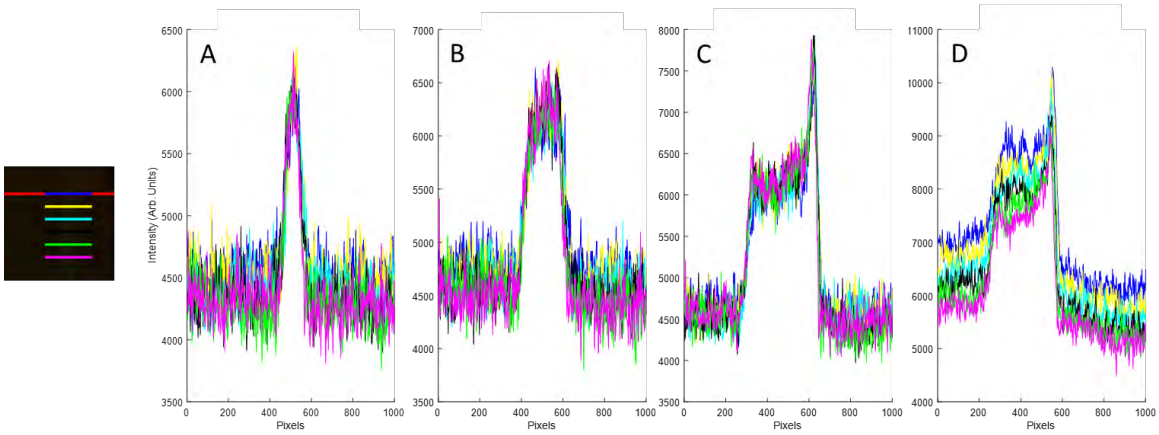

Figure 5. Image analysis results of broadband through Powell lens at diameters of 2–25 mm; A: 2 mm, B: 5 mm, C: 10 mm, D: 25 mm.

These figures show that as the input beam diameter of the source increased, the output line increased to a similar width up to an aperture diameter of 9 mm, the diameter of the Powell lens. If the input beam diameter was greater than 9 mm, aberrations around the lens occurred, but the width of the output beam did not change, as shown in C and D of Figure 4 and Figure 5. The relative intensity of the line varied with each width, but no trend was observed with either source, e.g., increasing intensity with increased diameter, which was expected.[10] These results demonstrate the ability to use a Powell lens to generate a line of light from a collimated broadband source of varying diameters complimentary to the spectrometer FOV.

Data cubes of the surface depicted in Figure 1 were collected using the illumination sources described in Section 3, with the results shown in Figure 6 and Figure 7 below. Each data cube was processed using an anomaly detection algorithm, with a black pixel representing background or non-anomaly, a red pixel representing a detected anomaly and a blue pixel representing a value of zero/non-data point due to limited illumination. As the dirt and gravel represent different surfaces, the data cubes were separated in post-processing and analyzed using two different data sets as background, if not the different background surfaces would all be classified as an anomaly. Under ideal conditions, only the Teflon™ and non-background surfaces will cause an anomaly to be detected. Overall, for the dirt samples, the fixed sources, with the exception of the stage light, had a high number of false anomalies and areas of no-data, as they do not provide even or complete coverage of the instrument FOV. The data collected with the stage, linear mounted halogen, and linear mounted flood lights produced fewer false anomalies and non-data points because the sources output is centered at the instrument FOV. The stage light, due to its larger projection diameter and more even coverage, produced fewer false anomalies or non-data points. Solar illumination produced poor results with the greatest amount of non-data points but did have few false anomalies. The high number of non-data points was due to shadows on the surface caused by the low azimuth angle of the sun.

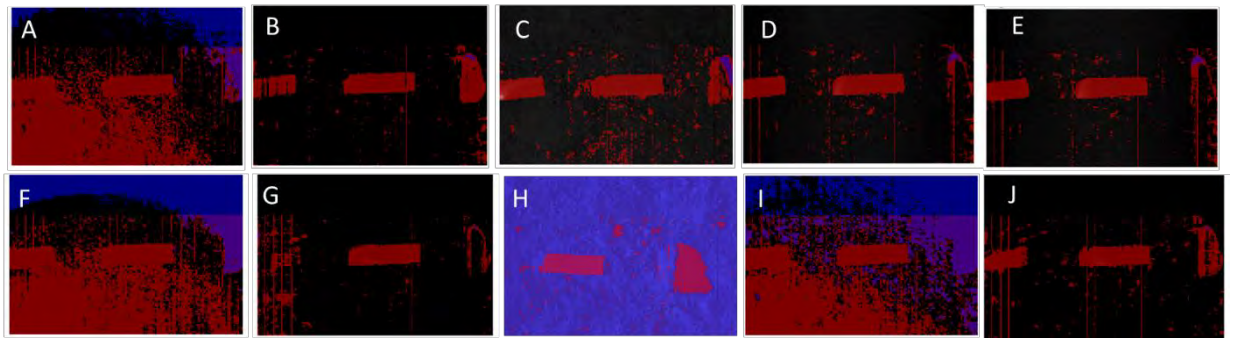

Figure 6. Algorithm results for gravel section of sample with illumination sources as follows: (A) Halogen, 24-inch, fixed; (B) Halogen, 24-inch, linear; (C) Stage, fixed; (D) Flood, fixed; (E) Flood, linear; (F) Halogen, 16-inch, fixed; (G) Halogen, 16-inch linear; (H) Solar; (I) Halogen, fixed; (J) Halogen, linear; Fixed = illumination source is stationary, Linear = illumination source is mounted to stage and tracks with spectrometer.

Results for the gravel samples, Figure 7, were similar to the dirt samples with the stationary illumination producing more false anomalies, while the linear mounted illumination samples produced less anomalies with less non-data points as well. In several of the gravel samples, specifically the fixed illumination, the lower right portion of the image is shown as non-data. This result is likely due to the uneven illumination or because the illumination source is mounted at an angle that is not complementary to the instrument FOV. Overall, the gravel samples had a greater number of non-data points because the surface is darker in color and thus reflects less light to the spectrometer under the same parameters used with the lighter dirt samples.

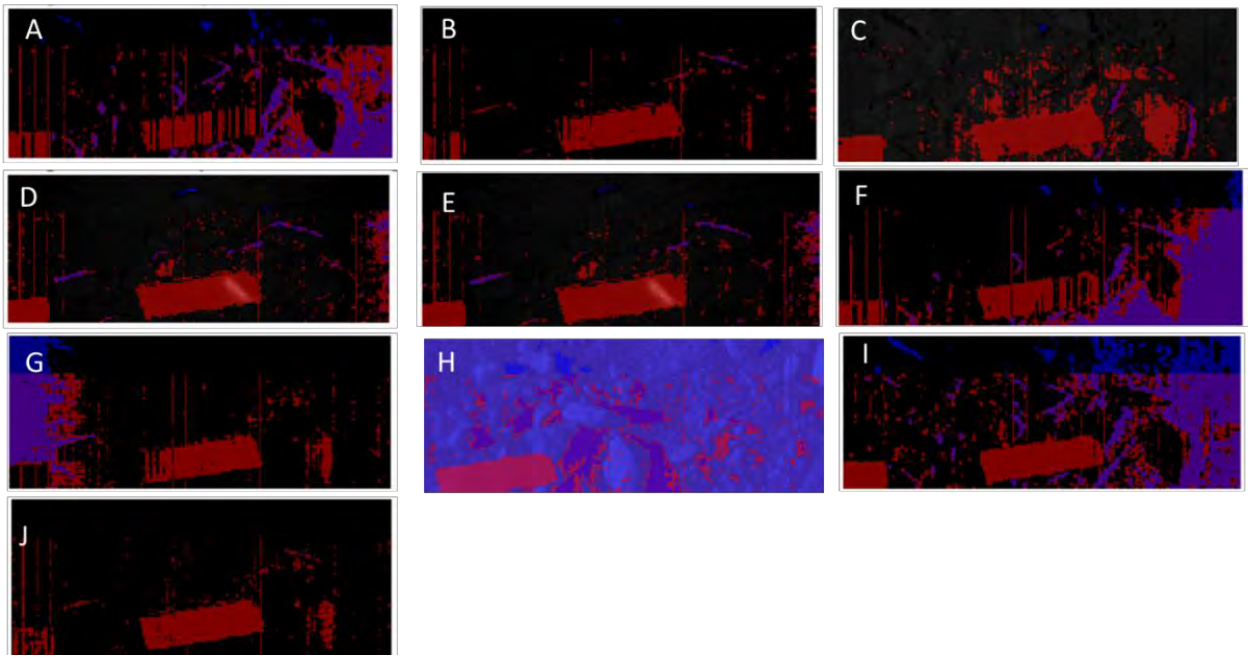

Figure 7. Algorithm results for dirt section of sample with illumination sources as follows: (A) Halogen, 24-inch, fixed; (B) Halogen, 24-inch, linear; (C) Stage, fixed; (D) Flood, fixed; (E) Flood, linear; (F) Halogen, 16-inch, fixed; (G) Halogen, 16-inch linear; (H) Solar; (I) Halogen, fixed; (J) Halogen, linear; Fixed = illumination source is stationary, Linear = illumination source is mounted to stage and tracks with spectrometer.

6. CONCLUSIONS

In conclusion, this work was able to demonstrate the ability of a compact halogen illumination source to provide a sufficient number of photons for a hyperspectral spectrometer to operate under non-daylight conditions. Due to the size and power consumption of the source, it along with the compact spectrometer, could be incorporated into a UAV/UGV for the detection of threats. As the halogen bulb is a commercially available item and is offered in a standard size with a range of power outputs, it could be tailored for a specific application, for example where a high output bulb is not required. While the Powell lens was demonstrated to work with a broadband source, a more complex and costly solution to co-align the compact source with the spectrometer FOV would be required to maximize the photon output. Within the current limitations, the compact halogen source could be integrated into a handheld package for short distance surface interrogation.

ACKNOWLEDGMENTS

Funding was provided by the Director, Combat Capabilities Development Command Chemical Biological Center under the authorities and provisions of Section 2363 of the FY 2018 NDAA to develop new technologies, engineer innovations, and introduce game-changing capabilities.

REFERENCES

[1] Elmasry, G.; Kamruzzaman, M.; Sun, D W.; Allen, P. Principles and applications of hyperspectral imaging in quality evaluation of agro food products: a review. *Crit. Rev. Food Sci Nutr*. 2012, *52* (11), pp 999–1023.

[2] Languirand, E.R; Curtiss, J.M; Emge, D. Field capability of a COTS instrument for on the move anomoly detection. *Presented at the 2019 Joint MSS Battlespace Acoustic, Seismic, Magnetic, and Electric-Field Sensing and Signatures Committee (BAMS) and National Symposium on Sensor & Data Fusion Committee (NSSDF) Conference.* Military Sensing Symposium, San Diego, CA, October 21–24 2019.

[3] Languirand, E.R; Emge, D. Higher order statistics for anomoly detection in hypersprectral imaging. In *Proceedings Volume 11010: Chemical, Biological, Radiological, Nuclear, and Explosives (CBRNE) Sensing XX*. SPIE Defense + Commerical Sensing. Baltimore, MD, June 22, 2019.
[4] Pecharromán Gallego, R. An overview on quantum cascade lasers: origins and development. In *Quantum Cascade Lasers*, Vasilios S.N, Ed.; InTech Open, 2017, p 22.
[5] National Aeronautics and Space Administration (NASA). *Solar irradiance*. [Online]; 2017. https://www.nasa.gov/mission_pages/sdo/science/solar irradiance.html. (Accessed 8 April 2021).
[6] Department of Commerce, National Institute of Standards and Technology. Technical Note 1504. *Precision Spectroscopy, Diode Lasers, and Optical Frequency Measurement Technology*. May 1998. https://nvlpubs.nist.gov/nistpubs/Legacy/TN/nbstechnicalnote1504.pdf (Accessed 2 June 2021).
[7] Lawrence, K.C; Park, B.; Heitschmidt, G.W.; Windham, W.R.; Thai, C. Evaluation of LED and tungsten halogen lighting for fecal contamination detection. *Applied Engineering in Agriculture*. 2007, *23* (6) pp 811–818.
[8] Cai, F.; Tang, R.; Wang, S.; He, S. A compact line detection spectrometer with a Powell lens. *Optik*. 2017, *155*, pp 267–272.
[9] Kosmatka, W. Faceted reflector for headlamps. U.S. Patent 4704661A, November 3 1987.
[10] Latimer, W. Efficient Transformation of Gaussian Beams into Uniform, Rectangular Intensity Distributions. Coherent, 2012. https://www.coherent.com/assets/pdf/Efficient Transformation of Gaussian Beams into Uniform Rectangular Intensity Distributions_FORMFIRST.pdf. (accessed 8 April 2021).

Antiviral copper-loaded polymer systems

Anne Y. Walker
U.S. Army Combat Capabilities Development Command Chemical Biological Center, Research & Technology Directorate, 8198 Blackhawk Rd, Aberdeen Proving Ground, MD 21010

ABSTRACT

Incorporation of copper into polymers could allow for the rapid production of passive antiviral materials that can slow the transmission of microbes, pertinently, SARS-CoV-2. Development of easily deployable copper-loaded systems (e.g. sprayable coatings) could allow for the use of these materials without having to retrofit equipment, thus providing a critical functionality with minimal logical burden. As such, this study focused on the development of copper-loaded polymer systems to serve as passive antiviral composites that could be used as coatings, in textiles, and as 3D printing filaments. This phase of the study centered on the formulation of copper-loaded systems made from inexpensive and readily-available commodity polymers (poly(vinyl alcohol), poly(acrylic acid), and poly(lactic acid)) and copper materials.

Keywords: antimicrobial, antiviral, polymer composites, additive manufacturing, coatings, formulation, poly(acrylic acid), poly(vinyl alcohol), functional materials

1. INTRODUCTION

Contact with contaminated surfaces and subsequent introduction of material into the body (chiefly through touching eyes, nose and mouth) is often a primary route of transmission of harmful microbes. This transmission route for infection and the danger it poses has been brought into sharp focus by the ongoing Coronavirus Pandemic. Though fomite-related transmission has been found not to be the major source of transmission, it still has not been ruled out as a means of introducing the virus.[1] The respiratory excretions of individuals infected with SARS-CoV-2 can land on surfaces, contaminating them for upwards of 72 hours. The SARS-CoV-2 virus can remain viable on surfaces for days (24 hours for cardboard, 2–3 days for stainless steel and plastics).[2] In contrast, coronavirus remains on copper surfaces for only four hours.[3] This is unsurprising, as copper has been shown to be an effective antimicrobial, particularly as compared to other commonly handled materials.[3,4] In particular, copper (I) has been shown to be especially effective against microbes.[4] Unfortunately, deploying copper metal on common-use surfaces is wildly impractical, especially in the face of a massive, globe-spanning pandemic. As such, it appears as though the development of easy to deploy copper-loaded systems that can act as passive antivirals could provide a means for helping slow the spread of infection while minimizing the overall logistical burden associated with replacing common-use surfaces with copper.

Though the production of copper-loaded plastics is not a new concept, many of the polymer systems used are difficult to formulate into easy-to-use coatings, difficult to fabricate into textiles, and unusable for 3D printing purposes. Previously-studied polymer systems include epoxies, poly(ethylene oxide), and polyethylene.[5,6,7] In addition to lacking requisite mechanical properties to match the needs outlined above, several of the polymers used in the past do not provide direct surface accessibility to the copper, attenuating its ability to effectively decontaminate microbes that land on the surface. Instead, for the production of a coating and textiles, this study instead focused on two commonly used membrane materials, poly(vinyl alcohol) (PVA) and poly(acrylic acid).[8,9] For the fabrication of 3D printing filaments, the study will focus on poly(lactic acid) and thermoplastic polyurethane. Though these exhibit the same accessibility issues as epoxies and polypropylene, they are simple to 3D print and may provide a means for post-processing schemes that can introduce antimicrobial functionalities after materials are printed. Overall, this study had three main guiding ideas: the formulated material must be easy to use and non-destructive, the base materials must be readily available and cost-effective, and the systems should be tailorable based on intended end use. We focused primarily on the formulation, use testing, and optimization of a sprayable, removable coating and tested the feasibility of 3D printing filament compounding and textile spinning.

2. MATERIALS AND METHODS

2.1 Materials

Copper (I) chloride, copper (II) chloride, and copper metal were selected as the antiviral portion of the system. Polyvinyl alcohol (99 % hydrolyzed, ~98 kDa) and poly(acrylic acid) (PAA) (450 kDa) were selected as carrier polymers for the coatings and electrospun systems. White thermoplastic polyurethane and clear polylactic acid 3D printing filament were obtained from MatterHackers (Lake Forest, CA) and Colorfabb (Belfeld, NL), respectively and used for filament compounding. Triton X-100 was used for system stabilization during electrospinning. All chemicals used in this study were obtained from MilliporeSigma® (St. Louis, MO) unless otherwise noted.

2.2 Coating formulation

2.2.1 Formulation

Stock solutions of PVA were produced by dissolving 10 % PVA by weight in distilled water and stirring at 80 °C overnight. Stock solutions of PAA were made by dissolving 4 % PAA by weight in either water or ethanol and stirring until dissolved. These solutions were used either as-is or diluted with water as needed.

Copper-loaded films were produced by mixing 0.05–1 % by weight copper material into polymer solutions and deposited via drop-casting, spraying using a standard sprayer bottle, or application to a surface via foam brush. In general, the copper salts dissolved readily in the polymer solutions, up to their solubility limit (47 g/L for CuCl and 730 g/L for $CuCl_2$). Since it is not readily soluble in ethanol, for ethanol-based PAA coatings, CuCl was dissolved in water and this solution was mixed with the PAA solution to achieve the desired copper concentration. Copper metal was introduced by pulverizing copper metal powder in a mortar and pestle and adding this powder to the prepared polymer solution. Due to the presence of carboxylate acid groups along its backbone, PAA can be rendered insoluble via chelation of divalent copper from $CuCl_2$. Because of this, $CuCl_2$ was not used for PAA systems in the coating formulation phase of the study.

2.2.2 Evaluation

Coated surfaces were subjected to tests to assess their peelability and wearability. Drying time was also recorded. For this study, glass petri dishes, a brass doorknob (Kwikset®), and a stainless-steel box wrench were coated (0.2 mL/in^2) for evaluation using a foam brush for application. For evaluation, 0.5 % by weight CuCl-loaded polymer solutions were tested against unloaded controls. All PVA, all PAA, 1:1 PVA:PAA, and 1:2 PVA:PAA were evaluated. Repetitive touch tests were performed using 20 cycles of the opening and closing of a gloved hand to determine wear behavior of the materials. A Brunel Hand 2.0 (Open Bionics™) was used to provide a consistent open and close force.

2.3 Electrospun system

For the electrospun system, stock solutions were generally prepared in the same manner described above for the coating formulation. For the PAA formulations, unloaded PAA, pulverized copper metal, CuCl were used. The unloaded PAA fibers were then post-processed via submersion in 1 M $CuCl_2$ solution to introduce copper to the system and render them insoluble.

Ethanol-based PAA systems were electrospun at 15 kV at a distance of 12 cm and a flow rate of 1 mL/hour. Water-based PAA systems were electrospun at 17.5 kV at a distance of 15 cm and a flow rate of 1 mL/hour. Polyvinyl alcohol systems were electrospun with 1 % Triton X at 20 kV with a distance of 10 cm and a flow rate of 1.5 mL/hour10.

2.4 3D Printing filament

Commercial thermoplastic polyurethane and polylactic (PLA) filament were pelletized and compounded with CuCl salt using a Filabot Ex 6 Desktop Extruder. Compounded filaments were made at 4:1 (polymer:salt) loading.

3. RESULTS AND DISCUSSION

3.1 Coating formulation

In most cases, the coatings were "self-leveling" on flat surfaces, yielding a fairly smooth, even coating of polymer. The optimal balance between thickness and dry time was determined to be at surface loading levels of 0.2 mL/in^2. This yielded water-based coatings that dried in 25 minutes, and ethanol-based coatings that dried in 45 seconds. Copper loading level did not have an appreciable effect on drying time across all types of copper used. In the systems loaded with copper salts, we observed a fairly uniform distribution of copper salts in most loading levels, giving the films a green or blue tint depending on the type of salt used (green for $CuCl_2$ as seen in Figure 1 below, blue for CuCl).

Figure 1. Unloaded PVA film (top) in comparison with 0.1 M CuCl2-loaded PVA film (bottom).

In contrast, at all loading levels, the copper metal-loaded coatings tended to aggregate, leaving a film with distributions of copper metal particles across the majority of the film interspersed with large islands of aggregated copper metal particle. This may be alleviated by introduction of a compatibilizer that could improve the particle-polymer interaction. On curved surfaces, water-based solutions tended to pool at the lowest point. The PAA-loaded ethanol systems did not experience this issue, owing to their significantly faster dry time. $CuCl_2$-loaded PVA films showed oxidation in some spots when applied to the doorknob and stainless-steel wrench. This was not evident in the CuCl systems. In general, the PAA films were the most uniform of all the coatings tested, as seen in Figure 2 below.

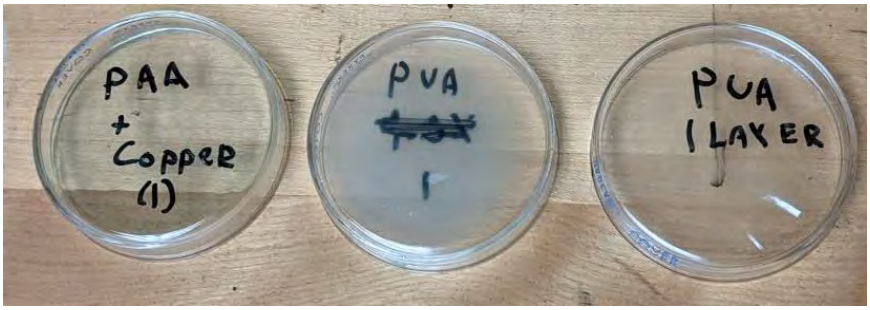

Figure 2. Comparison of films deposited onto glass petri plates. PAA (left) PVA (middle) and PVA with no copper (right).

Copper-loaded PAA systems yielded the clearest, most adhesive films across all forms of copper on all coated surfaces. In general, CuCl2-loaded films were significantly clearer than CuCl-loaded films, likely attributable to the differences in solubility between the two salts. PVA films were the easiest to remove from every surface tested. The adhesive character of blended PVA:PAA films increased as the PAA content was increased, introducing the ability to tailor the adhesive nature of the system depending on need. PVA-only films began to delaminate after five cycles of hand opening and closing across all surfaces tested. The 1:1 PVA:PAA systems showed some delamination beginning at cycle 15. In contrast, PAA-only films and 1:2 PVA:PAA films exhibited no delamination after 20 cycles. The testing apparatus for this evaluation is pictured in Figure 3 below.

Figure 3. Brunel hand gripping a doorknob coated in CuCl-loaded PVA (showing the closed hand position for this test).

Overall, the coating formulation that exhibited the best balance of properties was a 1:2 PVA:PAA system with an 0.5 % CuCl loading. This gave a good balance of resistence to wear while still allowing the user to peel the material off the surface and discard as needed. The optimal coating volume was found to be 0.2 mL/in^2 , yielding a formula that could coat roughly 150 ft^2 per gallon.

3.2 Electrospun system

Both PVA and PAA solutions were electrospun. PVA was much more difficult to spin due to its high sensitivity to an ambient environment and humidity. Though this can be controlled during the electrospinning process, the extra work required to ensure a narrow relative humidity condition made it less desirable as a base material for the fiber formulation. PAA loaded with pulverized copper metal, CuCl and $CuCl_2$, was successfully electrospun with varying fiber and mat quality. The pulverized copper metal systems yielded mats with a high degree of electrospray and some particle aggregation. CuCl-loaded PAA mats were relatively easy to spin and produced even, robust nonwoven textiles as pictured in Figure 4 below.

Figure 4. Electrospun poly(acrylic acid) loaded with CuCl, full mat backed with aluminum foil (left) and smaller peeled portion showing light transmissibility (right).

3.3 Compounded filament

Successful compounding of filament was achieved by using pelletized commercial 3D printing filament blended with copper salt. In general, the compounded filament was much more brittle than its commercial counterpart and exhibited an uneven cross section. These materials must be optimized before testing in a 3D printer, as brittle character and uneven cross section preclude testing on printers due to the possibility of damaging the systems. Compounded material is shown in Figure 5 below.

Figure 5. Compounded PLA filament loaded with CuCl (top), commercial copper metal-loaded filament (middle), and unloaded commercial PLA filament (bottom).

4. CONCLUSIONS AND FUTURE DIRECTIONS

This study represented the first phase of an investigation into copper-loaded passive antiviral materials. The most promising result was the successful formulation of a copper-loaded coating that can be tailored based on life needs, application style, and type of antimicrobial material loaded. PVA/PAA blends, and blends thereof, provide a good balance of peelability and adhesiveness depending on the situational need, and should provide sufficient accessibility to copper for antimicrobial efficacy. For these systems, more robust use testing will help further optimize the formulation. For the electrospun materials, wear testing, morphological characterization, and parameter optimization is necessary. In addition, a higher throughput fiber production method would be beneficial given scaling considerations. For the compounded 3D printing filament, evaluation of printability is the next step. Optimization of the filament for fused deposition molding and testing of the materials subsequent mechanical properties will be another focus of the next phase of this study.

The second phase of this investigation is the evaluation of the antimicrobial character of these systems. This testing will make up the bulk of the second phase of this study. Depending on the results of antimicrobial testing, the type or amount of antiviral material included may have to be changed, but the adaptable nature of this system makes that process much more straightforward. With that in mind, the coating system developed here may have uses beyond being an antiviral, and is perhaps adaptable for other passive decontamination schemes, including chemical warfare agents or toxic industrial chemicals.

ACKNOWLEDGMENTS

Daniel Barker, John Landers, and Cody Kendig provided general guidance, help with editing, and assistance with concept development. Melissa Sweat provided and assisted with use of the Brunel Hand for system evaluation.

Funding was provided by the Director, Combat Capabilities Development Command Chemical Biological Center under the authorities and provisions of Section 2363 of the FY 2018 NDAA to develop new technologies, engineer innovations, and introduce game-changing capabilities.

REFERENCES

[1] Lewis, D. COVID-19 rarely spreads through surfaces. So why are we still deep cleaning? https://www.nature.com/articles/d41586-021-00251-4 (accessed 30 April 2021)

[2] van Doremalen, N.; Bushmaker, T.; Morris, D.H.; Holbrook, M.G.; Gamble, A.; Williamson, B.N.; Tamin, A.; Harcourt, J.L.; Thornburg, N.J.; Gerber S.I.; Lloyd-Smith, J.O.; de Wit, E.; Munster, V.J. Aerosol and Surface Stability of SARS-CoV-2 as Compared with SARS-CoV-1. *N. Engl. J. Med.* **2020**, *382* (16), pp 1564–1567.

[3] Hutasoit, N.; Kennedy, B.; Hamilton, S.; Luttick, A.; Rahman Rashid, R.A.; Palanisamy, S. Sars-CoV-2 (COVID-19) inactivation capability of copper-coated touch surface fabricated by cold-spray technology. *Manuf. Lett.* **2020**, *25*, pp 93–97.

[4] Grass, G.; Rensing, C.; Solioz, M. Metallic Copper as an Antimicrobial Surface. *Appl. Environ. Microbiol.* **2011**, *77* (5), pp 1541–1547.

[5] Das, G.; Kalita, R.D.; Gogoi, P.; Buragohain, A.K.; Karak, N. Antibacterial activities of copper nanoparticle-decorated organically modified montmorillonite/epoxy nanocomposites. *Appl. Clay Sci*. **2014**, *90*, pp 18–26.

[6] Menazea, A.A.; Ahmed, M. K. Nanosecond laser ablation assisted the enhancement of antibacterial activity of copper oxide nano particles embedded though Polyethylene Oxide/Polyvinyl pyrrolidone blend matrix. *Radiat. Phys. Chem.* **2020**, *174*, p 108911.

[7] Gurianov, Y.; Nakonechny, F.; Albo, Y.; Nisnevitch, M. Antibacterial Composites of Cuprous Oxide Nanoparticles and Polyethylene. *Int. J. Mol. Sci.* **2019**, *20* (2), pp 439–455.

[8] Sapalidis, A.A. Porous Polyvinyl Alcohol Membranes: Preparation Methods and Applications. *Symmetry*. **2020**, *12* (6), pp 960–982.

[9] Kozawa, S.K.; Lord, A.; Scott-McKean, J.J.; Walker, A.Y.; Costa, A.C.S.; Wnek, G.E. Microcapillary Reactors via Coaxial Electrospinning: Fabrication of Small Poly(Acrylic Acid) Gel Beads and Thin Threads of Biological Cell Dimensions. *Gels*. **2021**, *7* (2), pp 37–46.

[10] Yang, S. B.; Kim, E. H.; Kim, S. H.; Kim, Y. H.; Oh, W.; Lee, J.- T.; Jang, Y.- A.; Sabina, Y.; Ji, B.C.; Yeum, J.H. Electrospinning Fabrication of Poly(vinyl alcohol)/Coptis chinensis Extract Nanofibers for Antimicrobial Exploits. *Nanomaterials.* **2018**, *8* (9) pp 734–748.

Cortical neurons for toxicological studies

Erin M. Gallagher[b], Julie A. Renner[a], Linnzi K. Wright[a], Theodore S. Moran[a], Russell M. Dorsey[a], Stanley W. Hulet[a]*
[a]U.S. Army Combat Capabilities Development Command Chemical Biological Center, Research & Technology Directorate, 8198 Blackhawk Rd, Aberdeen Proving Ground, MD 21010
[b]National Academies of Sciences, Engineering, and Medicine, NRC Research Associateship Program, 500 Fifth Street, NW, Washington, DC, 20001

ABSTRACT

The Operational Toxicology branch of the U.S. Army Combat Capabilities Development Command Chemical Biological Center maintains a colony of hairless guinea pigs that serve as a primary model for many toxicological assessments. Culturing of primary cortical cells can provide a useful model to measure the impact of chemical threat agents on neuronal signaling and investigate a mechanism of action. However, there are a lack of available published methodologies for culturing neurons from hairless guinea pigs. Cortical brain tissue was harvested from embryonic guinea pigs at different gestational periods of development. The 25–28 day gestational period was determined to be undesirable due to the small size of the brain and lack of structure. After tissue dissection, trypsin times, and cell culture plating densities were varied to determine the ideal conditions for promoting neuronal growth. The 30 minutes trypsin exposure with low seeding density (5,000 cells/cm^2) resulted in the best conditions for neuron growth.

Keywords: hairless guinea pig, primary cell culture, neurons, cortical neurons, glial cells, in vitro cell culture, method development

1. INTRODUCTION

The physiology of the brain, in response to threat agents, is not fully understood. This is in part due to the difficulty of using living brains for *in vivo* studies and a lack of relevant *in vitro* cell lines. Therefore, the ability to establish *in vitro* cultures of neuronal cells is essential to advance our understanding of brain function.[1] These neuronal cell lines can be used to measure the effects of chemical warfare agents (CWAs) and may help elucidate mechanisms of action within the central nervous system (CNS) cheaper and faster than traditional *in vivo* studies. Culturing primary neuronal cells is far more difficult than other cell lines that produce unlimited supplies of homogenous cells. Primary neurons also are not immortalized, which means the number of cells available for replicate experiments are limited.[1] Though difficult to culture, there are many published protocols that have established cortical neuron cell cultures derived from rat and mouse embryos.[1–6] However, there are far fewer protocols using guinea pig embryos and there is no published method for the hairless guinea pig model, a staple for U.S. Army Combat Capabilities Development Command Chemical and Biological Center's *in vivo* toxicity screening.[7–12] It is known that the embryonic development of the guinea pig differs substantially from that of rodents, but there is a lack of ontogeny information that has slowed the development of primary cell cultures from guinea pigs.[8] Establishing the optimal gestational day for harvesting hairless guinea pig neurons is necessary to develop an *in vitro* assay that will better align with *in vivo* toxicity assessments using the same model. In addition, neuronal cell cultures will allow for more uniform replicates to be tested in dose-response and time-course assays in an environment independent of hormonal, vascular, and inflammatory influences that otherwise would complicate whole-brain studies.[13] Developing primary CNS cell culture methodology can be used to assess neuronal function in the presence of threat agents and set the groundwork for primary receptor binding assays paramount to characterizing toxicity, identifying potential points for medical intervention, and for development of a neurovascular/blood brain barrier model.

2. METHODOLOGY

Literature reports various gestational days for successful harvesting of embryonic/fetal guinea pig CNS tissue ranging from 18–56 days.[7–12] Initially, we had chosen to harvest embryonic/fetal cortical neurons in 3 collection groups,

25–28 days, 34–37 days, and 44–46 days to determine the optimal gestational range for generating cultures. However, after the first two attempts at harvesting in the 25–28 day range that group was abandoned. For each collection group, pregnant sows were euthanized by carbon dioxide asphyxiation. Once death was confirmed, the guinea pig was placed in dorsal recumbency and the lower abdominal area was sprayed with 70 % ethanol (EtOH). An incision was made medially through the skin and muscles to expose the uterus and embryos/fetuses. The embryos/fetuses were removed from their amniotic sacs and euthanized immediately by decapitation.

Following resection, brains were placed in an ice-cold Hanks Balanced Salt Solution (HBSS, Sigma-Aldrich® H6648) bath. To maintain sterility, the dissection and subsequent procedures were completed in a PCR cabinet. The brains were dissected, retaining the cortex, sans meninges and blood vessels. The combined hippocampus, cortex, and cerebellum of all fetuses were mechanically minced using scalpels. Combined cells from all fetuses were placed into three 15 mL conical tubes and trypsinized with 0.25 % trypsin in HBSS for 15, 30, or 45 minutes in a 37 °C water bath. The trypsin cell solution was then neutralized with plating media (Dulbecco's Modified Eagle Medium-F12 Glutamax™ (Thermo Fisher Scientific, Inc. 10569010), 10 % fetal bovine serum (FBS) (Gibco™ 16140071), 25 mM d-glucose (Sigma-Aldrich® G8644), 1 % Penicillin-Streptomycin (Gibco™ 15140148)). Cells were triturated with 2 mL serological pipette and then passed through a 40 µm mesh screen (Falcon® 352340, Corning®). Next, the cells were pelleted by centrifugation for 5 minutes at 2,500 g.

The supernatant was aspirated, and the cell pellet was gently suspended in 2.5 mL of Plating Media and cell density was calculated by counting a sample using trypan blue. Cells were seeded at a density of 5,000, 10,000 or 50,000 cells/cm^2 in individual wells in a 96-well plate coated with poly-d-lysine (50 µg/mL, Gibco™ A3890401). Cells were incubated for 1 hour at 37 °C in a 5 % CO_2, then the media was changed to Neuron Media (Neurobasal™ medium (Thermo Fisher Scientific, Inc. 21103049), 50 mg/mL gentamicin (Gibco™ 15750078), 2 % B27 supplement (Gibco™ 17504044)). Half of the 200 µL media was changed every 2–3 days.

Cells were imaged daily and stained with NeuroFluor™ NeuO (StemCell™ Technologies 01801), a neuron stain, to differentiate between neurons and glia cells. A representative microscopic field image of cells stained positive for NeuroFluor™ NeuO can be seen in Figure 1A. The corresponding bright field image of the same cells is shown in Figure 1B to highlight glial cells in the culture. The cells were imaged in the green channel at an excitation of 468 nm and a 557 nm emission as well as in brightfield to capture both the stained and unstained cells. The images were then used to count the number of neurons and glial cells present in each condition using ImageJ multipoint counter.

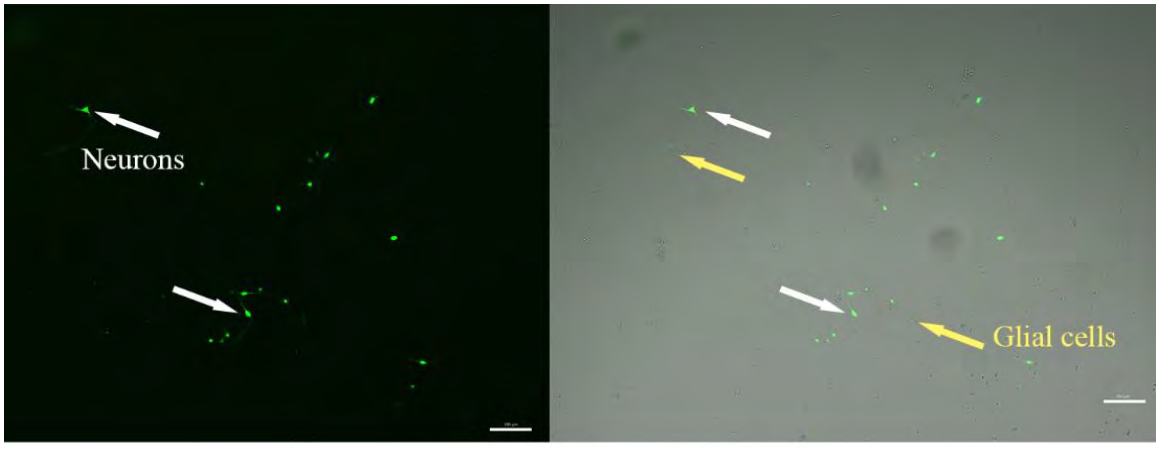

Figure 1. Brain isolate stained with 0.063 µM of NeuroFluor™ NeuO. A) The green fluorescent channel of the brain isolate highlighting the neurons brightly stained cell bodies. B) The overlay of bright-field and fluorescent channel of NeuroFluor™ NeuO stained cells. with select neurons in white and select glial cells in yellow. Note the brightly stained neurons and the unstained glial cells. Scale bar = 100 µM

3. RESULTS

Dissection was successfully performed on all the gestation ages. The latter two gestation ages (34–37 days and 44–46 days) were found to be the most viable for cortical isolation due to their larger size. In the younger gestation

age (25–28 days), the brain was too small to differentiate between the cortex and brain stem, resulting in difficulty isolating the cortex and removing the meninges.

Optimal seeding density and trypsin digest times were determined by splitting the harvested cells into three vials and trypsinizing them for 15, 30, or 45 minutes at 37 °C and then seeding at 5,000, 10,000, or 50,000 cells per cm^2

Cells were maintained in neuron media for 5 to 7 days and then dyed with NeurFluor™ NeuO stain. Cells were then washed for one hour in new media and imaged with one representative image per well.

The cell images were then analyzed using ImageJ Multipoint counter to count the two populations of cells. The first population was the intensely stained cells with small cell bodies and long processes, the second cell population was either faintly stained or unstained and had larger cell bodies with thicker foot processes.

Figure2A shows the percentage of neuron positive cells in cultures at each of the trypsin and seeding densities for brains isolated at gestational days (GD) 34–47. Figure 2B shows the percentage of neuron positive cells in cultures at each of the trypsin and seeding densities for brains isolated at gestational days (GD) 44–46.

No statistical significance was found using a one-way ANOVA. This is most likely due to the low number of harvests included. The larger mean of the 30 minutes trypsin exposure and low seeding density (Figure 2A) suggests that that is the best condition for neuron culture. Confidence in the results would be increased by evaluating more harvests. The total number of cells counted was N=4,215 cells, broken down the cells used to determine the gestation range of 34–37 was GD30=2,335 cells, the cell count for the gestation age of 44–46 was GD40=1,880 cells.

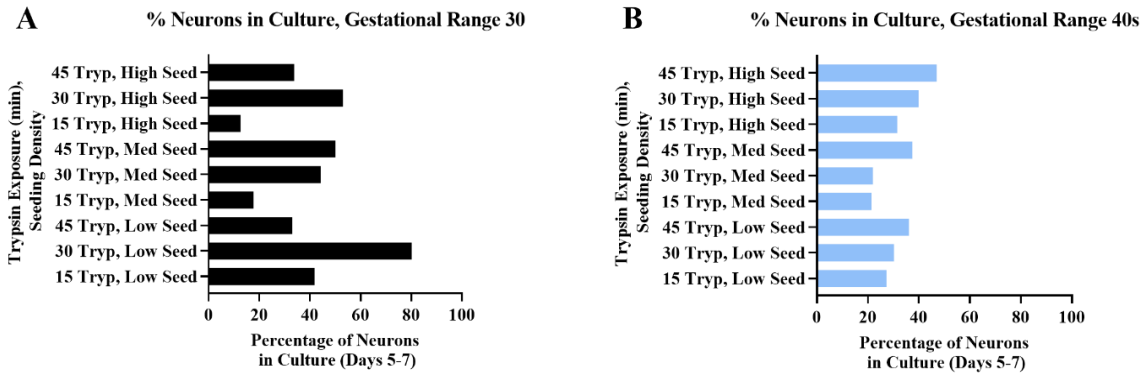

Figure 2. Percent of neurons in culture. Determined by cell stain NeuroFluor™ NeuO. High seeding density 50,000 cells/cm^2, medium seeding density 10,000 cells/cm^2, low seeding density 5,000 cells/cm^2 A) Cells harvested from fetuses in the 30-day gestation range. B) Cells harvested from fetuses in the 40-day gestation age range.

4. CONCLUSIONS

We have determined a method for successfully harvesting guinea pig neurons from fetal tissue. While no statistically significance difference was observed between the different methods, additional experiments could increase our confidence in the seeding and isolation method. We successfully isolated and maintained neurons for 20 days in culture. Antibody staining was less successful, due to the lack of commercially available guinea pig specific antibodies. In place of antibodies, we pivoted to using a neuron stain to quantify number of neurons in culture. From this stain, we quantified the number of neurons in culture per condition, narrowing down the different conditions. This resulted in optimizing the isolation protocol and the 30 minutes trypsin, 5,000 cells/cm^2 was found to yield the highest number of neurons.

ACKNOWLEDGMENTS

Funding was provided by the Director, Combat Capabilities Development Command Chemical Biological Center under the authorities and provisions of Section 2363 of the FY 2018 NDAA to develop new technologies, engineer innovations, and introduce game-changing capabilities

REFERENCES

[1] Gordon, J.; Amini, S.; White, M.K. General overview of neuronal cell culture. *Methods Mol. Biol*. **2013**, *1078*, pp 1–8.

[2] Darbinyan, A., Kaminski, R.; White, M.K.; Darbinian, N.; Khalili, K. Isolation and propagation of primary human and rodent embryonic neural progenitor cells and cortical neurons. *Methods Mol. Biol*. **2013**, *1078*, pp 45–54.

[3] Pacifici, M.; Peruzzi, F. Isolation and culture of rat embryonic neural cells: a quick protocol. *J. Visualized. Exp*. **2012**, (63), p 3634.

[4] Seibenhener, M.L.; Wooten, M.W. Isolation and culture of hippocampal neurons from prenatal mice. *J. Visualized. Exp*. **2012**, (65).

[5] van Niekerk, E.A.; Demuth-Zhang, H. Isolation and cultivation of viable adult mouse cortical neurons. *Miltenyi Biotec Inc*. **2018**.

[6] Viesselmann, C.; Ballweg, J.; Lumbard, D.; Dent, E.W. Nucleofaction and primary culture of embryonic mouse hippocampal and cortical neurons. *J. Visualized Exp*. **2011**, (47), p 2373.

[7] Barg, J.; Levy, R.; Simantov, R. Expression of the three opioid receptor subtypes, mu, delta, and kappa in guinea pig and rat brain cell cultures and in vivo. *Int. J. Dev. Neuroscience*. **1989**, *7* (2), pp 173–179.

[8] Beck, M.; Brückner, M.K.; Holzer, M.; Kaap, S.; Pannicke, T.; Arendt, T.; Bigl, V. Guinea pig primary cell cultures provide a model to study expression and amyloidogenic processing of endogenous amyloid precursor protein. *Neuroscience*. **1999**, *95* (1), pp 243–254.

[9] Cohen, E.; Dieni, S.; Rees, S.M; Small, D.H. Viable primary neuronal cultures from guinea pig embryos. *Toxicol. Methods*. **2008**, *10* (3), pp 231–238.

[10] Kari, B.; Gehrz, R. Susceptibility of fetal guinea pig brain cell cultures to replicating guinea pig cytomegalovirus infection is increased with increasing fetal age: infection of astrocytes. J. *Virol*. **1986**, *58* (3), pp 960–962.

[11] Paidi, M.D; Schjoldager, J.G.; Lykkesfeldt, J.; Tveden-Nyborg, P. Prenatal vitamin c deficiency results in differential levels of oxidative stress during late gestation in foetal guinea pig brains. *Redox Biol*. **2014**, *2*, pp 361–367.

[12] Schou-Pedersen, A.V.; Hanse, S.N.; Tveden-Nyborg, P.; Lykkesfeldt, J. Simultaneous quantification of monoamine neurotransmitters and their biogenic metabolites intracellularly and extracellularly in primary neuronal cell cultures and in sub-regions of guinea pig brain. *J. Chromatogr. B: Anal. Technol. Biomed. Life Sci.* **2016**, *1028*, pp 222–230.

[13] Brewer, G.J.; Torricelli, J.R. Isolation and culture of adult neurons and neurospheres. *Nat. Protoc*. **2007**, *2* (6), pp 1490–1498.

Determination of the rate of aging inhibited acetylcholinesterase by mass spectroscopy

Vanessa Funk, Li Kong, James M. Myslinski*
U.S. Army Combat Capabilities Development Command Chemical Biological Center, Research & Technology Directorate, 8198 Blackhawk Rd, Aberdeen Proving Ground, MD 21010

ABSTRACT

Organophosphorus nerve agents inhibit the enzyme acetylcholinesterase by covalently binding to the catalytically active Ser_{203}. Nerve agents that posses an alkoxy group, including organophosphorus nerve agents such as sarin and VX, are prone to becoming less susceptible to reactivation by known antidotes over time; this process is called aging. Herein, we describe a method to measure the kinetics of aging various acetylcholinesterase-organophosphorus complexes using mass spectroscopy, rather than measuring how well the activity of acetylcholinesterase can be rescued.

Keywords: Nerve Agent, Aging, Organophosphate, Acetylcholinesterase, Sarin, VX, Enantiomer, Stereoisomer

1. INTRODUCTION

Organophosphorus compounds (OPs) are commonly used as pesticides, but they have also been used as chemical warfare agents. Various members of this class of compounds have been used recently in attacks in Syria, Malaysia, England, and Russia. OPs work by inhibiting the enzyme acetylcholinesterase (AChE) in an essentially irreversible process by forming a covalent bond between the oxygen atom of Ser203 and the phosphorus atom of the inhibitor leading to an inactive enzyme. This covalent bond between an OP and AChE inactivates AChE, preventing the removal of ACh at synaptic clefts, causing neuron overstimulation and dysregulation.

The concept of aging nerve agent-inhibited AChE was first observed as a reduction in the maximum amount of AChE activity, as the aged form of the enzyme conjugate is completely resistant to restoration of the enzyme activity. However, measuring this "reactivatability" is limited to agents that are susceptible to reversal with certain oxime antidotes. However, the very presence of the oxime can interfere with the assay by significantly increasing the background. For some nerve agents, no antidote is known to effect 100 % reversal of the inhibition. Because this aging process cannot be measured for these compounds using traditional approaches, we developed a method to directly measure the aging process using mass spectroscopy. The aging process can be described as a dealkylation of the agent-enzyme complex, whereby the aged form of AChE resembles a transition state analogue of the natural reaction of AChE with acetylcholine,[1] and proceeds through an SN1 reaction involving a carbocationic intermediate.[2] A hydrogen bond between the aged complex and His447 is suspected to provide stabilization and inhibit reactivation by known antidotes.[1] Another hypothesis is coulombic repulsion between the negative charge on the phosphate and the nucleophilic oxime.[3]

The rate of such a process is described as an exponential decay that follows first-order kinetics

$$Rate = -\frac{d[AChE_i]}{dt} = k_a[\mathrm{AChE}_i]^1, \quad (1)$$

where $AChE_i$ is the concentration of inhibited AChE, t is time, and k is the first order rate constant. The identity of the aged enzyme complex has been identified by NMR, X-ray crystallography, and mass spectroscopy.[4]

Herein, we developed a method to examine the rate of aging using mass spectroscopy, which will be beneficial for difficult agents, such as those that have no known reactivator. It will also provide a method to *directly measure* the relative amounts of all species of AChE: uninhibited, inhibited (unaged), and inhibited (aged). Because the AChE enzyme varies between species in sequence and in substrate specificity, we used recombinant human AChE. The method could also have applications in measuring the rate of inhibition and reactivation, by changing only a few experimental parameters (e.g. concentrations and time points).

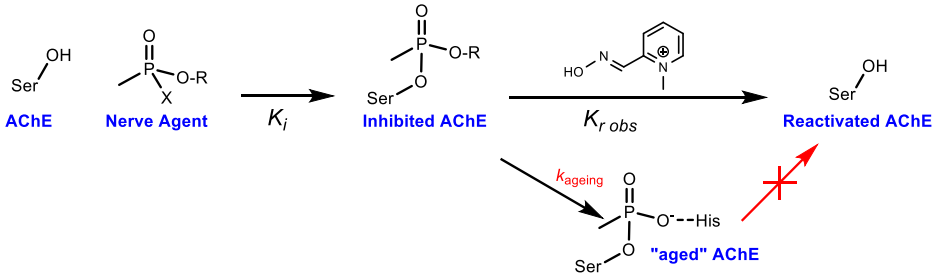

Figure 1. Diagram showing inhibition of AChE with a generic nerve agent.

For compounds with one or more stereogenic center, each rate is different. This phenomenon is evidenced in different toxicities for each enantiomer of GB, so it is important to examine both individually. Furthermore, GA presents an interesting case: it can age by either loss of its alkyl group or the loss of the *N*,*N*-dimethyl group, depending on the stereochemistry of the agent, the difference between these two pathways can be observed by mass spectroscopy.[2]

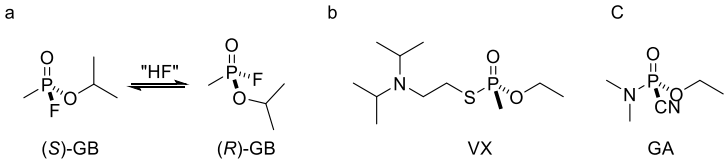

Figure 2. (a) Stereoisomers of GB racemize over time. (b) Structure of VX. (c) Structure of GA.

2. OPTIMIZATION OF MASS SPECTRAL METHOD

Due to the limitations of the instrument, the AChE needed to be digested prior to analysis. Pepsin was selected as the digesting enzyme as it should cut the relevant portion of AChE to a 9-mer suitable for MS. Investigational studies were performed without an internal standard to optimize the digestion. Semi-quantitative studies were then performed using the radiolabeled internal standard FGESAGAAS, which contains the modified serine residue.

Table 1. Predicted and Observed Masses for various species of AChE.* Aged VX and GB-inhibited complexes have the same mass.

Peptide	Theoretical mass $[M+H]^+$	Observed mass $[M+H]^+$	Mass error (ppm)
FGESAGAAS	796.34717	796.34738	-0.26
FGESAGAAS + GB	916.38119	916.38143	-0.26
FGESAGAAS + VX	902.36554	902.36532	0.24
Peptide aged*	874.33424	874.33427	-0.03

3. OPTIMIZATION OF INHIBITION

The known half-life of the unaged GB-inhibited enzyme is between 2.8 hours and 5.4 hours, depending on the source of AChE, pH, and additives,5–6 therefore time points were selected to capture the initial rate and over enough days to cover 5 half-lives. The enzyme was incubated using a large excess of GB, approximately 10 equivalents, to ensure full inhibition. The relative concentrations of each species (aged, unaged, and uninhibited enzyme fragment) need to be measured at various time points, but the enzyme had to be digested into fragments small enough to measure by MS. Because the aging process could theoretically continue during the digestion process, it was decided to halt the process by denaturation. Because heat accelerates the aging process, denaturation at 95 °C was not considered.7 Therefore, the enzyme was denatured using 5 M guanidine hydrochloride at 37 °C to halt the aging process at various time points, prior to pepsin digestion.

4. RATES OF AGING

Prior to receiving the internal standard, a semi-quantitative method was utilized to examine the kinetics of aging (*R*/*S*)-GB-inhibited AChE. Therefore, the sum of aged and unaged (inhibited) AChE was taken to be a constant, and the ratio of unaged to the sum was plotted relative to time (Figure 3). Based on these preliminary results, it was apparent that less frequent sampling was needed early in the time course, but more frequent sampling was needed between 4 and 24 hours to capture the decay. It was also noted that only about 25 % of the entire protein sample was inhibited, bringing into question the quality of the enzyme sample. Therefore, a new sample of AChE was prepared and inhibited with (*R*/*S*)-GB, and the time course measured. Further, the "reactivatability" of the enzyme was measured by incubating aliquots of the enzyme with a high concentration of 2-PAM, and measuring the activity by Ellman's Assay, relative to the inhibited and uninhibited enzyme, for comparison with the MS method (Figure 4).

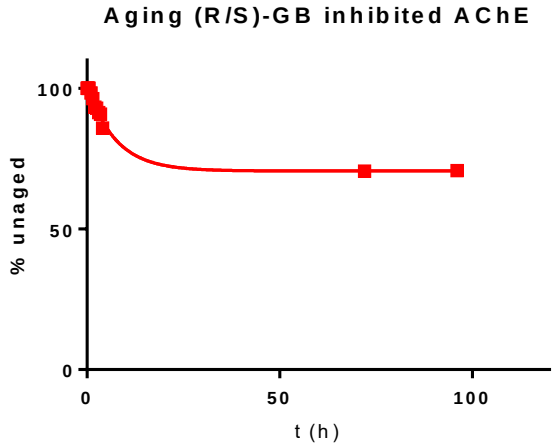

Figure 3. Preliminary aging experiment. The ratio of the aged complex and unaged complex were calculated as a percent of the total protein.

The rate constant for the aging process for racemic GB-inhibited AChE was determined to be 0.1559 and 0.1142 h-1 by MS and Ellman's Assay, respectively. This yields a half-life of and 4.4 hours and 6.1 hours, respectively. These values fall within the known range of GB aging. The rate of spontaneous reactivation for GB is about 4 % per day,7 but this was not taken into account in these preliminary experiments. However, some organophosphates have spontaneous reactivation rates that compete with the dealkylation. Therefore, future investigations should utilize either modified experimental conditions to suppress this rate, or it will have to be considered when deriving the rate constants.

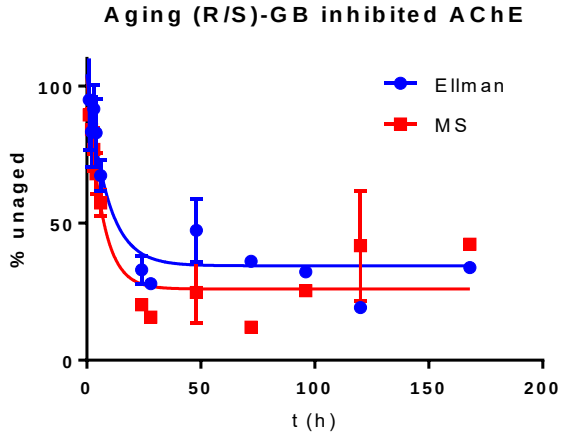

Figure 4. Comparison of the aging of R/S-GB-inhibited AChE by MS and Ellman Method.

The rate constants for aging AChE inhibited with each enantiomer of VX were also determined, essentially as described above, using VX enantiomers that had been separated by liquid chromatography-mass spectrometry and stored at -80 °C.

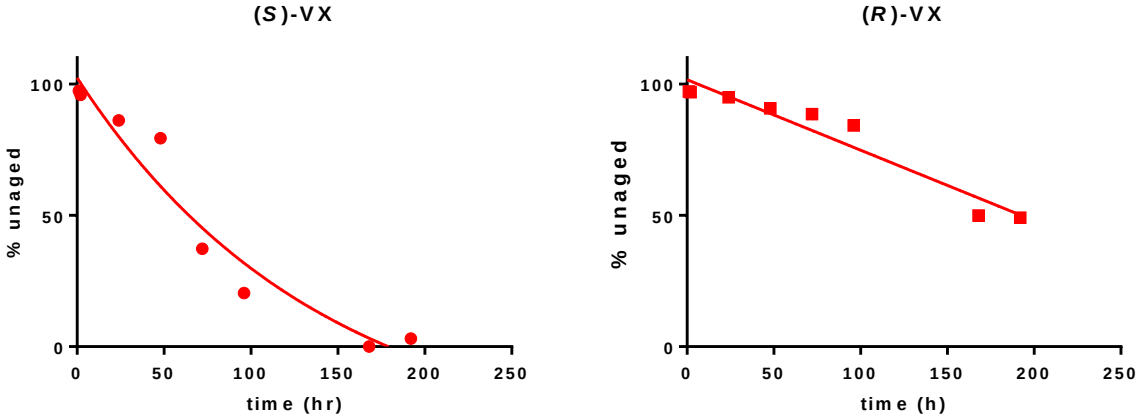

Figure 5. Aging of (*S*)-VX (left) and *(R)*-VX (Right).

The experiments were carried out a total of one time for each enantiomer. The rate constant of aging for (*S*)-VX inhibited AChE is 0.0072 h^{-1}, giving it a half-life of 96 hours. It could not be determined with any certainty for (*R*)-VX—due to it being a slow process not enough data points were captured. The literature half-life of the unaged (*R/S*)-VX complex is 36.5 hours,[8] whereas a similar inhibitor that should give the same inhibited complex had a half-life of 60 hours in another study.[7]

5. EXPERIMENTAL

5.1 Enzyme Inhibition

AChE was obtained as a stock solution frozen in buffer from 2017 (11.1 mg/mL), then buffer exchanged using a centrifugal filter unit (YM-10, MilliporeSigma®, 10 kDa MWCO, 14,000 x g, 60 minutes), replacing the buffer (500 µL, phosphate buffer, 100 mM, pH 7.4), and concentrated again (14,000 x g, 60 minutes), transferring the remaining solution (ca. 40 µL) to a microfuge tube, and adding buffer to bring the total volume collected to ca. 400 µL for each sample condition. The concentration was determined to be 2.9 mg/mL by UV-Vis (Nanodrop 1000, Thermo Scientific) prior to inhibition or was adjusted to obtain 2.9 mg/ml. OP ((*R/S*)-GB, (*R*)-VX, or (*S*)-VX) (1 µL) was diluted in phosphate buffer (99 µL, 100 mM, pH 7.4) and vortexed briefly, creating OP solution. OP solution (10 µL) was added to AChE (2.9 mg/mL, 400 µL), vortexed gently, and incubated at room temperature for 30 minutes. An uninhibited control sample was prepared and incubated under the same conditions by substituting buffer for OP. Excess agent was removed using Centrisep Spin Columns (Princeton Separations, Inc., CS-901), loading 400 µL of sample to pre-hydrated columns and centrifuged at (750 x g) for 2 minutes, and the eluent was collected and then passed through a second Centrisep column. The uninhibited AChE (control) was concurrently run through the Centri-Sep columns. The volumes and protein concentration of the resultant eluents were measured and compared to ensure the uninhibited and inhibited AChE were still comparable. An aliquot (20 µL) was removed for initial characterization experiments to determine that there was at least 95 % inhibition of AChE activity after incubation with the agent. Enzyme activity was determined by Ellman's assay using Ellman's Reagent (0.3 nM 5,5-dithio-bis-(2-nitrobenzoic acid)) (EQM Research, Inc.) and acetylthiocholine iodide (1 mM) (Sigma-Aldrich®, A5751) to produce a colored product (λ_{max} = 412 nm). The removal of the free GB via the Centri-Sep was confirmed by measuring the inhibitory activity of the inhibited enzyme, incubating the inhibited AChE with uninhibited AChE for 10 minutes, and comparing the activity with uninhibited AChE.

5.2 Aging

The reaction solution was incubated on a heat block at 37 °C, and at the desired time points measured from the addition of agent, aliquots (20 µL) were removed from the reaction mixture and placed into an PCR tube containing a solution of guanidine hydrochloride (100 µL, 6 M) at 37 °C for a minimum of 30 minutes to effect denaturation of the enzyme

and halt the aging process. The tubes were stored at -80 °C until the digestion could be performed.[9] The tubes were warmed to room temperature and the contents of each reaction tube was buffer exchanged using an Ultracel YM-10 centrifugal filter unit Microcon, 10,000 MWCO, 14,000 x g for 30 minutes) into aqueous formic acid (500 µL, 0.6 % formic acid) twice. The remaining solution was transferred to a new microfuge tube and the volume was brought up to ca. 200 µL. Pepsin (27 µL, 2 mg/mL) was added to each aliquot, which was then incubated at 37 °C for 3 hours. After incubation, the pepsin and any undigested AChE was removed by passing the solution through a size exclusion centrifugal unit (Amicon Ultra, 3k MWCO, 14,000 x g, 30 minutes), and the flow-through was collected for mass spectral analysis. A radiolabeled standard of the 9-mer fragment (10 µL, 50 µg/mL) was added to each sample (90 µL). The uninhibited control that had been prepared using buffer instead of OP was run identically.

5.3 Analysis

Ultra-high performance liquid chromatography–high-resolution mass spectrometry was performed on a Thermo Fisher Scientific, Inc. Vanquish UHPLC system coupled to an Orbitrap Fusion Tribrid mass spectrometer (Orbitrip Fusion TMS; Thermo Fisher Scientific, Inc., Waltham, MA, USA). Compound separation was achieved using a Luna® Omega Polar C18 column (100 x 2.1 mm i.d., 1.6 µm particle size, 100 Å pore size; Phenomenex) at a flow rate of 300 µl/minute. Mobile phase A was 10 mM ammonium formate aqueous solution with 0.1 % formic acid and mobile phase B was acetonitrile with 0.1% formic acid. The elution gradient was as follows: 0–2 minutes, an isocratic elution of 5 % B; 2–7 min, a linear gradient to 95 % B; 7–8.4 minutes, an isocratic elution of 95% B; 8.5 minutes, a gradient back to 2 % B and equilibration for 1.5 minutes. The total run time was 10 minutes. The injection volume was 2 µL. The autosampler chamber was maintained at 4 °C with a column temperature at 30 °C. Heated electrospray ionization (HESI) was utilized in positive ion mode and samples were analyzed from m/z 100–1,000. The parameters used for the mass spectrometer were as follows: spray voltage, positive 4,100 V; sheath gas flow rate, 40 respective arbitrary units; auxiliary gas flow rate, 20 respective arbitrary units; ion transfer tube temperature, 325 °C; vaporizer temperature, 300 °C; MS detector, Orbitrap; MS resolution, 240,000; MS scan range, 100–1,000; MS maximum injection time, 100 milliseconds; MS automated gain control (AGC) target, 100,000; S-lens radio frequency level, 60 V. In all experiments, active internal mass calibration was employed during the analysis. *X*calibur software (Thermo Fisher Scientific, Inc.) was used for the qualitative and quantitative analysis.

6. CONCLUSIONS

The rates of aging AChE inhibited with racemic GB, (*R*)-VX, and (*S*)-VX were determined by mass spectroscopy and found to be similar to the rates obtained from traditional methods. However, further experiments must be performed to determine the confidence in these values. To rule out racemization of the agent prior to inhibition, some control studies must be performed to determine the conditions at which the agents do not racemize. At this juncture we decided to delay examining the interaction of molecules belonging to the A-series with AChE.

MS was found to provide great insight into the AChE enzyme, including the quality of the enzyme. Furthermore, MS does not suffer some drawbacks that indirect methods to determine reaction rate suffer, such as inhibition or interference by the oxime with the assay, and interference of the agent with the assay. We hope that future studies will incorporate the valuable information that MS offers.

ACKNOWLEDGMENTS

Funding was provided by the Director, Combat Capabilities Development Command Chemical Biological Center under the authorities and provisions of Section 2363 of the FY 2018 NDAA to develop new technologies, engineer innovations, and introduce game-changing capabilities.

REFERENCES

[1] Millard, C. B.; Kryger, G.; Ordentlich, A.; Greenblatt, H. M.; Harel, M.; Raves, M. L.; Segall, Y.; Barak, D.; Shafferman, A.; Silman, I.; Sussman, J. L. Crystal Structures of Aged Phosphonylated Acetylcholinesterase: Nerve Agent Reaction Products at the Atomic Level. *Biochemistry.* **1999**, *38* (22), pp 7032–7039.

[2] Masson, P.; Nachon, F.; Lockridge, O. Structural approach to the aging of phosphylated cholinesterases. *Chem.Biol. Interact.* **2010**, *187* (1–3), pp 157–162.

[3] Barak, D.; Ordentlich, A.; Segall, Y.; Velan, B.; Benschop, H. P.; De Jong, L. P. A.; Shafferman, A. Carbocation-Mediated Processes in Biocatalysts. Contribution of Aromatic Moieties. *J. Am. Chem. Soc.* **1997**, *119* (13), pp 3157–3158.

[4] Bester, S. M.; Guelta, M. A.; Cheung, J.; Winemiller, M. D.; Bae, S. Y.; Myslinski, J.; Pegan, S. D.; Height, J. J. Structural Insights of Stereospecific Inhibition of Human Acetylcholinesterase by VX and Subsequent Reactivation by HI-6. *Chem. Res. Toxicol.* **2018**, *31* (12), pp 1405–1417.

[5] Sterri, S. H. Effect of imidazoles and pH on aging of phosphylated acetylcholinesterase. *Biochem. Pharmacol.* **1977**, *26* (7), pp 656–658.

[6] Crone, H. D. Can allosteric effectors of acetylcholinesterase control the rate of ageing of the phosphonylated enzyme? *Biochem. Pharmacol.* **1974**, *23* (2), pp 460–463.

[7] Berry, W. K.; Davies, D. R. Factors influencing the rate of "aging" of a series of alkyl methylphosphonyl-acetylcholinesterases. *Biochem.* **1966**, *100* (2), pp 572–576.

[8] Worek, F.; Thiermann, H.; Szinicz, L.; Eyer, P. Kinetic analysis of interactions between human acetylcholinesterase, structurally different organophosphorus compounds and oximes. *Biochem. Pharmacol.* **2004**, *68* (11), pp 2237– 2248.

Development and evaluation of temperature-controlled switches for synthetic biology

Julie Zacharko, Nathan D. McDonald*
U.S. Army Combat Capabilities Development Command Chemical Biological Center, Research & Technology Directorate, 8198 Blackhawk Rd, Aberdeen Proving Ground, MD 21010

ABSTRACT

The genomic age has paved the way for developing biological tools and systems for the benefit of society. Collectively, this area of research is oftentimes called synthetic biology which incorporates many fields of science, ranging from engineering to biology and materials sciences, among others. A key aspect of synthetic biology is identifying and utilizing genetic switches which can be implemented as controllers of a desired process. To date, numerous controllers have been identified, characterized, and optimized with new controllers continually being identified and developed. One drawback associated with many of these controllers is the need for an exogenous input to induce activity. Nature has provided many genetic systems which can elicit a response to abiotic inputs such as pH, physical stimulation, and temperature. The ability to harness these controllers will add a tool to the synthetic biology toolbox which can function without the need of additives. Here, we investigate the responsiveness and utility of two previously identified temperature responsive elements, Caf1R and TlpA. Both Caf1R and TlpA were constructed to control the production of a reporter green fluorescent protein and transferred into *Escherichia coli* to generate a temperature responsive biosensor. When grown under increased temperature, the Caf1R system was unable to induce green fluorescent protein expression whereas the TlpA system led to the production of green fluorescent protein. Further characterizations of TlpA found that it does in fact control green fluorescent protein expression in a temperature dependent manner at the temperatures of 25 °C, 30 °C, and 37 °C. Taken together, these data suggest that temperature responsive elements can be harnessed as synthetic biology controllers.

Keywords: synthetic biology, temperature, controllers

1. INTRODUCTION

The world of synthetic biology has discovered and engineered numerous controls, switches, and regulatory elements that can be used for a myriad of functions. As the library of inputs and genetic controls continues to grow, the possibilities of engineered genomes and synthetic microbes becomes more complex and feasible. However, as science continues to push the boundaries as to what is possible, the synthetic toolbox becomes limited. In many cases, controllers require exogenous inputs such as inducing molecules to act as gene promoters. When inducers are required, the risk of cross-reactivity or off-target effects increases. One recent study was able to engineer *Escherichia coli* strains to contain a set of 12 inducible systems with minimal cross-reactivity.[1] While these *E. coli* strains and their cognate controllers provide significant functionality, the system requires input for each step and as the science continues to develop it will again be limited. Alternatively, biological systems have optimized the control of complex regulatory pathways and can respond to a number of external cues that are independent of exogenous molecules.[2] One such abiotic inducer which has been underdeveloped as a tool for synthetic biology is temperature.[3] Organisms across life have numerous and diverse mechanisms to cope and respond to temperature fluctuations. Specifically, the families of heat shock and cold shock proteins are the best characterized in bacteria.[4] However, in addition to broad response system which have effects across the genome, there are several examples of temperature regulated proteins which can activate or repress a specific subset of genes.[4] Here, we characterize two previously identified bacterial protein thermometers which have been implicated in controlling gene expression, Caf1R from *Yersinia pestis* and TlpA from *Salmonella*.[5, 6] These genes were constructed in a plasmid to create a temperature responsive biosensor (Figure 1).

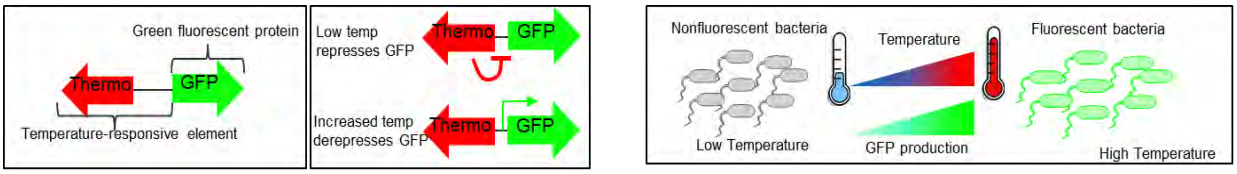

Figure 1. Schematic of temperature dependent biosensors.

2. MATERIALS AND METHODS

2.1 Obtaining and construction of temperature dependent biosensors

The sequence information for Caf1R and TlpA along with their cognate controller promoters were sequence optimized and ordered as gBlocks™ from Integrated DNA Technologies™. These gBlocks™ were cloned into the backbone plasmid through Gibson assembly and transformed into *E. coli* DH5a. The final biosensor plasmids were verified through restriction digest validation.

2.2 Growth and fluorescent readout of temperature biosensors

The biosensors were plated on selective agar plates and incubated at 37 °C overnight for single colonies. Single colonies were selected and grown overnight in Luria-Bertani (LB) broth with shaking at 37 °C. The overnight cultures were diluted 1:50 in LB in a 96-well plate and incubated with shaking in a Biotek® Synergy Neo2 plate reader at either 25 °C, 30 °C, or 37 °C for 16 hours. The absorbance was measured at 600 nm to determine bacterial growth. Fluorescence was measured at an excitation of 485 nm and an emission of 509 nm. Each temperature was measured with three technical replicates and at least two biological replicates.

3. RESULTS

To evaluate the utility of temperature responsive controllers, two biosensors were created from the protein thermometers Caf1R and TlpA designed to control the expression of green fluorescent protein (GFP) (Figure 2 (A)). These biosensors were confirmed by restriction digest screen (Figure 2 (B)).

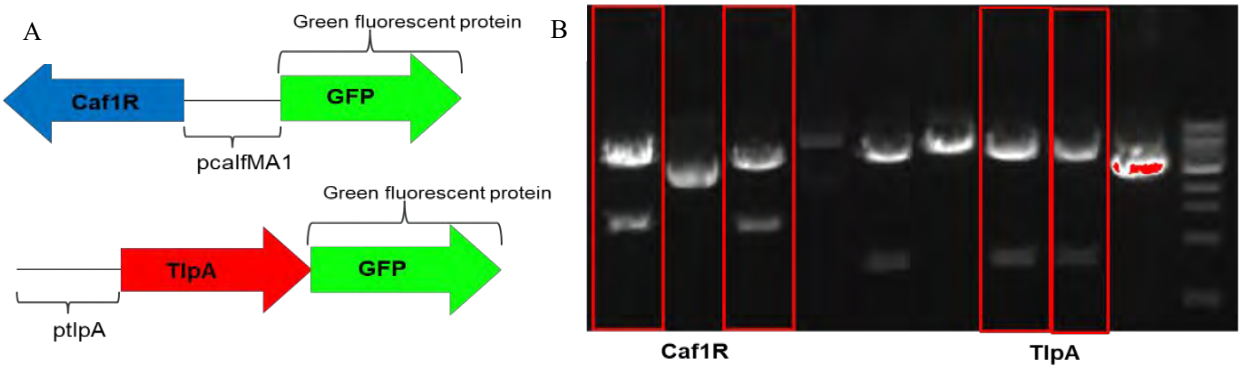

Figure 2. Design and confirmation of temperature thermometer biosensors. (A) Graphical design of protein-based biosensors. (B) Restriction digest confirmation of biosensors. Red boxes indicate validated constructs.

Having confirmed the construction of the biosensors, a preliminary test of the sensors was conducted following growth overnight at 37 °C which is expected to induce expression of the GFP. Following the test, only the TlpA sensor produced GFP at a level greater than the vector control whereas the Caf1R sensors did not (Figure 3).

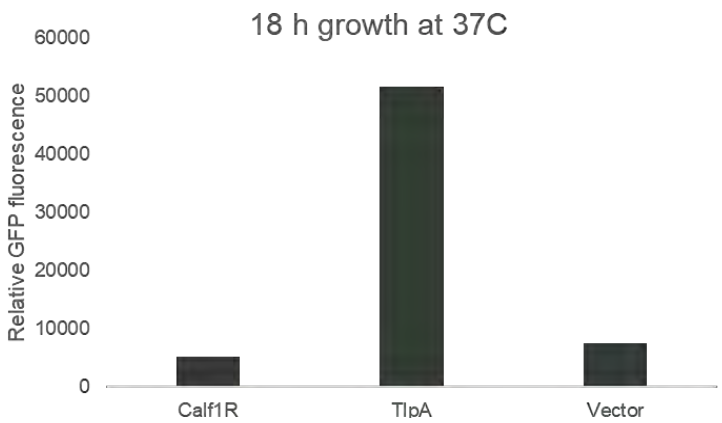

Figure 3. Initial screen of temperature responsive biosensors.

Having observed the functionality of the TlpA sensor, further testing was conducted to determine the temperature dependency of this sensor. *E. coli* transformed with the appropriate TlpA sensor genes or vector control were grown overnight in a BioTek®Synergy Neo2 plate reader at either 37 °C, 30 °C, or 25 °C and the GFP output and the optical density bacteria (to determine overall growth) were measured (Figure 4). As expected, at 37 °C, the biosensor and vector control strains grew maximally and the TlpA biosensor produced significantly more GFP than the vector control. At 30 °C, the bacteria again grew with a minimal lag and the TlpA sensor again produced significantly more GFP than the vector control. Finally, at 25 °C, the bacteria grew but with an extended lag phase. Despite the lag, as expected, there was no difference in GFP produced between the TlpA sensor and the vector control (Figure 4).

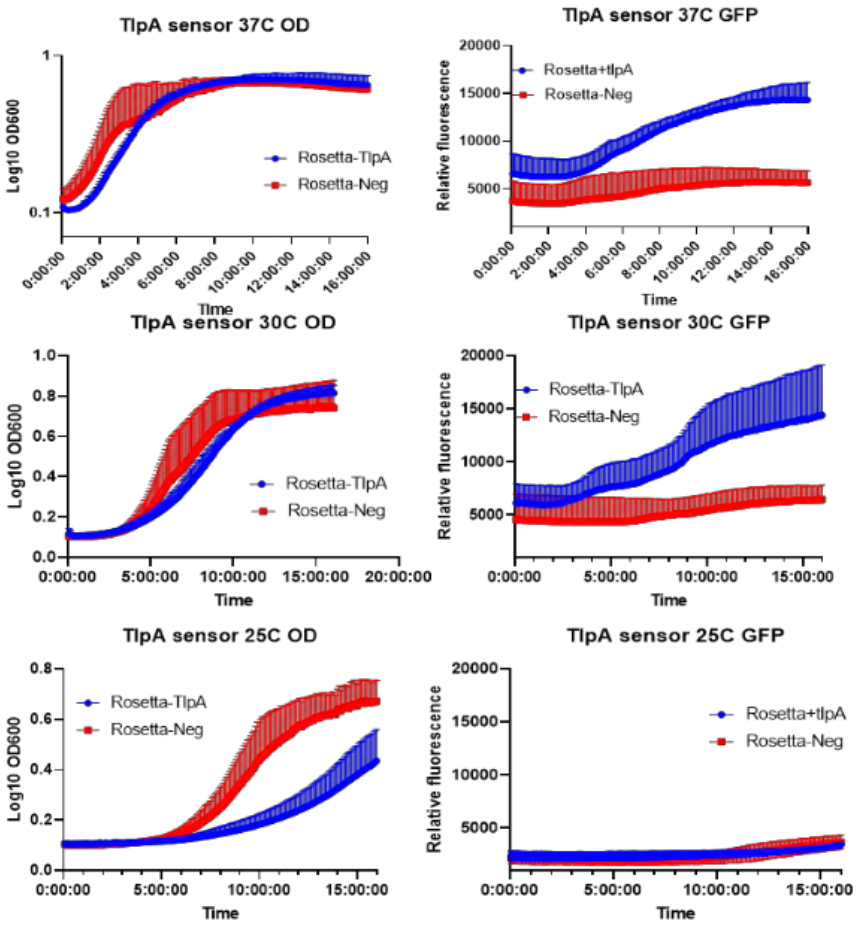

Figure 4. Temperature evaluations of the TlpA sensor at 37 °C, 30 °C and 25 °C.

4. DISCUSSION

The ability to add genetic switches for controlling gene expression is a continuing critical component of expanding synthetic biology. Here we examine the ability to implement protein thermometers which can regulate gene expression in response to temperature changes. We show that the protein TlpA can induce GFP expression at elevated temperatures without the need of additional inputs. The ability to modulate expression through time via tuning temperatures opens the door to creating complex regulatory circuits for a variety of biotechnological purposes. In addition, utilizing temperature as an inducer as opposed to small molecules can be cost saving and decreases burden in certain point-of-care or biomanufacturing applications of synthetic biology. Future work should be dedicated to further identifying characterizing and optimizing these genetic components which respond to environmental cues.

ACKNOWLEDGMENTS

Funding was provided by the Director, Combat Capabilities Development Command Chemical Biological Center under the authorities and provisions of Section 2363 of the FY 2018 NDAA to develop new technologies, engineer innovations, and introduce game-changing capabilities.

REFERENCES

[1] Meyer, A.J.; Segall-Shapiro, T.H.; Glassey, E.; Zhang, J.; Voigt, C.A. *Escherichia coli* "Marionette" strains with 12 highly optimized small-molecule sensors. *Nat. Chem. Biol.* **2019**, *15* (2), pp 196–204.

[2] Bervoets, I.; Charlier, D. Diversity, versatility and complexity of bacterial gene regulation mechanisms: opportunities and drawbacks for applications in synthetic biology. *FEMS Microbiol. Rev.* **2019**, *43* (3), pp 304– 339.

[3] Hoynes-O'Connor, A.; Shopera, T.; Hinman, K.; Creamer, J.P.; Moon, T.S. Enabling complex genetic circuits to respond to extrinsic environmental signals. *Biotechnol.Bioeng.* **2017**, *114* (7), pp 1626– 1631.

[4] Loh, E.; Righetti, F.; Eichner, H.; Twittenhoff, C.; Narberhaus, F. RNA thermometers in bacterial pathogens. In *Regulating with RNA in Bacteria and Archaea,* Chapter 4*;* Storz, G.; Papenfortm K., Eds.; Wiley, **2018**; pp 55–73.

[5] Al-Jawdah, A.D.; Ivanova, I.G.; Waller, H.; Perkins, N.D.; Lakey, J.H.; Peters, D.T. Induction of the immunoprotective coat of *Yersinia pestis* at body temperature is mediated by the Caf1R transcription factor. *BMC Microbiol.* **2019**, *19* (1), pp 1–12.

[6] Hurme, R.; Berndt, K.D.; Normark, S.J.; Rhen, M. A proteinaceous gene regulatory thermometer in Salmonella. *Cell.* **1997**, *90* (1), pp 55–64.

Evaluation of cold weather decontamination methods

Jana Kesavan[a], Daniel McGrady[b], Aime Goad[a], Amanda Schenning[a], Melissa Sweat[c]
[a]U.S. Army Combat Capabilities Development Command Chemical Biological Center, Research & Technology Directorate, 8198 Blackhawk Rd, Aberdeen Proving Ground, MD 21010
[b]MAG Aerospace, 12730 Fair Lakes Cir., Suite 600, Fairfax, VA 22033
[c]Defense Threat Reduction Agency Chemical Biological Research Center of Excellence, 8725 John J. Kingman Rd, Fort Belvoir, VA 22060

ABSTRACT

Most chemical or biological decontamination protocols have been driven by the need for fast and efficient methods that are relatively safe and easy to implement. As such, the focus has primarily been towards "general" environments—those in which water is readily available, and the ambient conditions are amenable to such techniques. Some of these include water showers, sprays with chemical decontaminants (e.g., soapy water or diluted bleach). However, there exist some scenarios in which water-based decontamination methods are not desirable. These include such regions as arid regions (water scarcity), specialized operations (method must be low volume/weight), and cold weather (water freezing). This study focuses on the cold weather challenge: identification of common methods for readily available decontamination and evaluation of their respective efficacies. Methods evaluated include wiping (with wet and dry wipes), blotting with moistened wipes, vacuuming, and the application and removal of adhesive tape. Results demonstrate that vacuuming and blotting (without overlapping targeted regions) are generally less effective than other wiping, blotting, and adhesive tape-based measures at removing bacteria from surfaces.

Keywords: decontamination, bacteria spores, wiping, vacuuming, blotting, adhesive tape, cold weather.

1. INTRODUCTION

It is important to decontaminate people quickly to mitigate adverse health effects. Assets are also decontaminated immediately to prevent spread of the contaminant. Many chemical decontamination processes involve applying a liquid decontaminant to humans, their personal protective equipment (PPE), and other contaminated assets.[1–5] However, certain venues requiring decontamination (decon) may not be conducive to methods requiring significant volumes of liquid—either due to scarcity (e.g., in a desert) or due to environmental conditions (e.g., temperatures below freezing). Generally, water-based decontamination methods are used when the outdoor temperatures are above 65 °F (~20 °C).[1] Ambient air temperature of 65 °F is considered as a "breakpoint" for decontamination based on comfort.[1] As the temperature decreases, outdoor decon transitions into heated tents where the personnel are also housed post decon.[1] Below 35 °F (~2 °C), water-based decons must be conducted indoors, or warfighters must transition to dry decon methods for outdoor operation.[1]

Environmental conditions were a point of consideration during the Arctic Eagle exercise in Alaska, performed in February 2020. This military exercise included the outdoor decon of personnel and dogs in heated tents using dry decon methods where the outdoor temperatures at approximately -20 °F (~-30 °C). At these temperatures, any decon method involving water was wholly impractical, resulting in the use of a variety of dry decon methods. These observed methods included vacuuming and wiping with paper towels (e.g., Scott® Rags in a Box), though an additional technique (applying and removing duct tape to a contaminated region) was considered but not observed. Regardless, the decon efficiency was unknown for all of these methods at the time of their employment during Arctic Eagle 2020, leading to a critical need to experimentally evaluate the removal efficacy of the aforementioned protocols—which will then enable the determination of whether further research is necessary to develop advanced dry decontamination methods. This manuscript describes the test methodologies employed, as well as the efficacy observed for each of the common cold weather decon methods.

A number of studies have endeavored to evaluate dry decon methods or other novel methods for decontamination.[1–3] Some of these include the development of novel materials (e.g., metal-organic frameworks),[2] and some are predominantly focused on the methods and materials of contamination removal (e.g., paper towels versus incontinence

pads; rubbing versus blotting).3,6–8 Previous guidance generally agree: time is critical, and water-based treatments are the most commonly recommended.1–4 This study builds on some of those previous ideas as they apply to the cold weather challenge in which water may not be readily available, or may be subject to freezing (whereby the efficacy of the water-based decon is unknown as the water turns to ice). Because the criticality of time is well known, decon using materials on-hand are generally seen as acceptable during a crisis.1 The general recommendation is to perform decon measures as quickly as possible, while trying to optimize doing the most good for the affected population, while minimizing any risks that may be incurred.1,9 This is a challenge as dry decon becomes more widely available, as the implementation of such methods is not necessarily as straight forward as a water shower.3 Implementation of dry decon is more likely to result in secondary contamination resulting from "movement" of contaminant in these events.3,10 Further, there is no standard decon procedures in the U.S. and this results in a varied response.11 Accordingly, these studies emphasize the need for increased evaluation of wiping protocols, as well as the need for effective communication of those results to those implementing dry decon procedures.

2. MATERIALS AND METHODS

2.1 Test substrates

Clear glass microscope slides (soda lime glass, Corning®; Corning, NY) were selected as the substrates for the wiping experiments. An aluminum tray was constructed to contain specially designed tracks to hold the microscope slides in a static configuration (e.g., to prevent sliding, rotating, etc., of the slides). This assembly is shown in Figure 1. Note that the glass slides are shown as opaque blue rectangles—this graphical representation is intended to describe how the slides were oriented in the tray. The slides themselves were made of clear glass. The arrow shown in the top row is indicative of direction of wiping, as described in the next section.

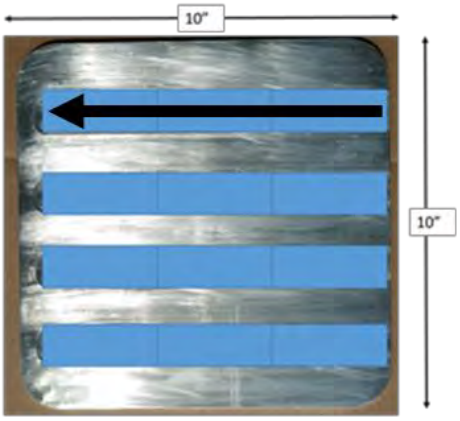

Figure 1. Twelve microscope slides as installed in the custom aluminum tray. Arrow depicts the direction of the wiping motion during wiping experiments. Each wipe will encounter three slides along a horizontal row, and each row represents a new wiping activity. For each tray, two rows were wiped, and two were not. The unwiped samples served as the controls for the evaluation.

Bacillus atrophaeus var. globigii (BG) was chosen as the test material for culture analysis. For each experiment, the BG spores were aerosolized and deposited onto twelve slides. The aerosolization and sample generation apparatus diagram is shown in Figure 2. Here, aforementioned glass slides in the aluminum tray were placed at the bottom of the chamber atop a rotating surface. The particles are dispersed in deionized water with 0.01 % Tween®80 (Sigma-Aldrich®) and aerosolized using a Sono-Tek aerosol generator (model 02809, Sono-Tek Corporation; Milton, NY). Air entering the chamber is heated and passed through the entry tube of the generator, carrying the aerosolized bacteria into the sample compartment of the test chamber. The particles were allowed to deposit on the surface of the microscope slides for at least 4 hours. During the particle deposition, the rotating table at the bottom of the chamber spins to ensure that all glass slides receive a uniform coating of particles. For those tests in which multiple decontamination methods were evaluated, the microscope slides were placed individually on the rotation surface for particle deposition followed by placement in the aluminum tray for each respective decontamination experiment. The aerosols generated were evaluated via an Aerodynamic Particle Sizer® 3321 (APS™) (TSI® Incorporated; Shoreview, MN) and observed to exhibit a bimodal size distribution. The number median distribution showed peaks at 1 µm and 3.4 µm, and the mass median diameters were observed at 1.4 µm and 4.8 µm.

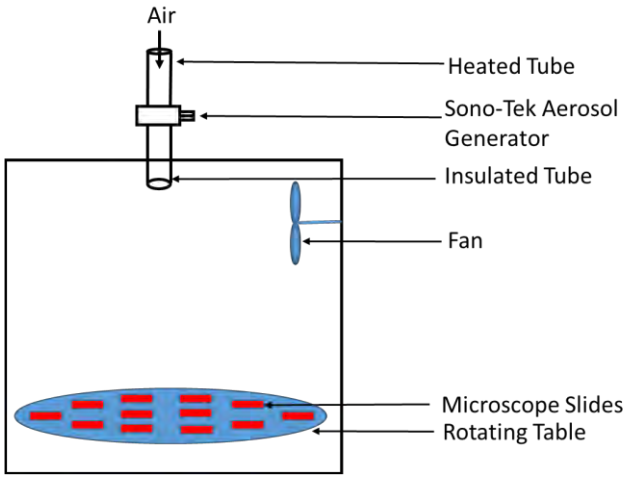

Figure 2. Aerosolization and sample generation apparatus. Air enters the heated tube at the top and carries the Sono-Tek generated particles to the insulated tube. After exiting the insulated tube, the particles are allowed to deposit on the glass slides at the bottom of the chamber. The glass slides are rotated to ensure even distribution of particles across the surface.

For each cold weather decontamination method evaluation, twelve slides were generated with aerosolized BG spores. Six of these were used as controls, and six were evaluated using the prescribed decontamination method.

2.2 Decontamination materials

Three decontamination methods were evaluated in this study: wiping, blotting, and tacky removal. The wiping experiments were performed with both wet and dry wipes. The blotting method used wet wipes only, and the tacky removal decon was performed using several adhesive tape products.

The specific wipes used in this study were FiberTect dry decontamination wipes (First Line Technology; Chantilly, VA) and Scott® Rags in a Box (Scott® Paper Company; Philadelphia, PA). Additionally, three adhesive tapes were evaluated: duct tape (Scotch™ brand, 3M™ ;Saint Paul, MN), 3M™ 2480 (3M™, Saint Paul, MN), and 3M™ 2476.

The FiberTect wipe is a commercial wipe comprised of three layers designed for optimal adsorption and absorption of toxic materials, including chemical warfare agents (CWA) and pesticides. The wipe is advertised as an inert, flexible, non-woven composite comprised of an activated carbon fibrous layer held between two fabric providing structure, mechanical strength, and other necessary physical properties to facilitate ease of use without damaging assets. For the dry wiping study, the 12 inch x 6 inch wipes were cut to produce 4 inch x 3 inch pieces. For the wet wiping evaluation, the wipes were sprayed with Dahlgren Decon™ A (DD-006-A-RTU, First Line Technology; Chantilly, VA). Dahlgren Decon™ is a very common wet decontaminant which is safe for use on PPE, sensitive equipment, and other such assets. Dahlgren Decon™ is stable for the life of a decontamination event, and usable in temperatures ranging from -20 °F to 160 °F (-20 °C to 71 °C). To produce a wet wipe, the decon solution was loaded into a spray bottle and sprayed onto the wipe from approximately 10–12 inches.

Scott® Rags in a Box (Scott® Paper Company;, Philadelphia, PA) is a common commercial off-the-shelf product that contains dry wipes usable for a wide variety of applications—wiping spills, absorbing waste liquid, etc. They are specifically manufactured for use in wet or dry-cleaning applications. Each wipe is 10 inches x 12 inches. These wipes were used as received for dry wiping applications.

The duct tape evaluated in this study was sourced from 3M™ (Saint Paul, MN). Duct tape is extremely strong and is manufactured using a natural rubber adhesive. This enables the tape to adhere to a variety of asset types—theoretically removing the contamination when the tape is peeled away from the surface. The duct tape was used as received.

However, because the duct tape may not be recommended for skin decon, a similar medical tacky tape could be used to avert any potential skin damage from the adhesivity of duct tape. This is, in part, the reason for including the 3M™ medical tacky tapes in this study. None of the products or methods considered in this study were evaluated for their impact on skin, PPE, or any other asset requiring decontamination.

3M™ 2480 (3M™; Saint Paul, MN) is a nonwoven polyester tape designed for use in the medical industry. The tacky side of tape is comprised of a proprietary silicone adhesive which allows the tape to be repositioned on skin without loss of adhesivity. The non-adhesive side of the tape is a white spunlace polyester. The tape was used as received.

Similarly, the 3M™ 2476 (Saint Paul, MN) is another commercial off-the-shelf nonwoven polyester tape. The tacky side of this tape is a proprietary silicone adhesive which also allows for repositioning on the skin. The principal difference between 2476 and 2480 is that the 2476 tape is less strongly adhesive than the 2480 option. Both tapes were evaluated, and both were used as received.

2.3 Decontamination methods

For all wiping applications, six slides were arranged in the aluminum tray as shown previously. The tray/slide assembly was placed on a scale (Ozeri USA; San Diego, CA), and the slides were wiped once with an applied mass of 2 lb. The wipe was placed at one end of the tray and translated across the surface of the glass slides until the wipe reached the opposite end of the tray. The wipe movement occurred in the direction of the glass slide as shown in Figure 1. The tray was fitted with stoppers to prevent the slides from being pushed off the tray. The wipe was first applied to the top row of slides. Once the top row was wiped, the wipe was folded before being applied to another row of slides to prevent cross-contamination.

The blotting technique was evaluated using wet FiberTect wipes. Much like the wiping evaluations, the tray/slide assembly was placed on a scale and blotted with an applied mass of 2 lb. The blotting technique required the wipe to be placed on the slide and translated a set distance away from the original location before removing the wipe from the glass slide. Multiple blots were performed on each slide to maximize coverage of the slide. The motion used is similar to wiping a liquid off a surface (e.g., removing ketchup from a counter). For the first blotting technique, the wipe was translated for a distance of a few millimeters. Additionally, the blotting areas did not overlap, but the same section of wipe was reused for multiple blotting actions. The second blotting method varied slightly—the translation distance was approximately a centimeter, the wiping areas overlapped, and a new area of the wipe was used for each blotting motion.

Due to the adhesive nature of the tape, the efficacy experiments were performed slightly different. The tape was placed on the scale with the adhesive side facing away from the scale. Then, a single contaminated slide was placed on top of the tape such that the contaminated face of the slide was in contact with the tape. The slide was pressed into the tape with an applied mass of 2 lb. Then, the tape was removed from the slide.

For the vacuuming evaluation, a commercial vacuum cleaner (WindTunnel®, Model UH70120, Hoover®; Austin, TX) was assembled per the instructions. The brush attachment was installed on the vacuum and placed in contact with the aluminum tray housing the contaminated slides. The vacuum was turned on, and the brush was translated along a single row of slides. The brush was then cleaned before being applied to the next row of slides. The air flow through the brush attachment was 1,239.13 liters per minute (lpm).

2.4 Efficacy calculations

Following the decontamination protocol, each slide (either control or test) was placed in a 50 mL centrifuge tube. Then 20 mL of phosphate buffered saline with 0.01 % Tween® (PBST) was added to the centrifuge tube, and the sample was vortexed for 10 minutes to maximize bacteria removal from the contaminated microscope slides. The samples were then plated in triplicate and incubated overnight, which allowed the observation of the number of culturable organisms in the sample from the control and decontaminated slides. The decontamination efficiency was determined by comparing the number of organisms removed by decontamination to the number of organisms in the control slides according to equation 1. In this equation, the decon efficacy describes the effectiveness of the decontamination method, where 100 % indicates a complete removal of the contaminant, and 0 % indicates that none of the bacteria were removed. The other terms refer to the number of observed CFUs in the agar plates after the overnight incubation for the decontaminated samples and the control samples. In the case of the control samples CFU, the value used is the average across all control samples.

$$Decon\ efficacy = \left(1 - \frac{cfu_{decon}}{cfu_{control}}\right) \times 100\% \quad (1)$$

3. RESULTS

This project successfully evaluated nine cold weather decon methods and the efficiency results are provided in Figure 3. In addition, the results are also shown numerically in Table 1. The column labelled average is the average percent of bacterial spores removed from the six samples collected for each decontamination method. The standard deviation is also provided.

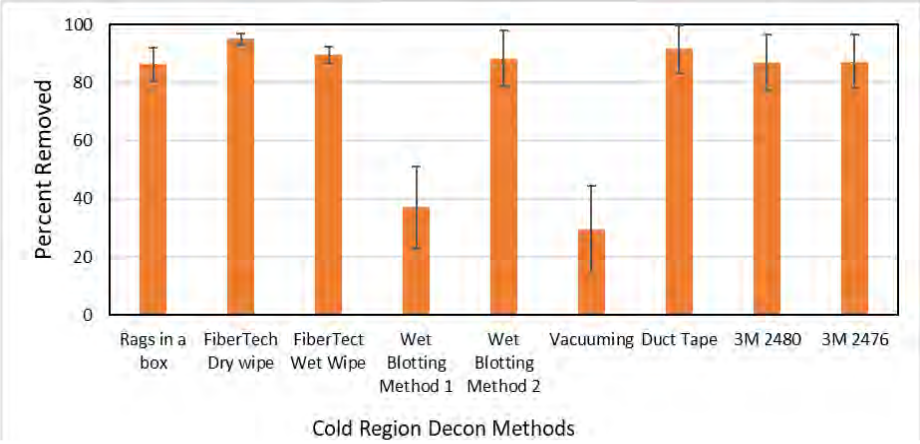

Figure 3. Amount of bacterial spores removed as a function of cold weather decontamination methods. Values are presented as the average percent of bacterial spores removed from six independent experiments. Error bars represent standard deviation.

Table 1. Amount of bacterial spores removed as a function of decontamination method.

	Percent Removed (%)	
Decon Method	**Average (%)**	**Std. Dev.**
Rag in a box	86.24	5.84
FiberTect (FT) Dry Wipe	94.93	1.77
FT Wet Wipe	89.53	2.79
Blotting Method 1 (FT)	36.95	14.16
Blotting Method 2 (FT)	88.23	9.56
Vacuuming	29.54	14.78
Duct Tape	91.44	8.27
3M™ 2480	86.77	9.57
3M™ 2476	87.12	9.30

Based on these results, the FiberTect dry wipe exhibits the highest percent removal from the glass slide. The vacuuming performs the poorest. Notably, however, the vacuuming is not distinctly different from the wet blotting method 1. This may be a result of either decontamination method missing contamination regions of the slide. In the blotting case, method 1 did not require the blotting motions to overlap. Because it is quite difficult to observe small particles on a clear substrate, the opportunity to miss contamination is greater than a method where caution is taken to overlap targeted areas. Similarly, the vacuum brush will not interrogate the glass slide with the efficiency of a handheld wipe. This clear operational deficiency is likely the cause of the decreased spore removal.

The remaining seven decon methods all performed very well—removing over 80 % of the contamination in all cases. The dry and wet wiping techniques all performed with very small deviation from the mean. Essentially, each wipe was repeatable. The wet blotting method 2 and the adhesive tape methods all exhibited greater deviation from the mean, indicating process variations had a more dramatic effect on total contamination removal. The ability to maintain a constant wipe is generally an easier motion than ensuring full contact of adhesive tape on a surface, for example.

Ultimately, this evaluation has provided significant insight into a number of cold weather decontamination techniques which have been previously observed in the field. Several of the techniques show promise in terms of contamination removal efficacy, specifically in terms of aerosolized bacterial removal, and a couple were considerably less effective. This work provides the basis for future research in terms of the contamination removal efficacy of an expanded range of contaminants (including hazardous particulate chemicals, pharmaceutical based agents, and liquid contamination). Further, the work shown here provides baseline data for understanding how cold weather affects decontamination efficacy of known dry decontamination techniques. There are a wide variety of potential contaminantes with different physical and chemical properties that can adhere to a plethora of surfaces with different properties that will require unique decontamination strategies, but this work provides a basis and a framework for this type of research to be considered.

ACKNOWLEDGMENTS

Funding was provided by the Director, Combat Capabilities Development Command Chemical Biological Center under the authorities and provisions of Section 2363 of the FY 2018 NDAA to develop new technologies, engineer innovations, and introduce game-changing capabilities.

REFERENCES

[1] Guidelines for Cold Weather Mass Decontamination During a Terrorist Chemical Agent Incident 2002; U.S. Army Soldier and Biological Chemical Command (SBCCOM), Edgewood area of the Aberdeen Proving Ground, MD.

[2] Cao, Y.; Hui, X.; Maibach, H. Effect of superabsorbent polymers (SAP) and metal organic frameworks (MOF) wiping sandwich patch on human skin decontamination and detoxification in vitro. *Toxicology Letters*. **2021**, *337*, pp 7–17.

[3] Amlot, R.; Carter, H.; Riddle, L; Larner, J; Chilcott, R. P. Volunteer trials of a novel improvised dry decontamination protocol for use during mass casualty incidents as part of the UK's initial operational response (IOR). *PLoS One*. **2017**, *12* (6), pp 1–18.

[4] Chan, H.; Zhai, H.; Hui, X.; Maibach, H. Skin decontamination: principles and perspectives. *Toxicology and Industrial Health.* **2012**, *29* (10), pp 955–968.

[5] Boyne, D. A.; Ruth, J. L.; Piesen, J. C.; Mantooth, B. A.; Eikenberg, J. H.; Smallwood, S. Q. Effect of Thickener on Measurement of Simulant Retention and Decontamination Performance for Materials. CCDC CBC-TR-1580; U.S. Army Combat Capabilities Development Command Chemical Biological Center: Aberdeen Proving Ground, MD, **2019**, UNCLASSIFIED Report (AD1073141).

[6] Larner, J.; Durrant, A.; Hughes, P.; Mahalingam, D.; Rivers, S.; Matar, H.; Thomas, E.; Barrett, M.; Pinhal, A.; Amer, N.; Hall, C.; Jackson, T.; Catalani, V.; Chilcott, R.P. Efficacy of different hair and skin decontamination strategies with ideantification of associated hazards to first responders. *Prehospital Emergency Care*. **2020**, *24* (3), pp 355–368.

[7] Novosselov, I.; Coultas-McKenney, C.; Miroshnik, L.; Kottapalli, K.; Ockerman, B.; Manley, T.; Gardner, M. Lareau, R.; Brady, J.; Sweat, M.; Smith, A.; Hargather, M.; Beaudoin, S. Trace explosives sampling for security applications (TESSA) study: Evaluation of procedures and methodology for contact sampling efficiency. *Talanta*. **2021**, *234*, p 234.

[8] Kassouf, N.; Syed, S.; Larner, J.; Amlot, R.; Chilcott, R. Evaluation of absorbent materials for use as *ad hoc* dry decontaminants during mass casualty incidents as part of the UK's Initial Operational Response (IOR). *PLOS One*. **2017**, *12* (2), pp 1–15.

[9] Guidelines for Mass Casualty Decontamination During a HAZMAT/Weapon of Mass Destruction Incident 2008; U.S. Army Chemical Biological, Radiological and Nuclear School and U.S. Army Edgewood Chemical Biological Center, Edgewood area of the Aberdeen Proving Ground, MD. 2009

[10] Chilcott, R.; Larner, J.; Durrant, A.; Hughes, P.; Mahalingam, D.; Rivers, S.; Thomas, E.; Amer, N.; Barrett, M.; Matar, H.; Pinhal, A.; Jackson, T.; McCarthy-Barnett, K.; Reppucchi, J. Evaluation of US Federal Guidelines (Primary Response Incident Scene Management [PRISM]) for Mass Decontamination of Casualties During the Initial Operational Response to a Chemical Incident. *Annals of Emergency Management*. **2019**, *73* (6), pp 671– 684.

[11] Power, S.; Symons, C.; Carter, H.; Jones, E.; Amlot, R.; Larner, J.; Matar, H.; Chilcott, R. P. Mass casualty decontamination in the United States: an online survey of current practice. *Health Secur*. **2016**, *14* (4), pp 226– 236.

Inhalation toxicity characterization of obscurants using human tissue

Jennifer R. Horsmon*, Tyler D.P. Goralski, Danielle L. Kuhn, Daniel J. Angelini
U.S. Army Combat Capabilities Development Command Chemical Biological Center, Research & Technology Directorate, 8198 Blackhawk Rd, Aberdeen Proving Ground, MD 21010

ABSTRACT

To offer a more biologically relevant screening model than current standard 2D cultures, 3D constructs can be utilized to determine the cytotoxicity of human lung tissue when exposed at the air-liquid interface. In this study, EpiAirway™ constructs, consisting of human-derived cell cultures of differentiated airway epithelial cells, were utilized to mimic human inhalation exposure to metallic particles that are currently being developed as a novel infrared obscurant. The objective was to do inhalation toxicity assessment of silica-coated aluminum particles using a 3D human airway tissue model. This model offers a higher throughput assessment that can be used for screening potential obscurant materials for toxicity. In this study, exposure to silica-coated aluminum particles produced no relevant cytotoxic effects following a 3-hour or a 24-hour exposure at the concentrations tested. These data suggest that exposure to these particles do not cause cytotoxicity in cultured pulmonary cells when exposed at operationally-relevant concentrations.

Keywords: air-lifted interface, apoptosis, cytokine, cytotoxicity, EpiAirway™, *in vitro*, obscurant, particulates

1. INTRODUCTION

Smokes and obscurants have been used by the military on the battlefield for centuries, as a way of impairing enemy sightlines and allowing for safe movement or relocation of military units. As technology advances, so do the obscurants utilized to protect the warfighter. Today's smokes and obscurants can offer screening protection against infrared electromagnetic regions, as well as visible spectrum of light. As new IR smokes are developed, it is essential to screen these particles to ensure they are safe for human inhalation and for the environment. Researchers are continuously attempting to reduce and replace animal experiments with *in vitro* exposures at a cellular level due to constant ethical concerns over animal testing models.[1,2] To meet the increased demand for this type of toxicology study, new exposure technologies allow toxicants to be tested in 3D organ cultures that incorporate primary cells to represent different organs/organ systems including the liver, heart, lung, and brain.[1] For experiments involving the lung, the airway epithelium provides a critical interface between the body and the external environment.[3] In a human, the epithelial tissue consists of basal cells, mucus producing goblet cells, tight junctions, and beating cilia.[4] By using the MatTek EpiAirway™ tissues, signs of respiratory-tract irritation, inflammation, and/or toxicity can be screened quickly and in a cost effective manner by exposing the apical layer of the tissues to the particle mixtures.

2. METHODOLOGY

2.1 EpiAirway™ cultures

Commercially available EpiAirway™ 3D human-derived tracheal/bronchial epithelial cells (AIR-100-HCF, MatTek Corporation, Ashland, MA) were used in this study. Cultures were ordered from the manufacturer in hydrocortisone-free media and were grown on 12-mm diameter membranes. When the tissue cultures arrived, they were transferred into two 24-well tissue plates with 1 mL of cold assay medium in each well and incubated overnight at 37 °C with 5 % CO_2, per the manufacturer's instructions. The next day, the basolateral side of the membranes received 1 mL of pre-warmed assay medium and 0.5 mL trans epithelial electrical resistance buffer to rinse any accumulated mucus from the apical surface. After the mucus wash, they were aspirated via pipet to ensure no disturbance of tissue surface prior to exposure.

2.2 Sample preparation

The silica-coated aluminum particles were generously given to us by Dr. Danielle Kuhn (Combat Capabilities Development Command Chemical Biological Center) suspended in 1x phosphate buffered saline (PBS) and vortexed thoroughly for 2 minutes. Airway constructs were exposed to five 10-fold serial dilutions from a stock concentration of 10 mg/mL (final concentrations: 1 to 0.0001 mg/mL). Media was used for the untreated samples, PBS was used for the vehicle control, and 10 % formalin was used as a positive control.

2.3 Exposure

The positive control, media control, vehicle control, and aluminum particle dilutions were warmed to 37 °C and mixed thoroughly before applying 100 µL of each sample to the cells on the apical side of the membrane. The constructs were exposed to five doses of silica-coated aluminum particles in the air-liquid interface for 3 hours at 37 °C with 5 % CO_2. At the end of the exposure period, the treatments were removed from the apical side of the inserts via pipet and then washed 3 times with 400 µL trans epithelial electrical resistance buffer. Three-hour samples (n = 24) were then processed for analysis. The 24-hour exposure tissues (n = 24) were then placed back into the incubator at 37 °C with 5 % CO_2. These samples were collected the following day for analysis.

2.4 Sample analysis

Tissue viability was assessed utilizing a kit included with tissue samples (MTT, MatTek). The MTT assay is a colorimetric assay that assesses the cell metabolic activity as an indicator of cell viability, proliferation, and cytotoxicity and was measured according to the manufacturer's instructions.

Cytotoxicity was assessed via lactate hydrogenase (LDH) Release Assay (CyQuant™ LDH Cytotoxicity Assay Kit, Invitrogen™) using the basolateral medium, which was collected from each Transwell, according to the manufacturer's instructions.

In order to measure inflammation levels, a Human Multiplex Cytokine ELISA kit (Creative Diagnostics®) was utilized to quantify the presence of 8 pro-inflammatory cytokines including interleukin 1α (IL-1α), interleukin 1β (IL-1β), interleukin 6 (IL-6), interleukin 8 (IL-8), granulocyte macrophage colony stimulating factor (GM-CSF), monocyte chemotactic and activating factor (MCAF), and tumor necrosis factor α (TNF-α) in cell culture supernatant and other biological samples. Responses were measured according to the manufacturer's instructions.

3. RESULTS

The results from this brief study showed that the silica-coated aluminum particles, which the Smoke and Target Defeat Branch are creating as an IR obscurant material, did not produce a detectable cytotoxic effect on lung tissues after a 3-hour and 24-hour exposure. The silica-coated aluminum particles suspensions were prepared in PBS to concentrations 1 mg/mL to 0.0001 mg/mL using 10-fold differences between particle concentrations. Dosed EpiAirway™ tissues were incubated for 3 hours (n = 24) or 24 hours (n = 24). At the conclusion of the exposure, no discernable cellular metabolic activity was detected at this exposure time point. The 24-hour samples were tested and only showed a slight response at the highest dose. Discernable levels of apoptosis were observed, which was more than likely due to cellular stress from particles coating the apical layer of the EpiAirway™ (Figure 1).

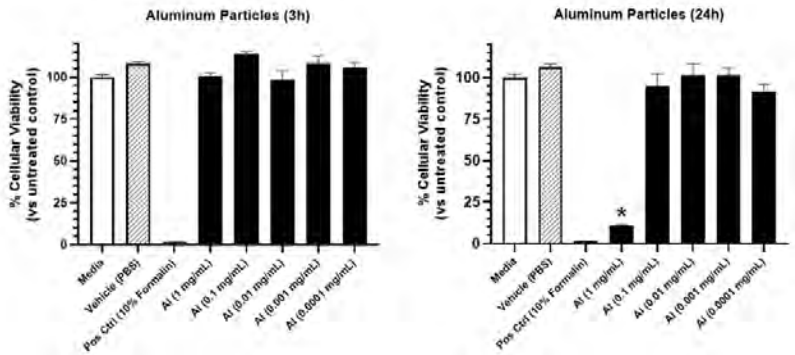

Figure 1. Tissue viability results at 3- and 24-hours post-exposure using a MTT assay and was expressed relative to the media and vehicle control tissues. Mean ± SEM; *p < 0.05 versus media control.

Downstream testing of the supernatant collected from the basolateral surface was performed to assess cytotoxicity and the presence of a pro-inflammatory response. The LDH assay is a cell death/cytotoxicity assay that can assess plasma membrane damage within a cell population. After a 3-hour exposure, there were no signs of cellular toxicity; and after 24 hours, there was only a slight indicator of toxicity at the highest particle concentration. Again, this response was more than likely due to cellular stress than actual plasma membrane damage (Figure 2).

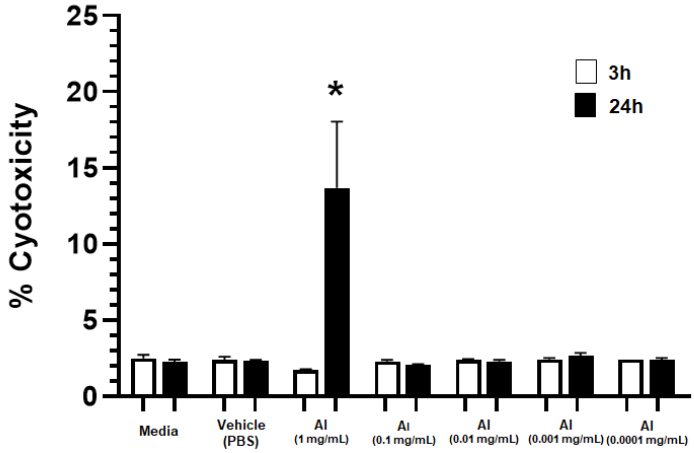

Figure 2. Cytotoxicity results at 3- and 24-hours post-exposure from the basolateral medium. There was no significant increase in LDH compared to the media and vehicle controls. The asterisk (*) represents the only slight difference over the controls but is not a high enough increase to represent a significant difference.

The final screen was a Human Cytokine ELISA that examined the tissues supernatant to determine if any pro-inflammatory cytokines were elevated after exposure to the silica-coated aluminum particles (Figure 3). This screen only showed a slight elevation of IL-1α at the highest concentration following a 24-hour exposure. The absorbance of this cytokine was below the lowest standard curve, which is not a discernable amount of inflammation.

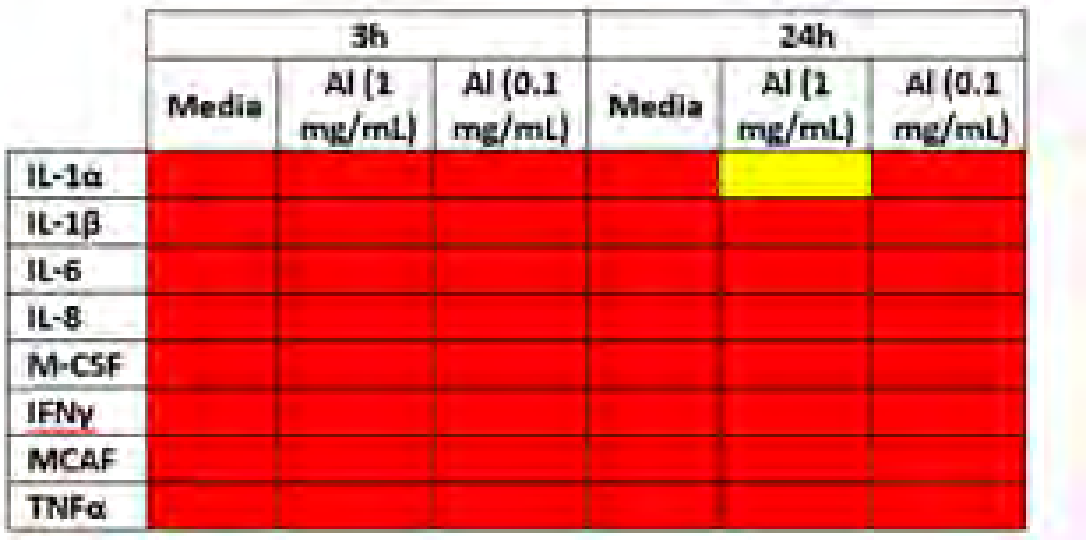

Figure 3. Inflammatory cytokine secretion was measured by ELISA at 3- and 24-hour post-exposure from the basolateral medium. There was no significant increase in inflammatory response over the controls. A slight increase in IL-1α was observed but fell below the standard curve.

4. CONCLUSIONS

The biological response of the EpiAirwayTM tissues provides a way of evaluating potential cytotoxicity and inflammation from the newly developed smoke and obscurant candidates. This in vitro study suggests that the currently developed particles do not elicit a pro-inflammatory response or cellular death in the airway epithelial cells. The slight increase of IL-1α in the inflammatory cytokine secretion assay in the 24-hour exposure leads to the need for follow on studies. IL-1α is a key danger signal that induces inflammation on release from necrotic cells.5 IL-1 is an important cytokine that is related to cell injury and homeostasis of cells, tissues, and organs. The 1 mg/mL 24-hour exposure tissues also showed a low-level response in the cytotoxicity and the tissue viability assays, which relates to the slight increase of IL-1α. With the currently performed assays, we cannot determine if the response is real, some other physiological stress, or a small amount of apoptosis occurring at the cellular level. We would need to perform more replicates with both 3- and 24-hour exposures and even multiple exposure screenings to fully characterize this model for inhalation toxicity. Alternately, we could use organ-on-a-chip systems to achieve higher granularity, and a potentially more physiologically accurate picture into how these particles effect the human body. This would also afford the ability to look at the effects of other organs that could be affected by the inhalation exposure, such as the liver.

It should be noted that even with this data, inhalation exposure to smoke and obscurant particulates should always be limited for personal health safety.

ACKNOWLEDGMENTS

I would like to thank Dr. Danielle Kuhn and the Smokes and Target Defeat Branch for supplying the infrared obscurant particles that were used for the testing of the human tissue cultures. I would also like to acknowledge Ms. Donna Hoffman for administrative support throughout the research and manuscript preparation process. Funding was provided by the Director, Combat Capabilities Development Command Chemical Biological Center under the authorities and provisions of Section 2363 of the FY 2018 NDAA to develop new technologies, engineer innovations, and introduce game-changing capabilities.

REFERENCES

[1] Caruso, J.A.; Stemmer, P.M. Petroleum coke exposure leads to altered secretome profiles in human lung models. *Hum. Exp. Toxicol*. **2018**, *37* (11), pp 1215–1232.

[2] Zavala, J.; O'Brien, B.; Lichtveld, K.; Sexton, K.G.; Rusyn, I.; Jaspers, I.; Vizuete, W. Assessment of biological responses of EpiAirway 3-D cell constructs versus A549 cells for determining toxicity of ambient air pollution. *Inhal. Toxicol*. **2016**, *28* (6), pp 251–259.

[3] Ji, J.; Hedelin, A.; Malmlöf, M.; Kessler, V.; Seisenbaeva, G.; Gerde, P.; Palmberg, L. Development of Combining of Human Bronchial Mucosa Models with XposeALI® for Exposure of Air Pollution Nanoparticles. *PLoS ONE*. **2017**, *12* (1), p e0170428.

[4] Ghio, A.J.; Dailey, L.A.; Soukup, J.M.; Stonehuerner, J.; Richards, J.H.; Devlin, R.B. Growth of human bronchial epithelial cells at an air-liquid interface alters the response to particle exposure. *Part. Fibre Toxicol*. **2013**, *10 (*25).

[5] Kaneko, N.; Kurata, M.; Yamamoto, T.; Morikawa, S.; Masumoto, J. The role of interleukin-1 in general pathology. *Inflamm Regen*. **2019**, *39* (12).

Large scale reflectin production through biomanufacturing

Krystina L. Hess*, Anna M. Crumbley[a], James M. Myslinskia, Robert Levenson[b], Brandon Malady[b], and Daniel E. Morse[b]
[a]U.S. Army Combat Capabilities Development Command Chemical Biological Center, Research & Technology Directorate, 8198 Blackhawk Rd, Aberdeen Proving Ground, MD 21010
[b]Department of Molecular, Cellular and Developmental Biology and the Institute for Collaborative Biotechnologies, University of California, Santa Barbara, CA 93106

ABSTRACT

Biomanufacturing has the potential to replace traditional petrochemical manufacturing of high-value chemicals and materials of interest to the Army. Some advantages of this method include a flexible and reusable infrastructure, scalability, small capital expenditures, and environmentally friendly production. Pilot scale facilities fill the crucial gap between benchtop and industrial production, producing enough material for prototyping and testing. The U.S. Army Combat Capabilities Development Command Chemical Biological Center's new biomanufacturing facility will operate on the pilot scale to produce materials for defense applications. One such material, a reflectin protein found in the skin cells of squids, can be used in camouflage and photonic applications. In order to produce enough material to prototype these applications, we aimed to develop translatable downstream processing methods for purifying reflectin from the growth cultures of organisms engineered to produce the protein. The novel method developed can be translated from the lab scale to the pilot scale and was able to provide crucial experience for the biomanufacturing team.

Keywords: Biomanufacturing, synthetic biology, biomaterial, scale-up, downstream processing

1. INTRODUCTION

The health of the U.S. defense industrial base is critical to military operations and the ability of the government to respond to national and international emergencies.[1] A 2018 interagency report to the White House indicated that unprecedented challenges were eroding the industrial base and threatening the Department of Defense's readiness.[2] The COVID-19 pandemic further revealed the vulnerability of U.S. supply chains when domestic inventories of national security materials, such as chemicals and textiles, neared depletion in a matter of weeks.[3] Biomanufacturing could provide a solution to bolstering domestic production capacity and minimizing reliance on foreign sole source suppliers.[4] Through biotechnology, materials can be produced in a more flexible, affordable, and environmentally friendly way than traditional petrochemical processes. There is a gap in funding and capabilities for pilot-scale production between benchtop-scale and industrial-scale production of biomaterials. This level of manufacturing, on the 1,000 L – 5,000 L scale, is crucial for production of enough material for advanced testing and prototyping and to optimize protocols before transitioning to industrial production. The limited number of existing pilot scale facilities are operating near capacity, causing domestic biotechnology companies to partner with sites outside the U.S. for their scale up needs. Security concerns associated with these international facilities limit usability for certain Department of Defense initiatives. In recognition of this bottleneck, the BioTechnology Branch of the U.S. Army Combat Capabilities Development Command Chemical Biological Center has secured funding for renovation of an existing bioprocessing facility to develop a pilot scale biomanufacturing facility with up to 2,000 L in fermentation capacity for scale up and robust downstream processing (DSP) capabilities for purification of materials of interest.

Biotechnologists have made huge advances in engineering organisms such as yeast and bacteria to produce novel materials, but protocols for scale up and DSP are often not prioritized until late in the process, increasing the risk of unexpected bottlenecks. One biomaterial of interest to the Army that can be produced by engineered cell strains is reflectin protein. Cephalopods, such as squids and octopuses, exhibit reflected colors from iridescent Bragg reflectors in skin cells called iridocytes.[5] These reflectors are primarily filled with reflectin proteins. In the squid *Doryteuthis opalescens*, the spacing, thickness, and refractive index of the reflectors are tunable. This tunability results in changes in the color and brightness of light reflected off the skin, which can create a camouflage effect or be used for communication.[6] One distinct reflectin protein that has been identified and fully characterized from *D. opalescens*

iridocytes is A1.[7] The lab of Dr. Daniel Morse at the University of California, Santa Barbara (UCSB) engineers *Escherichia coli* cells to produce reflectin A1 on the benchtop scale.[8] The U.S. Army Combat Capabilities Development Command Soldier Center is interested in harnessing the unique tunability of reflectin for incorporation into fabrics and solid-state electronic and photonic devices. To create enough material to prototype these applications, growth of the engineered organisms needs to be scaled up.

Reflectin produced by this method is produced in inclusion bodies, aggregates of recombinant protein that form due to high levels of expression. Benchtop-scale reflectin recovery involves the use of a detergent to lyse the cell membranes with subsequent detergent washing steps to purify the inclusion bodies. The protein can then be purified by chromatography. While effective on this scale, repeated centrifugation and resuspension of sticky pellets is highly difficult at the pilot scale. In this study, we aimed to develop novel DSP methods for inclusion body and reflectin purification that are translatable from the lab scale to pilot scale. These methods can be applied to produce reflectin on the gram or even kilogram scale for prototyping camouflage fabrics and electronic devices. Additionally, lessons learned from developing novel DSP methods from scratch provided crucial experience in linear scalability to the Chemical Biological Center biomanufacturing team.

2. MATERIALS & METHODS

2.1 Materials

All materials were purchased from MilliporeSigma® (St. Louis, MO) and Darmstadt, Germany unless otherwise stated.

2.2 Cloning

A codon-optimized reflectin sequence corresponding to the previously determined sequences of *D. opalescens* reflectin A1, inserted into a kanamycin-resistant expression plasmid, was obtained from Dr. Daniel Morse (UCSB) and ATUM (San Francisco, CA). N-terminal His6 affinity tags and adjacent TEV cleavage sites originally present were removed by oligonucleotide-directed mutagenesis.

2.3 Cell bank creation

Plasmids were transformed in RosettaTM 2(DE3) SinglesTM competent *E. coli* BL21-derrived cells. First, 1 µL of 94 µM A1 plasmid was added to 20 µL competent cells and incubated on ice for 5 minutes. The cells were then heat shocked at 42 °C for 30 seconds then immediately incubated on ice for 2 minutes. 80 µL of Super Optimal broth with Catabolite repression media was added and the cells were incubated at 37 °C with shaking at 250 rpm for 1 hour in an Innova 4230 Incubator Shaker (New Brunswick Scientific, Edison, NJ). The cells were then serially diluted in Super Optimal broth with Catabolite repression media and plated onto plates containing Luria-Bertani agar plates with 15 g/L agar, 50 µg/mL kanamycin, and 37 µg/mL chloramphenicol. Plates were incubated at 37 °C overnight and transferred to 4 °C for storage. Selected colonies were added to tubes containing 5 mL LB broth with 50 ug/mL kanamycin and 37 ug/mL chloramphenicol and incubated at 37 °C overnight with shaking at 200 rpm. A glycerol solution was made by sterile filtering 65 % glycerol with 25 mM Tris-HCl and 100 mM MgSO4 in water. 600 µL of overnight culture was combined with 400 µL of glycerol solution in cryogenic vials for storage at -80 °C prior to use.

2.4 Cell growth and protein expression at lab scale

One glycerol stock of A1 cells was thawed at room temperature and 20 µL was added to a 1 L flask containing 500 mL of 25 g/L autoclaved LB broth, 50 µg/mL kanamycin, and 37 µg/mL chloramphenicol. Flasks were incubated at 37 °C overnight with shaking at 200 rpm in an I24 Incubator Shaker (New Brunswick Scientific, Edison, NJ). Optical density readings of the overnight cultures were measured at 600 nm using a GENESYSTM spectrophotometer (Thermo Fisher Scientific, Waltham, MA). Overnight cultures were diluted to an OD600 of 0.5 in fresh 1 L flasks containing 500 mL of sterile LB broth, 50 µg/mL kanamycin, and 37 µg/mL chloramphenicol. During the first growth cycle, optical density of the culture was measured immediately after inoculation and at 2 hours, 4 hours, 6 hours, and 24 hours post inoculation. 6 hours after inoculation, 500 µL of 1 M isopropyl β- d-1-thiogalactopyranoside was added to each flask to induce expression of reflectin. The flasks were then incubated at 37 °C overnight with shaking at 200 rpm. Cell pellets were collected by transferring the overnight cultures into 250 mL centrifuge tubes and spinning at 7,000 rpm and 4 °C for 10 minutes in an Ivanti J-E centrifuge (Beckman Coulter, Indianapolis, IN). Pellets were stored at -80 °C until use.

2.5 Cell growth at pilot scale

To gain initial experience with operating the Micros 30L fermenter (New Brunswick Scientific, Edison, NJ), a growth curve of untransformed RosettaTM 2(DE3) SinglesTM competent E. coli cells was created. First, a pre-culture containing 10 µL of untransformed cells in 250 mL of LB broth was grown overnight at 37 °C with shaking at 200 rpm. The 30 L bioreactor was filled with 20 L of LB broth and 1 mL of Antifoam 204 and sterilized in place. 200 mL of the overnight pre-culture (i.e. 1 vol %) was added to the sterilized fermenter. Parameters set for overnight fermentation were as follows: 30 °C temperature, 20 standard liters per minute airflow, and 200 rpm mixing speed. These parameters, pH, dissolved oxygen, and pressure were measured by inline sensors.

2.6 Inclusion body recovery with detergent disruption method

Cell pellets from overnight cultures were resuspended in 5 mL BugBuster® per gram of cell paste and incubated with 1µL Benzonase® Nuclease per mL of BugBuster® for 10 minutes with shaking at 200 rpm. Inclusion bodies containing reflectin were then collected by centrifugation at maximum speed and 4 °C for 20 minutes. Inclusion bodies were then purified by resuspending pellets in 1 volume of BugBuster® with 5 kU rLysozyme™ and incubated for 5 minutes. 1 volume of BugBuster® diluted 1:10 in water was then added prior to centrifugation as before. Pellets were washed and centrifuged 3 times with 1 volume, 2 volumes, and 1.5 volumes of BugBuster® diluted 1:10 in water. Pellets were stored at -80 °C for up to 3 days.

2.7 Inclusion body recovery with mechanical disruption method

Cell pellets from overnight cultures were resuspended in 100 mL 1x phosphate-buffered saline (PBS). The M110P Microfluidizer® (Microfluidics, Westwood, MA) was first flushed with water and primed with 1x PBS. The cell suspension was then added to the microfluidizer and the lysed cell suspension was collected in a 250 mL centrifuge tube. The cell debris was collected by centrifuging the homogenized solution at maximum speed and 4 °C for 20 minutes. The inclusion bodies were then purified with the detergent method from above or by resuspending pellets in 10 mL PBS and centrifuging at 10,000 rpm and 4 °C for 10 minutes. Pellets were stored at -80 °C for up to 3 days.

2.8 SDS-PAGE gels

SDS-PAGE materials and equipment were purchased from Bio Rad (Hercules, CA) unless otherwise stated. Samples were collected throughout the reflectin recovery process and included: resuspended overnight culture cell pellet, post cell-lysis supernatant, unpurified inclusion bodies, and purified inclusion bodies. Samples were diluted 3 parts sample to 1 part sample buffer containing 5 % 2-mercaptoethanol in 4x XT Sample Buffer and boiled at 95 °C for 10 minutes in a GeneAmp® PCR System 9700 (Applied Biosystems, Waltham, MA). 10 µL of samples or 5 µL of Precision Plus Protein Dual Color Standards were then added to the wells of a Criterion™ XT Bis-Tris Precast Gel. Gels and XT MES Running Buffer were added to the electrophoresis cell and run at 200 V constant for 75 minutes. Gels were first washed 3 times by incubation in deionized water on an orbital shaker (Lab Line, Melrose Park, IL) for 5 minutes before incubation in SimplyBlue™ SafeStain (Thermo Fisher Scientific, Waltham, MA) for 1 hour on a plate shaker. Gels were then washed again by incubation in deionized water on a plate shaker for 1 hour and imaged with a ChemiDoc™ XRS+.

3. RESULTS

3.1 Cell growth at lab scale

A1 cells were grown on the benchtop scale in six 1 L shaker flasks. Optical density of the cultures was measured at 600 nm at the time of inoculation and every two hours after to determine the appropriate time to induce reflectin production (Figure 1A). After six hours, the average optical density of the cultures reached a level above 0.6. At this time, induction with isopropyl β- d-1-thiogalactopyranoside occurred, and the cultures continued to express for 18 hours. Optical density reached an average of 1.85 and cells were then collected by centrifugation and the mass of the wet cell paste was measured (Figure 1B). Cell mass was used to calculate volumes of detergent for cell lysis and inclusion body purification.

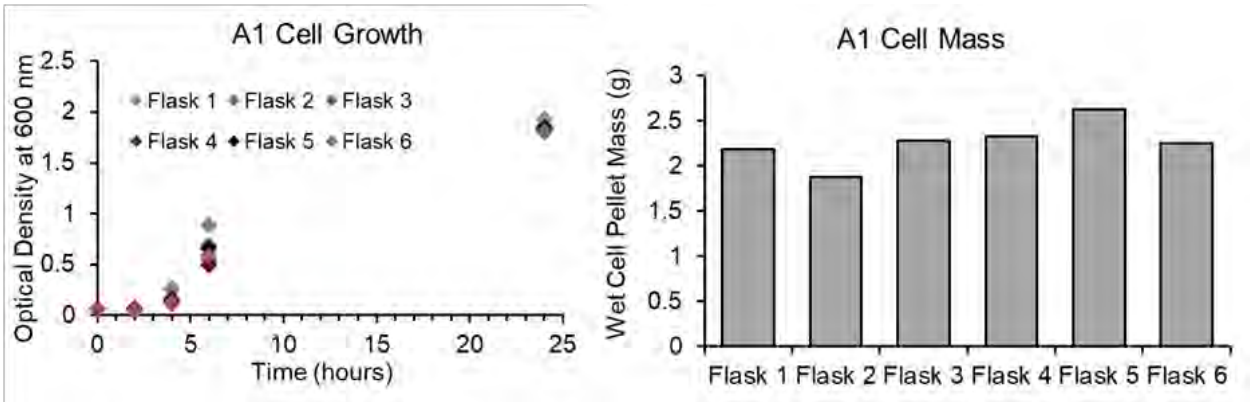

Figure 1. A1 cell growth data on the lab scale. (a) Optical density at 600 nm was measured over 24 hours. (b) Cell mass was measured after 24 hours.

3.2 Cell growth at pilot scale

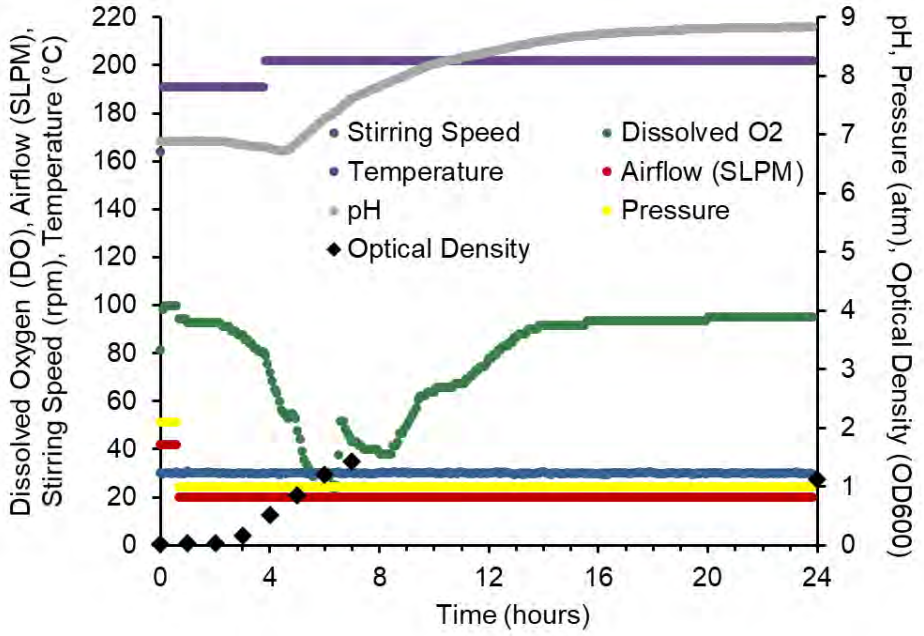

Figure 2. Growth curve and parameters of 20 L RosettaTM 2(DE3) fermentation. Optical density at 600 nm, temperature, pH, stirring speed, dissolved oxygen, airflow, and pressure were measured over 24 hours.

Untransformed RosettaTM 2(DE3) cells were grown in a 30 L bioreactor to gain crucial experience in small pilot scale fermentation. OD600 readings were taken manually approximately every hour for eight hours and at a final time point of 24 hours (Figure 2). The untransformed cells grew at a similar rate to A1 cells and reached a similar final optical density of 1.8. One advantage of the use of a bioreactor is the ability to control and measure important parameters including: temperature, pH, stirring speed, dissolved oxygen, airflow, and pressure. These parameters were measured with inline sensors over the entire 24-hour fermentation (Figure 2).

3.3 Inclusion body purification at lab scale

Following the method successfully used by the Morse lab, A1 cell pellets collected following a 24-hour growth period were resuspended in BugBuster® detergent with Benzonase® Nuclease to lyse the cells and degrade DNA, respectively. Reflectin is insoluble and produced in inclusion bodies which can be recovered by centrifugation. The inclusion bodies are then purified by repeated detergent washing steps. To investigate a method for recovering purified inclusion bodies that is more translatable to larger scales, A1 cell pellets were instead resuspended in PBS. The cell

suspension could then be run through a microfluidizer, a piece of equipment that also exists on the pilot scale, to mechanically lyse the cell membranes. Inclusion bodies could then be collected and purified either with repeated detergent steps or a simple PBS wash. An SDS-PAGE gel was run and visualized with SimplyBlue™ SafeStain on samples collected at the following stages: cell pellet, post-cell lysis supernatant, unpurified inclusion bodies, and purified inclusion bodies (Figure 3). The A1 sample in lanes 10 and 15 were both lysed and purified by detergent, the A1 sample in lanes 11 and 16 were lysed by the microfluidizer and purified by detergent, and the A1 sample in lanes 12 and 17 were lysed by the microfluidizer and purified by PBS. Qualitatively, the amount and purity of reflectin in the purified inclusion bodies does not vary based on the method of purification.

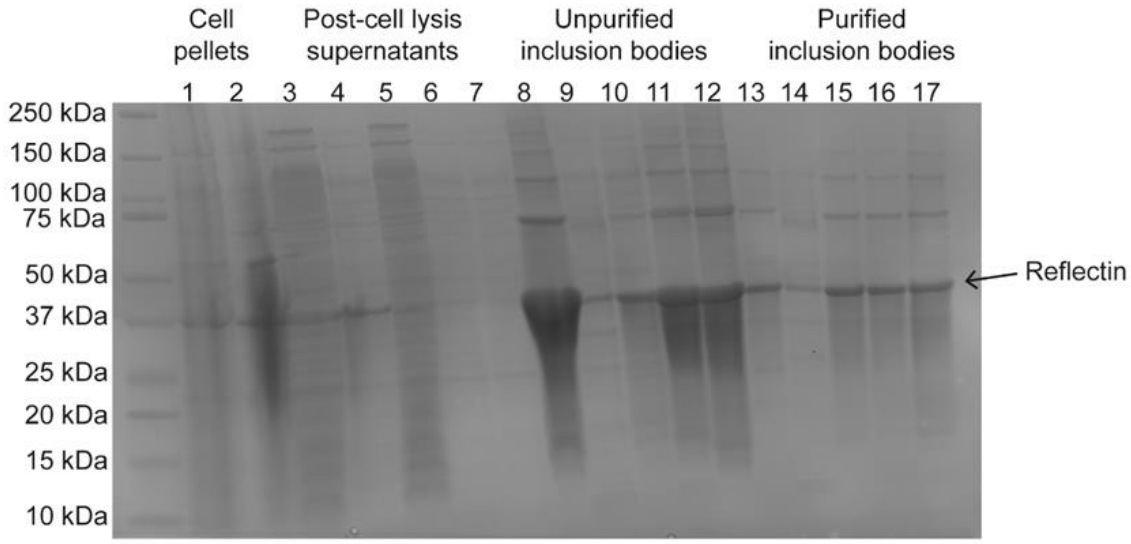

Figure 3. SDS-PAGE gel with uninduced, untransformed, and A1 samples purified by detergent, microfluidization, and PBS washing. Samples include cell pellets, lysed cell supernatants, and unpurified and purified inclusion bodies.

4. CONCLUSIONS

Biomanufacturing offers the ability to engineer organisms to produce materials of interest for the Army. There is currently a shortfall in domestic pilot scale production that the BioTechnology Branch aims to address through the renovation of the existing bioprocessing facility to enhance fermentation capabilities and add critical DSP and analytical technology. Many potential customers of this new facility have not developed DSP methods for material purification that are translatable from the benchtop scale to larger scales. One example, reflectin A1 produced in inclusion bodies by engineered *E. coli* cells, is purified through repeated detergent washing steps that involve high speed centrifugation and resuspension of sticky pellets. We developed a more translatable DSP method by mechanical lysing of cells and a simple wash step to produce purified reflectin inclusion bodies. Future experiments include confirming that reflectin can be further purified through chromatography and repeating this process on the 20 L scale using a bioreactor, a pilot scale microfluidizer, a tangential flow filtration unit, and a pilot scale simulated moving bed chromatography unit. Reflectin produced on this larger scale can be incorporated into fabric and electronic prototypes.

ACKNOWLEDGMENTS

I would like to acknowledge Dr. Daniel Morse, Dr. Robert Levenson, and Brandon Malady at UCSB for providing the reflectin-producing strain and assistance in protocol development. I also acknowledge Dr. Annie Crumbley for technical assistance throughout the project and Dr. James Myslinski for assistance in protocol development. I'd also like to thank Dr. Sandy Gibbons, Dr. Mike Kim, and Dr. Kelly Basi for assistance via intellectual discussion. Funding was provided by the Director, Combat Capabilities Development Command Chemical Biological Center under the authorities and provisions of Section 2363 of the FY 2018 NDAA to develop new technologies, engineer innovations, and introduce game-changing capabilities.

REFERENCES

[1] U.S. White House, National Security Strategy of the United States of America **2017**, pp 1–68.
[2] Report to President Donald J. Trump by the Interagency Task Force in Fulfillment of Executive Order 13806. Assessing and Strengthening the Manufacturing and Defense Industrial Base and Supply Chain Resiliency of the United States. **2018**, pp 1–146.
[3] Manuel, P.E. Commentary: Pandemic Lays Bare Supply Chain Vulnerabilites. *National Defense Magazine* **2020**.
[4] Delvigne, F.; Noorman, H. Scale-up/Scale-down of microbial bioprocesses: a modern light on an old issue. *Microb. Biotechnol.* **2017**, *10* (4), pp 685–687.
[5] DeMartini, D.G.; Krogstad, D.V.; Morse, D.E. Membrane invaginations facilitate reversible water flux driving tunable ridescence in a dynamic biophotonic system. *Proc. Natl. Acad. Sci. U.S.A.* **2013**, *110* (7), pp 2552−2556.
[6] Song, J.; Levenson, R.; Santos, J.; Velazquez, L.; Zhang, F.; Fygenson, D.; Wu, W.; Morse, D.E. Reflectin Proteins Bind and Reorganize Synthetic Phospholipid Vesicles. *Langmuir.* **2020**, *36* (10), pp 2673–2682.
[7] DeMartini, D.G.; Izumi, M.; Weaver, A.T.; Pandolfi, E.; Morse, D.E. Structures, Organization, and Function of Reflectin Proteins in Dynamically Tunable Reflective Cells. *J. Biol. Chem.* **2015**, *290* (24), pp 15238−15249.
[8] Levenson, R.; Bracken, C.; Sharma, C.; Santos, J.; Arata, C.; Malady, B.; Morse, D.E. Calibration between trigger and color: Neutralization of a genetically encoded coulombic switch and dynamic arrest precisely tune reflectin assembly. *J Biol. Chem.* **2019**, *294* (45), pp 16804–16815.

Spatial dynamics of infectious disease

Thomas E. Ingersoll
U.S. Army Combat Capabilities Development Command Chemical Biological Center, Research & Technology Directorate, 8198 Blackhawk Rd, Aberdeen Proving Ground, MD 21010

ABSTRACT

A method for estimating infective disease dynamics parameters when contact rates are heterogeneous, surveillance data are not systematically sampled, and cases are underreported is presented. An important parameter for predictive infectious disease models is R_e, the effective reproductive number. R_e determines the rate at which new infections occur, and responds to intervention strategies such as vaccination, quarantine, and social distancing. However, accurate estimation of R_e is complicated by shortcomings in surveillance data collection, which are difficult to mitigate through changes in sampling methods. The author proposes that estimation of R_e is not necessary to model changes in disease dynamics, rather, the basic reproductive number R_0 may be used along with contact parameters derived from network characteristics within the host population, characteristics that may be extracted from surveillance data. Further, estimates of R_0 can be derived from imperfect surveillance data through application of hierarchical methods that correct for underreporting by using explicit estimates of detection probabilities. A hierarchical data-assimilative method for improving parameter estimates in predictive models when data are imperfectly collected is demonstrated below. Accurate estimates of changes in disease dynamics can inform management decisions and mitigation strategies.

Keywords: CoViD-19, Network model, Parameter estimation, Surveillance, Susceptible Exposed Infectious Resistant model, Underreporting, Disease dynamics, Maximum likelihood.

1. INTRODUCTION

1.1 Purpose

A maximum-likelihood method for estimating infective disease dynamics parameters in metapopulations, where subpopulations exist in partial spatial isolation, surveillance data are not systematically sampled, and cases are underreported is presented. The author proposes that the basic reproductive number for an infectious disease, R_0, may be estimated along with network parameters for a host population, using only surveillance data, that is, without a-priori knowledge of network structure (Figure 1).

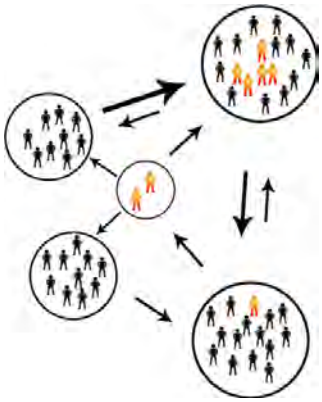

Figure 1. Structure of a hypothetical disease network showing nodes (circles) and links (arrows). Infected cases are in orange, while susceptible individuals are in black.

Further, such estimates of R_0 can then be used to parameterize a system of differential equations which can then predict changes in epidemic trajectory. A hierarchical data-assimilative method for improving parameter estimates in predictive models for networks with limited data collection is demonstrated below. Accurate estimates of heterogeneous disease dynamics can inform management decisions and mitigation strategies.

1.2 Background

Parameter estimates for predictive disease models typically rely on unsystematically sampled data. Sampling is limited to case reports of patients already known to be ill, which results in underreporting. Because only suspected cases are included in sampling, asymptomatic cases are overlooked. This results in underestimates for the number of infected hosts. Furthermore, host populations do not exhibit homogeneous contact rates. That is, portions of the population exist in partial isolation from others, resulting in populations that are not well-mixed. Underreporting, and incomplete mixing complicate our ability to estimate growth parameters for the spread of infectious disease, parameters such as R_0, the basic reproductive number. Rate parameters may appear to change erratically as the disease passes through different portions of the affected population, and as additional surveillance resources are brought to bear on an emerging outbreak.

Methods using hierarchical models are well-established for correcting underreporting.[1] These methods are particularly relevant for confirmatory samples because confirmatory samples tend towards high-specificity, where false-positives are limited.[2] However, methods for correcting inconsistent collection of confirmatory samples are more elusive. Correcting for unsystematic sampling would require that we supplement confirmatory samples with information more uniformly inclusive of the broader population.

Predictive dynamic models can produce data ranging across the breadth of the population and might be used to overcome problems with unsystematic data collection. This process would require that parameters are accurately estimated, that is, free of over and underestimates. Dynamic models could be combined with confirmatory samples in an ensemble model, to correct estimation inaccuracies while providing population-wide representation. Such models are called data-assimilative models, whose invention can be credited to Gauss.[3] Data-assimilation combines the strengths of dynamic models and confirmatory sampling while mitigating their weaknesses. Data-assimilation combined with hierarchical methodology could be used to adjust misestimates in dynamic model parameters, increasing reliability and the usefulness of model-based predictions.

A set of categories useful for describing the state of infection within hosts includes Susceptible (S) (individuals that are available to become hosts to the disease), Exposed (E) (recently exposed individuals that have not yet developed transmissible disease), Infective (I) (individuals that have acquired the disease and are able to spread it to others), and Resistant (R) (individuals that have acquired immunity so can no longer become hosts or transmit the disease to others). Models containing these categories are called SEIR models, and two goals of dynamic models are to estimate the number of individuals in each SEIR category at any given time, and to estimate the transition rates between categories,[4,5] rates such as the infection rate r, and the closely related basic reproductive number R_0. The cumulative count of cases, a number commonly reported in surveillance data, is the sum of I and R. SEIR models are approximations intended to predict population-level disease outcomes and can be expressed as a system of differential equations for the growth of each category. Terms of the equations are adjusted until model output resembles surveillance observations, then these equations are used to predict the future trajectory of the disease. Terms may be adjusted by expert judgement or may be estimated using statistical methods. An SEIR model was successfully applied to medical planning during the 2003 severe acute respiratory syndrome outbreak[6] using Bayesian methods for estimation. The author adapts this model to CoViD-19, as shown below. An important assumption of such models is that the population is well-mixed, that is, all individuals have an equal probability of encountering an infective host.[5] A method for relaxing this assumption using network models is shown below.

A method for estimating detection probability using predicted values from dynamic models, and count data from surveillance is found using Isaac Newton's Binomial Theorem[7]

$$P = \binom{n}{k} (p)^k (1-p)^{n-k}. \quad (1)$$

For our purposes, n is the day's cumulative case count from the dynamic model (I+R), k is the day's count from the surveillance data, p is the detection probability, and P is the probability of the parameters n and p, given the datum k. The product of P across all the data is called the model likelihood. The result is a maximum likelihood method for estimating the detection probability p, in turn, correcting underreporting expected to be present in the surveillance data. Newton's Theorem can be used to adjust observed imperfect counts to estimates of the true number of cases in the population, a number which often cannot be directly observed. The theorem also provides a vehicle to adjust the parameters for the dynamic model, also via maximum likelihood, which produce the value n. The result is data assimilation, where data are used to adjust a statistical model for detection, and terms of the dynamic model.

A critical and difficult to estimate parameter for SEIR models is R_0, the basic reproductive number,[5] which is the expected number of new infections arising from an infected host in an arbitrarily large, naïve population. R_0 is assumed to be fixed rate characteristic of a pathogen strain, and that changes in the infective rate, r, can be attributed to changes in contact rates between hosts.[5] This is sensible, because many otherwise susceptible individuals are not available for contact with infective hosts, because of spatial, environmental, or social distances, or mitigation strategies such as quarantine, each of which result in a population that is not well-mixed. Disease models for populations that are not well-mixed are called network models.[8] Network models have two fundamental components, nodes, which are subpopulations existing in incomplete isolation from other nodes within a metapopulation, and links, which are corridors of contact between nodes.[8] If we assume that R_0 is fixed, then changes in rate of growth r must be explained by changes in the number of affected nodes, the node sizes, and the timing of contact with links between nodes. Changes in R_0 would therefore not occur without pathogen mutation and emergence of new pathogenic strains.

1.3 Data sources

Open-source data for the CoViD-19 pandemic are available for the Diamond Princess Cruise Ship.[9] Diamond Princess began the sampling period with a population of 2,670 passengers and 1,100 staff. By the end of the sampling period all those infected had been removed shoreward into quarantine.[10] Additionally, by the end of the sampling period complete surveillance had been attained, so that all passengers had been repeatedly tested for SARS-CoV-2 using polymerase chain-reaction methods. Because testing frequency increased, and all passengers were tested repeatedly by the end of the sampling period, a valid model with underreporting should converge on testing results towards the end of the period, and estimated rates of detection should increase across the period towards $p = 1$.

2. METHODS

2.1 Methods development

Models were based on SEIR models developed for the 2003 Severe Acute Respiratory Syndrome infection.[6] These models were executed in the computational language R,[11] using the R library of differential equation solvers deSolve,[12] and functions written and archived by the author that use Newton's Theorem to estimate and model detection probability, adjust parameters for the differential equations, and estimate network characteristics using maximum-likelihood.

2.2 SEIR models and the well-mixed assumption

A series of SEIR models that conformed to the well-mixed assumption was produced (Figure 2).

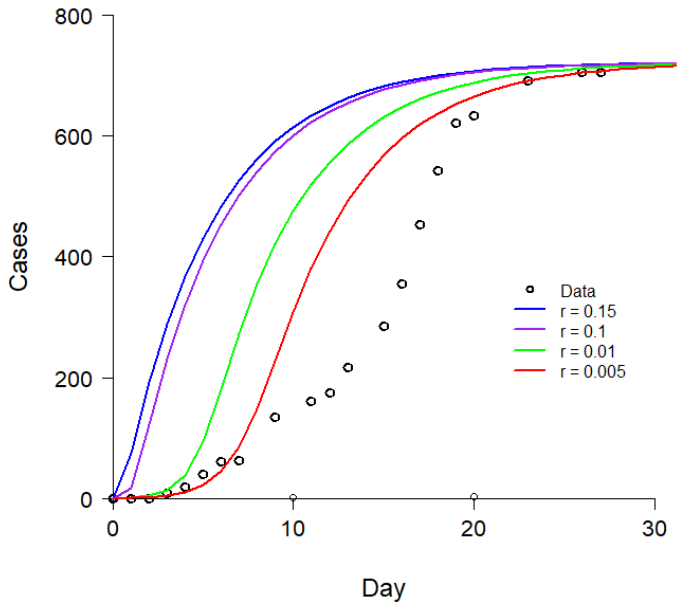

Figure 2. The failure of the well-mixed assumption.

The traces in Figure 2 represent predicted cases from well-mixed SEIR models with growth rate r. It was found that likelihoods produced when these models confronted the data were inestimably small, due to divergence of the model from data towards the middle of the series, regardless of the value of r. Alternatively, the author demonstrated, below, that network models with estimably high likelihoods could be produced from these data.

2.3 The detection model

The network model rendered estimable probabilities using Newton's Theorem and produced a maximum-likelihood estimate of daily detection probability. These values were then used to produce a logistic model for detection probabilities across the entire data series. The logistic detection model was then used to correct data for underreporting.

2.4 Maximum likelihood adjustments to the network model

Node size, link timing, and R_o were each sampled across a range of values. The combination of these values producing the highest likelihood, calculated from Newton's Theorem, was used to populate the preferred model, which could then be used for prediction. Selection between values for link timing are shown in Figure 3.

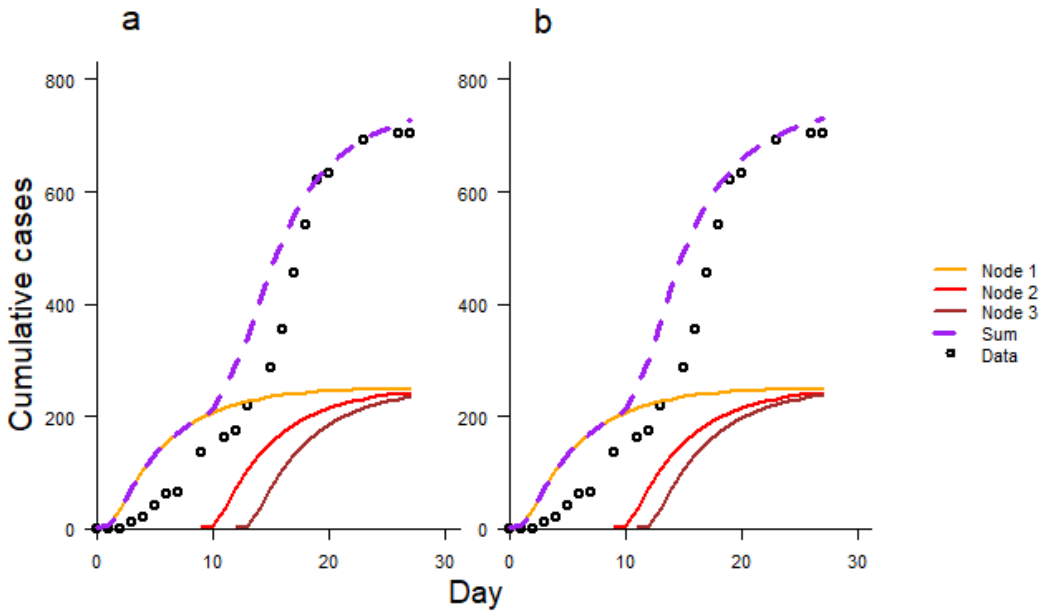

Figure 3. Selection between Day 12 (a) and Day 11 (b) for timing of a link to Node 3 (brown trace). The result is small change in the total trajectory of cases for the metapopulation (purple trace).

While the change in trajectory shown between Figures 3a and b appears subtle (purple traces), the result was an approximate doubling in model likelihood for the preferred model (Figure 3b), through shifting the link by only one day. Such small adjustments can be made until the best possible model parameters are estimated, given the data and computational resources.

3. DISCUSSION

3.1 The Diamond Princess outbreak

According to the selected model (Figure 3b), CoViD-19 began aboard the Diamond Princess in a node of 250 individuals. Detection probability (p) was low at first, and approached $p = 1$ towards the end of sampling period as passengers were subject to repeated testing. Because of its moderate infectivity (R_0 of 2.5), partial isolation from the rest those onboard, and low initial levels of detection, the disease was able to persist onboard undetected for an unknown number of days, and spread throughout the primary node until links with additional nodes on Days 9 and 11 triggered a steep period of spread. The pattern of spread seen early in the outbreak, with low-level persistence followed by eruption into exponential growth, cannot be explained by any of the well-mixed models (Figure 2). Exponential growth never reached its maximum, because the effects of emigration began to take over on Day 19, as passengers

disembarked into quarantine. It's possible that movement associated with disembarkation triggered the links on Days 9 and 11, as isolation was interrupted when passengers were repatriated via group air travel. According to the data, no new cases occurred after Day 27.

3.2 Predictive modeling

Predictive models used R_0 and network parameters extracted from the data-assimilated models, which were then used to predict the trajectories of simulated populations. We simulated two populations, a simulated shipboard population that differed from Diamond Princess only in initial population size (Figure 4a), and a simulated village population with node size selected to mimic small populations in China and Italy (Figure 4b) that were affected early in the pandemic.

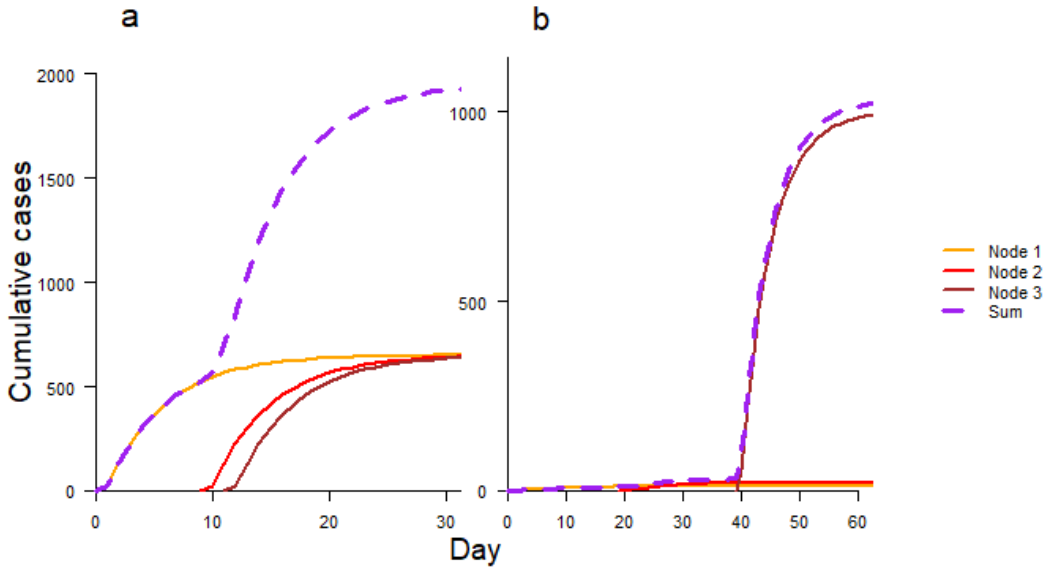

Figure 4. Predictive models for a hypothetical ship (a) and village (b). Population totals (purple trace) exhibit exponential growth following contact with Node 3 (brown trace).

The shipboard model (Figure 4a, purple trace) behaved exactly as expected, simply a larger version of the Diamond Princess model (Figure 3, purple trace). Infection started slowly, eventually saturating the primary node, then grew exponentially after encountering links with additional nodes at Days 9 and 11. Exponential growth then changed to logistic growth following emigration on Day 19. This demonstrates that the model can begin with prior knowledge of a similar system and be then adjusted for known differences in conditions to make predictions.

The village model (Figure 4b, purple trace) represented an outbreak that began in two small nodes where it persisted at low, largely undetected levels until encountering a link with a larger node at Day 39, whereupon exponential growth was initiated. This demonstrates that networked disease can persist undetected at low levels, then suddenly erupt into exponential growth. The well-mixed model cannot be made to resemble this pattern of rapid growth following low-level persistence (Figure 2). In fact, it is believed that the CoViD-19 outbreak began as early as early October 2019 in Italy and China,[13] and persisted undetected at low levels until its discovery in January 2020, coincident with eruption into exponential growth. The author has seen no other class of models, other than network models, that adequately explains this pattern.

3.3 Success of the demonstration

It was successfully demonstrated that a tool for estimating infective disease-dynamics parameters when contact rates are uneven, surveillance data are not systematically sampled, and cases are underreported could be developed. R_0, node size, and the timing of links were all successfully estimated using maximum likelihood, assuming constant R_0 and a logistic structure for the detection model. A proof-of-concept has been presented, above. That said, several tasks remain that will complete the tool as an effective aid to inform decision making. These tasks include further validation for more generalized cases, development of plausible confidence intervals, and especially, further automation through migration to a machine-learning environment. Increased automation will facilitate completion of validation and generalization.

ACKNOWLEDGMENTS

Funding was provided by the Director, Combat Capabilities Development Command Chemical Biological Center under the authorities and provisions of Section 2363 of the FY 2018 NDAA to develop new technologies, engineer innovations, and introduce game-changing capabilities.

REFERENCES

[1] Royle, J. A.; R. M. Dorazio. *Hierarchical Modeling and Inference in Ecology*. Elsevier, London. **2008**.
[2] Ingersoll, T. E. *Reducing false-positives via capture/recapture modeling for early-warning*. Proceedings of the Edgewood Chemical Biological Center, **2017**.
[3] Forbes, E.G. Gauss and the Discovery of Ceres. J. Hist. Astron. **1971**, *2* (3), pp 195–199.
[4] Kermack, W.O.; McKendrick, A.G. *A contribution to the mathematical theory of Epidemics*, Proceedings of the Royal Society, **1927**, A115, 700–721
[5] Anderson, R.; R. May, *Infectious Diseases of Humans, Dynamics and Control*, Oxford University Press, New York, **1991**.
[6] Riley, S.; Fraser, C.; Donnelly, C.A.; Ghani, A.C.; Abu-Raddad, L.J.; Hedley, A.J.; Leung, G.M.; Ho, L.-M.; Lam, T.-H.; Thatch, T. Q.; Chau, P.; Chan, K.-P.; Leung, P.-Y., Tsang, T.; Ho, W.; Lee, K.-H.; Lau, E.M.C.; Ferguson, N.M.; Anderson, R.M. Transmission dynamics of the etiological agent of SARS in Hong Kong: impact of public health interventions. *Science*. **2003**, *300* (5627), pp 1961–1966.
[7] Kline, M. *History of mathematical thought*. Oxford University Press. **1972**.
[8] Keeling, M.J.; Eames, K.T.D. Networks and epidemic models. *J. R. Soc. Interface*. **2005**, *2*, pp 295–307.
[9] Center for Systems Science and Engineering (CSSE). *COVID-19 Dashboard*. Johns Hopkins University (JHU). **2021**.
[10] CDC. Public Health Responses to COVID-19 Outbreaks on Cruise Ships — Worldwide, February–March 2020, *CDC Weekly*. **2020**, *69* (12), 347–352.
[11] R Core Team. *R: A language and environment for statistical computing*. R Foundation for Statistical Computing, Vienna, Austria. **2019**. https://www.R-project.org/.
[12] Soetaert, K., Petzoldt, T. and Woodrow, R. *Solving Differential Equations in R: Package deSolve*. J. Stat. Softw. **2010**, *33* (9) 1–25. http://www.jstatsoft.org/v33/i09
[13] van Dorp, L.; Acman, M.; Richard, D.; Shaw, L.P.; Ford, C.E.; Ormond, L.; Owen, C.J.; Pang, J.; Tan, C.C.S.; Boshiere, F.A.T.; Ortiz, A.T.; Balloux, F. Emergence of genomic diversity and recurrent mutations in SARS-CoV-2. Infect., Genet. Evol. **2020**, *83*, p 104351.

Standoff photoacoustic spectroscopy by thermally induced optical reflection of sound (THORS)

Daniel S. Kazal[a, b], Brian M. Cullum[b], Eric R. Languirand[a]*, Darren K. Emge[a]
[a]U.S. Army Combat Capabilities Development Command Chemical Biological Center, Research & Technology Directorate, 8198 Blackhawk Rd, Aberdeen Proving Ground, MD 21010
[b]University of Maryland, Baltimore County, Department of Chemistry, 1000 Hilltop Circle, Baltimore, MD 21250

ABSTRACT

The control and manipulation of soundwaves is of critical interest to many scientific and engineering fields such as photoacoustic sensing, acoustic engineering design, stealth technology, and secure communications. Traditionally, the means to manipulate sound has been limited to the use of physical acoustic structures that are often impracticable when considering their deployment for field use. A recently discovered phenomenon known as thermally induced optical reflection of sound provides a means to optically manipulate sound waves in air, without the need for physical acoustic barriers. By photothermally exciting the air with infrared laser light, an abrupt change in compressibility occurs at the edge of the laser beam. This change in air density at the laser's edge, results in the reflection of incident acoustic waves on the thermally induced optical reflection of sound barrier. Furthermore, if the excitation source is shaped into an optical tube an acoustic waveguide forms, which can enhance the distance transient acoustic waves can travel due to internal reflection. In this work, we demonstrate the ability to perform standoff photoacoustic measurements of ethanol vapor in ambient air. Additionally, the effect that thermally induced optical reflection of sound barriers and channels have on ultrasonic pulses is explored.

Keywords: photothermal, photoacoustic, standoff, acoustic reflection, acoustic waveguide, ultrasound, thermally induced optical reflection of sound

1. INTRODUCTION

In the past few years, the phenomenon known as thermally-induced optical reflection of sound (THORS) has been studied for its ability to manipulate sound waves without the need for traditional physical acoustic structures.[1–3] Early demonstrations of THORS were performed in an ethanol vapor environment, where a CO_2 laser, (9.6 μm) modulated by an optical chopper was used to excite the ethanol vapor and photothermally heat the surrounding air.[3] The heating of the air by the beam results in photothermal depletion of the surrounding media, and an abrupt air density change in the path of the beam (THORS barrier.) Incident acoustic waves on the THORS barrier will reflect due to this abrupt change in air density, i.e., internal reflection. Initial studies on THORS showed that fixed frequency sinusoidal sound waves, an incident on a THORS barrier, were suppressed when measured on the opposite side of the beam of the source and enhanced when measured on the same side as the source. Reflection efficiencies, as great as 40 % have been achieved in an ethanol vapor environment. When using multiple beams orthogonal to an incident sound wave, a suppression efficiency of virtually 100 % was achieved.

Further studies of THORS found that acoustic waveguides could be formed by expanding the CO_2 laser beam and masking its center, generating a donut shaped beam (THORS channel). To monitor the effect that a THORS channel had on transient sound waves, an earbud speaker emitting a fixed frequency sinusoidal sound wave was centered inside the channel, (facing down field of the laser) where its output amplitude was measured by a microphone inside the channel (facing up field of the laser.) By measuring the acoustic amplitude at varying distances along the channel, an acoustic decay profile was determined. In traditional acoustics, sound waves attenuate at a rate of 1/r with distance. With the THORS channel in ethanol, a significant enhancement in transient wave distances provided a decay profile of $1/r^{0.6}$ with distance. With an enhanced decay profile, this proof-of-principle study suggests that the enhancement of photoacoustic signals, over distance, would be significant.

The THORS technique is in contrast to other methodologies that are used to acquire standoff photoacoustic signals. These techniques require the use of large acoustic reflectors, which necessarily increase size, weight, and power,[4] or utilize a secondary method to understand the photoacoustic signal, without measuring the photoacoustic signal directly.[5] While these are viable methods, acoustic reflectors take additional processing techniques to reduce the acoustic noise being collected via the large reflector or other perturbations via the transduction method that is not photoacoustic. Utilizing THORS helps create a background-free technique that is not polluted by other acoustic signals as the THORS optical tubes provide a directional method for acquiring the acoustic signal.

In this work, we introduce the THORS phenomenon for the first time to ambient air and show standoff photoacoustic measurements of ethanol vapor. In addition to photoacoustic demonstrations, the ability to suppress and waveguide ultrasonic waves was evaluated.

2. RESULTS AND DISCUSSION

A CO laser (Coherent Inc.®, Model Diamond Series J-3-5) with an emission wavelength centered at 5.5 µm was used to generate THORS barriers due to the absorption and subsequent thermal relaxation by water vapor in the ambient air. The CO laser was modulated by applying an external transistor-transistor logic (TTL) square wave, provided by an arbitrary function generator at a 50 % duty cycle. The external TTL signal frequency varied between 500 Hz and 100 kHz but remained constant during each test. An internal pulse train of 1 MHz was simultaneously applied by the laser controller module, where it was set to a 40 % duty cycle, to control the output laser power.

To determine the effect that a THORS barrier generated by the CO laser has on incident ultrasonic waves, a 120 kHz ultrasonic transducer (Airmar Technology Corp.®, model AT120CH) was placed orthogonal to the laser beam and approximately 5 inches away, as seen in Figure 1a. The transducer was set to transmit 120 kHz ultrasonic pulses at a rate of 25 Hz. A second transducer was placed on the opposite side of the beam from the transmitting transducer approximately 5 inches away resulting in a total distance between the transducers of 10 inches. The second transducer was set to receive only mode to monitor the amplitude of the acoustic pulses passing opposite of THORS barrier. Both transducers were coupled to a digital oscilloscope where the transmitted and received pulses were monitored and triggered on the positive slope of the initial output pulse of the transmitting transducer.

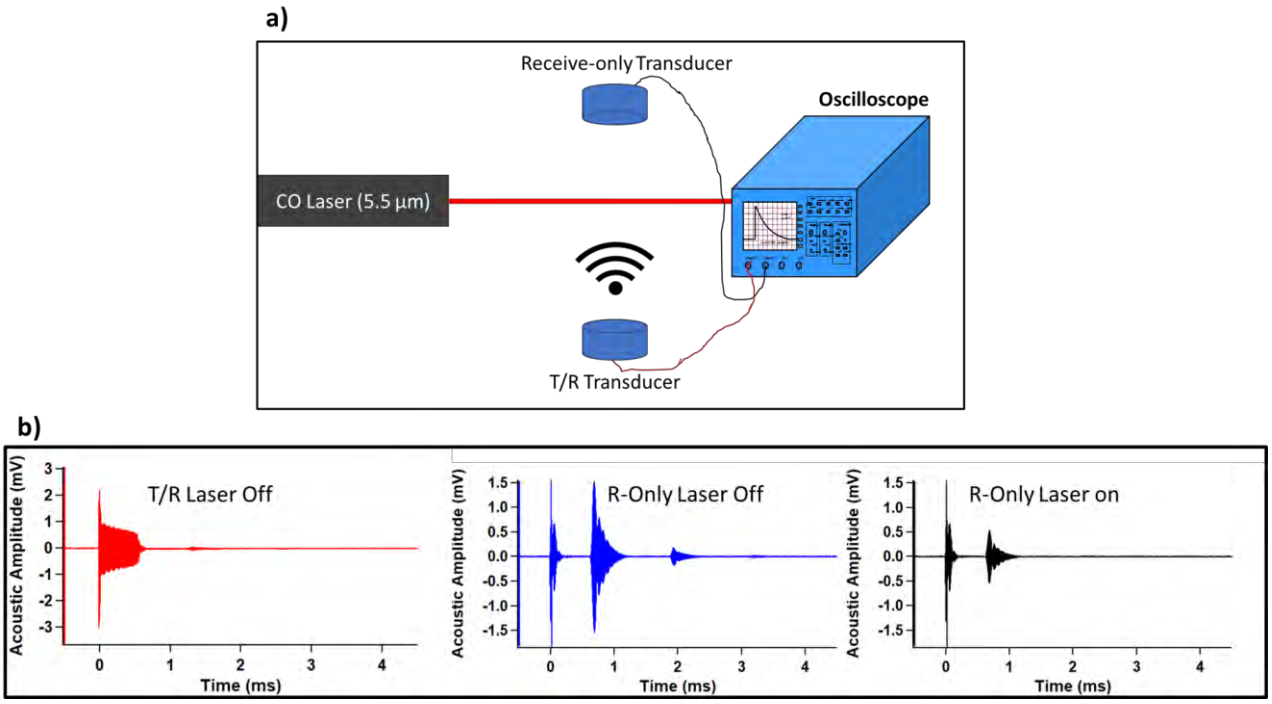

Figure 1. a) Experimental setup for THORS suppression measurements, using two 120 kHz ultrasonic transducers. b) Wave pulse data of ultrasonic transducers (T transmission and R receiver), where the initial output pulse (left), received pulse without the THORS barrier (middle), and the received pulse with the THORS barrier (right) are shown.

An initial output pulse by the transmitting transducer is observed at time zero (Figure 1b, left). With the CO laser shutter closed (laser/THORS off), the received signal from the initial pulse can be seen at 0.8 milliseconds. After opening the laser shutter (laser/THORS on), the received signal from the initial pulse is significantly attenuated, with a 59 ± 8 % THORS suppression efficiency. In the early work, characterizing THORS in an ethanol saturated environment using a CO_2 laser, THORS suppression efficiencies were typically in the range of 25–30 %.[1–3] Therefore, it appears from this initial work that either the THORS barrier performs better in ambient air or ultrasound is attenuated better than audible frequencies. To differentiate the origin of the enhanced suppression efficiency described here is outside the scope of this work, though is a planned area of future investigation.

To characterize the ability to generate THORS channels in ambient conditions, the CO laser beam was shaped into an annulus (hollow ring; THORS channel) by passing the beam through a calcium fluoride axicon lens, as seen in Figure 2a. Once a ring size of approximately 2 inches was reached, the THORS channel was recollimated through another axicon lens of identical geometry to the first lens. The CO laser was modulated at a rate of 3 kHz at a 50 % duty cycle and with an underlying pulse train of 1 MHz at a 40 % duty cycle. A metal plate shaped to fit inside the optical channel and was placed in front of the second axicon lens to act as an ultrasonic reflector. The ultrasonic reflector also acted as a mask to block any stray CO laser light inside the channel, this is only necessary in the current sensing geometry. A 120 kHz transducer was placed approximately 15 inches down field of the metal plate inside the optical channel and the mask ensured no damage to the transducer.

The 120 kHz transducer was set to transmit and receive reflected pulse waves and monitored on the oscilloscope. As shown in Figure 2b, the initial output pulse is observed at time zero in addition to the signal at approximately 2.3 milliseconds which is due to the reflection off the metal plate 15 inches away. When the laser shutter is closed (laser/THORS off), a reflected signal amplitude of 0.8 mV is observed. When the shutter is open (laser/THORS on) however, we see that the reflected signal is significantly increased, reaching enhancement efficiencies of 40 ± 1 % due to THORS. In comparison to the initial THORS studies in an ethanol saturated environment, THORS enhancement efficiencies reached approximately 30 %.[3]

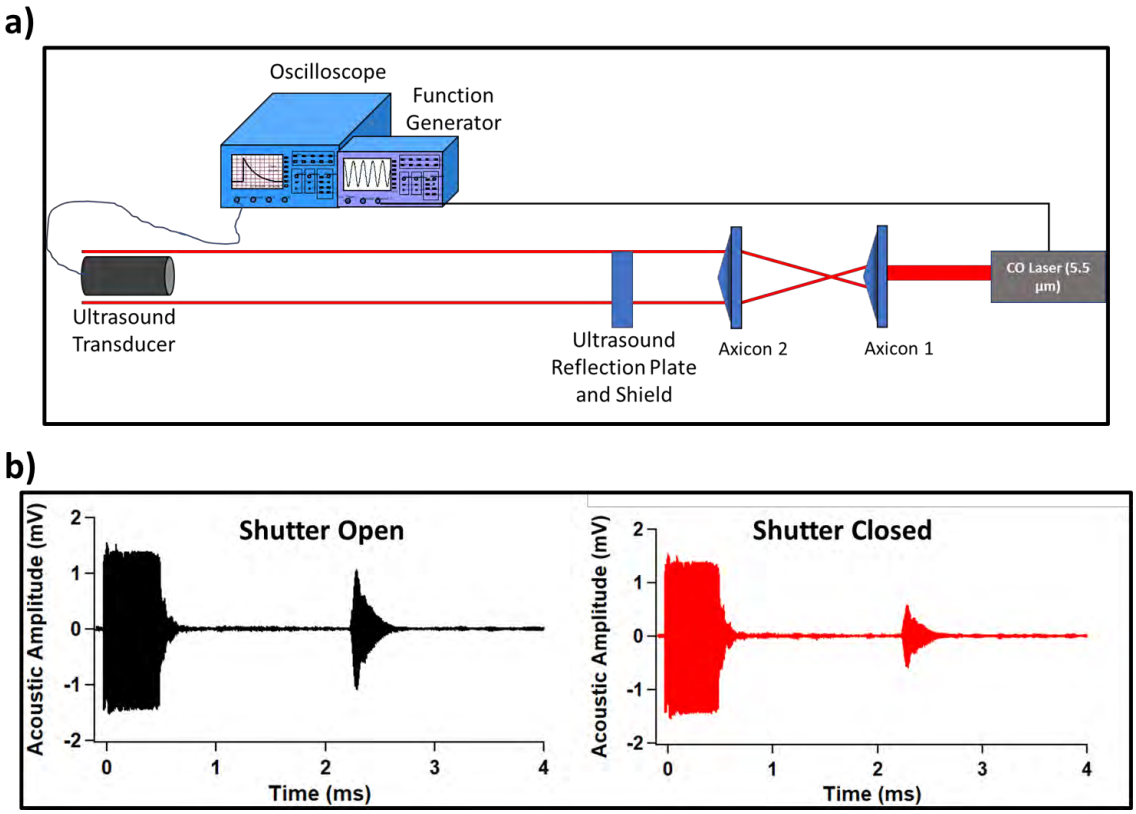

Figure 2. a) Experimental setup, to characterize THORS enhancement efficiencies of ultrasonic waves transmitted and received by a 120 kHz transducer. b) Pulse wave data from the 120 kHz transducer placed inside of the THORS channel. The reflected signal amplitude when the CO laser shutter is open (left), and the laser shutter is closed (right.)

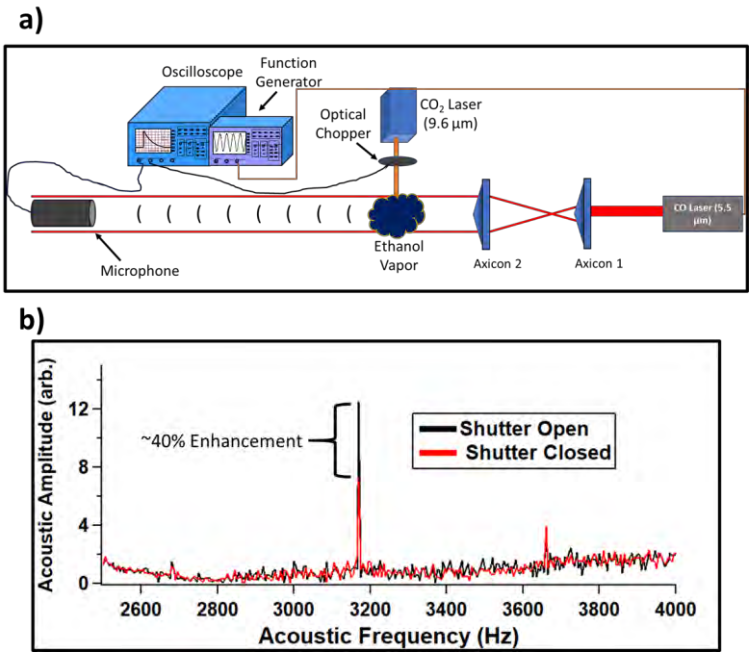

Figure 3. a) Experimental setup for the measurement of photoacoustic waves generated by the photothermal excitation of ethanol vapor inside a THORS channel. b) FFT data demonstrating the enhancement of 3.17 kHz photoacoustic waves generated by ethanol. The photoacoustic amplitude when the CO laser shutter is closed (red) and when the shutter is open (black).

To demonstrate the ability to employ THORS as a means to enhance standoff photoacoustic spectroscopy techniques, the experimental setup for the characterization of THORS enhancement efficiencies for ultrasound was slightly modified, as depicted in Figure 3a. The 120 kHz transducer was replaced with an audible microphone (ACO™ Pacific, Inc., Model PS9200KIT) which was necessary for transduction of the photoacoustic signal. The CO laser modulation frequency was set to 50 kHz at a 50 % duty cycle. An underlying 1 MHz pulse train was also applied to the CO laser modulation. A 4-inch diameter evaporation dish was filled with 200 proof ethanol and placed directly below the CO laser beam approximately 7 inches away from the microphone. A CO_2 laser (Laser Photonics, Model CL55WTVO) was tuned to emit a beam at a wavelength of 9.6 µm, passing directly through the center of the THORS channel, also 7 inches from the microphone. The CO_2 laser was modulated by an optical chopper (SciTech Services Inc., Model 300CD) at a frequency of 3.17 kHz to generate a photoacoustic signal due to the absorption by ethanol vapor.

To measure the photoacoustic signal generated by the ethanol vapor, the oscilloscope was set to trigger on the positive slope of the TTL signal from the optical chopper. The microphone wave signal was transformed via Fast Fourier Transform (FFT) to isolate the 3.17 kHz photoacoustic signal from external ambient noise. The measured 3.17 kHz photoacoustic signal can be seen in the FFT data in Figure 3b. In this trial a 40 % increase in the photoacoustic signal was realized when the CO laser shutter was opened (laser/THORS on), when compared to the signal with the laser shutter closed (laser/THORS off). In this study we found that the average photoacoustic signal enhancement at 7 inches was 30 ± 6 %.

3. CONCLUSION

We demonstrate for the first time that THORS barriers and channels are now capable of being generated in ambient air. This capability offers the potential for a new paradigm in standoff photoacoustic sensing by enhancing already available standoff sensing techniques. In addition to enhancing standoff photoacoustic sensing, THORS was used to demonstrate suppression and enhancement efficiencies in the ultrasound when compared to audible frequencies. Given the capability to generate a photoacoustic wave at ultrasonic frequencies in air, there is the potential to make even further improvements in standoff photoacoustic sensing by providing enhancements to a truly zero background sensing technique.

AKNOWLEDGMENTS

Funding was provided by the Director, Combat Capabilities Development Command Chemical Biological Center under the authorities and provisions of Section 2363 of the FY 2018 NDAA to develop new technologies, engineer innovations, and introduce game-changing capabilities. The authors would also like to acknowledge the Science, Mathematics, and Research for Transformation (SMART) Defense Scholarship Program for supporting Daniel Kazal during his internship at Combat Capabilities Development Command Chemical Biological Center while completing this work.

REFERENCES

[1] Kazal, D. S.; Holthoff, E.L.; Cullum, B.M. Thermally-induced optical reflection of sound (THORS) for photoacoustic sensing. *SPIE Defense + Commercial Sensing.* **2019**, *11020*, p 1102009.
[2] Kazal, D.S.; Ngo, A.; Holthoff, E.L.; Cullum, B.M. Acoustic Steering Using Thermally Induced Optical Reflection of Sound (THORS). *Appl. Spectrosc.* **2021***, 75* (10), pp 1320–1326.
[3] Cullum, B.M.; Holthoff, E.L.; Pellegrino, P.M. Optical reflection and waveguiding of sound by photo-thermally induced barriers. *Opt. Express.* **2017**, *25* (19), pp 22738–22749.
[4] Chen, X.; Cheng, L.; Guo, D.; Kostov, Y.; Choa, F.-S. Quantum cascade laser based standoff photoacoustic chemical detection. *Opt. Express.* **2011**, *19* (21), pp 20251–20257.
[5] Marcus, L.S.; Holthoff, E.L.; Pellegrino, P.M. Standoff Photoacoustic Spectroscopy of Explosives. *Appl. Spectrosc.* **2017**, *71* (5), pp 833–838.